Universidade do Minho
Escola de Engenharia

Rodrigo de Melo Lameiras

Sandwich structural panels comprising thin-walled SFRSCC and GFRP connectors: from material features to structural behaviour.

dezembro de 2015

Universidade do Minho
Escola de Engenharia

Rodrigo de Melo Lameiras

Sandwich structural panels comprising thin-walled SFRSCC and GFRP connectors: from material features to structural behaviour.

Tese de Doutoramento
Engenharia Civil - Engenharia de Estruturas

Trabalho efectuado sob a orientação do
Professor Doutor Joaquim António Oliveira de Barros
Professor Doutor Miguel Ângelo Dias Azenha

dezembro de 2015

STATEMENT OF INTEGRITY

I hereby declare having conducted my thesis with integrity. I confirm that I have not used plagiarism or any form of falsification of results in the process of the thesis elaboration.

I further declare that I have fully acknowledged the Code of Ethical Conduct of the University of Minho.

University of Minho, _____

Full name: Rodrigo de Melo Lameiras

Signature: *Rodrigo de melo Lameiras*

ACKNOWLEDGMENTS

ABSTRACT

An innovative sandwich structural panel composed of two outer Steel Fibre Reinforced Self-Compacting Concrete (SFRSCC) thin layers and a lightweight thermal insulating core material was developed for the walls of a pre-fabricated housing system. The stress transfer between the two SFRSCC layers was assured by Glass Fibre Reinforced Polymer (GFRP) connectors. SFRSCC was used to totally eliminate the need for conventional reinforcement and to decrease the thickness of the panel's outer layers, with consequent reduction of the global self-weigh of the panels, while GFRP connectors aimed to significantly decrease thermal bridging effects. The mechanical behaviour of SFRSCC under compressive and tensile loads were assessed. An in-depth investigation in the material scale was carried out in order to assess the pos-cracking behaviour of SFRSCC. A new test method was proposed to determinate the post-cracking behaviour of thin-walled SFRSCC elements and the results obtained with the proposed test method were compared with the ones resulted from the standard three-point bending tests (3PBT). Specimens extracted from a sandwich panel consisting of SFRSCC layers were also tested. The mechanical properties of SFRSCC were correlated to the fibre distribution by analysing the results obtained with the different tests. Finally, the stress-crack width constitutive law proposed by the *fib* Model Code 2010 was analysed in light of the experimental results. Eleven types of Glass Fibre Reinforced Polymer (GFRP) laminates consisted of polyester resin and differing on the kind of fibre reinforcement and on fibre content were produced by Vacuum Assisted Resin Transfer Molding (VARTM) and evaluated as material candidates for the production of connectors. All them were characterized under direct tensile tests. The shear behaviour of some of the GFRP candidates was investigated by means of the Iosipescu shear tests. Some GFRPs were also characterized under pin-bearing tests. Through linear static analyses and consideration of Ultimate Limit State loading scenarios, the sandwich panels were simulated using Finite Element Method (FEM). Parametric studies were performed in order to optimize the arrangement of the GFRP connectors and the thickness of the SFRSCC layers. Different arrangements of panels and production methods were explored. Moreover, models considering a specific nonlinear behaviour of SFRSCC were also constructed in order to simulate the progressive damage of the panel induced by cracking. In the scope of the nonlinear analyses, emphasis is given to parameter estimation of fracture modelling parameters for the fibre reinforced concrete based

on both inverse analysis and the *fib* Model Code 2010. An innovative connector system that consists on a GFRP perforated plate that is embedded into SFRSCC layers was proposed. The connection is strongly based in the mechanical interlock assured by the dowels originated from the SFRSCC passing through the holes opened on the GFRP plates. Experimental research devoted to the assessment of the pull-out and push-out shear behaviour of GFRP-SFRSCC connections were performed with specimens representative of the developed sandwich panel. For a better understanding of the proposed connection, the effect of the type of GFRP, number of holes of connectors and of existance of SFRSCC in front of connectors were experimentally investigated. Analytical frameworks to evaluate the load capacities of the connections when loaded transversally and longitudinally (i.e., pull-out and push-out loads, respectively) were developed based on experimental results. The feasibility of using the proposed connector was also determined trough an experimental work conducted with composite beam specimens using connectors made by two different types of GFRP laminates. In addition, the performed bending tests were simulated by using a computer program based on the FEM for assessing the stress field installed in the components that form the composite beam, in order to have a better knowledge on the stress redistribution between GFRP connector and surrounding SFRSCC that occurs during the loading process. Finally, an experimental program was conducted on the shear behaviour of the wall panels when subjected to in-plane loads, i.e., representative of the loading condition that the wall panels are subjected when seismic loads acts in the building. Full-scale panels (2.0 m by 2.0 m), with and without openings, were subjected to a constant vertical load representative of the slab reaction, while horizontal reversed cyclic loading was imposed to the panels. The seismic behaviour of panels were evaluated in terms of strength, stiffness, ductility and energy dissipation.

RESUMO

Neste trabalho é desenvolvido um painel estrutural inovador, do tipo sanduíche, constituído por duas camadas externas de Betão Auto-Compactável Reforçado com Fibras de Aço (BACRFA) de pequena espessura e uma espuma rígida, com elevada resistividade térmica, no seu núcleo. Os painéis foram projetados para serem aplicados como paredes portantes de um sistema pré-fabricado de casas modulares. No painel proposto, a transferência de tensões de corte entre as camadas de betão é garantida por connectores de material polimérico reforçado com fibras de vidro (PRFV). O BACRFA foi o material escolhido para as camadas de betão pensando-se em eliminar o uso de armaduras convencionais e assim possibilitar a execução de camadas de betão com espessuras reduzidas e, consequentemente, obter-se painéis com menor peso próprio total. O PRFV foi o material escolhido para os conectores de modo a se evitar pontes térmicas que poderiam levar a uma redução da eficiência energética do painel. Os comportamentos do BACRFA à compressão e tração foram determinados. Uma pesquisa ampla na escala do material foi realizada de modo que se fosse obtida uma melhor compreensão do comportamento à tração do BACRFA após a fissuração. Um novo método de ensaio para determinar o comportamento pós-fissuração do BACRFA foi proposto. O método proposto é bastante apropriado para a caracterização do material utilizado em elementos de pequena espessura, como é o caso do painel proposto nesta tese, pois permite determinar as propriedades do BACRFA fazendo-se uso de provetes com geometria semelhante a do elemento estrutural. Também foram realizados testes convencionais de caracterização através de vigota com entalhe, de onde as leis constitutivas tensão – abertura de fissura foram determinadas através de análises inversas. Provetes extraídos de painéis sanduíche foram ensaiados seguindo o método de caracterização proposto. Os resultados dos ensaios de caracterização do BACRFA obtidos com as diferentes metodologias empregadas foram comparados e correlacionados com a distribuição das fibras nos elementos. Finalmente, a lei constitutiva do tipo tensão – abertura de fissura proposta pelo *fib* Model Code 2010 foi comparada com os resultados experimentais. Foram estudados onze tipos de laminados de PRFV constituídos de matriz de resina poliéster e diferentes tipos de reforços de fibra de vidro, diferindo na disposição e quantidade de fibras. Todos eles foram produzidos por moldagem por transferência de resina sob vácuo e foram caracterizados através de testes de tração direta. Alguns laminados foram caracterizados ao corte ao longo de diferentes direções.

Ensaios do tipo "pin-bearing" também foram realizados com alguns dos laminados. Correlação Digital de Imagem foi utilizada para obter os campos de deformação nos ensaios de corte e nos ensaios do tipo "pin-bearing", apliando-se a compreensão do comportamento dos laminados. Simulações numéricas do comportamento mecânico dos painéis sanduíche foram realizadas fazendo-se uso de um pacote computacional baseado no Método dos Elementos Finitos (MEF). Fazendo-se uso de modelos numéricos lineares dos painéis sujeitos a combinações de carga relativas aos Estados Limites Últimos, foram realizados estudos paramétricos com o intuito de se otimizar o arranjo dos conectores e as espessuras das camadas de betão. Análises numéricas não-lineares também foram realizadas para simular o dano progressivo dos painéis induzidos pela fissuração das camadas de BACRFA com o aumento das ações laterais. No escopo das análises não-lineares, é dado ênfase para a estimativa dos parâmetros de fratura baseada em análises inversas e recomendações do *fib* Model Code 2010. Um conector de PRFV inovador chamado PERFOFRP foi proposto. De forma simplificada, o conector consiste em um laminado de PRFV com furos. A conexão é realizada através do intertravamento mecânico assegurado pelos pinos de betão que se formam devido à penetração do BACRFA durante o processo de betonagem dos painéis. O comportamento ao corte dos conectores PERFOFRP foram estudados através de ensaios de arrancamento e de corte longitudinal com provetes representativos das conexões nos painéis sanduíche. Para se ter uma melhor compreensão do PERFOFRP, os testes investigaram os efeitos do tipo de laminado de PRFV, do número de furos e da resistência frontal no compotamento mecânico das conexões. Um estudo preliminar da viabilidade de utilização dos conectores foi realizado com vigas sandwich produzidas com dois tipos de laminados de PRFV. Complementarmente, os testes de flexão foram simulados numericamente fazendo-se uso de um pacote computacional baseado no MEF, de onde foi possível obter-se uma melhor compreensão do comportamento das conexões. Finalmente, um programa experimental foi realizado com painéis submetidos a cargas no plano, representativas da condição de carregamento que as paredes estão sujeitas quando cargas sísmicas agem na edificação. Painéis com 2.0 m de altura e 2.0 m de largura, com e sem abertura, foram submetidos a um carregamento vertical constante para simular a reação de apoio das lajes, enquanto forças horizontais cíclicas foram impostas aos painéis. Os desempenhos dos painéis frente aos carregamentos cíclicos foram determinados determinando-se suas resistências, rigidezes, ductilidades e capacidades de dissipação de energia.

TABLE OF CONTENTS

LIST OF TABLES

LIST OF FIGURES

Chapter 1

INTRODUCTION

1.1 SCOPE AND MOTIVATION

Modern societies face tremendous global challenges in concern to the increase in worldwide energy demand, as well as depletion of non-renewable natural resources and the effect of gases generated due the use of fossil-fuel energy on climate change. It has been globally acknowledged that policies and solutions that lead to reducing energy consumption and greenhouse gas emission need to be definitely deployed more consistently in the near future (UNFCCC, 2015).

In the specific sector of housing construction, one relevant solution created by concrete-related industries to achieve sustainable and affordable buildings, was the development of concrete sandwich panels (*fib* T.G. 6.7, 2011). These panels present high thermal resistance, provided by the thermal insulation, while also keeping substantially high thermal inertia, provided by the internal concrete layer.

The ascending technology of concrete sandwich panels is based on the advantageous use of outer concrete layers together with the core consisted of a rigid thermal insulation material. A high thermal efficiency of panels can be achieved if no discontinuities are made to the thermal insulation material. However, especially in the case of prefabricated panels, it is normally necessary to establish mechanical connection between the outer concrete layers, which

inevitably involve local disruptions to the insulating layer. These connectors are responsible for keeping the concrete layers tied during stripping, transporting and erecting of panels. They also ensure the joint composite behavior of the whole system, providing a higher structural efficiency for the sandwich panels (PCI, 2011).

The earliest designs of concrete sandwich panels involved the use of steel connectors (Bush and Stine, 1994). However, the high thermal conductivity of steel causes regions with increased heat flow, usually referred as thermal bridges, which can jeopardize the thermal efficiency of panels. In recent years, the use of alternative materials for the steel was explored by several researchers (Einea *et al.*, 1994, Salmon *et al.*, 1997, Naito *et al.*, 2011, Rizkalla *et al.*, 2009b, Woltman *et al.*, 2013, Tomlinson, 2015). Glass Fibre Reinforced Polymers (GFRP), Carbon Fibre Reinforced Polymers (CFRP) and Basalt Fibre Reinforced Polymers (BFRP) were suggested. Different geometries and configurations for the connections were already studied. Nonetheless, the FRP still has a high cost, mainly the produced by pultrusion or using expensive fibres, such as carbon fibres. On the other hand, the concrete layers of the existing panels are always made with conventionally reinforced or prestressed concrete technology.

Overall, it can bestated that recent researches on effective and sustainable concrete sandwich panel solutions are still in their infancy. Much more investigation needs to be carried out to have a better understanding of the behaviour of this new approach to the existing technology of sandwich panels. Also, it is necessary to pursue alternatives for the existing sandwich panel technologies focusing on the balance of structural and thermal efficiencies with an acceptable production cost.

1.2 OBJECTIVES AND RESEARCH METHODOLOGY

The research conducted in this thesis addresses the proposal of an innovative solution for prefabricated structural sandwich façade panel, with focus on its adequate mechanical and thermal. The panel comprises thin-walled Steel Fibre Reinforced Self-Compacting Concrete (SFRSCC) as facing material on both outer layers, and a lightweight thermally insulating core material in the middle layer. Non-metallic shear connectors are used between both outer concrete layers as to avoid thermal bridging effects. The developed structural cladding wall system is able to incorportate embedded installations (water, electrical, network and telephone

connections), thermal insulation and finishes that is manufactured in a plant and transported to the construction site where the only tasks to be performed should be the ones related to placement of the panel and connections to foundations and adjacent elements. The wall system here proposed also acts as part of the primary load carrying system of the structure transferring gravity loads and lateral loads due to wind or seismic events to the foundation of the structure. The inner SFRSCC layer is designed to allow the support of flooring units, thus eliminating the need for any other vertical structural elements in the prefabricated building. By incorporating systems, the added value of panel is increased, the number of stages in the construction is diminished, the work efficiency is enhanced and, consequently, the overall cost of building is reduced.

The overall development of panels was guided by the objectives of decreasing the self-weight, improving durability and enhancing thermal insulation levels.

As a general summary of the research, it can be stated that different solutions for the components of the panels were proposed/optimized and the interaction between them was studied. To accomplish the objectives listed above, the work methodology to be followed encompasses the following steps:

At the material level:

- Evaluating if the standardized method to determine the post-cracking behaviour of SFRSCC is still valid for characterizing the material on thin-walled structural elements;
- Evaluating the effect of fibre orientation and distribution on scattering of mechanical properties of SFRSCC in thin-walled structural elements;
- Assessing mechanical properties of SFRSCC under compressive monotonic loading;
- Characterizing the tensile, shear and pin-bearing behaviour of GFRP laminates that are candidates for constituent material of connectors.

At the level of the structural system:

- Developing a new type of connector, hereinafter referred as PERFOFRP, that comprises perforated GFRP laminates which are in turn partially embedded into both opposing SFRSCC layers;
- Investigating some factors that intervene on the transversal shear behaviour of SFRSCC $\times$ PEFOFRP connections under monotonic pull-out tests;

- Investigating the factors intervening and determining the longitudinal shear behaviour of SFRSCC $\times$ PEFOFRP connections and by means of push-out tests;

- Proposing analytical approaches aiming to quantify the pull-out and push-out load capacities of SFRSCC $\times$ PEFOFRP connections;

- Evaluating the flexural behaviour of the connections on tests with reduced scale specimens.

At the full-scale level:

- Performing the linear and non-linear numerical modelling of the performance of the proposed panels and using the model to optimize the geometry and arrangement of the sandwich panels;

- Evaluating experimentally the performance of proposed sandwich panels, with and without openings, under in-plane vertical and cyclic lateral loads;

1.3 OUTLINE OF THE THESIS

The research investigation of the mechanical behaviour of concrete sandwich panels that is presented in this thesis is organized in ten chapters. Besides this introduction and the conclusions, the remainder eight chapters are related to the main stages of this research work, as follows:

- Chapter 2: Literature review on sandwich wall panels – This chapter provides a review of the available literature and current understandings about the technology of concrete sandwich panels. This literature review focuses on the available technologies, design requirements and the assessment of thermal and structural performances for this type of panel.

- Chapter 3: SFRSCC characterization – This chapter reports the characterization of two main types of SFRSCC and one type of Self-Compacting Concrete (SCC) from twenty two different castings. Focus is given to the determination of post-cracking behaviour of SFRSCC. A new methodology is proposed in order to obtain the parameters that characterize the post-cracking behaviour of SFRSCC. It is also investigated if the standardized method to determine the pos-crack behaviour and the method based on

inverse analysis of Three-Point Bending Tests (3PBT), are still valid for characterizing the SFRSCC used in thin-walled structural elements.

- Chapter 4: GFRP characterization − The manufacturing process of GFRP laminates used in this thesis is described and the results of direct tensile, shear and pin-bearing tests are reported. This chapter also presents the application of advanced full-field measurements, i.e., Digital Image Correlation (DIC), made in the shear and pin-bearing tests. Moreover, the capability of simulating the pin-bearing behaviour using models based on Finite Element Method (FEM) is also investigated.

- Chapter 5: Preliminary design of proposed sandwich panel − An innovative precast sandwich is presented. The proposed PERFOFRP connectors are here described. Simplified simulation models of the sandwich panels, based on the FEM and linear-elastic behavior of materials, are constructed to simulate the panels under service load conditions. The model is used to perform parametric studies focused on defining the required geometry and arrangement of connectors in the sandwich panels. FEM simulations that consider non-linear material behavior are also described in view of the evaluation of the post-cracking behaviour of panels.

- Chapter 6: Pull-out tests − A detailed experimental and analytical study of the pull-out behaviour of connections comprising PERFOFRP connectors and SFRSCC layers is performed in this chapter. The experimental part of the work involved pull-out tests with connectors made with different number of holes, with different GFRP materials and without fibre reinforcement of concrete are presented. A comprehensive analytical approach to predict the load capacity of connections is proposed and its predictive performance is assessed.

- Chapter 7: Push-out tests − This chapter reports the experimental program carried out to investigate the behaviour of PERFOFRP × SFRSCC connections when subjected to longitudinal shear, as well as a corresponding analyitical evaluation. Initially, the parcels of resisting mechanisms corresponding to the concrete dowel action, frictional resistance and concrete end-bearing effect are assessed experimentally. An analytical framework to predict the shear resistance of PERFOFRP when connected to SFRSCC layers that are representative of the sandwich panels is also presented.

- Chapter 8: Flexural behaviour − The behaviour of PERFOFRP × SFRSCC connections when subjected to combined effect of shear and flexural forces is assessed experimentally and numerically in this chapter. The influence of the type of GFRP

used in the PERFOFRP connector on the flexural behaviour of connection is investigated.

- Chapter 9: Seismic behaviour – This chapter deals with the experimental evaluation of in-plane cyclic behaviour of sandwich panels made with PERFOFRP connectors and SFRSCC outer layers. Results of quasi-static in-plane cyclic tests performed on real scale sandwich panels are presented.

Chapter 2

LITERATURE REVIEW ON SANDWICH WALL PANELS

This chapter presents a critical analysis of existing technologies for concrete sandwich wall panels. The literature review is divided in the following main topics: 1) general aspects; 2) available technologies, 3) design requirements and 4) assessment of thermal and structural performances.

2.1 GENERAL ASPECTS

Sandwich wall panels are structural panels typically composed by two outer layers and a thermal insulation core material. They are also referred to as Structural Insulated Panels (SIP), insulated wall panels or multilayered wall panels. These panels have been extensively applied in precast cladding panels, where the facing material provides insulation against mechanical damage, weather protection and vapour barrier, while the core provides thermal and acoustic insulation from the inside (PCI, 2011). Once these panels often form the outer skin of buildings, they must be designed to resist the usual loads caused by wind. In addition, they must be designed to accommodate the additional stresses and deflections caused by thermal bowing, which can occur for instance, when the one of the outer surface is heated by solar radiation, whereas the inner surface is shielded from such effect (Davies, 2001). In the specific case of prefabrication of the sandwich panel, other relevant issues need to be

carefully considered, particularly the need to be self-supporting in any phase of handling, transporting and erection.

The main advantage of using sandwich panels in building construction is related to the structural and thermal efficiency that can be achieved with this technology. By putting together thin, stiff and ductile concrete layers, with a thermally-efficient core material, it is possible to obtain lightweight panels that are energy efficient, and can be easily handled and erected.

Depending on how the outer concrete layers are arranged and connected, these panels can be designed to behave as non-composite, partially composite or fully composite (Figure 1). When the facings layers are connected with elements that have no capacity to transfer the in-plane-shear transfer, the panel is classified as a non-composite panel (Figure 1(a)). In fully composite panels, their outer faces are connected in such a way that both layers resist to the applied flexural loads as in a fully integrated manner, with full shear stress stransfer between components (Figure 1(b)). Partially composite behaviour is the intermediate situation, where only part of the in-plane-shear can be transferred from one layer to the other one. (PCI, 2011).
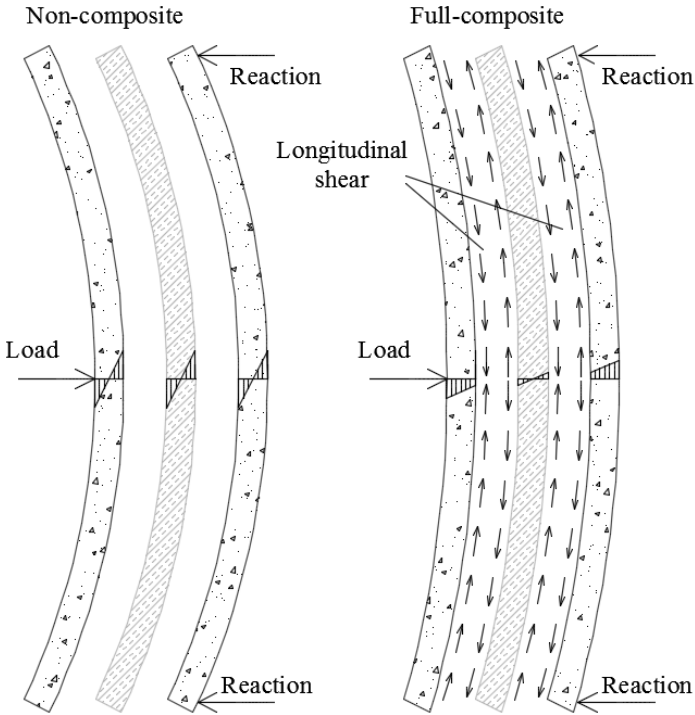
Figure 1: Schematic representation of shear forces that arises in sandwich panels under flexure for both non-composite and full-compsite behaviours.

The degree of composite action depends on the nature of the connections between the two concrete layers, particularly on type and arrangement of wythe connectors. Designing for a partial/full degree of composite action can significantly increase the structural efficiency and reduce both initial and lifecycle costs of a panel, compared with the fully noncomposite case (Rizkalla *et al.*, 2009a).

The typical design method for precast sandwich panels proposed by the 'Precast Concrete Institute' assumes non-composite behaviour (PCI, 2011). However, in practice, tests have shown that panels generally exhibit partially composite behaviour, transferring some level of shear between faces (Bush and Stine, 1994, Lee and Pessiki, 2008a, Frankl, 2008, Rizkalla *et al.*, 2009a, Pessiki and Mlynarczyk, 2003b). Considering this degree of composite action in design could expressively reduce costs. It is therefore fundamental to understand the influence of several parameters, such as connector types and arrangements, on the shear transference mechanisms.

Moreover, these panels, that generally comprise the building envelope, must be designed to meet energy performance requirements, generally prescribed in local thermal performance regulations for buildings, such as the Portuguese regulation RCCTE (2006). These codes often prescribe a minimum allowable thermal resistance (R-value) for building envelopes, which has consequences on the minimum insulation thickness required, thus impacting the geometry of panel.

2.2 AVAILABLE TECHNOLOGY

From their first applications in the early 20th century (Collins, 1954) until nowadays, many alternative forms of panels have been proposed by putting together different outer layer materials, connector types and core materials. When properly combined, the former materials and solutions allowed to attend the requirements for the intended applications. In the following sections, details are given about different technologies already applied in the manufacturing of sandwich panels.

2.2.1 Outer layer's materials

Traditionally, the external layers of precast concrete sandwich panels comprise reinforced or pre-stressed concrete layers. The thickness and material of each concrete layer depends on its structural function, concrete cover, anchorage of connectors, stripping and finishing (Einea *et*

al., 1991). They are generally made as thin as possible. Common non-composite structural sandwich elements made of concrete consist of a structural, load-bearing interior layer (with thickness ranging from 10 to 14 cm), and an exterior layer (façade) with no structural function (approximately equal to 7 cm) (Hegger and Horstmann, 2008). The minimum thicknesses of these concrete layers are relatively high due the necessary concrete cover for the steel reinforcement to comply with current design codes. The result is a robust and heavy panel with thick concrete layers.

In regard to the cross sectional geometry, rectangular sections are the most commonly used. Nonetheless, a variety of geometries were already used, including hollow cores, double-tees and corrugated concrete layers (PCI, 2011, Ricci *et al.*, 2013, Palermo *et al.*, 2014).The most common arrangement of the concrete layers consists on the use of two outer layers, however, the use of three layers has also been proposed by Lee and Pessiki (Lee and Pessiki, 2006).

The concrete layers of single storey panels are typically reinforced with steel welded wire mesh with reinforcement ratios being dictated by the minimum required for shrinkage and crack control. In the case of precast sandwich panels, unless they are carrying highly eccentric axial loads, flexural design is often governed by forces incurred during transport and handling as these loads often exceed those from wind (Tomlinson, 2015).

On the other hand, multi-storey sandwich panels are usually made using prestressed concrete layers (Bush and Wu, 1998, Rizkalla *et al.*, 2009b, Frankl, 2008, Lee and Pessiki, 2008a). Furthermore, the prestress of concrete layers is also used to help counteract thermal bowing of panels, by inducing nearly-uniform compression in the concrete layers.

An alternative for the reinforced concrete is the use of FRC, with the fibers replacing the steel reinforcement and allowing the adoption of thinner layers. Furthermore, these materials generally have improved water tightness and a better aesthetic finish due to their increased crack-width control capability (ACI Committe 544, 1997).

A type of FRC that has been largely used as face material on production of thin-walled skins for sandwich panels, especially for non-structural facings, is the Glass Fibre Reinforced Concrete (GFRC) (Precast/Prestressed Concrete Institute – PCI, 2001). In spite of the recognized advantages on use of GFRC, several researches have already shown that, even when using alkali-resistant glass fibre, the mechanical strength and toughness of GFRC decreases with ageing (Marikunte *et al.*, 1997, Purnell and Beddows, 2005, Lameiras, 2007),

leading to several problems along time, as extensive cracking and deformation of GFRC panels (Levitt, 1997, Correia *et al.*, 2006).

Steel Fibre Reinforced Concrete (SFRC) has been proposed as alternative for reinforced concrete and for GFRC in the production of precast facade panels (Cominoli *et al.*, 2004). The possibility of replacing the traditional surface reinforcement of sandwich panels with synthetic macro-fibres was demonstrated by Bigas *et al.*(2007).

Steel Fibre Reinforced Self-Compacting Concrete (SFRSCC) was proposed by researchers at the University of Minho (UM) (Barros *et al.*, 2007, Pereira *et al.*, 2008) for use in sandwich panels composed by two outer layers of 30 mm thickness and a grid of ribs of 100 mm width. The ribs correspond to regions where the insulation layer was omitted and had the purpose of connecting the concrete layers.

2.2.2 Insulating material

Concrete sandwich wall panels usually have a good thermal insulation performance due to the existence of insulation between two durable layers of concrete. The thickness and type of this insulation layer depends on the thermal properties of the insulation material used, and the desired thermal resistance of the panel. Insulation thicknesses have commonly varied from 25 to 100 mm (Einea *et al.*, 1991).

The first proposed concrete sandwich walls, in the early 1900's, used lightweight concrete or wood chips as core material. The use of rigid foams only began to be adopted as thermal insulation for sandwich panels in the 1950's (Leabu, 1965).

Although there are many insulation types available, sandwich panels generally utilize rigid insulations because of their compatibility with concrete at several levels: moisture absorption, dimensional stability and coefficient of expansion. The most commonly used types of insulations in sandwich wall systems are: moulded expanded polystyrene (EPS), extruded expanded polystyrene (XPS), polyurethane (PU), polyisocyanurate and phenolic (PCI, 2011). Basic features of some of the most used insulating materials are presented in Table 1.

Table 1: Basic features of the commonly met insulating materials (adapted from Papadopoulos (2005)).

	Material				
	Glass wool	Stone wool	Extruded polystyrene	Expanded polystyrene	Polyurethane foam
Density (kg/m³)					
Minimum	13	30	20	18	30
Maximum	100	180	80	50	80
Thermal conductivity (W/(m·°C))					
Minimum	0.030	0.033	0.025	0.029	0.020
Maximum	0.045	0.045	0.035	0.041	0.027
Temperature application range (°C)					
Minimum	-100	-100	-60	-80	-50
Maximum	500	750	75	80	120

Some researches have stated that the most currently employed thermal insulations (EPS and XPS) contribute to the shear transfer capacity of sandwich panels (Bush and Stine, 1994, Soriano and Rizkalla, 2013, Woltman *et al.*, 2013, Kim and You, 2015). Furthermore, some researchers have found that, even though XPS has higher strength, when EPS is used in replacement of XPS, a higher overall level of composite action under flexural loads and increased flexural capacity was achieved (Soriano and Rizkalla, 2013). This behaviour is justified by the increased surface area of the concrete/EPS interface. In fact, XPS plates are usually smoother than EPS plates, leading to weaker adhesive bond strength. Notwithstanding, designers often ignore this contribution to the shear transfer capacity with the assumption that this bond breaks during shipping and erection or due cyclic differential volume changes during the service life of the panel (Einea *et al.*, 1991). In the specific case of precast sandwich panels, this bond is only expected to last until the precast panel is installed (Ekenel, 2013).

2.2.3   Outer layers' connectors

The outer layers' connectors are the elements used to tie both concrete layers together during handling and under service conditions. Specifically in the case of precast sandwich panels, during stripping, transportation and handling of panels these connectors should be capable of resisting the forces created between the concrete layers due to self-weight.

In non-composite panels the type and arrangement of connectors are detailed to minimize in-plane shear transfer, so that the wythes may act independently. These types of connector are

often named as "non-shear connectors", "tie connectors" or "tension connectors". Typical tension connectors are pins, hairpins and C-ties (PCI Committee on Precast Sandwich Wall Panels, 1997).

In composite panels, the main connectors provide resistance to horizontal in-plane shear between the wythes. These connectors are usually called "shear connectors". Typical shear connectors include bent bars, sleeve anchors, areas of plain concrete and welded wire trusses (PCI Committee on Precast Sandwich Wall Panels, 1997). Their positioning and arrangement mostly depend on the panel width and degree of composite action desired. Non-shear connectors are also used in composite panels in which the distance between the shear connector exceeds an acceptable limit of approximately 600 mm (Einea *et al.*, 1991).

Some shear connectors are stiff in one direction and flexible in the other. These are called one-way shear connectors. They can be classified as concentrated and continuous connectors. Concentrated one-way connectors comprise small-size bent bars (Figure 2(a)). Continuous one-way connectors generally run the full length of the panel. This type of connector is the most commonly used and includes bent bars, trusses and perforated plates (Figure 2(b), Figure 2(c) and Figure 2(d)). Connectors that have comparable capacity in two directions in plane of the panel are the two-way shear connectors. Commonly used connectors of this type are: cylindrical sleeve anchors, crown anchors and concrete blocks (Figure 2(g) and Figure 2(h)) (Einea *et al.*, 1991).

Continuous steel bent bars and trusses are the most widely employed types of shear connector for sandwich panels. They have been studied by several researchers during recent decades (Bush and Stine, 1994, Bush and Wu, 1998, Benayoune *et al.*, 2007a, Benayoune *et al.*, 2008a).

Busch and Stine (1994) compared the efficiency of wire truss connector in comparison to a bent bar connector. Shear tests in three wythe configurations were performed to assess the shear resistance of each connector. Results have shown that a truss connector increased the shear stiffness up to 70% in comparison to bent bars connectors.
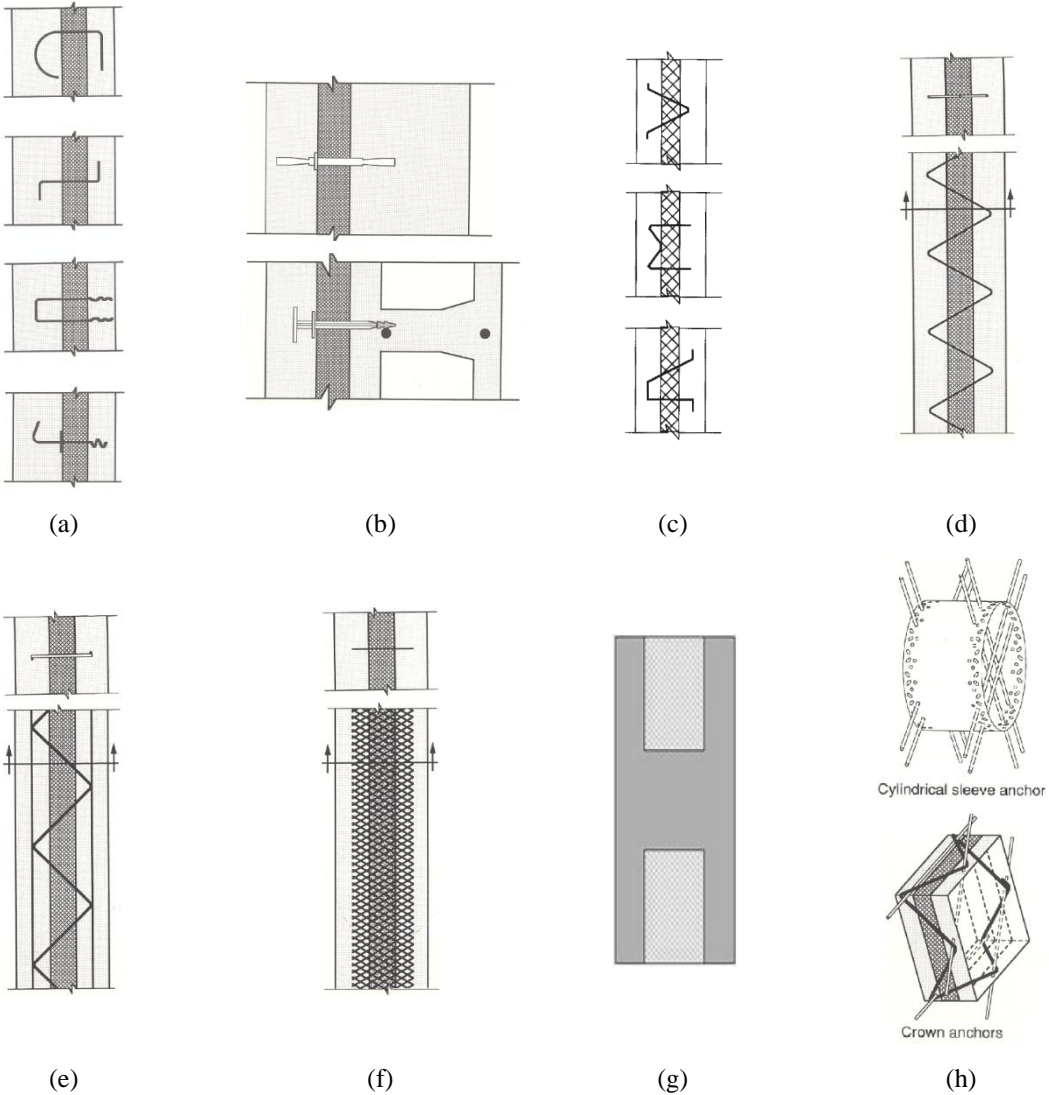
Figure 2: Outer layers' connectors. Non-shear connectors (Einea *et al.*, 1991): (a) metallic pin connectors and (b) plastic pin connectors. One-way concentrated shear connectors (PCI Committee on Precast Sandwich Wall Panels, 1997): (c) small-size bent bars. One-way continuous shear connectors (Einea *et al.*, 1991): (d) bent bars; (e) wire trusses and (f) perforated plates. Two-way shear connectors: (g) areas of plain concrete (Rizkalla *et al.*, 2009a); (h) sleeve and crown anchors (PCI Committee on Precast Sandwich Wall Panels, 1997).

During the 1960's and 70's, shear connections were typically provided from a combination of solid concrete regions and embedded steel truss connectors. These systems have high degrees of composite action at the cost of reduced thermal efficiency. Designers began to prefer non-composite wall designs in the 1980's (Tomlinson, 2015). Solid concrete regions were eliminated from many panels and steel trusses were replaced by small steel pin-type connectors in order to reduce thermal bridging and bowing (Leung, 1984).

Due to their high thermal conductivity, the steel connectors cause thermal bridging effects on

the building envelope that result in additional transmission losses, decreasing the thermal efficiency of the sandwich panel, and promoting the occurrence of condensation and mould problems (Lee and Pessiki, 2006). The existence of these thermal bridges increases the building energy demand for heating and cooling, and thus their avoidance is an essential challenge to achieve more energy efficient and sustainable buildings. According to previous research (McCall, 1985), the use of steel pin connectors that represent 0.08% of the sandwich panel area, can reduce the insulation performance (R-value) of a wall up to 38%. The same research also reports that a thermal performance reduction of 77% is expected when the connection between outer layers is made through 0.08% of steel pin connectors and 21.25% of solid concrete regions.

Alternatives to the steel shear and solid concrete regions connectors were proposed by researchers of University of Nebraska (Einea *et al.*, 1994). The proposed systems use continuous one-way glass FRP shear connectors with high thermal resistance. Candidates for such FRP connectors included a wide flange FRP beam, FRP diagonal straps and a prefabricated FRP bent bar. The bent bar connector was selected and tests of small scale specimens by push-off (pure shear) loading, small scale specimens by flexural loading and full scale specimens by flexural loading were carried out. Results showed that the connector provided sufficient strength to develop a high percentage of composite action. Salmon *et al.* (1997) have shown that sandwich panels with FRP bent bar connectors had a thermal efficiency 1.9 times higher than that of panels with concrete stems and 1.2 times higher than that of panels with steel truss connectors. The glass bent bar is commercially known as "Aslan 700" and is available by Hughes Brothers company (Figure 3).
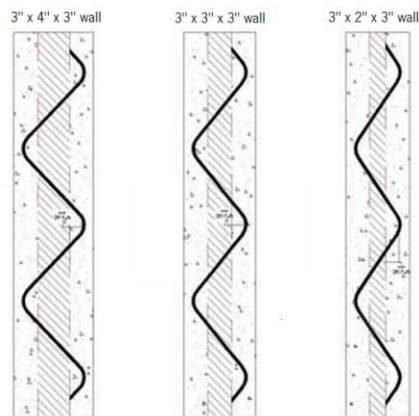
(a)

(c)

(d)

Figure 3: Glass bent bar Aslan 700 from Hughes Brothers company (Hughes Brothers, 2008).

Following the same concept, the Altus Group developed continuous one-way Carbon Fibre Reinforced Polymer (CFRP) grid, commercially known as C-GRID, in 2003. The Altus Group utilized the C-GRID in an orthogonal layout parallel to the long axis of the wall panels. Insel *et al.* (2005), followed by Geich (2007), proposed orienting the C-GRID in a truss like orientation (at a 45° angle) to provide adequate shear transfer between the concrete wythes (Figure 4).

Geich (2007) reported that CFRP grid connector technology has enabled concrete sandwich wall panel constructions with R-values equal to 32 m·K/W, while common values range from 11 to 16 m·K/W for sandwich panels with steel connectors or concrete connectors and with similar thicknesses.

Frankl (2008), Rizkalla *et al.* (2009a) and Lucier *et al.*(2010) performed full-scale tests with panels under combined effect of simulated vertical gravity loads and lateral cyclic loads. The measured deflections and strains indicated that the CFRP shear truss provided fully composite

action at service load levels. Testing and acceptance criteria were developed by Ekenel (2013) to evaluate the shear transfer capacities of CFRP grid connectors used in combination with rigid insulation in concrete sandwich panel construction.

(a)   (b)
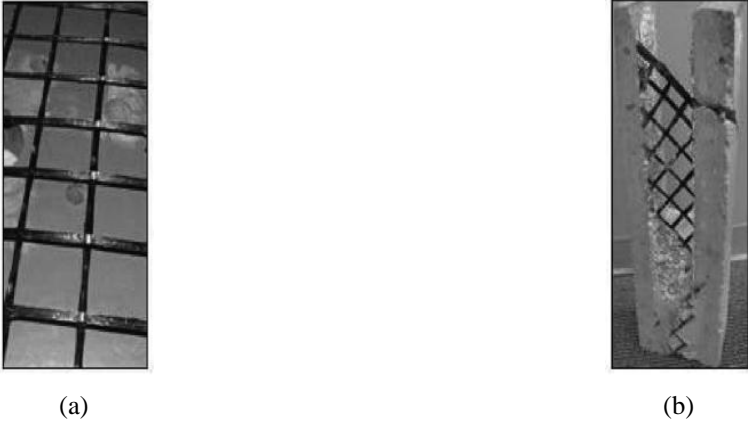
Figure 4: (a) C-GRID material sample; (b) Carbon FRP shear transfer mechanism in section cut from a tested panel (Rizkalla and Dawood, 2009).

Concentrated one-way glass FRP shear connectors "P-24 Delta Tie" are commercially available by Dayton Superior (Figure 5). The panel stiffness is altered, as necessary, by adjusting the tie distribution as a function of the shear and moment forces. In spite of the advantages associated with the use of this concentrated system, the level of achievable composite action is limited, requiring thicker concrete layers than the necessary when a higher degree of composite action is achieved.

(a)   (b)   (c)
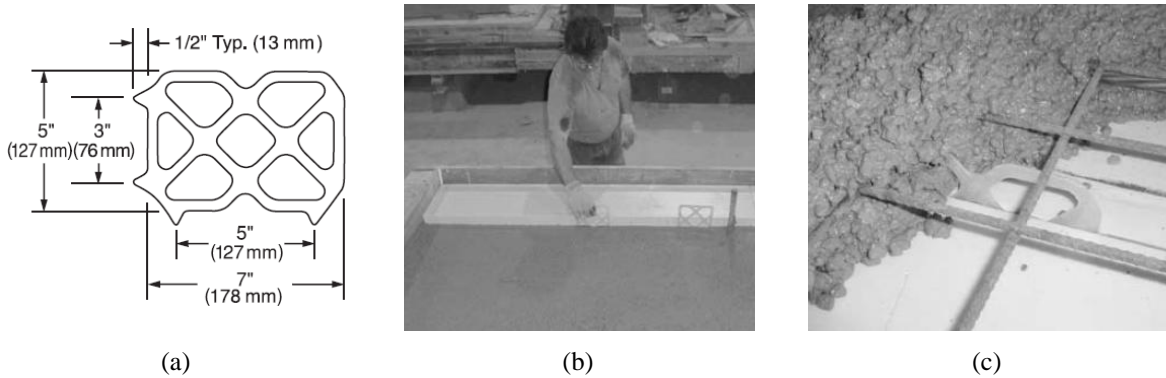
Figure 5: P-24 Delta Tie (Dayton Superior, 2006).

Pantelides and co-workers (2008) proposed a glass fibre reinforced polymer shell connector. Experiments carried out with single and double cage panels showed that panels can withstand out-of-plane loads while providing resistance to horizontal shear between the two concrete

wythes (Figure 6).

(a)   (b)

(c)
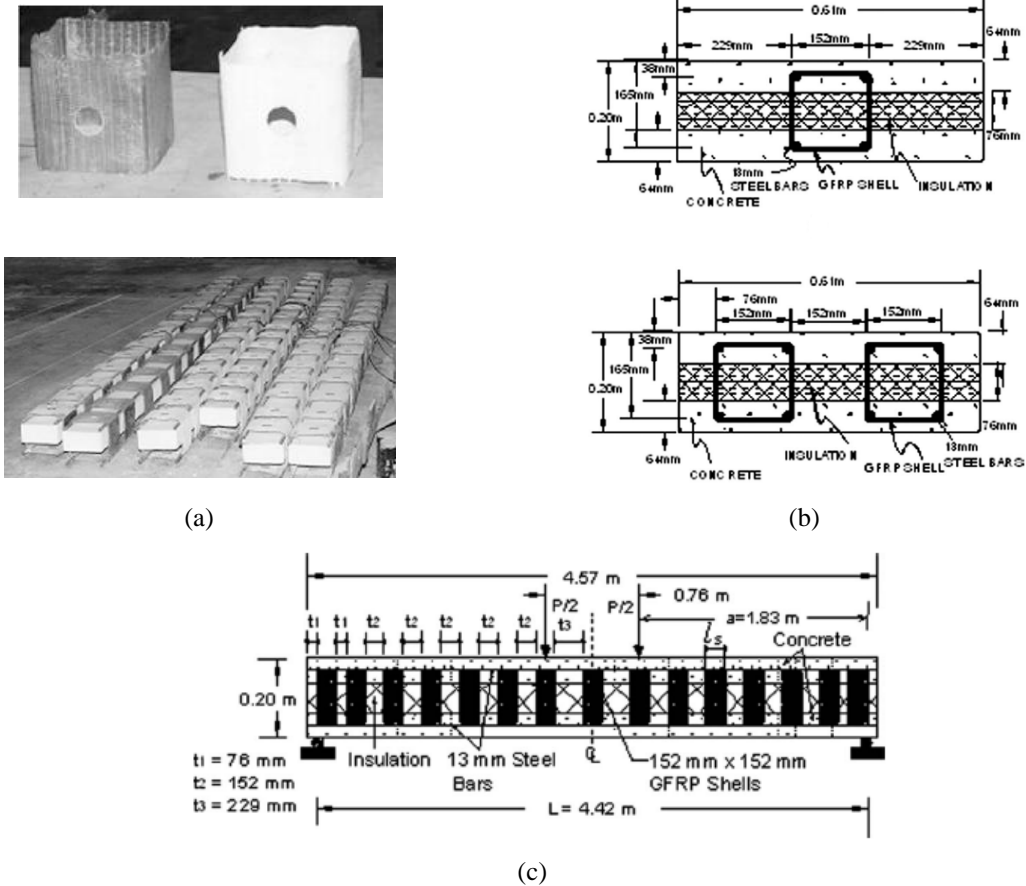
Figure 6: (a) epoxy-cured and urethane-cured GFRP shells; (b) cross-sectional view of single cage and double cage sandwich panels; (c) longitudinal view of panel (Pantelides *et al.*, 2008).

In recent past, Kim and You (2015) and Choi *et al.* (2015a) suggestsed the use of grid-type GFRP shear connectors for sandwich wall panels (see Figure 7). The connector is quite similar to the CFRP grid connector studied by the researchers of North Carolina State University (Frankl, 2008, Rizkalla *et al.*, 2009a, Lucier *et al.*, 2010, Bunn, 2011, Hodicky *et al.*, 2015), differing on the use of glass fibre reinforced epoxy in replacement of carbon fibre reinforced epoxy.
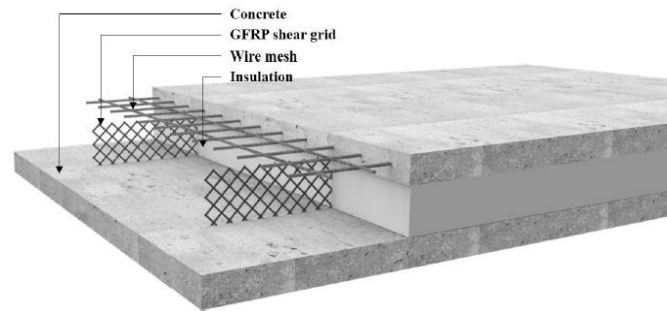
Figure 7: Grid-type GFRP shear connectors used by Kim and You (2015)and Choi *et al.* (2015a).

Recently, Chen *et al.* (2015) developed a roof/floor sandwich panel consisted of GFRP shear plate connectors made of Chopped Strand Mat (CSM) laminates. Continuous and discrete connectors were proposed by the researchers, as shown in Figure 8.

(a)

(b)
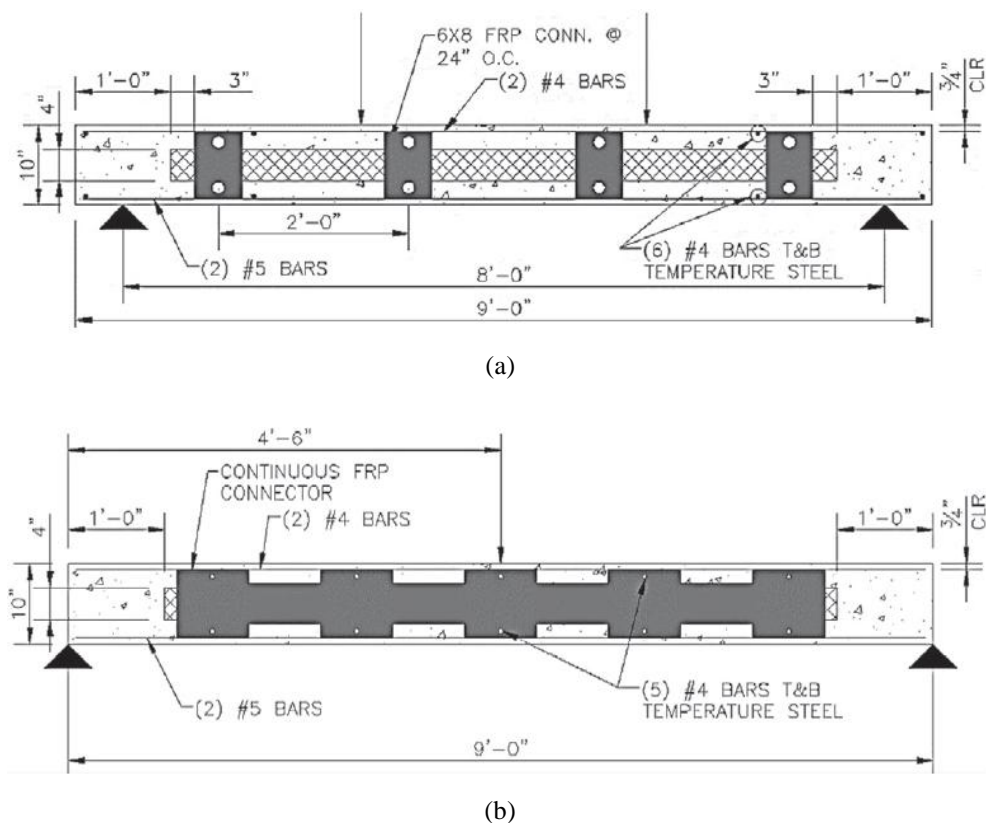
Figure 8: Plate GFRP connectors for roof/slab: (a) discrete; (b) continuous (Chen *et al.*, 2015).

Researchers of Queen's University of Kingston, Ontario, Canada (Teixeira, 2015, Tomlinson, 2015) have proposed the use of discrete connectors made of Basalt Fibre Reinforced Polymer (BFRP) bars. Each connection is made of a pair of L-shaped shear connectors: one inserted normal to the façade and the other placed at an angle, usually 45° (measured relative to the

normal connector), as shown in Figure 9. This arrangement of angled connectors was chosen to put the BFRP bars into tension when the panel is subjected to wind pressure and into compression when subject to wind suction (Tomlinson, 2015).

(a)

(b)
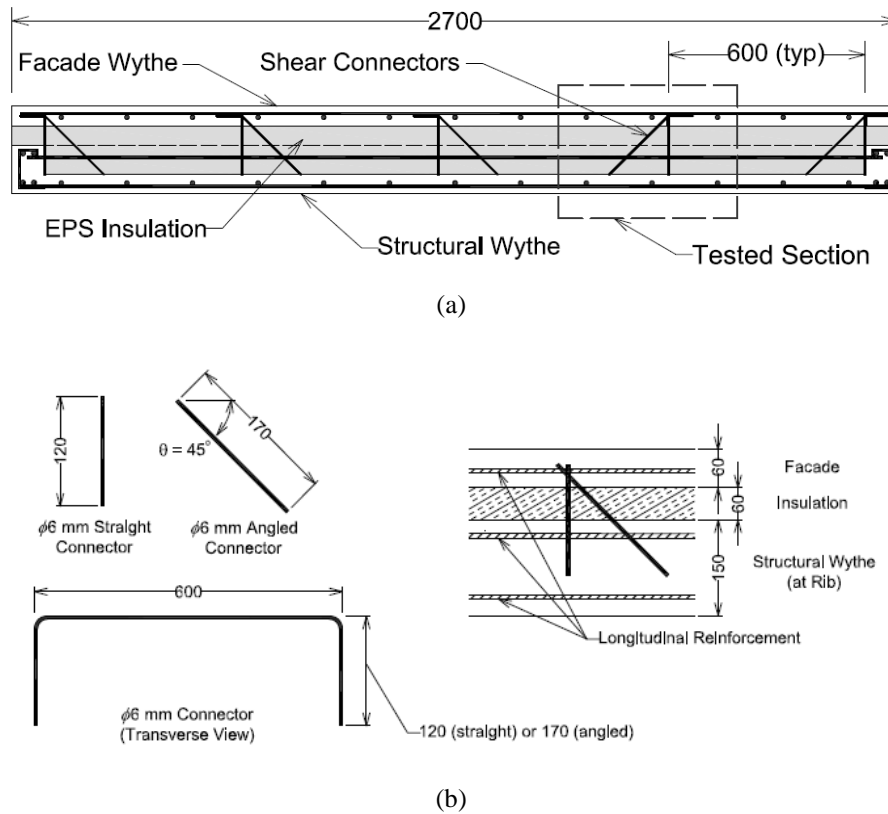
Figure 9: BFRP connectors for sandwich panels: (a) arrangement in the panel; (b) varation of geometry of connectors (Tomlinson, 2015).

Although adhesive bonding is extensively applied in many branches of industry (e.g., the automotive industry), it is less frequently used in Civil Engineering. Typical applications are the strengthening of concrete columns and beams with carbon fibre reinforced polymer strips and the bonding of facade elements to steel structures (Klapp, 2002). According to Gurtler (2004) the main advantage of adhesively-bonded connections over mechanical fastening is the avoidance of stress concentrations, which is important mainly when brittle materials, such as FRPs, are used. However, bonding as a method of connecting load-bearing members is still not widely used in Civil Engineering and no references where found in the literature focusing on its use to connect the concrete wythes of sandwich panels.

2.3   DESIGN REQUIREMENTS

2.3.1   Thermal requirements

The rapidly growing world energy consumption during the last decades has raised concerns over supply difficulties and environmental impacts. According to a recent study (United Nations Environment Programme, 2007) 30-40% of the energy in the world in 2007 was used by humans activities in residential and commercial buildings, and in Europe, there values rise up to 40–45%, exceeding the industrial and transportation sectors. Growth in population together with the increasing demand for building services and comfort levels lead to an upward trend in energy demand in the future.

It is under such circumstances that the regulatory bodies (i.e., Government, energy agencies, local authorities) introduced in different countries instruments for encouraging savings and maximizing energy efficiency in buildings (Decreto-Lei 80/2006, 2006, Real Decreto 314/2006, 2006, Energieeinsparverordnung für Gebäude, 2007, Italian Decree 192/2005, 2005, Office of the Deputy Prime Minister, 2006).

Specifically at European Union, from 2006, the European Directive on Energy Performance of Buildings - European EPBD (Directive 2002/91/EEC, 2003) requires member states to ensure that new buildings meet minimum energy requirements. It also requires that all buildings should undergo energy certification prior to sale. This policy led to a harmonization of all thermal regulations in the European Union and influenced regulations all around the world.

Building energy regulations, also referred to as building energy codes, have a prescriptive character, and their objective is to establish and limit the upper bound for the buildings energy consumption for heating, cooling and ventilation. Energy certification, in turn, is mainly a market mechanism whose main objective is to promote higher energy performance standards than the regulated ones. To reach this objective, energy certifications provide detailed information about the energy performance of building, allowing a comparative determination of the quality of buildings in terms of their energy use (Pérez-Lombard *et al.*, 2009).

Therefore, energy performance of buildings becomes an important aspect of innovative and cost-effective building design. In the case of new buildings, it is fundamental to make the

design of the thermal insulation to achieve the desired energy performance for the building. The thermal insulation of the outer shell of the building must be, at least enough to comply the minimum requirements imposed by the local regulations, or even higher, taking into account that regulations are being each day more strict, tightening the required average heat retention coefficient of the building´s outer shell (Galvin, 2010).

Although the most recent instruments of energy regulation and certification are aimed at the overall energy performance of buildings, they often also seek the optimization of the thermal protection of building envelopes by specifying limits to the heat transmittance values (U−values) or thermal resistance (R−values) for each component of the outer surface of the building, taking into account local climatic conditions. Emphasis is also placed on the need for continuity of insulation to avoid thermal bridging. For that, limits to avoid excessive thermal bridging effects are also imposed.

These decisions impact directly on design of building envelope components, like the sandwich wall panels proposed in this research. The following sections explain how these limitations affect the design of building envelope components.

Building regulations have historically set minimum insulation levels for the components of the outer shell of building in terms of elemental U−values (or R−values, which are the reciprocal of the U−values).

According to ASHRAE (2009) the heat transmittance (U−value) is the heat flux under steady-state conditions from the environment on the one side of a body to the environment on the other side, induced by the temperature difference between the surfaces of that body.

The U-value unit of measurement, $W/(m^2 \cdot °C)$, is an expression of how quickly energy passes through a square meter of the element for a given temperature drop between air on the inside and air on the outside of the element.

The theoretical concepts behind the computation of thermal transmittance of building elements which can be found elsewhere (ASHRAE, 2009, PCI Industry Handbook Committee, 2004). The overall heat transmittance of a building component (U) is determined as the reciprocal of its air-to-air thermal resistance to heat flow, as given in Eq. (1).

$$U = \frac{1}{R} \tag{1}$$

The air-to-air thermal resistance (R) is defined as the sum of the surface-to-surface thermal resistance (R_S) and the surface film resistances at both sides of element, of interior surface film (R_{fi}), and of exterior surface film (R_{fo}), as given by Eq. (2).

$$R = R_S + R_{fi} + R_{fo} \tag{2}$$

In turn, the surface-to-surface thermal resistance of a flat building assembly composed of parallel layers consists of the sum of the resistances of all layers in series, as shown in Eq. (3).

$$R_S = R_1 + R_2 + ... + R_i + ... + R_n \tag{3}$$

where R_i is the thermal resistance of an individual layer i, (m²·°C) /W.

The thermal resistance to heat flow of a single layer (R_i) is given by the ratio of its thickness to its apparent thermal conductivity (Eq. (4)).

$$R_i = \frac{t_i}{k_i} \tag{4}$$

where t_i is the thickness of the layer i (m) and k_i is the apparent thermal conductivity of the layer i, W/(m·°C).

The surface film resistances (R_{fi} and R_{fo}) specify the heat transfer to or from a surface by the combined effect of convection and conduction. Although these contributions are affected by surface roughness and temperature difference between the air and surface, the largest influence is that of air movement, turbulence, and velocity close to the surface. Because air movement at the envelope surface depends on wind speed and direction, as well as flow patterns around the building, which are usually unknown average film coefficients for interior and exterior heat transfer are normally used (ASHRAE, 2009).

The Portuguese regulation (Decreto-Lei 80/2006, 2006) establishes that the value adopted for the surface film resistances in the case of walls should be 0.04 (m²·°C)/W and 0.13 (m²·°C)/W, respectively for the exterior and the interior surfaces films.

The U−value calculation as described above is at its simplest for a building element which

consists solely of plane, parallel, uniform layers: the heat flow through such an element is directly from inside to outside in a straight line, and all that is needed to obtain the U−value is a simple sum of the thermal resistances of each layer. The consequence of these non-uniformities, or the presence of any layers that are not plane and parallel, is that the heat no longer travels in straight lines. That affects the total heat transfer through the element and needs to be allowed for in the determination of the U−value (Anderson, 2006). However, virtually all practical building components are non-homogeneous.

To overcome the limitation imposed by the non-homogeneity of elements, some simplified methods are normally adopted for U−value calculations (Lee and Pessiki, 2008b, BS EN ISO 6946:1997, 1997). These methods often involve calculation of the upper limit of thermal resistance of the element and the lower limit of thermal resistance. Any non-uniform layer is treated as a bridged layer and the U−value of the component is calculated by the mean of these limits.

However, the simplified calculation procedures are not valid for constructions bridged by thermal bridges, i.e., walls where the thermal insulation is perforated by repeating metal connectors (BS EN ISO 6946:1997, 1997). In these cases the thermal bridging effect may be greater than predicted by the simplified methods because the heat flow is very non–linear. Once the heat losses/gains are significantly increased in these regions, the effect of these thermal bridges should take full account when calculating the U-value of building elements which contain repeating thermal bridges.

For the calculation of thermal bridges there are standard methods described in details in ASHRAE handbook and EN 14683 (ASHRAE, 2009, ISO, 2007) that consist in integrating a linear thermal transmittance (ψ−value). Nevertheless, these methods underestimate the global heat losses through the walls in most cases (Déqué *et al.*, 2001). For these cases, a more accurate determination of the non-linear heat flow can be provided by two or three-dimensional numerical analysis, like the ones based on finite element method. For constructions comprised of precast elements that cannot be handled by the simplified methods, the best way to perform the thermal evaluation of the building is to calculate the U−value of the building component by numerical calculations only once, and then use the result in a simplified method.

The lower the U−value, the better the insulation provided by the element. So, the aim is to

slow down the rate of heat loss, which means a lower U−value. This is the reason that the building regulations generally assign an upper bound to the heat loss rate (U−value) for each element of the building envelope (e.g., wall, roof, glazing, etc). These values are generally categorized in the building regulations by type of building (new/existing, dwellings/others), portion of the building envelope and climate zone. Table 2 summarizes the recommended/required U−values for external walls the building regulations of different countries over the years.

Table 2: Required/recommended elemental U−values for external walls of new dwellings in buildings regulations of different countries over the years.

Country	Regulation	Year	Maximum U−value (W/(m²·°C))	Required / Recommended
England and Wales	The Building Regulations 1991 (Department of the Environment and The Welsh Office, 1991)	1991	0.45	Required
	The Building Regulations 2006 (Office of the Deputy Prime Minister, 2006)	2006	0.35	Required
	The Building Regulations 2010 (HM Government, 2010)	2010	0.28	Required
Germany	EnEV 2007 (EnEV 2007, 2007)	2007	0.35-0.45	Required
	EnEV 2009 (EnEV 2009, 2009)	2009	0.28-0.35	Required
France	Réglementation Thermique (RT) 2005 (Arrêté du 24 mai 2006, 2006)	2005	0.45	Required
	RT 2012 (Arrêté du 26 octobre 2010)	2010	0.36	Required
Portugal*	RCCTE 2006 (Decreto-Lei 80/2006, 2006)	2006	1.80, 1.60 and 1.45	Required
	RCCTE 2006 (Decreto-Lei 80/2006, 2006)	2006	0.70, 0.60 and 0.50	Recommended

*- respectively to climatic zones I1, I2 and I3.

Considering a sandwich panel comprised of two concrete layers of 60 mm thickness, taking into account the surface film resistances established by the Portuguese regulation and disregarding the heat losses due to thermal bridges, the thickness of insulation required in accordance with the Europeans building regulations would be those presented in Table 3.

Table 3: Required thickness of insulation for walls of new buildings to meet the current regulations (sandwich panel comprising two concrete layers of 60 mm thickness and disregarding the heat losses due to thermal bridges).

Country	Required / Recommended	Required/recommended insulating material thickness (mm)			
		Expanded polystyrene		Polyurethane foam	
		50 kg/m³	18 kg/m³	80 kg/m³	30 kg/m³
England and Wales	Required	96	136	66	90
Germany	Required	75 - 96	107 - 136	52 - 66	70 - 90
France	Required	73	103	50	68
Portugal*	Required	9, 11 and 13	12, 15 and 18	6, 7 and 9	8, 10 and 12
	Recommended	34, 41 and 51	48, 58 and 71	23, 28 and 35	32, 38 and 47

*- respectively to climatic zones I1, I2 and I3.

The considered thermal conductivity of concrete was 1.40 W/(m·°C) (Incropera *et al.*, 2006) and the considered thermal conductivities of the thermal insulations are those presented in Table 1.

Insulation materials are rarely continuous throughout a building element. When a highly conductive or non-insulating material takes place between the insulating layer, a low resistance path for heat is created. So, the heat flow this path of least resistance from the heater surface to the colder one. These paths, that are not necessarily perpendicular to the surfaces, are usually called thermal bridges.

According to Lowe and Bell (1998), thermal bridges in dwellings can be classified under six main headings:

- Quasi-homogeneous thermal bridges – defects in an element of the thermal envelope containing repeating thermal bridges. Examples include mortar joints and wall ties in masonry walls and ceiling joists in an insulated loft;

- Major structural thermal bridges – defects that arise when two elements of the thermal envelope intersect or abut. Examples includes wall-floor junctions and wall-roof junctions where the continuous layer of thermal insulation is cut or by-passed by a major structural element;

- Geometrical thermal bridges – occurs at edges and corners of the thermal envelope. Example: junction between a gable wall and non-gable wall or where the roof meets a wall or corner made by 2 external walls;

- Thermal bridging associated with services and loft hatches;

- Thermal bridging associated with window and doors reveals and

- Other thermal bridging associated with fenestration and doors, particularly frame and glazing edge losses.

The typical effects of thermal bridges are: significantly increase heat flow and give rise to low internal surface temperatures, with an associated risk of surface condensation or mould growth. Thermal bridges become even more important in the case of high thermal performance buildings.

To limit the thermal bridges to a reasonably low level, building regulations also includes thermal bridging targets. Different approaches are adopted in the building energy performance regulations. To achieve compliance with the British Building regulation (HM Government, 2010), the total heat loss through thermal bridging should be equal to or less than 10% of the total heat loss through the plane elements of the building. The German regulation establishes a maximum dimensionless temperature factor. The French regulation a maximum value is established for the thermal bridge linear transmittance (ψ-value) depending on the type of building. The Portuguese regulation gives explicit maximum value for areas. In Spain, to avoid the risk if mold formation, limits are established to maintain the indoor enclosures surface temperature at a high enough level.

The thermal mass or thermal inertia is the property associated to the ability of materials to absorb, store and later release significant amounts of heat. Physically, it is equivalent to thermal capacitance or heat capacity.

Numerous studies have demonstrated the beneficial effect on choose walls with high internal mass to the thermal performance of building, both for comfort and energy savings (Di Perna *et al.*, 2011, Kossecka and Kosny, 2002, Aste *et al.*, 2009). These materials absorb energy slowly and hold it for much longer periods of time than do lightweight materials, delaying and reducing heat transfer through the component. The main benefits associated with the use of materials with high thermal mass is that the peak loads are delayed and reduced, stabilizing the interior room temperature and also enabling a reducing of total loads in many climates and locations (Ogoli, 2003, Lindberg *et al.*, 2004).

In this context, due to its density, concrete construction, with its high thermal inertia and thermal storage properties, has an advantage over lightweight wall technologies (Precast/Prestressed Concrete Institute – PCI, 2006).

Once the building regulations are based on calculations of U-value made in a semi-stationary regime (steady state), they don´t take into account the effect of thermal inertia. The main reason for that is the complexity to assess these benefits, what requires transient simulations for an accurate evaluation.

2.3.2 Structural requirements

A wall construction shall be capable of accommodating with appropriate degree of reliability and in an economical way, all loads likely to occur during execution, its intended service life and ultimate limite state, including dead loads, live loads, roof loads, wind loads and seismic loads, and of transmitting the resulting loads to the supporting structural elements, i.e., foundations (ACI Committee 318, 2005).

Depending on the role of structural walls in the context of a structure, they may be classified as bearing walls or shear walls. Wight and MacGregor (2012) defines bearing walls as walls that are laterally supported and braced by the rest of the structure. This type of wall resists primarily in-plane vertical loads acting downward (primarily gravity loads) on the top of the wall. This load may act eccentrically with respect to the wall thickness, causing bending. On the other hand, shear walls are defined as walls that primarily resist lateral loads due to wind or earthquakes acting on the building. According to ACI Committee 318 (2005) these walls generally provide lateral bracing for the rest of the structure.

There is currently no legally adopted building code that defines design methods for concrete sandwich panels. The state-of-the-art of PCI (2011) provides guidelines for design of such sandwich wall panels. However, this document is not referenced by any legally adopted building code, and it does not provide any guidance in regard to capacity determination of composite shear connectors. It only states that composite shear connector capacities may be obtained from the connector manufacturers (Ekenel, 2013). Nonetheless, the ACI Building Code (ACI Committee 318, 2005), the PCI Design Handbook (PCI Industry Handbook Committee, 2004) and the ACI 533R-11 report (ACI Committee 533, 2012) give general provisions for the design of reinforced concrete walls that can be followed in the absence of specific document for concrete sandwich panels. These provisions are intended to ensure adequate strength to resist the design values of moments, shears and axial loads acting on it (ultimate limit states), while assuring satisfactory performance under normal service conditions (serviceability limit states).

The main particularity of design procedures for sandwich panels is that they may be designed to behave either in full-composite, non-composite or partially-composite action of concrete layers. The main difference between them is the level of longitudinal shear transferred between the concrete layers. The concrete layers of a full-composite panel act as one unit, resulting on a single neutral axis. The full-composite panels are more structurally efficient than the other types of panel. Considering panels made with the same thicknesses for the different layers, the strength and stiffness of a full-composite panel are higher than those of a partially- or non-composite panel. Furthermore, full-composite panels presents negligible shear deformation through the insulation material layer, resulting in null relative slip between its constituent layers. There are many advantages related to the use of fully composite panels, including reduced concrete layer's thickness and, consequently, reduced overall weight. Nonetheless, to attain a full-composite behaviour an increased number of shear connectors is required, reflecting on the cost of panel. Depending on the material of shear connector, an increased number of connectors can also lead to a reduction of the R−value of panel, jeopardizing the thermal performance of sandwich panel. Moreover, thermal bowing is a main concern on full-composite insulated panels. Tittelboom *et al.* (2015) stated that crack formation in the external concrete layer is often experienced in large sandwich panels, especially during the summer. This happens because the solar radiation heats up the external concrete layer while the temperature of the internal layer remains almost constant. Thus, the external layer expands with the temperature rise. If the panel presents a high degree of composite action, this deformation is restricted by the internal concrete layer, resulting in compressive stresses in the external layer. For this reason, some designers prefer to design and use non-composite walls, in spite of their reduced stiffness and reduced load capacity relative to full-composite panels.

The existing design provisions for reinforced concrete solid walls are often used to extrapolate the behaviour of sandwich panels by considering an equivalent flexural stiffness (*EI*) for the sandwich panels (Benayoune *et al.*, 2007b). For a non-composite panel the equivalent flexural stiffness is equal to the sum of each flexural stiffness. In the case of full-composite panels, the stiffness is equal to the stiffness of the composite section, taking into account the lack of concrete at the core and the location of the composite centroid. The methodology that may be adopted for the design of partially-composite panels is controversial among designers (Tomlinson, 2015). In a simplified way, it is assumed a percentage of composite action that is justified by testing and experience (PCI, 2011).

According to ACI 318 code (ACI Committee 318, 2005) , the maximum deflection due to service loads shall not exceed 1/150 of the span length. Deflection limits for precast wall panels are given by ACI Committee 533 (2012). According to this the ACI 533R-11, the immediate deflection due to combined effect of self-weight and superimposed dead load for load-bearing precast wall panels should be limited to 1/240 of the span length. The respective values for the immediate deflection due to live load in load-bearing panels and for the total deflection after installation of non-loadbearing panels likely to be damaged by large deflections are 1/360 and 1/480 of the span length. The ACI 533R-11 also impose a maximum deflection equal to 3/4 in.($\approx$19 mm) for all the cases.

In regard to limitations for crack opening, the ACI 533R-11 (2012) states that, for structural reason, if the crack width is narrow, not over 0.010 in. ($\approx$0.254 mm), the structural adequacy of the casting will remain unimpaired, as long as corrosion of the reinforcement is prevented. If the reinforcement is coated for corrosion resistance, wall panels containing cracks up to 0.005 in. ($\approx$0.127 mm) wide for surfaces exposed to weather and 0.010 in. ($\approx$0.254 mm) wide for surfaces not exposed to the weather should be acceptable. ACI 533R-11 (2012) indicates that the esthetic limitation for crack openings depends on the texture of the surface and the appearance required. For smooth surfaces in interior panels of high quality, the ACI 533R-11 states that a crack opening equal to 0.005 in. ($\approx$0.127 mm) is aesthetically acceptable.

Theoretically, as shown in Figure 10(a), the shear connectors used in sandwich panels should be designed to take into account the shear stresses τ_{LA} and τ_{LB} developed in the contact surface between the concrete layer and the connector. However, for the sake of simplicity and keeping in mind that the values used should be conservative for the design of the connectors, the shear stress τ_L developed in the mid thickness of panel can be considered (see Figure 10(b)).
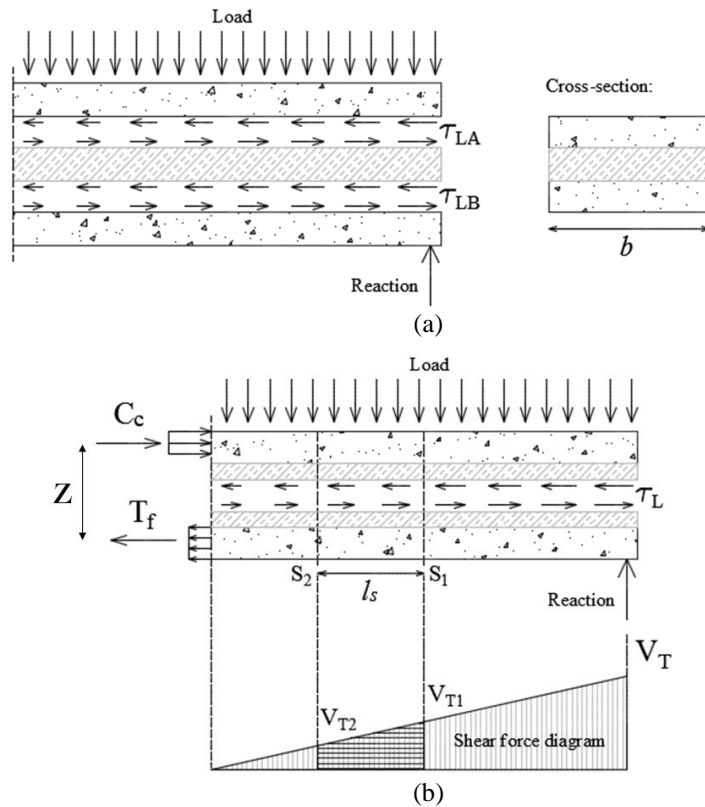
Figure 10: Schematic representation of shear forces that arises in sandwich panels under flexure: (a) τ_{LA} and τ_{LB} that form in the SFRSCC–GFRP connections; (b) τ_L computed in the mid-height of sandwich panel.

There are different ways for calculating the magnitude of the longitudinal shear stresses τ_L. Due to particularities related to their geometry, in the technology of ribbed connectors the shear stresses are preferably computed in terms of a longitudinal shear per unit length, also known as shear flow, that can be estimated from the Eq. (5).

$$q_L = \frac{V_T \cdot Q}{I_c} \tag{5}$$

where V_T is the shear force acting in the portion of panel where the shear flow is intended to be obtained (see (b), representing a simply supported panel submitted to a uniform distributed loading), Q is the first moment of area about the centroidal axis of the composite section for one part of the cross-section, and I_c is the moment of inertia of the entire composite section. Nonetheless, Eq. (6) applies to uncracked elastic members and is only a rough approximation for cracked panels.

Alternatively, the longitudinal shear can be computed from the variation in compressive force, C_c, or tensile force, T_f, in the panel (see Figure 10). By dividing the panel into a series of segments, the value of C_c or T_f at both ends of each segment are calculated, and the average longitudinal shear flow is obtained per segment by applying the Eq. (6).

$$q_L = \frac{T_{f2} - T_{f1}}{l_s}$$

(6)

where T_{f2} and T_{f1} are the larger and smaller tension forces on the extremities of a segment and l_s is the length of the segment (see Figure 10(b)). From the equilibrium of the sections, the tension force can be also taken as the moment due to applied force divided by the distance between the resultants of the compressive and tensile forces on the cross section (i.e., M_u/Z, where Z is defined in Figure 10 (b)). Thus, Eq. (53) can be written as a function of the variation of moment along the panel, as shown in Eq. (54). Further, knowing that the change in moment from one section to another is equal to the area of the shear-force diagram between the two sections, the longitudinal shear stress can be obtained from the shear-force diagram, as written in Eq. (7) (see V_{T2} and V_{T1} depicted in Figure 10(b)).

$$q_L = \frac{M_{u2} - M_{u1}}{Z \cdot l_s} = \frac{V_{T2} + V_{T1}}{2 \cdot Z}$$

(7)

Details about the above different methodologies can be found elsewhere (PCI, 2011, Wight and MacGregor, 2012).

Finally, the design of the shear connection in a sandwich panel consists on finding the quantity of connectors (*N*) that is necessary, per length of panel, to resist the expected shear stresses/flow due to the transversal loadings applied in the ultimate limit state. This is determined dividing the total shear flow to be transferred (q_L) by the design strength of the connector ($Q_{lo.d}$), as done in Eq. (8).

$$N = \frac{q_L}{Q_{lo.d}}$$

(8)

For conventional use of sandwich panels, where they should be designed for handling and wind loads, the design can be based on the application of Eq. (8), if the shear connector has a

ductile behaviour that allows a redistribution of shear stresses along the span. In general, a ductile response of connections is desirable for safety purposes. Moreover, if a ductile response is obtained, the design process of panels can be simplified. In fact, a ductile response of connections allows a redistribution of forces, maling it possible to consider that the connectors located between the positions corresponding to the null and maximum bending moments are equally loaded. In this approach, it is enough to know the shear flow to be resisted (q_L), calculated by Eqs. (5) to (8) and the design strength of the connector ($Q_{lo.d}$), that will be estimated in the following sections.

2.4 ASSESSMENT OF PERFORMANCE OF SANDWICH PANELS

This section focuses on the studies previously developed to assess the thermal and mechanical performances of sandwich panels. There are numerous testing programs, some analytical studies and few numerical investigations reported in the literature focusing on determination of the mechanical performance of sandwich panels based on distinct technologies.

Due to the non-linear behaviour of their constituent materials and the interaction between their various components, concrete sandwich panels usually present a complex mechanical behaviour. This convoluted behaviour has led researchers to mostly rely on experimental investigations backed by simple analytical studies (Benayoune *et al.*, 2006).

Some of the most relevant studies and their main contributions are reported in the following sections:

2.4.1 Thermal performance

The literature that addresses the assessment of thermal performance of concrete sandwich panels is scarce. Nonetheless, recently, two investigations were published concerning about this issue (Kim and Allard, 2014, Woltman, 2014).

The thermal performance of concrete sandwich panels subjected to typical cold region environment was investigated on reduced scale specimens by Kim and Allard (2014). The specimens were 230 mm high, 230 mm wide and 188 mm thick (two concrete layers 75 thick and thermal insulation material layer 38 mm thick). Polystyrene foam with thermal conductivity of 33 W/m·K was used as thermal insulation material. Three different steel pin connectors were used: W-, Z- and J-shaped. Each leg of W-shaped connector had diameter

equal to 2.56 mm, whilst the Z- and J-shaped connectors had diameters of 4.65 mm. The test consisted in exposing the external concrete surface to air at -30ºC while the internal concrete surface was exposed to temperature equal to 25ºC. They confirmed that thermal bridges are formed due the high conductibility of the steel connectors, in spite their reduced diameters.

Woltman (2014) tested ten full scale panels under steady-state conditions in a custom-built hot box apparatus. Steady-state conditions were obtained with the hot chamber at 24ºC and the cold chamber at -5ºC. Each specimen measured 2400 mm × 1550 mm × 254 mm. The panels consisted of two outer concrete layers and an intermediate insulation layer. Within the insulation layer there was a concrete frame featuring vertical studs measuring 100 mm deep by 75 mm wide, such that 25 mm of XPS was between the concrete stud and each outer concrete layer. The specimens also contained a header and footer to complete the stud framing. The assembly was connected by GFRP connectors passing through the concrete stud and embedded in the concrete layers. The specimens produced featured various stud spacing, connector spacing, connector sizes, and connector materials. For comparison purposes, some panels were fabricated with galvanized steel connectors used commercially in sandwich panels. From the recorded surface and internal temperatures and the thermal images of the panel surface, it was concluded that, although the regions of the panels containing the concrete studs had a significant thermal resistance (25 mm thick EPS for each side), it was the most significant source of heat transfer through the panel. When GFRP pin connectors were used, the connector locations were not visible in thermal images. On the other hand, the recorded temperatures and the thermal images clearly showed that the steel connectors were regions of preferential heat flow, despite having half the cross section area of the smallest GFRP connector.

2.4.2 Direct shear behaviour under pull-out and push-out loads

As mentioned earlier, the role of connections in the sandwich panels are: to keep the panel intact along its service life and to supply the panel with some degree of composite action, if designed to act as full- or partially- composite panel. Accordingly, the behaviour of the connections under pull-out loads (transversally to the concrete layers) and push-through (longitudinally) should be known for a correct design of panels.

Although pull-out failure of connections is occasionally reported in the literature concerning sandwich panels (Choi *et al.*, 2015b), no research works were found to focus on the pull-out characterization of connections for sandwich panels. This mechanism is even more important

for precast sandwich panels, that usually have the connections subjected to pull-out loads during stripping, transporting and erecting of panels.

A series of pull-out tests on FRP Perfobond rib shear connectors (perforated FRP plates) for FRP-concrete composite decks was reported by Cho *et al.* (2012). The test specimens, made with different number and size for the holes, were designed to examine only the effects of the resistance by rib holes. Constitutive equations were derived through regression analysis of the experimentally obtained load $\times$ displacement curves. It is expected that the obtained constitutive equations are useful for the analysis and design of connections made with similar materials and geometry.

With regard the longitudinal shear behaviour of connections, historically, the performance of shear connectors has been established from small-scale specimens following the procedures described in Eurocode 4 (CEN, 2004b). The test described in Eurocode 4 were proposed for connections in composite steel and concrete structures. The test specimen consists of two concrete layers connected by connectors that are welded within the flanges of a steel I-profile. The load $\times$ slip is obtained applying the load in the top end of the steel profile while the concrete layers are supported in their bottom end (see Figure 11).
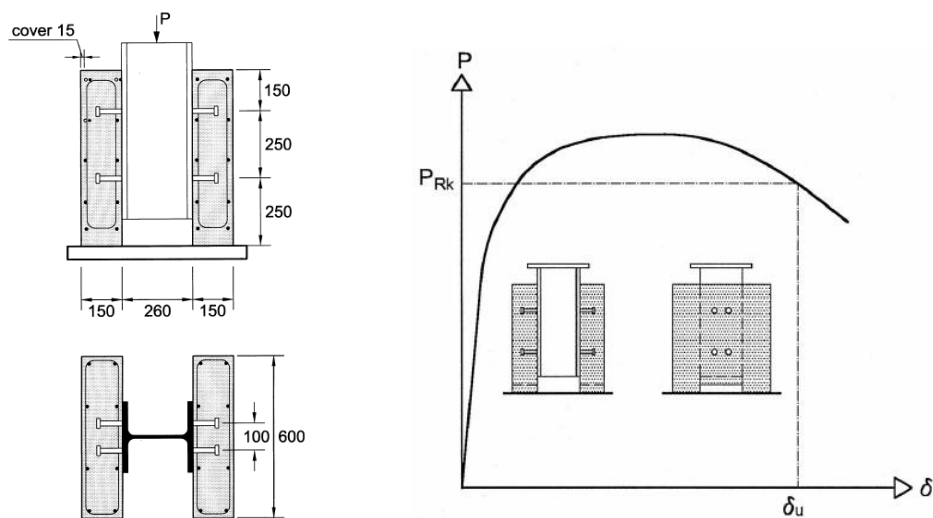
Figure 11: Push-out test setup and schematic representation of obtained load $\times$ slip curve that characterize the connection.

Although no standard procedure exists for the specific case of connections for sandwich panels, similar methodology was used by different researchers to assess and compare the shear behaviour of different shear connections mechanisms for sandwich panels. The test

configuration varied among the different researches. Two configurations are presented in Figure 12. In general, the specimens are comprised of three concrete layers made with connections that are representative of the system adopted in the sandwich panel.

(a)   (b)
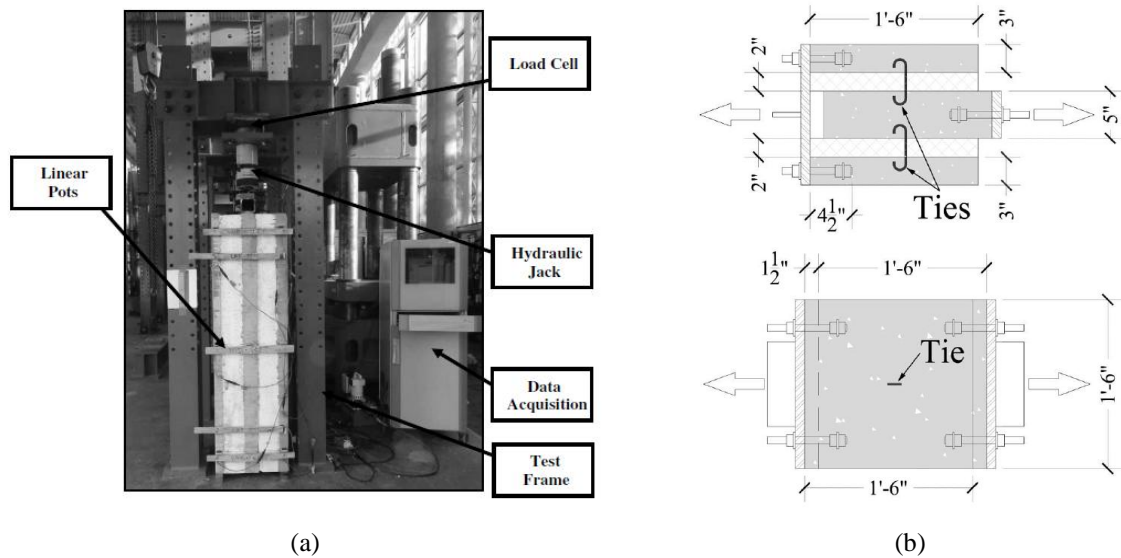
Figure 12: Test configurations to assess the direct shear behaviour of connectors for concrete sandwich panels.
(a) Hodicky *et al.* (2015); (b) Naito *et al.* (2012).

Einea (1992) performed push-out tests with specimens fabricated with different types of GFRP connectors. From the observation of test results, the importance of embedment length to develop the full strength of some connectors was evidenced. From the comparison of tests results of reference specimens with the results obtained with tests using plastic foil as bond-breaking between the concrete layers and the insulation, it was noticed that the bond between the insulation and the concrete contributes to shear resistance.

Choi *et al.* (2015b) evaluated the shear flow of specimens with the two different types of insulation materials (XPS and EPS) with and without a GFRP corrugated shear connector shear connector (made with two identical GFRP bent bars). They observed that, in specimens fabricated without shear connectors, shear strength and stiffness values at the interface between the concrete wall and XPS insulation are higher than those of the specimen with EPS insulation. Nonetheless, unlike the specimens without a shear connector, in the case of specimens with shear connectors and made with EPS insulation exhibited more shear flow than those with XPS insulation. They also observed that the use of EPS led to a more ductile failure as evidenced by the tearing out of the insulation. For the specimens made with XPS insulation it was evidenced the failure associated to the loss of bond strength between the

XPS and the concrete layer. The shear flow values for the EPS insulation and XPS insulation with GFRP shear connectors that had an embedded length of 50 mm were 137 kN/m and 130 kN/m, respectively. They also found that there was a noticeable difference in shear capacity with an increase in the embedded length of 10 mm. The shear flow values for the specimens made with EPS and XPS insulation averaged 111 kN/m and 103 kN/m, respectively, when an embedded length equal to 30 mm was used. The respective values were equal to 129 kN/m and 122 kN/m when the connector had an embedded length of 40 mm.

Pahn and Hanz (2012) carried out six direct shear tests to investigate how the characteristics of the bond between the concrete and the insulation material are affected by the type of insulation material used. The specimens consisted of concrete blocks with width × length × thickness equal to 300 mm × 300 mm × 150 mm that were cast on insulation plates (i.e., EPS or XPS). The load was applied in the concrete block parallel to the contact surface between the concrete and the insulations until the bonding failed. Afterwards, a sliding friction test was carried out. From the test results they noticed that the maximum adhesive shear stress of XPS−concrete is only 16% of the value obtained for the EPS−concrete interface. The average values of maximum adhesive shear stress were equal to 27.20 kN/m^2 for EPS−concrete specimens and 4.36 kN/m^2 for XPS−concrete specimens.

Other studies based on direct shear tests also indicated that the EPS insulation provides higher shear flow strength than those with XPS insulation (Yun *et al.*, 2012, Bunn, 2011). This behaviour is justified by the relatively high surface roughness of EPS insulation.

Naito *et al.* (2012) examined the pure shear behaviour of fourteen different commercially available connector types made with: steel, GFRP, BFRP and CFRP. The test results indicate that shear ties used in sandwich wall construction have considerable variation in strength, stiffness, and deformability. The average shear strength of the tested connectors varied from 5.5 kN to 18.5 kN for the discrete connectors and from 17.2 kN/m to 57.8 kN/m for the continuous connectors. The tie stiffness was found to be sensitive to the configuration of the tie geometry. Stiff truss-type ties provided greater initial stiffness than pin-type ties that work in a flexural mode. They observed that the shear strength was improved by 21% by the use of EPS insulation over XPS insulation when used in conjunction with CFRP truss shear connectors. Furthermore, they noticed that, for some types of connectors, the connection failed due to the rupture of the connector itself.

50 push-out tests were performed by Woltman *et al.* (2013) with specimens with dimensions equal to 254 mm × 254 mm × 900 mm. In this study they used only discrete shear connectors. Tests were performed with specimens consisted of plastic connectors (without fibre reinforcement), steel pin-connectors and connectors made with commercially available GFRP bars. The shear strength of specimens made with plastic connectors ranged from 22 MPa to 39 MPa (included the effect of friction between concrete and insulation material), whilst the connectors made with GFRP bars presented shear strengths ranging from 60 MPa to 112 MPa and the steel pin-connectors gave shear strengths ranging from 297 MPa to 365 MPa. Varying GFRP connector size, spacing, cross-section shape (i.e., circular and rectangular), or their end treatment had insignificant effect on the shear strength. Furthermore, they compared the responses of specimens made with the same type of GFRP connector but differing because while one was made with typical adhesion bond between concrete and insulation foam, the other was made with a bond breaker. It was noticed that adhesion bond and friction are quite significant and contribute about 28% to the overall strength.

Extensive experimental work was undertaken by researches from the North Carolina State University (Bunn, 2011, Hodicky *et al.*, 2015) on pure shear behaviour of continuous CFRP grid shear connectors. Bunn (2011) tested sixty-six specimens consisted of three concrete layers (5 cm thick external layers and 10 cm thick internal layer) and two layers of rigid insulation (i.e., EPS or XPS). The specimens were approximately 183 cm tall. The experimental program undertaken investigated the effects of type of insulation material (EPS or XPS), insulation thickness (from 50.8 mm to 203.2 mm) and grid spacing (from 304.8 mm to 914.4 mm). Moreover, the effect of vertical gaps along the length of grid (discontinuity of grid connectors) and the effect of using grid connectors in the transverse direction (perpendicular to the applied load) were also investigated. Test results indicated that, when using EPS foam, increasing the spacing between vertical lines of grid tends to increase the shear flow strength for a row of grid, likely due to the high bond strength of EPS foam. Further, increasing the spacing between grids for the XPS foam did not increase the shear flow strength for a given line of grid. Tests indicated that increasing the thickness of EPS insulation foam decreases the shear flow strength while increasing the thickness of XPS foam insulation (up to 101 mm) had minimal effect in shear transfer behavior. Results indicate that CFRP grid oriented in the transverse direction can provide considerable shear strength, perpendicular to the applied load (approximately 80% of the shear strength of case that connectors are parallel to the applied load). Based on the experimental data obtained by Bunn

(2011), Hodicky *et al.*(2015) developed a 3D nonlinear Finite Element (FE) model of the sandwich panel and conducted a parametric study to predict the shear flow strength of different FRP materials. They observed that the use of Basalt Fibre Reinforced Polymer (BFRP) and GFRP grids in replacement of CFRP grids leads to losses of between 5 to 10% and 10 to 25% of the shear flow strength, respectively.

2.4.3 Axial load and combined axial and bending loads

Besides resisting flexural loads, structural sandwich panels are also typically responsible for transmitting the roof/slab reactions by compressive force to the foundation/floor below. Despite that, possibly due to the complexity on performing tests under combined axial and bending loads, few investigations focused on the behaviour of sandwich panels subjected to this loading condition. Few works have already performed tests with different axial and/or eccentric loads. Among them there are the works run by Benayoune *et al.* (2006, 2007b), Frankl *et al.* (2011), Gara *et al.* (2012) and Tomlinson (2015).

Benayoune *et al.* (2006, 2007b) investigated the behaviour of six reinforced concrete sandwich panels subjected to axial (Benayoune *et al.*, 2007b) and other six under eccentric load (Benayoune *et al.*, 2006). The specimens consisted in panels with slenderness (i.e., height by thickness) ranging from 10 to 20 (1200 mm to 2400 mm high) and 1200 mm wide. Both reinforced concrete layers had thickness equal to 40 mm and the insulation material was 40 mm or 50 mm thick. The connection between the concrete layers was made by continuous steel truss-shaped connectors running the full height of panels. The panels had solid concrete regions at their uppermost and lowermost edges. They noticed that the first cracks occurred at about 44–79% and 38%−55% of the failure loads for axial and eccentric loads, respectively. It was also found that the panels tested under eccentric load, the failure modes showed separation of the concrete layers near the upper part of wall. Furthermore, they found that the strength of panels decreased nonlinearly with the increase of the slenderness ratio. This reduction was about 21% and 38% for axial and eccentric loads, respectively. In both experimental programs the panels behave on a fully composite manner till failure.

Gara *et al.* (2012) presented a study on 2.94 m long and 1.12 m wide in situ sandwich panels consisted of 35 mm thick outer sprayed concrete layers reinforced by metallic meshes. The concrete layers were connected by means of orthogonal steel wires welded to the meshes. Horizontal solid concrete regions along the uppermost ant lowermost edges of panels also connected both reinforced concrete layers. They performed compression tests with axial and

eccentric loads in panels with different thicknesses for the layer of expanded polystyrene (EPS) (i.e., 8 cm, 12 cm and 16 cm). Undulated (corrugated) and non-undulated EPS plates were used. In the tests with axial load, the load was applied at the panel axis, while in the eccentric compression test the load was applied at the axis of one of the concrete layers. The results of the experimental tests and FE simulations indicated that a partial degree of composite behaviour was attained by the tested panels. High ultimate loads, decreasing for increasing values of the slenderness ratios, were obtained. The numerical simulations indicated that the ultimate loads of axially loaded panels are close to the buckling loads which can be determined by performing a linear buckling analysis. Differently, the ultimate loads of eccentrically loaded panels, which are significantly lower than the buckling loads, can be simulated only by performing a non-linear analysis. They concluded that additional investigations are needed to develop simple, effective and rational methods for predicting the ultimate load of wall panels for different values of load eccentricity.

The behaviour sandwich panels made with CFRP grid connectors tested under their expected service conditions was studied by researchers from North Carolina State University (Frankl, 2008, Rizkalla *et al.*, 2009b, Frankl *et al.*, 2011). Six precast, prestressed full-scale sandwich panels were tested by Frankl *et al.* (2011) under combined vertical and lateral loads. The panels were 6.1 m $\times$ 3.7 m and were 200 mm thick. EPS (16 kg/m^3) and XPS (29 kg/m^3) were used as thermal insulations. Different layouts for the CFRP grids were investigated. The specimens were tested in the vertical position. Vertical loads were applied to the top of corbels positioned in the structural concrete layer to simulate the effect of a 18.3 m double-tee roof system. Lateral loads were applied by an actuator connected to a spreader steel beam system, which was used to push and pull the panel and simulate wind pressure and suction. After completion of 3890 fully reversed lateral load cycles loads equivalent to 45% (3710 cycles), 50% (177 cycles), 60% (1 cycle), 80% (1 cycle) and 100% (1 cycle); the lateral load was increased in one direction until failure. They concluded that panel stiffness and deflections are significantly affected by the type and configuration of the shear transfer mechanism and by the type of thermal insulation material. Further, they noticed that, for a given shear transfer mechanism, a higher degree of composite action can be achieved using EPS insulation rather that XPS insulation. They found percent composite actions near 100% with CFRP grid shear connections.

The first work focused on obtaining the complete axial force $\times$ bending moment interaction diagram accounting for partial composite action and slenderness effects was carried out by

Tomlinson (2015). He performed an experimental program with sandwich panels with BFRP shear connectors (see Figure 9). BFRP bars were also used to reinforce the concrete layers. The panels were tested in the horizontal position with various levels of constant axial loads applied to the structural layer of panels (bottom concrete layer during the tests). The flexural loading was increased gradually to failure. He found that the axial force × bending moment interaction diagrams have a tri-linear trend. At very low axial loads, shear compression failure of concrete structural wythe governed the maximum moment, after splitting of insulation and rupture of connectors. As axial load increased, splitting of the insulation governed the maximum moment, followed by connector rupture and/or structural wythe crushing. At very high axial loads, concrete crushing of structural wythe governed the maximum moment. Moreover, he found that the level of composite action by the strength method reduced from 47% to 3%, as axial load increased from 150 to 900 kN. The level of composite action by the stiffness method was much smaller, ranging from 2.5% to 7.8%.

2.4.4 Flexural behaviour

Fifty reinforced sandwich panels with a variety of solid concrete regions, steel pin-type and steel truss connectors were studied by Pfeifer and Hanson (1964). Flexural tests of sandwich panels were performed under uniform loading. The dimensions of specimens were 0.90 m × 1.50 m. They demonstrated that truss shaped connectors were more effective in transferring shear than the other connectors that had no diagonal members. Furthermore, they concluded that distributed solid concrete regions were able to provide equivalent structural capacity in comparison with panels made with longitudinal ribs and larger contact area between concrete layers.

The flexural behaviour of full-scale panels (1.8 m × 11.30 m) consisted of solid concrete regions and steel pin-type connectors (M-ties shown in Figure 2(c)) were evaluated by Pessiki and Mlynarczyk (2003a). They observed that, in spite of the high degree of composite action achieved (92%) in the panels made only with solid concrete regions, flexural cracking appeared earlier than expected due to the stress concentrations caused by the connectors. From test with sandwich panels made without connectors they concluded that the bond between the XPS and the concrete layers provides only 5% of composite action to the panel. They also found that the use of pin-type connectors leads to a panel with only 10% of the composite action obtained for a solution consisted of combination of solid concrete regions, M-ties and XPS foam.

Bush and Stine (1994) tested in flexure 203 mm $\times$ 2.44 m $\times$ 4.88 m precast sandwich panels with various connectors and construction details. The panels consisted of 76 mm thick prestressed concrete layers separated by 51 mm thick EPS insulation. Results of static testing indicated that a high degree of composite stiffness and composite flexural capacity (80% or more) can be attained using only steel truss connectors oriented longitudinally in the panels (with EPS insulation). The tests also provided evidence that the insulation strongly promoted composite behaviour. It was also found that stripping and handling inserts that extended through both concrete layers, typically used in precast panels, contributed more to longitudinal shear resistance than the truss shear connectors themselves. Some fatigue tests were also performed to simulate thermally-induced stresses in the concrete layers. Results indicated relatively minor stiffness loss (15% decrease) over 55000 loading cycles, which was attributed to the deterioration of the bond between the thermal insulation and concrete layers.

The flexural behaviour of sandwich panels also made with steel truss-shaped shear connectors was studied experimentally by Benayoune *et al.* (2008b). A total of six specimens were tested, being: two 2.00 m $\times$ 0.75 m one-way panels, two 1.50 m $\times$ 1. 50 m one-way panels and two panels with size 1.00 m $\times$ 0.50 m. All the panels were made with 40 mm thick reinforced concrete layers. From the test results, it was noticed that the ultimate strength and the degree of composite action were found to be depend to a large extent upon the stiffness of the shear connector used. In general, substantial degree of composite action was achieved by truss-type shear connectors.

Different types of GFRP connectors were suggested by Einea *et al.* (1994), including: wide flange profiles, dogbone section, diagonal strap connectors and fabricated bent bars. After preliminary tests, flexural behaviour of sandwich panels made with discontinuous GFRP bent bar connectors and 2.44 m long was explored by Einea *et al.* (1994). The GFRP bent bar connector systems achieved a satisfactory percentage of composite action. Defining the percentage of composite action at ultimate strength as the ratio between the measured ultimate strength and the 100 percent composite ultimate strength, they computed a composite action equal to 65% for specimen with one GFRP bent bar connector and with bond breaker sheets between the EPS insulation and the concrete layers, and composite action equal to 85% for specimen without bond breaker (standard panel). Test results showed that under flexural loads, the connectors were subjected to a combination of flexure and axial compression or tension. Similar conclusions were obtained by Maximos *et al.* (2007).They also presented results of two full scale tests on panels made with the GFRP bent bars and with dimensions

equal to 2.44 m × 9.14 m, 64 mm thick prestressed concrete layers and 76 mm thick EPS insulation. The panels were tested under uniformly distributed load, applied by an air bag.

The same researchers (Salmon *et al.*, 1997) compared the flexural behaviour of panels made with commercially available steel truss connectors with the proposed GFRP bent bar connectors. The tests were performed on prestressed panels with 2.44 m × 9.14 m subjected to uniformly distributed transversal load. The GFRP connectors were arranged longitudinally divided in three rows. The panel contained six 3 m long GFRP bent bars connectors (two for each row) in the edge most third of span and three connectors in three rows through the middle third of the span. were used n the proximity of supports, while only one 3 m long GFRP bent bar. In the panels with steel trusses, four connectors with diagonals having a cross sectional area of 30 mm^2 were used full length. They concluded that panels made with GFRP connectors generated 82% composite action and panels made with steel trusses had 88% composite action under service loads. The behaviour of sandwich panels containing GFRP bent bar connectors were further investigated by the same researchers from University of Nebraska (Maximos *et al.*, 2007, Morcous *et al.*, 2010) in order to optimize the design using this type of connector (also referred as NU-Tie connector). They recommended that panels with FRP connectors be designed such that connector failure occurs after yielding of longitudinal reinforcement to give adequate warning of failure.

The flexural behaviour of sandwich panels made with GFRP pin connectors was studied by Pahn and Hanz (2012) and Tomlinson (2015). The study performed by Tomlinson (2015) evaluated the effect of shear connector reinforcement ratio (i.e., ratio of total cross-sectional area of connectors located within the shear span to panel surface area in the shear span), in terms of using different diameters and spacing, on the flexural behaviour of panels. The specimens were 2.4 m long, 1.55 m wide and 26 cm thick (being two 5.5 cm concrete layers and 15 cm XPS foam insulation). The connectors consisted of pins fabricated from readily available GFRP bars. Three diameters of the GFRP connectors were used: 6.35 mm, 9.53 mm, and 12.7 mm. The spacing of connectors varied from 225 mm to 750 mm. He concluded that, as reinforcement ratio of GFRP shear connectors increased from 0.026% to 0.098%, the ultimate load of panels increased from 58% to 80% of the strength of the fully composite panel. For the tested panels, it was estimated that the strength of non-composite panel was equal to 20% of the fully-composite panel. It was estimated that the adhesion and friction between XPS foam core and concrete has contributed about 50% of the ultimate load. He observed relative slip between concrete layers at the end of the panel and associated to the

inherent low degree of composite action of panels.

In a recent past, Choi *et al.* (2015a) and Kim and You (2015) reported results of experimental programs conducted with sandwich panels consisted of GFRP shear grid connectors. Indeed, the GFRP shear grids are quite similar to the CFRP grid studied by the researchers from the North Carolina State University, differing mainly due to the use of glass fibre reinforcement of polymer. Both works tested concrete sandwich panels 3.6 m long, 1.2 m wide and 22 cm thick (6 cm thick concrete layers and 10 cm thick insulation material). In order to investigate the effect of the pull-out loads that the panels can be induced during their service life, i.e., induced by the wind suction, Choi *et al.* (2015a) tested panels under four-point bending tests with the panels in the horizontal position and the load applied in the positive (downwards) and negative (upwards) directions. The specimens were made with different types of insulation materials: EPS, XPS, and XPS plates with surface treatments (roughened surface and traction-free surface). The sandwich panels were made with two, three and four 1.10 m long GFRP grid connectors in each shear span. They found that the panels made with EPS foam, when loaded downwards, present similar flexural strength, with weak dependence on the number of connectors. Nonetheless, when loaded upwards, the results presented some dependence on the number of shear grids. This behaviour was justified by the fact that the pull-out forces weakened the adhesive bonds between concrete and EPS. The average degree of composite actions of panels made with EPS foam were equal to 26% and 57%, when calculated in terms of initial stiffness and ultimate strength, respectively.

An extensive experimental program was carried out by Naito *et al.* (2011) to evaluate the flexural behaviour of concrete sandwich panels. Three different experimental series were conducted: 42 specimens tested under single-span panels with idealized supports (0.53 m × 3.66 m and 0.81 m × 3.66 m). 12 two-span panels with intermediate connections (0.81 m × 7.30 m) and 4 single-span panels with end connections that are representative of the actual connectors used in sandwich panels construction (0.81 m × 3.66 m). Different layouts and types of commercially available connectors were investigated with reinforced and prestressed concrete panels. All the panels were tested under an approximate uniform load along the span. They found that, in general, reinforced concrete sandwich panels provided greater ductility than prestressed sandwich panels. The lowest degrees of composite action were obtained for plastic pin-connectors (without fibre reinforcement) and the highest values obtained when CFRP grid connectors were used. They also concluded that the use of stiff truss type ties results in a stiff flexural response, whereas the use of flexible steel C-clip ties

results in more appreciable softening of the flexural response after cracking.

Tomlinson (2015) performed seven flexural tests in order to investigate behaviour of panels made with BFRP connectors. The panels were 2.70 m long, 1.20 m wide and 27 cm thick. The panels consisted of two 6 cm thick concrete layers and a 150 mm thick XPS thermal insulation. The structural concrete layer had two ribs (approximately 9 cm high and 5 cm wide) along the length of the panel. The effect of type of reinforcement material (i.e., steel and BFRP) for the concrete layers were also investigated. For comparison purposed, some specimens were made with one type of steel shear connector. Both types of connectors, i.e., steel and BFRP, consisted of two bars: one positioned perpendicular to the concrete layers and other angled 45º. The connectors were arranged in two rows with five connectors each. The specimens were tested under four point bending configurations, with the load applied to the façade concrete layer to simulate the wind pressure. From the test results it was found that steel-reinforced walls showed a flexural strength-based composite action exceeding 90% with steel connectors and 75% with BFRP connectors. On the other hand, panels made with BFRP-reinforced walls and BFRP connectors showed only 51% composite action. When evaluating composite action based on deflection, rather than load, the walls generally had substantially lower composite action, ranging from 3.0% to 6.9%. This low value was justified both by the shear deformation through the panel, which reduces the effective stiffness, and the high stiffness of the theoretical fully composite case. Though composite action based on deflection is low, the tested panels showed between 1.9 and 3.0 times the stiffness of the theoretically non-composite case.

Recently, Chen *et al.* (2015) evaluated the flexural behaviour of six sandwich panels made with GFRP plates. The panels were 2743 mm long, 610 mm wide and 254 mm thick and consisted of two rows of connectors. All the panels also had 305 mm long solid zones in each extremity, which may collaborate to the shear transmission in the sandwich panel. They observed that the first failure of panels made with segmental and continuous connectors was due bending, while the panels made with discrete connectors presented a first failure associated to shear failure of panel. The degree of composite actions calculated based on deflections were 68%, 84% and 93% for discrete, segmental and continuous connectors, respectively. Finally, they concluded that continuous and segmental shear connectors performed better than discrete shear connector and that the use of discrete shear connector is not recommended.

2.4.5   Seismic behaviour

Since the 1950s, some research works have been developed to access the behaviour of prestressed/reinforced concrete walls under monotonic or simulated earthquake loading (Barda *et al.*, 1977, Paulay *et al.*, 1982, Kypros and Amr, 1995, Hidalgo *et al.*, 2002, Cevdet K. Gulec and Bozidar, 2008, Kuang and Ho, 2008, Cevdet K. Gulec and Bozidar, 2009, Massone *et al.*, 2009). Nonetheless, few attention was given for the use of precast/prefabricated wall systems as primary lateral load resisting system in seismic regions (Crisafulli *et al.*, 2002, Holden *et al.*, 2003, Perez *et al.*, 2003, Todut *et al.*, 2014). The seismic performance of precast/prefabricated structural wall systems is not well understood because experimental research on walls is quite difficult from a practical point of view (Pavese and Bournas, 2011). Moreover, most of these studies are focused on the behaviour of slender cantilever walls, giving relatively few attention for concrete walls with a height to length ratio of less than 2, hereinafter referred as squat walls.

Only few and recent research works are available concerning their behaviour under seismic loads. The works developed by Pavese and Bournas (2011) and by Ricci *et al.* (2013) present studies on the behaviour of single reinforced concrete cast-in-place squat sandwich panels under pseudo-static (cyclic) loadings. The behaviour of the complete structural system under earthquake (dynamic) loadings was investigated by Rezaifar *et al.* (2008) and Palermo *et al.* (2014).

Chapter 3

SFRSCC CHARACTERIZATION

The technology of the sandwich panel proposed in this thesis is based on the synergic combinations of two non-conventional materials for the construction: the SFRSCC for the external layers and the GFRP of the connectors and a thermal insulation material. To understand the behaviour of the structural panel is important to understand the behaviour of each of its singular components.

Fibre Reinforced Concrete (FRC) is a composite material that is characterized by an enhanced post-cracking tensile residual strength, also defined as toughness, due to the fibre reinforcement mechanisms provided by fibres bridging the crack surface (Prisco *et al.*, 2009b). Since fibre reinforcement mechanisms are mainly activated after cracking of the concrete matrix, fibres have marginal influence in the behaviour of uncracked elements. Therefore, concrete tensile strength is related to the matrix strength and is not influenced by fibres (ACI Committe 544, 1997, Bentur and Mindess, 2006a).

To enhance concrete toughness for structural applications, high-modulus fibres can be used to substitute, partially or totally, conventional reinforcement. Other types of fibres, having usually a low modulus and a small size (length of few millimetres and diameter of few microns) can be used to reduce shrinkage cracking and to enhance fire resistance (Prisco *et al.*, 2009b).

In special cases the use of high fibre contents can even completely replace conventional steel reinforcement showing a hardening controlled behaviour in bending. This feature is particularly interesting for thin elements, where traditional reinforcement cannot be easily used, because it requires minimum covers to guarantee durability (Prisco, 2009).

The synergy between Self-Compacting Concrete (SCC) and Fibre-Reinforced Concrete (FRC) combines the benefits of the former's superior fresh state behaviour with the enhanced performance of the latter in the hardened state. Due to the elimination of compaction and vibration and thanks to the suitably adapted rheology of the concrete matrix, a homogeneous dispersion of fibres within SFRSCC elements can be achieved, which is crucial for a reliable structural performance (Ferrara *et al.*, 2010).

Although SFRSCC mechanical properties have been already extensively studied (Groth, 2000, Grunewald, 2004, Schumacher, 2006, Cunha, 2010a, Laranjeira, 2010b), only few experimental data is available on tensile behaviour of SFRSCC. When compared to bending tests on concrete, tensile tests are much more difficult to perform due to the difficulties in assuring stable tests in the post cracking phase, which is the relevant for capturing the fibre reinforced benefits (Hordijk, 1991b).

Moreover, only limited research has been conducted on use of SFRSCC in thin-walled elements. In such materials the fibre orientation is strongly influenced by the method of casting and shape of the elements. The effect of alignment by the boundary conditions (wall effect), which is expected to occur in thin structural elements has to be recognized to get a more reliable basic stress-strain relation which reflects the mean basic behaviour of the fibre reinforced concrete (Walraven, 2009). Hence, the mechanical properties of SFRSCC determined from specimens cast in small moulds may not represent the material behaviour of the material with the same mix proportioning in the actual structural element.

This chapter arises from the necessity of understand the mechanical behaviour of the SFRSCC used in the other investigations developed in this thesis. In what concerns the mechanical properties of the SFRSCC, the most contribution of fibre reinforcement is to the post-cracking behaviour of material. Thus, it is expected that the main mechanical properties of the SFRSCC may be also affected by this variables. Indeed, some recent researches have attempted to clarify this issue (Ferrara and Meda, 2006, Stähli *et al.*, 2008, Martinie *et al.*, 2010, Ferrara *et al.*, 2012c, Abrishambaf *et al.*, 2013, Švec *et al.*, 2014), but none of them are

conclusive on how the traditional characterization tests procedures leads to values divergent to the actual properties of the material on the structural element and further research is required for a better understanding of this aspect.

In summarized manner, this Chapter encompasses:

- the characterization of some properties of SFRSCC related to the mechanical behaviour of the sandwich panels;
- research in the material scale to evaluate if standardized method to evaluate the post-cracking behaviour is still valid for characterizing the material on a structural element, despite its geometry and;
- investigation to achieve a better understanding of how the concrete flow of self-compacting concrete affects the SFRSCC properties, obtain acceptable design values for the parameters that characterize the post-cracking behaviour of SFRSCC and to correlate the properties of the material on the structural element with the obtained from the well know standardized tests.

3.1   RAW MATERIALS AND COMPOSITIONS

The materials used in the composition of the concretes used in this thesis are: Cement CEM I 42.5R (C), water (W), superplasticizer of third generation (S) based on polycarboxylates (SIKA 3005 HE), limestone filler (L_{FI}), fine river sand (F_S), coarse river sand (C_S), coarse aggregate and hooked end steel fibres.

Two main types of SFRSCC are here investigated, hereafter denominated types A and B. The SFRSCC type A corresponds to concrete produced with granite coarse aggregates (G_{CA}) and the type B corresponds to a concrete obtained with limestone coarse aggregates (L_{CA}). These concretes also differ on the type of fibre adopted. Both are produced with hooked end steel fibres. However, these fibres are produced by different manufacturers and differ on their geometry properties, as can be verified on Table 4. The SFRSCC A and B uses, respectively, the steel fibres A (S_{FA}) and steel fibres B (S_{FB}).

Table 4: Geometric properties of the hooked end steel fibres used in this research

Type of fibre	Type of fibre	Wire diameter d [mm]	Fibre length L_f [mm]	Aspect ratio $\lambda = L_f/d$ [mm]	Tensile strength [N/mm^2]
A	Radmix RAD 65/35 HW	0.50	35	70	1300
B	Ibermix HER 0.55/35 BL M	0.55	35	65	1244 - 1446

The mix composition has followed the procedures described elsewhere (Pereira *et al.*, 2004) in order to take into account the influence of the fiber content and properties on the skeleton organization of the aggregates, and the paste percentage.

The Table 5 summarizes the composition of the different castings corresponding to the two types of SFRSCC and to one type of Self-Compacting Concrete (SCC) made with the same constituent materials and similar composition of the cementitious matrix used for SFRSCC A.

Table 5: Compositions of the concretes used in this research

Type of Concrete	Casting	C [kg]	W [kg]	S [kg]	L_{FI} [kg]	F_{RS} [kg]	C_{RS} [kg]	C_{GA} [kg]	C_{LA} [kg]	S_{FA} [kg]	S_{FB} [kg]
SFRSCC A	1-7	412	124.0	7.83	353	179	655	588	-	60	-
SFRSCC B	8-10	413	148.0	7.83	353	233	700	-	582	-	-
	11	413	179.1	7.83	353	233	700	-	582	-	60
	12	413	186.9	7.83	353	233	700	-	582	-	60
	13-15	413	174.7	7.83	353	233	700	-	582	-	60
	16-19	413	182.4	7.83	353	233	700	-	582	-	60
SCC	20-21	412	106.0	7.83	353	179	655	588	-	60	-
	22	413	116.0	7.83	353	179	655	588	-	60	-

The SFRSCC A and B also differ on the manufacturing conditions adopted. The concrete type A is produced in a lab condition, using a mixer with 200 l capacity. The concrete B is produced in a precast concrete plant by using an industrial mixer of vertical axis, with 1000 l capacity.

Attention is paid to the fact that the water/cement ratio and the content of aggregates between the two types of SFRSCC also slightly differ due to the required adjustments to attain self-compatibility with the different constituent materials and production conditions. Even

between different castings of the SFRSCC type B, the water content of the concretes slightly differs to compensate for the aggregate absorption (see Table 5).

3.2   FLOW SPREAD OF FRESH CONCRETE

The flow spread (D_{fl}) values of SFRSCC from each casting, shown in Table 6, were obtained in the fresh state by using the inverted Abram's cone and following the recommendations of EFNARC (EFNARC, 2005). Average flow spreads equal to 671 mm, 661 mm and 733 mm were obtained for SFRSCC A, SFRSCC B and SCC, respectively. A relatively reduced value was obtained for the SFRSCC B, casting 10. Possibly this reduced value was caused by a sum of effects: the reduced water content and the higher period of time between its mixing phase and the flow test.

3.3   COMPRESSIVE BEHAVIOUR

From each concrete batch, 150×300 mm (diameter $\times$ height) cylinders were taken for compressive tests. All the specimens were cured under the same laboratory temperature and humidity conditions that the respective structural specimens were exposed. The tests of specimens from different castings were carried out at the ages indicated in Table 6.

To obtain the compressive strengths of different castings of both SFRSCC and SCC used in the experimental program, tests were performed based on the procedures given in EN 12390-3 (CEN, 2009). The tests were carried out in a servo-controlled machine with 3000 kN maximum load carrying capacity. To obtain the full stress-strain curves, some tests performed to obtain the compressive strength of concretes were performed under displacement control, under a displacement ratio of 10 μm/s. The tests were controlled by a LVDT mounted to measure the longitudinal displacement of the upper loading platen. The values registered by this LVDT are adopted to compute the longitudinal strain of the specimen, dividing the registered displacement by the length of specimen, for each data point.

The stress $\times$ strain diagrams presented in Figure 13 had the initial slopes corrected in order to disregard nonlinearities related to the friction between the plates of the machine and the specimen. This correction was made computing the slope corresponding to each 13 points until the peak load for each curve. Then, the greatest value of slope was identified and the

experimental points of the curve prior to this points were disregarded. So, the curve was translated in order to transform on the new origin the point that the line with the slope equal to the maximum value computed and that contain the point of the curve corresponding the maximum slope meets the x-axis. The strain at peak stress (ε_c) were determined from these corrected curves, being, by definition, the strain corresponding to the maximum stress attained during the test.

The energy dissipated per unit volume under compression (G_c) was calculated as the area under the corrected stress × strain curve, using the Eq. (9). The G_c value was determined for two ultimate deformations (ε_u): 7500 µε and 10000 µε.

$$G_c = \int_0^{\varepsilon_u} \sigma_c d\varepsilon \tag{9}$$

where σ_c is the stress in the SFRSCC.

Non-destructive elastic modulus tests were performed on some of the cylinders following the procedures described by the Portuguese standard LNEC E397 (1993) that are similar to the procedures of other standards, such as RILEM TC 14-CPC (1975) and ASTM C469 (1994). According to this specification, the test should be carried out under force control over a certain number of cycles. First, a stress corresponding to $\sigma_b = 0.5$ MPa is imposed to the specimen and the corresponding strain, ε_b, is registered. The stress is then increased at a velocity equal to 0.2 MPa/s until another stress level, σ_a, corresponding to 1/3 of the compressive strength of concrete ($f_c/3$). The stress σ_a, is maintained for 90s and in the last 30s of this interval, the strains ε_a are recorded. After this, the load is decreased to a stress level equal to σ_b. This stress level is also maintained for 90s and the corresponding strains are also recorded in the last 30s. The modulus of elasticity is then computed for the nth cycle using the Eq. (10). The modulus of elasticity of concrete is taken as the average value obtained in the cycles.

$$E_{c,n} = \frac{\sigma_{a,n} - \sigma_{b,n}}{\varepsilon_{a,n} - \varepsilon_{b,n}} \tag{10}$$

The strain was calculated from measurements of the displacements over a reference length equal to 10 cm. The longitudinal displacements were measured using three LVDTs evenly distributed along the perimeter of specimen (120° from each other). The LVDTs were attached to the specimens making use of steel rings positioned distancing 10 cm from each other. The average values and respective coefficient of variation (CoV) obtained for compressive strength (f_c), strain at peak (ε_{c1}), energy dissipated under compression (G_c) and modulus of elasticity (E_c) are presented in Table 6. The full compressive stress × strain relationship obtained in the tests performed under displacement control, for some castings of SFRSCC A and SFRSCC B, are presented in Figure 13.

Table 6: Values of flow spread of fresh concrete, compressive strength (f_c), strain at peak (ε_{c1}), energy dissipated under compression (G_c) and modulus of elasticity (E_c).

Type	Casting	Flow spread of fresh concrete [mm]	Compressive test											Modulus of elasticity test			
			Age [days]	N. of specim.	Compressive strength f_c [MPa]		Strain at peak stress ε_{c1} [με]		Energy dissipated G_c [MPa]				Age [days]	N. of specim.	Modulus of elasticity E_c [GPa]	
									up to $\varepsilon_c = 7500$ με		up to $\varepsilon_c = 10000$ με					
					Avg.	CoV	Avg.	CoV	Avg.	CoV	Avg.	CoV			Avg.	CoV
SFRSCC A	1	620	28	2	70.9	7.3%	-	-	-	-	-	-	28	2	37.17	2.6%
	2	620	28	1	68.99	0.0%	-	-	-	-	-	-	28	1	32.85	0.0%
	3	640	28	3	68.24	1.4%	-	-	-	-	-	-	28	2	34.2	1.5%
	4	720	21	2	70.87	12.0%	-	-	-	-	-	-	21	2	40.11	3.1%
	5	750	21	3	61.88	4.3%	-	-	-	-	-	-	21	3	37.02	6.5%
	6	680	77	4	68.77	7.5%	6427	0.6%	0.351	2.4%	0.496	1.4%	77	1	36.21	0.0%
	7	-	50	6	50.81	4.5%	5313	10.9%	0.259	4.7%	0.331	8.4%	50	4	33.26	4.8%
SFRSCC B	8	620	31	2	45.48	2.5%	5015	16.4%	0.175	4.8%	0.192	3.6%	31	2	33.93	0.6%
	9	700	31	1	44.74	0.0%	4356	0.0%	0.142	0.0%	0.153	0.0%	31	2	34.03	0.3%
	10	485	94	4	45.6	8.5%	3695	15.5%	-	-	-	-	94	2	34.6	3.5%
	11	600	66	4	56.39	3.4%	3774	14.2%	0.251	1.5%	0.294	0.0%	66	2	35.06	10.5%
	12	715	66	3	61.23	2.5%	4591	3.9%	0.271	5.5%	0.351	1.9%	66	2	35.89	16.1%
	13	680	67	4	61.94	5.2%	4340	6.1%	0.279	5.1%	0.323	5.7%	67	2	41.61	0.6%
	14	-	64	4	60.22	3.3%	4145	14.2%	0.255	4.0%	0.3	4.1%	64	2	41.17	3.3%
	15	-	52	4	60.06	7.2%	4430	12.2%	0.238	3.6%	0.274	0.8%	52	2	41.34	1.2%
	16	740	66	5	60.66	3.4%	4452	7.4%	0.251	10.6%	0.347	0.0%	66	3	40.44	0.3%
	17	-	66	3	63.46	2.2%	4265	16.5%	0.262	13.6%	0.339	2.1%	66	2	40.86	2.4%
	18	-	66	4	54.81	2.7%	3898	7.7%	0.226	8.1%	-	-	66	2	35.97	8.8%
	19	745	66	4	64.83	2.3%	4776	8.3%	0.271	1.6%	0.312	9.9%	66	2	42.2	2.6%
SCC	20	700	28	4	65.32	4.5%	-	-	-	-	-	-	38	2	34.27	17.3%
	21	730	28	4	72.15	2.0%	-	-	-	-	-	-	38	5	37.35	3.7%
	22	770	21	4	59.12	3.4%	-	-	-	-	-	-	21	3	34.63	2.7%

* - compressive tests of concretes corresponding the castings 1-5 and 20-21 were performed under loading rate control.
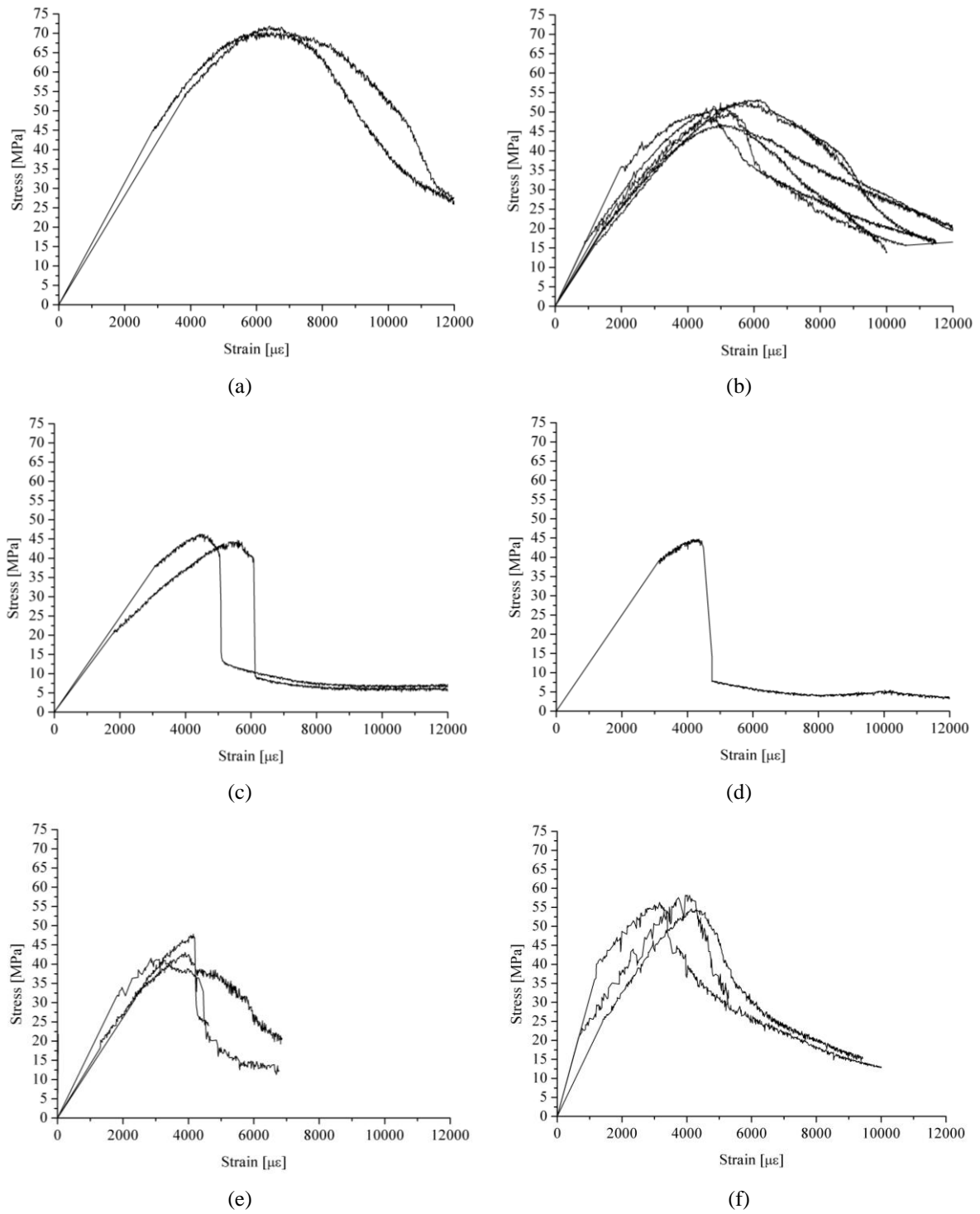
Figure 13: Experimental stress – strain relationships for SFRSCC A, castings: (a) 6 and (b) 7; and SFRSCC B, castings: (c) 8, (d) 9, (e) 10 and (f) 11.

(g)

(h)

(i)

(j)

(k)

(l)
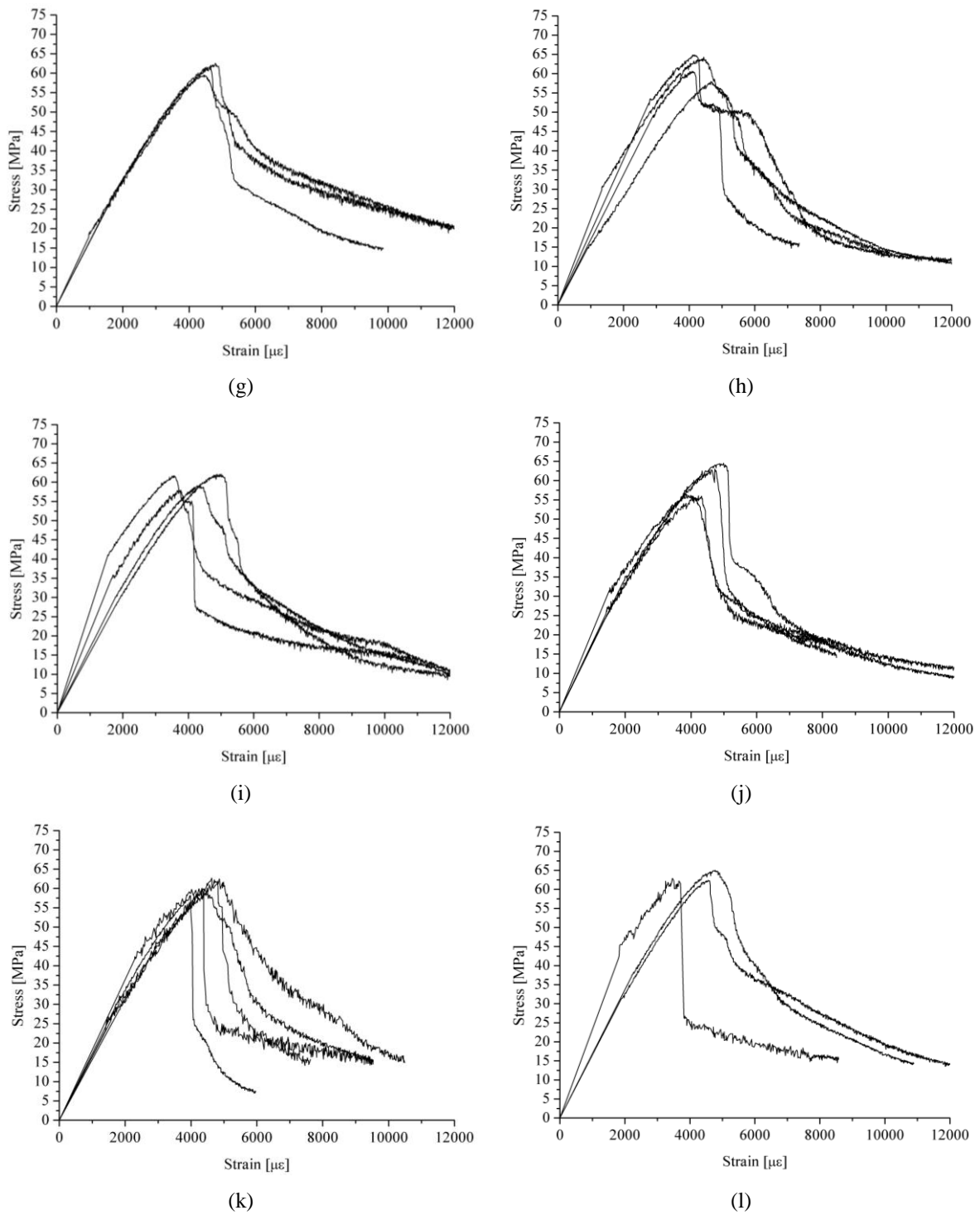
Figure 13: Experimental stress – strain relationships for SFRSCC A, castings: (g) 12, (h) 13, (i) 14, (j) 15, (k) 16 and (l) 17.

(m)   (n)
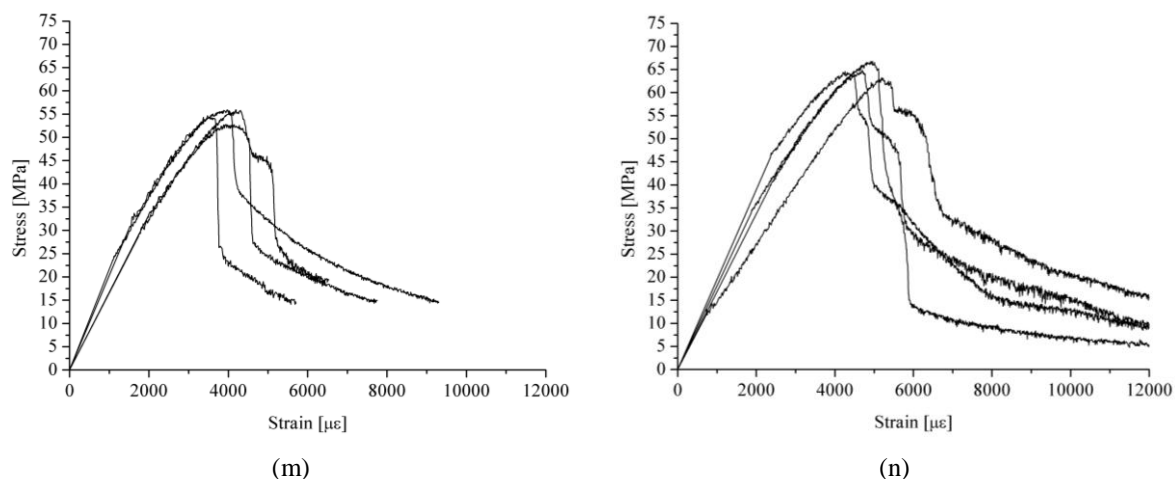
Figure 13: Experimental stress – strain relationships for SFRSCC A, castings: (m) 18 and (n) 19.

The results indicate average values of compressive strength equal to 63 MPa (CoV equal to 14%), 58 MPa (CoV equal to 11%) and 65 MPa (CoV equal to 9%) for SFRSCC A, SFRSCC B and SCC, respectively.

It is observed that the coefficients of variation of the results of compressive tests were high, and the differences registered amongst the groups are also significant, mainly between the casting group 8-10 and the remaining castings. Nevertheless, it is considered that this is a minor issue for the main objectives of the present research, since in spite of the recognized favorable effect of the compressive strength on a better mobilization of the reinforcement mechanisms, the available research in this respect suggests that the obtained differences do not have significant impact in this context, as long as the fibre failure mode is not changed, such was the case (Bentur and Mindess, 2006b).

The average values and respective coefficients of variation (CoV) obtained for the modulus of elasticity of SFRSCC were equal to 35.8 GPa (CoV equal to 7.7%), 38.2 GPa (CoV equal to 9.6%) and 35.9 GPa (CoV equal to 7.5%), respectively for for SFRSCC A, SFRSCC B and SCC.

Figure 14 shows the relationship between the compressive strength and modulus of elasticity of each casting corresponding to the studied SFRSCCs and SCC. Additionally, the analytical relationship between compressive strength and modulus of elasticity of plain concrete suggested by the European standard EN 1992-1-1 (2004) is plotted together with the experimental data.

(a)

(b)

(c)
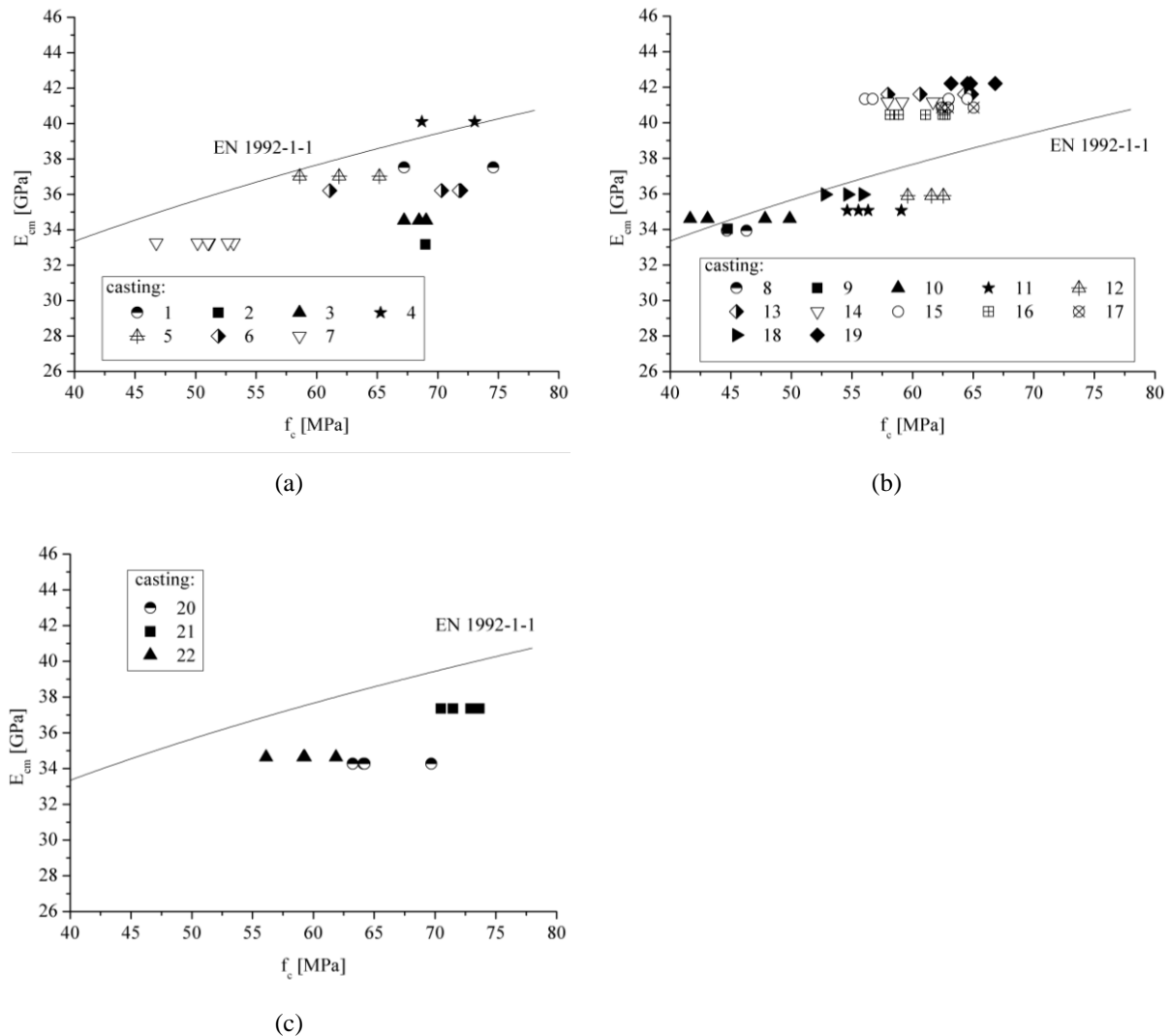
Figure 14: Relationship between the compressive strength and the average modulus of elasticity for:
(a) SFRSCC A; (b) SFRSCC B; (c) SCC.

3.4   POST-CRACKING BEHAVIOUR OF SFRSCC

Identification of the tensile constitutive behaviour of Fibre Reinforced Concrete (FRC) is an important aspect of the design of structural elements using this material. Although an important step has been made with the introduction of guidance for the design with regular FRC in the recently published *fib* Model Code 2010, a better understanding of the behaviour of this material is still necessary, mainly for that with self-compacting properties.

A new test method is proposed herein for assessing the post-cracking behaviour and the results obtained with the proposed test method are compared with the ones resulted from the standard three-point bending tests (3PBT). Specimens extracted from a sandwich panel

consisting of SFRSCC layers are also tested. The mechanical properties of SFRSCC are correlated to the fibre distribution by analysing the results obtained with the different tests. Finally, the stress-crack width constitutive law proposed by the *fib* Model Code 2010 is analysed in light of the experimental results.

The use of fibre reinforcement for concrete structures is a steadily increasing technology that is competitive in several applications. It is particularly attractive for statically indeterminate structures, since cracking control through fibre reinforcement mechanisms can provide high levels of stress redistribution, leading to load carrying capacity and deformability levels that are much higher than the cracking load and its corresponding deformation. In fact the energy dissipated on the concrete fracture propagation is the property that most benefits from including fibre reinforcement. This dissipated energy is, however, quite dependent on the fibre orientation and distribution (Kooiman, 2000, Markovic, 2006, Cunha, 2010b, Laranjeira, 2010a).

Therefore, accurate design approaches require the knowledge of fibre dispersion and orientation that is expected to be found into the structural element. These two parameters are, however, governed by several factors like: mixing and placing technology of fibre reinforced concrete (FRC), rheology of FRC, geometric and mechanical properties of the FRC constituents, mainly of fibres, and geometry of the structure (Dupont and Vandewalle, 2005, Gettu *et al.*, 2005, Ferrara *et al.*, 2008, Vandewalle *et al.*, 2008, Boulekbache *et al.*, 2010, Ferrara *et al.*, 2012a, Ferrara *et al.*, 2012b, Torrents *et al.*, 2012). These aspects are even more relevant in steel fibre reinforced self-compacting concrete (SFRSCC), due to the high flowability of this composite and the higher density of these relatively stiff fibres, leading to the tendency of fibres to align orthogonally to the concrete flux lines, as well as to sink into the SCC medium (Ferrara and Meda, 2006, Stähli *et al.*, 2008, Martinie *et al.*, 2010, Ferrara *et al.*, 2012c, Abrishambaf *et al.*, 2013, Švec *et al.*, 2014).

Several test methods have been proposed to assess the fracture mode I of the post-cracking behaviour of FRCs (RILEM TC 162-TDF, 2001, RILEM TC 162-TDF, 2002, CEN, 2005a, CEN, 2006a, CEN, 2006b). These methods are, in general, based on direct assessment (e.g., uniaxial tensile tests) or indirect approaches through bending, indirect tensile (Brazilian) and plate tests. These indirect approaches require further procedures to derive the constitutive law that, eventually, can simulate the fracture mode I propagation in FRC. Fracture mode I is characterized by the stress at crack initiation, σ_{cr}, the fracture energy, G_F, and the shape of the

stress (σ) *vs* crack width (*w*) diagram, σ−*w*. G_F corresponds to the energy dissipated on the formation of a unit area of crack surface, i.e., the area between the σ−*w* diagram and the abscissa axis representing the crack width, up to the ultimate crack width, w_u, that corresponds to null tensile stress:

$$G_F = \int_o^{w_u} \sigma(w) \cdot dw \qquad (11)$$

A direct tensile test under closed-loop displacement control is the most suitable method to determine G_F of a material (Hordijk, 1991a). This test generally uses notched specimens in order to create a weaker section, inducing the appearance of a single crack across the notched section of the specimen and favoring a more stable test. This increased stability is related to the fact that the control system generally follows the signal recorded in displacement transducers that are almost exclusively measuring the crack opening at the notched section (Hordijk, 1991a, Barros, 1995). However, due to the fibre pullout reinforcement mechanisms, mainly when using relatively long fibres, w_u is generally not attained in FRCs, resulting in estimated values of G_F that can be lower than the ones that actually characterize the material (Barros, 1995, Barragán, 2002). In an opposite way, a unique fracture surface is almost impossible to be guaranteed in FRCs, mainly when strain hardening cement composites are tested (Pereira *et al.*, 2012), therefore the evaluated G_F can result in overestimations.

Apart from these concerns on the evaluation of G_F, the direct tensile test is expensive and time consuming. Moreover, there is a multiplicity of technical problems that make the uniaxial tensile test difficult to be performed, namely the perfect alignment of the specimen with the actuator in order to avoid undesired bending, and the difficulties of properly fixing the specimen to the equipment (Hordijk, 1991a, Barros, 1995, Shah *et al.*, 1995, Van Mier, 1997, Bažant and Planas, 1998, Cunha, 2010b).

Owing to the difficulties in performing direct tensile tests, standard test methods for assessing the post-cracking behaviour are generally based on notched beam bending tests (RILEM TC 162-TDF, 2002, CEN, 2005a, CEN, 2006a, ASTM Standard C1550, 2010). Three and four point bending tests (3PBT and 4PBT, respectively) are commonly adopted. Among the different standards and proposals, differences can also be found in the size of specimens and in the presence or absence of a notched section. In spite of its simplicity, this type of test is known to have limitations, such as the necessity of performing inverse analysis procedures to obtain the stress *versus* crack opening relationship (σ-*w*). Furthermore, in the case of SFRSCC

testing, the standardized geometries and casting procedures can conduct to a material that is not representative of the SFRSCC employed in the actual structure. This is aggravated in the cases where SFRSCC is used in thin structural elements (e.g., shell structures) (Ferrara and Meda, 2006, di Prisco *et al.*, 2009).

In an attempt to avoid the limitations of the aforementioned tests, Ozyurt *et al.* (2007) and Carmona and Aguado (2012) proposed the adoption of Splitting Tensile Test (STT), also known as Brazilian test, to evaluate the post cracking behaviour of FRC. This is a relatively simple test method in which the specimen can be obtained through drilling (either from a prototype, or even from the actual structure). The main limitation of this test is the fact that it is an indirect test, with the overlapping of compressive and tensile stresses at the fractured section of specimen.

Seeking the advantages of the splitting test, and trying to minimize its limitations, some authors proposed similar alternatives, like the Double Edge Wedge Splitting (DEWS) test and the Modified Splitting Tensile Test (MSTT).

The DEWS test was originally conceived by Brühwiler and Wittmann (1990) for plain concrete, and was recently suggested by di Prisco *et al.* (2013) for the characterization of FRC. It consists of a rectangular specimen with angular notches at the proximity of the load application. This test aims to assure absence of accompanying compression fields perpendicularly to the load direction in the central region of the specimen by adopting angular notches in its loaded regions. These notches also induce the formation of only one fracture plane in the central part of specimen.

In turn, the MSTT was introduced by a group of researchers from the University of Minho (Abrishambaf *et al.*, 2013). It consists on the use of a cylinder specimen with vertical notches along the loading plane, obtaining a weakened section in the middle of specimen.

The main differences between the DEWS and MSTT are the geometry of the specimens (cylindrical for MSTT and prismatic with square section for DEWS), and the process used to form the fracture plane at the middle of specimen. An advantage of the DEWS is the fact that in this test the crosswise compressive stresses are deviated from the ligament by means of the angular notches and a pure mode I fracture is likely to be induced along the fractured section. Nevertheless, despite the actions taken to induce only one fracture surface, the formation of

multiple parallel cracks has been reported by di Prisco *et al.* (2013) for some tests made adopting the DEWS.

The DEWS and MSTT have been used to evaluate the influence of the FRC flowability on the fibre distribution and orientation, and corresponding consequences on the fracture properties of this composite (Ferrara and Meda, 2006, Ozyurt *et al.*, 2006, Ozyurt *et al.*, 2007, Stähli and van Mier, 2007, Stähli *et al.*, 2008, Boulekbache *et al.*, 2010, Torrijos *et al.*, 2010, Akcay and Tasdemir, 2012, Ferrara *et al.*, 2012a, Zerbino *et al.*, 2012). Analytical and numerical approaches have been also presented in this respect, respectively, by Laranjeira *et al.* (2012) and Cunha *et al.* (2011). Nonetheless, it is still not clear for structural designers how these aspects should be taken into consideration while designing a structural element made with SFRSCC.

In the present work experimental tests were carried out with standard 3PBT specimens, with specimens extracted from prototypes and from real scale sandwich panels formed by outer SFRSCC layers and a polystyrene foam core (thermal insulation). A new test method, which arose from adaptation of DEWS and MSTT test methods was proposed. The tests were planned for assessment of the influence of casting conditions on fibre distribution and orientation. Finally, the results obtained from the different tests are compared in order to discuss the capacity of the different characterization tests in regard to modelling SFRSCC behaviour of actual structures where such material is applied.

3.4.1 RILEM TC 162-TDF recommendations

For the characterization of the post-cracking behaviour of SFRC, RILEM TC 162-TDF initially recommended the evaluation of the equivalent flexural tensile strength parameters, one to be used for the design at serviceability limit states, $f_{eq,2}$, and the other for the design at ultimate limit states, $f_{eq,3}$, in regard to reference vertical deflections (δ) during the experiment (RILEM TC 162-TDF, 2000a, RILEM TC 162-TDF, 2000b). Later, RILEM TC 162-TDF has proposed the replacement of f_{eq} for the concept of residual flexural tensile strength, f_R, which gives the stress for distinct deflections or crack mouth opening displacements, (CMOD) (RILEM TC 162-TDF, 2002). Although this last concept has the advantage of being easier to evaluate, it is more susceptible to the irregularities of the force-deflection relationships registered in the tests.

The specimen geometry proposed by RILEM TC 162-TDF recommendations (RILEM TC 162-TDF, 2002) is shown in Figure 15. For specific information on the method for casting the specimens, the curing procedures, the position and dimensions of the notch sawn into the specimen, the loading and specimen support conditions, the characteristics for both the equipment and measuring devices and the test procedures, the reader is forwarded to the RILEM TC 162-TDF recommendations. Such specific information has been omitted here for the sake of brevity.
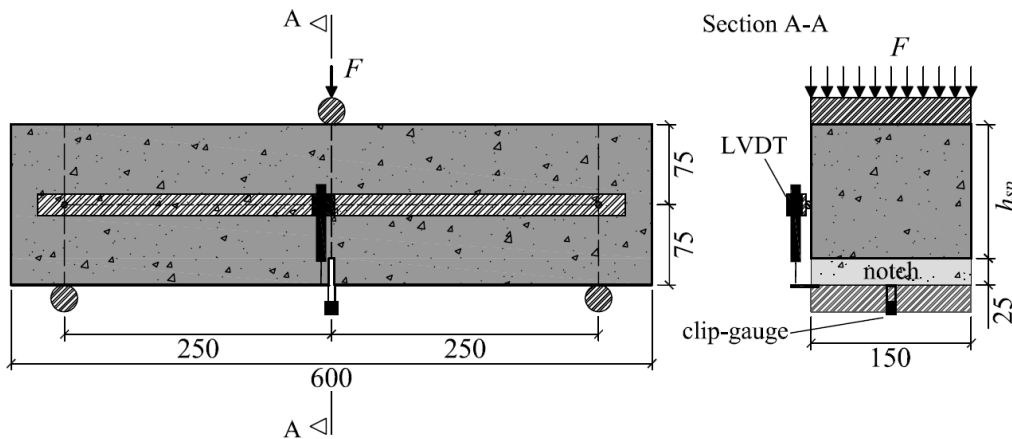
Figure 15: Three-point bending test setup (RILEM TC 162-TDF, 2002) (units in millimetres).

A typical force (F) deflection (δ) relationship, F-δ, for this 3PBT testing procedure is shown in Figure 16. If a displacement transducer is mounted at the notch mouth, the F-$CMOD$ relationship can also be recorded. Using these relationships, RILEM TC 162-TDF proposed the evaluation of the load at the limit of proportionality (F_L), the equivalent ($f_{eq,2}$ and $f_{eq,3}$) and the residual ($f_{R,1}$ and $f_{R,4}$) flexural tensile strength parameters (RILEM TC 162-TDF, 2000a, RILEM TC 162-TDF, 2003). F_L is the highest value of the load recorded up to a deflection (or $CMOD$) of 0.05 mm. The parameters $f_{eq,2}$ and $f_{eq,3}$ are related to the material energy absorption capacity up to a deflection of δ_2 and δ_3 ($\delta_2 = \delta_L + 0.65$ mm and $\delta_3 = \delta_L + 2.65$ mm, where δ_L is the deflection corresponding to F_L) provided by fibre reinforcement mechanisms ($D^f_{BZ,2}$ and $D^f_{BZ,3}$), as seen in Figure 16. $D^f_{BZ,2}$ and $D^f_{BZ,3}$ are computed following the procedures described elsewhere (RILEM TC 162-TDF, 2000a). The parameters $f_{R,1}$ and $f_{R,4}$ are the stresses for the forces $F_{R,1}$ and $F_{R,4}$, respectively, at deflection of $\delta_{R,1} = 0.46$ mm and $\delta_{R,4} = 3.0$ mm. According to RILEM TC 162-TDF, the limit of proportionality ($f_{fct,L}$), the equivalent (RILEM TC 162-TDF, 2000a) and the residual (RILEM TC 162-TDF, 2002) flexural tensile strength parameters are obtained from the following equations:

$$f_{fct,L} = \frac{3}{2} \frac{F_L L}{bh_{sp}^2}$$ (12)

$$f_{R,1} = \frac{3}{2} \frac{F_{R,1}L}{bh_{sp}^2} \quad ; \quad f_{R,4} = \frac{3}{2} \frac{F_{R,4}L}{bh_{sp}^2}$$ (13)

$$f_{eq,2} = \frac{3}{2} \frac{D_{BZ,2}^f}{0.50} \frac{L}{bh_{sp}^2} \quad ; \quad f_{eq,3} = \frac{3}{2} \frac{D_{BZ,3}^f}{2.50} \frac{L}{bh_{sp}^2}$$ (14)

where b (=150 mm) and L (=500 mm) are the width and the span of the specimen, and h_{sp} (=125 mm) is the distance between the tip of the notch and the top of the cross section.
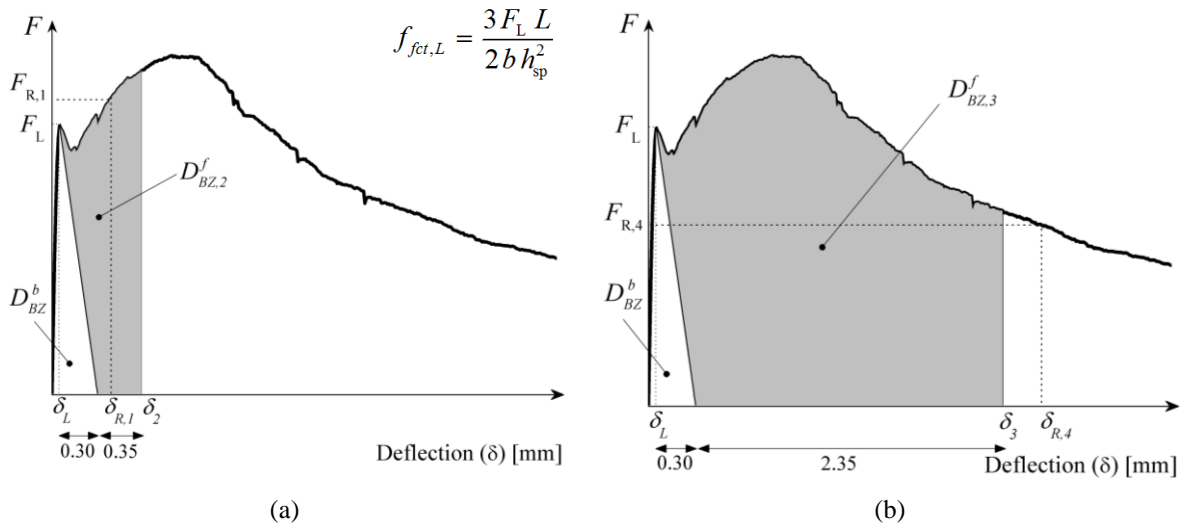
Figure 16: Evaluation of: a) $f_{eq,2}$ and $f_{R,1}$, b) $f_{eq,3}$ and $f_{R,4}$ flexural tensile strength parameters according to RILEM TC 162-TDF (RILEM TC 162-TDF, 2000a, RILEM TC 162-TDF, 2002)

3.4.2 *fib* Model Code 2010 recommendations

While the RILEM approach makes use of equivalent flexural tensile strength parameters ($f_{eq,2}$ and $f_{eq,3}$), the *fib* Model Code 2010 is based solely on the residual parameters ($f_{R,j}$). Furthermore, in the *fib* Model Code 2010 the deformations are expressed in terms of CMOD, not being necessary to measure deflections, as recommended by the RILEM TC 162-TDF (RILEM TC 162-TDF, 2000a).

A typical Force-*CMOD* relationship obtained from a three-point beam bending test following the *fib* recommendations is represented in Figure 17. The geometry and the production of the

specimen are the same ones recommended by RILEM TC 162 TDF, as well as the loading and support conditions (RILEM TC 162-TDF, 2000a).
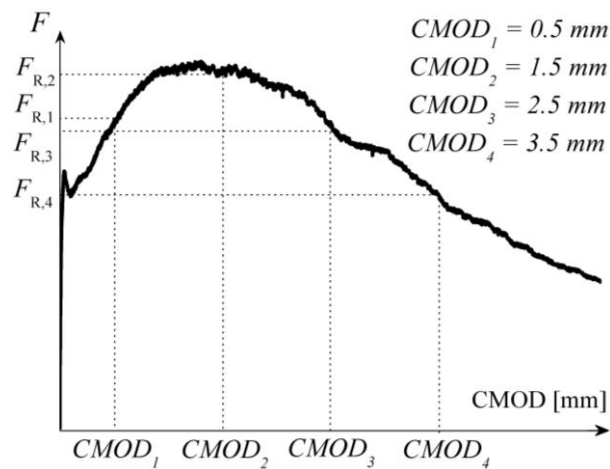
Figure 17: Typical load F – $CMOD$ curve for FRC (*fib*, 2012a, *fib*, 2012b).

Based on the force values for the $CMOD_j$ ($j=$ 1 to 4, see Figure 17), the corresponding force values, F_j, are obtained, and the derived residual flexural tensile strength parameters are determined from the following equation:

$$f_{R,j} = \frac{3 F_{\mathrm{j}} L}{2 b h_{\mathrm{sp}}^2}$$

(15)

where f_{Rj} [N/mm^2] and F_j [N] are, respectively, the residual flexural tensile strength and the load corresponding to $CMOD = CMOD_j$ [mm].

3.4.3   Experimental Program: Three-point bending test (3PBT)

A total of 47 beams of size $150 \times 150 \times 600 \text{ mm}^3$ were cast according to the recommendations of EN 14651 standard (CEN, 2005a) by using SFRSCC from the castings 3 and 5 (SFRSCC A), 10 to 13 and 16 to 19 (SFRSCC B). The beams were notched at midspan by using a saw-cutting equipment. The depth of the notch was about 25 mm along the width of the specimen's cross section. The final dimensions of all the specimens were measured and were taken into consideration on the evaluation of the results.

Three-point bending tests (3PBTs) on notched specimens were carried out in accordance with the recommendations of RILEM Technical Committee TC 162-TDF (2002) – see schematic representation and photo in Figure 18. The tests were performed under displacement control with a servo-hydraulic testing machine by using a linear transducer (LVDT). Until a

deflection of 1 mm, the test was performed at a constant rate of 0.2 mm/min. When this deflection was reached, the deflection rate was increased to 0.4 mm/min. Two additional LVDTs were used to measure the Crack Mouth Open Displacement (CMOD) placed at the locations shown in Figure 18(a). Following the recommendations of RILEM TC 162-TDF in terms of the loading and casting directions, the deflection and the CMOD were measured as illustrated in Figure 18. The $CMOD_T$ and $CMOD_B$ represent, respectively, the CMOD registered in the top and bottom surfaces considered in the casting process of the specimen.

(a)   (b)
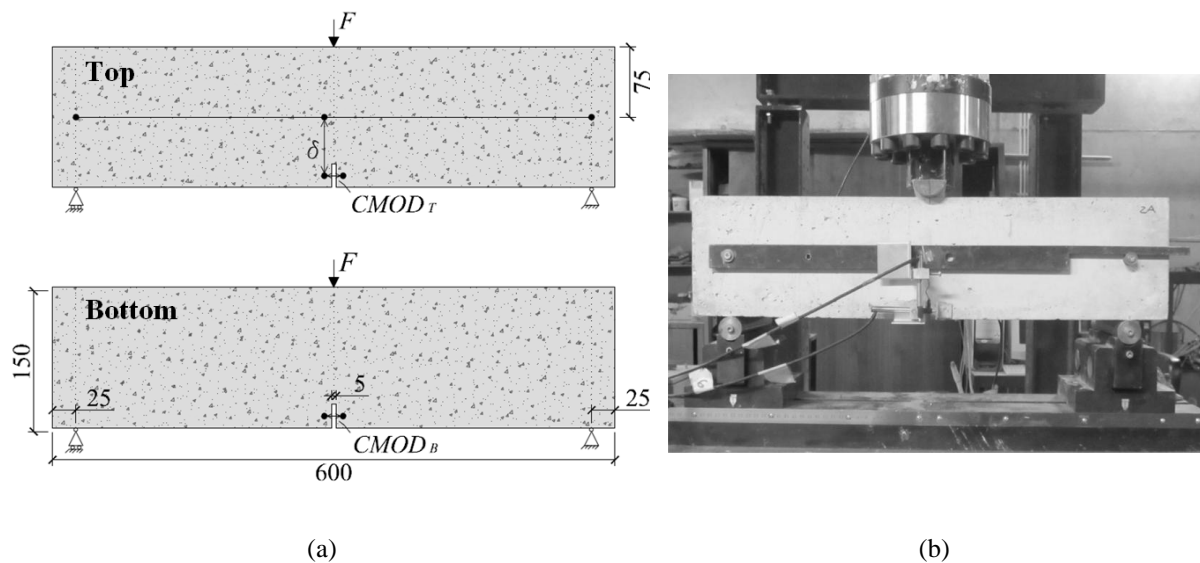
Figure 18: Test set-up of 3PBT: (a) schematic representation; (b) general view of top surface (units in millimetres; Top/Bottom: refers to the casting position of specimens).

From the 3PBT, the following results were computed: limit of proportionality ($f_{fct,L}$); equivalent flexural tensile strength ($f_{eq,2}$ and $f_{eq,3}$) and residual flexural tensile strengths. These results were obtained corresponding to the following the CMOD equal to 0.5, 1.5, 2.5 and 3.5 mm (f_{R1}, f_{R2}, f_{R3} and f_{R4}, respectively), as recommended by the *fib* Model Code. All the 3PBT were performed up to a midspan deflection equal to 4.0 mm, which was verified to be almost coincident to a crack width of 4.0 mm, what was already expected based on the relationships between deflection and CMOD reported in the literature (RILEM TC 162-TDF, 2000a). The 3PBT were always conducted 28 days after the casting of specimens.

3.4.4   Experimental Program: Splitting test

For the splitting tests, only the SFRSCC from casting 16 (SFRSCC B) was considered. The specimens used in this study were obtained by drilling from a flat plate (laboratory prototype)

and from a full-scale sandwich wall panel developed by the authors in the context of the research presented in Chapter 9. The tests carried out in specimens extracted from these elements will therefore allow to take conclusions about the flow induced orientation and dispersion of fibres on the post-cracking behaviour of this material.

The flat plate has the dimensions of $1.5 \times 1.0 \times 0.06 \ \text{m}^3$ and was casted with the SFRSCC feeding permanently at its central point (see Figure 19(a)), letting the SFRSCC to flow radially until complete filling of the steel formwork. Abrishambaf *et al.* (2013) have shown that for a plate with dimensions $1.5 \times 1.0 \times 0.06 \ \text{m}^3$, a uniform flow profile that diffuses outwards radially from the centre of the panel is achieved. This casting process was chosen since the high flowability of the developed SFRSCC suggests high probably of being adopted in several real applications. The sandwich wall panel (shown in Figure 19) was poured in accordance with the procedures commonly adopted in the precast plant of the industrial partner, with the SFRSCC feeder moving along all the surface of the panel. The SFRSCC layer thickness of the sandwich panel from which the specimens were extracted was equal to the thickness of the flat plate, that is, 60 mm. In both cases, no specimens were extracted from the vicinity of the edges of the formwork, as shown in Figure 19, in order to reduce the interference of the wall effect from the lateral formwork on the results. The drilling operation was performed when the panels were already in their hardened-mature phase. In the flat plate the specimens were extracted from a distance of 300 mm and 600 mm from its centre (see Figure 19(a)). In the sandwich panel, the specimens were extracted from the bottom layer of the panel, that was cast over the same steel surface used for casting the flat plate, thus keeping similar flowing conditions. As shown in Figure 19(b), the specimens of the sandwich panel were obtained from the lateral regions of its opening, in the region between the embedded Glass Fibre Reinforced Polymer (GFRP) connectors. These GFRP plate connectors were positioned perpendicularly to the surface of the SFRSCC layers and were embedded on these layers, as is described in Lameiras *et al.* (2013c). Due to its flat nature and the relative proximity of these connectors, it is believed that, independently of the casting procedure, the SFRSCC had the tendency of flowing along the corridors formed by the connectors (*y*-direction in Figure 19(b)). In the $1.5 \times 1.0 \ \text{m}^2$ flat plate, the extracted specimens were submitted to a loading direction coincident with the notched plane executed in the specimen (Figure 19 and Figure 22). Since notched planes parallel and orthogonal to the flux lines of the SFRSCC were cut, the test results can provide information about the influence of the casting technology on the post-cracking behaviour of this material. With the same aim, the

notched planes on the specimens extracted from the sandwich panel were cut in the *x*-direction and *y*-direction, since as already indicated, these are the critical directions in terms of fibre orientation and distribution. Before the drilling process, the positions and the notched planes of the specimens were marked, as shown in Figure 19(c) and Figure 19(d).

(a)

(b)

(c)

(d)
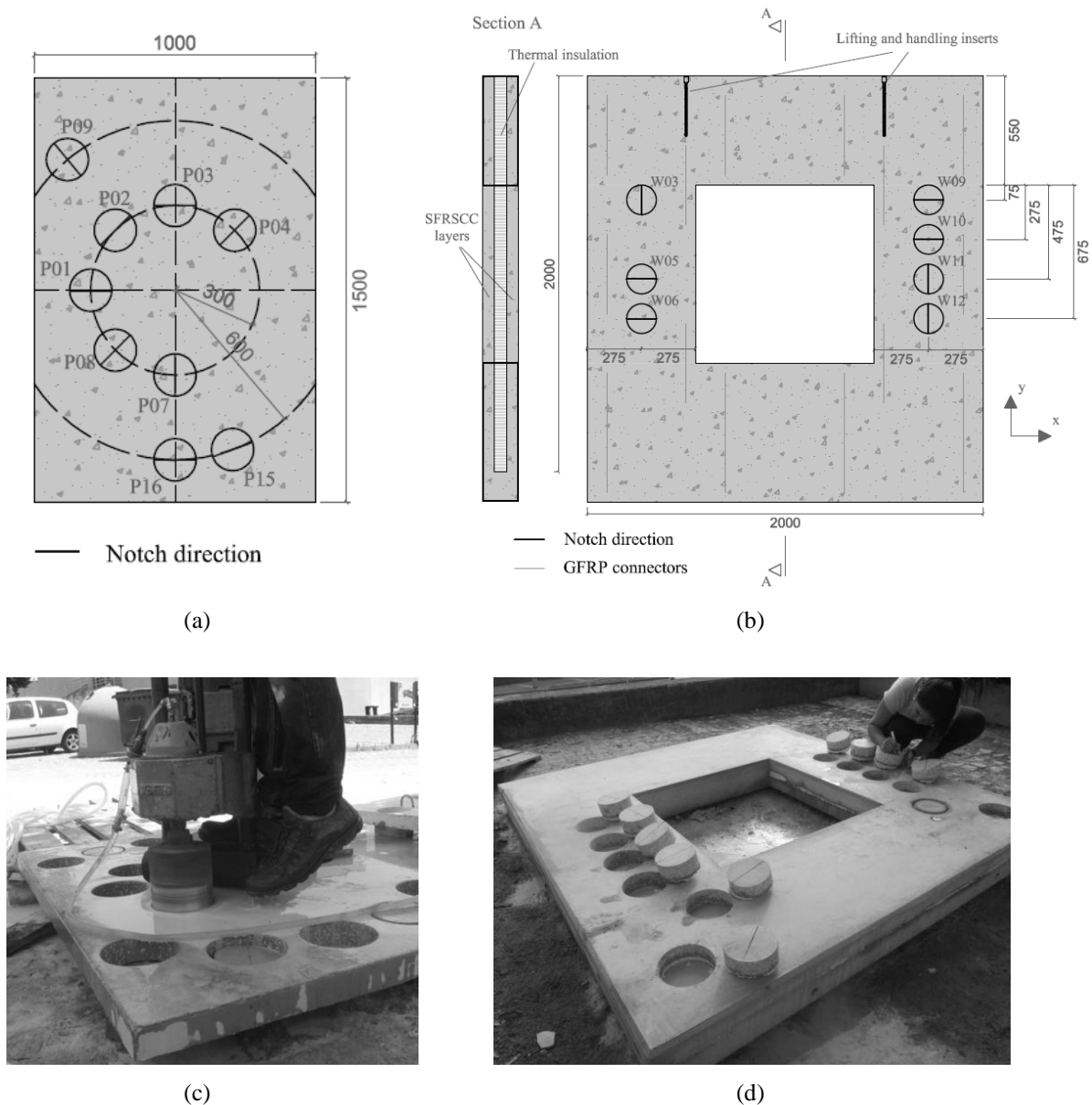
Figure 19: Schematic representation of the specimens sawn out from: (a) flat plate; (b) sandwich panel. Overall view of the drilling process for: (c) flat plate; (d) sandwich panel (units in millimetres).

All the specimens had a diameter of 150 mm. In terms of thickness, the specimens obtained from the 1.5×1.0 m^2 flat plate had a thickness that varied from 60.9 to 69.9 mm, while in the sandwich wall panel, the thickness ranged from 50.2 to 63.1 mm. This variation was probably a consequence of a non-perfectly flatness of the steel base of the formwork, and a certain

lifting of polystyrene foam during the casting process. Nine specimens were sawn out from the 1.5×1.0 m^2 flat plate, six at a distance of 300 mm and three of 600 mm from the centre of the plate. Among the specimens distanced 300 mm from the centre, four were used for tests with the load being applied parallel to the SFRSCC flux lines (P01, P04, P07 and P08), while the other two specimens were tested with the load being applied perpendicularly to the flux lines (P02 and P03). In the specimens obtained from a distance of 600 mm from the centre, only one specimen was tested with the load being applied parallel to the flow (P09), while the other two specimens were tested with the load applied perpendicular to the flux lines (P15 and P16).

As already indicated, one of the objectives of the present research was to improve the test setup proposed by Abrishambaf *et al.* (2013) in order to determine, as directly as possible, the stress-crack width relationship that can be representative of the material behavior in real structures. As reported in the cited work, the specimens used for the splitting tests were cylindrical, with a 150 mm diameter and had 5 mm deep notches parallel to the loading direction, in order to localize the specimen's fracture surface along the notched plane (see notch 2 in Figure 21). Nonetheless, in the present research two additional notches were executed following the procedures adopted by di Prisco *et al.* (2013). In fact, in an attempt of inducing a stress field corresponding to an almost pure fracture mode I in the notched plane, a V-shaped groove with 45° inclination has been cut at the extremities of the notched plane at the +45° and -45° directions, as illustrated in notch 1 of Figure 21. The load is then applied by using steel rollers of 20 mm diameter that are accommodated into these grooves and directly pushed by the machine device, as shown in Figure 20. This configuration aims to deviate the compressive stresses from the notched plane, creating, as much as possible, a uniaxial tensile stress field in the notched plane, orthogonal to this plane, as was done by di Prisco *et al.* (2013). Furthermore, following what was implemented by di Prisco *et al.* (2013), two more 5 mm deep straight notches at the direction 90º (see notch 3 in Figure 21), originating from the vertices of the V grooves are executed to force the crack opening at the reduced section and to move the crack tip away from the load application zones, where high stress concentrations generally rise. All the specimens were measured (see Table 7 and Table 8) and the actual measurements were used to calculate the results.

(a)

(b)

(c)

(d)
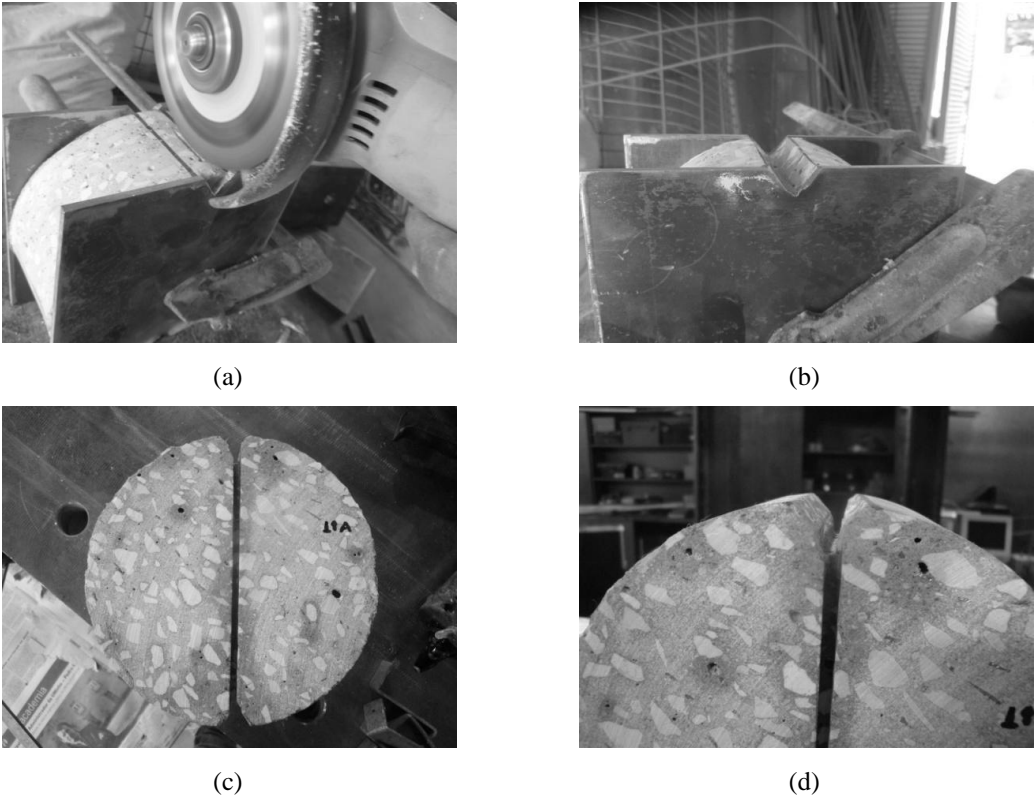
Figure 20: Specimen preparation: (a) procedure to obtain one of the v-notches (notch 1) of the specimens; (a) detail of the v-notch; (c) straight notch through the load direction (notch 2); (d) detail of the notch 3.
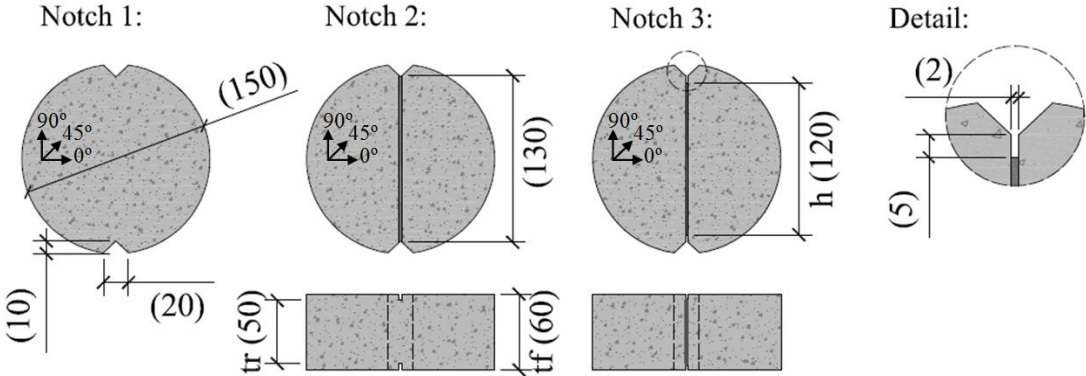
Figure 21: Sequencing of implementation of the notches made on the specimens. Nominal dimensions inside the parentheses (units in millimetres; t_f: total height; t_r: height of net area of notched plane).

Table 7: Dimensions of specimens extracted from the 1.5m × 1.0m panel.

Specimen	Tensile stress direction (normal / parallel)	Distance from the centre (mm)	Thickness without notches (mm)		Thickness with notches (mm)		Height (mm)	
		Lc	tf.1	tf.2	tr.1	tr.2	h.1	h.2
P01	normal	300	67.7	67.8	45.9	47.9	118.3	118
P02	parallel	300	65.7	65.6	54.6	53.2	122	120.8
P03	parallel	300	65.4	65	48.9	49.1	119.4	116.8
P04	normal	300	66.1	66.3	48.3	48.6	117.8	119.3
P07	normal	300	69.9	69.7	50	49.4	115.8	118.4
P08	normal	300	68.2	67.8	43.4	45.9	115.2	115.3
P09	normal	600	61.9	61.7	46.6	46.1	122.9	122.5
P15	parallel	600	61.7	60.9	46.3	47	120.6	120.5
P16	parallel	600	66.5	66.2	44.2	43.4	127.6	127
Average			65.8		47.7		119.9	
St. Dev.			2.7		3		3.6	
Min			60.9		43.4		115.2	
Max			69.9		54.6		127.6	

Table 8: Dimensions of specimens extracted from the sandwich wall panel.

Specimen	Tensile stress direction (x / y)	Thickness without notches (mm)		Thickness with notches (mm)		Height (mm)	
		tf.1	tf.2	tr.1	tr.2	h.1	h.2
W03	y	60.9	60.8	45.2	45.4	110	111.2
W05	x	58.3	58.7	40.3	40.6	111.4	110.9
W06	x	56.2	57.8	42	41.6	102.2	102.3
W09	x	63.1	62.8	44.1	44.6	108	105.3
W10	x	61.1	61.5	45.7	45.3	108.2	110.6
W11	y	61.8	61.6	45.4	46	103.5	101.7
W12	y	62.5	62.5	44.1	44.8	110.8	111.4
Average		60.7		43.9		107.7	
St. Dev.		2.1		2		3.8	
Min		56.2		40.3		101.7	
Max		63.1		46		111.4	

The test was conducted under displacement control of the piston of the load machine by using the following displacement rates: 1.0 μm/s up to the displacement of 2.0 mm; 2 μm/s from 2.00 mm up to 3.0 mm; 4 μm/s until the end of the test. For an accurate detection and tracking of the crack propagation, five LVDTs of 5 mm stroke were used to measure the crack opening

displacement: three at the side of the specimen corresponding to the upper side during casting, and the two remaining at the other side of specimen (corresponding to the side in contact with the metallic formwork). The exact position of each LVDT is schematically represented in the Figure 22(d). The adopted disposition of the LVDTs allows the evaluation of the in-plane and out-of-plane rotation of the specimen in consequence of the fibre orientation and distribution in the notched plane. The load is registered by means of a 150 kN load cell. All the splitting tests were carried out 56 days after casting.

(a)   (b)

(c)   (d)
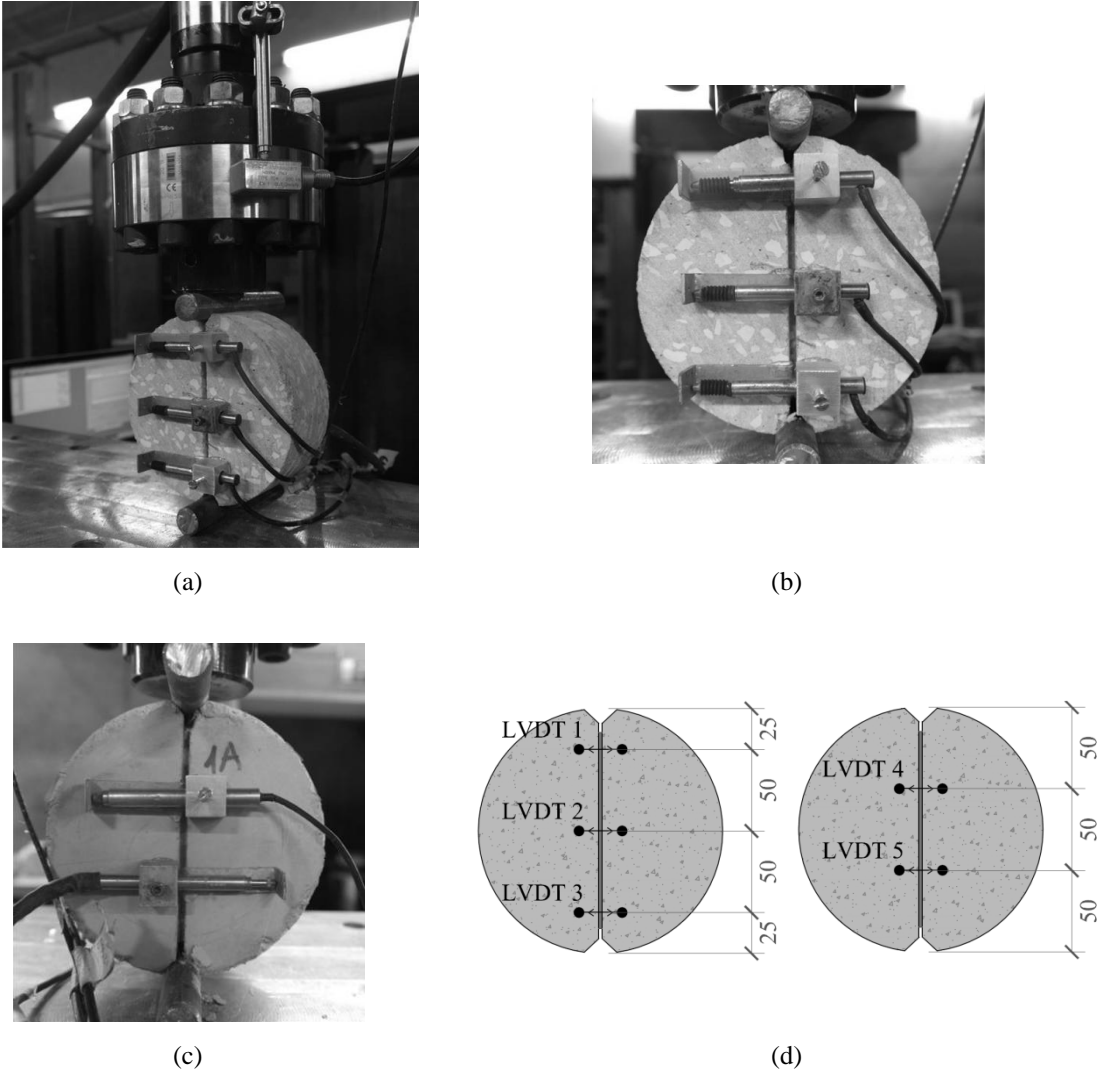
Figure 22: Experimental set-up. (a) general view; (b) detail of the upper side during casting; (c) bottom side during casting and (d) positions of LVDTs (units in millimetres).

3.4.5 Assessment of the number of effective fibres

After testing, each of the two faces of the fracture surface of a splitting tensile specimen was divided in four equal regions in order to evaluate the fibre distribution (see Figure 23(a), Figure 23(b) and Figure 23(c)). A similar procedure was adopted for the 3PBT specimens. However, for the 3PBT specimens, each of the two faces of the fracture surface was divided in nine regions as shown in Figure 23(d). The fibre distribution was evaluated by counting the number of effective fibres crossing the fractured surfaces (Figure 23(d)). A fibre was considered effective when it was broken or when its visible length was, at least, two times larger than the length of the hooked part of fibre. Attention should be paid to the fact that this procedure for determining the number of effective fibres allows to draw conclusions about their orientation and distribution in the structural element.

(a)

(b)

(c)

(d)
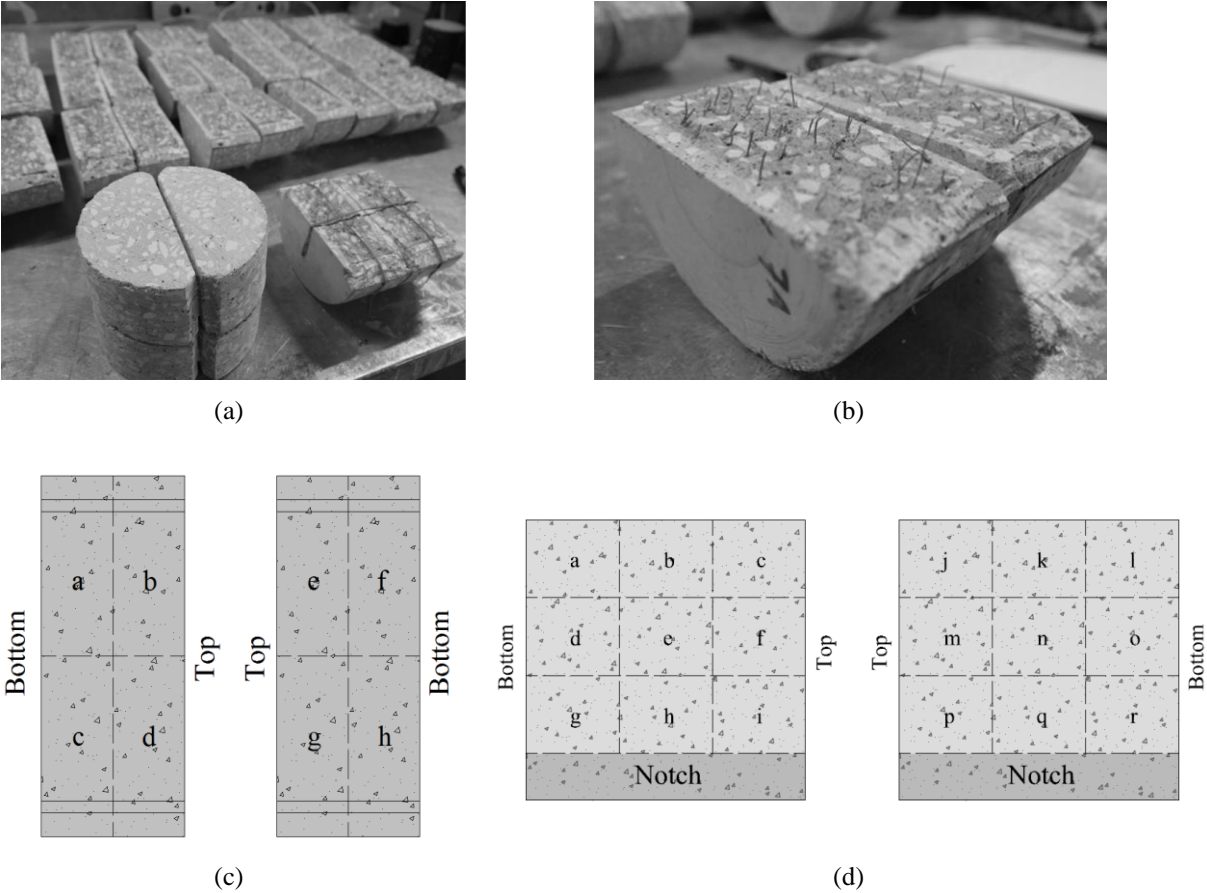
Figure 23: Assessment of the fibre density in the fractured zone of specimens. (a) Overall view of fibre counting for splitting test specimens; (b) detail of fibres at the fractured zone of splitting test specimen; (c) schematic representation of the regions of measurement of fibres in the splitting test specimen; (d) schematic representation of the regions of measurement in the 3PBT specimen.

3.4.6   Results and Discussion: Three-point bending tests (3PBTs)

For 27 out of the 40 specimens made with SFRSCC B tested in 3PBT only one visible crack was formed in the notch plane. Nonetheless, due to the relatively high content of fibres, failures with multiple cracks concentrated in the midspan region of specimens were also observed (13/40 of specimens). For 11/40 of specimens the desirable fracture plane was not attained at all. Instead of that, an irregular surface fracture was observed because the crack tip deviated from the notched section However, for computing the equivalent and residual strengths all the tests were taken into account. The typical failure modes are depicted in Figure 24(a) to Figure 24(c).
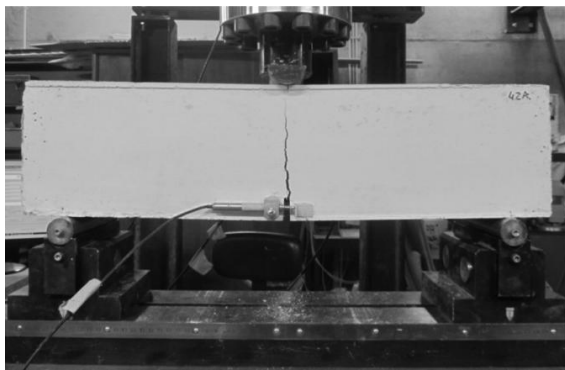
(a)
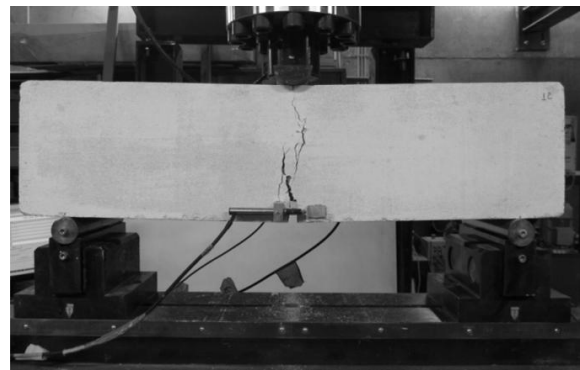
(b)
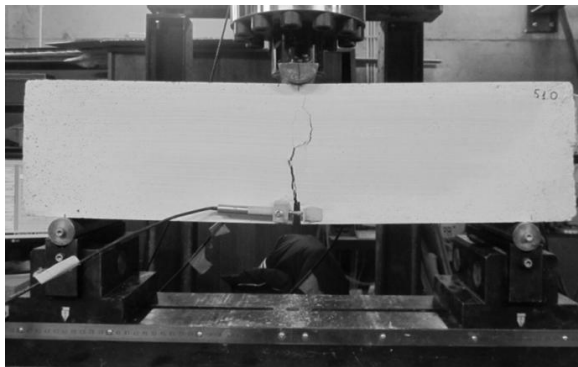
(c)

Figure 24: Typical failure modes found in the 3PBT. (a) only one visible crack formed in the notch plane, (b) multiple cracks concentrated in the midspan region, (c) deviation of the main crack tip.

The average and envelope deflection *versus* CMOD relationship obtained for all the performed tests with SFRSCC B are presented in Figure 25. A relatively low dispersion of the results was obtained for this relationship. It was also verified that the average observed relationship fits very well the corresponding equation proposed by RILEM TC 162-TDF (RILEM TC 162-TDF, 2002), which gives support on the reliability of this equation.
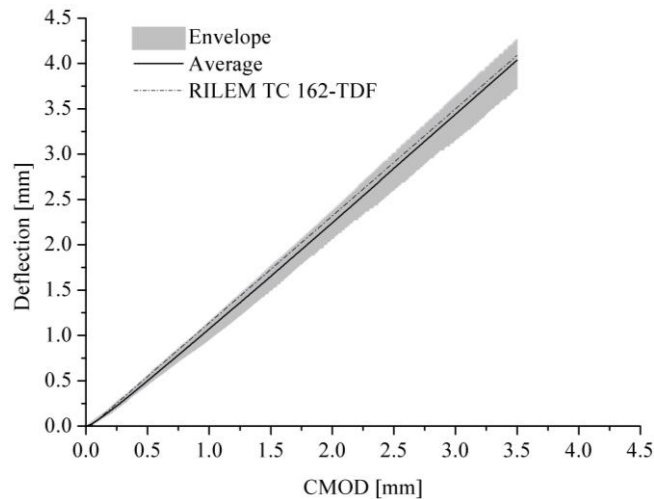
Figure 25: Deflection *versus* CMOD relationship for SFRSCC B.

The average and the envelope load *versus* CMOD curves of these tests are depicted in Figure 26. The results for the SFRSCC B are grouped in Figure 26(a) and a detailed view of the initial part of the experimental response is depicted on Figure 26(b). The curves corresponding to the upper bound (U.B.) and lower bound (L.B.) with a confidence level equal to 95% are also presented. Table 9 shows a summary of the strength parameters, presenting the average (Avg.), coefficient of variation (CoV) and the lower bound value (characteristic value) obtained for a confidence level of 95% (L.B.$_{95}$). The results are presented by separating the values obtained from different castings. From Table 9 it is verified that $f_{fct,L}$ is similar for all the SFRSCC castings. This parameter is less affected by the fibre reinforcement and is mainly dependent on the matrix properties. Figure 27(b) shows that the dispersion of results among specimens was significantly increased after crack initiation, since this testing stage is mainly governed by the fibre reinforcement mechanisms, whose effectiveness is dependent on the fibre orientation and distribution. This dispersion is also denoted in the CoV of the strength parameters that characterize the post-cracking behaviour of these composites, as noticeable in the values indicated in Table 9.

Table 9: Average and characteristic post-cracking parameters for different castings of SFRSCC.

Concrete type / casting (number of specimens)			$f_{ct,L}$ [MPa]	f_{ct} (0.7$f_{ct,L}$) [MPa]	Equivalent flexural tensile strength		Residual flexural tensile strength			
					$f_{eq,2}$ [MPa]	$f_{eq,3}$ [MPa]	$f_{R,1}$ [MPa]	$f_{R,2}$ [MPa]	$f_{R,3}$ [MPa]	$f_{R,4}$ [MPa]
SFRSCC A	3 (2)	Avg.	6.62	4.63	9.80	5.20	10.04	4.79	2.77	1.83
		CoV	3.3%	3.3%	8.8%	24.9%	5.5%	37.1%	40.7%	32.8%
		L.B.$_{.95}$*	6.32	4.42	8.61	3.41	9.27	2.33	1.21	0.99
	5 (5)	Avg.	6.18	4.20	9.75	8.87	9.60	8.68	6.84	5.54
		CoV	6.6%	3.9%	7.2%	13.5%	8.0%	19.2%	23.8%	26.2%
		L.B.$_{.95}$*	5.72	3.95	9.13	7.82	8.92	7.08	5.38	4.27
SFRSCC B	10 (5)	Avg.	5.80	4.06	9.62	8.10	9.21	8.11	6.82	5.70
		CoV	13.3%	13.3%	12.4%	15.0%	13.8%	15.4%	15.7%	18.5%
		L.B.$_{.95}$*	5.13	3.59	8.57	7.03	8.10	7.02	5.88	4.77
	11 (3)	Avg.	5.25	3.67	8.46	7.21	8.22	7.13	5.42	4.13
		CoV	0.9%	0.9%	4.5%	0.8%	4.2%	2.7%	10.7%	19.4%
		L.B.$_{.95}$*	5.20	3.64	8.03	7.15	7.82	6.91	4.76	3.22
	12 (7)	Avg.	5.11	3.58	7.63	6.57	7.44	6.77	5.52	4.61
		CoV	13.2%	13.2%	26.8%	26.4%	27.2%	24.6%	28.6%	26.3%
		L.B.$_{.95}$*	4.61	3.23	6.12	5.28	5.94	5.54	4.35	3.72
	13 (5)	Avg.	5.23	3.66	6.98	6.12	6.82	6.25	5.38	4.69
		CoV	8.5%	8.5%	18.9%	19.2%	41.4%	20.7%	22.2%	22.5%
		L.B.$_{.95}$*	4.84	3.39	5.82	5.09	5.69	5.20	4.46	3.90
	16 (5)	Avg.	5.09	3.56	6.87	5.92	6.67	5.97	5.26	4.54
		CoV	17.5%	17.5%	29.0%	28.5%	29.7%	27.8%	27.6%	25.5%
		L.B.$_{.95}$*	4.31	3.02	5.12	4.44	4.93	4.51	3.98	3.53
	17 (5)	Avg.	5.54	3.88	8.64	7.51	8.39	7.59	6.52	5.66
		CoV	8.4%	8.4%	7.4%	8.3%	7.2%	8.3%	11.0%	12.0%
		L.B.$_{.95}$*	5.13	3.59	8.08	6.96	17.15	7.84	6.96	5.92
	18 (5)	Avg.	5.63	3.94	8.55	7.38	8.36	7.47	6.40	5.59
		CoV	7.9%	7.9%	7.5%	7.3%	7.4%	7.2%	9.6%	11.4%
		L.B.$_{.95}$*	5.24	3.67	7.39	6.35	7.22	6.42	5.47	4.80
	19 (5)	Avg.	4.91	3.66	6.90	5.87	6.62	6.01	5.16	4.55
		CoV	10.9%	7.0%	15.6%	13.7%	16.0%	13.7%	12.6%	13.7%
		L.B.$_{.95}$*	4.44	3.34	5.96	5.17	5.69	5.29	4.59	4.01

*- lower bound considering a level of confidence equal to 95%
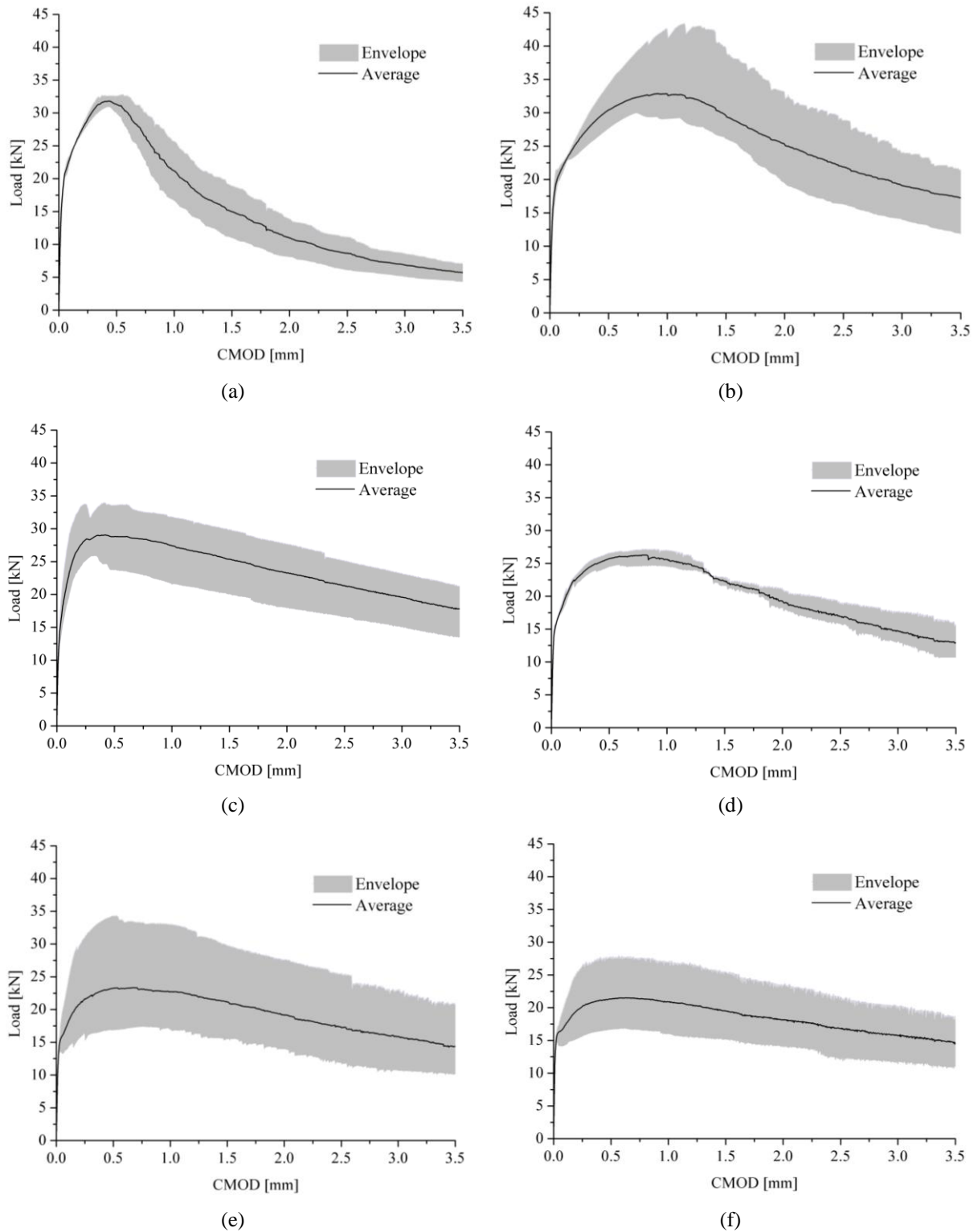
Figure 26: Experimental load - CMOD relationships for SFRSCC A, castings: (a) 3 and (b) 5; and SFRSCC B, castings: (c) 10, (d) 11, (e) 12, (f) 13.
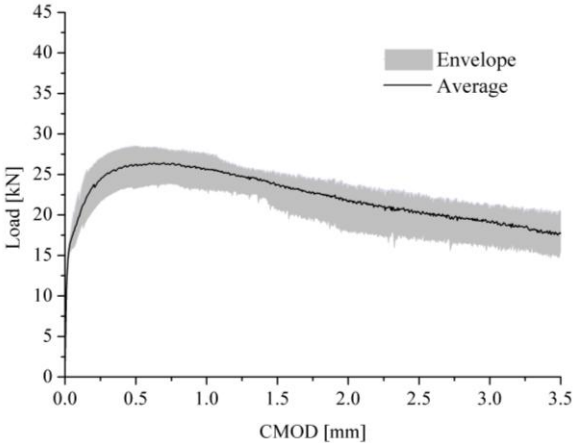
(g)
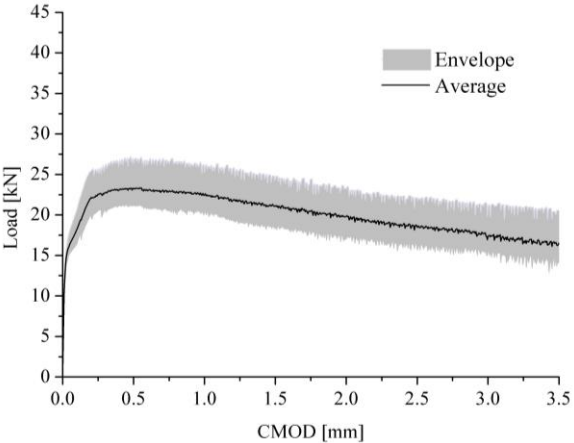
(h)
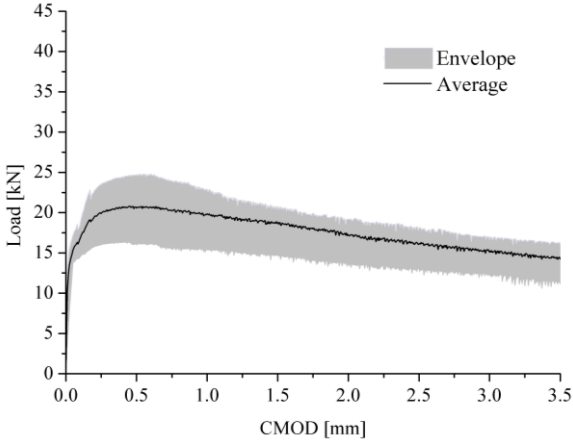
(i)

Figure 26: Experimental load - CMOD relationships for SFRSCC B, castings: (g) 17, (h) 18 and (i) 19.
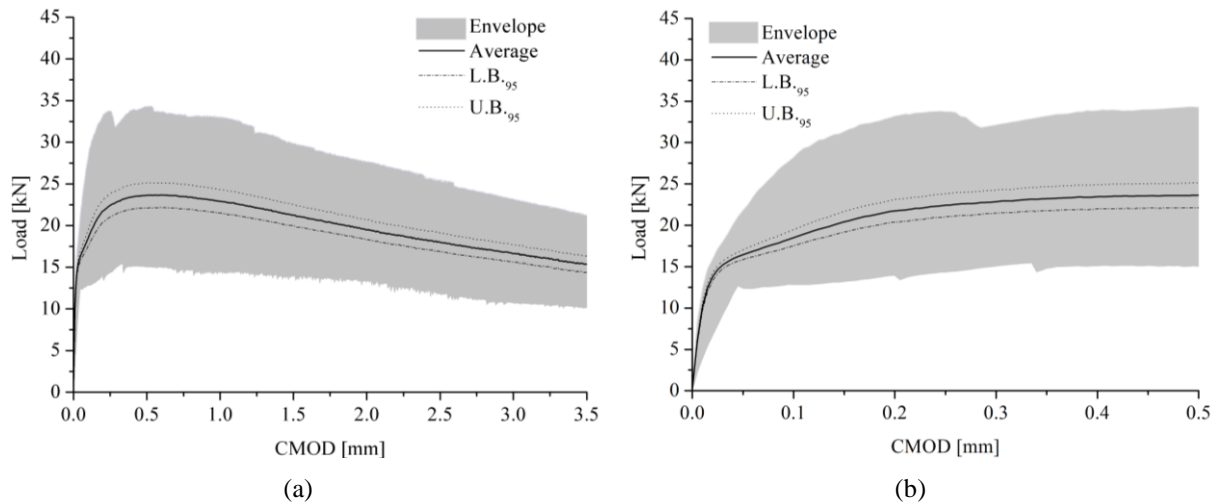
Figure 27: Results from 3PBT for SFRSCC B: (a) load *versus* CMOD curves, (b) detailed view of the load *versus* CMOD curves up to a CMOD equal to 0.5 mm.

The results from the fibre counting of SFRSCC B, represented in Figure 28, show that some fibre segregation has occurred. Due to higher density of steel, the fibres have tended to settle to the bottom part of the specimens.
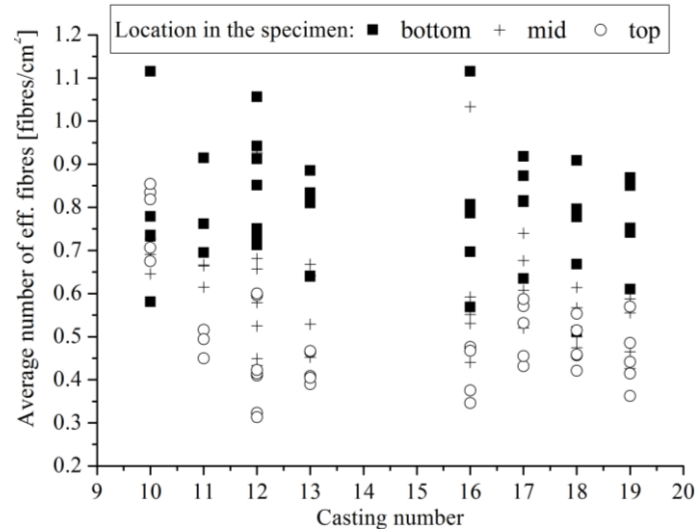
Figure 28: Fibre distribution at the cross section of the 3PBT's specimens.

The observed relationships between the strength parameters ($f_{fct,L}$; $f_{R,1}$; $f_{R,2}$; $f_{R,3}$; $f_{R,4}$; $f_{eq,2}$ and $f_{eq,3}$) and the average number of effective fibres per cm^2 at the fracture surface of 3PBT's specimens made with SFRSCC B are depicted in Figure 29(a) to Figure 29(g).
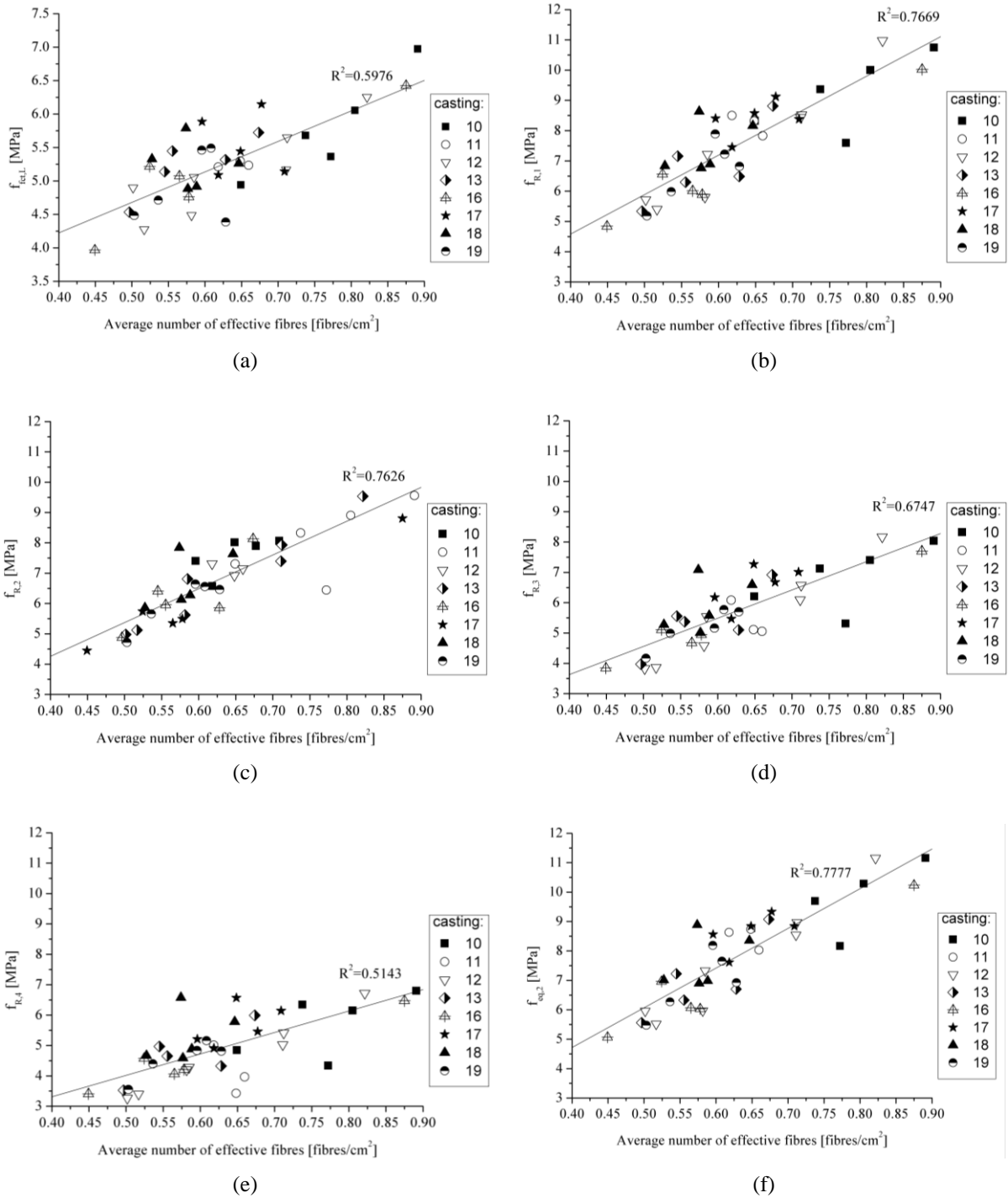
Figure 29: Relationships between the average number of effective fibres per square centimeter and the post-cracking parameters: (a) $f_{fct,L}$; (b) $f_{R,1}$; (c) $f_{R,2}$; (d) $f_{R,3}$; (e) $f_{R,4}$ and (f) $f_{eq,2..}$
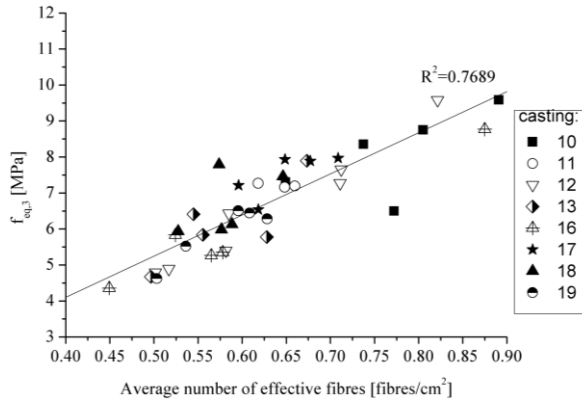
(g)

Figure 29: Relationships between the average number of effective fibres per square centimeter and the post-cracking parameters: (g) $f_{eq,3}$.

Regarding the limit of proportionality ($f_{fct,L}$), as expected, no significant relation is observed with the number of effective fibres at the specimen's fracture surface. However, for the f_R and f_{eq} parameters, an almost-linear tendency to increase can be observed, when these are related with the number of effective fibres. This behaviour was expected, since the stress transfer during the crack propagation is intimately related to the number of mobilized fibres. It is also possible to notice a tendency for decrease of the R^2 of the linear fit with the increase of the crack width at which the f_R and f_{eq} are evaluated, especially in the f_R, since as larger is the crack width as smaller is the effectiveness of the fibre reinforcement mechanisms of the adopted fibres. The f_{eq} parameters are not so sensitive to this aspect, because f_{eq} is obtained by considering the energy dissipated up to the crack with it corresponds, while f_R parameters are determined by taking the load at the crack with it corresponds.

3.4.7 Results and Discussion: Splitting Tests

Figure 30 and Figure 31 show the splitting tensile stress ($\sigma_{t,split}$) *versus* crack width curves, where $\sigma_{t,split}$ is determined from the following equation:

$$\sigma_{t,split} = \frac{2 \cdot P}{\pi \cdot t_r \cdot h}$$
(16)

where P is the compressive load applied in the specimen, t_r is the height of the SFRSCC cylinder and h is the diameter of the remaining SFRSCC cylinder after the notches are executed in the specimen, as shown in Figure 21. The nominal values for t_r and h are equal to 50 and 120 mm, respectively.

The crack width of the abscissa axes of Figure 30 and Figure 31 corresponds to the average of the values measured in the five LVDTs installed in the splitting tensile specimen (Figure 22). The average, envelope and Lower Bound (L.B.) and Upper Bound (U.B.) characteristics curves corresponding to a confidence level (k) equal to 95% are also presented in Figure 30 and Figure 31. The questionability of using Eq. (16) for the characterization of the tensile stress on the post-peak phase of splitting tensile tests is conceptually the same as that of using the theory of elasticity for the evaluation of the f_R and f_{eq} for flexural tests, as recommended by RILEM TC 162-TDF (2000a).

(a)

(b)
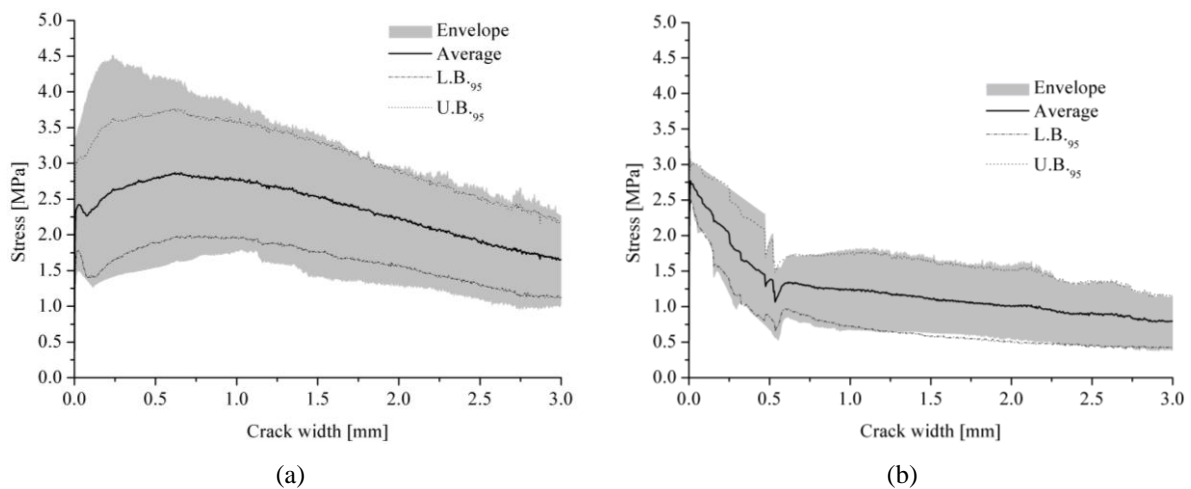
Figure 30: Splitting tensile stress *versus* crack width relationship for the specimens obtained from the $1.5 \times 1.0 \ m^2$ plate, and with loading direction (a) parallel, and (b) perpendicular, to the SFRSCC flux lines.

(a)

(b)
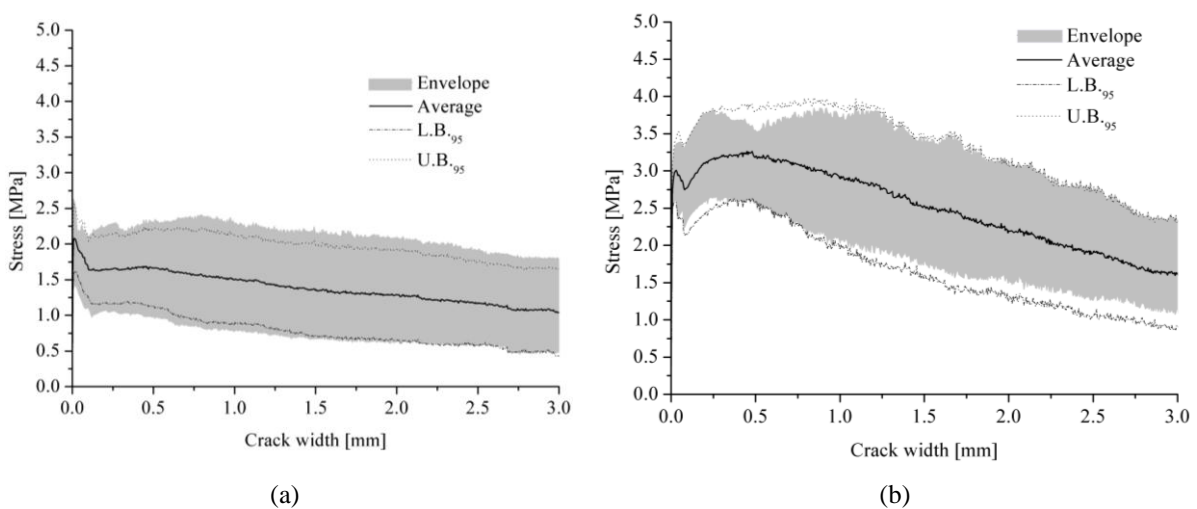
Figure 31: Splitting tensile stress *versus* crack width relationship for the specimens obtained from the sandwich wall panel, and with the loading direction in (a) *x*-, and (b) *y*-direction.

As already shown by Ferrara *et al.* (2012b), and di Prisco *et al.* (2013), the local dispersion and orientation of fibres are responsible for the obtained experimental scattering in stress-crack width curves. Despite the high dispersion of the results observed in specimens collected from the 1.5×1.0 m^2 panel (see Figure 30), it is quite evident that the stress at crack initiation, and mainly the post-cracking tensile strength, were higher in the specimens loaded in the direction of the SFRSCC flux lines than in the orthogonal direction, since, as already demonstrated by Abrishambaf *et al.* (2013), the fibres have the tendency to orientate orthogonally to the SFRSCC flux lines.

The same tendency was observed in the specimens obtained from the sandwich panel (Figure 31). As already indicated, due to the procedures adopted for casting and considering the geometry of panel, the SFRSCC has preferentially flowed along the *y*-direction in the left and right sides of the opening. This fact explains the similarities between the experimental responses in Figure 30(a) and Figure 31(b), corresponding to specimens loaded in a direction parallel to the SFRSCC flux lines. Similar arguments explain the similarity of the experimental responses obtained in the specimens with the loading direction perpendicular to the SFRSCC flux lines (Figure 30(b)) and in the specimens cored from the sandwich panels with the loading direction parallel to the *x*-direction (Figure 31 (a)).

In the specimens tested with loading direction parallel to the SFRSCC flux lines (Figure 30(a) and Figure 31(b)), it is noticeable that upon crack initiation there is a small load decay followed by slight strain-hardening branch, whereas in the specimens with loading direction perpendicular to the SFRSCC flux lines, after the first crack, only a strain-softening branch is verified.

The relevant conclusions taken from the stress *versus* crack opening relationships can be also confirmed by determining the residual strength parameters (σ_{w*}) and the energy absorption during the fracture process (G_{Fw*}), determined as schematically represented in Figure 32, and values are presented in Table 10 to Table 13. It is noted that the value attributed to the subscript "*w**" represents the crack width at which σ_w and G_F are evaluated.
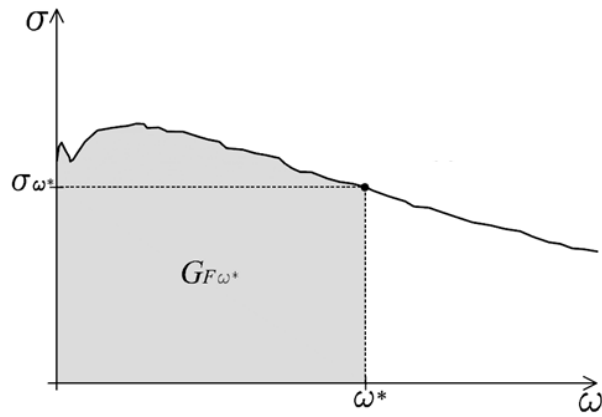
Figure 32: Determining the fracture energy of SFRSCC corresponding to a crack opening width ω *.

(a)

(b)

(c)

(d)
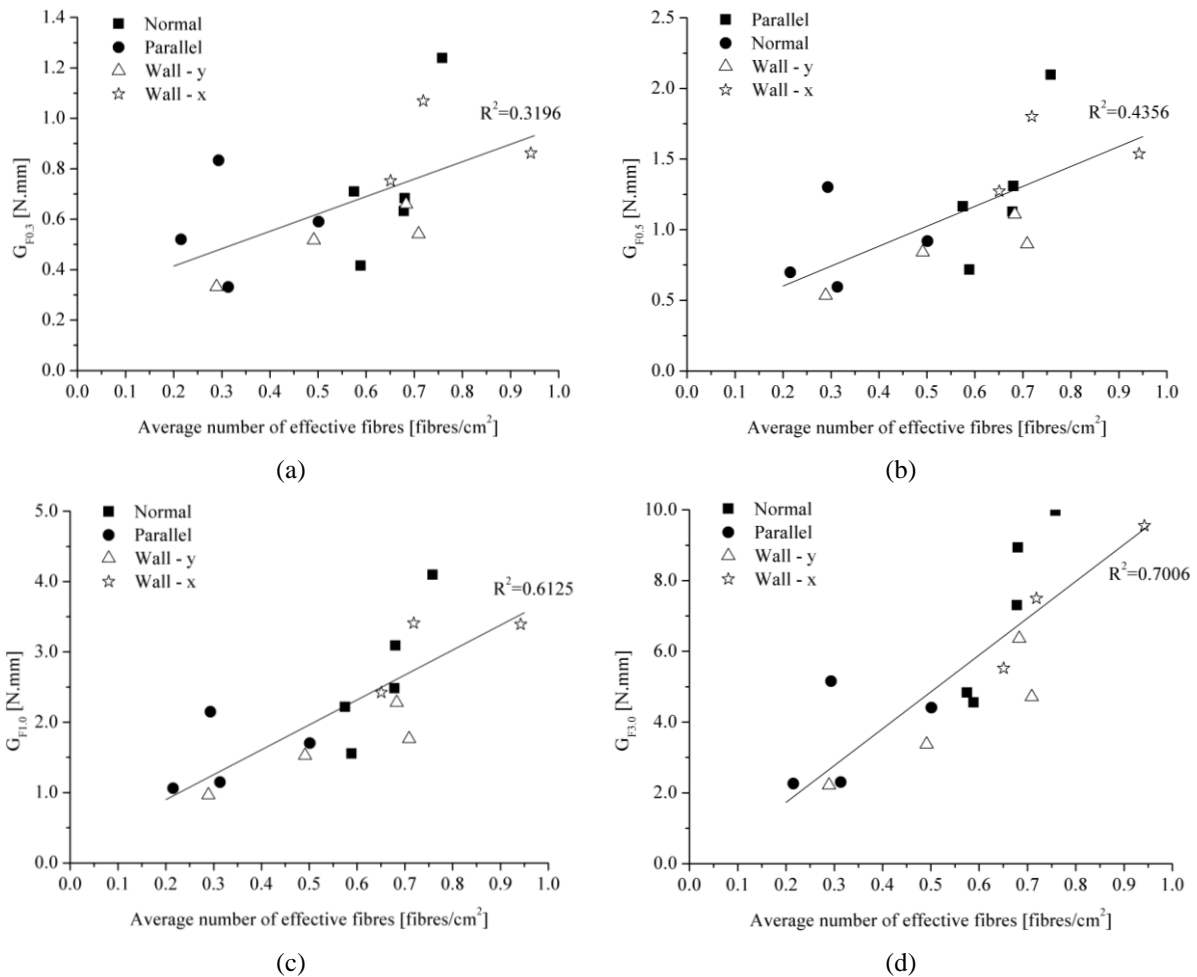
Figure 33: Relationships between the average number of effective fibres and the toughness: (a) $G_{F0.3}$; (b) $G_{F0.5}$; (c) $G_{F1.0}$; (d) $G_{F3.0}$.

Table 10: Maximum stress, residual stress and dissipated energy for the specimens extracted from 1.5×1.0 m^2 plate and with load applied parallel to the SFRSCC flux lines.

Specimen	σ_{max} [MPa]	$\sigma_{0.3}$ [MPa]	$\sigma_{0.5}$ [MPa]	$\sigma_{1.0}$ [MPa]	$\sigma_{1.5}$ [MPa]	$\sigma_{3.0}$ [MPa]	$G_{F0.3}$ [N/mm]	$G_{F0.5}$ [N/mm]	$G_{F1.0}$ [N/mm]	$G_{F1.5}$ [N/mm]	$G_{F3.0}$ [N/mm]
P01	4.66	4.38	4.18	3.78	3.42	2.26	1.24	2.10	4.10	5.89	9.97
P04	3.20	2.31	2.25	1.91	1.44	1.04	0.71	1.17	2.22	3.03	4.83
P07	3.06	2.34	2.57	2.83	2.87	1.63	0.63	1.13	2.48	3.84	7.30
P08	3.75	2.78	3.43	3.53	3.14	2.25	0.68	1.31	3.09	4.78	8.94
P09	1.87	1.46	1.55	1.78	1.79	1.07	0.42	0.72	1.55	2.45	4.56
Average	3.31	2.65	2.80	2.76	2.53	1.65	0.74	1.28	2.69	4.00	7.12
CoV	31%	41%	37%	33%	34%	37%	41%	39%	36%	34%	34%

Table 11: Maximum stress, residual stress and dissipated energy for the specimens extracted from 1.5×1.0 m^2 plate and with load applied perpendicular to the SFRSCC flux lines.

Specimen	σ_{max} [MPa]	$\sigma_{0.3}$ [MPa]	$\sigma_{0.5}$ [MPa]	$\sigma_{1.0}$ [MPa]	$\sigma_{1.5}$ [MPa]	$\sigma_{3.0}$ [MPa]	$G_{F0.3}$ [N/mm]	$G_{F0.5}$ [N/mm]	$G_{F1.0}$ [N/mm]	$G_{F1.5}$ [N/mm]	$G_{F3.0}$ [N/mm]
P02	3.49	1.81	1.31	0.94	0.66	0.39	0.33	0.60	1.15	1.54	2.30
P03	2.71	1.75	1.58	1.56	1.48	1.13	0.59	0.92	1.70	2.47	4.41
P15	3.04	2.58	1.93	1.81	1.66	1.12	0.83	1.30	2.15	3.03	5.15
P16	3.09	1.01	0.68	0.68	0.64	0.55	0.52	0.70	1.06	1.39	2.26
Average	3.08	1.78	1.37	1.25	1.11	0.80	0.57	0.88	1.52	2.11	3.53
CoV	10%	36%	38%	42%	48%	48%	37%	36%	34%	37%	42%

Table 12: Maximum stress, residual stress and dissipated energy for the specimens extracted from sandwich wall panel and with load applied parallel to the *x*-direction.

Specimen	σ_{max} [MPa]	$\sigma_{0.3}$ [MPa]	$\sigma_{0.5}$ [MPa]	$\sigma_{1.0}$ [MPa]	$\sigma_{1.5}$ [MPa]	$\sigma_{3.0}$ [MPa]	$G_{F0.3}$ [N·mm]	$G_{F0.5}$ [N·mm]	$G_{F1.0}$ [N·mm]	$G_{F1.5}$ [N·mm]	$G_{F3.0}$ [N·mm]
W05	1.81	1.02	0.98	0.78	0.69	0.49	0.33	0.53	0.96	1.33	2.22
W06	2.74	1.62	1.60	1.28	0.97	0.58	0.52	0.84	1.53	2.59	3.38
W09	2.23	1.73	1.80	1.65	1.60	1.30	0.54	0.90	1.76	2.57	4.72
W10	2.69	2.21	2.29	2.29	2.14	1.79	0.66	1.11	2.28	3.39	6.36
Average	2.37	1.65	1.67	1.50	1.35	1.04	0.51	0.85	1.63	2.47	4.17
CoV	19%	30%	32%	42%	48%	59%	26%	28%	33%	34%	43%

Table 13: Maximum stress, residual stress and dissipated energy for the specimens extracted from sandwich wall panel and with load applied parallel to the *y*-direction.

Specimen	σ_{max} [MPa]	$\sigma_{0.3}$ [MPa]	$\sigma_{0.5}$ [MPa]	$\sigma_{1.0}$ [MPa]	$\sigma_{1.5}$ [MPa]	$\sigma_{3.0}$ [MPa]	$G_{F0.3}$ [N·mm]	$G_{F0.5}$ [N·mm]	$G_{F1.0}$ [N·mm]	$G_{F1.5}$ [N·mm]	$G_{F3.0}$ [N·mm]
W03	3.93	3.79	3.54	2.94	2.35	1.41	1.07	1.80	3.41	4.73	7.50
W11	2.76	2.62	2.59	2.03	1.81	1.14	0.75	1.27	2.42	3.39	5.52
W12	4.03	3.20	3.45	3.71	3.44	2.34	0.86	1.54	3.39	5.22	9.55
Average	3.57	3.21	3.19	2.89	2.53	1.63	0.89	1.54	3.07	4.44	7.52
CoV	20%	18%	17%	29%	33%	38%	18%	17%	18%	21%	27%

The above mentioned preferential alignment of fibres are corroborated by the results of effective fibre counting at the fractured surface of splitting specimen, shown in Table 14 and Table 15 for the specimens obtained from the $1.5 \times 1.0 \text{ m}^2$ plate and from the sandwich wall panels, respectively. The values presented in the Table 14 and Table 15 highlight the correlation between the post-cracking response of specimens and the effective fibre counting at the fractured specimens. Moreover, when the data in Table 14 corresponding to the $1.5 \times 1.0 \text{ m}^2$ plate are evaluated separately by load direction, it is verified that the average number of effective fibres in the specimens loaded parallel to the SFRSCC flux lines is twice the average number of fibres counted in the specimens with the load applied perpendicularly to the SFRSCC flux lines. For the sandwich wall panel (see Table 15) the ratio of the average number of fibres counted in the specimens with load applied parallel to the *y*-direction *versus* *x*-direction is 1.4, which is not as high as the value observed in the other panel due to the distinct flux conditions in the two types of panels. Furthermore, when the data contained in Table 14 is separated according to the distance of the specimens from the centre of the panel, the tendency of having higher number of effective fibres in the proximity of point from where the mould was fed by SFRSCC can be confirmed. The average number of effective fibres in the specimens collected nearer the centre of the plate was 13% higher for the specimens with the load applied parallel to the concrete flow. This percentage was 64% for the specimens with the load applied perpendicular to the concrete flow. Nonetheless, although the results obtained with the splitting tests seem consistent with this information, quantitative conclusions cannot be issued due to the relatively small number of tested specimens. The results obtained in the specimens drilled from $1.5 \times 1.0 \text{ m}^2$ plate and from the sandwich panel are in accordance to the data presented by Abrishambaf *et al.* (2013) and di Prisco *et al.* (2013), since higher post-cracking parameters were obtained in the specimens with the fracture plane parallel to the SFRC flow direction. In these mentioned works, the difference of residual strengths was ascribed to a preferential fibre alignment influenced by the SFRC's flow, in accordance to the observations of the current research work.

Table 14: Fibre counting at fractured surface of specimens extracted from 1.5×1.0 m^2 plate.

Loading direction	Distance from centre (mm)	Specimen	Average number of fibres [fibres/cm^2]				
			Per specimen			Summary	
			Bottom	Top	Total	Per load direction	Per distance
Parallel to flow	300	P01	0.87	0.65	0.76		
	300	P04	0.61	0.54	0.57		0.67
	300	P07	0.64	0.72	0.68	0.66	
	300	P08	0.78	0.58	0.68		
	600	P09	0.62	0.56	0.59		0.59
Perpendicular to flow	300	P02	0.34	0.29	0.31		0.41
	300	P03	0.57	0.43	0.50	0.33	
	600	P15	0.37	0.21	0.29		0.25
	600	P16	0.16	0.27	0.22		

Table 15: Fibre counting at fractured surface of specimens extracted from the sandwich wall panel.

Loading direction	Specimen	Average number of effective fibres [fibres/cm^2]			
		Per specimen			Summary per direction
		Bottom	Top	Total	
x	W05	0.42	0.16	0.29	
	W06	0.44	0.54	0.49	0.54
	W09	0.74	0.68	0.71	
	W10	0.50	0.86	0.68	
y	W03	0.60	0.84	0.72	
	W11	0.70	0.60	0.65	0.77
	W12	1.05	0.83	0.94	

The results obtained by the splitting tests indicate that the properties are too affected by the fibre orientation caused by the concrete flow conditions and geometric characteristics of the casted structural element. Thus, the aforementioned observations reinforce the remark of di Prisco *et al.* (2009) that, for the characterization of the FRC used in structural elements, there is a need to use specimens that can reproduce the real fibre reinforcement mechanisms of the actual structural element. This is particularly important in the case of elements with reduced thickness (slender slab-like type elements), where the "wall effect" gives to the FRC a pronounced orthotropic and even anisotropic behavior that should be properly captured for a correct design. Furthermore, the results obtained in this work reiterate that, for the FRC with

self-compacting properties, it is also necessary to take into account its flow characteristics and the casting procedure. It is believed that the method employed in this work, which consists in casting a plate with the same thickness of the structural element, and applying a casting methodology similar to the one adopted in the corresponding real application, is a promising procedure to determine the values of the fracture parameters of SFRSCC to be assumed in the design of the actual structural element. In this context, the residual strength could be defined by considering the results of tests performed with specimens extracted from different distances from the feeding point, perpendicularly and parallel to the concrete flow, as was done in this work. By knowing the fibre orientation and distribution, different constitutive laws for the fracture process can be attributed to each representative volume by considering the crack orientation towards the governing fibre orientation, under the framework of the FEM-based material nonlinear approaches.

3.5 POST-CRACKING BEHAVIOUR OF SFRSCC ACCORDING TO THE *FIB* MC 2010 APPROACH

3.5.1 *fib* MC 2010 constitutive law

fib MC 2010 proposes the stress *versus* crack width constitutive law represented in Figure 34 with basis on the values of f_{Rj} determined according to the approach described in Section 3.4. In the constitutive law represented in Figure 34, f_{Fts} represents the serviceability residual strength, defined as the post-cracking strength for serviceability crack openings, and f_{Ftu} represents the ultimate residual strength. These two parameters are calculated through the following equations (*fib,* 2012a, *fib,* 2012b):

$$f_{Fts} = 0.45 f_{R1} \qquad (17)$$

$$f_{Ftu} = f_{Fts} - \frac{w_{ac}}{CMOD_3}(f_{Fts} - 0.5 f_{R3} + 0.2 f_{R1}) \geq 0 \qquad (18)$$

The maximum crack opening accepted in structural design (w_{ac} presented in Figure 34) was assumed equal to 0.3 mm.
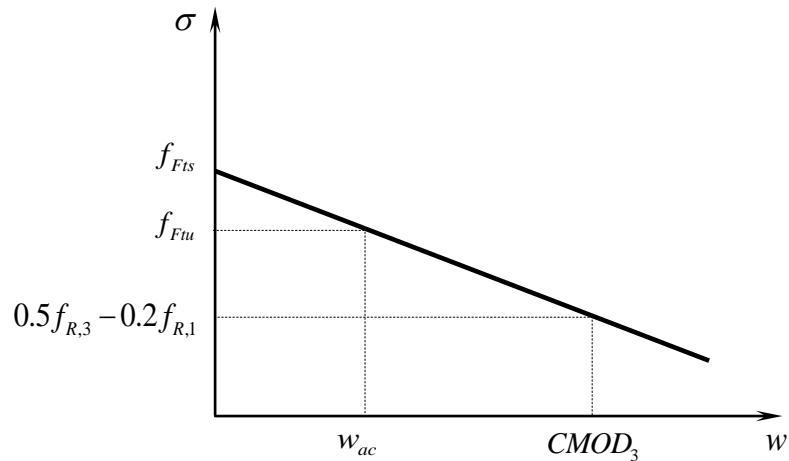
Figure 34: Stress-crack width constitutive law proposed by *fib* MC 2010 [44, 45].

3.5.2 *fib* MC 2010 model approach applied to the obtained experimental results

In this research, the experimental data from the 3PBT was used to compute the envelopes and characteristics curves, i.e., lower bound and upper bound with a confidence level (k) equal to 95%. Figure 35 depicts a comparison between the experimental results obtained from the splitting tests and by using the model proposed by the *fib* Model Code 2010 formulation, up to a crack width of 0.5 mm.
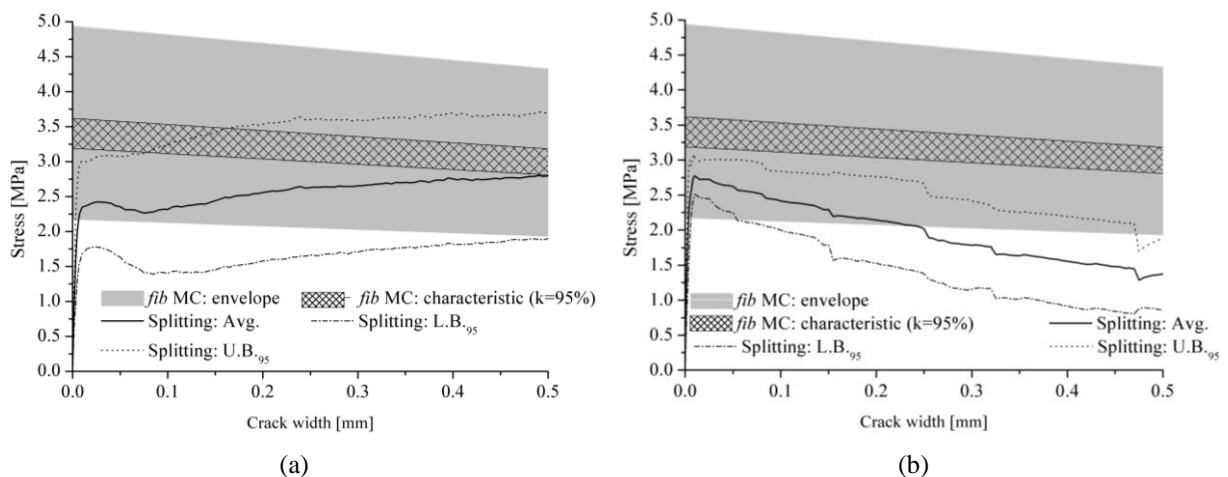
Figure 35: Comparison between the stress *versus* crack width diagrams obtained considering the *fib* MC 2010 approach and the experimental results from splitting tests corresponding to the loading: (a) parallel to the SFRSCC flow and (b) perpendicular to the SFRSCC flow.
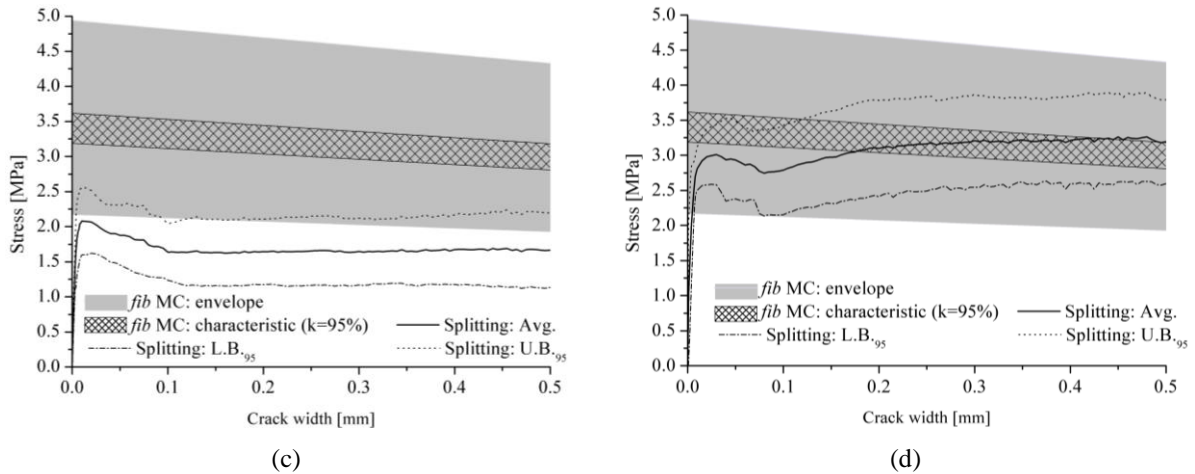
(c)   (d)

Figure 35: Comparison between the stress *versus* crack width diagrams obtained considering the *fib* MC 2010 approach and the experimental results from splitting tests corresponding to the loading: (c) parallel to the *x*-direction (wall) and (d) parallel to the *y*-direction (wall).

The results presented in Figure 35 show a tendency of the approach of MC 2010 to overestimate the post-cracking tensile capacity of the adopted SFRSCC. This assertion is further confirmed in Figure 36, which plots the ratios between the energy absorption capacity during the fracturing process, computed from the experimental data and the one calculated from the simplified MC 2010 approach. In this figure $G_{F0.5,MC}$ is this energy, evaluated up to 0.5 mm of crack with and by using the MC approach, while $G_{F0.5,split}$ is the corresponding one obtained from the splitting tests.

Figure 35 and Figure 36 interestingly show that the *fib* MC 2010 approach for the constitutive modelling of fibre reinforced concrete overestimates the energy absorption capacity even for the directions in which SFRSCC presents the uppermost energy absorption capacities (i.e., with the loading applied parallel to the concrete flow), due to the flow induced orientation of fibres. This tendency was already observed by Salehian and Barros (2014).
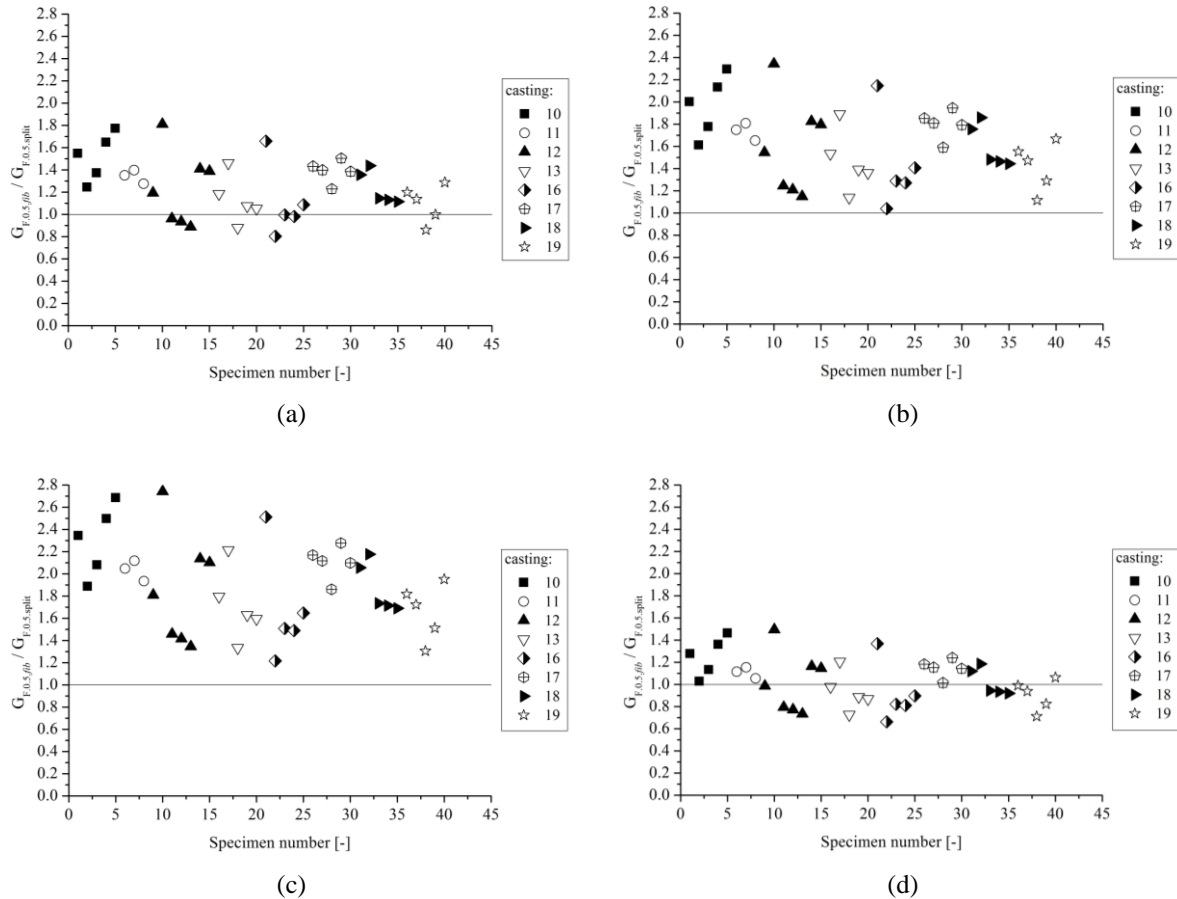
Figure 36: Comparison between the toughness related to the average post-cracking diagram obtained considering the *fib* MC 2010 approach ($G_{F0.5,MC}$) and the splitting tests ($G_{F0.5,split}$) up to $w = 0.5$mm with the splitting test corresponding to the loading: (a) parallel to the SFRSCC flow; (b) perpendicular to the SFRSCC flow; (c) parallel to the *x*-direction (wall); (d) parallel to the *y*-direction (wall).

3.6 COMPUTING THE $\sigma{-}\omega$ CURVES FROM THE EXPERIMENTAL DATA

In spite of its heterogeneity, the concrete mechanical behaviour at the post-cracking stage can be modeled considering the material as homogeneous. This approach, commonly called smeared crack approach is reasonable and advantageous due to the simplicity that is given to the model, not being necessary to explicitly consider the concrete's constituents and the interaction among them (Bažant, 1991, Bažant, 1994). In this approach, the softening behaviour of concrete in mode I fracture can be assumed as a constitutive property of material that is characterized by the dissipated specific energy after the localization in the cracked

region (G_F) and the tensile strength obtained by direct tensile test (f_{ct}) (Hillerborg, 1985). Furthermore, the shape of the softening branch of that relates the residual stresses to the crack opening displacement also has a critical importance (Hordijk, 1991a, Rots and De Borst, 1989). Unlike plain concrete, for which the post-cracking behaviour can be modeled by a linear diagram, for fibrous concrete it is more suitable to represent the softening branch through more complex functions. Michels *et al.* (2013) quoted that using a bilinear softening diagram is adequate. Nonlinear diagrams are proposed by (Cornelissen *et al.*, 1986, Hordijk, 1991a) and trilinear diagrams by (Hillerborg, 1980, Barros *et al.*, 2005, Cominoli *et al.*, 2007). The use of poly-linear functions is also recommended by some authors (Kurihara *et al.*, 2000, Kitsutaka, 1997) to increase the fitting quality of $\sigma - \omega$ curves.

In this research, the option for representing the softening behaviour of the SFRSCC by a poly-linear function comprising four branches is made (see Figure 37). It was initially tried to use a trilinear diagram, but during the inverse analyses of 3PBT, it was noticed that would be hardly possible to simulate the load-CMOD with an acceptable accuracy representing the $\sigma - \omega$ diagram by using such shape.
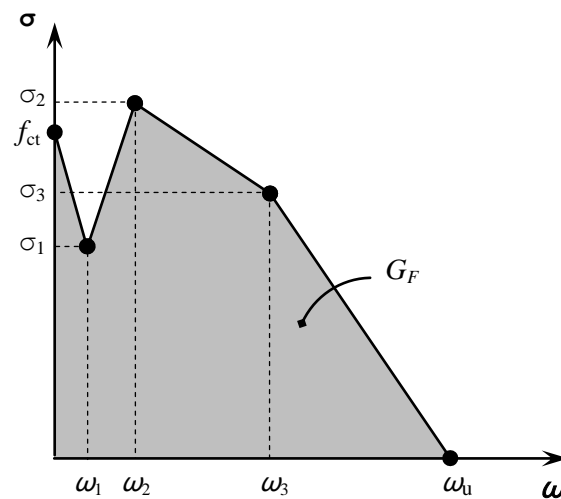
Figure 37: Schematic representation of the quadrilinear diagram for the post-cracking behaviour of the concrete.

This work adopts two indirect tensile tests to obtain the post-cracking behaviour of SFRSCC: 3PBT and splitting. Then, theoretically the $\sigma - \omega$ curves cannot be obtained directly from the tests. It is necessary to perform an inverse analysis to found the $\sigma - \omega$ diagram corresponding

to an direct tensile test that reproduces better the experimental results when the test is performed according the indirect method.

3.6.1 Quadrilinear functions obtained from splitting tests

It is known that the loading condition in the splitting test produces an almost uniform tensile stress distribution acting horizontally in the larger portion of cylinder. It is estimated that the high horizontal compressive stresses developed in the vicinity of the loading points act for about 1/6 depth of specimen and the remaining 5/6 depth is subjected to tension due to poisson's effect (Mehta and Monteiro, 2014). Thus, it can be considered that the $\sigma - \omega$ diagrams are rough approximations of the direct tensile responses of SFRSCC. Assuming that this is true, the average, lower bound with 95% of confidence interval (L.B.$_{95}$), upper bound with 95% of confidence interval (U.B.$_{95}$), lower bound corresponding to envelope (L.B.$_{EN}$) and upper bound corresponding to envelope (U.B.$_{EN}$) were fitted by poly-linear functions consisted of four branches. Some of these diagrams are shown in Figure 38 and the parameters of the quadrilinear functions are grouped in Table 36.
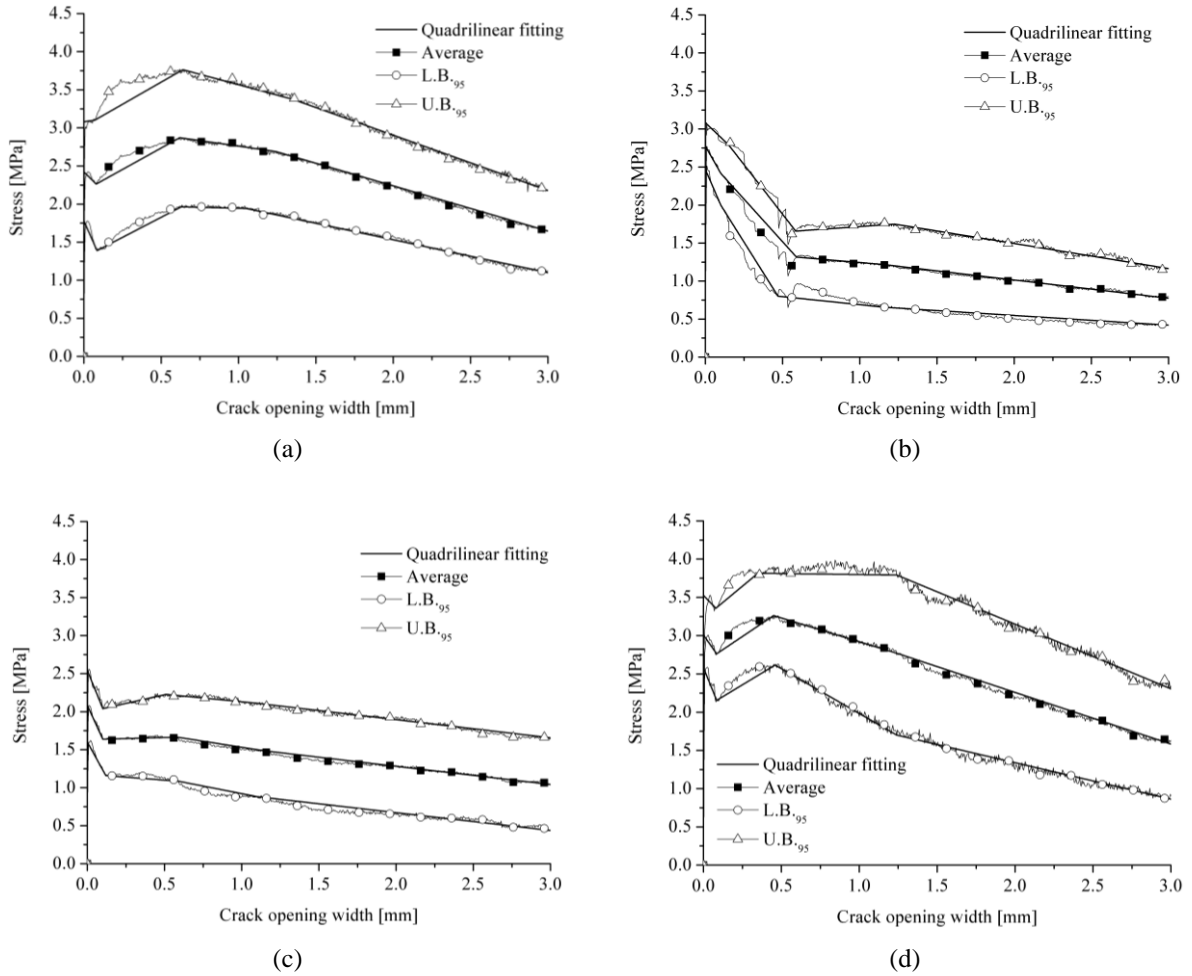
Figure 38: Fitting of the average and characteristics stress *versus* crack opening width curves obtained from the experimental results of splitting tests with the loading applied: (a) parallel to the SFRSCC flow; (b) perpendicular to the SFRSCC flow; (c) parallel to the *x*-direction (wall); (d) parallel to the *y*-direction (wall).

Table 16: Fracture parameters for the SFRSCC considering a quadrilinear diagram for its post-cracking tensile behaviour.

		f_{ct}	w_1	σ_1/f_{ct}	w_2	σ_2/f_{ct}	w_3	σ_3/f_{ct}	w_u	G_F	$\eta_{0.5}$	$\eta_{1.0}$	$\eta_{2.0}$	$\eta_{3.0}$
		[MPa]	[mm]	[-]	[mm]	[-]	[mm]	[-]	[mm]	[N·mm]	[%]	[%]	[%]	[%]
Plate - normal	Avg	2.423	0.080	0.93	0.620	1.19	1.240	1.11	5.774	9.40	-2.5	-1.2	-0.6	-0.1
	L.B.EN	1.497	0.110	0.86	0.625	1.09	1.160	1.24	4.537	4.98	-0.5	0.2	5.5	4.0
	U.B.EN	3.378	0.170	1.30	0.505	1.24	1.000	1.12	5.887	13.34	0.1	-0.1	0.3	0.2
	L.B.95	1.779	0.085	0.78	0.630	1.10	1.050	1.09	5.545	6.23	-2.3	-1.5	-1.3	-0.8
	U.B.95	3.080	0.070	1.01	0.640	1.22	1.355	1.09	6.003	12.56	-3.6	-1.7	-1.4	-0.8
Plate - parallel	Avg	2.773	0.100	0.87	0.590	0.47	1.150	0.44	6.225	4.98	6.3	4.8	3.2	2.3
	L.B.EN	2.467	0.100	0.83	0.450	0.22	1.135	0.27	5.509	2.55	4.1	-3.6	-3.7	-2.9
	U.B.EN	3.185	0.100	0.91	0.620	0.53	1.245	0.56	6.207	7.00	-1.8	-0.4	-0.6	-0.7
	L.B.95	2.467	0.100	0.81	0.470	0.33	1.160	0.27	6.288	2.93	7.7	1.0	1.3	2.4
	U.B.95	3.083	0.150	0.91	0.585	0.54	1.225	0.57	6.533	7.14	0.1	-0.4	-0.2	-0.4
Wall - y	Avg	2.081	0.100	0.79	0.580	0.80	1.140	0.71	7.360	6.49	0.9	1.3	1.5	1.1
	L.B.EN	1.426	0.120	0.68	0.500	0.69	1.220	0.51	6.880	3.17	-2.6	0.1	-0.2	-0.3
	U.B.EN	2.627	0.095	0.79	0.500	0.87	1.150	0.86	10.023	12.63	-0.3	-1.5	-0.8	-0.5
	L.B.95	1.600	0.120	0.72	0.590	0.68	1.100	0.55	4.871	2.86	-1.1	1.7	3.3	2.2
	U.B.95	2.541	0.100	0.80	0.510	0.88	1.090	0.83	9.930	11.70	0.6	0.0	0.2	0.3
Wall - x	Avg	3.008	0.085	0.92	0.450	1.08	1.245	0.92	5.346	9.42	-1.0	-0.5	0.2	0.5
	L.B.EN	2.579	0.080	0.87	0.350	1.03	1.160	0.77	5.072	6.63	-1.3	-0.3	0.8	0.3
	U.B.EN	3.381	0.075	0.98	0.350	1.09	1.240	1.10	5.866	13.12	-1.1	-0.6	-0.2	0.0
	L.B.95	2.579	0.085	0.84	0.460	1.01	1.240	0.66	4.814	5.82	-1.3	-0.4	-0.3	0.1
	U.B.95	3.527	0.080	0.95	0.350	1.08	1.240	1.08	5.727	13.14	-0.8	-1.5	-0.6	-0.2

$\eta_{\omega*}$ is the cumulative error of the area under the fitted diagram until the prescribed crack opening equal to $\omega*$ mm.

3.6.2 Inverse analysis of three-point bending test (3PBT)

As the 3PBT is an indirect tensile test, an inverse analysis procedure is necessary to determine the best fit parameters of $\sigma - \omega$ curve. For this purpose, in this investigation the experimental tests are simulated using a finite element program developed by the one of the co-authors, FEMIX (Azevedo *et al.*, 2003b). Firstly, the geometrical boundary conditions of the specimen are introduced and the parameters defining the post-cracking tensile behaviour of the material are initialized. The parameters used to represent the post-cracking behaviour of SFRSCC are schematically represented in Figure 37.

The test is here simulated considering a plane stress state. In spite of the fact that the width of specimen is equal to its height, it is considered feasible to suppose that the beam endures a plane stress state. Figure 39 depicts the mesh and type of elements adopted for the simulations. For the elements located in symmetry axis of the beam is used an integration scheme with two integration points (IP), whereas for the remaining elements a Gauss-Legendre integration scheme with 2×2 IP is adopted. Only four-node elements are used in the model. The elements located in the vicinity of the fracture zone of the element (see again the Figure 39) are modeled with consideration for the nonlinear behaviour for the material. For simplification and aiming to reduce the numerical cost, the remaining elements are modeled considering linear elastic behaviour for the SFRSCC. In compression, the SFRSCC is considered linear elastic. In tension, for the elements in which material nonlinearity is taken into consideration, the material behaviour is assumed linear elastic until the uniaxial tensile strength f_{ct} is reached. After that, the constitutive material law of SFRSCC is modeled by a decreasing stress-strain branch. For all simulations, a value of 37.0 GPa is considered for the modulus of elasticity of concrete (E_c), corresponding to the average experimental value for the concrete of all castings. The density adopted for the SFRSCC is 2.4×10^{-5} N/mm^3 and the Poisson's ratio equal to 0.2.

Prescribed displacements at the *y*-direction are specified in the *c* and *d* nodes (see axes and points in Figure 39). The displacements are restrained at the *y*- and *x*- directions in the node *a* and at the *y*-direction in the node *b*. The CMOD from the numerical model is computed taking into consideration the displacements at the *x*-direction of nodes *e* and *f*.
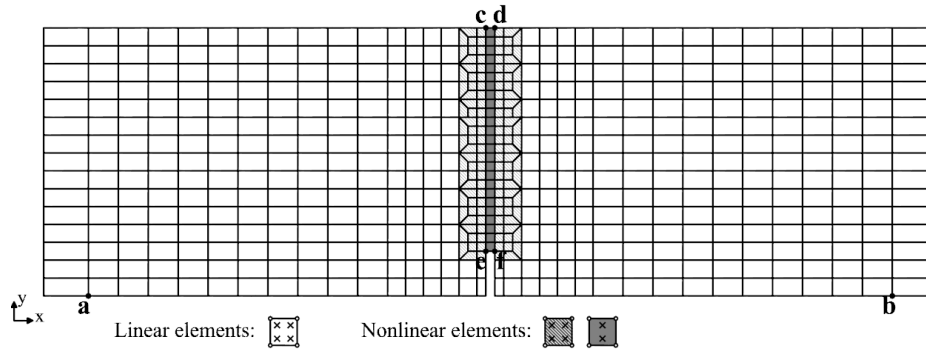
Figure 39: Finite element mesh, details of geometry and constraint conditions adopted to simulate the 3PBT.

The transition between the discrete (stress-crack opening relationship) and the smeared (stress-strain relationship) is made by the parameter called characteristic length (l_c). The characteristic length plays the role of correlate a minimum volume around each single point of the continuum that make the parameters measured at macroscale meaningful. Theoretically, the characteristic length is the distance over which the concrete undergoes plastic deformation. This concept was firstly introduced by Bažant and co-workers in the crack band model (Bažant and Oh, 1983, Bažant and Pijaudier-Cabot, 1989). There is no consensus in the scientific literature about the evaluation of the characteristic length for FRC (Montaignac *et al.*, 2012). In general, it is considered that it is influenced by the specimen geometry, fibre type and content. In the present investigation the characteristic length was set equal to the square root of the area of the corresponding integration point.

In order to perform the inverse method for determining the stress-crack width ($\sigma - \omega$) diagram from the experimental load-CMOD curve on pre-notched beams, a simplified graphical method is developed. The developed methodology is based on the principle that each parameter that represents the direct tensile behaviour of SFRSCC has a major influence in a determinate/limited branch of the load-CMOD response of the 3PBT. The detailed procedures adopted to perform the inverse analyses can be summarized as follows:

Step 1: Initialization of the parameters defining the pos-cracking tensile behaviour of the SFRSCC. The parameters to be obtained by the inverse analysis procedure are: f_{ct}, σ_1, σ_2, σ_3, ω_1, ω_2, ω_3 and ω_u. They are schematically represented in Figure 37. A first approximation considered reasonable for ω_u is to consider equal to the 8th part of the fibre length ($L_f/8$). The reference crack opening widths (ω_i) kept constant during all the process are: 0.2, 1.0 mm and

2.5 mm, for i = 1, 2 and 3, respectively. The values of σ_2 and σ_3 are initialized taking in order to have σ_2/f_{ct} = 1.0 and σ_3/f_{ct} = 0.5. The values of f_{ct} and σ_2 are initialized at the following step;

Step 2: Find out the value of f_{ct} that leads to the best adjustment of the initial branch of the experimental load-CMOD curve. This is made by ranging the value of f_{ct} for two different ratios σ_1/f_{ct} (0.8 and 1.2). The tensile strength of the concrete f_{ct} is ranged from $0.5 \cdot f_{ctm.EC2}$ and $0.9 \cdot f_{ctm.EC2}$, where $f_{ctm.EC2}$ is equal to the direct tensile strength of concrete, computed as indicated by the EN 1992-1-1 (2004) from the value of the maximum stress obtained by the splitting test. The values of σ_1 are chosen lower than $f_{ctm.EC2}$ because it is believed that the notched specimens lead to maximum stress much lower than the cracking stress of concrete due to the stress concentration that arises in the nearby of notches. The value of f_{ct} is chosen graphically in order to obtain the best adjustment of the first branch of the load-CMOD curve (for a better understanding of the procedures, see Figure 40, where the procedure is applied to the experimental data obtained in the 3PBT with the studied SFRSCC). Each curve represents the load-CMOD response obtained from the numerical simulation of the experimental test for the matching set of parameters;

Step 3: Determining σ_1/f_{ct}. The value of $f_{ct}/f_{ctm.EC2}$ is kept constant and equal to the value obtained in the step 2 and σ_1/f_{ct} is ranged together to σ_2/f_{ct}. Nine values are chosen for the principal variable (σ_1/f_{ct}) and 2 values for the secondary variable (σ_2/f_{ct}). From this step, the value of σ_1/f_{ct} that leads to the best fit of a second branch of the experimental load-CMOD data is taken;

Step 4: Determining σ_2/f_{ct}. σ_2/f_{ct} is found out using the same methodology adopted in the step 3, but considering σ_2/f_{ct} for the principal variable, and σ_3/f_{ct} for the secondary variable;

Step 5: Determining σ_3/f_{ct}. σ_3/f_{ct} is determined following the same methodology described in the step 3 and 4, but considering σ_3/f_{ct} for the principal variable, and ranging the value adopted for ω_u from $L_f/10$ to $L_f/4$;

As long the stress-crack width ($\sigma-\omega$) diagram is obtained, the fracture energy (G_F), represented in the Figure 37, can be evaluated by the Eq. (11), considering that ω_{lim} is equal to ω_u.
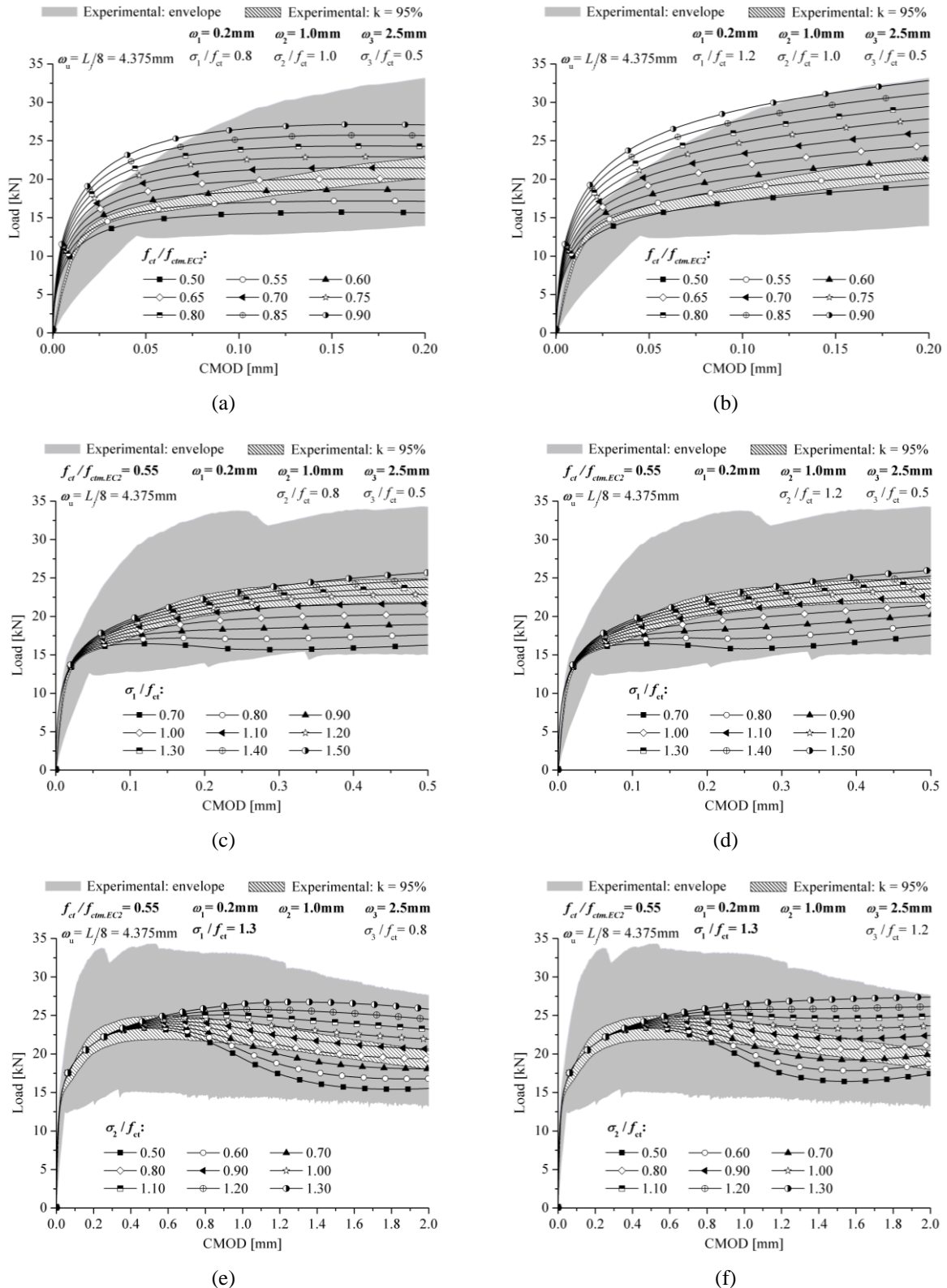
Figure 40: Inverse analysis of 3PBT to determine the fracture parameters for the average behaviour of SFRSCC

B. Parameters studied: (a) f_{ct} : $\sigma_1/f_{ct} = 0.8$; (b) f_{ct}: $\sigma_1/f_{ct} = 1.2$; (c) σ_1/f_{ct}: $\sigma_2/f_{ct} = 0.8$; (d) σ_1/f_{ct}: $\sigma_2/f_{ct}= 1.2$; (e) σ_2/f_{ct}: $\sigma_3/f_{ct} = 0.8$ and (f) σ_2/f_{ct}: $\sigma_3/f_{ct} = 1.2$.
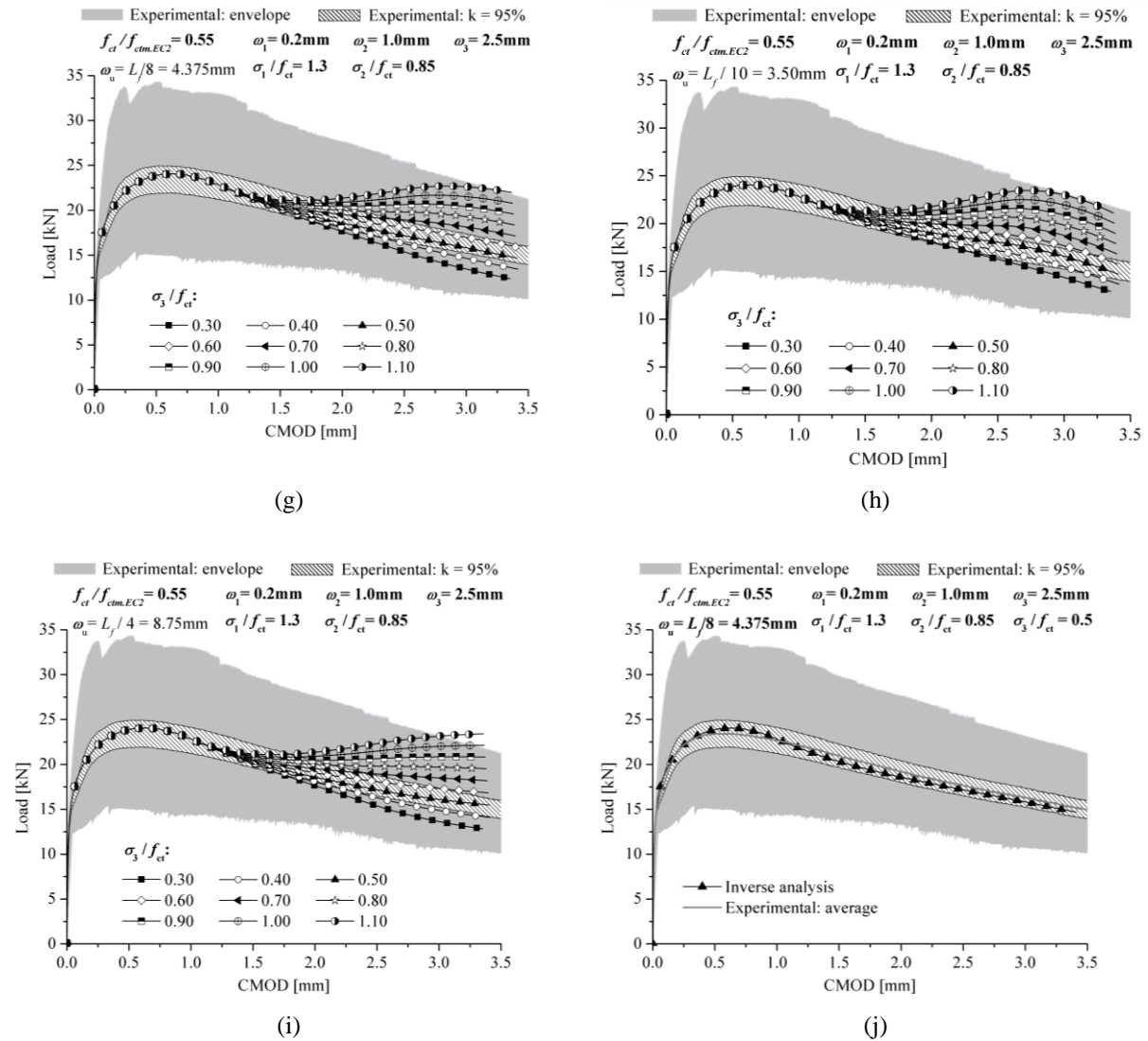
(g)

(h)

(i)

(j)

Figure 40: Inverse analysis of 3PBT to determine the fracture parameters for the average behaviour of SFRSCC B. Parameters studied: (g) σ_3/f_{ct}: $\omega_u = L_f/8$; (h) σ_3/f_{ct}: $\omega_u = L_f/10$ and (i) σ_3/f_{ct}: $\omega_u = L_f/4$. (j) Result of the inverse analysis of the average behaviour.
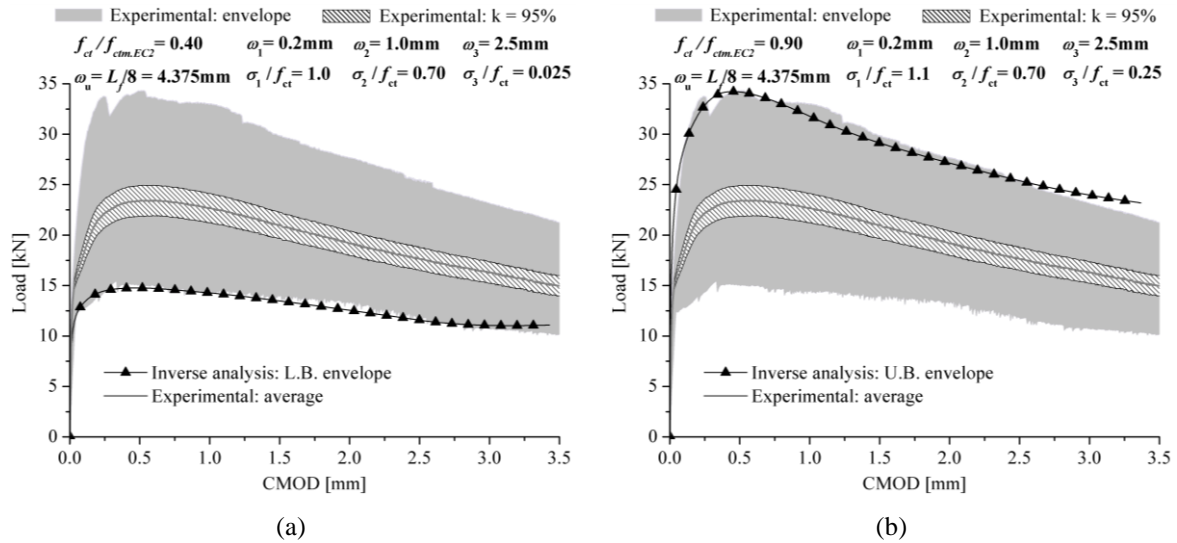
Figure 41: Results of inverse analyses of 3PBTs to determine the fracture parameters for the envelope behaviour of SFRSCC B: (a) lower bound and (b) upper bound.

The fracture parameters that define the average and envelope behaviour of SFRSCC B obtained by inverse analysis of 3PBTs are grouped in Table 17.

Table 17: Fracture parameters for the average, lower bound and upper bound behaviour of SFRSCC B obtained by inverse analysis of 3PBTs.

	f_{ct}	w_1	σ_1	w_2	σ_2	w_3	σ_3	w_u	G_F
	[MPa]	[mm]	[-]	[mm]	[-]	[mm]	[-]	[mm]	[N·mm]
Avg	2.232	0.20	2.902	1.00	1.897	2.50	1.116	4.375	5.74
L.B.$_{\cdot EN}$	1.623	0.20	1.623	1.00	1.136	2.50	0.041	4.375	2.35
U.B.$_{\cdot EN}$	3.652	0.20	4.018	1.00	2.557	2.50	0.913	4.375	7.16

Figure 42 depicts a comparison between the stress *versus* crack width constitutive law obtained by inverse analysis of the 3PBTs results of SFRSCC B, the experimental results obtained from the splitting tests and by using the model proposed by the *fib* Model Code 2010 formulation and up to a crack width of 3.5 mm.

The results presented in Figure 42 show that, although the approach of MC 2010 seems to overestimate the post-cracking tensile capacity of SFRSCC B, it fits well the average stress *versus* crack width constitutive response obtained by inverse analysis of the 3PBTs.
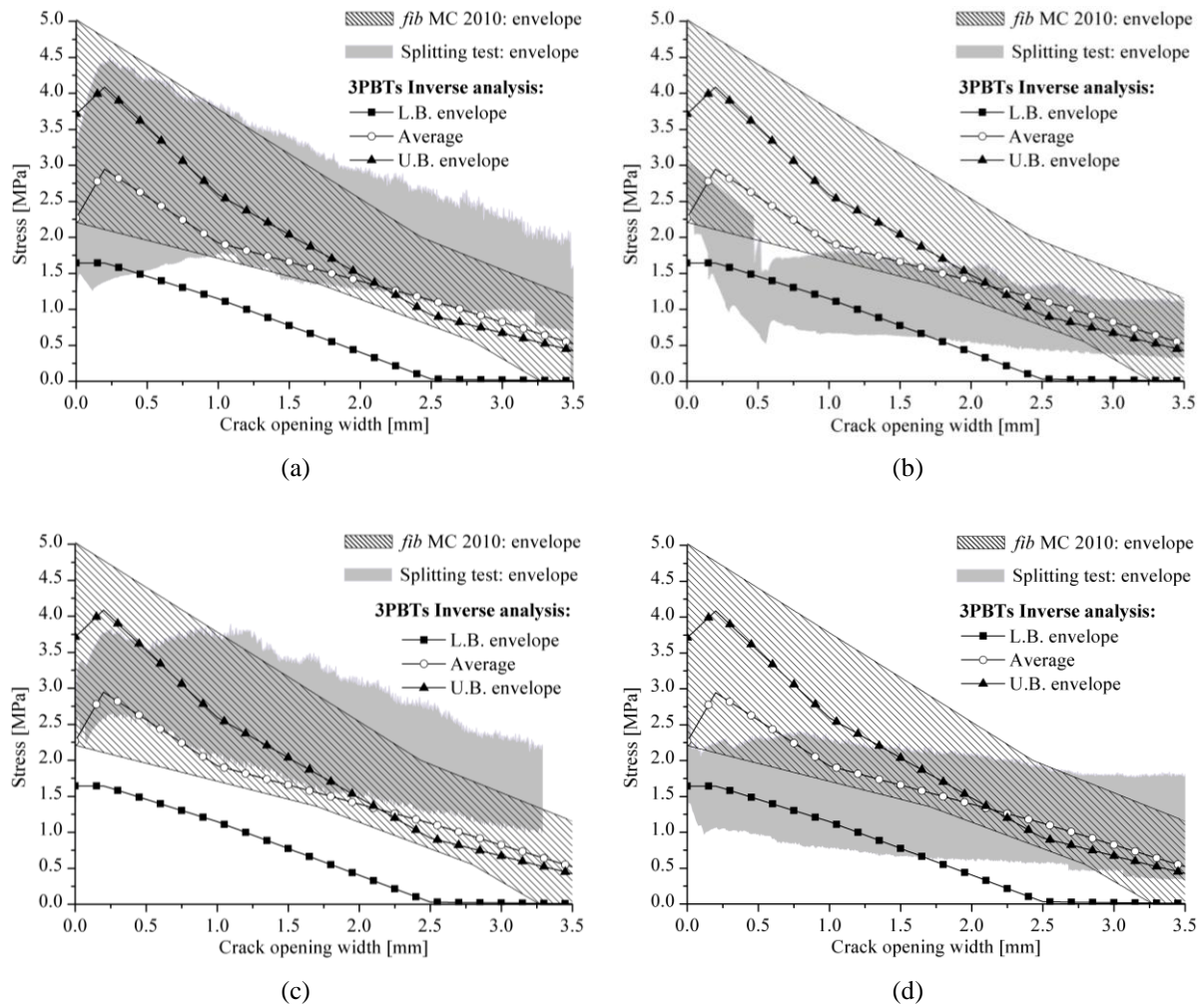
Figure 42: Comparison between the stress *versus* crack opening width diagrams obtained from the inverse analyses of 3PBTs, considering the *fib* MC 2010 approach and the experimental results from the splitting tests with force: (a) parallel to the SFRSCC flow; (b) perpendicular to the SFRSCC flow; (c) parallel to the *x*-direction (wall); (d) parallel to the *y*-direction (wall).

A verification of the validity of the direct use of the stress *versus* crack opening diagrams obtained from splitting tests to represent the direct tensile response of SFRSCC B was made by comparing the experimental load–CMOD curves obtained in 3PBTs with results of FE models of the 3PBTs using the parameters listed in Table 16 to model the post crack behaviour of SFRSCC. The geometry, boundary conditions, loading conditions and other properties of SFRSCC adopted in these models were the same used for the inverse analyses discussed above. Figure 43 illustrates the aforementioned comparison.
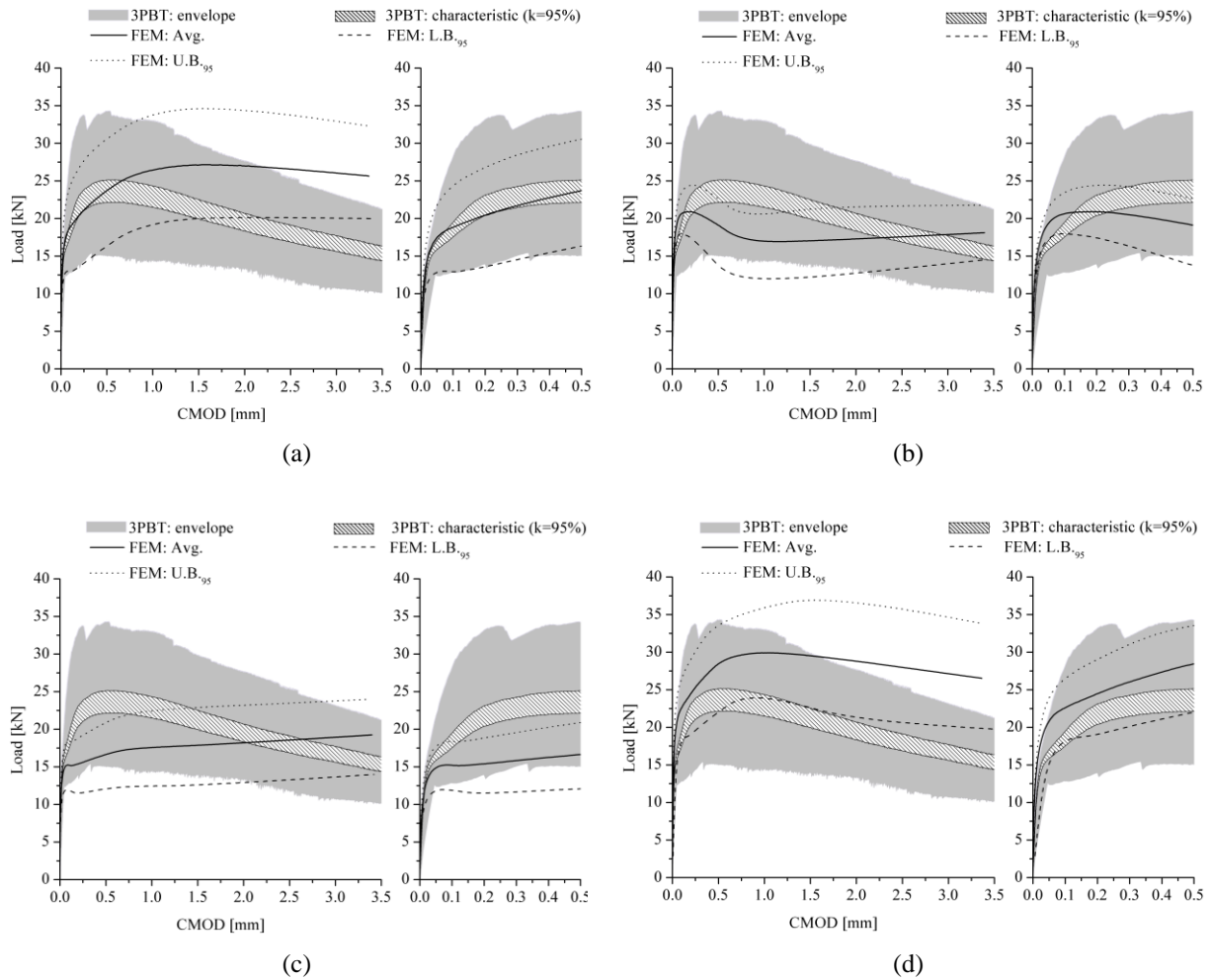
Figure 43: Comparison between the experimental load−CMOD curves and the ones obtained from the FEM of the 3PBT considering the quadrilinear diagram fitted from splitting tests: (a) parallel to the SFRSCC flow; (b) perpendicular to the SFRSCC flow; (c) parallel to the *x*-direction (wall); (d) parallel to the *y*-direction (wall).

3.7 THERMAL DILATION COEFFICIENT (TDC)

The interest in the thermal dilation coefficient of concrete is related to the fact that this property can affect the curling and axial stresses of the concrete sandwich panels. The knowledge of the TDC of concrete is an especially important consideration in the design of concrete structures exposed to the daily/yearly environmental temperature changes. Particularly in the case of the sandwich panels, the thermally induced loads are a main concern on the design of the elements and their connections (PCI, 2011). The stress level that arises on the structural element when subjected to a temperature change/gradient is strongly dependent on this property.

Concrete is a composite material and its TDC is dependent on material factors such as the type and amount of constituent materials (i.e., coarse aggregate, sand, cement paste, etc); and also on moisture condition of the concrete (Neville, 1996, Mehta and Monteiro, 2014). On the concrete technology, a common practice of technicians is to estimate the TDC and other thermal properties of concrete from the weighted average of the TDC of constituent materials (Neville, 1996). However, this hypothesis may not be still valid for SFRSCC due to the insertion of the steel fibres. The CTE of hardened plain concrete in the saturated state is reported to generally vary between 5.5 με/°C and 14 με/°C (Neville, 1996, Bamforth, 2007)

In this work, an experimental program was planned to determine experimentally the TDC of the SFRSCC B.

3.7.1 Test specimens and method

Several test methods are available to obtain the TDC of plain concrete cycles (Laplante and Boulay, 1994, Loser *et al.*, 2010, Loukili *et al.*, 2000, Bjøntegaard and Sellevold, 2001, Kada *et al.*, 2002, Sarkis *et al.*, 2002, Turcry *et al.*, 2002, Hammer and Bjontegaard, 2006, Cusson and Hoogeveen, 2006, Ozawa and Morimoto, 2006, Viviani *et al.*, 2007, Maruyama and Teramoto, 2011). The procedures described by AASHTO T336 (2011) were chosen to be followed in this work. This test consists on a linear technique, based on the measurement of the longitudinal length change of the specimen when subjected to controlled temperature changes.

The test was performed only with SFRSCC B from castings 13 and 19 (see Table 5). For that, one cylinder with 300 mm of height and 150 mm of diameter was cast for each of the casting studied. The specimens were instrumented with a vibrating wire strain gauge embedded in the center of specimen, positioned in order to measure the longitudinal (along its height) strain, as shown in Figure 44. The test was performed when the specimens were 210 and 212 days old, respectively for casting 13 and 19.

Figure 44: Detail of the vibrating wire sensor prior to the casting of specimen for TDC test.

Once there are evidences that the moisture content of the concrete affects the TDC (Emanuel and Hulsey, 1977), the specimens were sealed prior to the tests. Furthermore, in order to control the water absorption during the tests, the weight of both specimens are taken before and after the test.

(a)

(b)

Figure 45: Determination of the TDC. (a) Detail of sealing procedure of the specimens prior to the casting of specimen; (b) view of the sealed specimens submerged in the bath used to perform the test.

The specimens were submerged in a tank with circulating water under controlled temperature. Several thermocouples type K were used for monitoring the temperature in different positions in the water in the tank and also in different points located in the surface of specimens. The internal temperature of specimens was registered by a thermistor temperature sensor located in the vibrating wire sensor.

Prior to the test, the specimens were submerged to the water, the temperature of water was elevated up to T1 (approximately equal to 30ºC), and they the specimens were allowed to reach thermal equilibrium with the surrounding bath. Then, the temperature was elevated up to T2 (approximately equal to 35ºC) and, once again, the necessary time was allowed to ensure full thermal equilibrium of the specimen with the surrounding bath. After that, the temperature was dropped to the target temperature T1 and the 1st cycle completed. 4 similar cycles were performed in the test. The strains in the specimens were measured continuously along the test. The TDC of the cycle *j* was calculated for heating and cooling branches using Eq. (19). The TDC of each specimen was taken equal to the average of values registered for all the cycles.

$$TDC_j = \frac{\varepsilon_{T2,j} - \varepsilon_{T1,j}}{T2_j - T1_j} \tag{19}$$

where $T1_j$ and $T2_j$ are the registered temperatures after the equilibrium for the cycle *j* and $\varepsilon_{T1,j}$ and $\varepsilon_{T2,j}$ are the respective registered strains.

3.7.2   Test results

Both specimens presented increases of the weight during the test. Nonetheless, these values corresponded to only 0.35% and 0.77% of the initial weight of specimen, respectively, for the specimen of casting 13 and 19.

The registered internal and surface temperatures are compared for in Figure 46(a). The values of temperature and strain measured after the equilibrium for each cycle and the respective computed TDC are shown in Table 18.

(a)

(b)
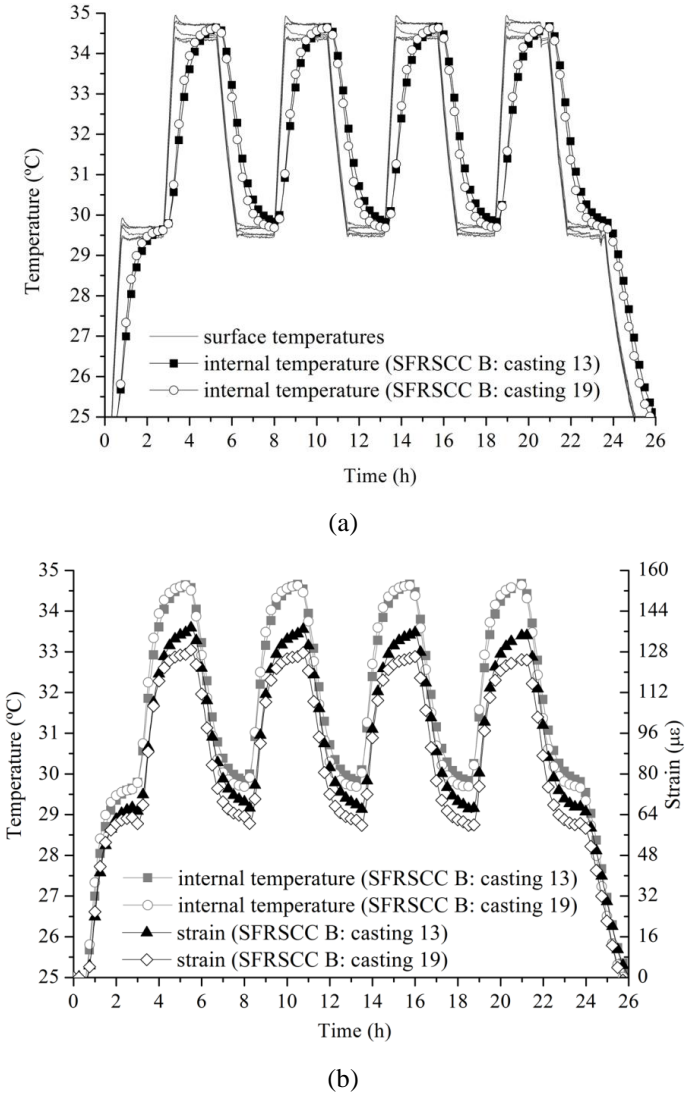
Figure 46: TDC test results. (a) progress of surface and internal temperatures; (b) progress of strain in the SFRSCC specimens due to temperature changes.

Table 18: Values measured in the TDC test.

Cycle		Instant		Casting 13		Casting 19	
				ΔT	TDC	ΔT	TDC
		[h]		[°C]	[$\mu\varepsilon$/°C]	[°C]	[$\mu\varepsilon$/°C]
1	Heating	initial	2.7				
		final	5.2	5.0	13.81	5.0	12.83
	Cooling	initial	5.2				
		final	7.8	-4.7	13.82	-4.9	12.89
2	Heating	initial	7.8				
		final	10.3	4.8	13.68	4.9	12.71
	Cooling	initial	10.3				
		final	13.0	-4.7	13.87	-4.9	12.97
3	Heating	initial	13.0				
		final	15.7	4.8	13.71	4.9	12.76
	Cooling	initial	15.7				
		final	18.3	-4.8	13.91	-4.9	12.99
4	Heating	initial	18.3				
		final	20.6	4.8	13.72	4.9	12.77
	Cooling	initial	20.6				
		final	23.3	-4.7	13.85	-4.9	12.98
Average					13.80		12.86
CoV					0.61%		0.84%

3.8 FINAL REMARKS

The work described in this chapter pertained to an experimental investigation focused on the determination of the mechanical behaviour of the SFRSCC and SCC used in this thesis. While not all the properties determined are essential for the design of the sandwich walls, they give an insight on possible failure modes that can occur during tests. Moreover, the obtained mechanical properties are valuable for numerical analyses dealing with modelling of the mechanical behaviour of structural element.

In this chapter, special attention was given to the tensile constitutive behaviour of SFRSCC (post-cracking behaviour). A modified splitting test was proposed and making use of the developed test method, the influence of the flow driven orientation of fibres on the post-cracking behaviour of SFRSCC was assessed. Results from standard 3PBT method, proposed by RILEM TC 162-TDF for the characterization of regular FRC, were compared with the results obtained from specimens that are more representative of the actual structural element

where the material is intended to be applied. Finally, the validity of *fib* MC 2010 approach for the constitutive modelling of SFRSCC applied to thin-section elements was questioned. From the research presented in this chapter, the following conclusions can be drawn:

- Although some undesirable failure modes were still obtained, the proposed test method is a promising procedure for the determination of the post-cracking behaviour of SFRSCC. Some optimization of the geometry of specimen (i.e., diameter, dimensions of notches) is still necessary;

- For the materials and casting conditions used in this research, the fibre orientation seems to be highly affected by the concrete flow. Specifically for the flow conditions used in this research, i.e., radial flow, the fibres tend to be oriented perpendicularly to the concrete flow;

- The post-cracking tensile behaviour of SFRSCC is affected by the fibre alignment resulting from the concrete flow and from the geometric characteristics of the structural element casted, but other parameters not covered in the present work also influence this behaviour, which deserves further research on the topic. Thus, the characterization of the material used in structural elements comprising SFRSCC should employ specimens that are geometrically representative of the actual structural element. Furthermore, to define the design value of the fracture properties the flow of concrete and the casting procedures should be taken into account;

- The method employed in this work, that consisted in obtaining the specimens from a plate with the same thickness of the structural element feeding the concrete in the center of the plate and performing splitting tests with load applied parallel and perpendicular to the flow, is a promising procedure to determine the values of the fracture parameters of SFRSCC to be adopted in the design of the thin-section structural elements. Having knowledge of the upper and the lower bounds of the expected behaviour (i.e., obtained the proposed splitting tensile test with the load applied parallel and perpendicular to the concrete flow, respectively), and considering partial safety factors, the design values can be obtained.

- The *fib* MC 2010 approach for the constitutive modelling of fibre reinforced concrete seems to overestimate the energy absorption capacity even for the directions in which SFRSCC presents the uppermost energy absorption capacities (i.e., with the loading applied parallel to the concrete flow), due to the flow induced orientation of fibres.

Chapter 4

GFRP CHARACTERIZATION

4.1 CONSTITUENT MATERIALS AND MANUFACTURING PROCESS

Glass Fibre Reinforced Polymer (GFRP) is a composite material having as matrix a polymer and as reinforcement, continuous or discontinuous glass fibres. Combining these two constituent materials is possible to achieve a composite material characterized by high strength and stiffness, combined with low density, when compared with bulk materials.

This thesis deals with different types of GFRP. All the laminates were produced in the installations of the Pole for Innovation in Polymer Engineering (PIEP). The manufacturing process chosen to produce the GFRP laminates was the Vacuum Assisted Resin Transfer Molding (VARTM). When compared to conventional autoclave processes, the VARTM has lower tooling cost, reduced energy cost for curing composite parts, and an almost unlimited part size (i.e., no size constraints based on autoclave size). When compared to the traditional resin transfer molding (RTM) process, it has a lower tooling cost and shorter start-up time. With the VARTM is possible to form a uniform composite with a fibre content as high as 60 to 70 percent fibre by weight (Carlsson *et al.*, 2014).

In a simplified manner, the VARTM can be described as the composite manufacturing process in which the dry fibres are assembled/laid into a form/tool with the desired geometry,

followed by the impregnation of the entire laminate in a single step making use of a vacuum pump. It has been developed as a variant of the traditional resin transfer molding (RTM) process. The VARTM eliminates the need of a matched metal mold, replacing it by a flexible film/bag.

A schematic representation of the VARTM procedure adopted in this research is shown in Figure 47.
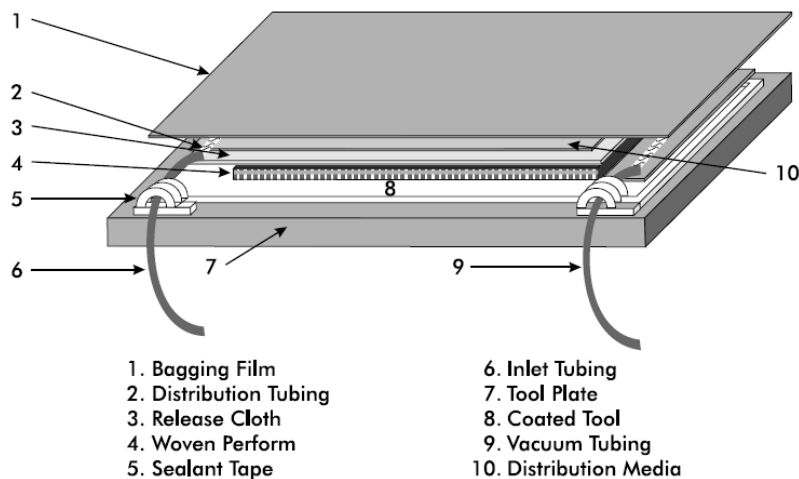
Figure 47: Illustration of a VARTM setup (Carlsson *et al.*, 2014) .

Typically, a thermosetting polymer of relatively low viscosity is used in the VARTM process. The composites used in the connectors employed in this thesis are made with polyester resin matrix. The option for this type of resin is related to its low cost and also because of the fact that it is one of the most common thermosetting resins used in the reinforced plastics.

Continuous and discontinuous E-glass fibres were adopted in the production of the composites used in this thesis. Two main types of reinforcements were used in the manufacturing of laminates: Chopped Strand Mat (CSM) and Stitched Roving Fabric (SRF). Discontinuous-fibre composites are normally somewhat random in alignment, which dramatically reduces their strength and modulus. However, discontinuous-fibre composites are generally much less costly than continuous-fibre composites. Therefore, continuous-fibre composites are used where higher strength and stiffness are required (but at a higher cost), and discontinuous-fibre composites are used where cost is the main driver and strength and stiffness are less important (Campbell, 2010).

In what concerns to the geometry of GFRP elements, two different main types of elements were produced for this research: profiled and flat elements. The production of both types of elements by the VARTM were similar and can be described in general by the following steps:

- Mold preparation

The mold used depended on the geometry of the composite element to be produced. In the VARTM process a metallic, wooden or glassy surface is normally used. In this research, a float glass plate was adopted for the production of the flat plates and metallic profiles to produce the profiled elements. First the tool/form was cleaned using sandpaper and acetone. Then, a frame corresponding to the borders was created using masking frame. Several coats of a release agent are applied to the form surface inside the masked frame. After that the masked tape was removed;

- Sealant bagging tape

Strips of silicone bagging tape, also called gum tape or tip tape, were applied to the tool surface in place of the masking tape. These strips provided an added adhesive surface for attachment of the inlet and outlet tubing (see Figure 48).

| (a) | (b) |
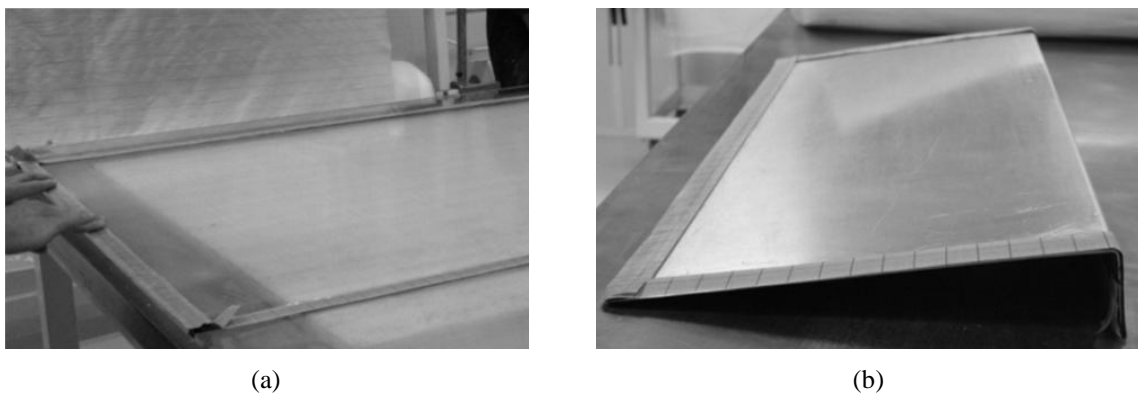
Figure 48: Detail of sealent tape applied to the mold: (a) glassy surface used as mold; (b) metallic profile used as mold.

- Bottom release material

The bottom release material was cut and applied, covering all mold surfaces (see Figure 49(a)). This bottom release fabric, also called as peel ply, is a porous release material that allows the easy removal of the fabricated element from the mold surface.

- Fabric lay-up

First, the different plies of the Chopped Strand Mat (CSM) or Stitched Roving Fabric (SRF) E-Glass fibres were cut. The fibre preform stack was then mounted by laying-up the different plies that compose the reinforcement following the designed stacking sequence. The number and type of plies differed for the different types of GFRPs used on this research (see details on Table 19). Once mounted, the fibre preform was then placed inside the sealant tape frame (see Figure 49(b)). A gap was kept between the silicone tape and the edges of the preform where the tubing was installed. Nonetheless, no gap existed between the sealant tape and the fibre preform along the panel width, in order to avoid providing an alternative resin flow pathway outside the preform from the inlet to the outlet tubing.

- Top release material

Another layer of porous release film (peal ply) was cut and positioned on top of the preform. This material allowed the composite laminate to release from the distribution media.

- Distribution media (flow mesh)

Due to the low injection pressure (1 atm), a resin distribution media with high permeability was incorporated to facilitate the resin flow in the preform (see Figure 49(c)). Once the distribution media provided a low resistance resin pathway, the resin easily filled this material, and then leaked downward, wetting the preform. The use of this material reduces the processing time, improves the uniformity of the impregnation of the preform and also protects the element from the wrinkles on the vacuum bag.

- Distribution/inlet and vacuum/outlet tubing

Polyethylene spiral wire wrap tubes were used as the resin distribution (inlet) and vacuum lines (outlet). These lines are laid above the distribution media at the two edges along the length of the preform. In the case of the resin distribution line, the resin line was closed at one end and connected to resin supply at other end. The vacuum line was closed at one end and connected to a vacuum pump through the vacuum gage.
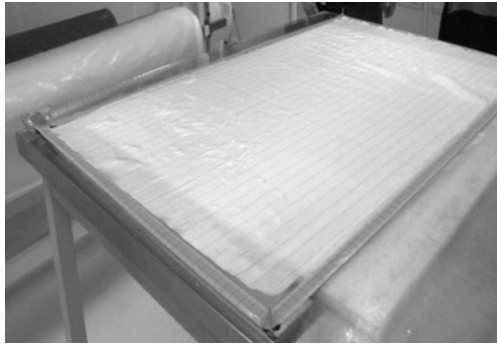
(a)

(b)
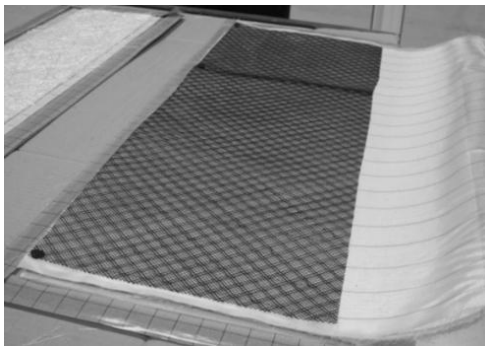
(c)

Figure 49: Manufacturing process of GFRP connectors: (a) bottom release material; (b) preform; (c) distribution media.

- Vacuum bag

Nylon bagging film was cut and used as vacuum bag. This film was spread over the mold area and it was airtight sealed with the tool surface using the sealant bagging tape (see Figure 50(a) and Figure 50(b)). Prior to the resin infiltration, the laminate was fully evacuated using the vacuum pump. Through this procedure was possible to detect bag leaks or leaks at the nylon material and the sealant interface. These leaks were prevented because they can result in void or poor consolidation of the final composite.

- Resin degassing

After mixing the resin components and before impregnation, the resin was degassed to remove air bubbles that were introduced during mixing. This procedure took place in a vacuum chamber. After that, the resin is contained in a bucket.

- Resin infiltration

The resin infiltration begun keeping the bagged laminate under full vacuum and then submerging the end of the supply tubing in the resin bucket. The resin flowed through the distribution tubing and across the width of the preform as it entered the distribution media. The flow-front of resin through the preform can be viewed in Figure 50(c). The vacuum pump was kept on for a while longer there were no more bubbles in the resin outlet line.

(a)	(b)
(c)	(d)
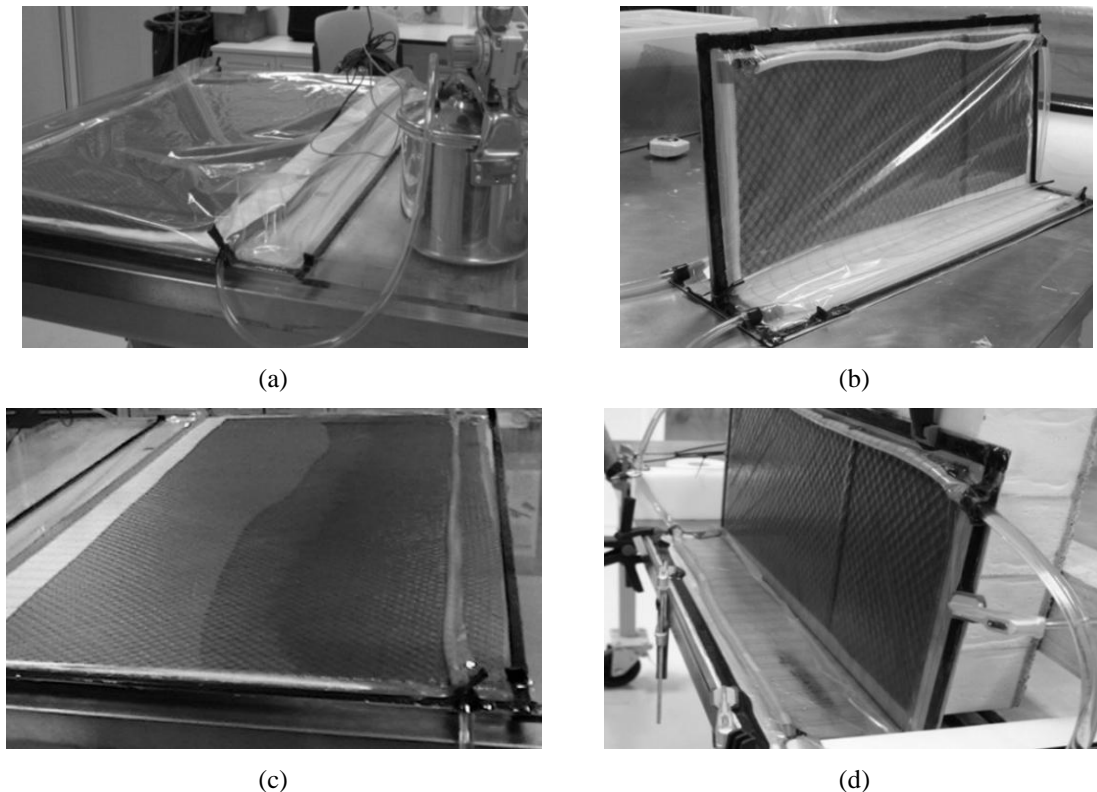
Figure 50: Manufacturing process of GFRP connectors. Vaacum bag applied to: (a) flat plate; (b) profiled element. Resin infiltration of: (c) flat plate; (d) profiled element.

- Curing

The curing of the elements was made keeping the mold at room temperature up to complete cure of the composite. This procedure took from 12 to 24 h.

- Demolding, cutting of elements and finishing works

After the cure the GFRP plates and profiles were cut and, in the case of perforated plates, the holes were made using a driller. To finalize, the edges and holes were sanded and the peel plies adhered to the GFRP surface were removed.

(a)
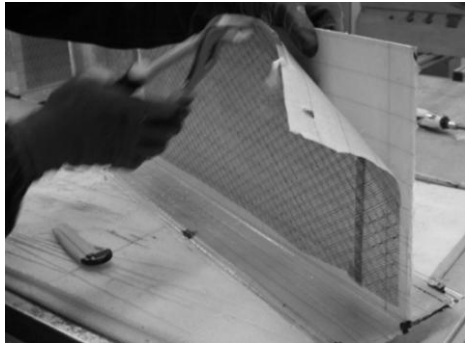
(b)

(c)

(d)

(e)

(f)

(g)
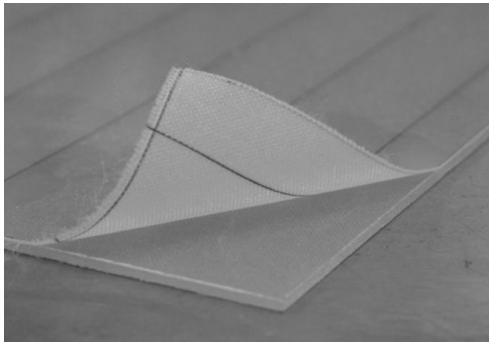
(h)

Figure 51: Manufacturing process of GFRP connectors: (a) demolding flat plates; (b) demolding profiled elements; (c) cutting of flat plates; (d) cutting of profiled elements; (e) perforating flat plates; (f) detail of hole perforated in a flat plate; (g) sanding; (h) remotion of peel ply.

Throughout the experimental programs developed as part of this thesis, 11 composites were used as material candidates for the connectors, being 9 laminates and 2 sandwich composites. All these materials are listed in Table 19. The nomenclature adopted for the composites denotes the stacking sequence of laminates, and is based on the Laminate Orientation Code, used almost universally by the composites community. The stacking sequence is indicated by the ply angles separated by a comma, from the outermost ply up to the one disposed in the midplane of the laminate. When two or more plies are grouped together, the angles of these plies are written once with a subscripted number denoting the number of plies in the group. Square brackets are used to indicate the beginning and end of the code. A subscript capital "S" following the closing square bracket is used to indicate that the laminate is symmetric and that only the plies on one side of the midplane is shown. In the other hand, a subscript capital "T" following the closing square bracket is used to indicate that the total laminate is presented. When a symmetric laminate contains an odd number of plies of the same material, the centre ply is designated with an overbar. For instance, the composite $L/[(+45,-45)_4; \bar{0}_3]_S$ is a laminate comprising three layers of a mat with fibres oriented in the 0° direction, positioned at the midplane of laminate, and 8 layers of a mat with fibres in the ±45° directions in each side, totalling 9 layers.

The first three laminates of Table 19, hereinafter referred as CSM, are made of Chopped Strand Mat (CSM) reinforcement. This reinforcement is characterized by short length fibres randomly oriented in its plane, as shown in Figure 52(a). These laminates were produced in different stages of the research and differ on the total content of glass fibres per m^2. The fourth and fifth laminates of Table 19, hereinafter referred as BIA, comprise long fibres arranged on ±45° directions. The reinforcement used in these solutions are supplied in biaxial Stitched Roving Fabric (SRF), containing layers of 400 g/m^2 and 450 g/m^2 each. The sixth laminate listed in Table 19, hereinafter referred as TRI, is comprised of a biaxial SRF and an unidirectional mat with their long fibres arranged on ±45° and 0° directions, respectively. Laminates consisted of different contents of long fibres arranged in 0°, 90° and ±45° directions were also investigated. These laminates are hereinafter called MU2 and MU4. The MU2 and MU4 laminates were produced using the same manufacturing process, the same constituent materials and the same fibre volumetric proportion. They differed only on the number of layers and, consequently, on the total thickness of the laminates. The laminate of the third material alternative (MU2) was obtained by stacking 6 layers of 400 g/m^2 ±45° stitched-bonded mats and one layer of 0°/90° containing 300 g/m^2 in each direction,

positioned in the symmetry plane. On the other hand, the fourth material alternative (MU4) included 12 layers of 400 g/m^2 ±45° stitched-bonded mats and one layer of 0°/90° containing approximately 600 g/m^2 in each direction. A quasi-isotropic laminate, referred as QUA, complete the list of laminates used in this thesis. In preliminary studies, the possibility of use of sandwich composites was also investigated. They are referred as SAC and SAQ. These sandwich composites consist of 5 mm of polyurethane foam (PU foam) of density 35 kg/m^3 as core material, and 2 outer skins laminates. The SAC composite differs from SAQ because the outer skins laminates of former composite consisted on 2 sheets of the same mat adopted in the production of the QUA laminate, while the later consisted of the same CSM mat adopted in the manufacturing of the CSM 1 laminate.

The QUA laminate was chosen because it is the GFRP adopted in the connectors of a preliminary research performed. The other laminates, namely: CSM, BIA, MU2, MU4, TRI and the sandwich structures: SAC and SAQ, are an attempt to reduce the costs, by adopting a mat with a lower cost (the case of CSM), or by reducing the content of the more expensive component (i.e., reducing the number of layers of E-glass mat, as done in the sandwiched solutions). The sandwich composites (SAC and SAQ) were the most competitive solutions to avoid instability derived from using thin laminates. In these composites the core material increases the internal arm of the resisting external layers, leading to an increase of the flexural stiffness of the sandwich composite without substantial increment in weight and cost of the final product.

Details about the composite layup and the thickness of laminates are grouped in Table 19 and the total amount of fibres per direction is given in Table 20. The average final thickness of composites were obtained taking two measurements of at least twenty specimens of the same material. The obtained average values are grouped in Table 19.

Table 19: Composites lay-ups and thicknesses.

Type / Ref.		Laminate Orientation Code	Stacking sequence		Thickness			
			N. of layers	Material of the layer	Avg. [mm]		N. of spec.	CoV [%]
LAMINATE	CSM 1	L/[CSM$_5$]$_T$	5	CSM/450	2.0		50	13.3
	CSM 2	L/[CSM$_5$]$_T$	5	CSM/450	2.0		50	19.7
	CSM 3	L/[CSM$_5$]$_T$	5	CSM/500	2.5		282	5.4
	BIA 1	L/[(+45,-45)$_8$]$_T$	8	SRF/+45-45/400	2.2		50	8.2
	BIA 2	L/[(+45,-45)$_8$]$_T$	1	SRF/+45/450	2.4		50	8.2
			1	SRF/-45/450				
			1	SRF/+45/450				
			2	SRF/-45/450				
			1	SRF/+45/450				
			1	SRF/-45/450				
			1	SRF/+45/450				
	TRI	L/[(+45,-45)$_4$; $\overline{0}_3$]$_S$	1	SRF/+45/450	6.0		50	13.3
			1	SRF/-45/450				
			1	SRF/+45/450				
			1	SRF/-45/450				
			6	SRF/0/450				
			1	SRF/-45/450				
			1	SRF/+45/450				
			1	SRF/-45/450				
			1	SRF/+45/450				
	MU2	L/[(+45,-45)$_3$; $\overline{(0,90)}$]$_S$	3	SRF/+45-45/400	2.2		50	6.6
			1	SRF/090/1200				
			3	SRF/+45-45/400				
	MU4	L/[(+45,-45)$_6$; $\overline{(0,90)}$]$_S$	6	SRF/+45-45/400	4.0		50	11.8
			1	SRF/090/600				
			6	SRF/+45-45/400				
	QUA	L/[(0,90,+45,-45)$_6$]$_T$	6	SRF/QUA/1203	5.1		56	8.7
SANDWICH	SAC	S/[CSM$_2$; $\overline{PU}$]$_S$	2	CSM/500	2.0	9.0	20	2.3
			1	PU foam	5.0			0.0
			2	CSM/500	2.0			2.3
	SAQ	S/[(0,90,+45-45); $\overline{PU}$]$_S$	1	SRF/QUA/1203	1.4	7.8	20	9.2
			1	PU foam	5.0			0.0
			1	SRF/QUA/1203	1.4			9.2

CSM

BIA

TRI

90°
+45°
0°
-45°

(a)

(b)

(c)

MU2, MU4 and QUA

(d)
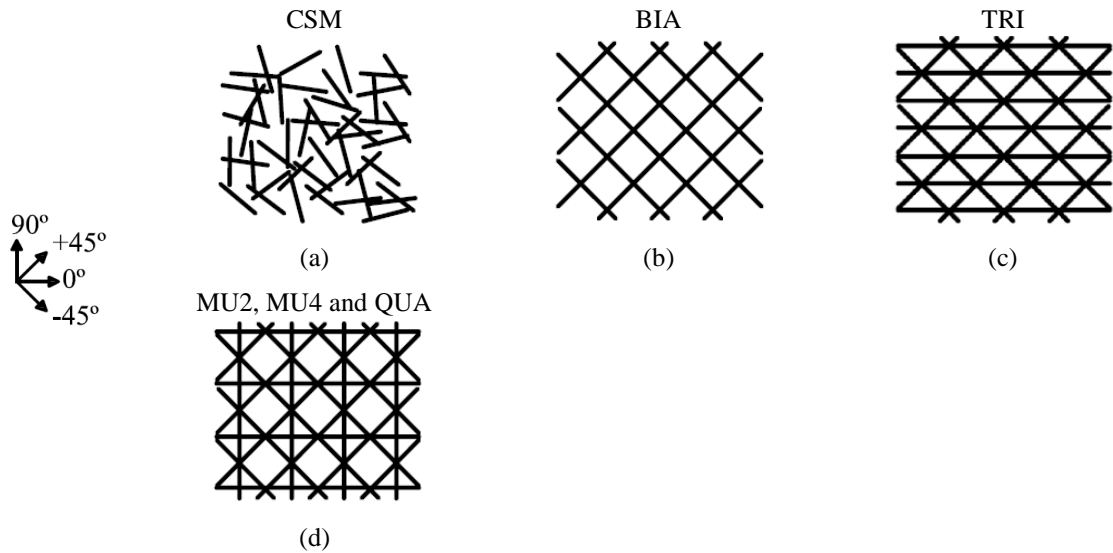
Figure 52: Schematic representation of used materials: (a) CSM; (b) BIA; (c) TRI and (d) MU2, MU4 and QUA.

Table 20: Total amount of glass fibre per composite.

Composite	Total content of glass fibre per composite [g/m^2]					
	Per direction					Total
	CSM	0°	90°	-45°	45°	
CSM 1	2250	0	0	0	0	2250
CSM 2	2250	0	0	0	0	2250
CSM 3	2500	0	0	0	0	2500
BIA 1	0	0	0	1600	1600	3200
BIA 2	0	0	0	1800	1800	3600
TRI	0	2400	300	1800	1800	6300
MU2	0	300	300	1200	1200	3000
MU4	0	590	610	2400	2400	6000
QUA	0	1800	1782	1818	1818	7218
SAN 1	2000	0	0	0	0	2000
SAN 2	0	600	594	606	606	2406

4.2   VOLUME FRACTIONS OF FIBRE AND RESIN

The properties of the composites materials are strongly dependent on the fibre volume fraction (Gay *et al.*, 2003). Thus, this parameter is an important quality measure of such materials that allows to estimate the properties of the composite, especially those that are not dependent on the fibre direction. This section presents the results of the measurements of the volume fraction of glass fibres on some of the composites used in this research.

The method adopted is the burn-off technique ASTM D 2584 (2011). This method is appropriate for glass fibre composites because this type of fibre is resistant to oxidation at the temperatures required to burn off the matrix (500 to 600ºC) (Carlsson *et al.*, 2014). The burn-off technique consists in the determination of the volume fraction by removing the matrix from the composite. The composite´s specimens are weighed at the beginning and the remaining fibres are weighed after the matrix to be volatilized. The weight of the fibres W_f are directly obtained after the burning process. The weight of matrix W_m is determined as the weight of composite minus W_f. The volume fractions are thus computed from the densities of the constituents from Eq.(20):

$$V_f = \frac{\rho_m W_f}{\rho_f W_m + \rho_m W_f} \tag{20}$$

where V_f is the volume fraction of fibres, ρ_m is the density of matrix and ρ_f is the density of fibres. For these calculations, it is assumed that the void content of the composite is negligible, what is acceptable for the composites produced by VARTM process (Carlsson *et al.*, 2014).

The test was performed for 8 types of laminated composites used in this research. 4 to 5 specimens of each type of composite were tested. The samples had all nearly 25 mm × 25 mm × thickness. They were weighed to the nearest 1.0 mg and then ignited in an electric muffle furnace. The specimens were heated at 565 °C for 6 h, time enough for the polyester matrix to disappear according to ASTM D 2584 (2011). After cooling to room temperature, the glass fibres were weighted to the nearest 1.0 mg. Figure 53 illustrates the specimens and stages of burn-off test.

<table>
<tr><td>(a)</td><td>(b)</td></tr>
</table>

Figure 53: Determination of volume fraction of fibres in the studied composites. (a) glass fibres corresponding to the composites after ignition; (b) weighing the remaining fibre of one specimen.

The Table 21 presents the volume fractions of fibre and resin for each type of laminated composite. The volume fractions are obtained assuming for E-glass fibres and polyester resin the respective densities: 2.6 g/cm^3 and 1.2 g/cm^3 (Gay *et al.*, 2003).

Table 21: Volume fractions of fibre of laminated composites.

Composite	N. of spec.	V_f	CoV
CSM 1	4	40.9%	0.6%
CSM 2	5	40.8%	0.6%
CSM 3	5	42.2%	0.6%
BIA 1	5	50.9%	0.5%
BIA 2	4	48.5%	1.1%
TRI	4	48.0%	3.1%
MU2	5	49.1%	0.8%
QUA	5	55.0%	0.5%

4.3 DIRECT TENSILE BEHAVIOUR

For the determination of the mechanical properties of the composites, direct tensile tests under constant head-speed rate of 2 mm/min were executed. In the case of the laminates BIA, TRI and QUA, in which the content of fibre is different in the different directions, tests were carried out loading the laminate in tension along other directions besides 0°.

Plates were manufactured using the same process that was chosen for the production of connectors, and test specimens were cut from the flat plate using a diamond saw wheel. The specimens were 25 mm wide and 250 mm long. The test procedures described in ASTM D3039 (2008) were followed, and tensile strength, stiffness and stress-strain relationship up to failure were determined. A clip-gauge with reference length of 50 mm, fixed in the middle of each specimen, was used to measure the strain in the longitudinal direction (see Figure 54(a)). To provide appropriate anchorage during testing and to diffuse the clamping stresses, rectangular aluminium tabs (50mm $\times$ 25mm $\times$ 1mm) were bonded at the extremities of the laminate specimens, as shown in the Figure 54(b). In the case of the sandwich composites the thickness of each laminate skin was increased to 3mm in the extremities of the specimens to avoid gripping damage. In the extremities of these specimens the polyurethane foam was replaced by a wood plate to prevent premature failure, as result of crushing the foam in the region where the specimen is gripped by the clamps (Figure 54(c)).

During the tests with sandwich composites, a premature delamination of the specimens was verified prior to the failure of the skin laminates. Representative failure modes can be observed in Figure 54(d).

The tensile stresses of the laminate specimens were calculated for each data point simply dividing the registered force by the average cross-sectional area of specimen. For the sandwich composites the tensile stresses were computed only considering the contribution of the laminate skins, disregarding the sectional area of the foam. The tensile strain at any data point was obtained dividing the displacement registered by the extensometer at data point by the extensometer gauge length.

The longitudinal and transversal tensile strengths, $\sigma_{pt.u}$, were defined as the ultimate values of stress obtained in a test. The ultimate strains, $\varepsilon_{pt.u}$, are the strains corresponding to $\sigma_{pt.u}$. The tensile chord modulus of elasticity, E_{pt}, was calculated as the division of the difference in applied tensile stress between the two points of reference contained in the lower half of the stress $\times$ strain curve, by the difference between the strain corresponding to the same points. The two points adopted as reference corresponded to 25% and 50% of determined ultimate strain.

The direct tensile test results are presented in Table 22, and the experimental stress-strain curves are depicted in Figure 55.

(a)   (b)

(c)   (d)
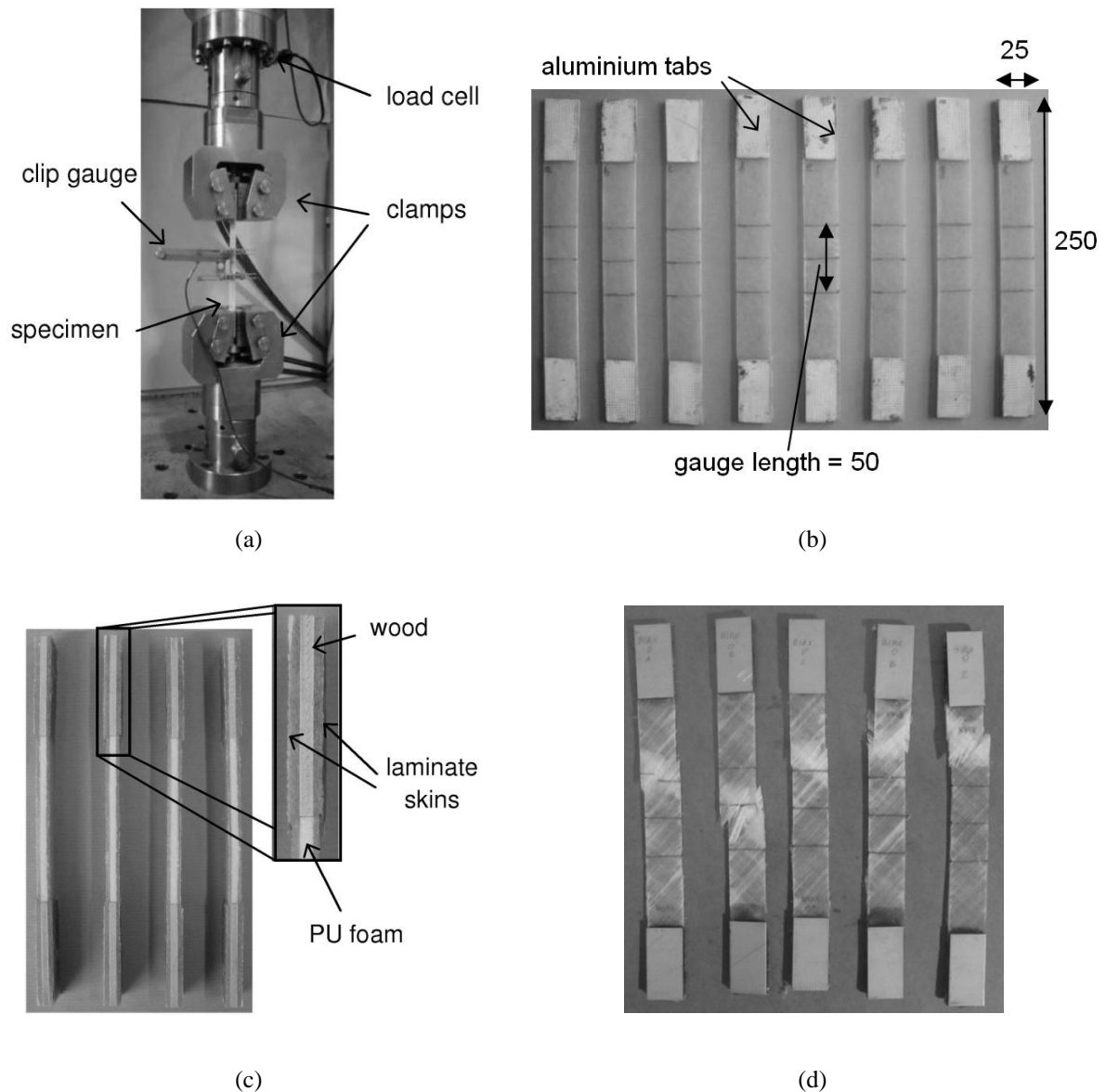
Figure 54: Direct tensile tests on GFRP laminates: a) test setup; b) CSM 1 specimens prior tests; c) detail of the SAC specimens; d) ruptured BIA 2 specimens tested along 0° (units in millimetres)

As shown in Figure 55, the responses of all laminates are not exactly linear in the loaded directions. This behaviour was expected due the high content of fibres transversally positioned to the load direction. From the results, it should be also noted that the laminates comprising longer fibres (BIA, MU2, MU4 and QUA) presented higher ultimate tensile strength and strain (see Table 22) than the similar composites comprising CSM laminates. In these cases, an elastic limit strain was determined creating a best linear fit for each of the two linear regions and these lines were extended until they intersected. The elastic limit strain was

taken equal to the strain that corresponds to the intersection point. The elastic limit stress, $\sigma_{pt.el}$, was made equal to the stress in the stress × strain curve corresponding to $\varepsilon_{pt.el}$.

Among the types of GFRP investigated, the CSM laminate was the material considered the most promising to produce the connectors due to its relative low cost, production simplicity and satisfactory mechanical properties.

Table 22: Direct tensile test results.

Ref.	Dir.	N. of spec.	Ultimate tensile stress $\sigma_{pt.u}$		Ultimate tensile strain $\varepsilon_{pt.u}$		Elastic limit stress $\sigma_{pt.el}$		Elastic limit strain $\varepsilon_{pt.el}$		Tensile Modulus of Elasticity E_{pt}	
			Avg. [MPa]	CoV	Avg. [με]	CoV	Avg. [MPa]	CoV	Avg. [με]	CoV	Avg. [GPa]	CoV
CSM 1	0°	6	252.54	8.5%	18029	9.8%	252.54	8.5%	18029	9.8%	14.64	7.4%
CSM 2	0°	8	199.49	7.9%	13981	13.2%	199.49	7.9%	13981	13.2%	14.35	6.1%
CSM 3	0°	8	201.97	4.4%	17881	5.4%	201.97	4.4%	17881	5.4%	12.65	3.7%
BIA 1	0°	6	119.59	3.2%	174231	3.2%	71.42	1.2%	9965	6.3%	13.33	1.4%
BIA 2	0°	5	90.73	3.2%	26745	1.7%	60.03	8.1%	5334	15.5%	14.42	9.8%
	45°	5	417.7	7.3%	21650	8.6%	417.7	7.3%	21650	8.6%	19.29	2.4%
TRI	0°	6	439.51	2.4%	23052	3.9%	439.51	2.4%	23052	3.9%	20.97	6.4%
	30°	7	141.65	5.7%	9188	8.3%	141.65	5.7%	9188	8.3%	20.39	4.1%
	45°	7	152.43	5.0%	24683	49.6%	72.11	3.9%	4210	8.0%	18.04	8.5%
	60°	7	126.04	5.5%	16488	12.7%	55.51	7.1%	3551	9.3%	16.93	10.6%
	90°	7	89.85	4.8%	22266	5.9%	44.84	1.4%	3929	8.8%	14.1	10.9%
MU2	0°	6	175.72	3.0%	24093	8.5%	69.4	7.1%	4788	9.1%	16.23	2.3%
MU4	0°	6	183.48	8.5%	26788	2.3%	73.44	4.3%	5016	3.8%	16.7	3.0%
QUA	0°	5	363.41	4.7%	26185	7.6%	363.41	4.7%	26185	7.6%	14.3	2.2%
	90°	6	350.11	3.7%	25912	5.8%	350.11	3.7%	25912	5.8%	13.52	2.0%
SAC	0°	4	194.69	2.8%	21911	12.5%	194.69	2.8%	21911	12.5%	9.51	2.5%
SAQ	0°	4	100.83	2.8%	16462	11.6%	100.83	2.8%	16462	11.6%	6.89	6.0%
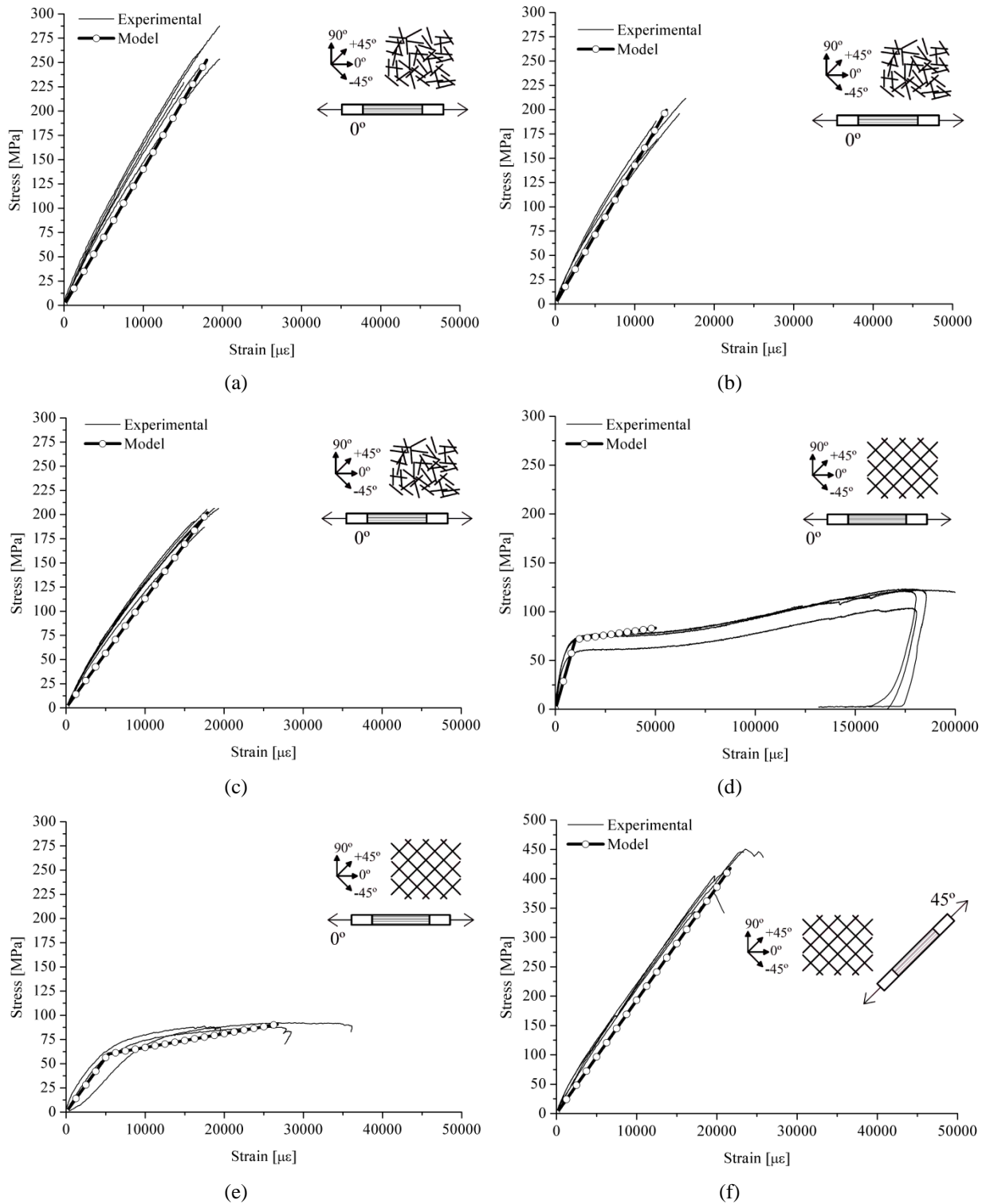
Figure 55: Experimental and modeled stress × strain curves for the direct tensile behaviour of the GFRPs: (a) CSM 1 at 0°; (b) CSM 2 at 0°; (c) CSM 3 at 0°; (d).BIA 1 at 0°; (e) BIA 2 at 0° and (f) BIA 2 at 90°.
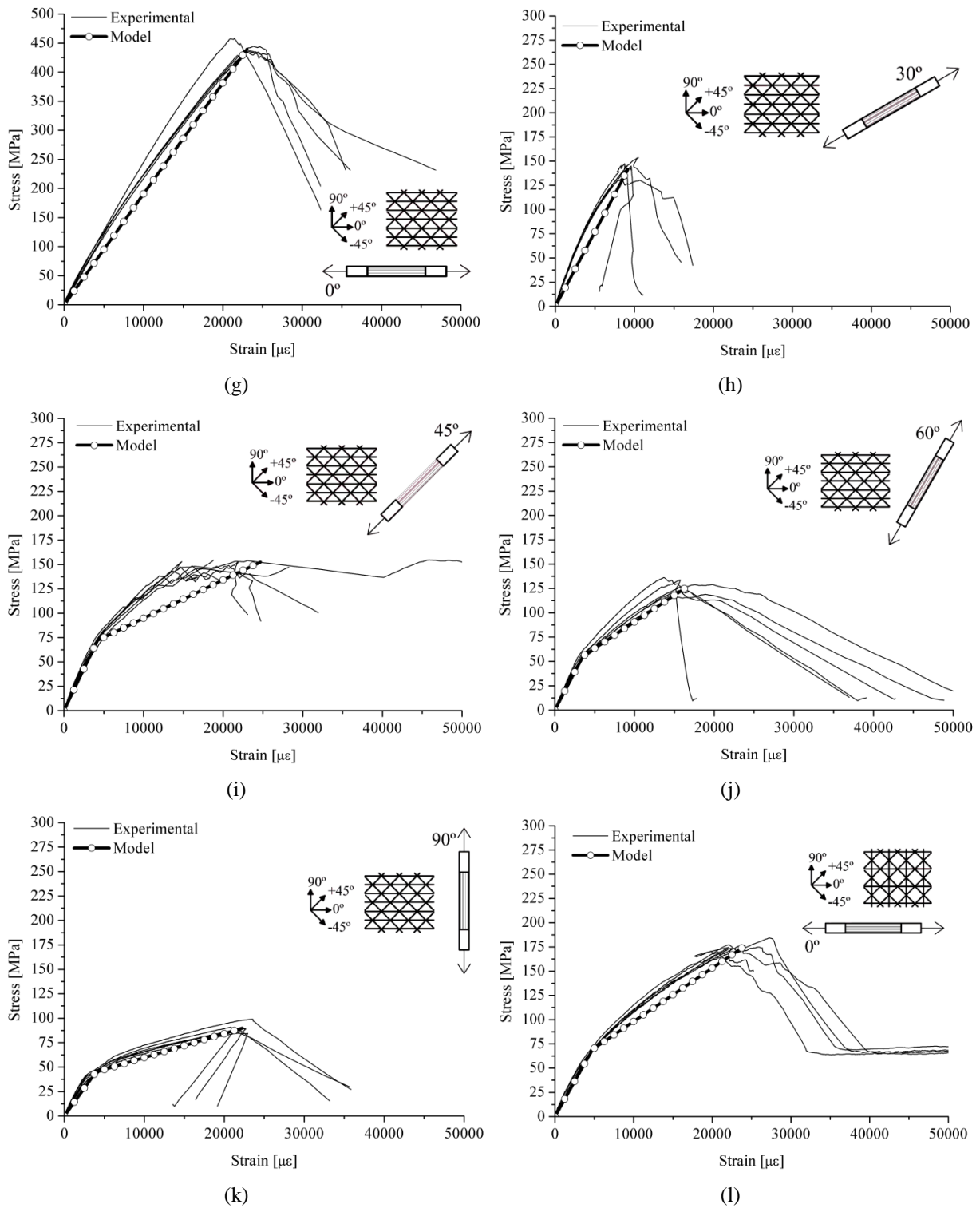
Figure 55: Experimental and modeled stress × strain curves for the direct tensile behaviour of the GFRPs: (g) TRI at 0°; (h) TRI at 30°; (i) TRI at 45°;(j) TRI at 60°; (k) TRI at 90° and (l) MU2 at 0°.
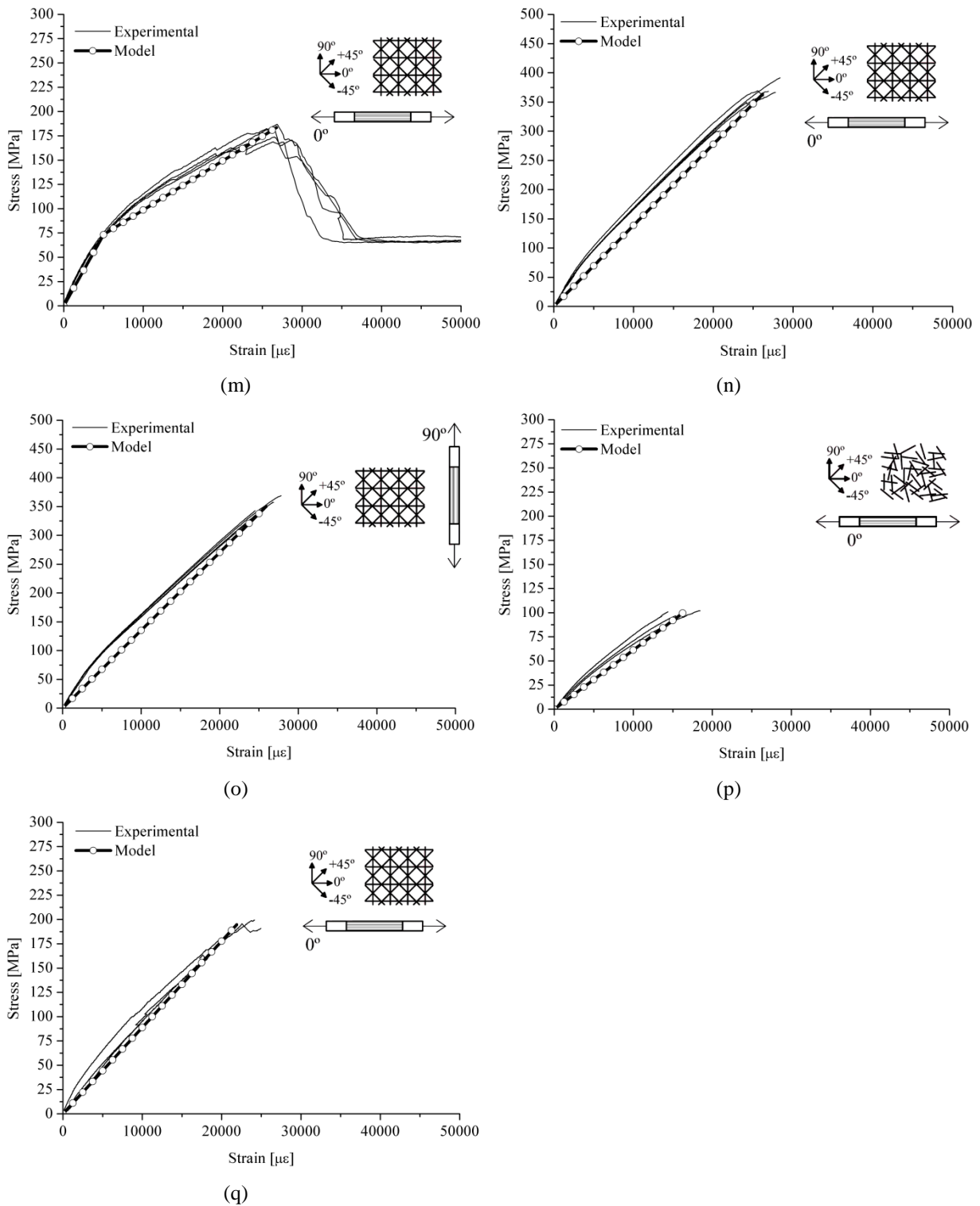
(m)

(n)

(o)

(p)

(q)

Figure 55: Experimental and modeled stress × strain curves for the direct tensile behaviour of the GFRPs: (m) MU4 at 0°; (n) QUA at 0°; (o) QUA at 90°; (p) SAC at 0° and (q) SAQ at 0°.

Figure 55 also plotted a model to represent of the tensile behaviour of GFRPs for each test. This model was developed to represent, in a simplified mode, the behaviour of the composites in the tested directions. They were built representing the curves as linear or bilinear curves.

When the response of the composite was better represented by a linear curve, the model was built with the origin and a point represented by the average values of $\sigma_{\text{pt.u}}$ and $\varepsilon_{\text{pt.u}}$. When a bilinear behaviour fitted better the response of the direct tensile tests, the stress $\times$ strain curve was modeled as schematically shown in Figure 56. If the ultimate failure did not occur within 50000 $\mu\varepsilon$, the data is truncated to the data corresponding to the strain of the data point nearest to this value.
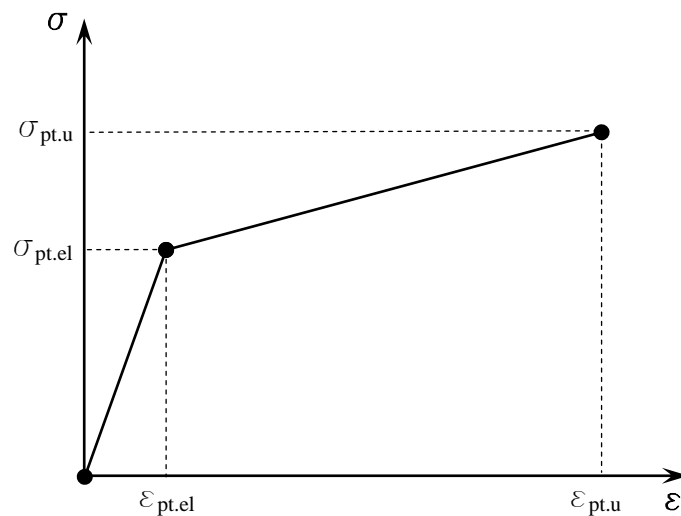
Figure 56: Schematic representation of the bilinear constitutive law for the GRRP.

4.4 SHEAR BEHAVIOUR

In this section, the shear behaviour of multi-directional Glass Fibre Reinforced Polymers (GFRP) is investigated by means of the Iosipescu shear test. In particular, the influence of the lay-up configuration on both in-plane shear properties and quality of test procedure is analysed. The in-plane shear modulus and strength of three types of GFRP that differ on type, amount and direction of reinforcement fibres.

The accurate measurement of mechanical properties of GFRPs is a fundamental requirement for their utilization as a structural material. In particular, their shear behaviour must be determined independently through a suitable shear test. However, the correct measurement of in-plane shear properties of composite materials is a complex problem, well known as one of the most difficult types of mechanical quasi-static tests (2000). During the last decades,

several methods have been proposed for measuring in-plane properties of composite materials (Boller, 1969, Sims, 1973, Rosen, 1972, Chamis and Sinclair, 1977, Whitney and Halpin, 1968, Iosipescu, 1967, Arcan *et al.*, 1978, ASTM, 2012b).

Among the proposed test methods there is the Iosipescu shear test method. This method was first developed for homogeneous, isotropic materials such as metals (Iosipescu, 1967). In the Iosipescu shear test, the specimen has the shape of a rectangular flat strip with two 90° symmetrical V-notches located in the middle length of the specimen. The specimen is inserted into a fixture with the notch aligned along the line of action of loading. The fixture is comprised by two halves that are compressed while monitoring load. One side of the fixture is displaced vertically while the other remains stationary (Figure 57).
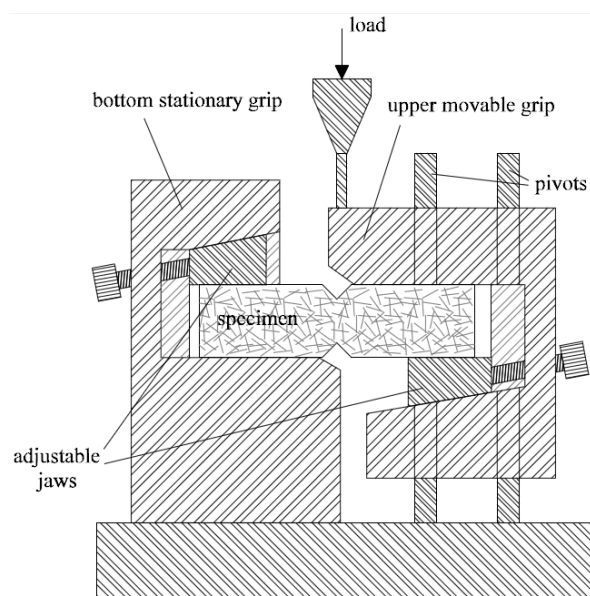
Figure 57: Schematic representation of a typical modified Wyoming fixture for Iosipescu shear test.

The original idea of Iosipescu (1967) was to obtain a four-point asymmetric bending test with a notched specimen. Theoretically, in this test configuration, the notched zone of specimen is only under pure shear forces (see Figure 58).
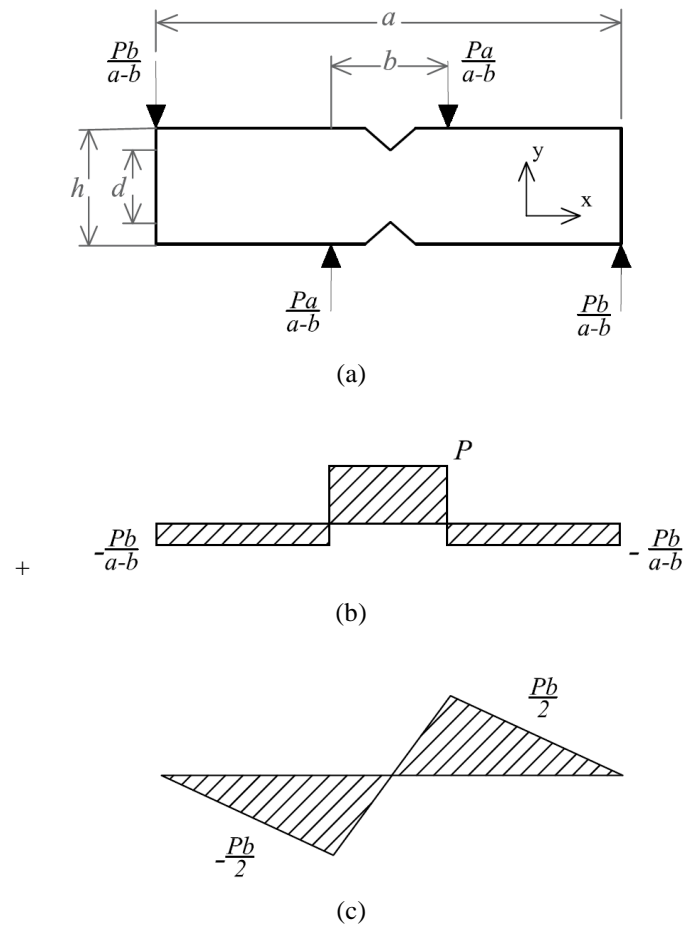
Figure 58: Iosipescu shear test method: (a) Idealized force during test; (b) idealized shear diagram on the specimen; (c) idealized moment diagram on the specimen.

Walrath and Adams (1983) first proposed the use of this test method for polymeric composite materials. Later, in order to avoid large compressive stresses generated in the gauge section of the specimen, an alternative fixture design was proposed by the same authors (Adams and Walrath, 1987), known as "modified Wyoming fixture". This modified Iosipescu shear test is standardized on ASTM D 5379 (ASTM, 2012a). This standard assumes that the strains are uniform along the area of the cross-section between the notches. Thus, shear strains are generally measured by use of electrical strain gauges (ESG) glued at the central portion of the specimen. However, it is known that such uniformity is not achieved for all materials, and that the lack of uniformity increases with the degree of anisotropy of the material (Pierron, 1998). Some authors have already shown that normal stresses can appear over the reduced section during the tests with anisotropic composites, not obtaining the desirable pure shear stress state (Kumosa and Hull, 1987, Broughton *et al.*, 1990, Morton *et al.*, 1992, Pierron and Vautrin, 1998, Odegard, 1999, Odegard and Kumosa, 2000). Thus, when this occurs, the ultimate

shear stress, $\tau_{xy.ult}$, and the shear modulus of elasticity, G_{xy}, both computed by the procedures described in ASTM D 5379 (ASTM, 2012a) cannot be interpreted as the real material properties.

Other limitations of the Iosipescu shear test outlined by previous works are (Ho *et al.*, 1994, Odegard and Kumosa, 2000): specimen sliding within the fixture; premature damage caused by crushing due to the specimen-to-fixture contact and premature intralaminar damage in the gauge region after the formation of axial splits. These factors generally appear for higher loads, and they generally introduce additional non-linearity to the load-displacement and stress-strain responses, thus affecting the determination of the shear properties of the tested material.

This work aims at obtaining a better understanding of shear behaviour of multi-directional fibre reinforced polymeric composites. Specifically, the tests were performed with laminates comprising polyester matrix and glass fibres reinforcements that differ among themselves in the type of reinforcement used (i.e., quantity and fibre orientation) and on the total thickness of the composite. To access the hypothesis of uniformity of shear stresses in the notched section and for a better understanding of the test performed with polymeric composites, an optical full-field measurement technique was used for determination of strains on the zone around the notched section. The digital image correlation (DIC) technique was adopted. The DIC is attractive for this purpose because it allows to identify strain gradients due to distributed mechanical properties and if the mechanical setups are causing parasitic effects (Grédiac, 2004). Finally, the strain measurements obtained with DIC were compared with the values obtained by the use of ESG and, based on the results, the validity of the standard test method was addressed.

4.4.1   Experimental program

The experimental program included a total of 23 Iosipescu tests, with at least two identical specimens of each variant. Details about the adopted materials, specimen's geometry, instrumentation and experimental procedures are presented in the following sections.

4.4.2   Material

Three types of GFRP were used: 1) CSM 2; 2) BIA 2 and 3) TRI. For the sake of simplicity, in this section, these composites are referred as CSM, BIA and TRI. The relative orientation

of the plies in the specimens used for the Iosipescu shear test are shown in Figure 59. Detailed information about the fibre content per direction for each laminate are presented in sections 4.1 and 4.2.
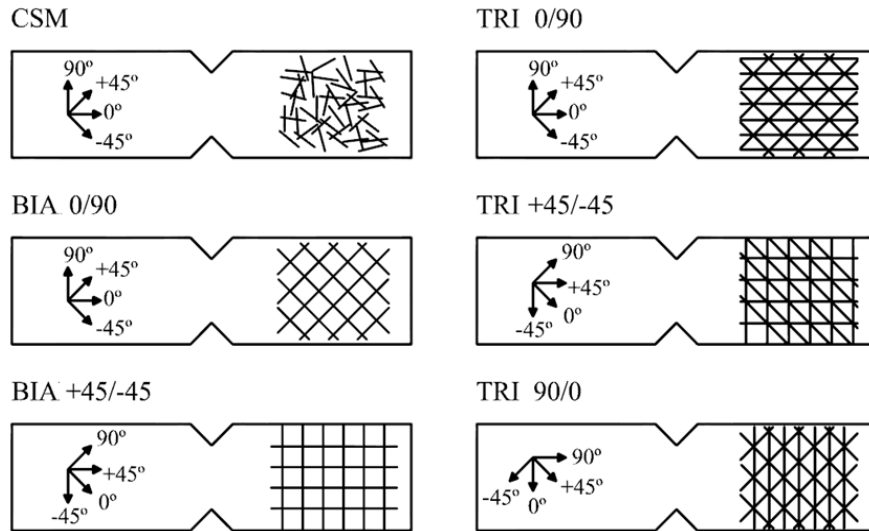
Figure 59: Schematic representation of the specimens and nomenclature adopted to identify the Iosipescu shear tests.

2.2.2 Iosipescu shear tests

All the Iosipescu specimens were obtained from 500×500 mm^2 flat plates. One plate of each type of composite was produced. The specimens were sawn through laser cutting to obtain more precision on their final dimensions. Due to their anisotropic nature, in the case of BIA and TRI laminates, specimens oriented in other directions than the 0/90 were also obtained (see Figure 59). The composites were cured at 20 °C during, at least 60 days.

The nomenclature adopted to identify the material orientation in the specimens consists on identifying the directions along the length of specimen and parallel to the loading axis, separated by a slash, i.e., the TRI 0/90 indicates that the test is performed with a specimen comprising TRI material with the 0° parallel to the length of specimen and the 90° parallel to the loading axis.

The nominal dimensions of the specimens are presented in Figure 60. These dimensions follow the recommendations of the ASTM D 5379-12 (ASTM, 2012a). Before the tests, the width w_{io} and height h_{io} of the specimen across the notch is measured and reported. The

cross-sectional area is calculated as: $A_{io} = w_{io} \cdot h_{io}$. The geometric properties of the specimens were taken at least for two sections. The average values obtained for each specimen are shown in Table 23.

(a)

(b)

(c)

(d)
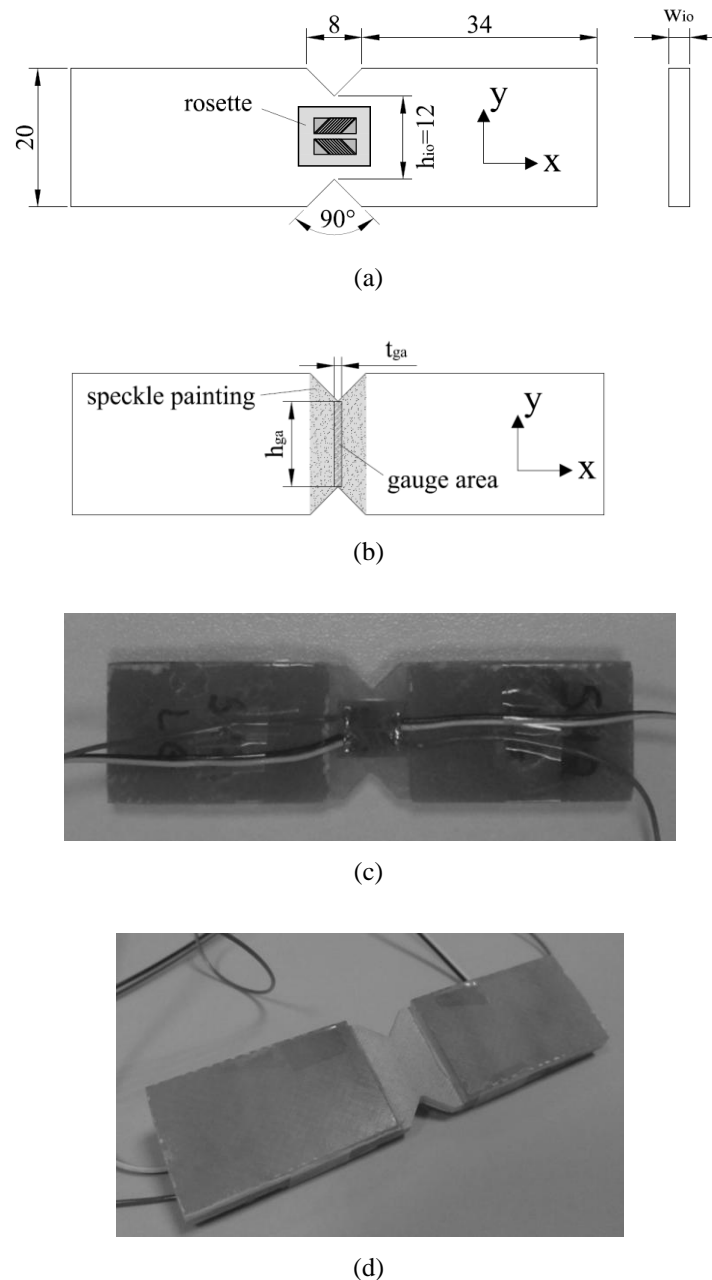
Figure 60: Dimensions of specimens and detail of instrumentation of specimens used on the Iosipescu shear test: (a) schematic representation of specimens with electrical strain gauge (back surface); (b) schematic representation of speckle painting for DIC technique (front surface). Detail of tabbing and instrumentation of: (c) specimens with electrical strain gauge; (d) speckled surface for DIC (units in millimetres).

Table 23: Measured dimensions, strain measurement method and use of tabs on the Iosipescu shear test.

Composite laminate	Specimen's number	Material planes alignment		Dimensions of reduced section		Measurement method		Gauge area (DIC)		Tab
		x	y	w_{io} [mm]	h_{io} [mm]	Elect. strain gauge	DIC	t_{ga} [mm]	h_{ga} [mm]	
CSM	1	-	-	2.19	11.73	✗	✓	0.94	11.02	✗
	2	-	-	2.13	11.66	✗	✓	0.94	11.02	✗
	3	-	-	1.95	11.86	✗	✓	0.94	11.02	✗
	4	-	-	2.04	11.65	✓	✗	-	-	✓
	5	-	-	2.15	11.06	✓	✗	-	-	✓
BIA	6	0°	90°	2.79	12.05	✓	✓	0.94	11.49	✓
	7	0°	90°	2.72	11.90	✓	✓	0.94	11.26	✓
	8	45°	-45°	2.82	12.00	✓	✓	0.94	11.26	✓
	9	45°	-45°	2.69	11.93	✓	✓	0.94	11.96	✓
	10	45°	-45°	2.69	11.95	✓	✓	0.94	11.26	✓
	11	45°	-45°	2.72	11.81	✓	✓	0.94	11.73	✓
	12	45°	-45°	2.92	12.01	✓	✗	-	-	✓
	13	45°	-45°	2.74	11.98	✓	✗	-	-	✓
TRI	14	0°	90°	6.69	12.03	✓	✓	0.94	11.96	✗
	15	0°	90°	6.08	12.16	✓	✓	0.94	11.73	✗
	16	0°	90°	6.28	12.12	✓	✗	-	-	✗
	17	0°	90°	6.89	12.05	✓	✗	-	-	✗
	18	45°	-45°	6.19	11.94	✓	✓	0.94	11.26	✗
	19	45°	-45°	6.18	11.96	✓	✓	0.94	11.96	✗
	20	45°	-45°	6.12	11.82	✓	✗	-	-	✗
	21	90°	0°	6.28	12.15	✓	✓	0.94	11.73	✗
	22	90°	0°	6.25	11.90	✓	✓	0.94	11.26	✗
	23	90°	0°	6.25	12.20	✓	✗	-	-	✗

✓: presence. ✗: absence.

In order to avoid undesirable premature failure modes induced by the reduced thickness of specimens (i.e., local crushing failure and twisting of specimen), in the case of CSM and BIA laminates, polyamide tabs with thickness equal to 2 mm were locally bonded on both sides of the extremities of the specimens, as shown on Figure 60(c) and Figure 60(d).

At least two specimens of each type were instrumented with electrical resistance strain gauges (ESG). The strain gauge used consists on a stacked rosette with two orthogonal strain gauges

glued to the centre of the specimen at a ±45° to the loading axis. The active gauge length is 1.4 mm and it is 120 Ω. The matrix dimensions of the rosettes are 7.0×3.4 mm^2. In order to provide compensation for temperature-induced changes in the circuit, both individual strain gauge elements of rosettes are connected independently to a Wheatstone bridge in a quarter-bridge arrangement. The gauge fixing procedure followed the recommendations of the manufacturer. The gauge is attached to the composites by an adhesive (cyanoacrylate). The DIC technique was employed in 15 specimens, as shown in Table 23.

To obtain the necessary textured pattern for DIC measurements, the central region of interest of the Iosipescu specimens was painted. A matte white thin layer was firstly applied to the background (see Figure 61(a)) and a random pulverization of fine droplets of black paint was achieved by means of an airbrush guaranteeing suitable contrast and speckle size over the field of view (see Figure 61(b)). The final aspect of the faces of specimens instrumented with the ESG and for measurements with DIC are shown, respectively, in Figure 60(c) and Figure 60(d).

<table>
<tr><td>(a)</td><td>(b)</td></tr>
</table>
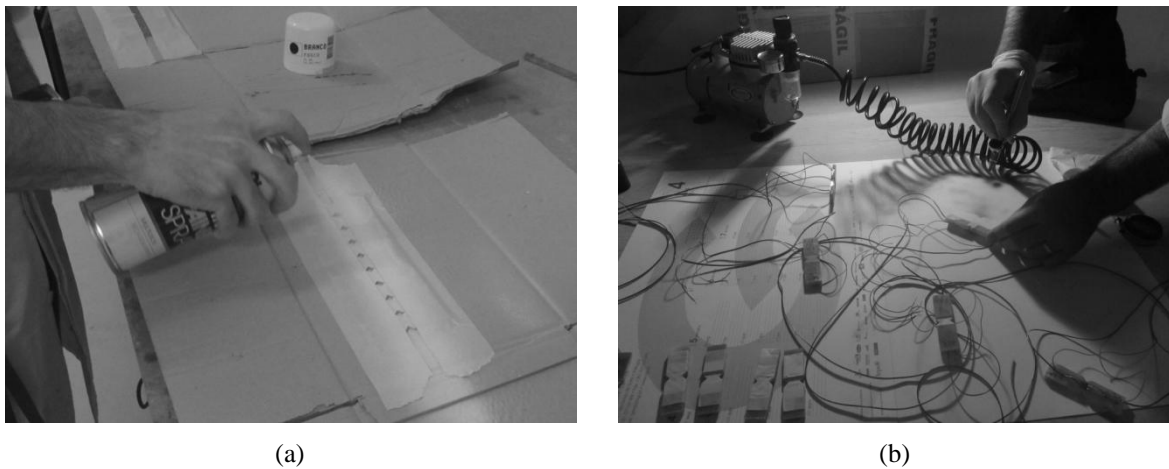
Figure 61: Preparation of specimens for DIC: (a) white background; (b) pulverization of black paint to obtain the speckle painting.

While keeping the specimens centred, the left-hand-side jaw was lightly tightened so that the specimens were contacting the lower grip surface. Then, the jaw of the right-hand grip was also lightly tighten until the specimens contacted the upper grip surface. A pre-load equal to 3 N was applied to the specimens to provide some adjustment between the specimens and the fixture.

The tests were performed on a Shimadzu universal testing machine, at a controlled displacement rate of 1 mm/min. The applied force was monitored using a load cell with 50 kN capacity. The force and strain outputs are recorded on a portable computer through a data acquisition system at a frequency of 10 Hz, while the images obtained for DIC technique are recorded through an independent acquisition system at a frequency of 1 Hz.

The mode and location of failure of the specimens were recorded. Then, the failure modes were identified among one of the acceptable types indicated in the ASTM D5379 (ASTM, 2012a) and shown in Figure 62.
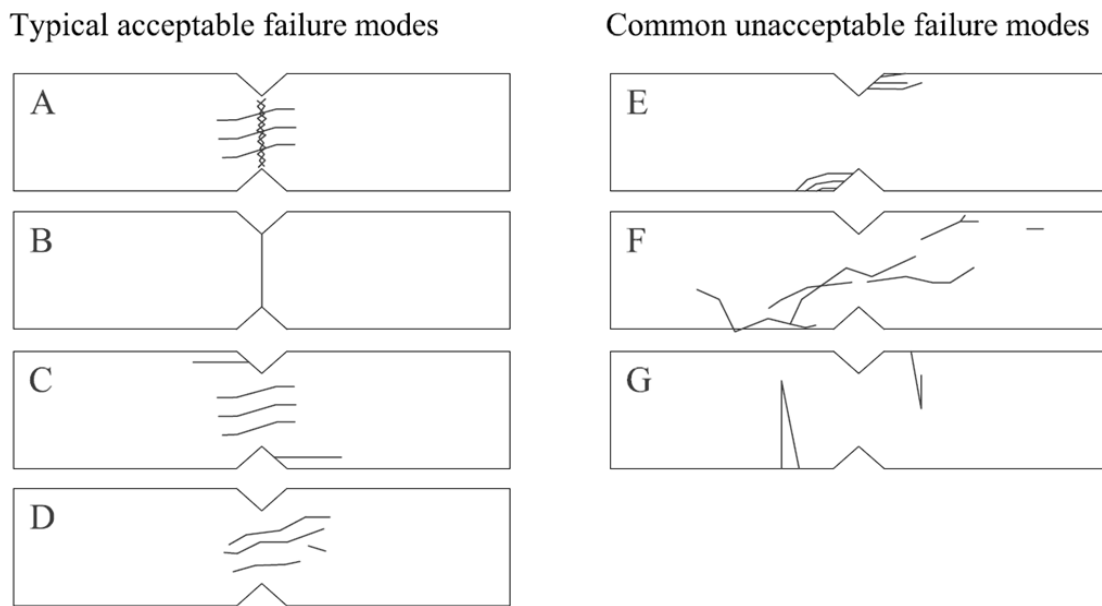
Figure 62: Typical failure modes for the Iosipescu shear tests (adapted from ASTM D5379 (ASTM, 2012a)).

When electrical strain gauges were employed, the engineering shear strains γ_{xy} at i[th] data points were obtained by Eq. (21).

$$\gamma_{xyi} = \left|\varepsilon_{+45°i}\right| + \left|\varepsilon_{-45°i}\right| \tag{21}$$

where $\varepsilon_{+45°i}$ and $\varepsilon_{-45°i}$ are the strains measured by the strain gauges positioned at +45° and -45°, respectively, for the ith data point. The shear stresses were obtained by considering a uniform stress distribution along the reduced cross-section of the specimens. The values of this shear stress at i[th] data point were computed by Eq. (22).

$$\tau_{xyi} = \frac{P_i}{A} \tag{22}$$

Where P_i is the load applied to the fixture at i[th] data point and A is the reduced cross-sectional area of the specimen. Considering that P_u is the load at the occurrence of failure, the ultimate shear stresses carried out by the specimens were computed by Eq. (23).

$$\tau_{xyult} = \frac{P_u}{A} \tag{23}$$

Following the procedures recommended by the ASTM D5359 (ASTM, 2012a), if the ultimate failure did not occur within 50000 με, the data was truncated to the data corresponding to the strain of the data point nearest to this value. The ultimate shear strain γ_{xyult} was defined as the shear strain corresponding to the ultimate load. The values obtained of τ_{xyult} and γ_{xyult} for a certain specimen are only considered for the computing of the ultimate shear stress and ultimate shear strain of laminate when the specimen presents one of the acceptable failure modes indicated in the ASTM D5379 (ASTM, 2012a).

The shear chord modulus of elasticity was computed by Eq.(24).

$$G_{xy} = \frac{\Delta\tau_{xy}}{\Delta\gamma_{xy}} \tag{24}$$

where $\Delta\gamma_{xy}$ and $\Delta\tau_{xy}$ were respectively the difference between two strain points and the respective difference in applied shear stress for the same points. The shear chord modulus of elasticity was computed using Eq.(24) applied over a 4000 ± 200 με engineering shear strain range, with the lower strain point in the range between 1500 and 2500 με.

The values defined above were calculated considering a uniform distribution of the stress and strain along the area of the cross-section between the notches.

Through DIC the deformation of composites was assessed by comparing the geometrical deformation of the random textured pattern (speckled painting), that is assumed perfectly bonded to the material. DIC deformation measurements can assist in this case to inspect both uniformity and predominant shear response of the Iosipescu specimens. Moreover, it allows

the measurement of shear strain component integrated along the V-notch section, contracting with the punctual measurement by using a strain gauge.

In this work, the ARAMIS DIC-2D was used (GOM, 2009, Xavier *et al.*, 2012). The optical system consisted on 8-bit Baumer Optronic FWX20 camera coupled with a telecentric lens OPE-TC-06-39. The working distance was defined as 103.5 mm with a magnification factor of 0.018 mm/pixel. Lighting and shutter time was adjusted in order to extent the histogram of the speckled image over the dynamic of the CCD sensor, avoiding under and over pixel saturation. Considering the region of interest, average speckle size and pixel size on the object plane, a subset size of 15×15 pixels^2 was chosen, in a compromise between resolution and spatial resolution. The shear components were then determined from in-plane displacements by numerically differentiated, using a gauge length of 5 subsets. The typical resolution of the measurements was in the range of 0.01 pixel and 0.02-0.04 % for displacement and strain evaluation, respectively (Sousa *et al.*, 2011a, Sousa *et al.*, 2011b). Two photos of the test setup are shown in Figure 63.

(a)   (b)

Figure 63: Test setup: (a) overall view; (b) detailed view of specimen positioned in the fixture and the position of the camera..

4.4.3   Failure mechanisms of the Iosipescu specimens

In general, the Iosipescu shear test proved to be inappropriate for use with the tested composites, excepting for the CSM and BIA 45/-45. For these laminates, the use of tabs to increase the thickness of laminates in the gripping regions proved to be essential for obtaining the desired failure by shear in the notched section. For the specimens 01 to 03, comprised of

CSM laminate and tested without the use of tabs, the specimens presented a premature failure by local crushing of the laminate at the gripping region of the fixture. A typical evolution of these tests is presented in the Figure 64, where the premature crushing is indicated by white arrows. The same premature crushing was observed for the TRI 0/90, TRI 45/-45 and TRI 90/0 (see Figure 67). A distinct failure mode was observed for the BIAX 0/90 06 and 07. For these specimens, a premature failure in the tabs was noticed (see Figure 66). In the Figure 64 to Figure 67, the item (c) generally indicates the first failure noticed in the front face of specimens with a white arrow. It is noted that, even when these undesirable premature failures have occurred, they apparently started at shear strain always higher than 9500 µε. This is more than twice the strain level used to compute the shear modulus of material.
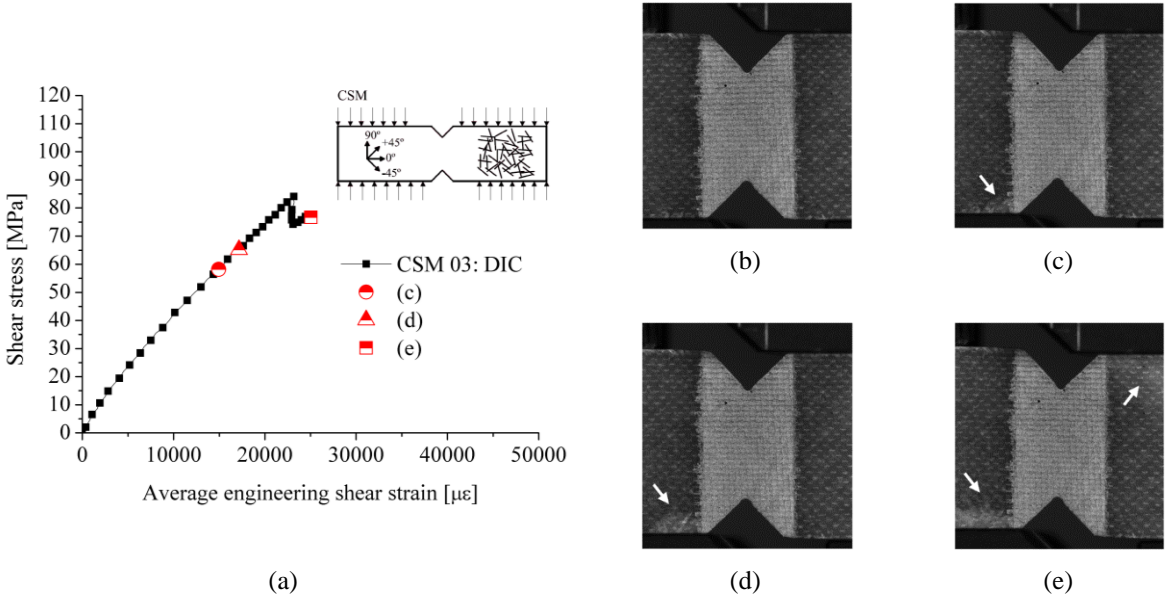
Figure 64: Damage evolution on specimen CSM 03 (a) stress vs. strain relationship; (b) load equal to 0 kN; (c) load equal to 1.339 kN (15400 µε); (d) load equal to 1.491 kN (17600 µε); (e) load equal to 1.708 kN (25000 µε).

(a)
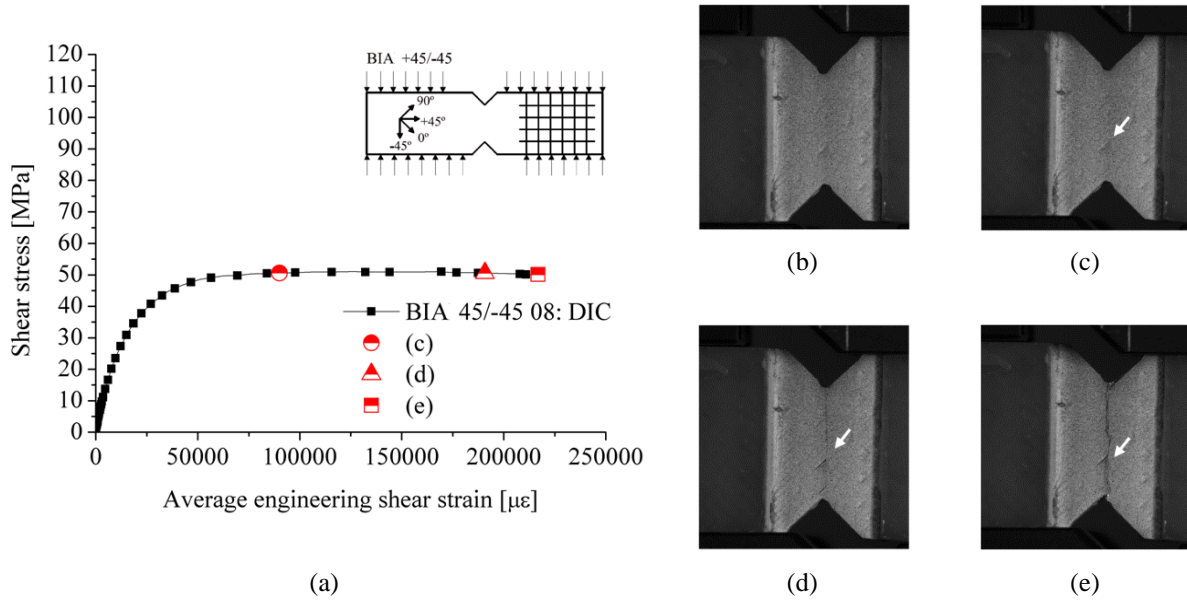
Figure 65: Damage evolution on specimen BIA 45/-45 08: (a) stress vs. strain relationship; (b) load equal to 0 kN; (c) load equal to 1.672 kN (90040 µε); (d) load equal to 1.688 kN (190720 µε); (e) load equal to 1.193 kN (216750 µε).

(a)
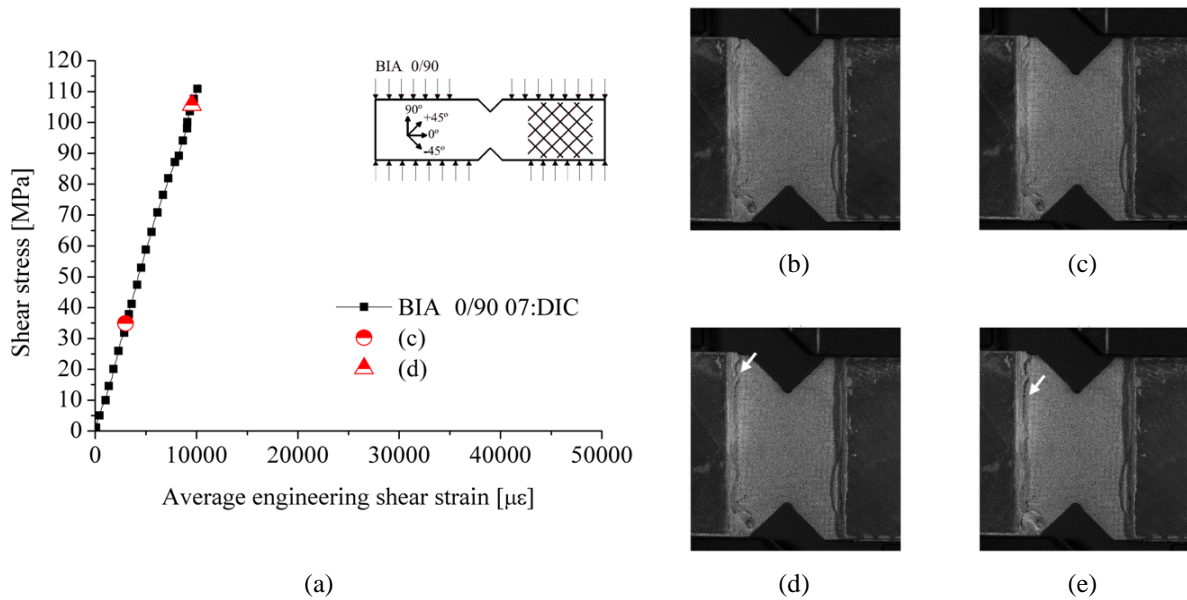
Figure 66: Damage evolution on specimen BIA 0/90 07: (a) stress vs. strain relationship; (b) load equal to 0 kN; (c) load equal to 1.112 kN (3000 µε); (d) load equal to 3.371 kN (9500 µε); (e) final aspect.

<div align="center">(a)</div>
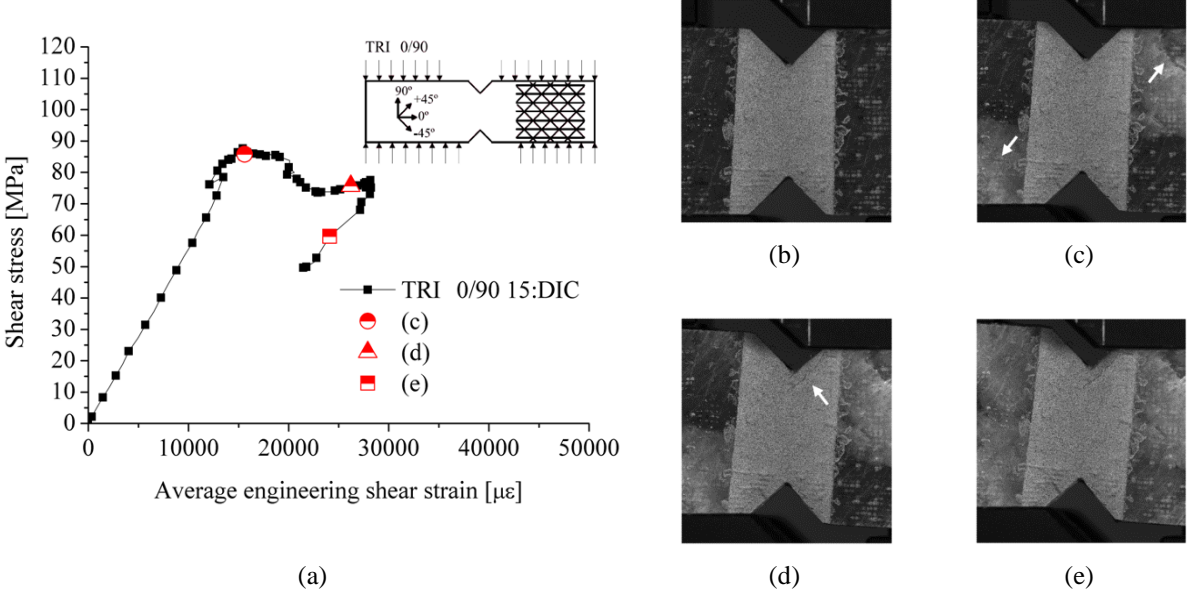
Figure 67: Damage evolution on specimen TRI 0/90 15: (a) stress vs. strain relationship; (b) load equal to 0 kN; (c) load equal to 6.363 kN (15600 με); (d) load equal to 5.615 kN (26200 με); (e) load equal to 4.422 kN (24100 με).

The final physical condition of some specimens after the tests are shown in Figure 68. Attention is paid to the characteristic failure by pure shear obtained for the specimen BIA presented in Figure 68(b) and Figure 68(c). Similar aspect was obtained for all the other BIA specimens and CSM specimens in which tabs were applied to the specimens. The delamination observed for some TRI specimens is shown in the Figure 68(g).
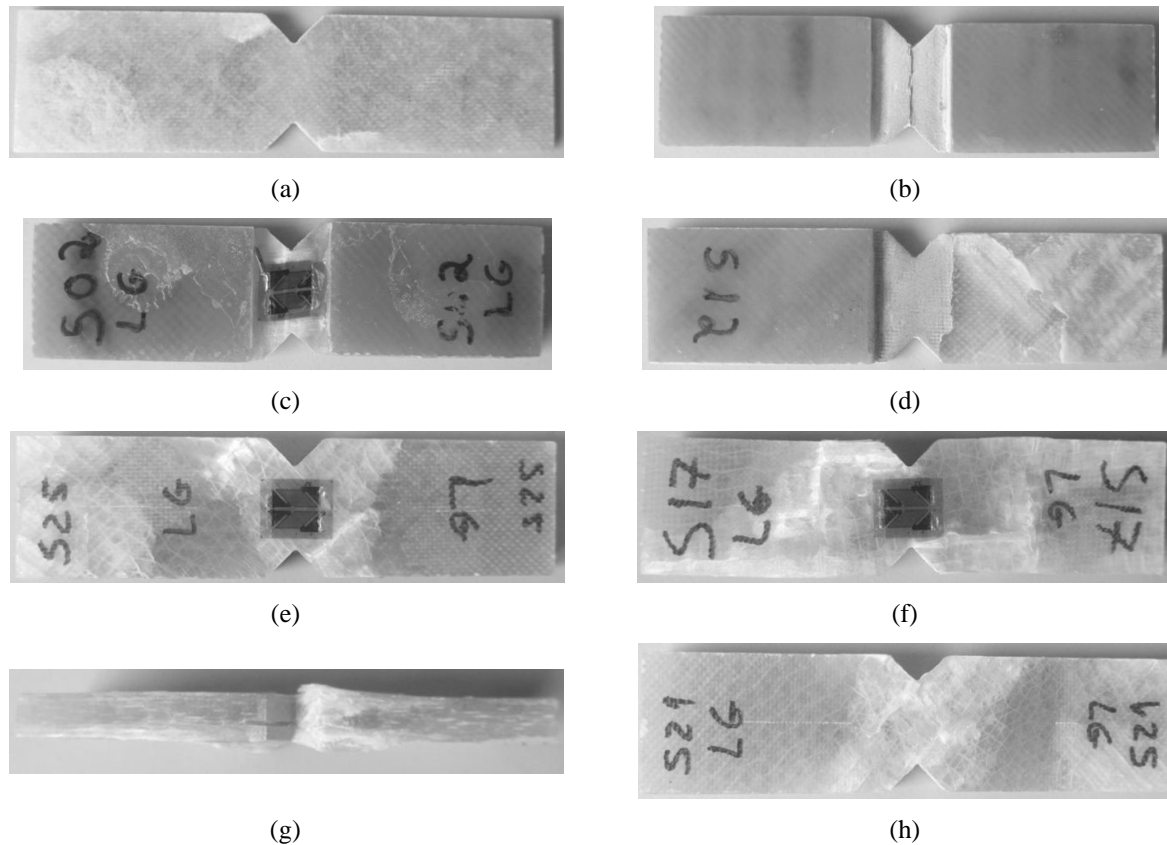
Figure 68: Final physical condition of the test specimens following testing: (a) CSM 03: front view; (b) BIA 45/-45 08: front view; (c) BIA 45/-45 08: back view; (d) BIA 0/90 06: front view; (e) TRI 0/90 14: back view; (f) TRI 45/-45 18: back view; (g) TRI 45/-45 18: top view; (h) TRI 90/0 22: back view (after removal of strain gauge).

4.4.4   Strain fields and test validation

Two issues are of interest to evaluate qualitatively the results obtained from the Iosipescu shear tests: 1) the uniformity of the stresses between the notches and 2) the amount of normal stresses in the reduced section. Concerning the measurement of shear modulus, Pierron and Vautrin (1998) state that it is not necessary to have a state of pure shear in the reduced section. Although, the authors draw attention to the fact that the transverse compressive strains that tend to arises during the Iosipescu tests must be accounted for measurement of the shear strength. According to the authors, these compressive strains tend to delay fracture, hence increasing the ultimate stress of the specimen.

In this section, two studies are performed to evaluate these two issues. First, to verify the existence of a state of pure shear in the gauge section, the normal and shear strain fields obtained by DIC are plotted. An example for the case of specimen BIA 45/-45 08 is depicted

in Figure 69. These fields are plotted for a stage where the maximum shear strains are between 2000 $\mu\varepsilon$ and 4000 $\mu\varepsilon$. This interval is chosen because it pertains to the interval considered for computing the shear modulus.
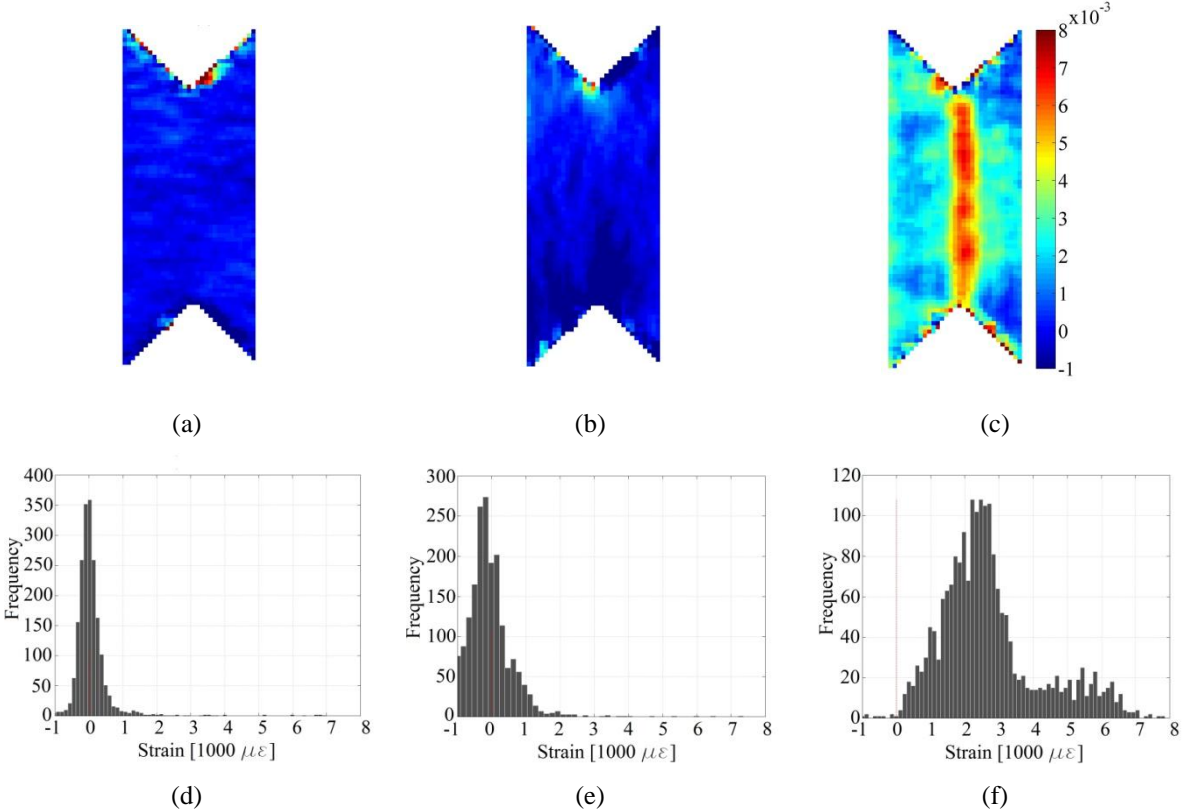
Figure 69: Strain fields corresponding to BIA 45/-45 08 (corresponding to load equal to 500.3 N): (a) normal strain ε_x; (b) normal strain ε_y and (c) shear strain ε_{xy}. Strain histogram in the gauge area: (d) normal strain ε_x; (e) normal strain ε_y and (f) shear strain ε_{xy}.

The uniformity of the stresses on the gauge section and the evolution of the normal and shear strains up to the failure can be observed in the Figure 70 to Figure 75.

τ_{xy}^{avg} :	14.42 MPa	23.38 MPa	27.53 MPa	31.90 MPa	43.49MPa
γ_{xy}^{avg} :	2800 με	5200 με	6400 με	7500 με	10900 με

(a)   (b)   (c)   (d)   (e)
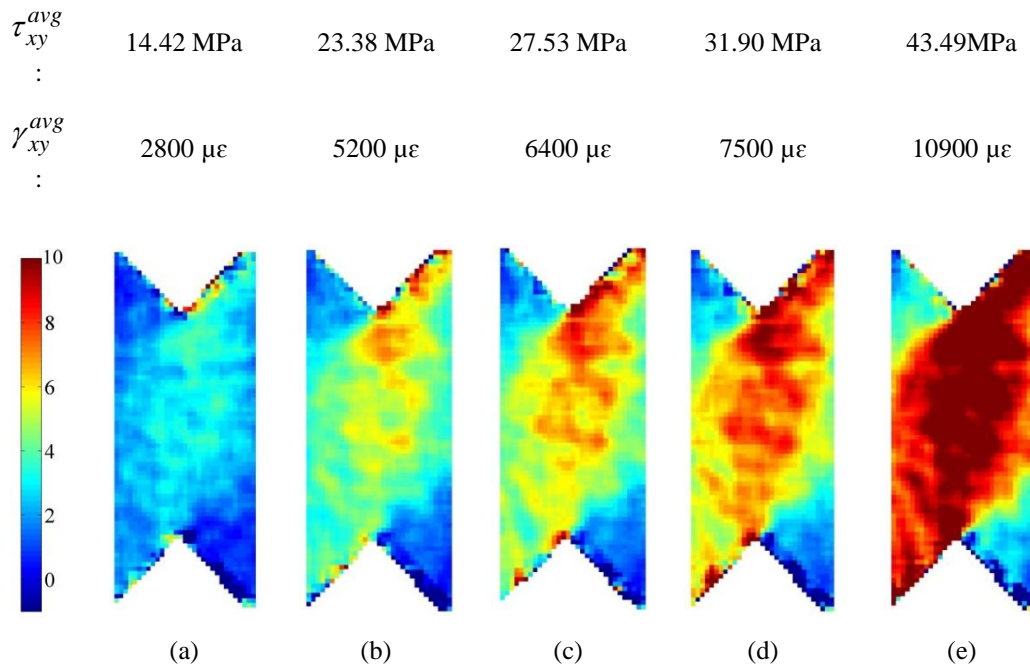
Figure 70: Evolution of engineering shear strain in the specimen CSM 03: (a) 2800 με; (b) 5200 με; (c) 6400 με; (d) 7500 με; (e) 10900 με (units in 1000 με).

τ_{xy}^{avg} :	12.02 MPa	31.38 MPa	52.15 MPa	72.60 MPa	87.90 MPa
γ_{xy}^{avg} :	1200 με	2900 με	4500 με	6400 με	8300 με

(a)   (b)   (c)   (d)   (e)
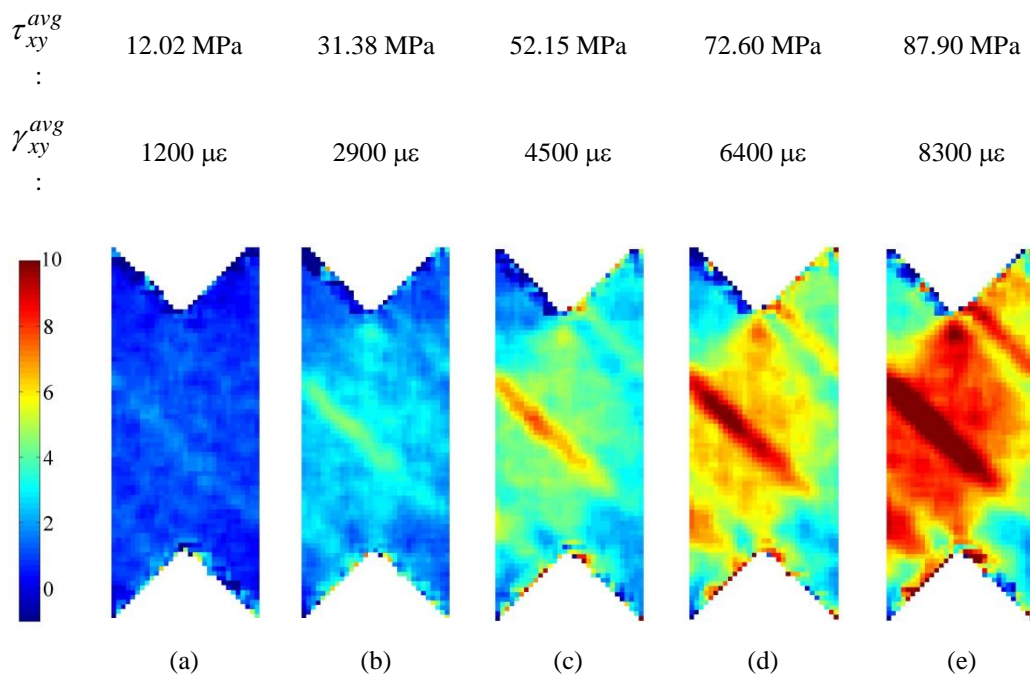
Figure 71: Evolution of engineering shear strain in the specimen BIA 0/90 07: (a) 1200 με; (b) 2900 με; (c) 4500 με; (d) 6400 με; (e) 8300 με (units in 1000 με).

τ_{xy}^{avg} :   3.58 MPa   10.01 MPa   14.78 MPa   23.00 MPa   30.16 MPa

γ_{xy}^{avg} :   924 με   3300 με   5300 με   9600 με   15000 με

(a)   (b)   (c)   (d)   (e)
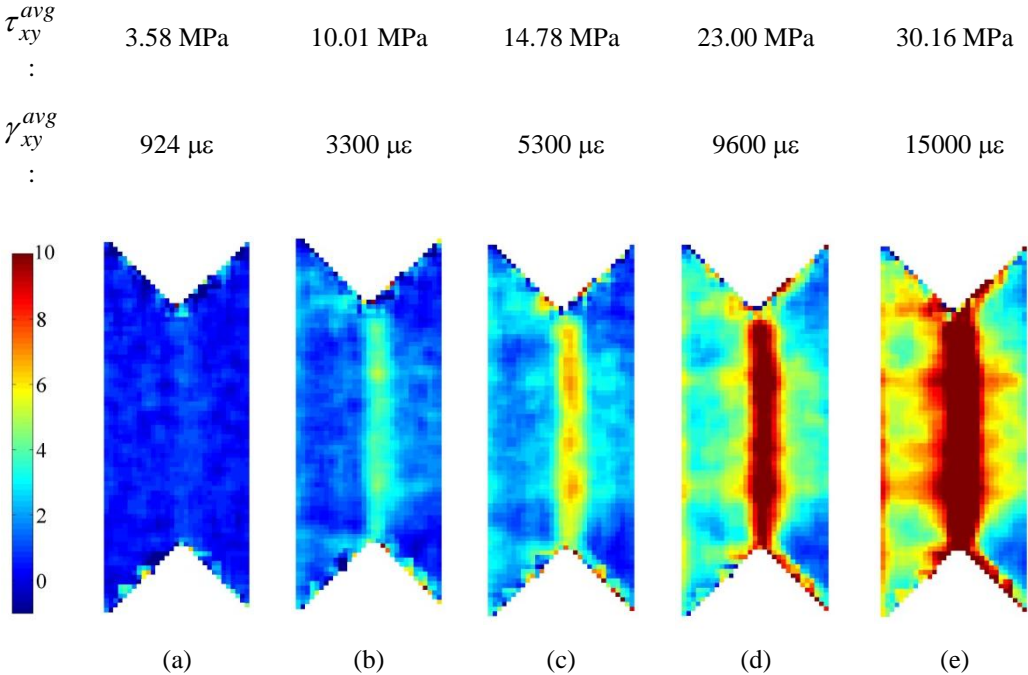
Figure 72: Evolution of engineering shear strain in the specimen BIA 45/-45 08: (a) 924 με; (b) 3300 με; (c) 5300 με; (d) 9600 με; (e) 15000 με (units in 1000 με).

τ_{xy}^{avg} :   15.31 MPa   23.10 MPa   35.82 MPa   49.01 MPa   57.76 MPa

γ_{xy}^{avg} :   2700 με   4000 με   6500 με   8800 με   10400 με

(a)   (b)   (c)   (d)   (e)
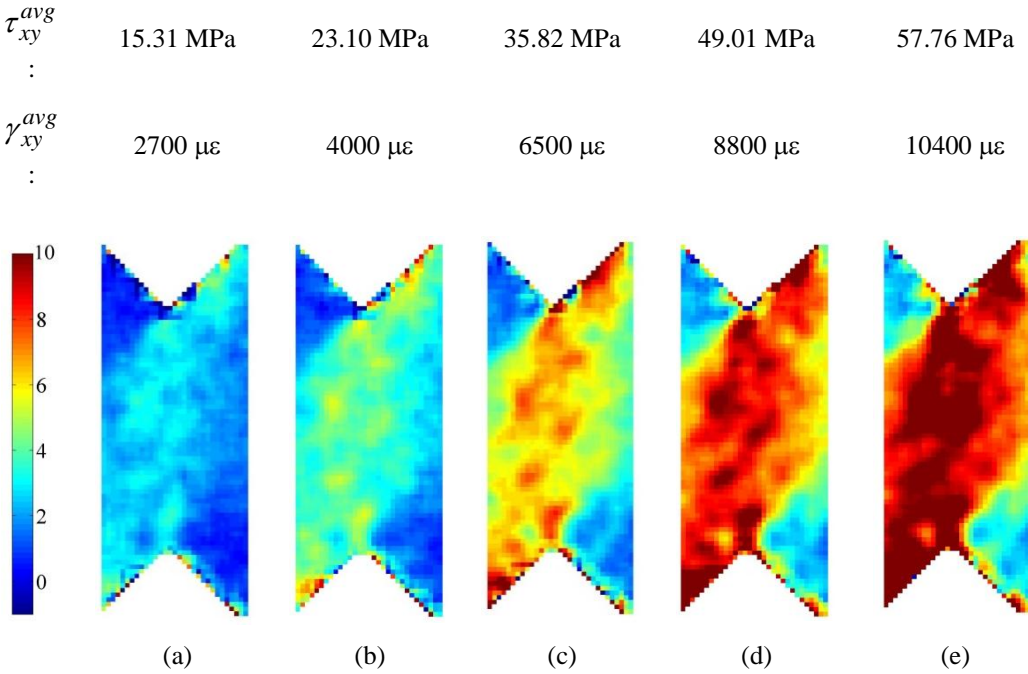
Figure 73: Evolution of engineering shear strain in the specimen TRI 0/90 15: (a) 2700 με; (b) 4000 με; (c) 6500 με; (d) 8800 με; (e) 10400 με (units in 1000 με).

| τ_{xy}^{avg} : | 7.38 MPa | 12.24 MPa | 17.64 MPa | 23.79 MPa | 30.70 MPa |
| γ_{xy}^{avg} : | 2000 με | 3900 με | 5700 με | 7900 με | 10000 με |

(a)　　　　(b)　　　　(c)　　　　(d)　　　　(e)
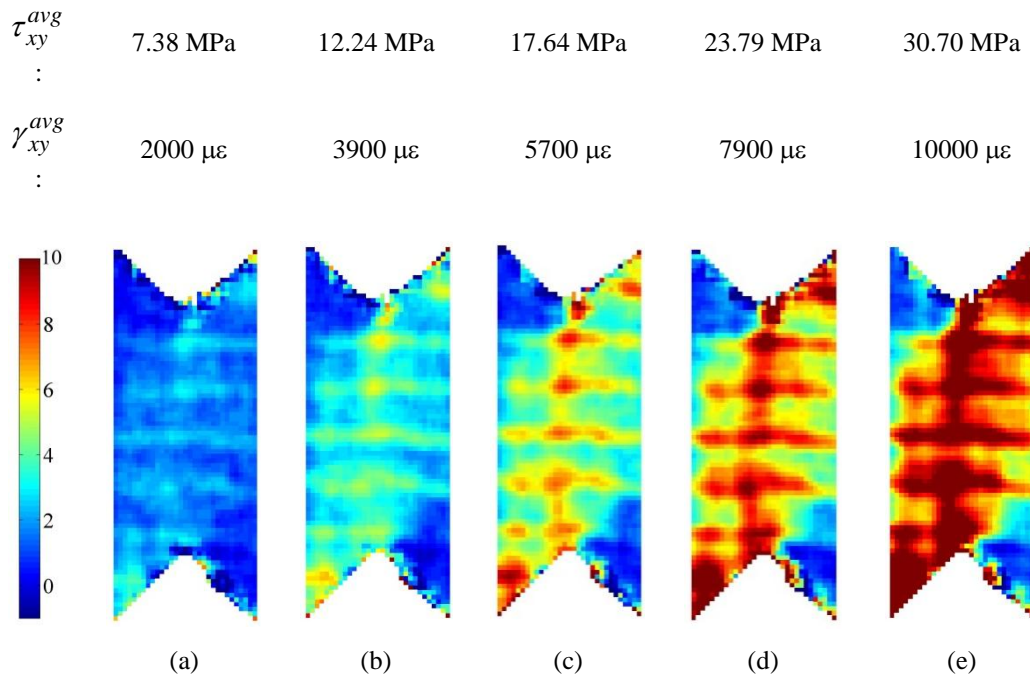
Figure 74: Evolution of engineering shear strain in the specimen TRI 45/-45 19: (a) 2000 με; (b) 3900 με; (c) 5700 με; (d) 7900 με; (e) 10000 με (units in 1000 με).

| τ_{xy}^{avg} : | 12.03 Mpa | 21.13 MPa | 29.35 MPa | 39.95 MPa | 48.45 MPa |
| γ_{xy}^{avg} : | 2100 με | 4000 με | 5600 με | 7700 με | 9400 με |

(a)　　　　(b)　　　　(c)　　　　(d)　　　　(e)
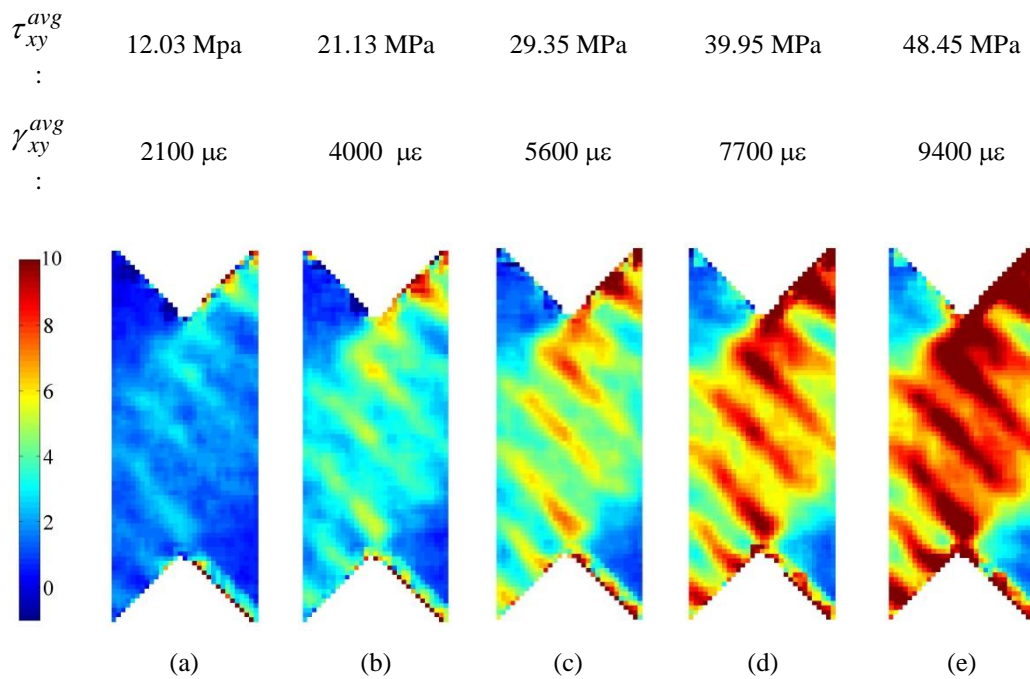
Figure 75: Evolution of engineering shear strain in the specimen TRI 90/0 22: (a) 2100 με; (b) 4000 με; (c) 5600 με; (d) 7700 με; (e) 9400 με (units in 1000 με).

4.4.5 Shear modulus, ultimate stress and strain

Table 24 reports the average (AVG) values and coefficient of variation (CV) of the shear modulus. Values obtained by the two employed measurement methods, i.e., ESG and DIC, are shown. The ratio between the values obtained by the ESG to the corresponding value obtained by DIC are presented for the specimens where both techniques were applied.

Table 24: Shear modulus

Composite laminate	Spec. number	Material planes alignment		Shear modulus (G_{xy})						$G_{xy}^{ESG}/G_{xy}^{DIC}$
		x	y	Electrical resistance strain gauges (ESG)			Digital image correlation (DIC)			
				Value	Avg	CV	Value	Avg	CV	
				[GPa]	[GPa]	[%]	[GPa]	[GPa]	[%]	[ ]
CSM	1	-	-	-			4.02			-
	2	-	-	-			3.85			-
	3	-	-	-	5.41	27.5	4.03	3.97	2.5	-
	4	-	-	6.46			-			-
	5	-	-	4.36			-			-
BIA	6	0°	90°	9.18	9.15	0.6	8.36	10.30	26.7	1.10
	7	0°	90°	9.11			12.25			0.74
	8	45°	-45°	3.49			2.47			1.41
	9	45°	-45°	3.39			2.30			1.47
	10	45°	-45°	3.44	3.56	7.3	3.66	3.05	25.2	0.94
	11	45°	-45°	3.89			3.75			1.04
	12	45°	-45°	3.26			-			-
	13	45°	-45°	3.87			-			-
TRI	14	0°	90°	6.84			4.15			1.65
	15	0°	90°	7.94	7.19	7.2	5.45	4.80	19.1	1.46
	16	0°	90°	6.84			-			-
	17	0°	90°	7.16			-			-
	18	45°	-45°	7.12			2.43			2.93
	19	45°	-45°	6.66	6.38	14.28	2.63	2.53	5.66	2.53
	20	45°	-45°	5.36			-			-
	21	90°	0°	7.90			5.70			1.38
	22	90°	0°	7.42	7.53	4.3	5.22	5.46	6.3	1.42
	23	90°	0°	7.28			-			-

The results presented in Table 24 indicate that, the values obtained for the shear modulus seem to be affected by the technique used to make the measurements (ESG or DIC). Probably this is a consequence of the lack of uniformity on the strain fields at the notched zone of

specimen, as observed in Figure 70 to Figure 75, particularly for TRI specimens and for with BIA specimens with the load applied parallel to the 90° direction. Indeed, the ESG measures the strain on a small area located in the center of specimen, this measurement is more prone to inaccuracies due to the lack of uniformity. On the other hand, the measurements obtained by DIC result of measurement of strains in the area that extends along all the height of the notched section.

Table 25 reports the values of the maximum shear stress at failure of the specimens and the failure modes observed for each specimen.

Table 25: Ultimate shear stress and failure mode

Composite laminate	Spec. number	Material planes alignment x	y	Ultimate shear stress $(\tau_{xy\,ult}{}^{app})$ Value [MPa]	Avg [MPa]	CV [%]	Failure mode	
CSM	1	-	-	85.34			NOT OK	E
	2	-	-	82.58			NOT OK	E
	3	-	-	84.11	106.25	28.69	NOT OK	E
	4	-	-	138.43			OK	C
	5	-	-	140.78			OK	C
BIA	6	0°	90°	95.86	104.09	11.19	NOT OK	other
	7	0°	90°	112.33			NOT OK	other
	8	45°	-45°	48.60			OK	B
	9	45°	-45°	49.42			OK	A
	10	45°	-45°	62.32	53.28	12.53	OK	A
	11	45°	-45°	61.39			OK	A
	12	45°	-45°	49.79			OK	A
	13	45°	-45°	48.16			OK	A
TRIA	14	0°	90°	85.62			NOT OK	G
	15	0°	90°	87.64	91.92	6.74	NOT OK	F
	16	0°	90°	96.37			NOT OK	F
	17	0°	90°	98.04			NOT OK	F
	18	45°	-45°	81.38			NOT OK	G
	19	45°	-45°	79.66	94.47	25.59	NOT OK	G
	20	45°	-45°	122.38			NOT OK	E
	21	90°	0°	87.49			NOT OK	F
	22	90°	0°	100.81	95.82	7.58	NOT OK	F
	23	90°	0°	99.16			NOT OK	G

Table 26 shows the values of the ultimate shear strain computed for each test.

Table 26: Ultimate shear strain

| Composite laminate | Spec. number | Material planes alignment | | Ultimate shear strain ($\gamma_{xy\,ult}$) | | | | | | $(\gamma_{xy\,ult})^{ESG} / (\gamma_{xy\,ult})^{DIC}$ |
| | | | | Electrical resistance strain gauges (ESG) | | | Digital image correlation (DIC) | | | |
		x	y	Value [$\mu\varepsilon$]	Avg [$\mu\varepsilon$]	CV [%]	Value [$\mu\varepsilon$]	Avg [$\mu\varepsilon$]	CV [%]	[ ]
CSM	1	-	-	-	27919	4.8	18170	19510	16.4	-
	2	-	-	-			17200			-
	3	-	-	-			23160			-
	4	-	-	26969			-			-
	5	-	-	28869			-			-
BIA	6	0°	90°	6880	9445	38.4	12490	11345	14.3	0.55
	7	0°	90°	12010			10200			1.18
	8	45°	-45°	50300	49839	1.6	51240	50820	1.1	0.98
	9	45°	-45°	50150			51380			0.98
	10	45°	-45°	50000			50440			0.99
	11	45°	-45°	48230			50220			0.96
	12	45°	-45°	50354			-			-
	13	45°	-45°	50000			-			-
TRIA	14	0°	90°	12860	17517	28.8	16550	15980	5.0	0.78
	15	0°	90°	24170			15410			1.57
	16	0°	90°	18554			-			-
	17	0°	90°	14484			-			-
	18	45°	-45°	30930	33293	17.4	30540	28665	9.3	1.01
	19	45°	-45°	29070			26790			1.09
	20	45°	-45°	39878			-			-
	21	90°	0°	12110	13317	28.5	16560	16370	1.6	0.73
	22	90°	0°	10270			16180			0.63
	23	90°	0°	17571			-			-

4.4.6 Shear stress *versus* shear strain relationships

The shear stress *versus* average engineering shear strain curves obtained using different strain acquirement technique are plotted in Figure 76 for each specimen. Through the analysis of Figure 76 it is possible to have a better idea of the representativeness and limitations of the ESG and DIC technique for each type of GFRP tested.
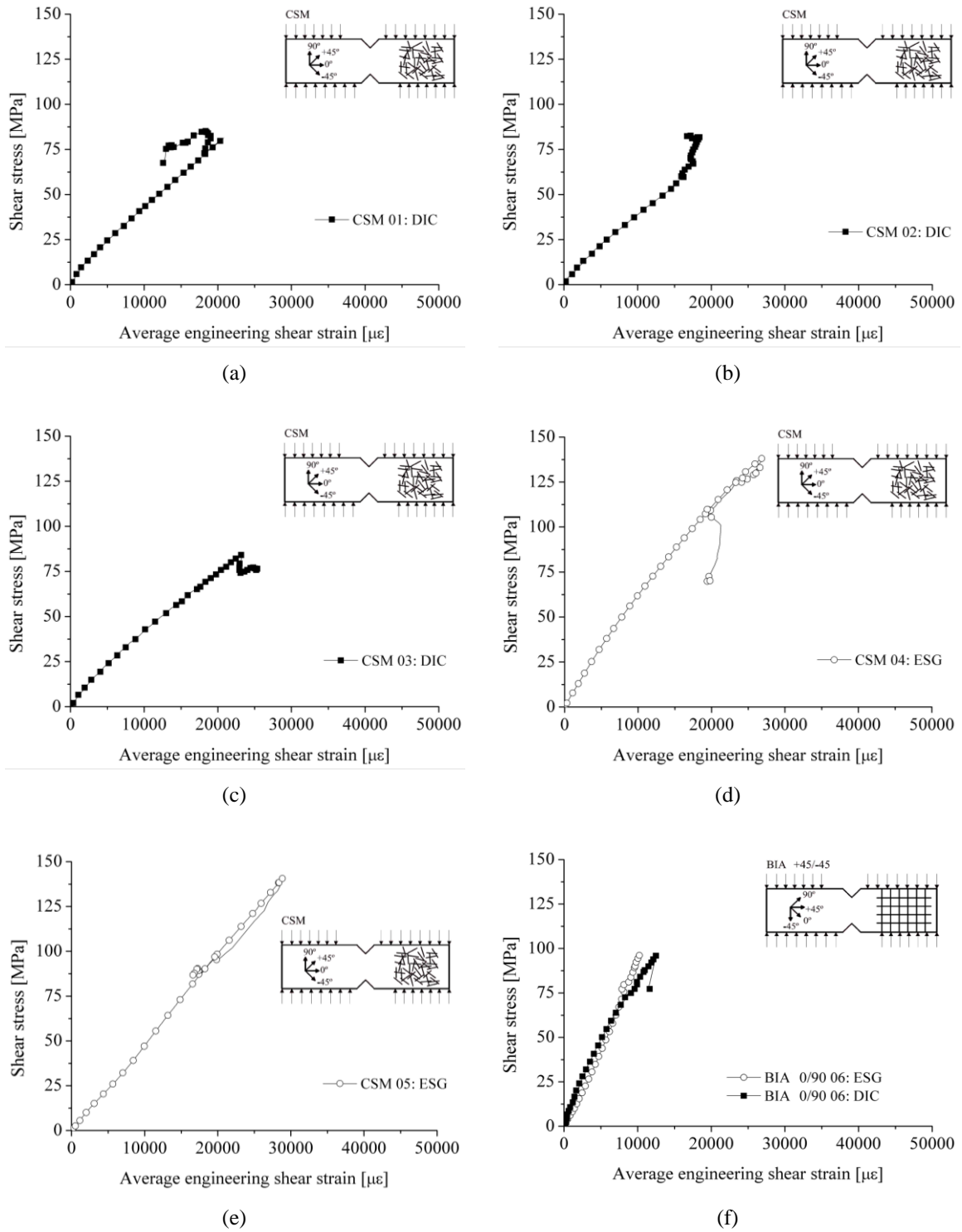
Figure 76: Shear stress-strain relationships obtained for the individual specimens: (a) CSM 01; (b) CSM 02; (c) CSM 03; (d) CSM 04; (e) CSM 05 and (f) BIA 0/90 06.

(g)

(h)

(i)

(j)

(k)

(l)
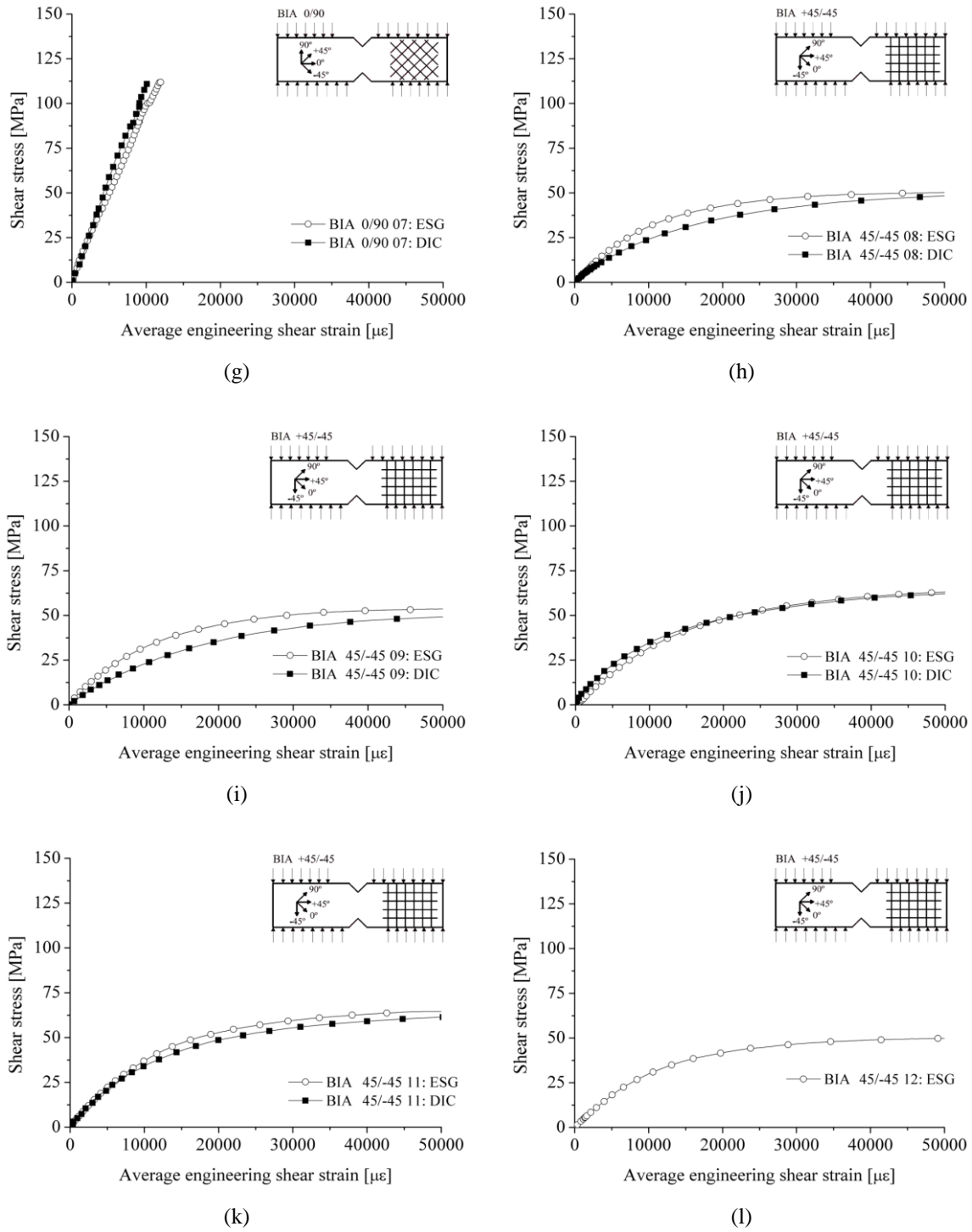
Figure 76: Shear stress-strain relationships obtained for the individual specimens: (g) BIA 0/90 07; (h) BIA 45/-45 08; (i) BIA 45/-45 09; (j) BIA 45/-45 10; (k) BIA 45/-45 11 and (l) BIA 45/-45 12.

(m)

(n)

(o)

(p)

(q)

(r)
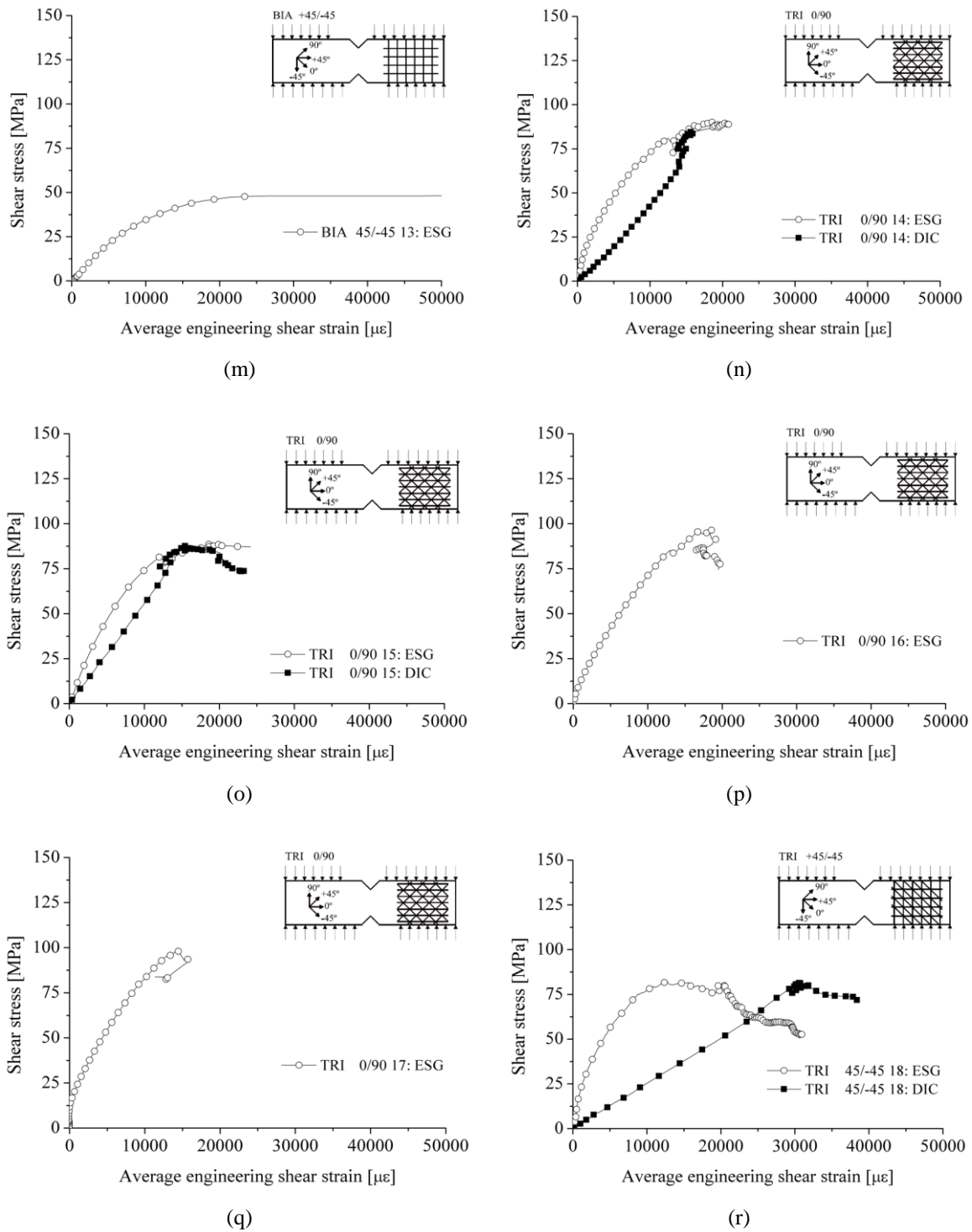
Figure 76: Shear stress-strain relationships obtained for the individual specimens: (m) BIA 45/-45 13; (n) TRI 0/90 14; (o) TRI 0/90 15; (p) TRI 0/90 16; (q) TRI 0/90 17 and (r) TRI 45/-45 18.
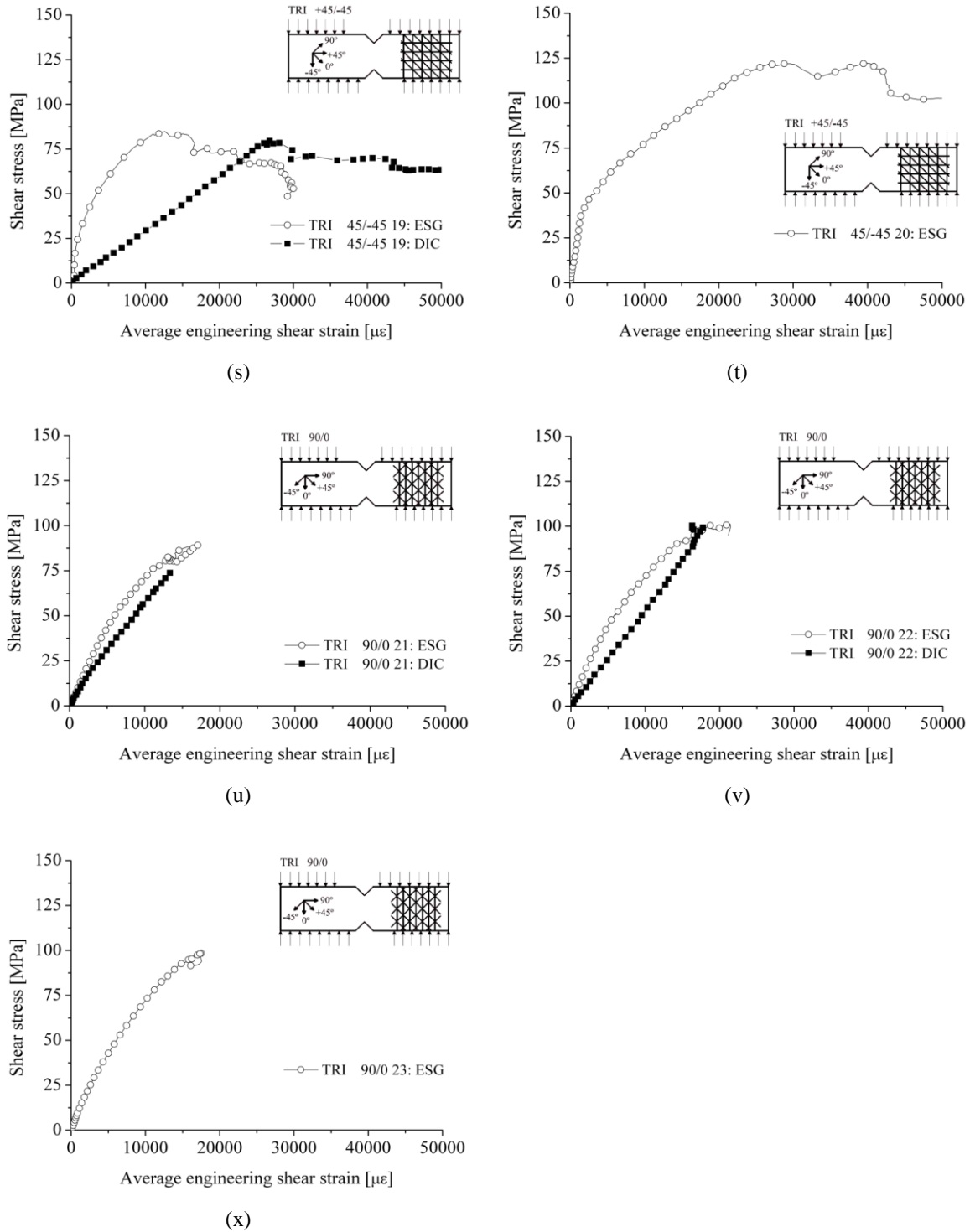
Figure 76: Shear stress-strain relationships obtained for the individual specimens: (s) TRI 45/-45 19; (t) TRI 45/-45 20; (u) TRI 90/0 21; (v) TRI 90/0 22 and (x) TRI 90/0 23.

The stress *versus* strain relationships obtained for all the specimens produced with the same material are grouped in the same chart in Figure 77.
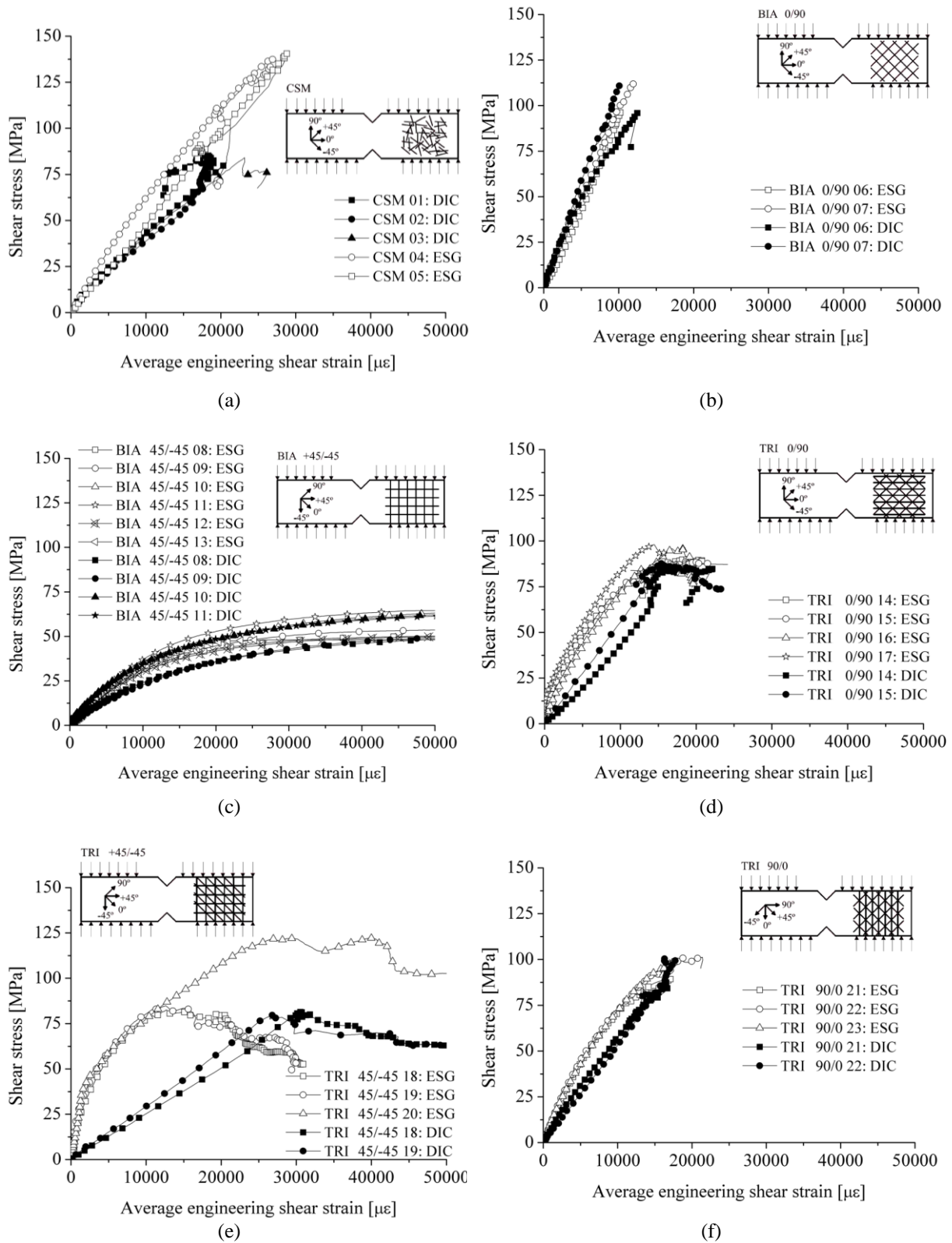
Figure 77: Shear stress-strain relationships grouped by type of GFRP: (a) CSM; (b) BIA 0/90; (c) BIA 45/-45; (d) TRI 0/90; (e) TRI 45/-45; (f) TRI 90/0.

4.5   PIN-BEARING BEHAVIOUR

Preliminary pull-out tests, reported in (Lameiras *et al.*, 2013c), have shown that the failure of the GFRP $\times$ SFRSCC connection, when subjected to pull-out forces, can occur in different modes, depending on the geometry and materials used in the connections. The pull-out experimental program evidenced that, for a promising solution for the connections consisted on perforated GFRP plates embedded in the SFRSCC (hereinafter called PERFOFRP connections), the load capacity can be conditioned by failures in the concrete or even in the GFRP connector itself, in the vicinity of holes. Nonetheless, although the connector failure was evidenced in the post testing inspection, due to the fact that the connector is embedded in the concrete, the conditions at which the rupture actually occurs and the underlying mechanisms could not yet be fully understood nor explained. Despite the relatively high tensile strength of the GFRP in the context of the materials used in concrete sandwich panels, failure through the GFRP can irremediably compromise the structural performance of this type of panels, since the these materials generally present a brittle behaviour, thus leading to an undesirable sudden rupture of the panel.

In the technology of the perforated composites for mechanically fastened connections this issue could be solved by establishing minimum distances from the holes to the border of the laminate to be followed in the design process. However, in the case of proposed PERFOFRP connections, the diameter of holes and the distance from border are limited by the application given to the connector. In fact, when compared with the geometries of the usual perforated plates for mechanically fastened connections, the diameter of the hole used in the PERFOFRP is larger (usually ranges between 3 and 10 mm for fastened connections) and the distance between the hole and the border is shorter (Collings, 1977, Karakuzu *et al.*, 2008). The diameter of holes should permit the aggregates and fibres of concrete to pass through the holes and promote the expected mechanical interlocking between the concrete and the connector.

For conventionally reinforced concrete, this value could be equal to the clear distance between individual parallel bars recommended by EN 1992-1-1 (CEN, 2004a), that is given by the maximum size of aggregate plus 5 mm (i.e., 12 mm + 5 mm = 17 mm for the materials used in this research). Nonetheless, the steel fibres used as reinforcement of concrete has length equal to 35 mm. To avoid fibre congestion, the diameter of holes was set equal to 30 mm. The distance of hole from the border is limited by the relatively small thickness of

concrete layer, that, based on the recommendations made in a first study (Lameiras *et al.*, 2013a), was set at only 60 mm. Considering a minimum cover to the GFRP of 15 mm, value also limited by the maximum diameter of aggregate used in the concrete, the length that remains for the distance from the centre of hole to the laminate border is only 22.5 mm, meaning that the distance from the edge of hole to the laminate border is only 7.5 mm. On the other hand, even with all the aforementioned constraints, in a preliminary investigation (Lameiras *et al.*, 2013a, Lameiras *et al.*, 2013b), the authors confirmed that the load capacity possible to be attained with the proposed PERFOFRP connection was enough to be used as connector for sandwich wall panels, enabling to take the advantages related to the use of this type of connector.

Although the bearing behaviour of GFRP laminates is a subject well-researched and reported in the literature (Collings, 1977, Chang *et al.*, 1984, Liu and Raju, 1999, Pierron *et al.*, 2000, Okutan, 2002, Karakuzu *et al.*, 2008), the authors considered that it was necessary to perform bearing tests that were representative of the geometry of proposed connections for a better understanding of the mechanical behaviour of the this particular type of connector. Thus, an experimental program was also undertaken in the scope of the present research, as to determine the failure mechanisms and the strain field around holes of this type of GRP connectors. More specifically, tensile tests were carried out on specimens formed by a multi-directional GFRP plate including a hole (herein designated as single-hole plate), where the hole was supported with a metallic pin to reproduce, as much as possible and in a feasible way, the anchorage conditions expected for the GFRP connector embedded in the sandwich panel concrete layers. The tests were performed for a range of laminate configurations and different positions of the hole relatively to the free-stress contour of the GFRP plate. Furthermore, the strain field in the vicinity of hole was assessed by using a full-field measurement technique, and also registering local measurements with electrical strain gauges.

4.5.1 Expected failure modes

Despite the specificities of the PERFOFRP connectors, some similarities with the plates used in bolted joints can be still be found. For instance, apart from failure of the concrete pin in either shear or compression, it can be considered that the potential failure modes might be expected to be similar. Specific literature on strength of perforated plates for mechanically fastened joints (ASTM, 2013, Caprino *et al.*, 2005) generally considers that the failure of the

connection occurs in one of the four potential modes illustrated in Figure 78: net-tension, shear-out (or tear-out), bearing, and cleavage.
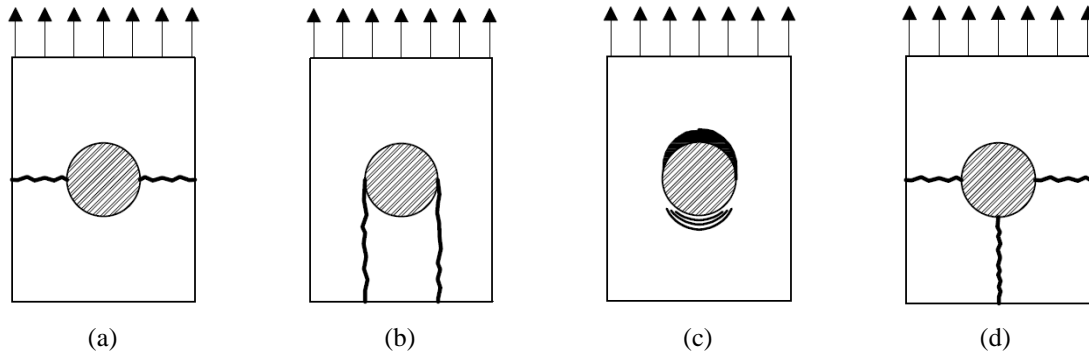
Figure 78: Common failure modes described in the literature: (a) net-tension; (b) shear-out; (c) bearing; (d) cleavage.

Net-tension is a lateral failure at the minimum cross-section perpendicular to the loading direction (Figure 78(a)). The stress that is introduced in net section is schematically represented in the (see Figure 79(a)) and can be determined from Eq. (25).

$$\sigma_{nt} = \frac{Q}{\left(W - D_h\right) \cdot t_p}$$

(25)

where Q is the applied load, W is the width of the specimen, D_h is the diameter of the hole, and t_p is the thickness of the laminate. This failure mechanism takes place when σ_{nt} reaches the direct tensile strength of the composite in the load direction.

Shear-out or tear-out is the rupture of the part below the hole due to the occurrence of two lateral failure surfaces with origin in the lateral extremities of the hole (Figure 78(b)). The shear stress can be computed with Equation (26),

$$\tau_{so} = \frac{Q}{2 \cdot e \cdot t_p}$$

(26)

where e is the distance from the bottom edge to the lateral extremity of the hole (see Figure 79(b)). If the shear stress τ_{so} reaches the shear strength of material, shear-out or tear-out failure occur.

Bearing failure involves a local compression in the composite immediately beneath the loading pin (see Figure 78(c)). Despite the variation of compressive stress along the perimeter contact between the pin and the hole, it is usually assumed that the applied load acts uniformly on the projection of the perimeter of the bottom semi-circumference of the hole on a surface perpendicular to the load direction (see Figure 79(c)). The bearing stress is thus obtained with Equation (27).

$$\sigma_{be} = \frac{Q}{D_h \cdot t_p}$$ (27)

Some researchers (Caprino *et al.*, 2005) have pointed out that due to the lack of plasticity of GFRP, a ductile behaviour for the connection is only attained when a bearing failure is observed. This happens because during bearing failure mode, the joint is able to support significant load after first failure.

The cleavage is considered a mixed failure mode between the shear out and net tension that occurs due to relatively small edge distance (Rosner and Rizkalla, 1995, Valenza *et al.*, 2007).

(a)   (b)   (c)
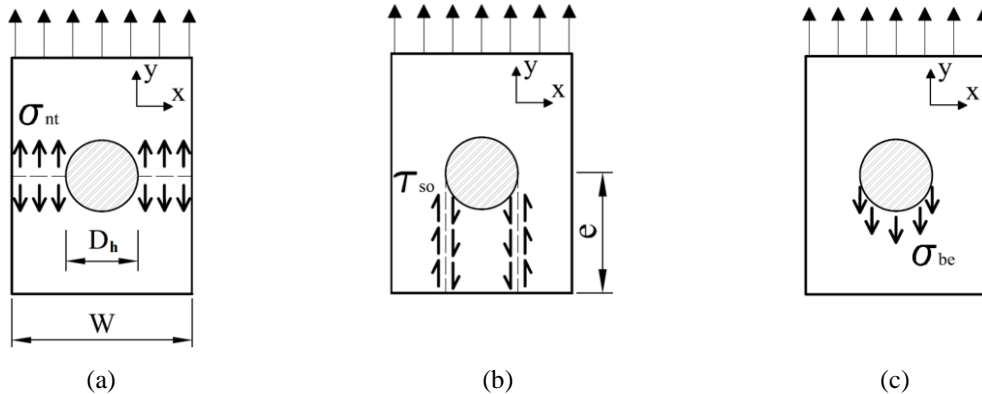
Figure 79: Schematic representation of the stresses computed for: (a) net-tension; (b) shear-out; (c) bearing.

4.5.2   Factors affecting failure

Several researchers (Collings, 1977, Slagter, 1992, Cooper and Turvey, 1995, Wu and Hahn, 1998, Liu and Raju, 1999, Okutan, 2002, Caprino *et al.*, 2005) indicate that the type of failure mode that occurs in a fastened joint is mainly dependent on the width-to-diameter (W/D_h) and edge-to-diameter (e/D_h) ratios. They also indicate that while a low W/D_h favours the occurrence of net-tension, a low e/D_h induces shear-out or cleavage failure modes.

The type of composite material can also affect the overall behaviour of the connection. In an experimental investigation on bearing behaviour of an E-glass/vinyl-ester epoxy composite, Wu and Hahn (1998) verified that a quasi-isotropic composite has higher ultimate bearing strength than chopped strand materials composite (CSM). Nonetheless, Smith and Pascoe (1986) found that, for GFRP, the effect of different stacking sequence did not influence significantly the bearing strength.

The effect of the lateral restraint on the material bearing strength for this type of test was evaluated in several studies (Slagter, 1992, Cooper and Turvey, 1995, Caprino *et al.*, 2005) by comparing bolted to pinned bearing tests and also by evaluating the effect of the clamping torque on the bearing behaviour. These studies showed that lateral restraint always improved the bearing capacity of glass-fibre and glass-fibre/aluminium laminates. This occurs when pure bearing failures mode are expected. This failure mode is related to the compressive forces in the composite immediately beneath the pin. Furthermore, delamination of laminate has also a tendency to occur, resulting in a mixture of compressive and delamination failure at the bolt hole. Thus, the applied clamping force prevents the expected delamination , which increases the failure load.

In the specific case of PERFOFRP, the concrete tends to promote some lateral confinement of the laminate. Nonetheless, in the regions where the concrete is mainly under tensile stresses or if there is some transverse flexure, this favourable confinement effect can be rendered irrelevant.

Previous studies (Pyner and Matthews, 1979, Godwin and Matthews, 1980, Kretsis and Matthews, 1985, Karakuzu *et al.*, 2010) have shown that, when the composite plate is loaded by multiple pins, the bearing strength of the composite is dependent upon the ratio between the distance between the holes and their diameter. This aspect seems to be very significant on the proposed laminate connector, since it is comprised of several aligned holes (see Chapter 5).

4.5.3 Experimental program

The experimental program, carried out at the Laboratory of the Structural Division of the University of Minho, included a total of 29 pin-bearing tests, with at least 3 identical tests of each variant. Emphasis was given on investigating the effect on failure modes and strength of

single-hole plate of using: (i) different multi-directional GFRP; (ii) diverse distances between the hole and the free-stress edges of the specimen.

In addition to the CSM and MU4 laminates employed in the tests with the GFRP × concrete connections under pull-out loads (see Chapter 6), in the pin bearing tests, two other materials were employed: BIA 1 (in this section referred as BIA) and MU2. Detailed description of laminates and the material properties of the four laminates employed in the pin-bearing tests are given in the Chapter 4.

4.5.4 Test specimens

For each one of the four types of materials tested, a large rectangular flat plate was prepared with about 1500×1000 mm^2. The specimens are cut out from the plates by a diamond saw. The longer dimension of the specimens (see Figure 80) coincided with the 0° or 90° orientation axis of the material according to the referential shown in Figure 80. The pin holes were then drilled by a 30 mm diamond grit hole saw.

Two types of tests, using different specimen geometries, were carried out for the determination of bearing strength. The specimens had different (W/D_h) and (e/D_h) ratios. These ratios intended to be representative of the two failure modes in the GFRP connectors observed on the pull-out tests presented in the preliminary tests (Lameiras *et al.*, 2013c). The BEL specimen type (Figure 80a) was designed to induce the cleavage failure mode in the region of the laminate immediately below the hole, while the LAT specimen type (Figure 80b) was specially designed to cause a net-tension failure mode. The chosen values for the W/D_h and e/D_h ratios are representative of the connectors investigated in the first part of this companion paper (Lameiras *et al.*, 2015), where a distance of $2.5 \cdot D_h$ between centre of holes was adopted. To simplify, in this paper the effect of multiple holes was not considered, and thus, the tested specimens with only comprise a single hole. The distances between the holes adopted in the connectors presented in Lameiras *et al.* (2015) were based on recommendations resulted from studies with similar steel connectors (Oguejiofor and Hosain, 1994, Oguejiofor and Hosain, 1997), where the ratio between distance between holes and the diameter of hole is mainly conditioned by concrete properties.
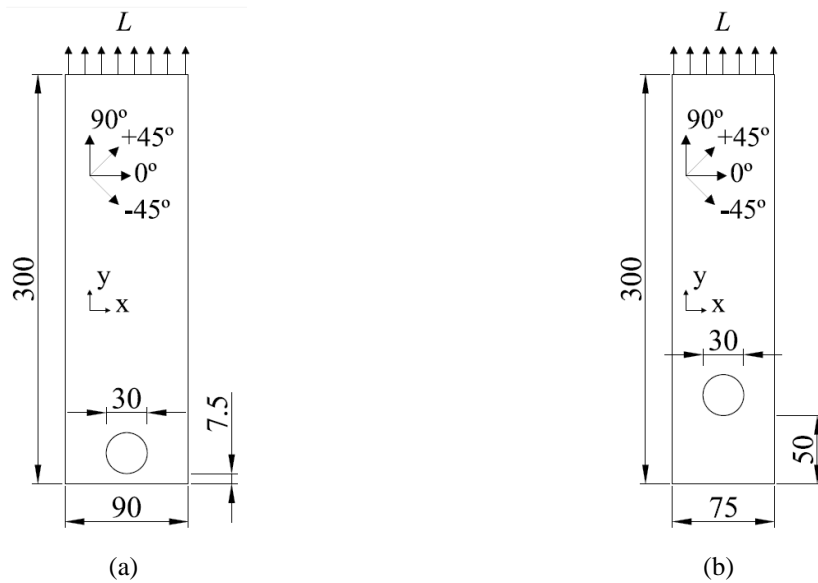
Figure 80: Type of specimens: (a) BEL; (b) LAT (dimensions in millimeters).

4.5.5 Test setup

The test set-up used in this investigation was designed to be as representative as possible of the conditions imposed in pull-out tests performed with GFRP connectors in the Chapter 6.

Despite disregarding the confinement effect of the concrete surrounding the connector, the pin-bearing test configuration was the selected one for the present tests since it provides conservative results in terms of the strength capacity and ductility when compared to the expected behaviour of the connector when embedded in the sandwich panel.

An aluminium pin with 30 mm diameter was tightly attached to the circular hole of specimen in the bottom extremity of the composite, and the gripping was made by a manual mechanical action wedge grip located on the top extremity of specimen (see Figure 82(a)) To increase the specimen-grip friction and to avoid any specimen's slippage, rough inner surface grips were used. An anchorage length of 90 mm for the GFRP laminate was always adopted to assure proper gripping conditions for all types of laminates tested. Steel tabs with 1 mm thickness, 90 mm height and with the same width of the specimens were glued on their both sides in the gripping region. This was done as an attempt to assure, as much as possible, an uniform distribution of shear stresses in the zone where the load was transferred from the grip to the specimen, contributing to prevent a premature rupture of the specimen.

More representative conditions of the reality would be obtained if a SFRSCC pin was used in the tests. However, besides some complexity associated with the production of a concrete pin, it would be possible to experience earlier failures in these pins, for a load level lower than the ones corresponding to the failure modes of the GFRP. Thereby, avoiding the occurrence of these types of failures modes was critical for the study of the intended mechanisms of rupture. Hence, aluminium was the selected material, in replacement of a commonly employed steel pin, because its modulus of elasticity is more approximated to that of concrete, while still maintaining tensile/shear strength levels that are high enough to avoid the failure within the pin.

A double-lap single-pin joint was considered for the experimental model. The aluminium pin passed through a specially manufactured steel fork support that was attached to the base of the test machine crosshead, as represented in Figure 81(a) and Figure 81(c). A variation of this test setup was also used in five additional tested specimens in order to have full visual access to one surface of the specimen during the tests, allowing to record the damage initiation and propagation for the different failure modes by using an optical full-field measurement technique. This variation of the test setup is illustrated in Figure 81(c) and Figure 81(d), and was obtained by removing one side of the steel fork fixture where the aluminium pin was attached. By removing this part from the original device of the test setup, the aluminium pin became a cantilevered element (see Figure 81(d)). Hereinafter the original and modified test setups were designated by SIM (simply supported) and CAN (cantilevered), respectively.
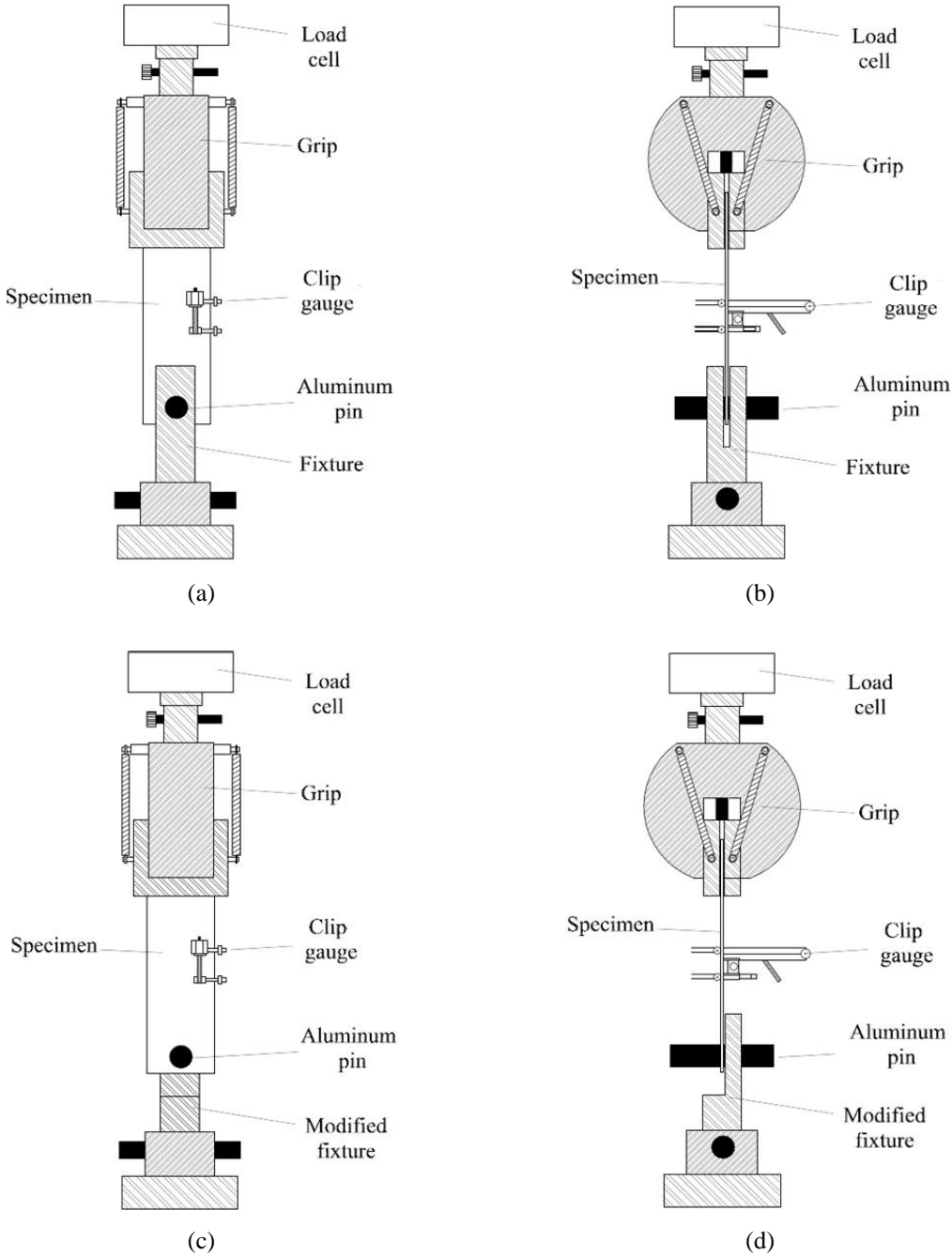
Figure 81: Schematic representation of test-setups adopted for the pin-bearing tests: (a) original test setup (SIM): front view; (b) SIM: lateral view; (c) modified test setup (CAN): front view; (d) CAN: lateral view.

All the tests were performed in tension on a MicroTest (SCM4000) universal test machine (Figure 82(a)), by imposing a displacement control, at constant cross-head speed of 2 mm/min.

4.5.6 Instrumentation

For each test, load *versus* displacement plots were obtained, where the displacement is obtained from the cross-head movement. The load was measured by a 200 kN load cell at a rate of 2 Hz. The load cell was connected in series to the cross-head and to the loading clamp device (Figure 82(a)).

The nominal axial strain was measured in all tests using a clip gauge with a reference length of 50 mm, attached to the middle part of the specimens (see Figure 81 and Figure 82(a)). The strain distribution in the vicinity of the hole was experimentally determined by using several electrical strain gauges (ESG). As represented in Figure 82, at least one specimen of each test configuration and also of each GFRP material was instrumented with ESG. One ESG was placed immediately below the hole in the BEL specimens and one pair of ESG was glued at the left and right sides of the hole in the LAT specimens. These positions were chosen because they are the most susceptible to the occurrence of the highest strain gradients. The two ESG used in the LAT specimens were placed on the front and rear sides of the laminate in order to evaluate the symmetry of test, identifying the possible occurrence of bending due to some misalignment. For a better understanding of the strains development in the proximity of holes, one LAT/MU4 specimen (i.e., LAT test configuration with a specimen comprising MU4 material) comprised additional strain measurement by using four electrical strain gauges arranged as illustrated in Figure 82(d).
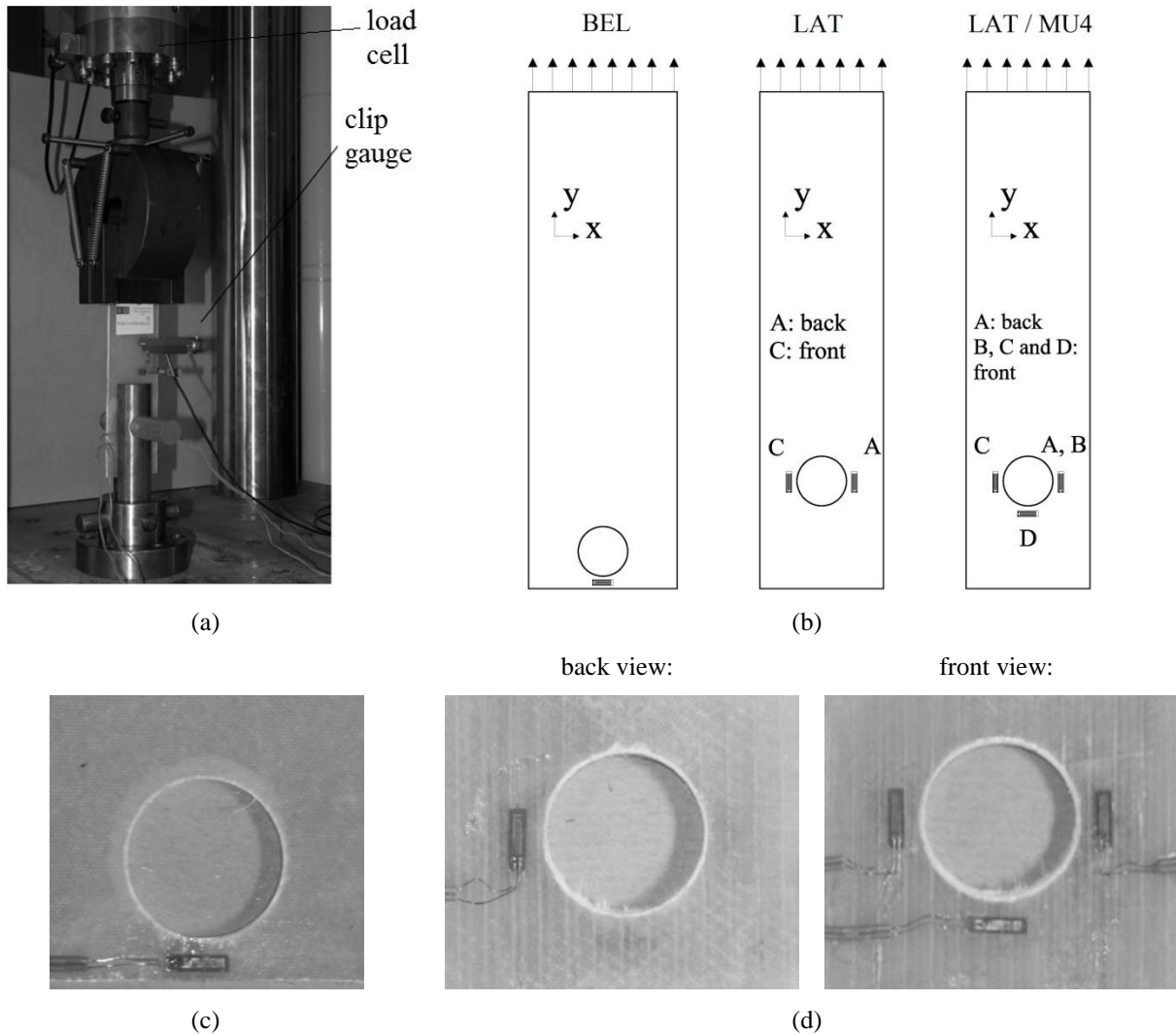
Figure 82: Instrumentation adopted: (a) clip-on gauge in the middle section of specimen; (b) schematic representation of three configurations adopted to measure the deformation in the proximity of hole; (c) detail of the ESG glued immediately below the hole of BEL specimen; (c) detail of ESG glued next to the hole of LAT / MU4 specimen.

The strain field around the hole connection was also evaluated by means of Digital Image Correlation (DIC). This white-light optical technique provides the full-field displacement of a target surface by correlating images recorded at different instants. The material surface must have a textured pattern, defining locally an unique feature-based region. At the scale of observation, a speckle pattern is created using a white-to-black spray painting technique to ensure suitable contrast and granular size. The quality of this pattern is relevant to ensure a good balance between spatial resolution and accuracy, which is particularly crucial in this application. In this work, the ARAMIS system by GOM was used (Sousa *et al.*, 2011b, Xavier *et al.*, 2012, Xavier *et al.*, 2014). The optical system was equipped with an 8-bit

Baumer Optronic FWX20 digital camera coupled with a Zoom-Nikkor 28-105mm f/3.5-4.5D IF. The aperture, the lighting intensity and the shutter time were set to enhance contrast of the speckle image. Considering the characteristic dimensions of the region of interest, the optical magnification and the quality of the speckled pattern, a subset of 15×15 pixel^2 (1.08×1.08 mm^2), with an overlapping of 2 pixels for enhancing the strain spatial resolution, was chosen. The strain fields were determined by numerical differentiation of the displacement fields by least-square regression over a base length of 5×5 subsets^2 (5.4×5.4 mm^2). From rigid-body translation tests (Xavier *et al.*, 2012, Sousa *et al.*, 2011c), an accuracy of 0.01-0.02 pixel (0.72-1.44 μm) and 0.012-0.035% was obtained for the DIC measurements of displacement and strain, respectively.

4.5.7   Failure modes

In general, the BEL specimens presented a cleavage failure mode as the sequence exemplified in Figure 83(a). All BEL specimens exhibited similar behaviour, with initiation of failure at the zone of the minimum cross section area, immediately below the hole, followed by the appearance of two inclined failure lines due to the formation of two cantilevers in the second stage of failure propagation (see photos of BEL specimens after having been tested in Figure 84). The failure mechanism was almost the same in all the BEL samples, differing only on the ductility of the responses. Still within BEL specimens, for the CSM laminates, the second failure lines occurred more abruptly than in the specimens comprising other types of laminates, as evidenced in Figure 86. This may be justified by the existence of a high content of fibres on the ±45° directions in the other three laminates studied here. In fact, the behaviour of the ±45° laminates under direct tensile tests along the 0°/90° directions was always more ductile (Bunsell and Renard, 2005). This effect was probably more pronounced in the bearing tests due to the higher anchorage length of the fibres arranged on the ±45° directions.

On the other hand, bearing and net-tension were the failure modes observed in the case of the LAT specimens. Most specimens showed a mixed bearing and net-tension failure mode as schematized in Figure 83(b). From the observations made during tests it was verified that the beginning of failure was characterized by a bearing damage followed by net-tension failure of the laminate. This was the failure mode found for all specimens comprising BIA and MU4 laminates (see tested specimens in Figure 85). For these specimens the failure occurred in a relatively ductile fashion. In the specimens with ±45° plies, a whitening of a limited region was observed prior the net-tension rupture (see Figure 85). This whitish region was limited by

lines that start in the hole edge and finish in the free lateral edges, at an angle approximately equal to $\pm45°$ with the x axis. It was verified that this pattern was associated to the occurrence of a progressive delamination/damage due to the mobilization of inclined fibres. When the net-tension failure took place, it happened in a sudden way, generally with the propagation of a horizontal crack from the hole edge to the lateral edges of specimen.
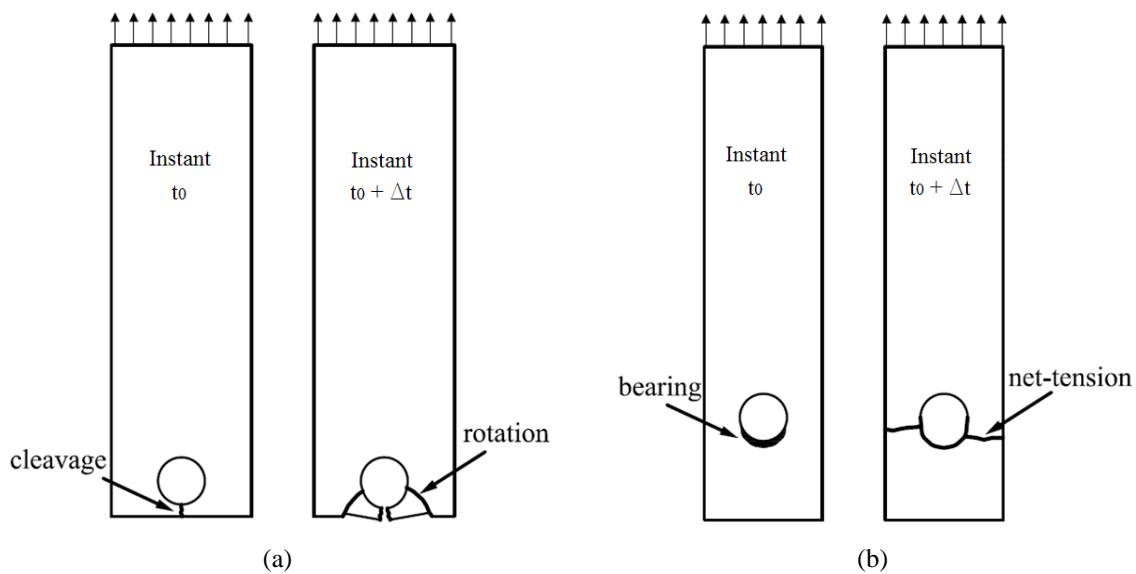
Figure 83: Typical mixed failure sequence for: (a) BEL specimens; (b) LAT specimens.

The difference between the failure modes of BEL and LAT specimens was attributed to the larger e/D_h (0.75 and 2.17, for BEL and LAT specimens, respectively) and smaller W/D_h (3.00 and 2.50, for BEL and LAT specimens, respectively) ratios of LAT specimens.

In the case of the four specimens tested according to the CAN test setup, a pronounced out-of-plane displacement was observed in all the specimens tested. Both CAN-BEL specimens present failure by cleavage, while both CAN-LAT specimens failed by bearing.

Geometry / Material	Damaged specimens		
	01	02	03
BEL/CSM			
BEL/BIA			
BEL/MU2			
BEL/MU4			

Figure 84: Final appearance of BEL specimens.
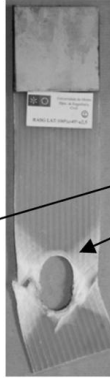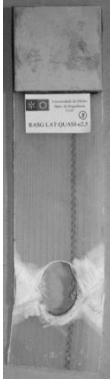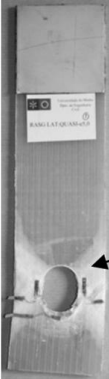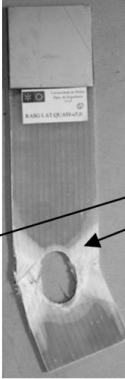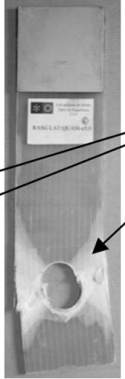
Geometry / Material	Damaged specimens			
	01	02	03	04
LAT/CSM				
LAT/BIA				
LAT/MU2				
LAT/MU4				

Figure 85: Final appearance of LAT specimens.

4.5.8 Bearing behaviour and strength

The general bearing behaviour of laminates was obtained from the load *versus* displacement relationship. This relationship for BEL and LAT specimens is presented in Figure 86 and Figure 87, respectively.
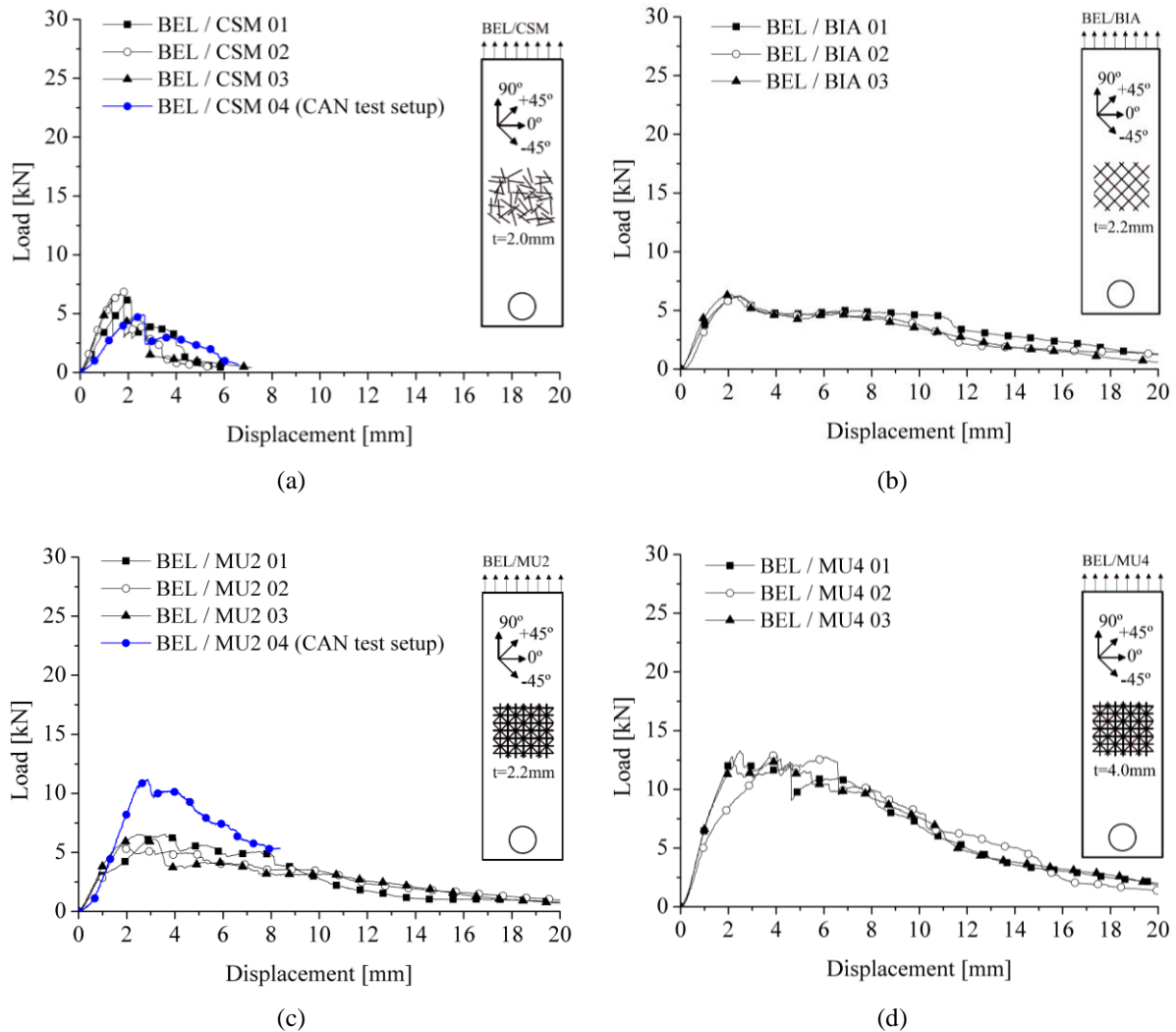
Figure 86: Load *versus* displacement curves for the BEL specimens: (a) CSM; (b) BIA; (c) MU2; (d) MU4.

It was noticed that changing the test setup from a balanced solution (SIM) to a cantilevered fixture (CAN) led to different results. In general, different failure modes were obtained with CAN: the initial slope of the force *versus* displacement curves was smaller than the slope obtained for specimens tested under the SIM test setup, and the ultimate loads were significantly different from the ones obtained when the specimens are tested using the SIM configuration, but without a clear tendency. This particular behaviour obtained for the specimens tested under the CAN test setup possibly have been induced by the out-of-plane

displacements observed during the tests when this configuration was used. Since in the real connection, within the sandwich panel, the laminate is surrounded by concrete that avoids the out-of-plane movements, the authors believe that the results obtained in the CAN configuration were less representative of the laminate working conditions in the sandwich panel than the results obtained in the SIM test setup. For this reason, the results obtained with the CAN test setup were disregarded in the analyses in terms of failure mode and ultimate load. The results from DIC technique, applied exclusively to the specimens tested with CAN setup, were then only used to obtain information on the strain concentrations in the vicinity of holes.

Figure 86 and Figure 87 show that a similar load *versus* displacement response was obtained in all specimens of same geometry and material tested in SIM conditions, which is an indication of the reliability of this test setup.

In general, the load *versus* displacement curves showed a linear response of the specimens, followed by a nonlinear behaviour due to damage in the laminate zones of higher strain gradients adjacent to the hole. This nonlinear branch was longer and more pronounced in the LAT specimens, where the progressive damage due to bearing was more evident. Apart the BEL/CSM and LAT/MU4 specimens, above the deformation corresponding to maximum load the specimens continue to sustain significant part of the peak load up to relatively large axial deformation. In the post-peak load stage of BEL/CSM and LAT/MU4 specimens, the load carrying capacity decreased pronouncedly (see Figure 86(a) and Figure 87(d)). For the LAT specimens a more clear load plateau was noticed, followed by a series of small loading and unloading cycles. Based on observations during tests, this behaviour was associated to visible successive damages related to bearing failure mode. The final failure of specimens occurred more abruptly when a net-tension failure took place (e.g., compare the responses of LAT/MU4 specimens, which failed by net-tension after a short branch of progressive damage associated to bearing mode, with the responses of the other LAT specimens). This observed behaviour seems consistent with the results published by other authors (Bank, 2013, Bank and Arora, 2007).

The ultimate loads, taken as the maximum sustained load for each specimen, are presented in Table 27.
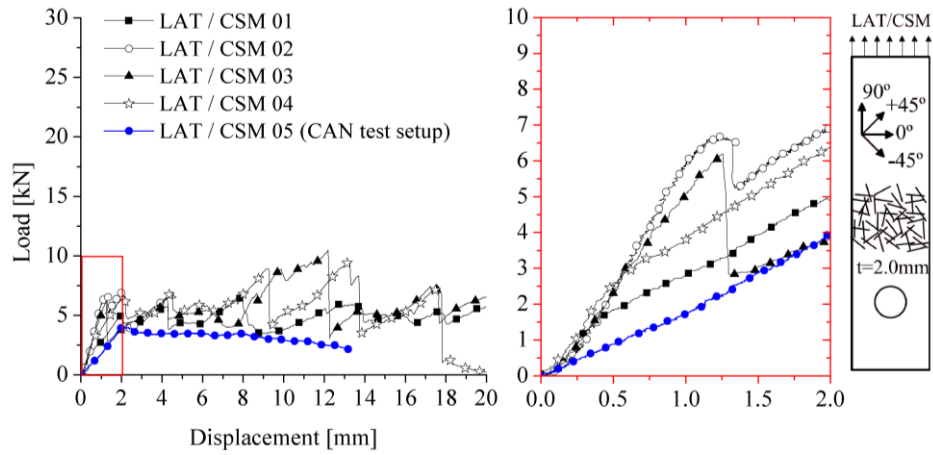
(a)
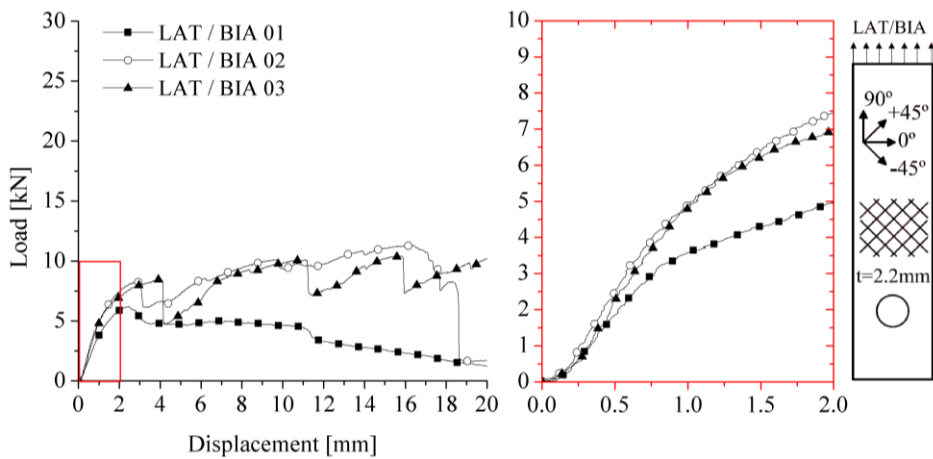
(b)
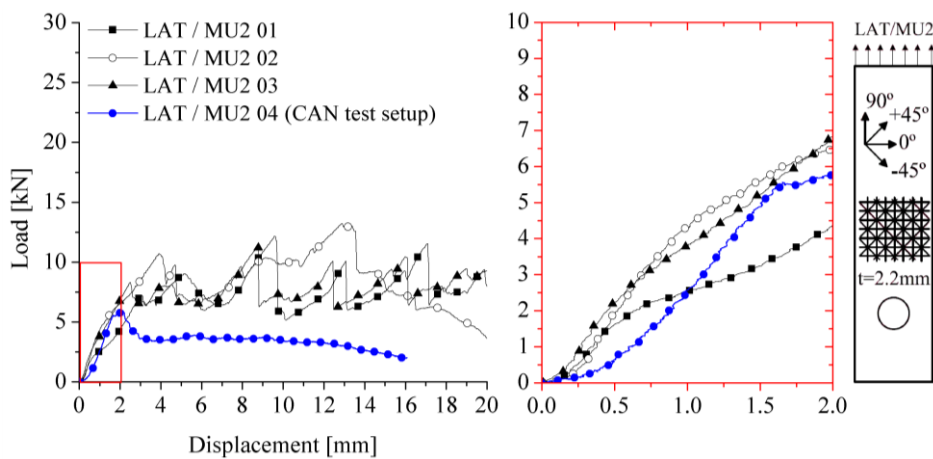
(c)

Figure 87: Load *versus* displacement curves for the LAT specimens: (a) CSM; (b) BIA and (c) MU2.

(d)
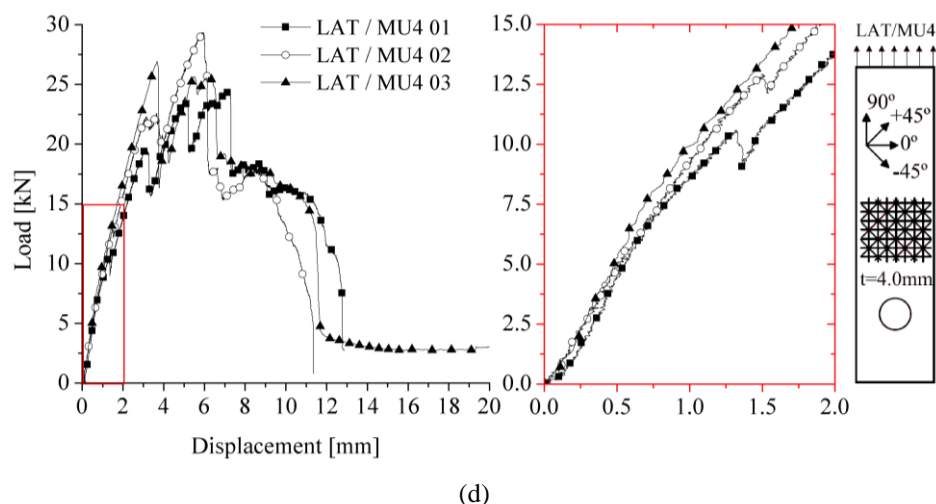
Figure 87: Load *versus* displacement curves for the LAT specimens: (d) MU4.

Apart the laminate MU4, small variation on ultimate load was observed between specimens fabricated with different types of laminates (see Table 27). The ratios between the average ultimate loads of BEL specimens comprising other types of laminates and the CSM laminate was: 0.96, 0.95 and 1.99, for BIA, MU2 and MU4 laminates, respectively. For LAT specimens the respective ratios were: 1.13, 1.26 and 2.76. The higher ultimate load of MU4 in both specimen geometries (BEL and LAT) was due to its larger sectional area. In fact, while the ultimate loads obtained for the BEL and LAT specimens comprising MU2 laminate were, respectively, 6.22 kN and 12.24 kN, the average ultimate load obtained for the correspondent MU4 specimens were 12.96 kN and 26.93 kN, that is, a factor 1.97 and 2.08 for the BEL and LAT specimens. These factors were similar to the ratio between the thicknesses of MU4 and MU2, that was equal to 1.82. This becomes clear when the results are presented in terms of stress, as shown in Figure 88 to Figure 90. These stresses were computed by Equations (25) to (27) at the maximum load.

Attention is paid to the fact that different failure modes led to similar ultimate loads in the LAT specimens made of CSM and MU2 laminates (see Table 27). This behaviour may indicate that for these specimens the bearing strength and the tensile strength in the net-section were achieved for similar load levels.

Table 27: Failure mode and ultimate load for each specimen.

Geometry of specimen	Laminate	N.	Failure mode	Ultimate Load (L_u)		
				Individual value	Avg.	CV
				[kN]	[kN]	[%]
BEL	CSM	01	cleavage	6.27	6.51	5.3
		02	cleavage	6.90		
		03	cleavage	6.35		
	BIA	01	cleavage	6.20	6.28	1.5
		02	cleavage	6.25		
		03	cleavage	6.39		
	MU2	01	cleavage	6.54	6.22	8.7
		02	cleavage	5.59		
		03	cleavage	6.53		
	MU4	01	cleavage	13.28	12.96	2.5
		02	cleavage	12.96		
		03	cleavage	12.63		
LAT	CSM	01	bearing + net-tension	7.04	9.74	21.1
		02	bearing + net-tension	11.91		
		03	bearing	10.49		
		04	bearing + net-tension	9.50		
	BIA	01	bearing + net-tension	11.32	11.06	4.0
		02	bearing + net-tension	11.32		
		03	bearing + net-tension	10.54		
	MU2	01	bearing	12.17	12.24	7.7
		02	bearing + net-tension	13.22		
		03	bearing	11.34		
	MU4	01	bearing + net-tension	24.53	26.93	12.7
		02	bearing + net-tension	29.37		
		03	bearing + net-tension	26.89		

By comparing the ultimate loads of BEL and LAT specimens (see Table 27), it was verified that for all tested laminates the failure by cleavage (BEL specimens) happens at a load level lower than the ultimate load corresponding to the bearing/net-tension failure on LAT specimens. The ratios between the average ultimate loads obtained by the LAT specimens and by the BEL specimens were equal to 1.50, 1.76, 1.97 and 2.08 to CSM, BIA, MU2 and MU4 laminates, respectively. This behaviour is consistent with that observed by the authors in the

pull-out tests with GFRP connectors embedded in SFRSCC in the Chapter 6. In fact, in the pull-out tests with perforated plate connector comprising CSM composite, failure usually occurred within the GFRP connector by cleavage immediately below the holes. Net-section failure only occurred in few cases. No bearing failure was observed for the specimens geometries tested in the pull-out tests.

(a)   (b)
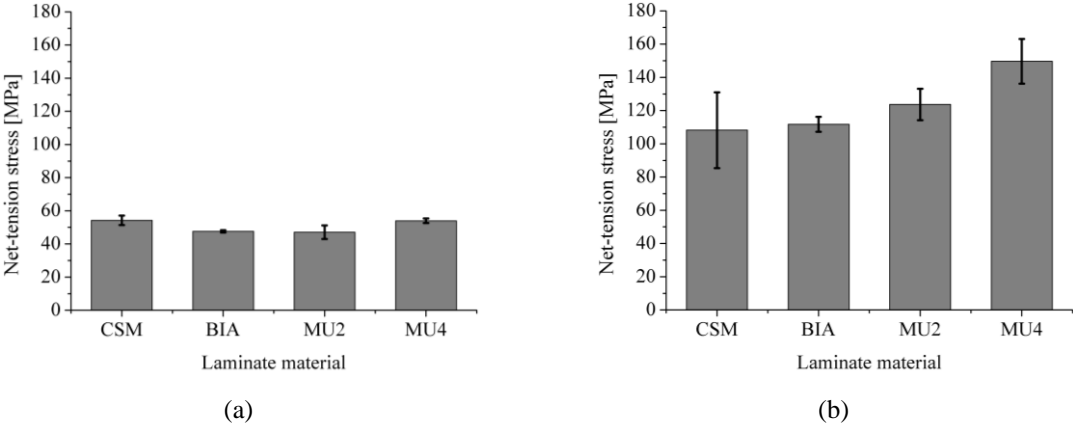
Figure 88: Net-tension stress corresponding to the ultimate load for the different laminates with: (a) BEL geometry; (b) LAT geometry.

(a)   (b)
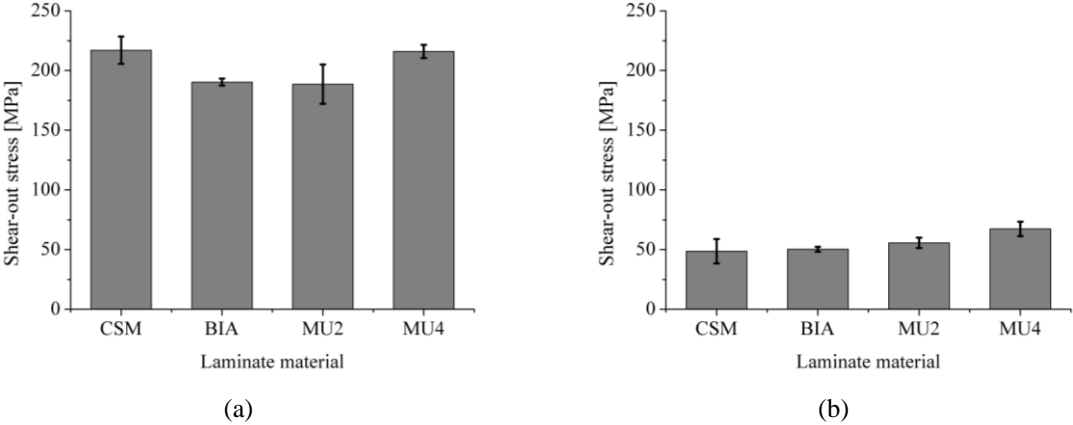
Figure 89: Shear-out stress corresponding to the ultimate load for the different laminates with: (a) BEL geometry; (b) LAT geometry.

(a)   (b)
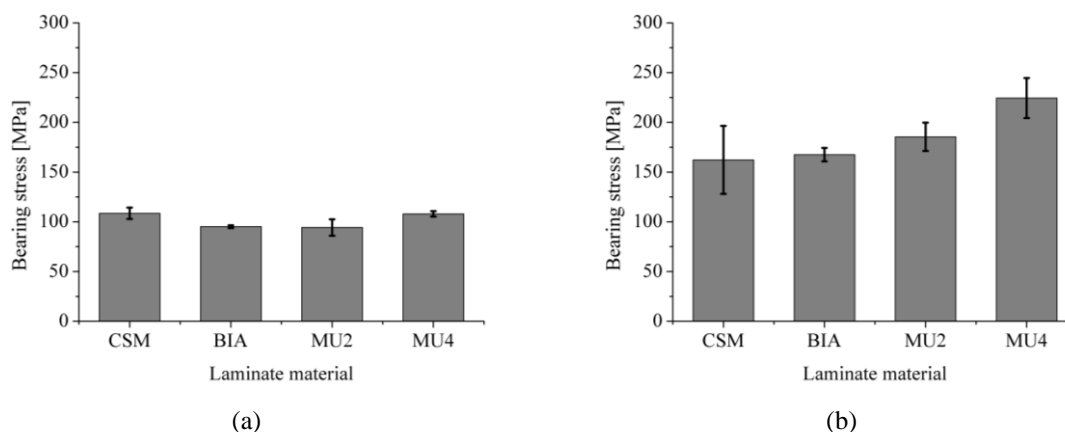
Figure 90: Bearing stress corresponding to the ultimate load for the different laminates with: BEL geometry; (b) LAT geometry.

By comparing the results obtained in the laminates BIA and MU2 (see Table 27 and Figure 88 to Figure 90) is possible to conclude that for the studied fibre content, there was no relevant contribution of the fibres that are parallel and perpendicular to the load direction on the bearing strength of the connection, independently of the failure mode expected: cleavage or bearing. Moreover, the similar load capacity of the specimens failing by cleavage, regardless the type of laminate, suggested that for the geometry studied the load capacity was conditioned by the resin strength, not by the fibre content, type or arrangement. Such observed behaviour diverges from that found in the literature (Yýlmaz and Sýnmazçelik, 2007). This probably happens due to the particular geometry of the specimens adopted in this work, that was set based on the constrains imposed by the geometry of the structural elements where the PERFOFRP connector is going to be applied.

Figure 88 to Figure 90 show, respectively, the net-tension, shear-out and bearing stresses corresponding to the maximum load. Attention should be given to the fact that the shear-out stress was computed considering that two failure planes appear in the specimens, what was not verified in the tests. Nevertheless, the shear-out stress gave a good idea on how the composite was prone to fail by shear-out/cleavage.

Looking at the results in Figure 88 to Figure 90, it was verified, as expected, that the net-tension and bearing strengths in the BEL specimens were much lower than in the LAT specimens. The ratio between the average strength in the LAT and BEL specimens was equal to 2.43 and 1.82 for net-tension and bearing strength, respectively. On the other hand, the

Figure 89 shows that the shear-out strength was much lower in the LAT than in the BEL specimens (LAT/BEL ratio equal to 0.27).

It is important to emphasize that even for materials with quite different tensile strength in 0°/90° direction (see Table 27), the LAT specimens failed for similar net-tension stresses (see Figure 88(b)). The same occurred for the BEL specimens that failed by cleavage (see Figure 88(a)). In general, the stresses corresponding to the ultimate load seemed to be independent of the type of reinforcement used in the laminate.

By comparing the ultimate loads obtained in the tests with BEL and LAT specimens, it can be concluded that, independently of the laminate used, the geometric configuration proposed for the connector in the experimental program presented in Chapter 6 was more prone to suffer a failure by cleavage immediately below the hole than a net-tension failure or even a bearing failure. Thus, it can be concluded that, for the materials and geometries studied in this research, the strength capacity of the proposed connectors was limited by the distance between lateral extremities of the hole and the below free edge of specimen (distance e indicated in Figure 79). In the case of the proposed connectors, this distance was conditioned by the thickness of the SFRSCC layers of the sandwich panels (see Chapter 5), and a value of 22.5 mm was adopted (7.5 mm + $D_h/2$).

4.5.9   Strains

Table 28 provides a summary of the experimental data in terms of maximum strains measured in the gross-section of laminate of all the specimens (in the reference length of the clip-gauge). The results indicated that in the BEL specimens a maximum of 77.8% of the elastic limit strain and 18.1% of the ultimate limit strain are attained respectively for one of the specimens comprised of MU4 and CSM laminates. Moreover, when LAT geometry was considered, apart from CSM laminate, all the other laminates present strains in the gross section higher than the elastic limit strain, attaining a maximum of 299.4% of the elastic limit strain in the BIA laminate. However, the strains were always lower than the ultimate limit strain of the respective laminates since failure at the gross-section was not observed in these laminates.

Table 28: Strain attained in the gross section of specimen.

Geometry of specimen	Laminate	N.	Maximum gross strain (ε_{gr})			ε_{gr} / $\varepsilon_{pt.el}$	ε_{gr} / $\varepsilon_{pt.u}$
			Individual value	Avg.	CV		
			[$\mu\varepsilon$]	[$\mu\varepsilon$]	[%]	[%]	[%]
BEL	CSM	01	1908	2475	27.9	10.5	10.5
		02	3246			18.1	18.1
		03	2272			12.3	12.3
	BIA	01	2422	2388	7.6	24.5	1.4
		02	2549			25.9	1.5
		03	2193			21.9	1.3
	MU2	01	1963	1924	15.5	47.9	9.5
		02	1607			32.9	6.5
		03	2201			47.0	9.3
	MU4	01	2470	2800	35.8	56.5	10.6
		02	3927			77.8	14.6
		03	2003			39.0	7.3
LAT	CSM	01	3388	6735	72.8	18.9	18.9
		02	4576			25.5	25.5
		03	14020			78.0	78.0
		04	4956			27.5	27.5
	BIA	01	29845	22232	30.7	299.4	17.1
		02	20227			203.2	11.6
		03	16625			167.0	9.6
	MU2	01	8019	9389	23.3	166.3	33.1
		02	8233			171.5	34.1
		03	11914			248.3	49.4
	MU4	01	6547	9764	19.0	131.2	24.6
		02	9175			232.2	43.5
		03	13569			271.0	50.7

The shear-out stress *versus* local strain curves obtained from the surface strain gauges placed immediately below the holes of BEL specimens are shown in Figure 91. From the results in this figure, the different ductility of both types of laminates for this loading conditions is quite visible. An initial linear response was observed followed by a branch that progressively becomes nonlinear. This nonlinear branch was, however, not observed in the CSM laminate. In fact, this laminate presented an almost linear relationship up to a brittle failure occurrence. In this test, the ultimate stress was attained for a strain approximately equal to 13500 $\mu\varepsilon$. This value corresponds to 75% of ultimate limit strain obtained from the direct tensile tests with

the laminate. This apparent premature failure may reflect the fact that the strain gauge was attached to the laminate at a distance of approximately 3 mm from the hole edge, while it was expected that the highest strain levels are developed immediately in the vicinity of the hole.

As might be expected from a knowledge of the direct tensile behaviour of the studied composites, the BIA laminate presented the most nonlinear response, and the MU2 and MU4 showed an almost bilinear response up to attain a pseudo-plastic phase (see Figure 91(c) and Figure 91(d)). This pseudo-plastic stage was also developed in BIA laminates after the ultimate limit strain was attained (see Figure 91(b)).
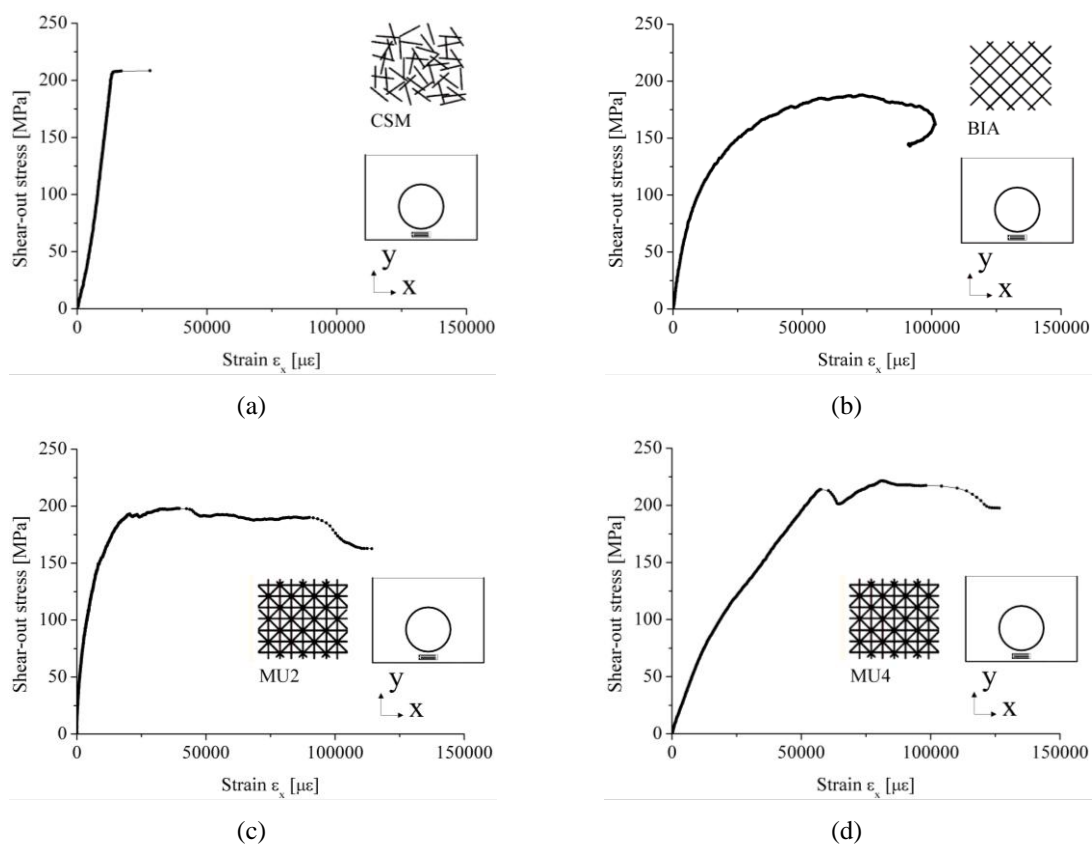
Figure 91: Shear-out stress vs. engineering strain εx in the proximity of hole corresponding to BEL specimens. Laminates: (a) CSM; (b) BIA; (c) MU2; (d) MU4.

The bearing stress *versus* local strain curves obtained from the longitudinal and transversal strain gauges are shown in Figure 92. By comparing the readings from strain gauges symmetrically positioned in laminates, it can be concluded the out-of-plane deformation was almost null (see Figure 92(a) to Figure 92(e)). Apart from CSM specimens, the remaining specimens exhibited a pronounced nonlinear behaviour. For the CSM and MU2 unloading was observed in a stage when the strain level in the lateral vicinity of the hole was much

lower than the ultimate limit strain of the respective laminates (see Figure 92(a) and Figure 92(c)). After this unloading occurrence, the initial stress-strain trend was not maintained and a reduction in the strains in the CSM specimen was observed (see Figure 92(a)). In the MU2 specimen, an asymmetric behaviour was noticed after the unloading (see Figure 92(c)). These responses can be justified by considering the damage configuration in specimens shown in Figure 85, since it was caused by the progressive failure by bearing. This reduction of strain level at the lateral vicinity of the holes was expected to happen, once the hole was elongated down by bearing, leading to maximum strains occurring in the region located near the pin.
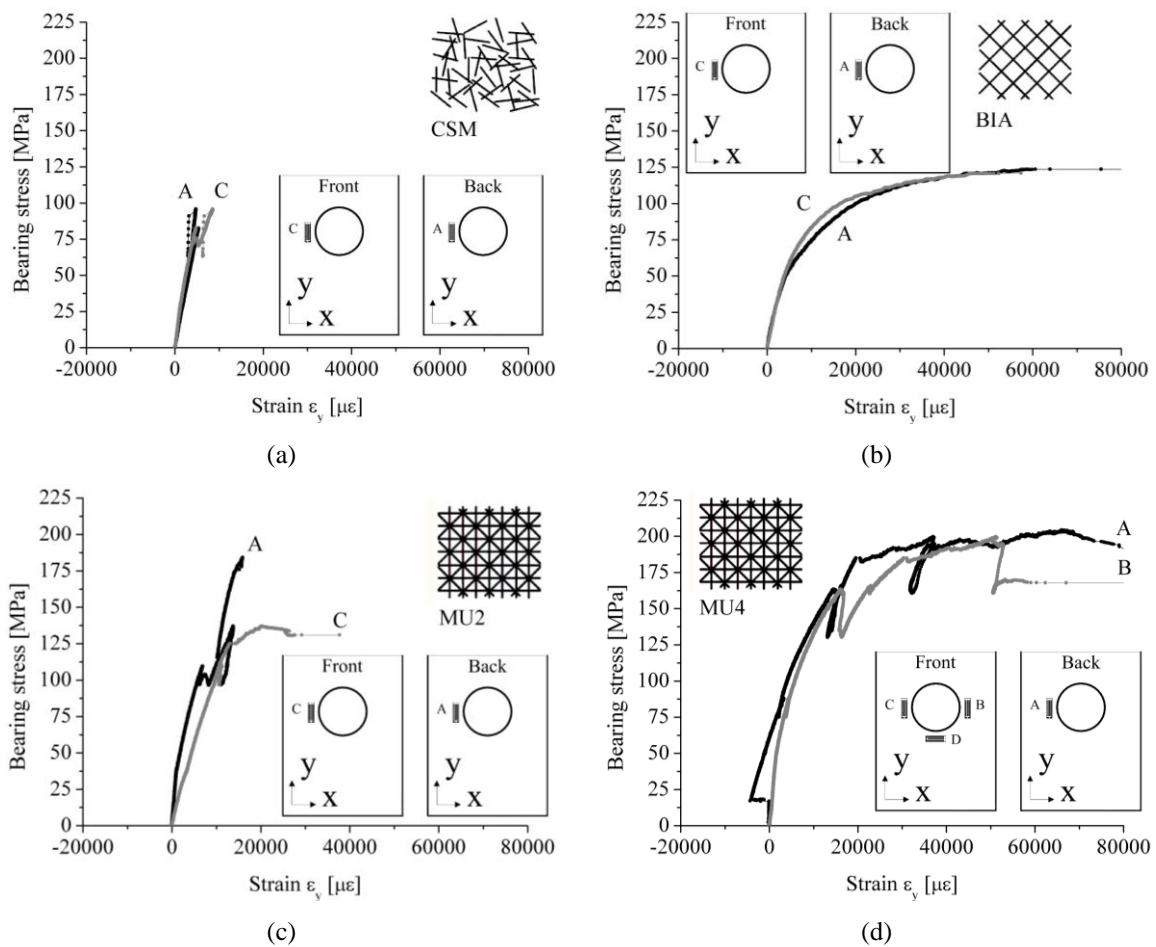
Figure 92: Bearing stress vs. engineering strain in the proximity of hole corresponding to LAT specimens: (a) CSM; (b) BIA; (c) MU2 and (d) MU4 – front and back.
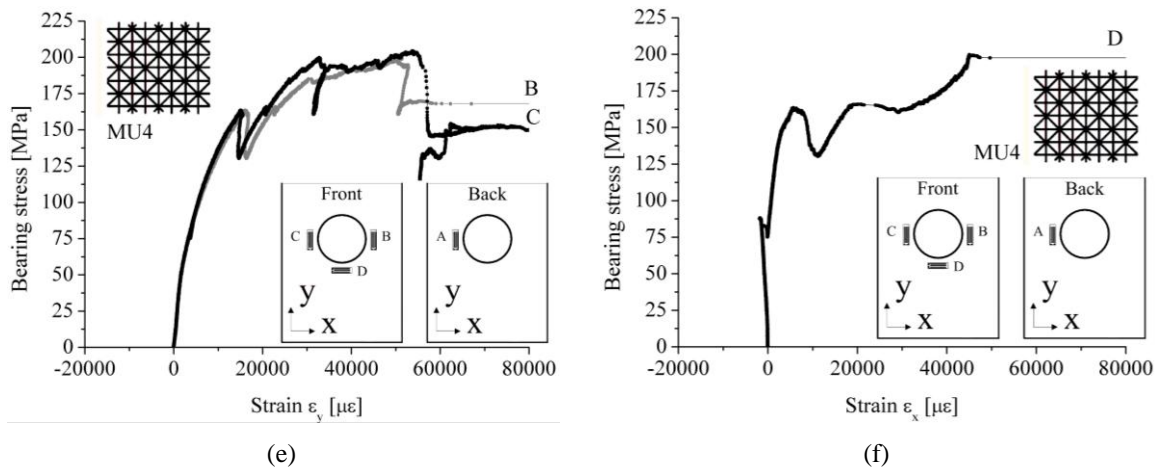
(e)

(f)

Figure 92: Bearing stress vs. engineering strain in the proximity of hole corresponding to LAT specimens: (e) MU4 – left and right; (f) MU4 – below.

Strain fields during the loading process were obtained for all the specimens using Digital Image Correlation (DIC) technique. Figure 93 and Figure 94 represent the variations of strain fields on a BEL specimens, while the variations of strain fields on LAT specimens are presented in Figure 95 and Figure 96. In the Figure 93 to Figure 96, normal compression strain is positive and shear strain is positive if it represents a decrease on the angle between the sides of an element of material (see axis in Figure 92).
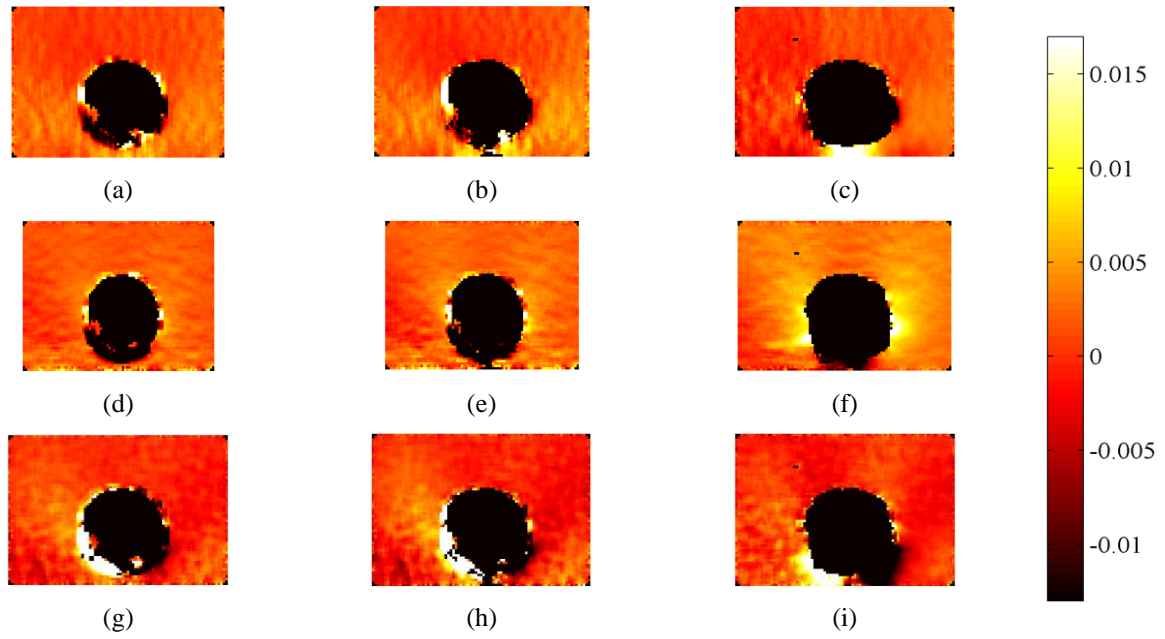
Figure 93: Engineering strain field evolving along the test for a BEL/CSM specimen. (a) ε_x (50% F_{max}); (b) ε_x (75% F_{max}); (c) ε_x (100% F_{max}); (d) ε_y (50% F_{max}); (e) ε_y (75% F_{max}); (f) ε_y (100% F_{max});(g) γ_{xy} (50% F_{max}); (h) γ_{xy} (75% F_{max}); (i) γ_{xy} (100% F_{max}). Units: [ ].
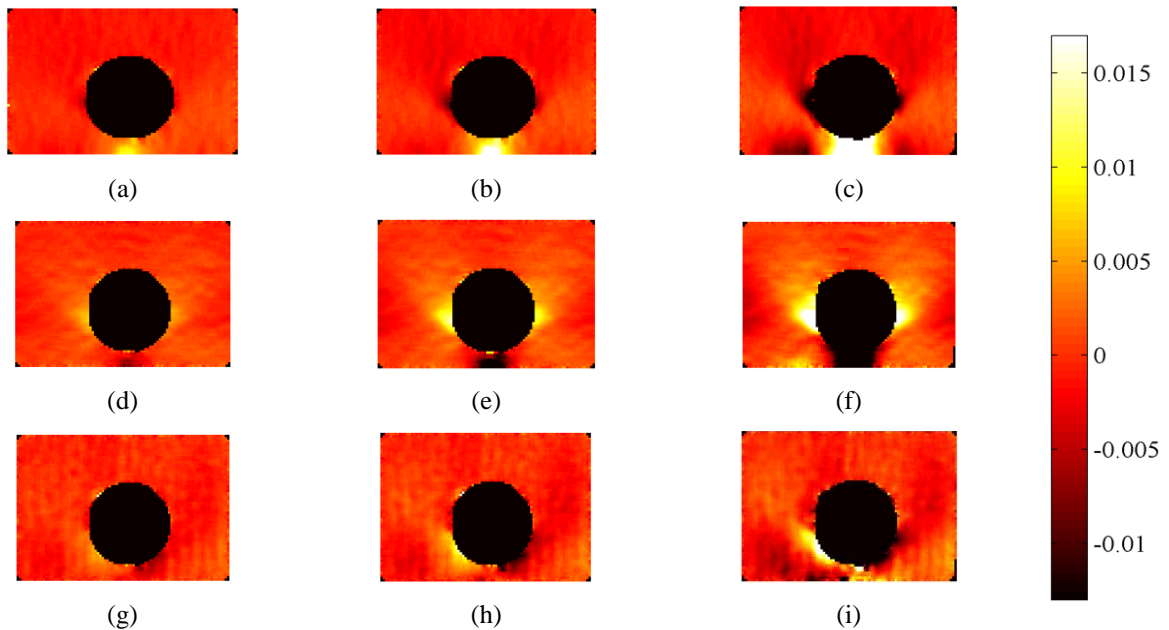
Figure 94: Engineering strain field evolving along the test for a BEL/MU2 specimen. (a) ε_x (50% F_{max}); (b) ε_x (75% F_{max}); (c) ε_x (100% F_{max}); (d) ε_y (50% F_{max}); (e) ε_y (75% F_{max}); (f) ε_y (100% F_{max});(g) γ_{xy} (50% F_{max}); (h) γ_{xy} (75% F_{max}); (i) γ_{xy} (100% F_{max}). Units: [ ].
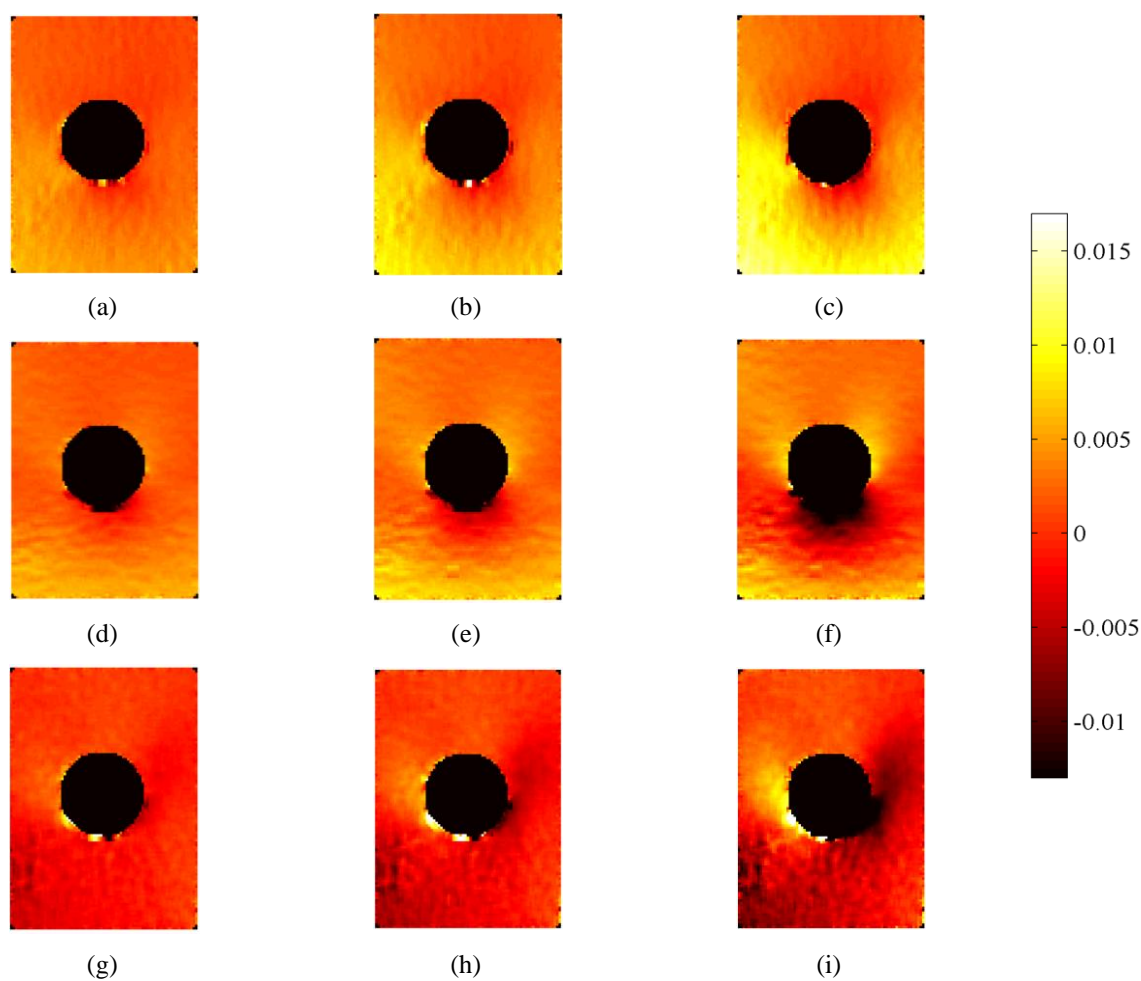
Figure 95: Engineering strain field evolving along the test for a LAT/CSM specimen. (a) ε_x (50% F_{max}); (b) ε_x (75% F_{max}); (c) ε_x (100% F_{max}); (d) ε_y (50% F_{max}); (e) ε_y (75% F_{max}); (f) ε_y (100% F_{max});(g) γ_{xy} (50% F_{max}); (h) γ_{xy} (75% F_{max}); (i) γ_{xy} (100% F_{max}). Units: [ ].
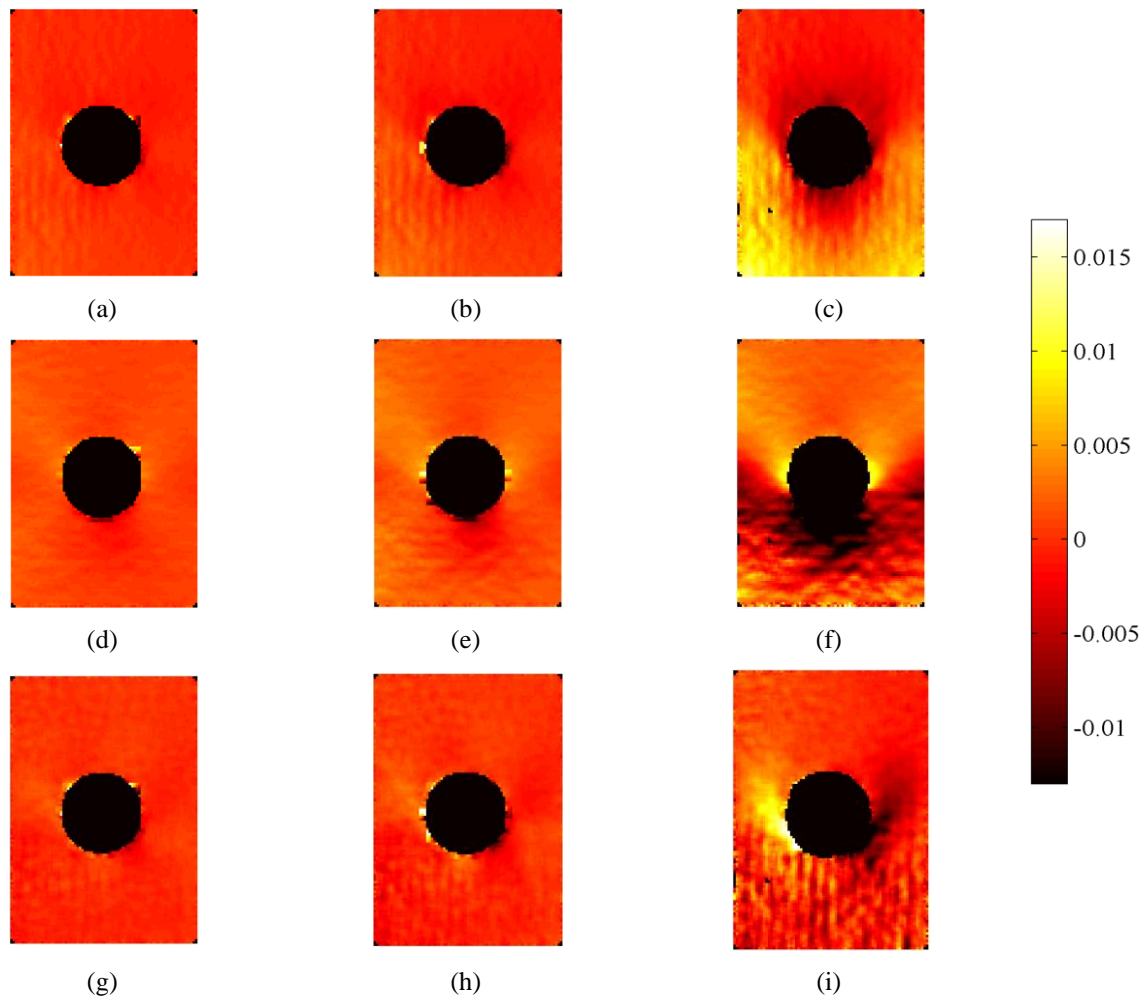
Figure 96: Engineering strain field evolving along the test for a LAT/MU2 specimen. (a) ε_x (50% F_{max}); (b) ε_x (75% F_{max}); (c) ε_x (100% F_{max}); (d) ε_y (50% F_{max}); (e) ε_y (75% F_{max}); (f) ε_y (100% F_{max});(g) γ_{xy} (50% F_{max}); (h) γ_{xy} (75% F_{max}); (i) γ_{xy} (100% F_{max}). Units: [ ].

The engineering normal and shear strain diagrams along four representative sections (L1 to L4), obtained using Digital Image Correlation (DIC) for different load levels, are presented in Figure 97 and Figure 98 for BEL specimens and Figure 99 and Figure 100 for LAT specimens.

(a)

(b)

(c)

(d)

(e)

(f)
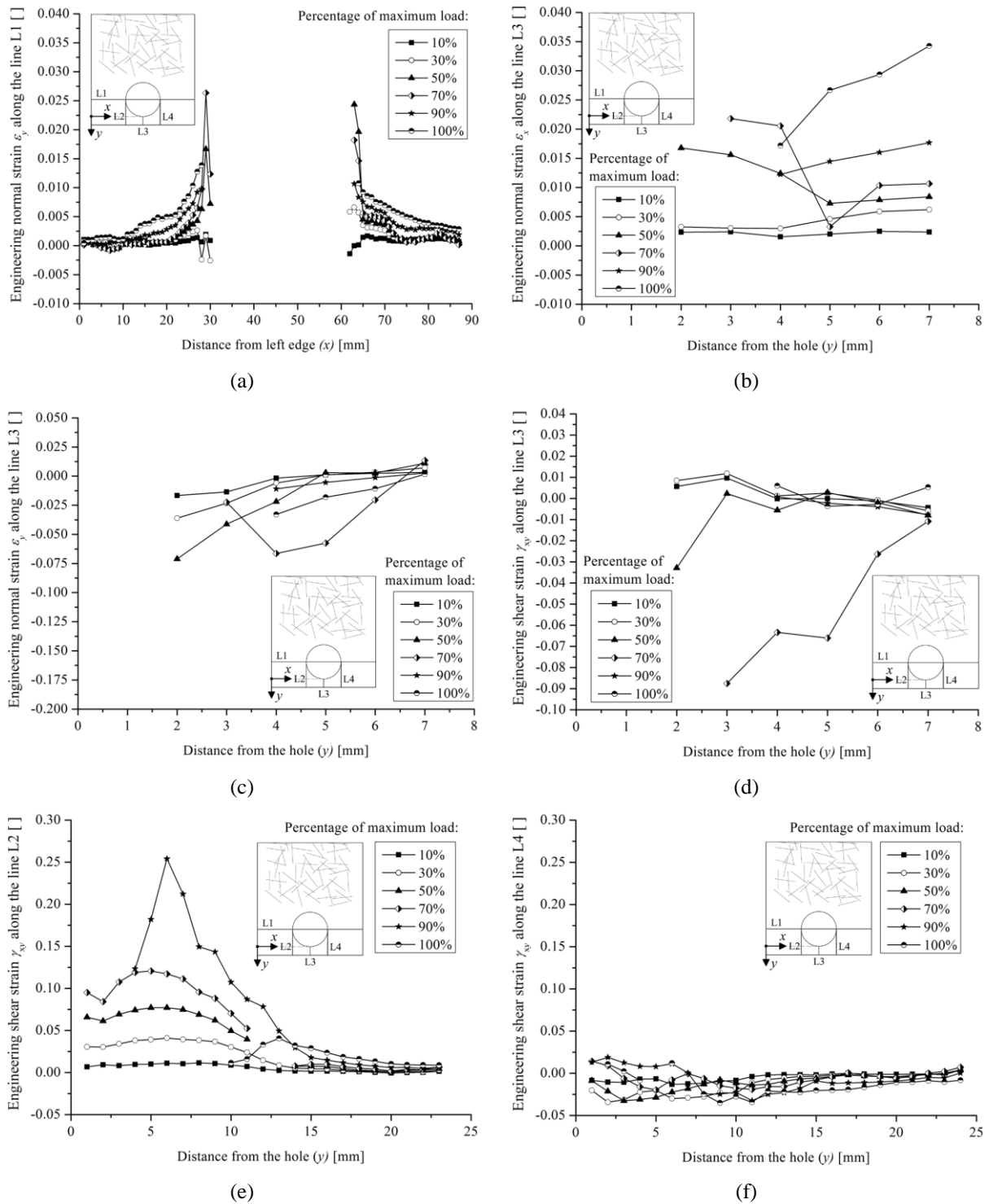
Figure 97: Engineering strain evolving along representative lines for a BEL/CSM specimen: (a) ε_y along line L1; (b) ε_x along line L3; (c) ε_y along line L3; (d) γ_{xy} along line L3; (e) γ_{xy} along line L2; (f) γ_{xy} along line L4.
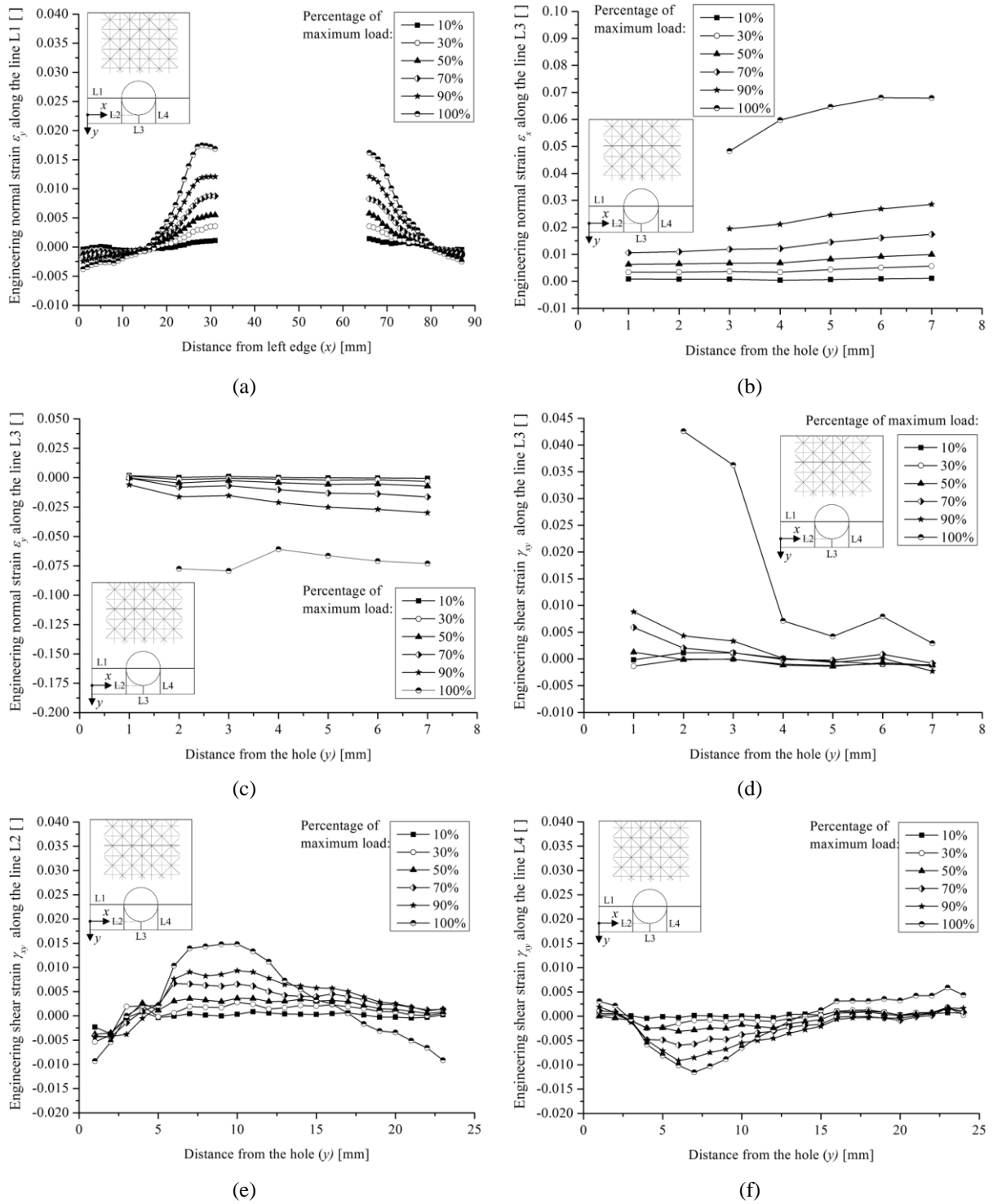
Figure 98: Engineering strain evolving along representative lines for a BEL/MU2 specimen: (a) ε_y along line L1; (b) ε_x along line L3; (c) ε_y along line L3; (d) γ_{xy} along line L3; (e) γ_{xy} along line L2; (f) γ_{xy} along line L4.

(a)

(b)

(c)

(d)

(e)

(f)
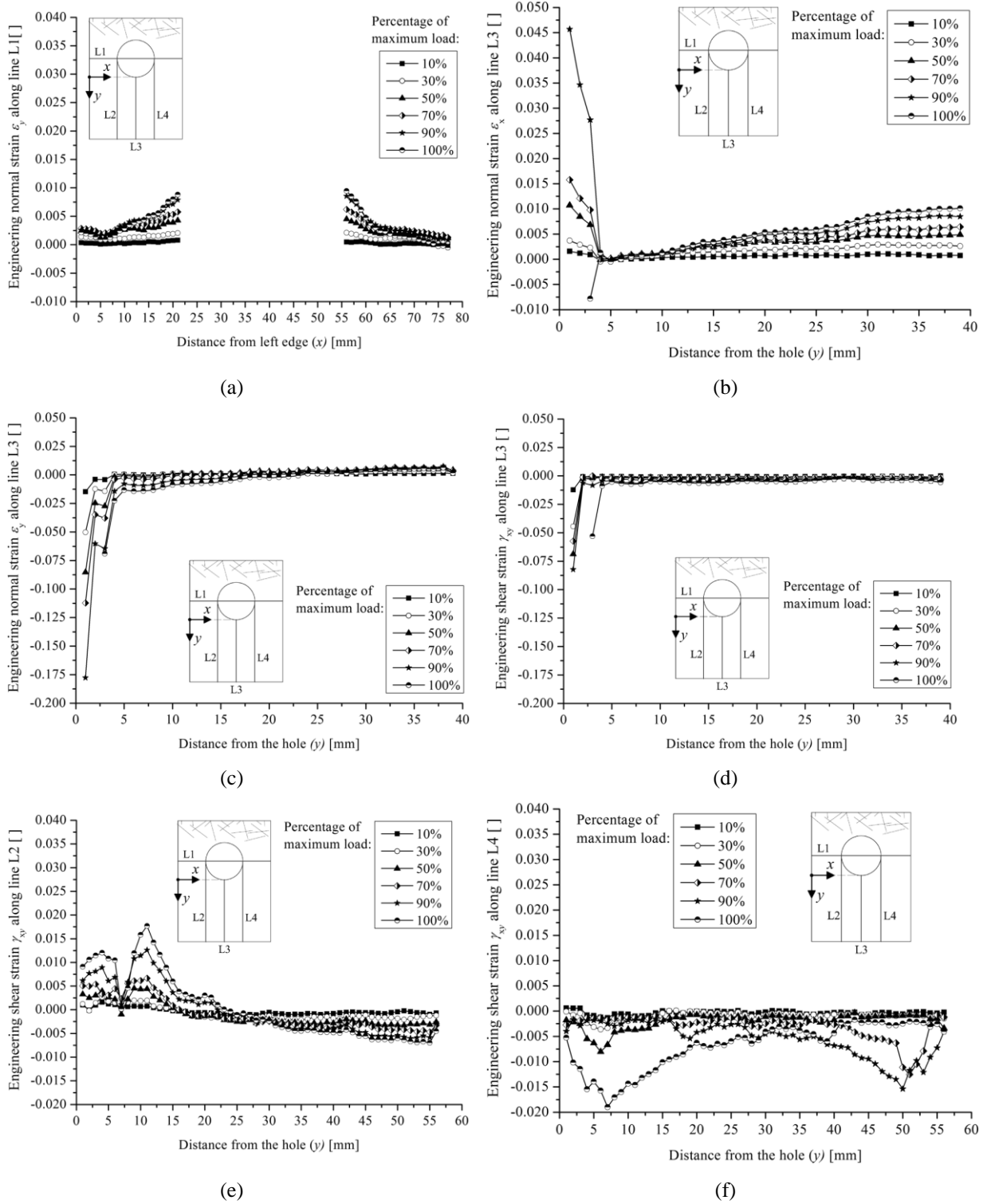
Figure 99: Engineering strain evolving along representative lines for a LAT/CSM specimen: (a) ε_y along line L1; (b) ε_x along line L3; (c) ε_y along line L3; (d) γ_{xy} along line L3; (e) γ_{xy} along line L2; (f) γ_{xy} along line L4.
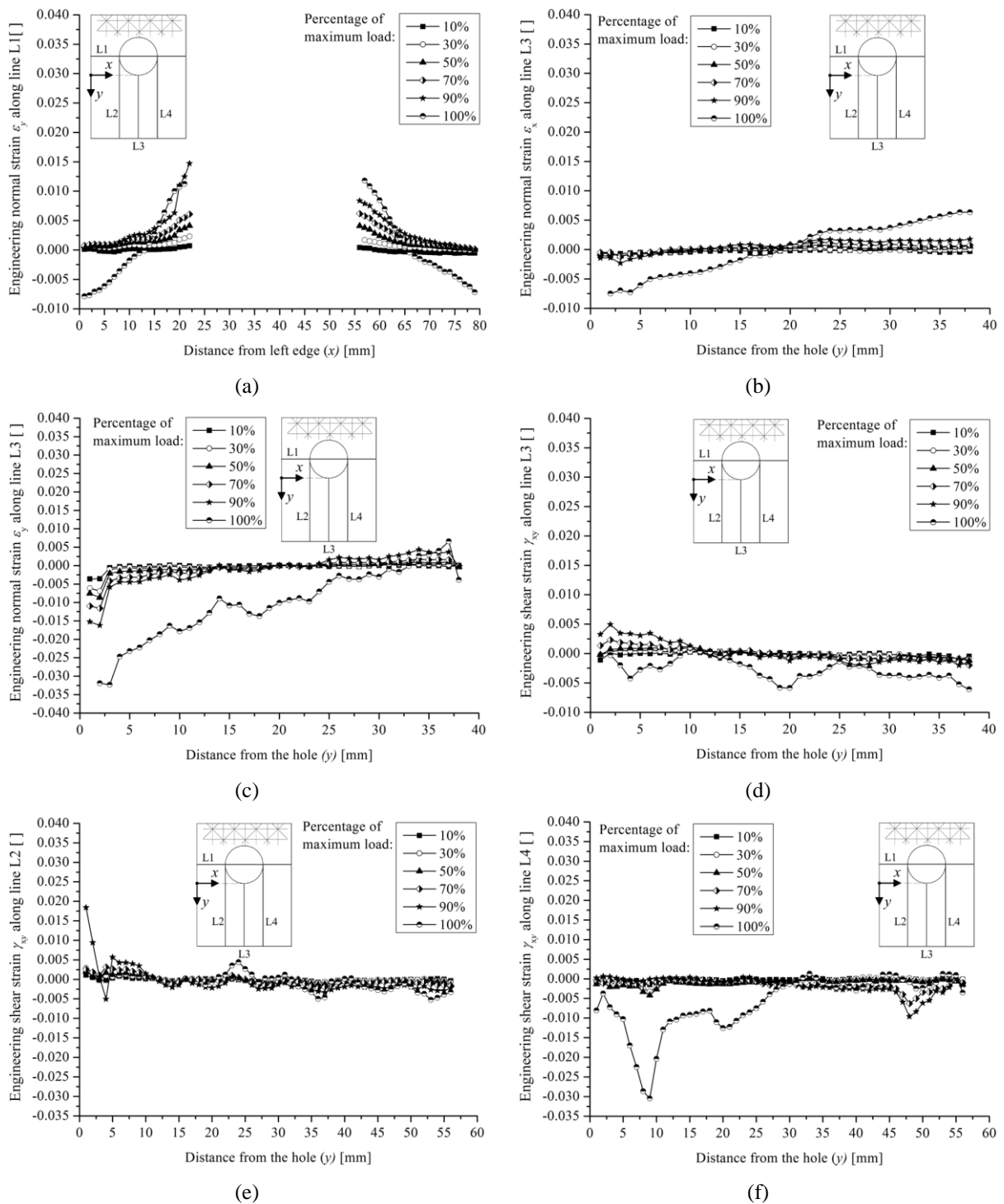
Figure 100: Engineering strain evolving along representative lines for a LAT/MU2 specimen: (a) ε_y along line L1; (b) ε_x along line L3; (c) ε_y along line L3; (d) γ_{xy} along line L3; (e) γ_{xy} along line L2; (f) γ_{xy} along line L4.

For all the specimens, it is clear that the loading leads to an increasingly higher strain concentration at the y−direction in the nearby the hole, along section L1 (see Figure 97(a), Figure 98(a), Figure 99(a) and Figure 100(a)). In this case, the strain values in BEL/CSM specimens were a little higher than the strain values measured in BEL/MU2 specimens.

Nonetheless, for BEL specimens, the highest tensile normal strains were found for at x–direction along the line L3, between the hole and the bottom edge (see Figure 97(b) and Figure 98(b)). In L3 alignment, the tensile normal strains were higher in BEL/MU2 specimens than in BEL/CSM specimens. This pattern is coherent to the failure modes obtained for this type of specimen. Furthermore, it is clear in Figure 98(b) that there was some flexure in the region below the hole, with higher tensile strains in the nearby of the bottom edge of specimen. Shear strains along lines L2 and L4 present similar magnitude in BEL/MU2 specimen (see Figure 98(b) and Figure 98(e)), indicating that the test was performed in a symmetric way. The same does not happen for the BEL/CSM specimen (see Figure 97(d) and Figure 97(e)).

On the other hand, the engineering strain diagrams along the representative lines of LAT specimens, presented in Figure 99 and Figure 100, show that the tensile normal strain ε_y level attained in the BEL specimens was not achieved in LAT specimens, but similar strain distribution patterns were found, as these values increase towards the proximity with the holes in all tested specimens. However, a high compressive strain at y–direction in the vicinity of the hole was observed for both LAT specimens along line L3 (see Figure 99(c) and Figure 100(c)). In fact, the existence of this strain concentration just below the hole explains the bearing failure in the LAT specimens.

4.5.10 FE modelling the bearing behaviour of GFRP

In order to investigate the capability of modelling the pin-bearing behaviour of GFRP plates, a two-dimensional finite element model was built using the FEMIX program (Azevedo *et al.*, 2003a).

The following assumptions were made while building the model: (a) the aluminium pin is considered as perfectly rigid, (b) the friction between the pin and GFRP is disregarded; (c) no clearance or slacks are considered between the perforated plate and the aluminium pin and (d) the tabs are disregarded and the load is applied as a line force uniformly distributed in the top of the specimen. For simplicity, only half of the plate was modelled, since there is a symmetry on geometry and loading conditions with respect to $y - z$ plane as shown in Figure 101, which also depicts meshing and loading conditions. Meshes of 944 and 640 total elements are used respectively for BEL and LAT specimens.
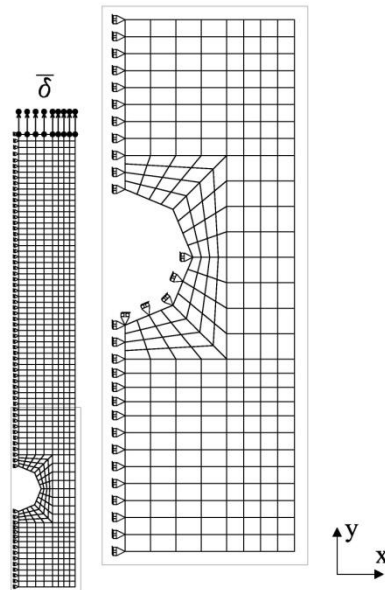
Figure 101: Mesh, loading and boundary conditions (LAT specimen).

The pin was simulated by radially restraining the displacements on the bottom part of the hole edge. The nodes on the symmetry axis were restrained from moving along the horizontal *x*-direction. A prescribed displacement was applied progressively to the nodes on the top edge of specimen.

For simplicity, only the CSM material was considered on the numerical study. This material was chosen due to its isotropic properties. Moreover, the CSM is the material with the greater potential to be employed as material of the connectors according to the findings reported in the previous sections of the current chapter.

Both a linear and a nonlinear model were constructed. All calculations were performed by considering mean stiffness and strength values instead of design values. This strategy was adopted in order to make it possible to directly compare results with the experimental data. In both elastic linear and nonlinear modeling, the CSM GFRP was assumed with $E_{pt} = 14.64$ GPa, based on the data reported for CSM 1 in Table 22. The Poisson's ratio of the CSM laminate was considered equal to 0.2. 8-node Serendipity plane stress elements with 2×2 Gauss-Legendre integration scheme were used. In both modelling approaches (linear and nonlinear), a linear elastic behaviour under compression was adopted.

For the nonlinear modeling, a multi-fixed smeared crack model was used. In the smeared crack approach, localized inelastic deformations are smeared over a band of a certain width in terms of stress $\times$ strain relations and thus the cracking process is modelled in a continuous

way. This approach is widely used to simulate the fracture process in the concrete (Hillerborg, 1980, Bažant and Oh, 1983, Hordijk, 1991a). The propagation of cracks is driven by the shape of the tension-softening constitutive law and the fracture energy of material in mode I cracking (G_f). In this approach, a new crack is initiated when the maximum principal stress reaches the uniaxial tensile strength, and the angle between the direction of the existing cracks and the direction of the maximum principal stress exceeds the value of a predefined threshold angle.

In the present study, the post cracking behaviour of the GFRP under tension was assumed to follow the multi-linear softening behaviour presented in Figure 102. A relatively abrupt decay of strength of laminate is considered as to adequately simulate the brittle rupture observed in the direct tensile tests for the CSM. The parameters ϕ_i and ξ_i ($i=1$ to 3) that define the shape of the tension-softening behaviour are presented in Figure 102. The crack band width was assumed equal to the square root of the area of the finite element in order to assure that the results are not dependent on the mesh refinement. Here, the threshold angle was assumed constant and equal to 30° and a maximum of 2 cracks per integration point is allowed to arise. The results from the FE modelling are then discussed taking in consideration the limit stress failure criteria.
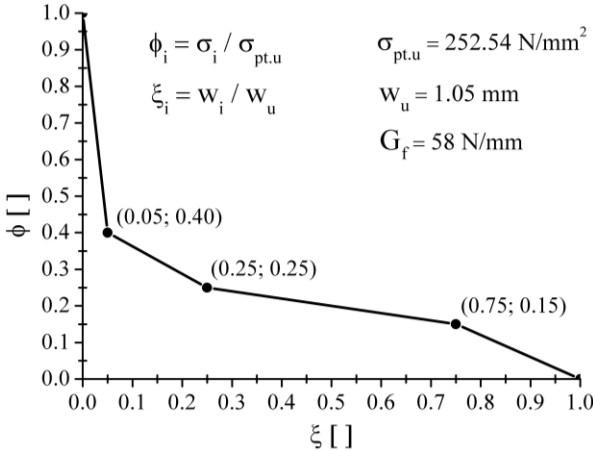
Figure 102: Post-cracking softening diagram adopted for the GFRP in the nonlinear material analyses.

Initially, the feasibility of the FE modelling was assessed by comparison of the deformed mesh obtained from an elastic analysis and the undeformed mesh. Figure 103 illustrates this comparison for a prescribed displacement of 1mm on the top edge of both BEL and LAT specimens. The deformed shapes were plotted at a magnification factor of 10. From these

images is possible to note that the results are qualitatively coherent to the boundary and loading conditions imposed to the models.

(a)   (b)
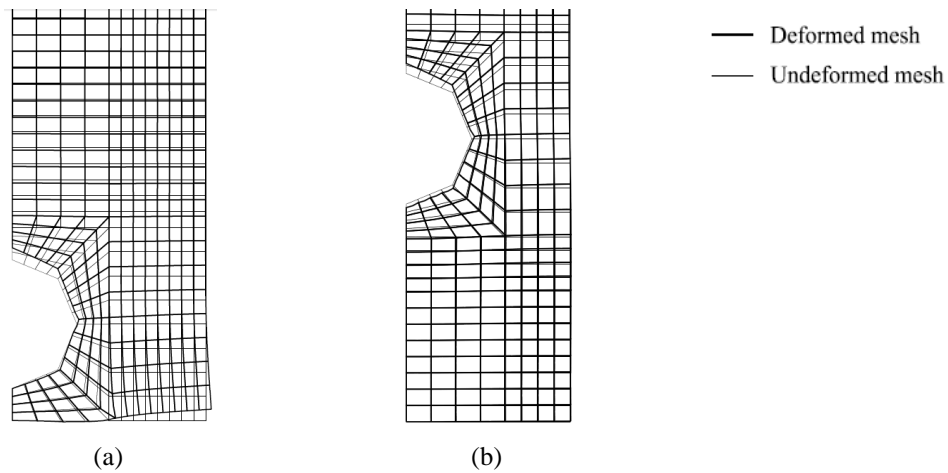
Figure 103: Details of deformed mesh when the prescribed displacement is equal to 1 mm: (a) BEL specimen; (b) LAT specimen (magnification factor: 10×).

At 1mm prescribed displacement, Figure 104 and Figure 105, respectively show, for BEL and LAT specimens, the elastic stress fields for the normal engineering stresses in the x and y directions: σ_x, σ_y; and for the shear engineering stress(τ_{xy}).

$\sigma_x{}^{max} = 221MPa$ $\sigma_y{}^{max} = 272MPa$ $\tau_{xy}{}^{max} = 67MPa$

$\sigma_x{}^{min} = -175MPa$ $\sigma_y{}^{min} = -35MPa$ $\tau_{xy}{}^{min} = -103MPa$

(a)   (b)   (c)
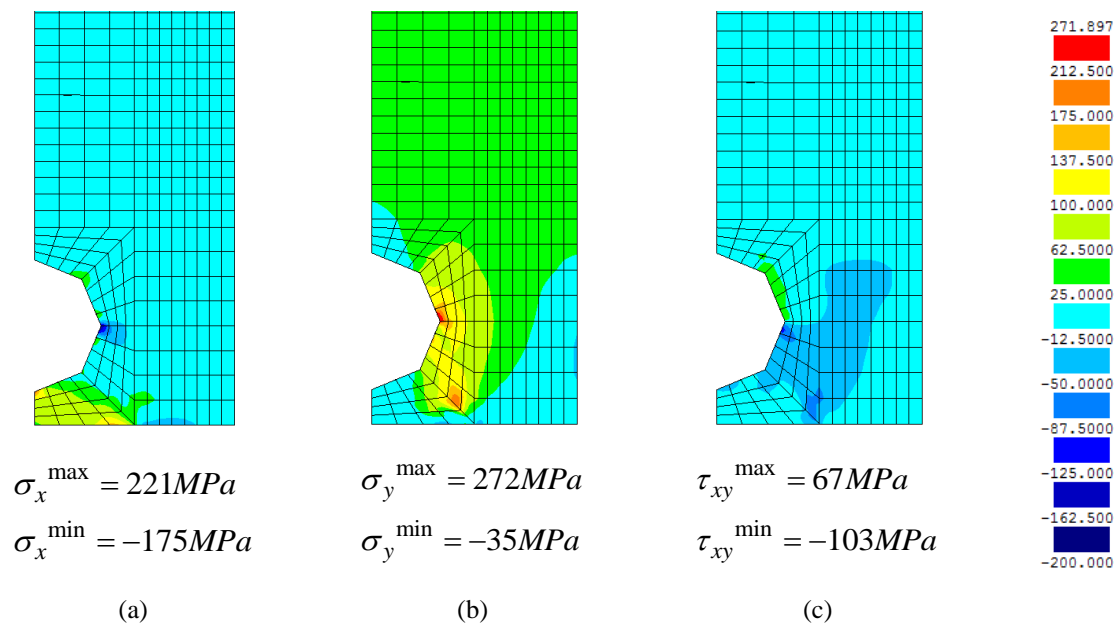
Figure 104: Engineering stress field obtained for the BEL specimen corresponding to a prescribed displacement on top edge of specimen equal to 1.00 mm: (a) σ_x; (b) σ_y; (c) τ_{xy} (units in MPa; negative values corresponds to compression).

$$\sigma_x{}^{max} = 148MPa \qquad \sigma_y{}^{max} = 243MPa \qquad \tau_{xy}{}^{max} = 91MPa$$

$$\sigma_x{}^{min} = -172MPa \qquad \sigma_y{}^{min} = -184MPa \qquad \tau_{xy}{}^{min} = -168MPa$$

(a)   (b)   (c)
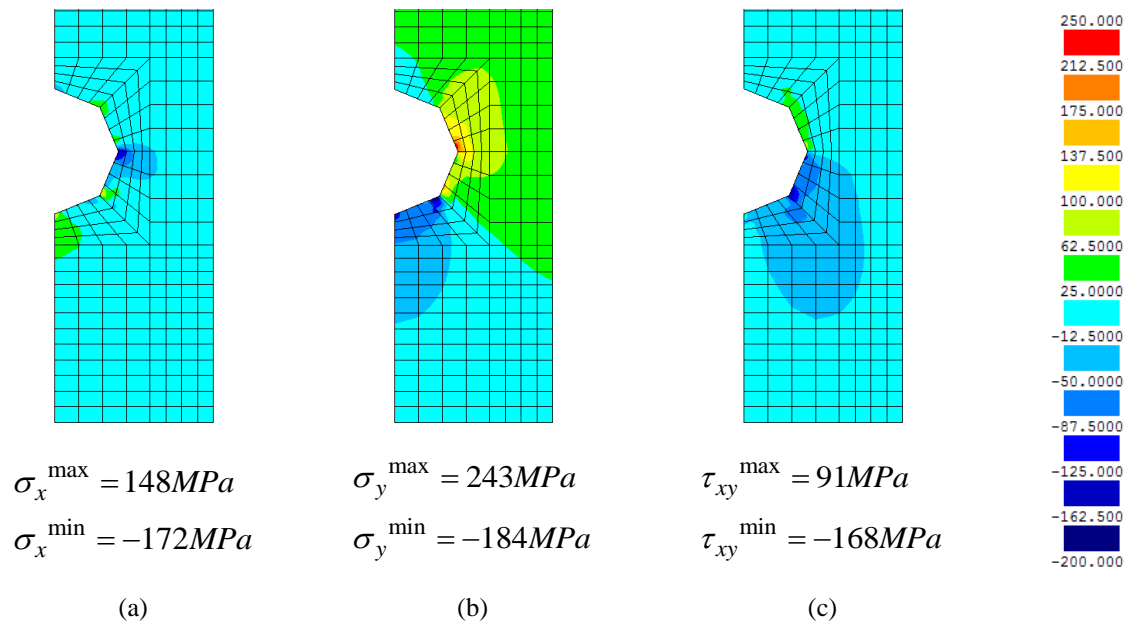
Figure 105: Engineering stress field obtained for the LAT specimen corresponding to a prescribed displacement on top edge of specimen equal to 1.00 mm: (a) σ_x ; (b) σ_y ; (c) τ_{xy} (units in MPa; negative values corresponds to compression).

Considering that CSM laminate is isotropic and taking into account the results shown in Figure 104, based on a limit stress rupture analysis, one would conclude that is expected that the specimen would fail by a net-tension failure, even in the BEL specimens. Nonetheless, in the experimental program it was observed that, with the exception of two specimens, all the others presented a failure mode by cleavage immediately below the hole. Probably this is related to the fact that, due to the reduced distance that remains of GFRP between the hole edge and the bottom edge of specimen, the GFRP properties in this zone may not actually match those obtained through the characterization tests. In fact, at this region below the hole a few number of fibres kept intact, with the required anchorage length to contribute to the strength of the composite. Possibly the properties of the laminate in this region approach the strength of the matrix.

The FEM results indicate that, as is experimentally evidenced, the LAT specimens are more prone to present a failure mode by net-tension. Attention should be paid to the high compressive stress σ_y attained at the hole edge immediately bellow the pin (45° with y-direction). This compressive stress may be associated to the bearing failures that were experimentally observed.

Considering the maximum and minimum stresses presented in Figure 104 and Figure 105 and the direct tensile and shear strengths obtained from the characterization tests for the CSM laminate, it is expected that in both types of specimen, the ratio between the extreme stresses to the strength are the lowest for the case of shear stress. This indicates that the shear failure is not expectable for the conditions under study.

The evolution of the σ_x and σ_y fields for three levels of imposed deformation on the top edge (0.40 mm, 0.60 mm and 1.00 mm) are respectively shown in Figure 106 and Figure 107.

$$\sigma_x^{max} = 88MPa$$
$$\sigma_x^{min} = -70MPa$$
(a)

$$\sigma_x^{max} = 133MPa$$
$$\sigma_x^{min} = -105MPa$$
(b)

$$\sigma_x^{max} = 221MPa$$
$$\sigma_x^{min} = -175MPa$$
(c)
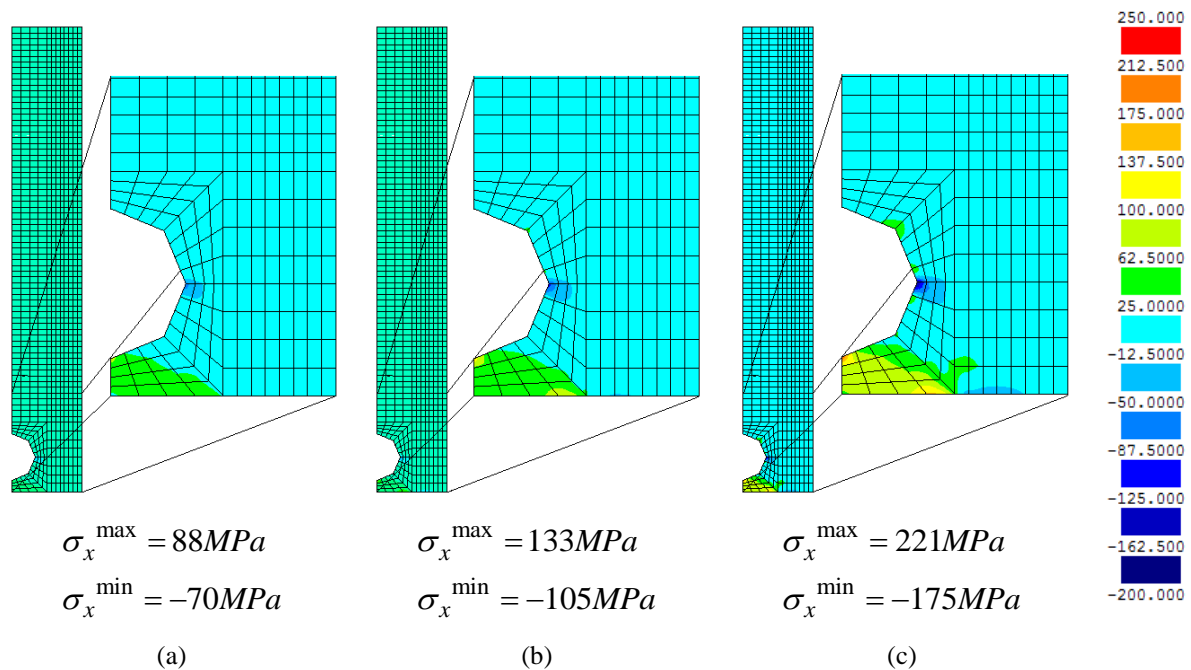
Figure 106: Evolution of engineering normal stress field σ_x obtained for the BEL specimen corresponding to the following prescribed displacements: (a) 0.40 mm; (b) 0.60 mm and (c) 1.00 mm (units in MPa; negative values corresponds to compression).

$$\sigma_y^{\max} = 97 MPa \qquad \sigma_y^{\max} = 146 MPa \qquad \sigma_y^{\max} = 243 MPa$$

$$\sigma_y^{\min} = -74 MPa \qquad \sigma_y^{\min} = -110 MPa \qquad \sigma_y^{\min} = -184 MPa$$

(a)   (b)   (c)
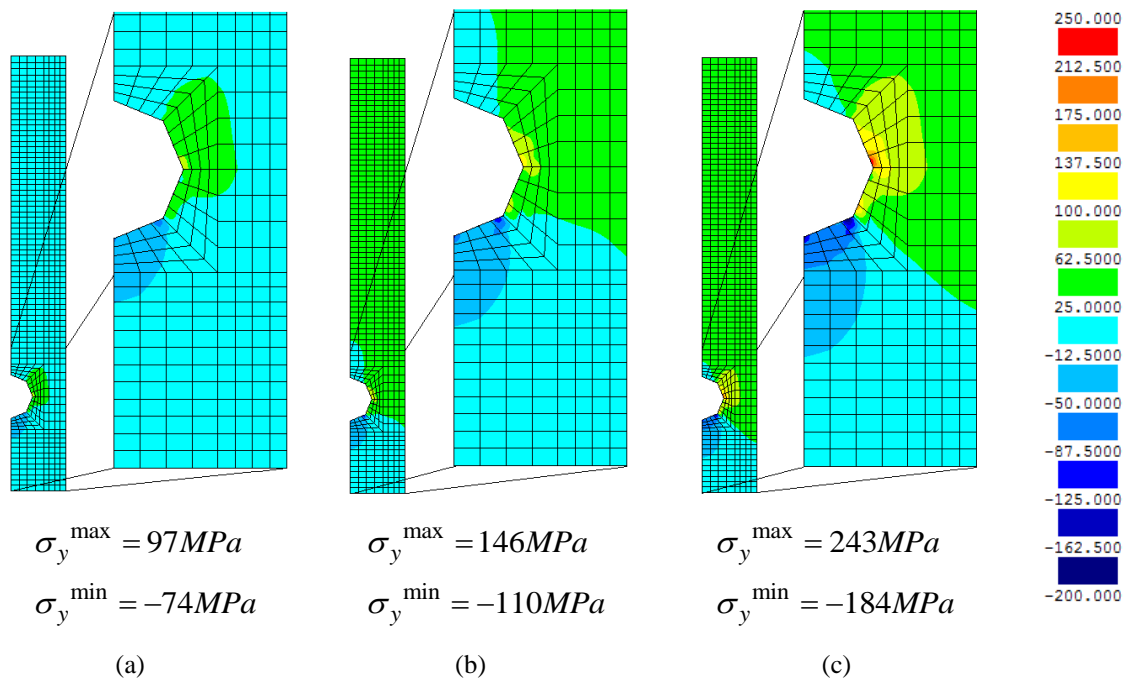
Figure 107: Evolution of engineering normal stress field σ_y obtained for the LAT specimen corresponding to the following prescribed displacements: (a) 0.40 mm; (b) 0.60 mm and (c) 1.00 mm (units in MPa; negative values corresponds to compression).

The progressive damage of the BEL and LAT specimens obtained by the nonlinear numerical analyses are illustrated respectively in Figure 108 and Figure 109.

(a)   (b)   (c)
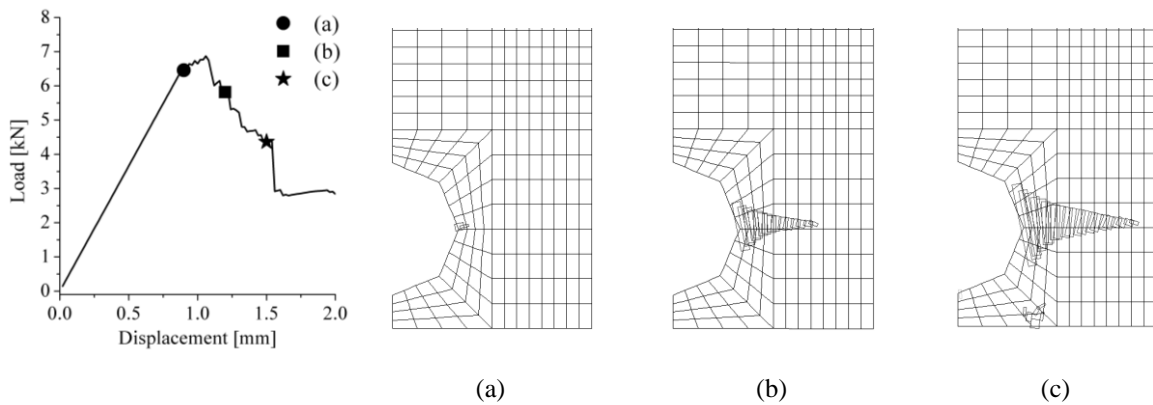
Figure 108: Crack patterns for the nonlinear modeling of BEL specimen corresponding to the following prescribed displacements: (a) 0.90 mm (crack initiation); (b) 1.2 mm; (c) 1.5 mm (crack width factor: 5; crack length factor: 2).

(a) (b) (c)
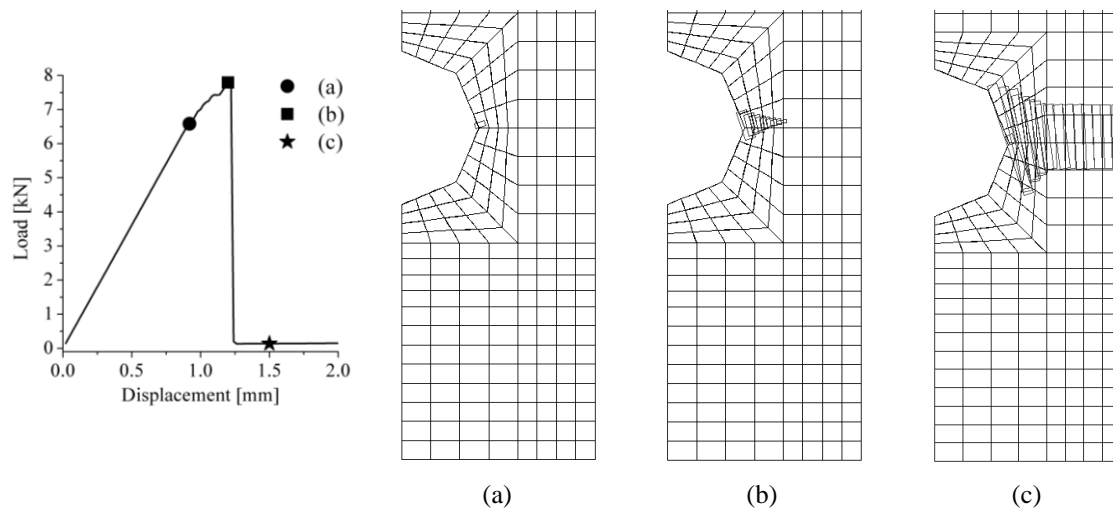
Figure 109: Crack patterns for the nonlinear modeling of LAT specimen corresponding to the following prescribed displacements: (a) 0.92 mm (crack initiation); (b) 1.2 mm; (c) 1.5 mm. (crack width factor: 5; crack length factor: 2).

The conclusions obtained from the stress fields considering a linear elastic behaviour of laminate (Figure 106 and Figure 107) are confirmed by the crack patterns presented in Figure 108 and Figure 109. As expected, the failure mode predicted to BEL specimens is the same obtained for the LAT specimens: by net-tension failure. Nonetheless, this failure mode is obtained experimentally only for the LAT specimens. The hypothesis that can explain this behaviour was discussed earlier in this study.

Comparisons between the experimental and numerical force *versus* displacement relationships are given in Figure 110(a) and Figure 110(b). In these figures, both the linear elastic and nonlinear responses are presented.

From the comparison between the numerical and experimental data it can be seen that the experimental curves show some initial non-linearity, but after this branch the curves are almost linear. A possible explanation for this initial non-linearity lies in the adjustment of the pin to the hole edge due to the existence of some clearance or even localized slacks/imperfections. As a consequence of this adjustment, for both cases, the numerical curves show a delay in relation to the experimental data. A similar behaviour was reported by McCarthy and McCarthy (2003). Whereas in the LAT specimen this delay seems constant, in BEL specimen the numerical curve shows a slight tendency to stiffen with increasing load.

Despite the fact that the failure modes observed in the experimental program for the BEL specimens are different from the failure mode obtained from the FE modelling, the predicted

ultimate strength is in quite good agreement with the experimental values. This may indicate that, in these specimens, the failure due to net-tension (obtained in the model) is attained in a value quite similar to the value obtained for the failure by cleavage obtained experimentally. It might be argued that the net-tension failure was eminent in the tested specimens, and would really actually have happened, were it not for the anticipation of the cleavage failure mechanism.
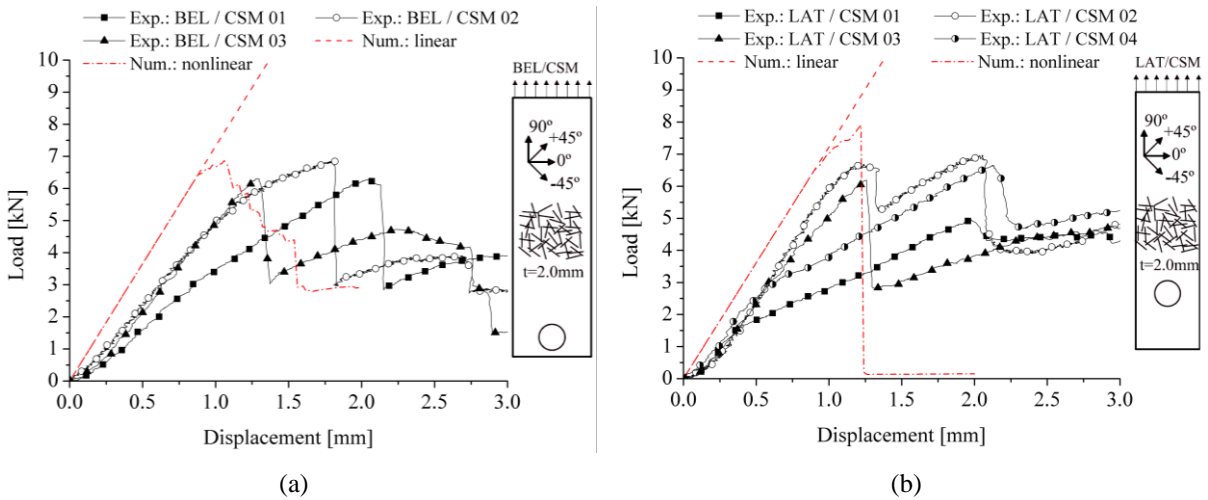
Figure 110: Comparison between the experimental and numerical load *versus* displacement curves for: (a) BEL specimen; (b) LAT specimen (displacements at *y*–direction in the top edge of specimen).

On the other hand, the post-cracking behaviour obtained numerically for the LAT specimens occurs in a much more brittle mode than the one observed experimentally. This is related to the fact that in all LAT specimens there was the evidence of bearing failure prior to the net-tension failure. This bearing failure mode is not caught by the numerical model due to the limitation of modelling the compressive behaviour of laminate as elastic linear. Another finding from Figure 110 is that, due to the geometric configuration of BEL specimens, the load *versus* displacement responses tends to be more ductile than the rupture by net-tension in LAT specimens. This occurs due to mechanism changing after the first failure in the BEL specimens and consequent appearance of other failure lines (see Figure 108).

Comparison between the engineering strains in the proximity of hole edges are presented in Figure 111.
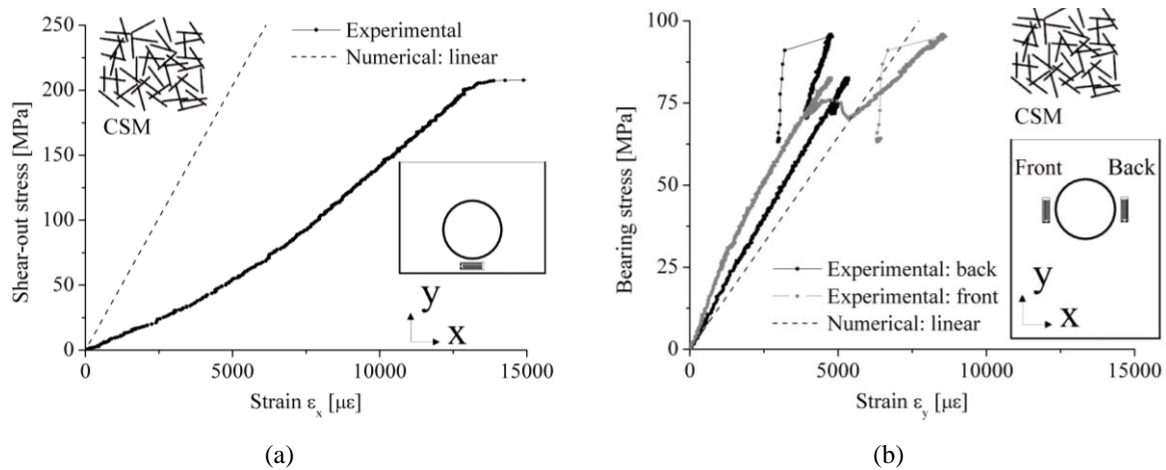
Figure 111: Comparison between the engineering strains in the vicinity of holes obtained by numerical analysis and measured by ESG: (a) BEL specimen; (b) LAT specimen.

From the results presented in Figure 111a is clear that whereas the numerical results for the test with a LAT specimen provide a good approximation to the experimental data, the numerical modelling of BEL specimen leads to an overestimation of response stiffness as compared to the measurement of the strain gage. This is a strong indication that the elastic modulus of material bellow the hole might be lower than the elastic modulus adopted in the model. This result support the previously raised hypothesis, which speculated that the drilling of the hole at a distance of only 7.5 mm might be reducing the number of fibres crossing the minimum sectional area between the hole and the laminate edge. Furthermore, the fewer number of fibres at this section have a reduced anchorage length, contributing to a decrease of the load capacity of the composite. In this region the properties of the composite would dominated by the properties of matrix. In fact, the elastic modulus of the polyester matrix is quoted to be between 2.06 and 4.41 GPa in the literature (Callister and Rethwisch, 2009). This value represents at about ¼ of the elastic modulus of the composite (14.64 GPa).

A better understanding of the behaviour of bearing capacity of the perforated plates is attained plotting the evolution of the principal stresses in the elements where the maximum stresses are attained. The evolution of principal stresses for 2 integration points (IPs) for the BEL specimens and 3 IPs for the LAT specimens are depicted in Figure 112 and Figure 113, respectively. The chosen integration points correspond to the ones where the extreme values for the principal stresses are attained.
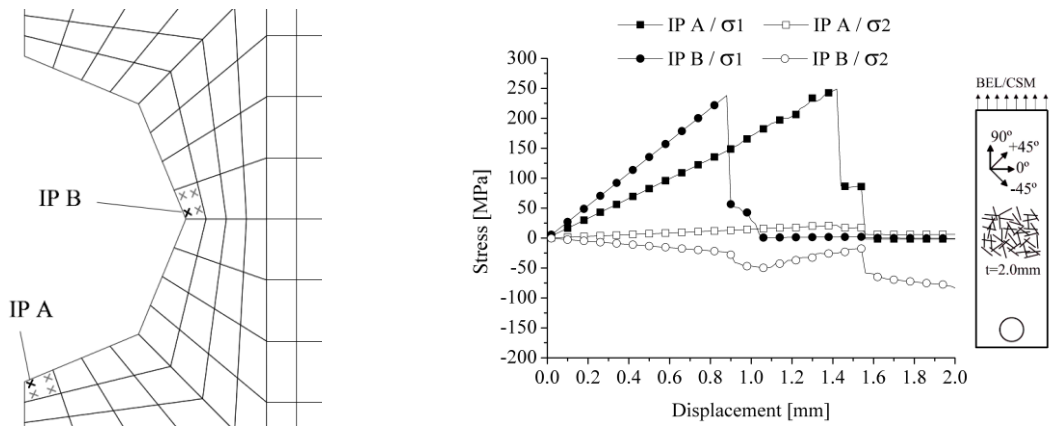
Figure 112: Evolution of principal normal stresses obtained for integration points (IP) corresponding to elements where the maximum stresses are attained in BEL specimen (negative values corresponds to compression).
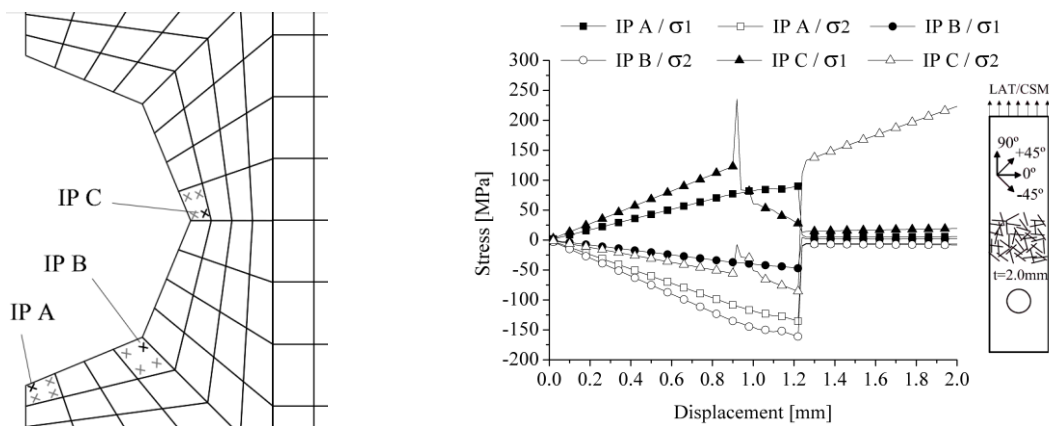
Figure 113: Evolution of principal normal stresses obtained for integration points (IP) corresponding to elements where the maximum stresses are attained in LAT specimen (negative values corresponds to compression).

4.6 FINAL REMARKS

In this chapter, the manufacturing process used to produce different GFRP candidates to be used in the production of connectors was addressed. The main properties of interest of the GFRP candidates were evaluated. The characterization was limited to the determination of fibre content, direct tensile, shear and pin-bearing behaviour.

According to these tests, it was concluded that a simple and low-cost GFRP such as the one made by chopped strand mat (CSM) can be used in the production of the connectors that are part of the sandwich panel. Furthermore, the characterization tests gave a better understanding of the overall behaviour of the connections and giving valuable information necessary to their correct design. From the test results a set main conclusions can be drawn, and are sequentially addressed in the following paragraphs.

In the shear tests, premature failure by local crushing of laminate at gripping region of the fixture was obtained for tests with CSM laminates without the use of tabs, BIAX 45/-45, TRIAX 0/90, TRIAX 45/-45 and TRIAX 90//0. This failure mode made it impossible to obtain the ultimate shear stresses for these tests. Nonetheless, it was observed that, for the strain range within which the shear modulus were computed, a state of pure shear was achieved in the gauge section of all specimens. Furthermore, the measurements obtained by ESG demonstrated to be prone to inaccuracies for tests with laminates with high material anisotropy, due to the lack of uniformity of the shear strain in the gauge area. In the other hand, the DIC demonstrated to be very useful because it allows measuring strains along a reduced area in the nearby of the notched section, not being necessary to use correction factors.

For the geometries and materials used in this investigation, the results of pin-bearing tests (pull-out forces) indicated that the load capacity of the connectors is limited by the distance between the hole and the bottom edge of specimen, independently of the composite used. Furthermore, the advantage of using BIA and MU2 laminates instead of CSM is related to the more ductile rupture mode obtained when these materials are employed. In absence of the geometrical constrains encountered in this research that limit the distance between the hole edge and the bottom edge of connector, it is recommended to design the connector in order to avoid rupture by cleavage. The experimental results obtained with LAT specimens indicate that, for all the materials studied and considering a connector with holes distanced 2.5 D apart, when a ratio e/D equal to 2.17 is adopted, the rupture tends to be more ductile. From observations during tests, this pseudo-ductile behaviour is associated to successive damages related to bearing failure mode.

Chapter 5

PRELIMINARY DESIGN OF PROPOSED SANDWICH PANEL

In this chapter an innovative precast sandwich panel with suitable structural and thermal performance is proposed. The panel is devised as a fundamental part of a construction system for modular buildings. This system is intended to be cost competitive with focus on reduction of construction time and material optimization. The proposed sandwich panel for exterior bearing walls comprises GFRP connectors of controlled cost, and two thin outer layers of Steel Fibre Reinforced Self-Compacting Concrete (SFRSCC).

The role of SFRSCC is related to the inherent benefits of using this material instead of concrete with conventional reinforcement. Firstly, it allows reducing the volume of concrete necessary to produce the external layers, since the requirement of minimum concrete cover for the reinforcements in conventional reinforced concrete structures is not applicable to SFRSCC elements (Prisco *et al.*, 2009a). So, more structurally efficient and lightweight elements can be obtained. Another advantage is related to the possibility of reducing non-value adding activities on the production line and the related labour costs. Specifically, SFRSCC technology eliminates the tasks of placing the reinforcement (mesh or bars), and compacting/levelling concrete, thus allowing easier standardization of the production tasks. Furthermore, since the proposed panels are supposed to constitute the building envelope, it should be ensured that the width of the cracks in these elements is small enough to satisfy

requirements concerning serviceability (functionality and appearance) and durability of the structure. In this context, SFRSCC has several properties that makes it attractive: it generally presents high crack-width control capacity, ductility, impact resistance, and water tightness due to the fibre reinforcement mechanisms provided by fibres bridging the microcracks, and the relatively high content of fine constituents. Furthermore, the costs of maintenance derived from corrosion of conventionally reinforced concrete layers are suppressed, since corrosion effects in SFRSCC have been reported to be negligible or even non-existing if crack width is limited to 0.3 mm (Nemegeer *et al.*, 2003, Bernard, 2004).

As already mentioned in the literature review presented in Chapter 2, different types of Fibre-Reinforced Polymer (FRP) connectors have been proposed by several researchers for reinforced/prestressed concrete sandwich panels (Einea *et al.*, 1994, Lucier *et al.*, 2010, Pantelides *et al.*, 2008, Woltman *et al.*, 2010), and some of them are even commercially available (Naito *et al.*, 2012). SFRSCC was also suggested as the material for sandwich panels, in which the connection between the concrete layers is assured by solid zones of concrete (Barros *et al.*, 2007). Nevertheless, the combination of SFRSCC panels with FRP connectors to obtain a sandwich panel that takes advantage of both materials is unknown at present phase, thus motivating the research developed in this thesis.

This chapter begins with a brief description of the proposed building system. Different possibilities to materialize the connection of SFRSCC layers were identified. For a better understanding of the structural behaviour of the panels, the second part of this chapter centres efforts for assessing the best solutions for the geometry of the panel and arrangement of GFRP connectors, through parametric analyses. The parametric studies included both linear and non-linear numerical analyses of the panel subjected to the combined action of axial loadings and wind pressure.

5.1 PROPOSED BUILDING SYSTEM

The building system that was developed is composed of pre-fabricated sandwich structural panels for both walls and slabs, which are connected to each other *in situ*. The idea was to develop a structural exterior wall system that incorporates all the installations (water, electrical, network and telephone connections), thermal insulation and finishes. The entire system is prefabricated at a plant and transported to the construction site, where the remaining

tasks to be performed are placement of the panels and application of connections to foundations and adjacent elements. Even though this construction system can be deployed for multi-storey buildings, the research efforts were centred in single-storey buildings.

The prefabricated structural sandwich panel comprising thin-walled SFRSCC is schematically shown in Figure 114(a), where the various components involved are identified, and a possible arrangement of connectors is indicated. This wall system acts as the primary load carrying component of the structure transferring the loads to the foundation of the structure. The single storey wall panels span vertically between foundations and floor/roof panels without the need for additional intermediate supports. Horizontal floor and roof panels shall behave as one-way slabs, continuously supported on the inner concrete layer of wall panels, as shown in Figure 114(b). This eliminates the need for beams and columns along exterior walls. The horizontal panels shall also act as diaphragms that transfer the lateral loads to the walls.
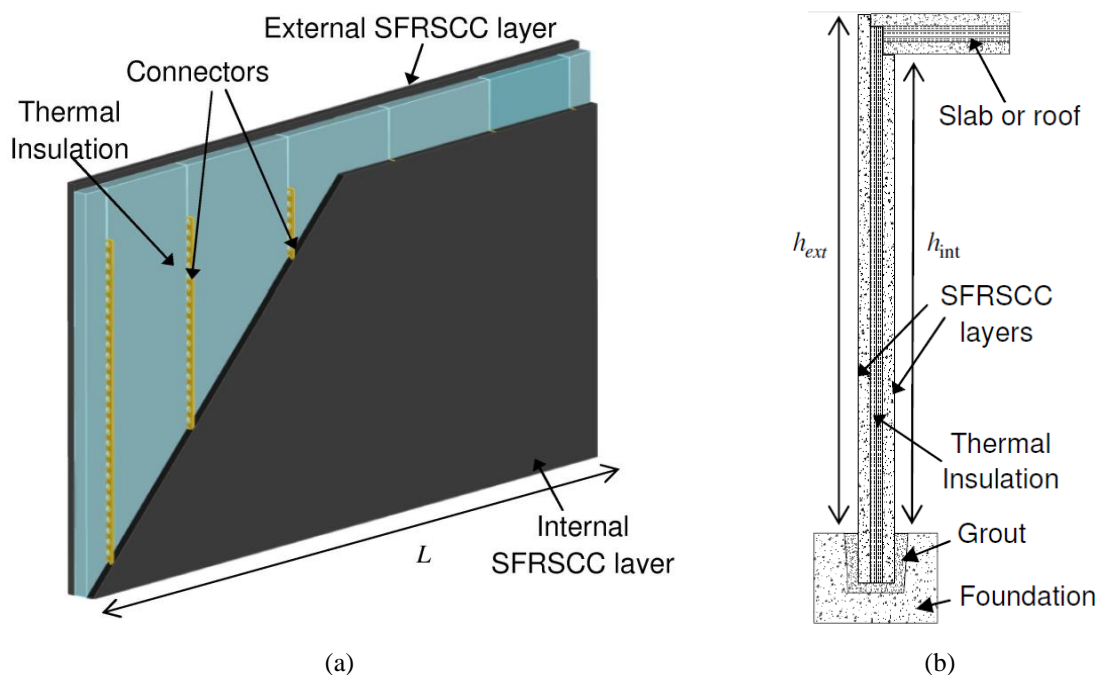
Figure 114: Proposed building system: (a) components of the devised load-bearing sandwich wall panel; (b) system cross section.

The horizontal joints connect floor and wall units. In the case of dwellings, the principal forces to be transferred are vertical loads from the roof. The connection methods to be employed in these joints can be grouting, bolting, welding or a combination of these techniques (Elliott, 2002, Engström *et al.*, 2008). The author suggests the use of bearing pads combined to grouting dowels projected from the wall panel and from the roof/slab members.

If the slab is used with a composite concrete topping, the connection can also be achieved using dowels from the wall to the cast-in-place topping.

Continuous footings are suggested to support the lower surface of the wall. The connection between the panel and the corresponding footing can be made through cast-in-place grout, as indicated in Figure 114(b).

5.1.1   Geometry of panels

The maximum possible length and weight of a panel is determined based on handling, transportation and installation requirements. Its dimensions should be as large as possible to reduce costs by diminishing the number of panels needed and, consequently, the number of joints and connections required. The thicknesses of the SFRSCC layers are as thin as possible to withstand the imposed loads over its service life, while being thick enough to make viable connections between both concrete layers and between the panel itself and adjacent horizontal/vertical panels. The thickness of the insulation material is primarily tailored to meet the desirable thermal performance for the building envelope. However, this thickness can be also specified based on structural or even on constructive requirements, since it influences the flexural stiffness and capacity of the panel, and the core can be also used to accommodate other installations.

5.1.2   Connections between the concrete layers

The connection between the two SFRSCC layers of a sandwich panel is assured by discrete or continuous one-way GFRP connectors. While the continuous connectors extend along the full height or length of the panel, the discrete connectors have much lower length than the in-plane dimensions of the panels, and are strategically positioned to ensure optimized strength/stiffness benefits.

Since these connectors are the main load transfer mechanism between both SFRSCC layers, they must resist to the forces resulting from loadings to which the panel may be subjected. It should be noticed that, if the panels are stripped from the horizontal position, their connectors must be designed to resist the tensile forces caused by the self-weight of the lower SFRSCC layer as well as the suction from the form generated during the lift up movement. Moreover, the connectors are also mobilized to transfer the shear stresses caused by flexural bending, as well as the in-plane stresses due to temperature variation and shrinkage.

For the GFRP × SFRSCC connection two main types of connectors are proposed: embedded (Figure 115(a) and Figure 115(b)) and adhesively bonded (Figure 115(c)). The first ones are embedded into both concrete layers. Among the embedded connectors there are simply perforated plates (Figure 115(a)) and connectors with a profiled shape (Figure 115(b)). The simply perforated plates consist of a GFRP plate with a number of uniformly spaced holes, through which SFRSCC can flow. During casting, the openings in the GFRP promote the formation of SFRSCC dowels, which increase the mechanical anchorage between the GFRP connector and the SFRSCC layer, providing shear resistance along the connector alignment and preventing the separation between the SFRSCC layers in the direction orthogonal to their planes. The second embedded profiled connector (Figure 115(b)) consists of a I-shaped GFRP that is embedded into concrete, and the mechanical interlock provides the anchorage of the connector. When submitted to shear loading, the flanges of the I-shaped connector presents frontal bearing strength and the I web resists to shear stresses. These connectors are similar to the steel Perfobond and I-shaped connectors adopted in steel-concrete composite structural elements (Valente and Cruz, 2004). GFRP connectors similar to the simply perforated plates (Cho *et al.*, 2010) and I-shaped (Keller *et al.*, 2007) have already been proposed for hybrid GFRP-concrete bridge decks.
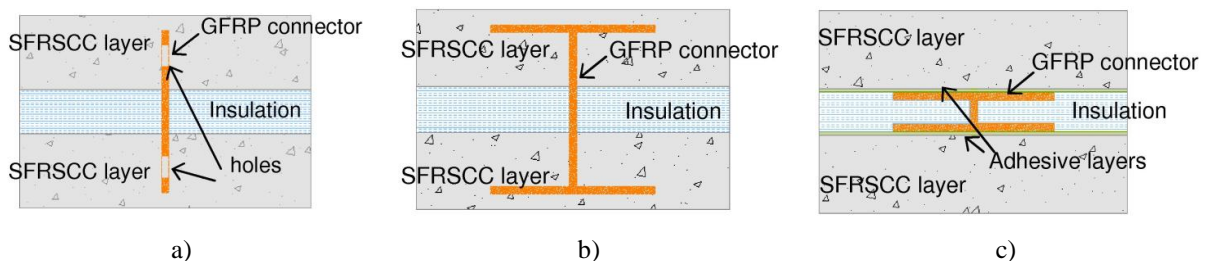
Figure 115: Cross-sectional scheme of investigated connections for sandwich panels: a) embedded – simply perforated plate; b) embedded – profiled and c) adhesively bonded.

An alternative to the embedded connectors is the adoption of adhesively bonded connections, where the SFRSCC layers, the GFRP profiles and the thermal insulation blocks are connected by an adhesive joint (see Figure 115(c)). Adhesive bonding is a connection method that has been extensively used in repair and strengthening of concrete structures for more than a decade (Bakis *et al.*, 2002). This technique has been proposed for application in some FRP-concrete composite structures, especially in bridge decks (Deskovic *et al.*, 1995, Kim and Fam, 2011). The main benefit commonly associated to this technique is the assurance of a rather uniform stress distribution over the section of the composite structure, unlike the case

of embedded connectors, which favour the occurrence of zones of high stress gradients (Luo *et al.*, 2012). As shown in Figure 115(c), the adhesive is spread in the entire surface of the panel. However, due to practical and economical restraints, a simpler alternative can be considered, which consists in spreading the adhesive layer only in the flanges of the I-profiles whereas the insulation plates could be connected through a male-female connection.

5.2 MANUFACTURE OF THE PROPOSED PANEL

5.2.1 Panels comprising embedded connectors

Traditionally, the construction of sandwich reinforced concrete panels is made by cutting, bending, tying and placing the reinforcement; pouring the first concrete layer, followed by the placement of the thermal insulation blocks and of the connectors prior the concrete set time. Then, reinforcing steel and lifting inserts are placed and, finally, the panel is finished by pouring the second concrete layer. However, if this traditional construction system was adopted by simply replacing the conventional concrete by the SFRSCC, the probability of obtaining fibres passing through the holes of the perforated GFRP plate connector would be reduced, since the connectors are positioned after the casting of the first SFRSCC layer. So, to overcome this limitation of the traditional system, particularly in the case of using perforated GFRP connectors, a new manufacturing system is proposed that permits the steel fibres to flow through the holes of the connectors. This system is described in the following paragraph and is schematically represented in Figure 116.

A sandwich panel is cast on a planar formwork system that includes four slidable members. The overall thickness of the sandwich panel is achieved by adjusting the height of these members. Once the dimensions of the panel are configured, the connectors are positioned and held firmly in position with the aid of temporary supports (see Figure 116(a)). Then, the first layer of SFRSCC mix is poured into the panel form (see Figure 116(b)). At this stage, the bottom perforated part of the connectors becomes submerged to the SFRSCC layer. Afterwards, while the first concrete layer hardens, insulating material plates are placed on top of the first concrete layer. In order to make the internal SFRSCC layer have a shorter height than the external layer (see Figure 114(b)), placeholders are used according to the scheme of Figure 116(c). These placeholders can also be used to materialize openings, such as windows and doors. After putting all of the insulating blocks on the top of the first SFRSCC layer,

handling inserts and/or plate inserts are installed above the insulating blocks for the connection of these panels to the roof/floor elements. Later, the SFRSCC mix is poured, thus materializing the second SFRSCC layer (see Figure 116(d)). After initial curing, the panel is removed from the mould and stocked.

a)

b)

c)

d)
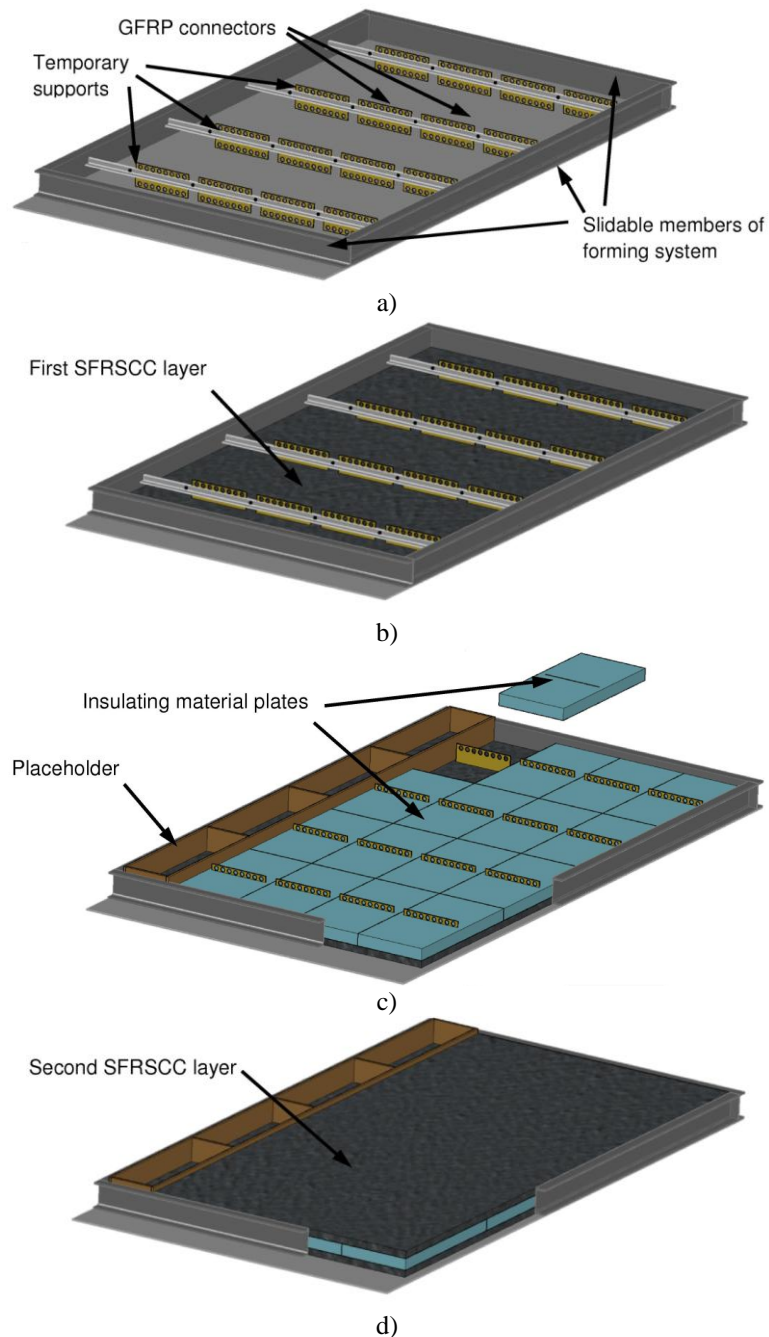
Figure 116: Phases of manufacture of a sandwich panel with pre-positioned embedded one-way discrete connectors: a) connectors positioned before casting; b) pouring the first SFRSCC layer; c) positioning the insulating material plates; d) pouring the second SFRSCC layer.

5.2.2 Panels comprising adhesively bonded connectors

The main difference on the manufacturing process of adhesively bonded panels is that the assemblage of panels is done independently of the concrete layers casting process. Firstly, both SFRSCC layers are cast in completely equal conditions. After the concrete curing time, the adhesive layer is spread in the proper surfaces of the concrete layers, and the panel is assembled by putting the thermal insulation foam and the GFRP profiles in their position.

Despite the practicality of using embedded connectors, such technique requires a minimum concrete thickness to ensure the effectiveness of the connection. The use of adhesively bonded connections allows overcoming this limitation with the advantage of obtaining two smooth surfaces (surfaces in contact to the mould) turned to the inner and outer side of building. On the other hand, a limitation of this technique is related to the number of stages and timeouts, namely the time required to cure the SFRSCC layers and the adhesive, with the consequent delay to join the parts together. Another potential problem related to this technology is the possibility of warping of the SFRSCC layers during stripping and handling before assembling the panel.

5.3 PARAMETRIC STUDIES FOR THE DESIGN OF THE SANDWICH PANELS

To better understand the structural behaviour of the panel, a set of systematic parametric studies based on linear elastic modelling of the sandwich panels was carried out. At an initial stage, focus was given to the optimum arrangements and properties of the parts of the sandwich panel. The parameters considered in these studies were: the position, orientation and continuity of the GFRP connectors and the thickness of the SFRSCC layers. The FEM-based software FEMIX (Azevedo *et al.*, 2003b) was used for these analyses. A linear and elastic analysis was adopted for this phase of the design process, since preliminary tests with small size prototype systems of the sandwich panel have indicated that damage due to cracking of SFRSCC had minor relevance even for loading levels corresponding to the ultimate limit state design conditions (CEN, 2004a). This decision was also caused by the relatively high computing time of material nonlinear analysis of real size sandwich panels requiring to find the best configuration for the constituent elements of the panel.

5.3.1 Common features: geometry, mesh, loading, support conditions and material properties

In this work all the analyses were limited to a reference sandwich panel of 8.00 m length, with an external (h_{ext}) and an internal (h_{int}). SFRSCC layer of 2.60 m and 2.40 m free height, respectively (see Figure 114). The length of the panel was determined by transportation and handling constraints. In turn, the height of the internal SFRSCC layer was related to the minimum ceiling height of the building. The height of the external SFRSCC layer was defined as the height of the internal layer plus the thickness of the slab or roof that is supported by the internal layer. The thickness of the insulating material was kept equal to 100 mm, whereas the thickness of the SFRSCC layers was one of the variables studied. These dimensions are consistent with the ones of the conventional sandwich panels, according to the PCI Committee on Precast Sandwich Wall Panels (2011).

Similar finite element (FE) meshes were adopted for the different panels, differing only on the position of connectors. The FE meshes of the sandwich panels consisted of Reissner-Mindlin flat shell eight nodes finite elements for modelling the internal and external SFRSCC wythes, as well as the GFRP connectors (see Figure 117). The FE mesh coincides with the middle surface of these components of the sandwich panel. The Gauss-Legendre integration scheme with 2×2 points was used in all elements. The FE models assumed that bond between materials (SFRSCC and GFRP) is perfect. In preliminary studies (Lameiras *et al.*, 2013c), the pullout responses for different types of connections were assessed and a high initial rigidity of these connections was observed. In the authors' opinion, this observed behaviour justifies the possibility of considering perfect bond between both materials during the linear stage.

The contribution of the thermal insulating material for the structural behaviour of the panel is disregarded. In fact, previous experimental research has shown that the contribution to the composite action of sandwich panels provided by the bond between the concrete layers and insulation is less than 5% (Pessiki and Mlynarczyk, 2003a). Moreover, due the movements that the panels are subjected, caused by thermal gradients and/or wind load, the bond between concrete and insulating material cannot be guaranteed along all the service life of the structure.
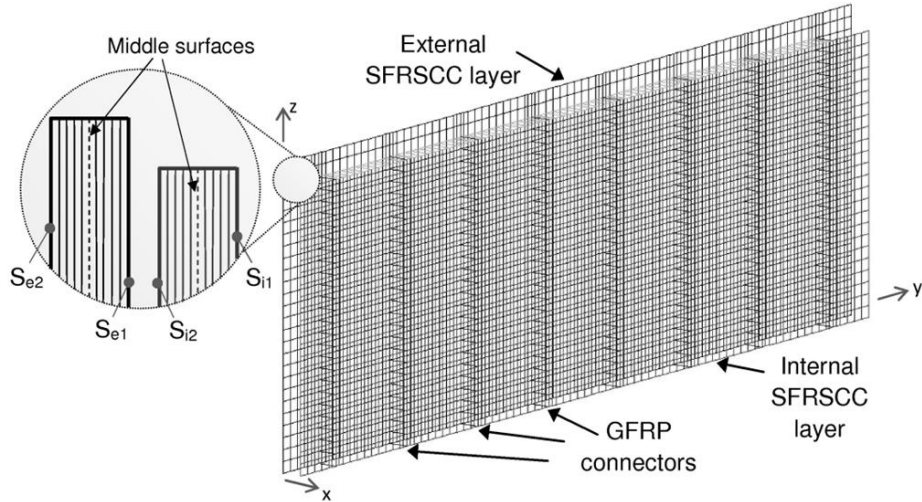
Figure 117: View of FE mesh adopted for panels consisting of arrangements C, D and E, and detail of the layered shell elements.

The panels are subjected to both horizontal (x direction according to the referential defined in Figure 117) and vertical loads (z direction). It is considered that the roof/floors transfer the vertical forces to the load-bearing walls and into the foundation through the SFRSCC layer that faces the interior of the building, herein designated as internal layer of the sandwich panel (Figure 118). The lateral loads (i.e., wind) are withstood by the sandwich wall panels that span between the floor/roof and the foundation. Floor/roof systems, herein designated as slabs, are considered to act as horizontal diaphragms, in the sense that horizontal loads are carried through these diaphragms into the shear walls (the sandwich wall panels in orthogonal direction to the panel studied herein). These supporting conditions are shown in Figure 118.
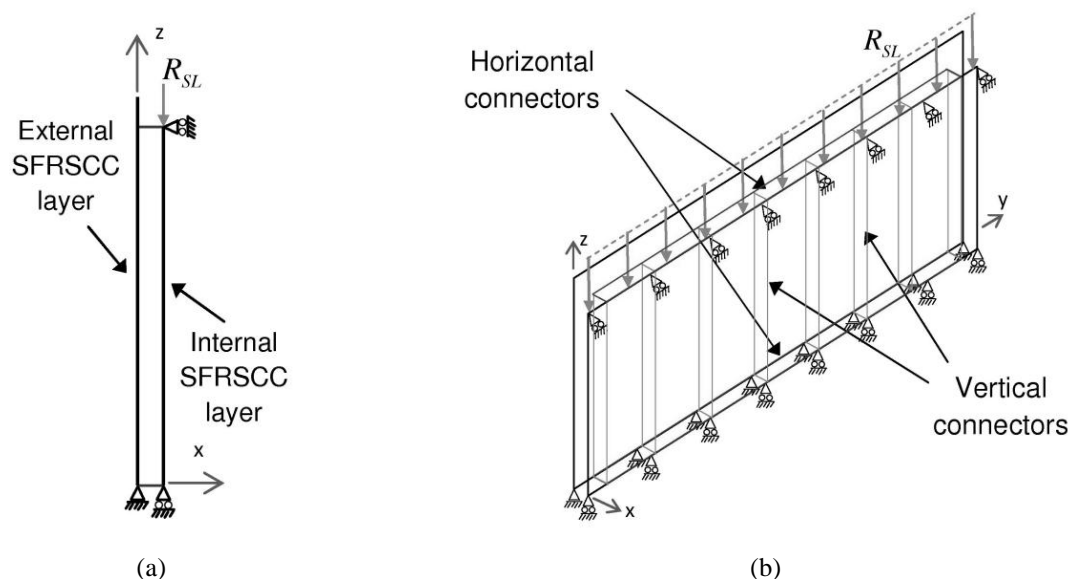
Figure 118: Schematic representation of support conditions and forces transferred by the slab: (a) cross-section; (b) perspective view.

The vertical loads correspond to the self-weight of the wall panel and the load (R_{SL}) transferred by the slab (10.0 m of span), which is simulated by a centred line force applied to the upper edge of the internal SFRSCC layer (see the schematic representation in Figure 118). In order to guarantee this condition in practice the connections between the wall panels and the slabs are designed to transmit only the vertical load centred in the internal SFRSCC layer, not transmitting moments (e.g., simply supported slabs over neoprene strips installed centred in the top surface of the internal SFRSCC layer).

The wind loading is computed following the simplified procedure described in the Eurocode 1 – Part 1-4 (CEN, 2004a), with consideration of an open building situation. In consequence, the wind load acts as a uniform pressure, directly towards the surface, or suctions, directly away from the surface, on the external and internal surfaces of the panel. The values that lead to the most unfavourable conditions considered in the Portuguese National Annex are chosen. The described load cases are included in three different relevant Ultimate Limit States (ULS) combinations: LC1 − external SFRSCC layer under pressure and internal SFRSCC layer under suction; LC2 − external SFRSCC layer under suction and internal SFRSCC layer under pressure; and LC3 − both layers under suction (see Figure 119, Table 29 and Table 30). These load cases and values are defined depending on the aspect ratio of building and on the size and distribution of the openings in the building envelope. The values indicated in Table 29

and Table 30 are defined in the *x*, *y*, *z* Global Coordinate System (GCS), so a negative value means that the direction of the applied force is opposite to the corresponding axis of the GCS.
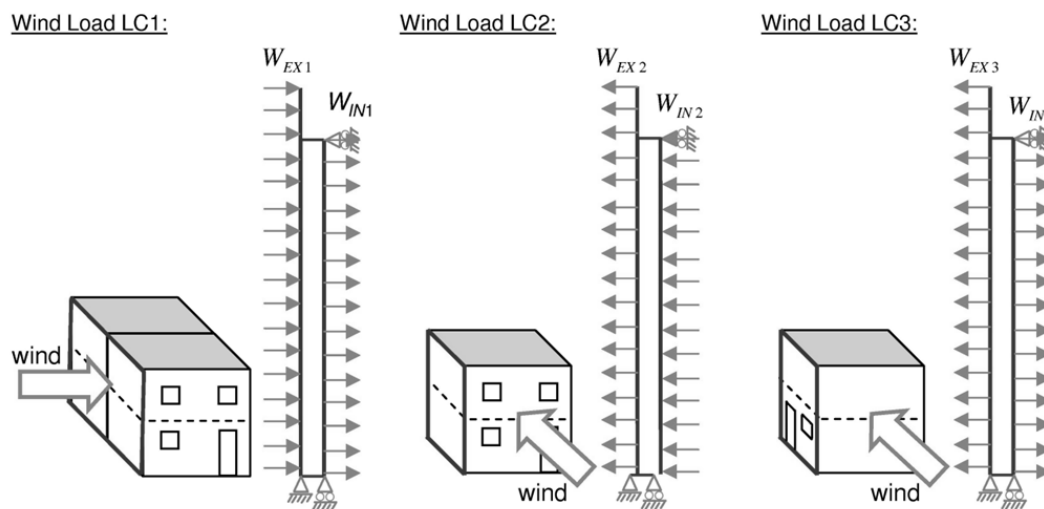
Figure 119: Wind load cases.

Table 29: Adopted values for the load cases.

Load cases		
Gravity Load	G	-
Slab reaction (design value)	R_{SL}	-48.75 N/mm
LC1 – External wind force	W_{EX1}	+1.021e-03 N/mm^2
LC1 – Internal wind force	W_{IN1}	+6.381e-04 N/mm^2
LC2 – External wind force	W_{EX2}	-1.531e-03 N/mm^2
LC2 – Internal wind force	W_{IN2}	-4.466e-04 N/mm^2
LC3 – External wind force	W_{EX3}	-1.531e-03 N/mm^2
LC3 – Internal wind force	W_{IN3}	+6.381e-04 N/mm^2

Table 30: Load combinations.

Load combinations (ULS)	
LC1	$1.35G+1.0R_{SL}+1.5(W_{EX1}+W_{IN1})$
LC2	$1.35G+1.0R_{SL}+1.5(W_{EX2}+W_{IN2})$
LC3	$1.35G+1.0R_{SL}+1.5(W_{EX3}+W_{IN3})$

The SFRSCC and GFRP properties used in the panel simulations are the ones experientally determined and presented in the Chapter 3. The SFRSCC was characterized by the average

modulus of elasticity of 35.45 GPa SFRSCC A (see Table 6). The GFRP was characterized by a modulus of elasticity equal to the average value obtained for CSM 3, i.e., 12.65 GPa (see Table 22). The Poisson's ratios considered were 0.15 and 0.40, respectively for the concrete and GFRP. Moreover, both materials were simulated assuming a linear and isotropic behaviour. The thickness of the GFRP flat shell connectors was held constant with 2.5 mm, value equal to the average thickness of CSM 3 (see Table 19).

5.3.2 Effect of the arrangement of the connectors on the maximum stresses and transversal displacements of the panel

In a first stage, the effect of the arrangement adopted for the connectors of the sandwich panels on the maximum tensile principal stresses and on the deformability of the proposed panel was studied in order to determine the most effective arrangements. Both vertical and horizontal connectors were considered. The use of continuous and discrete connectors was explored. The arrangements studied are described in Figure 120.

Arrangement A consists of three vertical continuous connectors and one horizontal connector. The vertical connectors are spaced 3.50 m from each other. In arrangements B and C, the distance between vertical connectors are, respectively, 1.75 m and 1.00 m. Arrangement D is similar to arrangement C but without the horizontal connector. Arrangement E consists of eight vertical lines of three discrete connectors each, spaced horizontally 1.00 m from each other as in arrangement D. These discrete connectors are 0.40 m long each, regularly distributed along the height of internal concrete layer and vertically spaced of 0.60 m. Since the total cost of the panel is influenced by the number and length of connectors employed, it is important to stress that the different arrangements influence the total length of connectors (Figure 120).

Figure 120: Arrangements of connectors studied: (a) A; (b) B; (c) C; (d) D and (e) E (units in metres).

It may be considered that the panel is casted in the horizontal position and that the panel is stripped by the internal SFRSCC layer. Then, the load corresponding to the weight of the external SFRSCC layer is transferred to the internal SFRSCC layer through the GFRP connectors. For SFRSCC layers of 75 mm, assuming that the unit weight of SFRSCC is 25 kN/m^3 and that a total volume of $8.00 \times 2.65 \times 0.075$ m^3 (1.59 m^3) is lifted, a total weight of 39.75 kN should be withstood by the connections. Moreover, if a suction/adhesion of 3 kN/m^2 is assumed to be imposed by mould during demoulding process (HALFEN-DEHA, 2008), and considering the area of contact between the external SFRSCC layer and the mould of 8.00×2.65 m^2 (21.2 m^2), a value of 63.6 kN should be added to the weight of the unit. So, a total of 103.35 kN must be supported by the connections. Considering the arrangement with the minimum length of connector (arrangement E, with 9.6 m), the total applied load per unit length is equal to 10.76 kN/m, which corresponds to 15% of the average load capacity of adhesively bonded connectors (the connector that presents the lower load capacity between

the studied types). The author is aware of the simplicity of the assumption that the stresses on the connectors are uniform during demolding, which probably does not occur in practice. However, as the stress level is much lower than the tensile strength of the connectors, it is expectable that even for more complex lifting configurations the strength of the GFRP is not attained. It should be noted that, for all the arrangements proposed and based on the experimental study presented in the first part of the paper, the GFRP $\times$ SFRSCC connections work in their linear stage during the critical situation that occurs when the panel is first lifted out of the formwork.

The thickness of the SFRSCC flat layers remain constant and equal to 75 mm, which is a typical thickness for concrete layers of sandwich panels (PCI, 2011).

Figure 121 shows the evolution of the maximum principal tensile stress (σ_1) in both SFRSCC layers and also in the GFRP connectors for the five panel configurations studied. From these results, it is possible to infer that a lower spacing between the vertical connectors reduces the stress level in both SFRSCC layers. It may be further noted that the omission of horizontal connectors (arrangement D) does not imply relevant changes in terms of principal stresses in SFRSCC and GFRP. It can be also observed that, independently of the arrangement, the maximum tensile stress in the GFRP connectors is always much lower than the tensile strength of the material, reaching a maximum of 3.6% of the corresponding ultimate capacity for the arrangement A. For SFRSCC layers of 75 mm, the maximum principal tensile stress does not reach the tensile strength of SFRSCC in any of the studied arrangements. For arrangements B, C, D and E the maximum stress level is similar in both layers, which is a desirable situation, since the material and the thickness adopted for both layers are the same. In addition, the use of discrete connectors does not lead to a significant increase of the maximum principal stresses in the SFRSCC neither in the GFRP. Thus, from these obtained results it can be concluded that the arrangement E, with only discrete vertical connectors with 0.40 m length, distanced vertically of 0.60 m and horizontally of 1.00 m from each other, can be adopted, keeping a low stress level in the SFRSCC layers and GFRP connectors.

(a) (b)
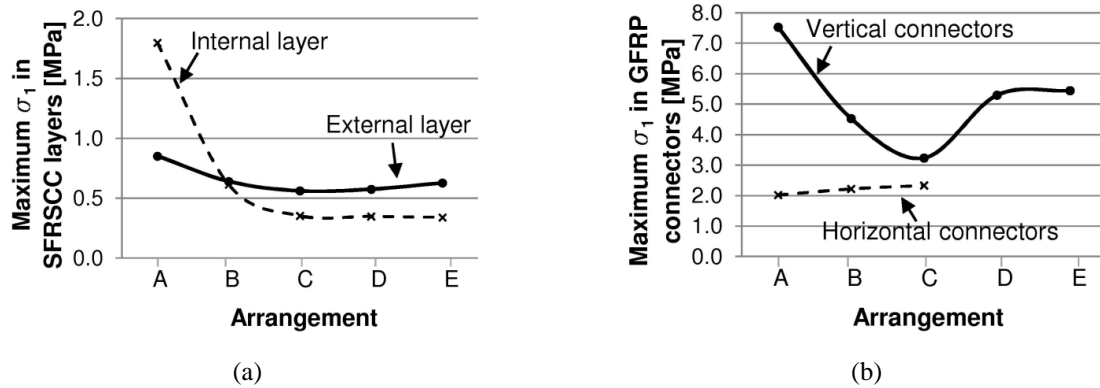
Figure 121: Influence of connector arrangement on the maximum principal stresses (σ_1) of: (a) SFRSCC layers; (b) GFRP connectors (positive values signify tension).

The influence of the connectors' arrangement on the maximum transversal displacements of SFRSCC layers (*x* direction) is presented in Figure 122.
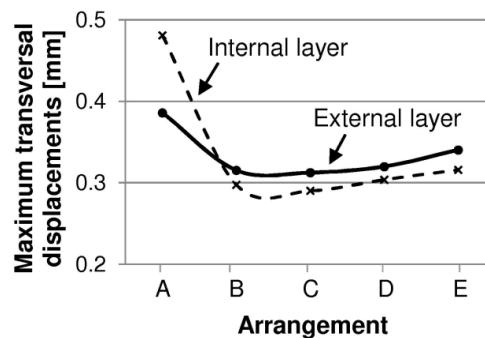
Figure 122: Influence of connector arrangement on the maximum transversal displacement in the panel.

The obtained results show that the transversal displacements in the panel are relatively small for all the arrangements studied, even in panels consisting of vertical discrete connectors. Moreover, the results show that for the arrangements B, C, D and E, the maximum transversal displacements are similar for both concrete layers, which does not happen for the arrangement A. For this reason, and considering that panels with the arrangement E use exactly half total length of connectors used in arrangement D, the arrangement E was chosen as the most attractive solution to be adopted in the following studies.

5.3.3 Effect of the thickness of SFRSCC layers on the maximum stresses and transversal displacements in the panel

From the economic point of view, it is advantageous to design the sandwich panels by minimizing the consumption of raw materials. Since the SFRSCC is a material with relatively high impact in the global costs of the building, the thickness of the concrete layers should be reduced as much as possible. In order to assess the possibility of reducing the thickness of the concrete layers, numerical analyses of panels with the connector arrangement E (Figure 120e) and SFRSCC layers thickness of 35, 45, 55, 65 and 75 mm were performed.

The effect of the thickness of SFRSCC layers on the maximum value of the principal tensile stresses in these layers and on the GFRP connectors are depicted in Figure 123. From the obtained results, it may be observed that even for sandwich panels comprising layers of 35 mm thickness, the maximum principal tensile stresses are lower than half of the tensile strength of SFRSCC. It is also observed that the reduction of the thickness of SFRSCC layers from 75 to 35 mm is accompanied by an increase of the maximum tensile stresses in the connectors from 5.45 to 9.22 MPa. These values are not significant when compared to the connector's tensile strength, once they correspond to only 2.6% and 4.4% of the ultimate GFRP tensile strength, respectively.
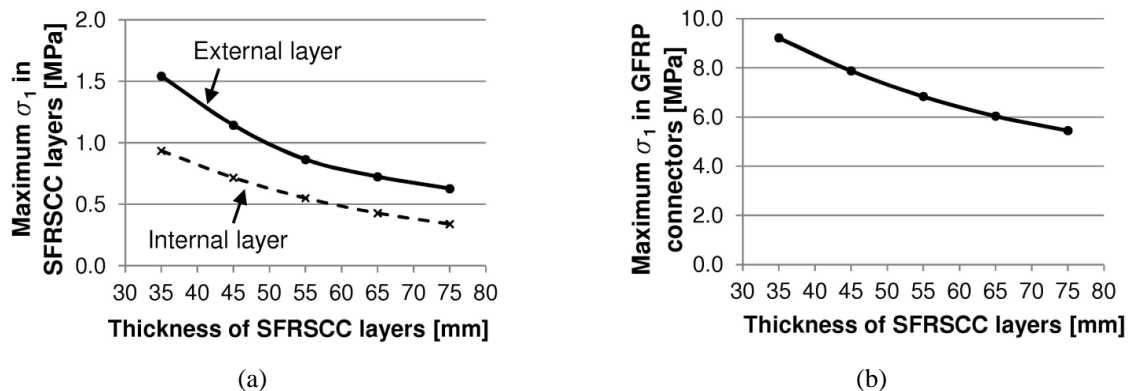
Figure 123: Influence of thickness of SFRSCC layer on the maximum principal stresses (σ_1) in: a) SFRSCC layers; b) GFRP vertical connectors (positive values signify tension).

The influence of the thickness of SFRSCC layers on the maximum transversal displacements is depicted in Figure 124. These results show that the maximum transversal displacement of the panel increases with the decrease of thickness on the SFRSCC layers. The maximum transversal displacement reaches a maximum of 1.09 mm in a panel consisting of SFRSCC layers with 35 mm thickness. The panel spans 2.40 m between the foundation and the slab

and, therefore, this displacement corresponds to h/2200 for ultimate limit state. This value is much lower than the deflection limit of h/480 (5 mm) given in the literature for precast wall panels under service loads (ACI Commitee 533, 1993).

After the results presented in Figure 123 and Figure 124, it was concluded that the thickness of the concrete layers could be much less than 75 mm. However, if an effective connection is to be achieved with embedded shear connectors, it is important to ensure a minimum thickness, so that the connector can be positioned inside the concrete layer in order to effectively transfer the stresses between the two SFRSCC layers. Considering this, it was decided to select a SFRSCC layer thickness of 60 mm.
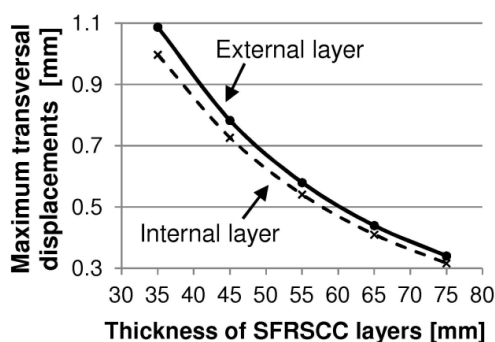
Figure 124: Influence of the thickness of SFRSCC layers on the maximum transversal displacement in the panel with the arrangement E.

The in-plane stress fields in the z and y directions in the external SFRSCC layer for a panel with arrangement E and SFRSCC layers of 60 mm thick, submitted to the load combination LC2 (most critical one) are shown in Figure 125. It can be observed that the highest stresses are localized at the middle zone of the panel and at the top extremity of the top connectors, due to the fundamental flexural behaviour of the panel in the xz plane. However, the calculated stress values are much lower than the compressive and tensile strength of the developed SFRSCC.
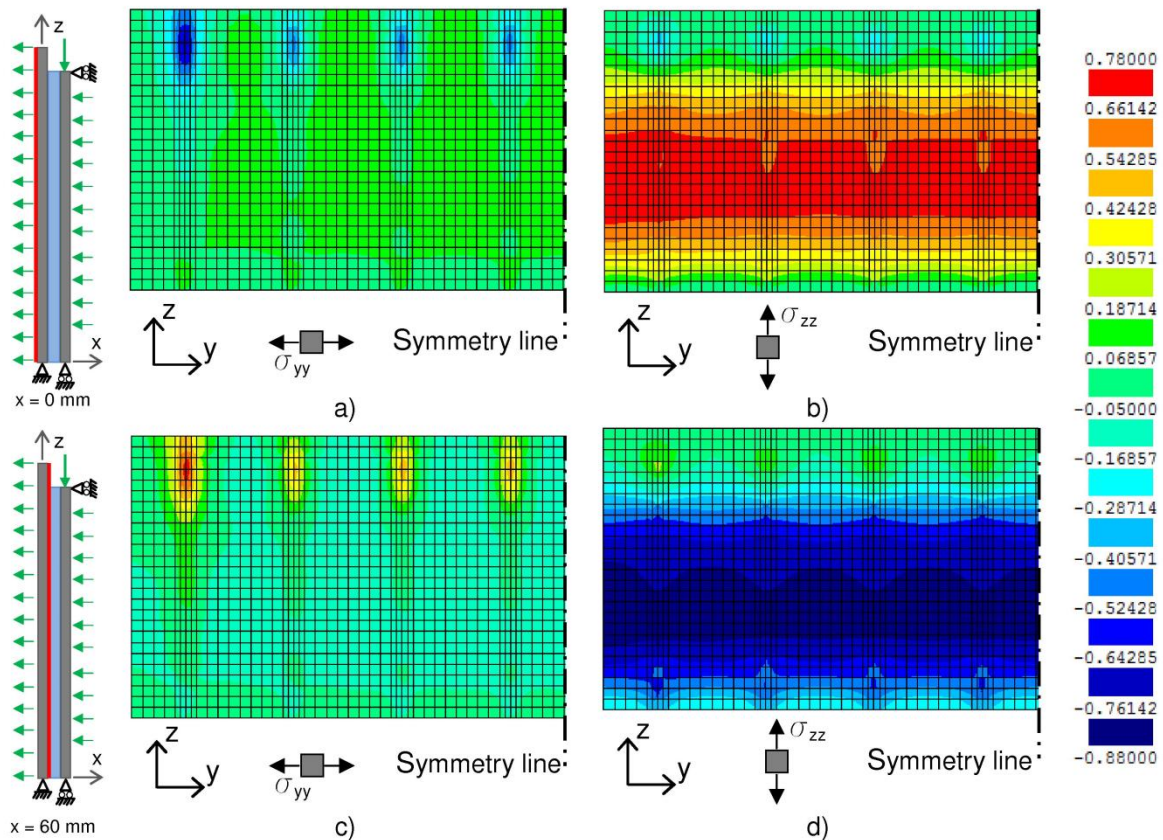
Figure 125: In-plane stress fields in the external SFRSCC layer: (a) y direction and x = 0 mm (S_{e2}); (b) z direction and x = 0 mm (S_{e2}); (c) y direction and x = 60 mm (S_{e1}); (d) z direction and x = 60 mm (S_{e1}). Units in MPa / positive values signify tension.

5.4   MATERIAL NONLINEAR ANALYSIS

In order to predict the behaviour of the selected sandwich panel configuration up to relatively high damage levels (only probable at extreme loading conditions), a FEM-based material nonlinear analysis is performed in the present section.

To simulate the material nonlinear behaviour of the panel due to crack initiation and propagation in SFRSCC, the FEMIX computer program (Azevedo *et al.*, 2003b) was used, since it is capable of modelling the post-cracking behaviour of fibre reinforced concrete materials.

The geometry, mesh and support conditions were those of the parametric study described in the previous section. The analyses of the present section pertain to the arrangement E of connectors, and thickness of SFRSCC layers of 60 mm.

In order to simulate the progressive damage induced by cracking, the concrete shell element thickness was discretized in layers, where each of them was considered in a state of plane stress. The concrete cracking was simulated with a multi-directional fixed smeared crack constitutive model, which is conceptually justified due to the diffuse crack patterns expected to be formed during the loading process of the panel. According to Barros and Figueiras (2001) the fracture energy is dissipated over a crack band width, l_b. In the present simulations, it is assumed a crack bandwidth equal to the square root of the area of the corresponding integration point. More details about the model are described by Sena-Cruz *et al.* (2004).

5.4.1   Constitutive laws and loads

In the performed numerical simulations the fracture mode I behaviour of SFRSCC, characterized by a stress $\times$ crack width relationship ($\sigma-\omega$), was modelled by using the following two approaches: 1) the tri-linear $\sigma-\omega$ diagram represented in Figure 126(a) that was obtained by inverse analyses; and 2) the linear $\sigma-\omega$ diagram represented in Figure 126(c) that was obtained from the recommendations of *fib* Model Code (*fib, 2012a, fib, 2012b*), where the $f_{R,i}$ parameters were determined from the three-point beam bending tests for SFRSCC A presented in the Chapter 3. In both approaches the lower bound of the experimental load *versus* CMOD curve was taken into account (level of confidence equal to 95%). Also in both approaches, the measured crack width was converted into crack normal strain by dividing the crack width by the crack band width. As there is no comprehensive formulation to estimate crack band width in structures that solely have fibre reinforced concrete, the adopted assumption is deemed valid.

The tri-linear softening behaviour of SFRSCC is defined by the values attributed to the stress at crack initiation, f_{ct} , the pair of points σ_A, ω_A and σ_B, ω_B, and the fracture energy (G_F), as shown in Figure 126(a).

(a)

(b)

(c)
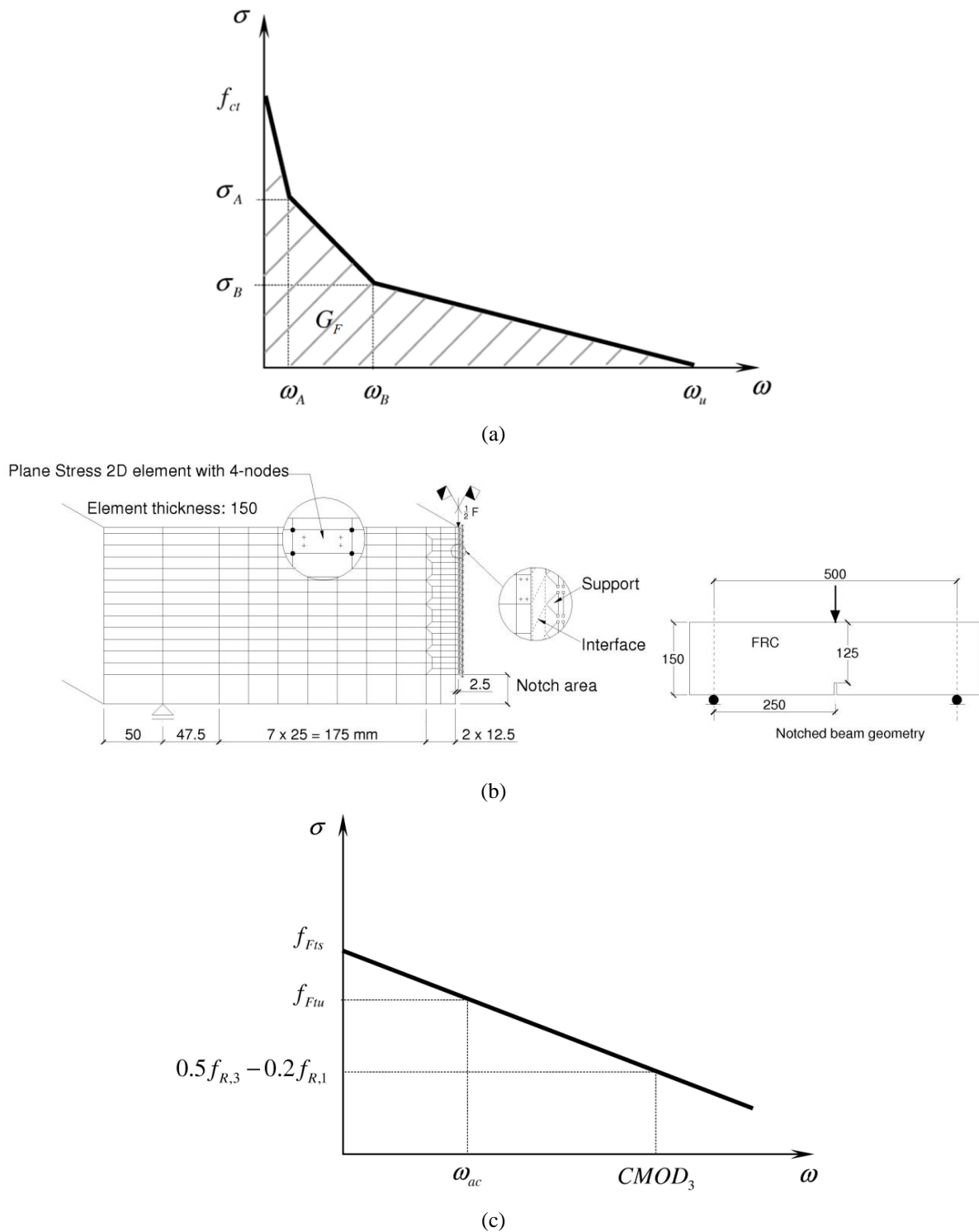
Figure 126: Stress × crack width diagrams adopted for modelling the fracture mode I propagation in SFRSCC: (a) tri-linear diagram obtained by inverse analysis; (b) finite element mesh adopted in the inverse analysis (units in millimetres); (c) linear diagram determined according the recommendations of *fib* Model Code 2010.

The inverse analysis for obtaining the parameters that define the stress−crack width diagram represented in Figure 126(a) is based on the process described elsewhere (Sena-Cruz *et al.*, 2004, Slowik *et al.*, 2006, Pereira *et al.*, 2008). The procedure consists on the evaluation of

the parameters that minimise the deviation between the experimental and the numerical load-CMOD curve, by brute force analysis. The error (err_{CMOD}) was calculated by Eq. (28).

$$err_{CMOD} = \left| A_{F-\delta}^{\exp} - A_{F-\delta}^{num} \right| \Big/ A_{F-\delta}^{\exp} \qquad (28)$$

where $A_{F-\delta}^{\exp}$ and $A_{F-\delta}^{num}$ are the areas below the experimental and the numerical load-CMOD curves, respectively, up to a certain CMOD. The optimization procedure in the inverse analysis was restricted to the interval of CMOD 0-0.5 mm. Adopting this strategy, it is possible to obtain the stress-crack width diagram that best simulates the crack opening propagation of the developed SFRSCC up to a limit that captures the fundamental behaviour of the sandwich panel, not only for serviceability limit states, but also up to a crack opening above the maximum limits of the *fib* Model Code 2010.

In this work, the optimisation was done considering the experimental curve corresponding to the characteristic lower bound of the load-CMOD relationship. The numerical curve consisted of the results of a FE model to simulate the geometry of the specimens, the loading and support conditions of the three point bending tests presented in Chapter 3 for SFRSCC A. The specimen was modelled by a mesh of 8 node plane stress finite elements. The Gauss-Legendre integration scheme with 2×2 integration points was used in all elements, with the exception of the elements at the specimen symmetry axis, where only 1×2 integration points were adopted. With this integration point layout a vertical crack may develop along the symmetry axis of the specimen, in agreement with the experimentally observed crack initiation and propagation. Linear elastic behaviour is assumed in all the elements, with the exception of those above the notch (see Figure 126(b)). For these elements, an elastic-cracked material model in tension is adopted using the discrete crack model available in the FEMIX computer program.

The values that defined the tri-linear $\sigma-\omega$ diagram, obtained by inverse analysis, are indicated in Table 31

Table 31: Values of the parameters of the tri-linear $\sigma-\omega$ diagram computed by inverse analysis.

f_{ct}	ω_1	σ_1	ω_2	σ_2	ω_u	G_f	$err_{0.5}$	$err_{1.0}$	$err_{2.0}$
[MPa]	[mm]	[MPa]	[mm]	[MPa]	[mm]	[N/mm]	[%]	[%]	[%]
3.30	0.050	2.64	0.300	3.63	2.300	4.56	2.5	1.9	6.9

The linear $\sigma-\omega$ diagram of Figure 126(c) is proposed in the *fib* Model Code 2010, which is characterized by the parameters f_{Fts} and f_{Ftu}. These parameters are obtained with Eqs. (29) and (30). The values considered for the flexural tensile strength parameters $f_{R,1}$ and $f_{R,3}$ were the lower bound characteristic values obtained from the three-point notched beam bending tests presented in the first part of this paper. The maximum crack opening accepted in structural design ($\omega_{ac}\omega_{ac}$) was assumed equal to 0.3 mm.

$$f_{Fts} = 0.45 \cdot f_{R,1} \tag{29}$$

$$f_{Ftu} = f_{Fts} - \frac{\omega_{ac}}{CMOD_3}\left(f_{Fts} - 0.5 f_{R,3} + 0.2_{R,1}\right) \geq 0 \tag{30}$$

The $\sigma-\omega$ diagrams obtained from the two approaches are depicted in Figure 127, where a good mutual similarity can be confirmed.
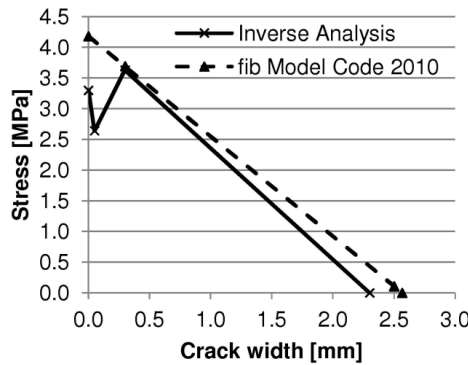
Figure 127: $\sigma-\omega$ diagrams adopted in the material nonlinear analysis of the panels.

Since the linear analyses showed that the GRFP connectors always remain at stress levels well below their strength limits, they were simulated assuming a linear elastic behaviour.

For this study the same load geometry, mesh, loading and support conditions adopted in the previous sections were considered. In the same way it was done in the linear elastic analyses, the perfect bond between was considered between the connectors and the SFRSCC layers. Firstly, the self-weight of the panel and the load transferred by the slab were applied, and then

the wind loading was gradually applied, by multiplying the characteristic value of the wind pressure by an increasing wind load factor k.

5.4.2 Results

Figure 128 and Figure 129 represent the crack patterns for the panel under the load case LC2, respectively at the external and internal surfaces of the external SFRSCC layer (S_{e2} and S_{e1}).

It can be observed that a distributed pattern of fine cracks was obtained on an extensive area of the external surface of the external SFRSCC layer due to a stress field constituted predominantly by tensile stresses in the z direction (external surface). In the internal surface (Figure 129), the cracks are wider at the top extremity of the top connectors, due to the existence of the horizontal support at this region.

(a)   (b)
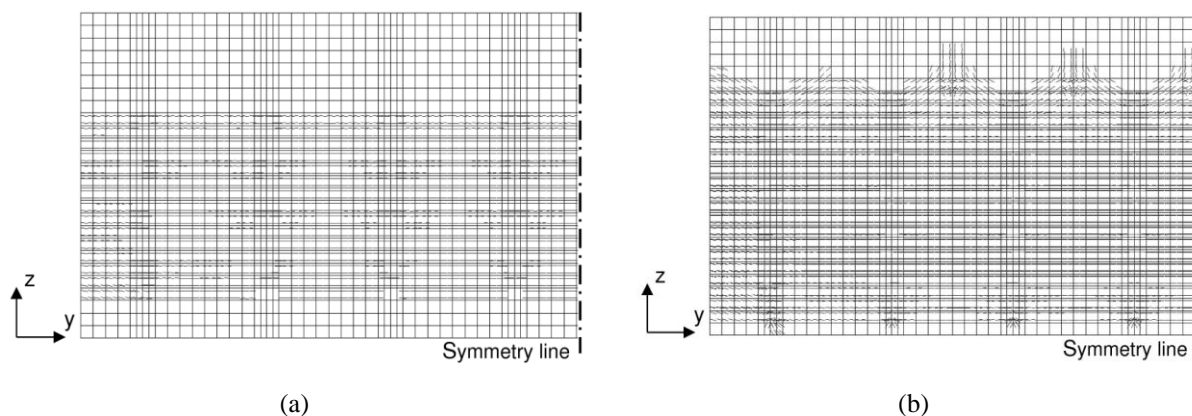
Figure 128: Crack pattern at the external surface of the external SFRSCC layer (S_{e2}) for the load case LC2, and for a load factor corresponding to a maximum crack width of: (a) 0.01 mm and (b) 0.10 mm.

(a)   (b)
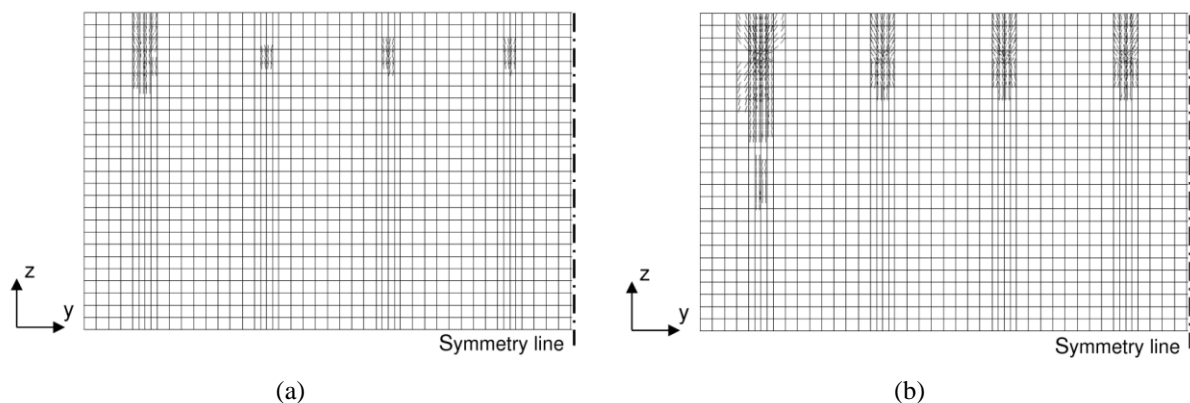
Figure 129: Crack pattern at the internal surface of the external SFRSCC layer (S_{e1}) for the load case LC2, and for a load factor corresponding to a maximum crack width of: (a) 0.01 mm and (b) 0.10 mm.

The relationship between the maximum crack width and the wind load factor *k* in both SFRSCC layers is depicted in Figure 130, where S_{ej} and S_{ij} represent the surfaces turned to the interior (j=1) and exterior (j=2) of the external (S_e) and internal (S_i) SFRSCC layers. These results correspond to the models with the constitutive law obtained by the inverse analysis.

The results shown in Figure 130 indicate that the greatest crack widths are attained for the load combination LC2. Attention should be given to the fact that, depending on the wind load factor, due to the stress redistribution effects, the maximum crack width is obtained in different SFRSCC layers (internal or external) and/or in different surfaces (outer or inner surface of a specific SFRSCC layer). Specifically, in the case of the LC2, up to a wind load factor of 25.0, the maximum crack width was attained in the outer surface of the external SFRSCC layer. Above this wind load factor the maximum crack width was reached in the internal surface of the external SFRSCC layer.

(a)

(b)

(c)
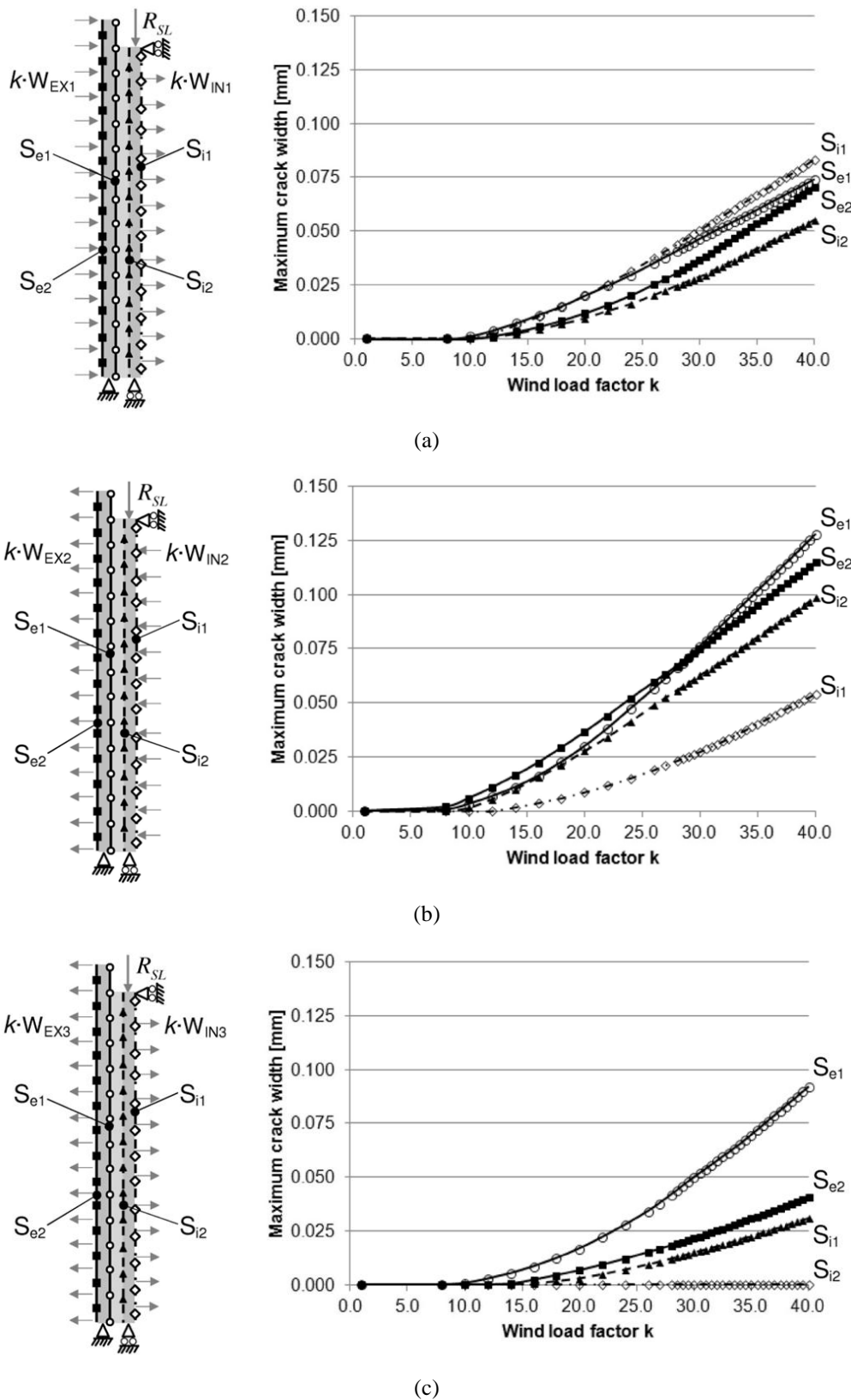
Figure 130: Relationship between the maximum crack width in the SFRSCC layers and the k wind load factor for the following load combinations: a) LC1; b) LC2 and c) LC3.

Considering the most adverse load case (LC2), although the first crack opening in the SFRSCC layers appears for a wind load factor of 8.00, a maximum crack opening of 0.10 mm is only attained for a wind load factor equal to 34.50 (equivalent to 23 times the wind load factor for the ULS). At this stage, the maximum compressive stress in the SFRSCC layers is 15.90 MPa and the correspondent transverse displacement at the middle point of the internal and the external concrete layers is, respectively, 13.15 mm (h/182) and 13.54 mm (h/177). For this wind load factor the maximum principal tensile and principal compressive stresses in the GFRP connectors are, respectively, 184 and 169 MPa, which means that, even for transversal loads as high as 23 times the corresponding to ULS, the rupture of the GFRP connectors is not expected.

The relationships between the maximum crack width and the wind load factor, determined by using the $\sigma-\omega$ diagrams obtained from the inverse analysis and *fib* Model Code approaches, are represented in Figure 131. Since the inverse analysis conducted to a $\sigma-\omega$ diagram that has a smaller post-cracking residual strength and, consequently, smaller fracture energy, than the $\sigma-\omega$ diagram determined according to the recommendations of *fib* Model Code 2010, it was expected that the former approach predicted larger maximum crack width for any wind load factor. As expected this discrepancy has a tendency to increase with the wind load factor. Despite the fact that using the constitutive law proposed by the *fib* Model Code 2010 the maximum crack width obtained is slightly lower, it seems to be an acceptable simplification, capable of predicting the behaviour of the structure with a reasonable accuracy.
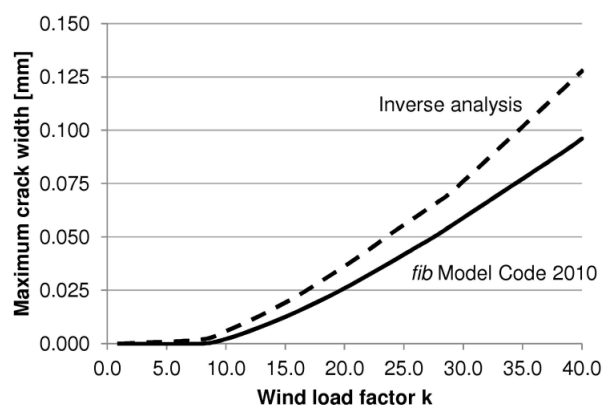
Figure 131: Relationship between the maximum crack width and the wind load factor for the two approaches adopted to determine the $\sigma-\omega$ diagram.

5.5   FINAL REMARKS

In this study an innovative sandwich panel comprising SFRSCC layers and GFRP laminate connectors was proposed and its behaviour was investigated by numerical research. The geometry and arrangement of the panel components were optimized through a FE linear modelling. The structural behaviour of the sandwich panel was also assessed up to a relatively high damage level, by simulating the material nonlinear behaviour of SFRSCC layers due to crack initiation and propagation.

The maximum tensile stress in the SFRSCC layers was significantly affected by the arrangement of the GFRP connectors. However, for a panel configuration comprising vertical GFRP connectors spaced 1 m from each other, the omission of the top horizontal connector did not imply relevant changes in the principal stresses in SFRSCC and GFRP. Furthermore, the obtained results have shown that it is possible to adopt an arrangement with only discrete vertical 0.40 m connectors, distanced vertically 0.60 m and horizontally 1.00 m from each other, keeping the ULS stress level in the SFRSCC layers and in the GFRP connectors comfortably under the corresponding strength of these materials.

Regardless of the arrangement and thickness of the SFRSCC layers, for serviceability limit state conditions, the maximum tensile stress in the GFRP connectors was always much lower than the tensile strength of the material, which leads to conclude that, disregarding local effects in the connections, the weakest components in the panel are the SFRSCC layers. However, even for the panels composed of SFRSCC layers of 35mm thickness, the maximum principal tensile stresses were lower than the characteristic tensile strength of SFRSCC. Nevertheless, as evidenced in the experimental program presented in the first part of this paper, using thicknesses of less than 60 mm for the SFRSCC may pose practical problems to the realization of the embedded connection to join the GFRP connector to the SFRSCC layers.

The results obtained from the material nonlinear simulations of the sandwich panels have shown that the proposed configuration for the panel presents a ductile behaviour, even for wind load factor that is 23 times the load factor corresponding to the ULS. Ongoing experimental research with real scale prototypes is being carried out to appraise the relevant predictions provided by the FEM-based material nonlinear analysis carried out in this paper.

Despite the fact that the material nonlinear simulations of the panels, by using a constitutive law derived from the recommendations of *fib* Model Code 2010, have obtained slightly lower maximum crack widths, this methodology seems to be a good simplification, capable of predicting the behaviour of the sandwich panels with a reasonable accuracy.

Chapter 6

PULL-OUT TESTS

The performance of the composite panel is highly influenced by the mechanical behaviour of the connections in the longitudinal and transversal directions of the panel. The longitudinal stiffness of the shear connection affects the flexural rigidity of the composite section and defines its degree of composite action. In fact, the full composite action is practically attained when the longitudinal stiffness is high and, consequently, the corresponding transversal deflections in the sandwich panel are small enough to accomplish the serviceability limit state conditions. In addition, the longitudinal strength of these connections is especially important to the case of precast panels that are generally transported in the vertical position, as shown in Figure 132(a), since the panels are generally transported by suspending one of the layers, therefore the deadweight of the other layer is transferred through the connectors. On the other hand, the transversal behaviour is related to how the connection resists the forces that tend to separate both concrete layers. Such type of transversal tensile stresses arises mainly during stripping and erection operations of panels (Figure 132(b)). The magnitude of these tensile stresses is difficult to estimate due to dynamic effects that are involved during these operations. During the panel's service life, these connections also experience continuous variation of transversal tensile stress due to thermal cycles and wind action. Thus, the panel should have a performance in the transversal direction that assures the required resisting tensile capacity.

(a)

(b)
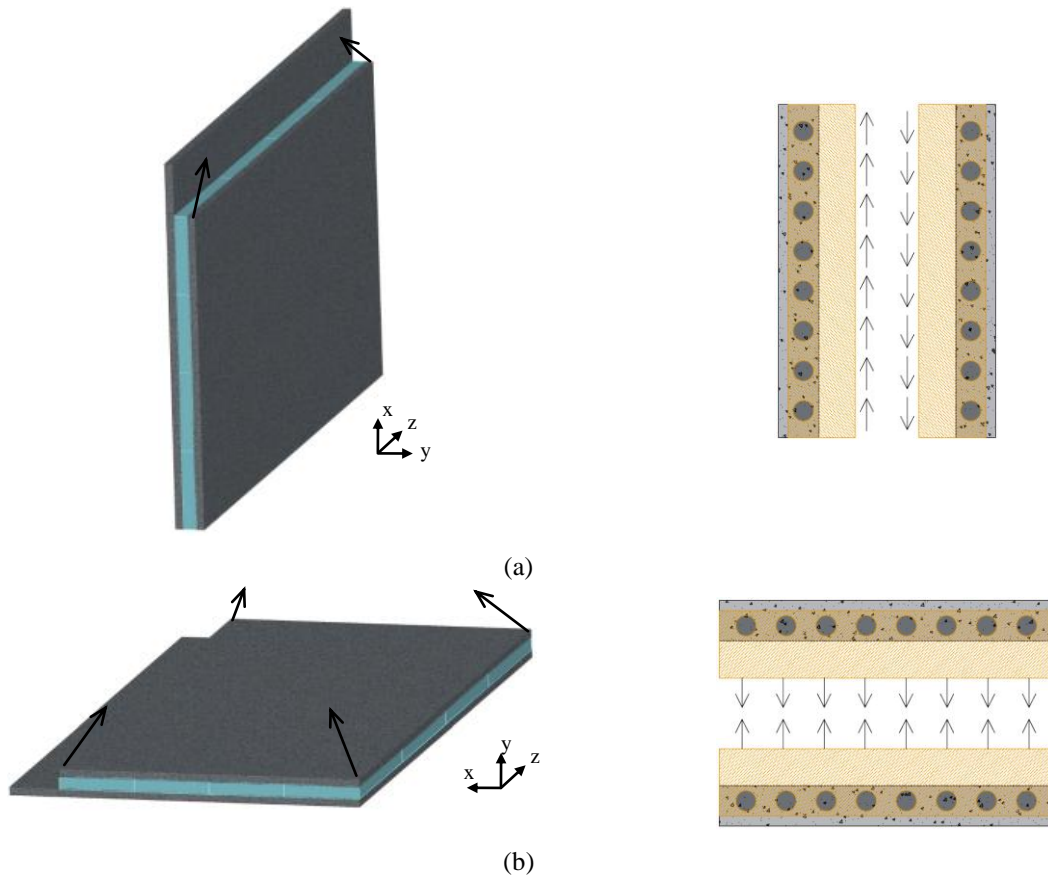
Figure 132: Bearing loads acting on the connectors: a) longitudinal shear (e.g., during transporting); b) transversal shear (e.g., during stripping and transporting).

Numerous works have been devoted to the parametric study of steel Perfobond connectors based on tests and numerical simulations (Oguejiofor and Hosain, 1997, Medberry and Shahrooz, 2002). Moreover, formulations have been proposed to estimate the shear strength of this type of connection (Oguejiofor and Hosain, 1994, Oguejiofor and Hosain, 1997, Verissimo, 2007, Vianna *et al.*, 2009, Ahn *et al.*, 2010).

The geometry of the PERFOFRP connector is similar to the Perfobond connector, but the overall design and mechanical behaviour of this connection differs from the steel Perfobond due to the lower strength and elastic modulus of GFRP comparatively to steel. According to preliminary tests carried out by Lameiras *et al.* (2013a), the main concern of connections made with PERFOFRP connectors is their shear capacity. It is expected, therefore, that in addition to the failure modes resulting from the rupture of the concrete itself (Figure 133(a), Figure 133(b) and Figure 133(c)), the possible failure modes of the PERFOFRP connector must be also considered (Figure 133(d), Figure 133(e) and Figure 133(f)).

The present chapter aims to deeply investigate the behaviour of the PERFOFRP connectors when subjected to tensile stresses. For this purpose, pull-out tests were conducted with PERFOFRP connectors by using specimen and loading configurations capable of reproducing, as much as possible, the conditions found in a sandwich panel.
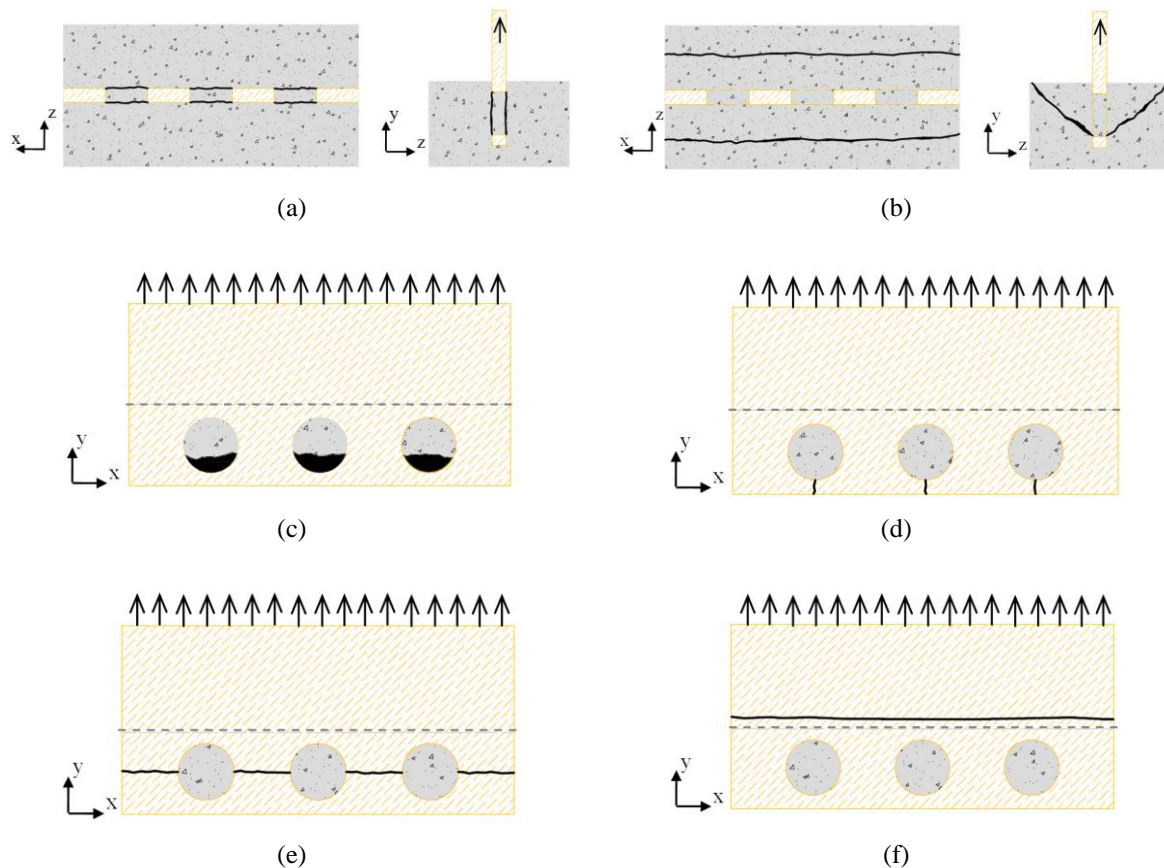
Figure 133: Failure mechanisms likely to occur when the connections are subjected to transversal shear. On SFRSCC: (a) shear of the dowels; (b) concrete cone rupture and (c) crushing. On GFRP connector: (d) rupture of the GFRP below the SFRSCC dowels; (e) rupture of the GFRP between the SFRSCC dowels and (f) rupture of the GFRP on the free section

The variables investigated included the type of GFRP, the number of holes of connector, and the type of concrete (conventional and fibre reinforced self-compacting concrete). The contributions of the resisting mechanisms (i.e., SFRSCC dowel effect and frictional resistance, schematically represented in Figure 134) were evaluated by comparing the results of tests on connectors with and without holes.
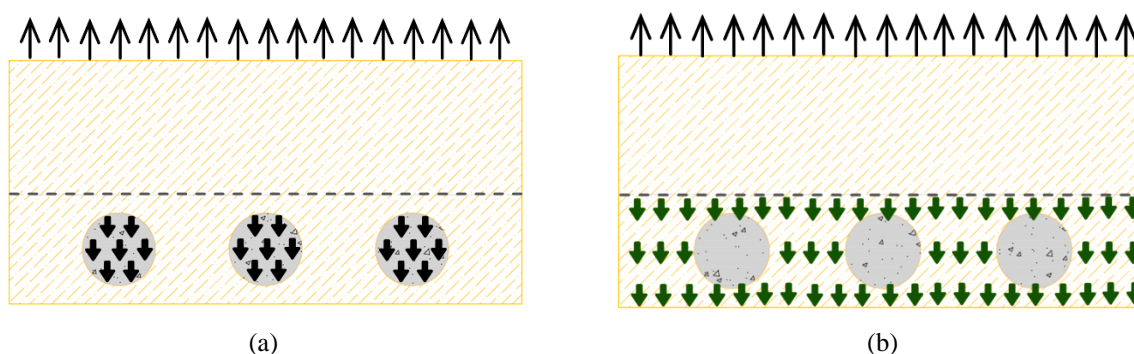
Figure 134: Main load transfer mechanisms acting on the connectors due to loads applied transversally to the concrete layer: a) SFRSCC dowel effect (including the fibre reinforcement mechanisms); b) friction/adherence resistance between GFRP and SFRSCC.

6.1 EXPERIMENTAL PROGRAM

The experimental program, carried out at the Laboratory of the Structural Division of the University of Minho, included a total of 24 pull-out tests on GFRP connectors embedded in bulk concrete blocks.

6.1.1 Material properties

Pull-out tests were performed with two distinct concrete mixes: (i) SFRSCC A from casting 5 (see Table 6); and (ii) SCC from casting 22 (see Table 6), without any kind of fibre reinforcement. The use of this second mix has the purpose of evaluating the influence of steel fibre reinforcement on the mechanical behaviour of the connections. The mix compositions adopted for SCC and SFRSCC are very similar (Table 5).

Two types of GFRP were used on the production of connections: CSM 1 and MU4 (see Table 19). The first laminate was made of a Chopped Strand Mat (CSM) reinforcement. This solution had already demonstrated satisfactory behaviour when employed as a constituent material for connectors in preliminary tests (Lameiras *et al.*, 2013a). The MU4 laminate comprised long fibres arranged on 0°, ±45° and 90° directions (see a schematic representation of the material in Figure 52(b)). Further details about the GFRPs can be seen in Chapter 4.

6.1.2 Specimens

The geometry and details of pull-out specimens are shown in Figure 135. All the specimens were made of a concrete block (i.e., SFRSCC or SCC) and a GFRP connector embedded in its centre. The concrete block had an overall thickness of 100 mm and 400 mm×246 mm of plan dimensions.
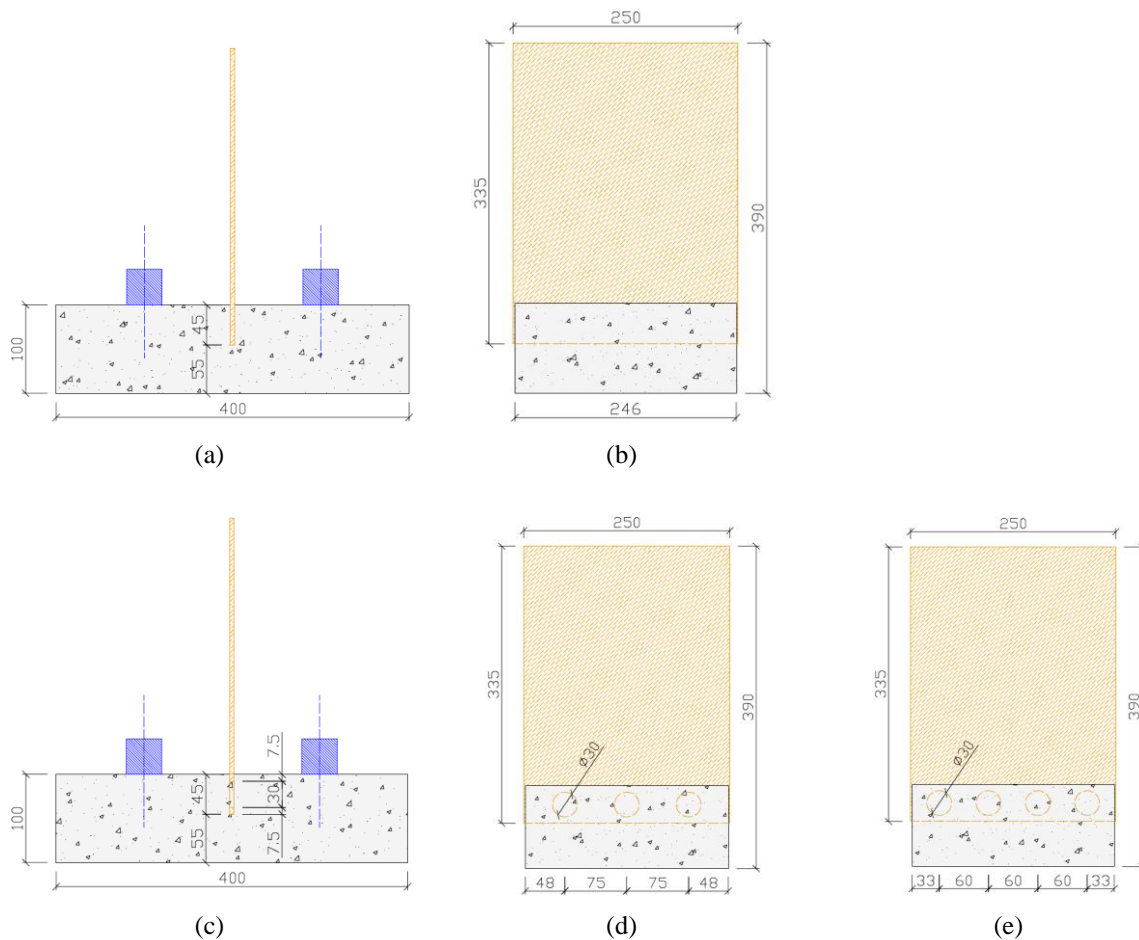
Figure 135: Layout of specimens: (a) front view and (b) lateral view of 0H connector; (c) front view of PERFOFRP connectors; (d) lateral view of 3H connector; (e) lateral view of 4H connector (dimensions in millimeter).

As shown in Figure 135, the geometry of the GFRP connectors was conditioned by the following constraints: diameter of the holes, thickness of the concrete layer, thickness of concrete cover (between the connector and the mould), and thickness of concrete above the hole. Taking into account these variables, a constant diameter of 30 mm was assumed for the holes on the GFRP plates in all perforated connectors, which allows the passage of aggregates (max. diameter equal to 12 mm) throughout the holes.

The thickness of the concrete blocks was different of the concrete layers of the sandwich panels (i.e., 60 mm of thickness) proposed by the authors in a previous work (Lameiras *et al.*, 2013a). The option for a thicker concrete block in this research has the purpose of decreasing the flexural stresses in the concrete during the pull-out tests, in an attempt of avoiding premature ruptures through concrete. Nonetheless, the depth of embedment of the GFRP connector remains equal to that used in the previous work (45mm), in order to be representative of the connection in a sandwich panel comprising SFRSCC layers with 60 mm of thickness. The concrete cover of the connectors was kept constant and equal to 55 mm in all the specimens (see Figure 135). This value would correspond to a SFRSCC cover of 15 mm in case of a SFRSCC layer thickness of 60 mm in the sandwich panel, which is near the minimum acceptable for assuring proper concrete flow conditions in these zones. With these aforementioned values, the thickness of concrete above the holes was equal to 7.5 mm (see Figure 135c). The GFRP connectors were 250 mm wide and 335 mm tall. The width of the connector was slightly larger than of the concrete block (250 mm × 246 mm) in order to more easily fix the connector to the form, thus facilitating casting procedures, as shown in Figure 136. The connectors were cut out from GFRP flat plates with approximately 2.5 m × 2.0 m and, for the PERFOFRP connectors, the holes were drilled afterwards.

(a)	(b)

Figure 136: Production of pull-out specimens: (a) overall view of formwork; (b) pouring of 3H-MU4-SCC specimen.

Concrete blocks were cast orthogonally to their largest surfaces, in order to reproduce, as much as possible, the casting procedures adopted for the sandwich panels (see Figure 136). To also reproduce the fabrication conditions, the connectors were positioned and fastened to the mould prior to the concrete pouring (see Figure 136). Placing the connector in-place

before casting provides a higher probability of having fibres passing through the holes of PERFOFRP connectors (thus improving shear behavior of the dowel when compared to plain concrete).

The test variables were the number of holes on the GFRP connector (0, 3 or 4), the type of GFRP (CSM and MU4), and the type of concrete (SCC and SFRSCC). Figure 137 presents an overview of the executed experimental program, as well as the nomenclature for the tested specimens. The following designations are adopted: 0H – without holes; 3H – with 3 holes; 4H – with 4 holes; CSM - chopped GFRP strand mat; MU4 – multidirectional GFRP; SFRSCC – steel fibre reinforced self-compacting concrete; SCC – self-compacting concrete. The configurations of the perforated connectors are shown in Figure 135. The distance between holes were $2.5 \cdot D$ (D – diameter of the hole) and $2.0 \cdot D$ for the connectors with 3 and 4 holes, respectively. These values are near the distance of $2.25 \cdot D$ indicated by Oguejiofor and Hosain (1997) as the minimum distance between holes to avoid the deleterious influence of adjacent concrete pins on the dowel effect. Hereinafter, in coherence with the scheme of Figure 137, the specimens are labeled as "XH-YYY-Z", where "X" refers to the number of holes (i.e., 0H, 3H or 4H), "YYY" refers to the type of GFRP laminate (i.e., CSM or MU4) and "Z" refers to the type of concrete adopted (i.e., SCC or SFRSCC).

In general, 3 specimens for each type were tested, except for type 3H-CSM-SCC, 0H-MU4-SFRSCC and 0H-MU4-SCC, where only 2 specimens were tested.
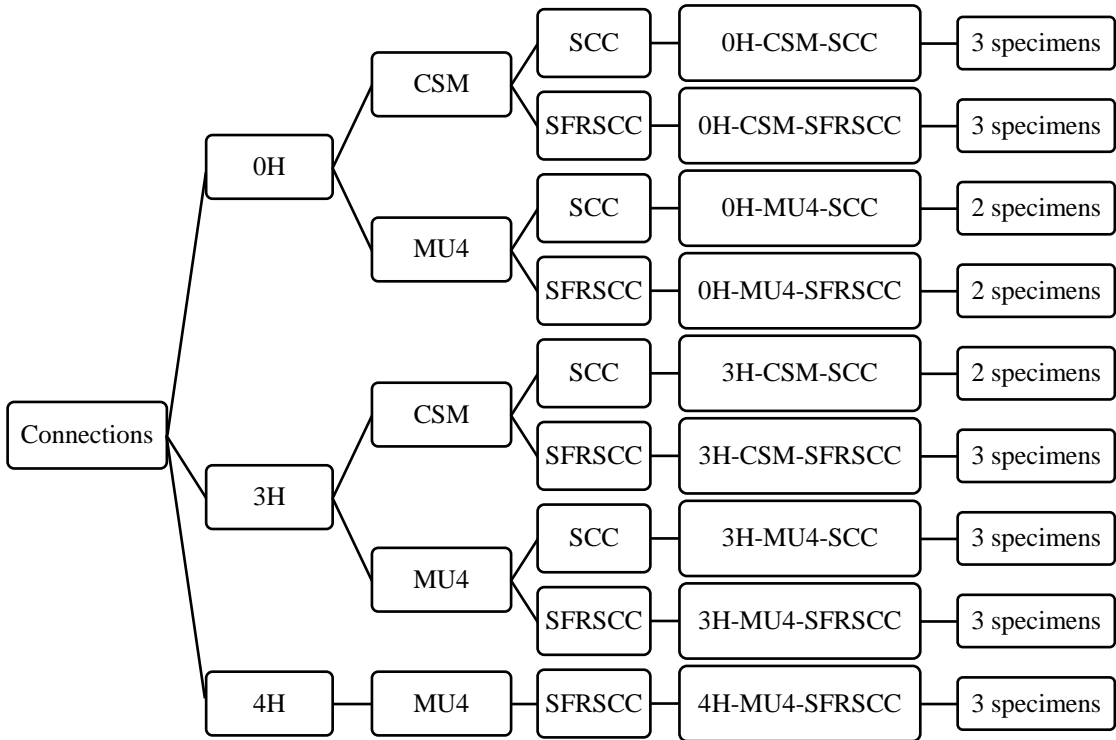
Figure 137: Experimental program: nomenclature of specimens and overall explanation.

6.1.3 Pull-out test setup

The pull-out test setup is shown in Figure 138. Tests were performed in displacement control with a rate of 0.6 mm/min using a universal testing machine. As can be observed from Figure 138, the movement of the concrete block of each specimen was restrained by two stiff steel bars (one in each side of the GFRP plate) by close tightening four high strength threaded rods of 20 mm diameter fixed to the base of the testing machine. The stiff steel bars have a square cross section of 40 mm edge and are distanced 200 mm from each other (see Figure 138). The vertical load was applied to the GFRP making use of grips where steel plates were tightened to the GFRP plate with four high strength steel bolts. The inner surfaces of such steel plates were made rough in order to increase their bond to the GFRP connector. An anchorage length of the GFRP laminate of 150 mm was always adopted to assure its proper gripping to the testing machine. A hinged connection was adopted between the gripping system and the testing machine in order to reduce the bending effect of a possible misalignment of the specimen in relation to loading axis of the testing machine (see Figure 138).
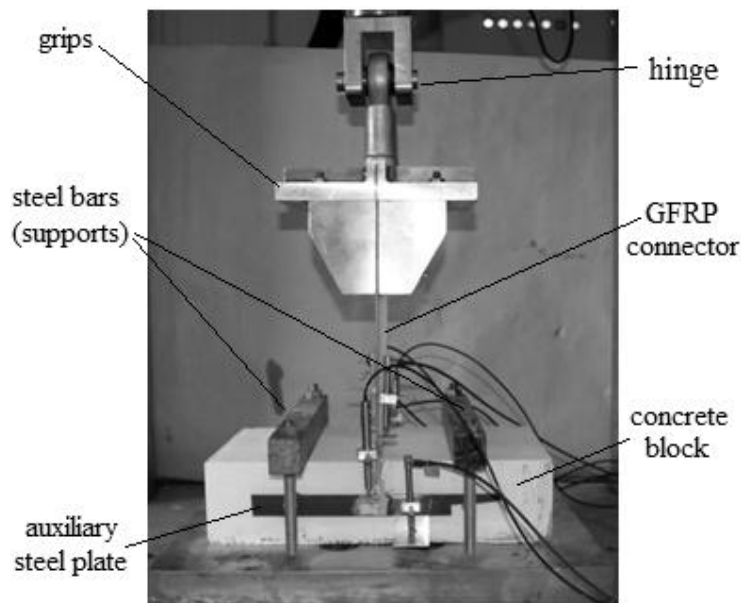
Figure 138: Overall view of pull-out test setup

The specimens were properly instrumented with linear variable displacement transducers (LVDTs) to monitor strains in selected zones of the GFRP laminate out of the concrete block, as well as the differential displacement (slip) occurring between the GFRP laminate and the concrete block. In particular (see Figure 139):

- LVDTs A and D monitored the relative displacement between the GFRP laminate and the auxiliary steel plate fixed to the concrete block, in the front and rear sides of specimen, respectively. These LVDTs have a stroke of ±10 mm;

- LVDTs B and E monitored the deflection of the concrete block in the mid-span position in the front and rear sides of specimen, respectively. The deflection is obtained from measurements with the LVDTs fixed to the auxiliary steel bar in order do not include parasitic displacements (Japan Society of Civil Engineers, 1984). The deflection of concrete block is used to control the overall behaviour of specimen during the tests, and to obtain the real slip between the GFRP laminate and the concrete block. These LVDTs have a stroke of ±2 mm;

- LVDTs C, F and G were used to evaluate the average strains in the GFRP regions between the supporting points of these LVDTs, which were separated by 60 mm. For practical reasons, these supporting points were distanced 10 mm and 70 mm from the top surface of the specimen (see Figure 138). A main concern of the test setup adopted was related to the possible existence of high bending stresses/strains that result from

an eventual misalignment between the specimen and the loading axis of the machine. Making measurements of strain in the GFRP in both sides of the laminate and in different positions along the width of specimen was considered a good away to control and evaluate the quality of the test results. These LVDTs have a stroke of ±2 mm.

To minimize potential effects of bending, the real slip between the GFRP connector and the concrete block was obtained for each specimen as the average value from the front and rear side of the specimen. The real slip in the front of the specimen was obtained by subtracting the measurement of LVDT B from the measurement of LVDT A, while the real slip in the rear side of the specimen was obtained by subtracting the measurement of LVDT E from the measurement of LVDT D.

The applied load was registered by a 200 kN load cell attached to the piston of the actuator. The acquisition system was set to continuously acquire the raw data at 2 Hz.

The surface cracks in the concrete blocks were signalized during the loading process. The test was finished when the specimen was already in its softening stage, at a load decay of at least 50% in regard to the registered peak load.
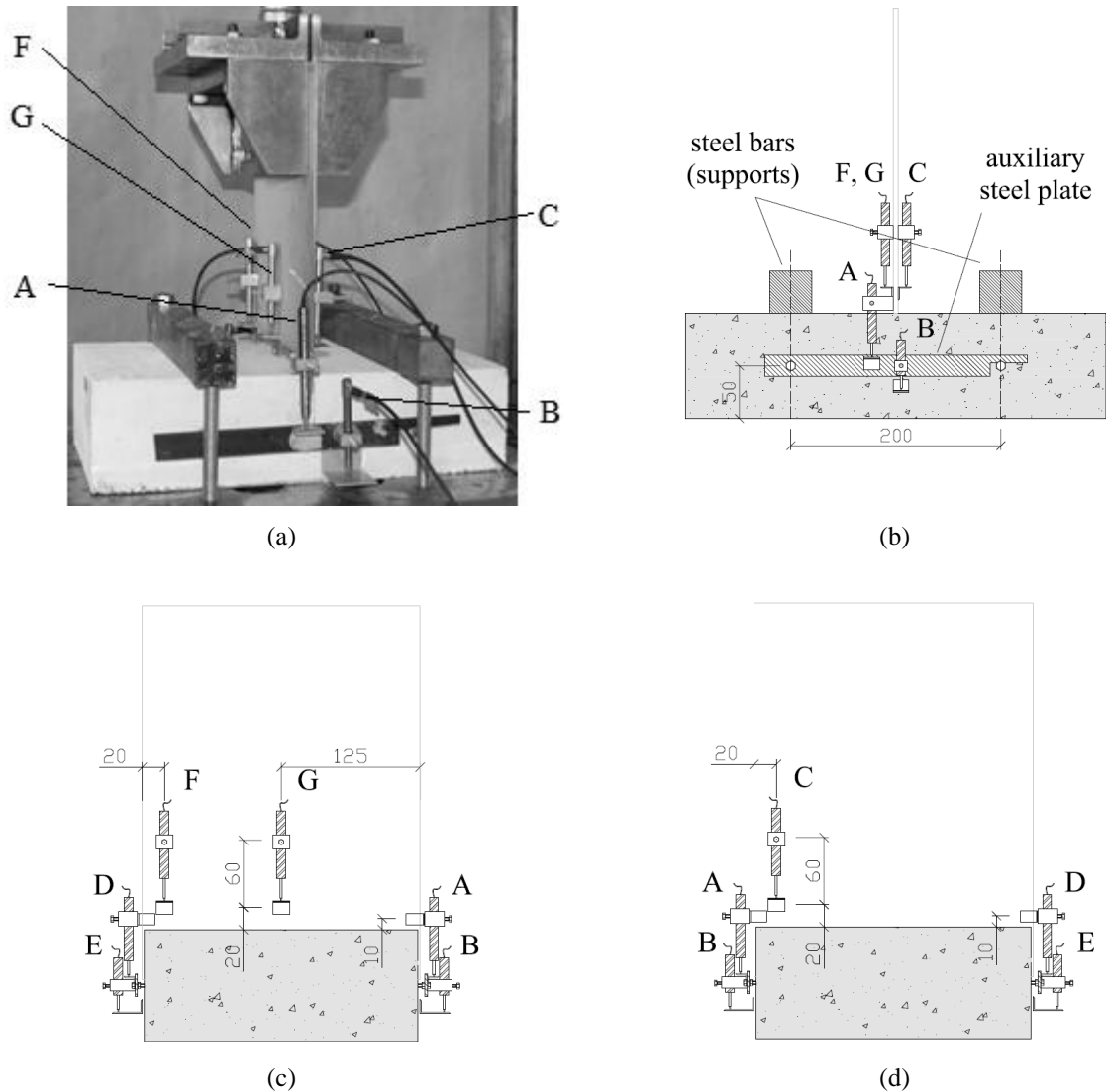
Figure 139: Pull-out instrumentation: (a) Schematic representation of layout of LVDTs: (b) front view, (c) left view, (d) right view (dimensions in millimeter).

6.2 EXPERIMENTAL RESULTS

6.2.1 Failure modes

The interpretation of the failure modes is made taking into account the observations made during the tests and also the post testing inspection of the specimens. The interpretation of the damages observed in the embedded part of the GFRP plate was based on this post testing inspection.

It was observed that, in general, independently of the type of concrete and of the connector, for a certain load stage the interface between concrete block and GFRP connector started to become disconnected, which generated in a crack that has progressively propagated towards the bottom surface of the block, as shown in Figure 140, by splitting the concrete block in two parts. For the specimens with SCC, this almost vertical crack developed rapidly throughout the entire thickness of the specimen when the peak load was reached, with a crack width that continuously got wider, and at the end of the test the maximum crack width was larger in the SCC than when using SFRSCC. On the other hand, in the specimens with SFRSCC, the crack width propagation was arrested by the steel fibres bridging the crack, keeping the width much lower.

<center>(a)</center>

<center>(b)</center>
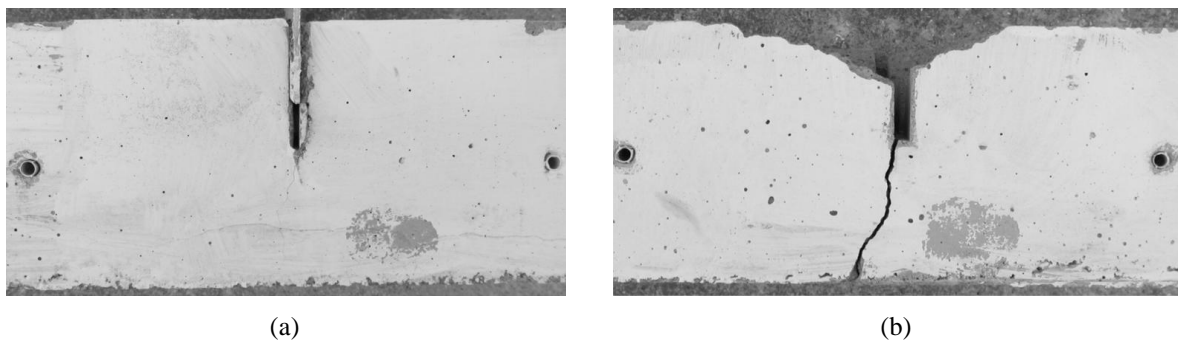
Figure 140: Detail of typical vertical cracking of concrete blocks: (a) 3H-CSM-SFRSCC and (b) 3H-CSM-SCC.

For the specimens made with CSM PERFOFRP connectors, the failure occurred due to the rupture of the connector in the vicinity of the holes (see Figure 141). This behaviour was observed for specimens with SCC and SFRSCC blocks. An exception occurred in 3H-CSM-SCC 01 specimen, where no rupture of the connector was observed.
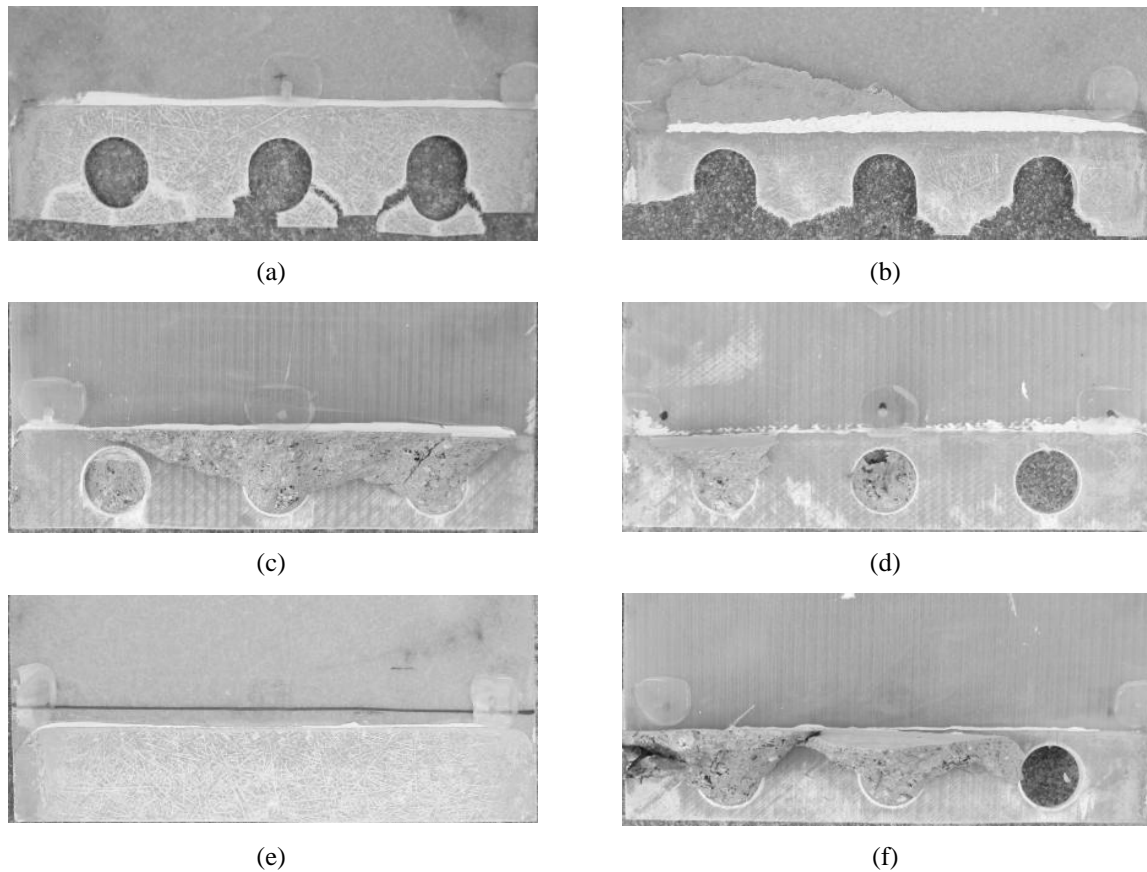
Figure 141: Representative aspect of GFRP connectors after failure: (a) 3H-CSM-SCC 02; (b) 3H-CSM-SFRSCC 01; (c) 3H-MU4-SCC 01; (d) 3H-MU4-SFRSCC 02; (e) 0H-CSM-SFRSCC 01; (f) 4H-MU4-SFRSCC 01.

For the connectors made with the CSM laminate three typical failure lines were observed in the vicinity of holes of GFRP connectors: two inclined at approximately 45°, and one at 90° with the horizontal (see Figure 142). These failure lines generally crossed the connector from the hole edge to the connector bottom edge (see Figure 142). Apparently, the CSM connectors were not capable of causing a shear failure of the concrete dowels. This may be caused by the rupture of the connector itself that has occured before the shear strength related to the rupture by shear in the surface between the PERFOFRP connector and the concrete block, due the combined effect of concrete dowel and friction/adhesion, is attained. Similar failure modes were obtained in the preliminary pull-out tests (Lameiras *et al.*, 2013a).

(a)   (b)
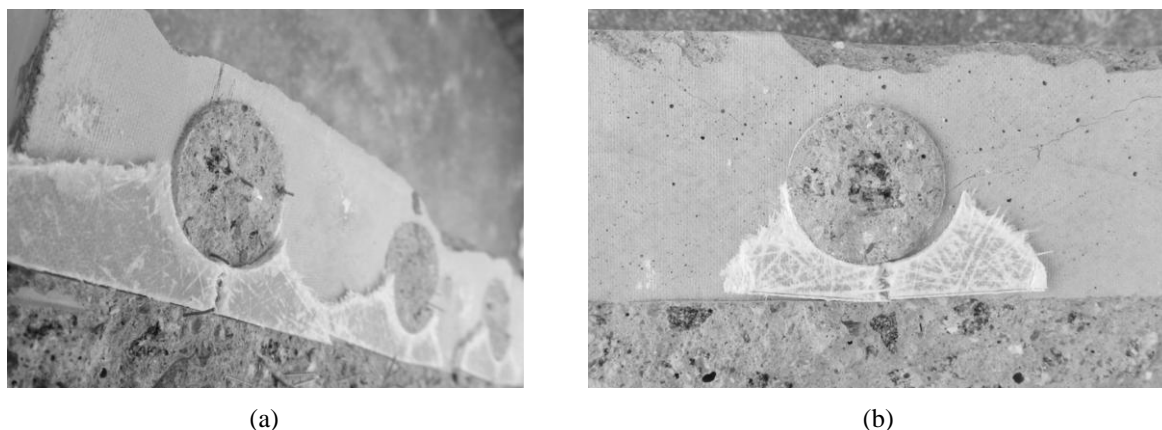
Figure 142: Detail of typical failure modes of specimens comprising CSM laminate with holes: (a) 3H-CSM-SFRSCC; (b) 3H-CSM-SCC.

Due to the larger thickness of the MU4 laminate, rupture of the concrete block was observed in the corresponding specimens. As observed in Figure 141(d) and Figure 143(a), a slice of concrete dowel remains in many holes at the end of the tests. These observations confirm the higher efficacy of this type of connector in mobilizing the concrete dowels. In fact, concrete failure was the dominant failure mode in the specimens with MU4 laminate. Two main types of failure were observed: shear failure along the interface plans between both materials (shear failure of the concrete dowels plus shear failure by friction/adhesion) and concrete cone failure. Sometimes both failure modes were observed for different holes of the same connector (see Figure 143(a)). Possibly this occurred due to an occasional difference of stiffness of the concrete dowels, any geometric imperfection, eccentricity of the load applied to the specimen, or any combination of these effects. Apparently, the connectors produced with MU4 laminate would be able to attain higher loads, since the small embedment depth of the dowels/holes, which was limited by constructive restrictions (i.e., thickness of concrete layer, minimum distance between the connector and the mould, etc), has promoted the occurrence of a premature rupture by the formation of a superficial concrete cone (see Figure 143(b)).

(a)   (b)
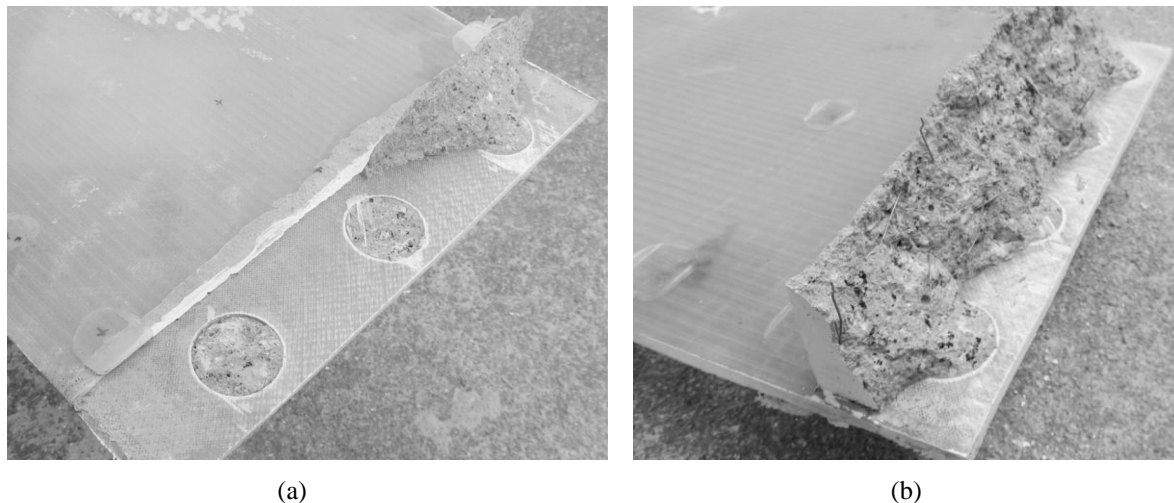
Figure 143: Detail of typical failure modes of specimens comprising MU4 laminate with holes: (a) 3H-MU4-SCC; (b) 4H-MU4-SFRSCC.

The failure modes obtained for the connections consisting MU4 PERFOFRP connectors with 3 and 4 holes were quite similar. For all the specimens, it was observed the formation of concrete fracture cones that extended from the top surface of the concrete blocks and with their apex in the lower edge of the concrete dowels formed by the passage of concrete through the holes of the connectors (Figure 143(a)). The horizontal distance measured in the top surface of the concrete block from the connector to the crack corresponded to the concrete cone had an average length of approximately 35 mm. Considering the apex of the cone in the point immediately below the hole, located at a depth of 30 mm + 7.5 mm measured vertically from the top surface of the concrete block, an angle of about 47° between the surface of the cone and the horizontal was obtained. In any case, the failure line did not reach the supports (i.e., the stiff steel bars positioned on the top surface of concrete blocks). It was also noticed that the fracture lines that defined the concrete cone generally did not appear at the same instant in both sides of specimens.

With regard to the GFRP laminates without holes, such as specimens 0H-CSM-SCC, 0H-CSM-SFRSCC, 0H-MU4-SCC and 0H-MU4-SFRSCC, no damage was visible in the GFRP, apart some superficial scratches resulting from friction between the concrete block and the GFRP (see Figure 141(e)).

6.2.2 Engineering normal strain in the laminate

Table 32 presents the maximum engineering normal strains obtained from the measurements of LVDTs C, F and G, positioned in the region of the GFRP between the concrete block and the grips.

Table 32: Maximum engineering normal strains in the region of the GFRP connectors between the concrete block and the grips.

Specimen	Maximum strain - ε_{max} [$\mu\varepsilon$]			$\varepsilon_{max} / \varepsilon_{pt.el}$	$\varepsilon_{max} / \varepsilon_{pt.u}$
	LVDT C	LVDT F	LVDT G		
3H-CSM-SCC 01	1737.45	1028.35	1429.10	9.6%	9.6%
3H-CSM-SCC 02	3439.05	1966.92	2038.25	19.1%	11.3%
3H-CSM-SFRSCC 01	2572.97	802.40	1317.38	14.3%	7.3%
3H-CSM-SFRSCC 02	13.70	1291.03	1397.68	7.8%	7.8%
3H-CSM-SFRSCC 03	3108.87	2973.08	2901.40	17.2%	16.5%
3H-MU4-SCC 01	1252.20	58.22	949.57	25.0%	3.5%
3H-MU4-SCC 02	1625.63	997.30	1109.77	32.4%	4.1%
3H-MU4-SCC 03	1562.33	890.83	709.28	31.1%	3.3%
3H-MU4-SFRSCC 01	997.95	1474.75	1442.80	29.4%	5.5%
3H-MU4-SFRSCC 02	1467.40	990.92	1115.03	29.3%	4.2%
3H-MU4-SFRSCC 03	974.75	1129.57	1396.43	27.8%	5.2%
0H-CSM-SCC 01	953.65	2321.23	3073.20	17.0%	17.0%
0H-CSM-SCC 02	2033.90	1609.22	1676.77	11.3%	9.3%
0H-CSM-SCC 03	2067.65	1938.27	1159.30	11.5%	10.8%
0H-CSM-SFRSCC 01	*	*	*	*	*
0H-CSM-SFRSCC 02	1298.60	341.58	1607.20	8.9%	8.9%
0H-CSM-SFRSCC 03	*	1344.97	1503.92	8.3%	8.3%
0H-MU4-SCC 01	1126.67	1001.45	685.05	22.5%	3.7%
0H-MU4-SCC 02	1480.07	236.78	201.30	29.5%	0.9%
0H-MU4-SFRSCC 01	905.12	560.90	500.60	18.0%	2.1%
0H-MU4-SFRSCC 02	881.92	547.87	568.05	17.6%	2.1%
4H-MU4-SFRSCC 01	1483.22	1406.83	981.20	29.6%	5.3%
4H-MU4-SFRSCC 02	1162.53	809.03	537.48	23.2%	3.0%
4H-MU4-SFRSCC 03	*	923.28	993.83	19.8%	3.7%

*- value not registered.

Comparing the values registered by the different LVDTs in each test, it can be observed that there are significant differences between the tensile strains in the monitored regions of the laminate. These values indicate the existence of bending in the laminates during the tests, which is almost impossible to exclude completely, regardless the type of test setup used. The

relevant information extracted from these results is that the maximum registered strains (ε_{max}) was much lower than the ultimate strain of the adopted GFRPs ($\varepsilon_{pt.u}$), never exceeding 17% (see Table 32). It can be concluded that for the configuration adopted for the connections, regardless the type of concrete, connector (with or without holes) and type of GFRP (CSM or MU4), the laminates were always far from the rupture in the region between the concrete block and the grips.

6.2.3   Pull-out load capacity and load *versus* slip behaviour

Table 33 summarizes relevant results obtained from the twenty four pull-out tests of the experimental program. In detail, such table reports the average values (avg.) and coefficient of variation (CoV) of: the ultimate load ($Q_{tr.u}$), the slip corresponding to the ultimate loads ($s_{tr.u}$), the cracking load ($Q_{tr.cr}$), the slip corresponding to the cracking loads ($s_{tr.cr}$) and the initial stiffness ($K_{tr.i}$).

Table 33: Results of pull-out tests: ultimate load ($Q_{tr.u}$), slip corresponding to the ultimate load ($s_{tr.u}$), cracking load ($Q_{tr.cr}$), slip corresponding to the cracking load ($s_{tr.cr}$) and initial stiffness ($K_{tr.i}$).

Connection	$Q_{tr.u}$ Avg. [kN/m] (CoV) [%]		$s_{tr.u}$ Avg. [mm] (CoV) [%]		$Q_{tr.cr}$ Avg. [kN/m] (CoV) [%]		$s_{tr.cr}$ Avg. [mm] (CoV) [%]		$K_{tr.i}$ Avg. [kN/mm/m] (CoV) [%]	
3H-CSM-SCC	80.4	(20)	0.18	(18)	80.4	(20)	0.18	(18)	104.9	(12)
3H-CSM-SFRSCC	95.1	(6)	1.18	(21)	71.7	(2)	0.11	(37)	78.8	(35)
3H-MU4-SCC	93.4	(7)	0.31	(104)	86.2	(2)	0.07	(23)	193.3	(13)
3H-MU4-SFRSCC	108.2	(7)	1.25	(44)	71.2	(12)	0.05	(31)	145.3	(30)
0H-CSM-SCC	74.5	(9)	0.14	(16)	72.7	(11)	0.14	(16)	109.5	(32)
0H-CSM-SFRSCC	58.1	(18)	0.58	(138)	58.1	(18)	0.12	(19)	92.4	(11)
0H-MU4-SCC	88.8	(13)	0.1	(64)	88.8	(13)	0.1	(64)	143.7	(2)
0H-MU4-SFRSCC	80.9	(2)	0.14	(30)	80.9	(2)	0.14	(30)	119.1	(13)
4H-MU4-SFRSCC*	112.1	(2)	0.4	(3)	83.1	(6)	0.05	(31)	180.8	(32)

*- results of 4H-MU4-SFRSCC 02 were disregarded.

The ultimate load ($Q_{tr.u}$) corresponds to the maximum load attained in each test. The cracking load ($Q_{tr.cr}$) is the one for which the first crack appeared in the concrete block. The initial stiffness ($K_{tr.i}$) of the connections was calculated from the Eq. (31):

$$K_{tr.i} = \frac{Q_{tr.50} - Q_{tr.25}}{s_{tr.50} - s_{tr.25}} \qquad (31)$$

where $Q_{tr.50}$ and $Q_{tr.25}$ are the loads corresponding to 50% and 25% of the $Q_{tr.cr}$, respectively, while $s_{tr.50}$ and $s_{tr.25}$ are the corresponding slips.

Representative pull-out load *versus* slip curves, with the identification of some of the observed failure modes, are depicted in Figure 144.

(a)

(b)

(c)
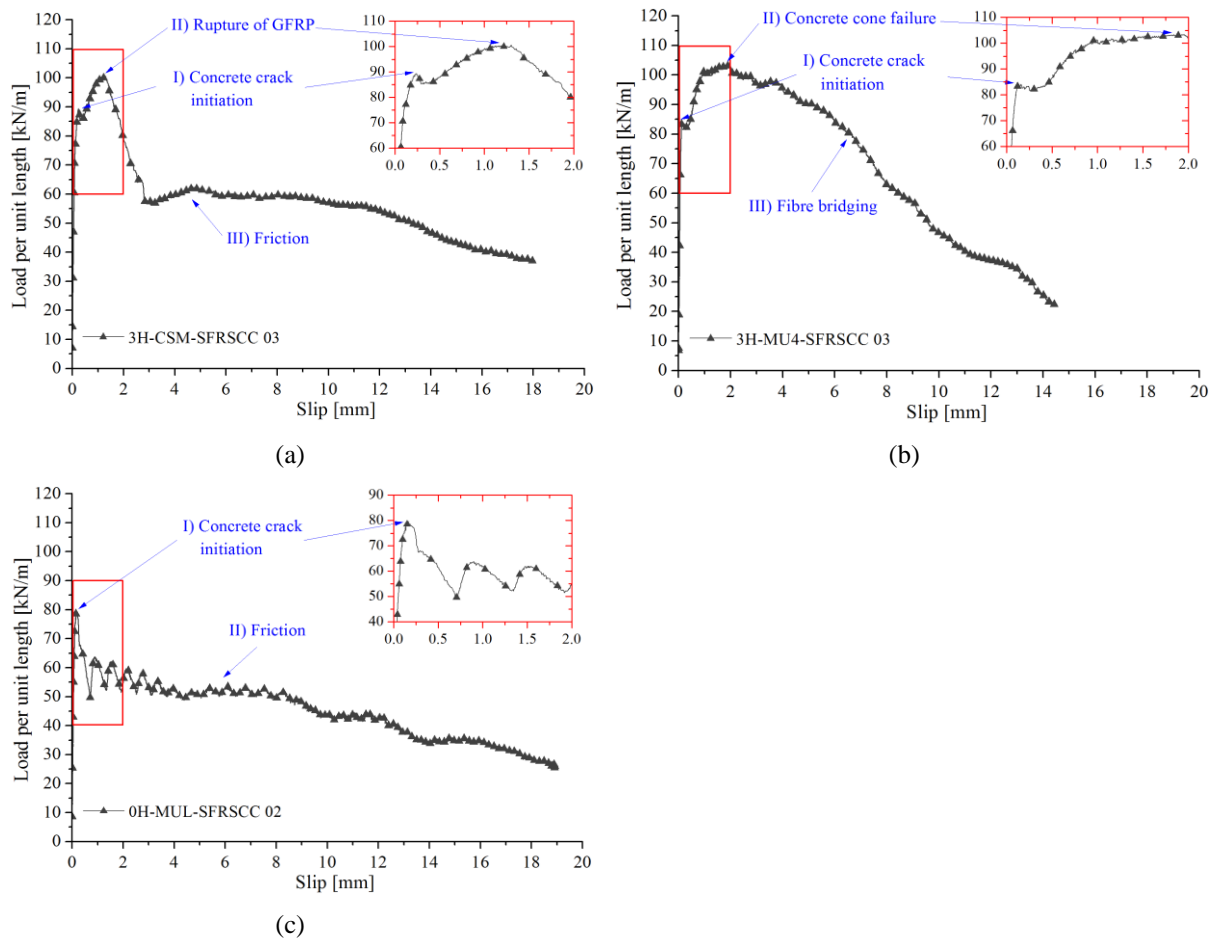
Figure 144: Representative pull-out load *versus* slip relationship, with identification of the observed failure modes: (a) 3H-CSM-SFRSCC; (b) 3H-MU4-SFRSCC and (c) 0H-MU4-SFRSCC

The presented curves were obtained for each specimen averaging the slips measured in the front and rear sides of the specimen. Although some divergence was obtained in the results registered from the front and rear sides of the same specimen, it was observed that similar conclusions were taken when the data was analyzed separately or in terms of average values. Therefore, for the sake of brevity, only the average values are presented. All the curves

obtained in the pull-out tests are presented in Figure 145 to Figure 147. The curves are grouped for helping in the analysis of the following effects: concrete type (Figure 145), type of GFRP laminate (Figure 146), and number of holes in the connector (Figure 147). In Table 33 and in the curves presented in Figure 144 to Figure 147, the load is indicated as "load per unit length of connector". This value was obtained dividing the experimental load by the width of the connector of specimen that was 246 mm.
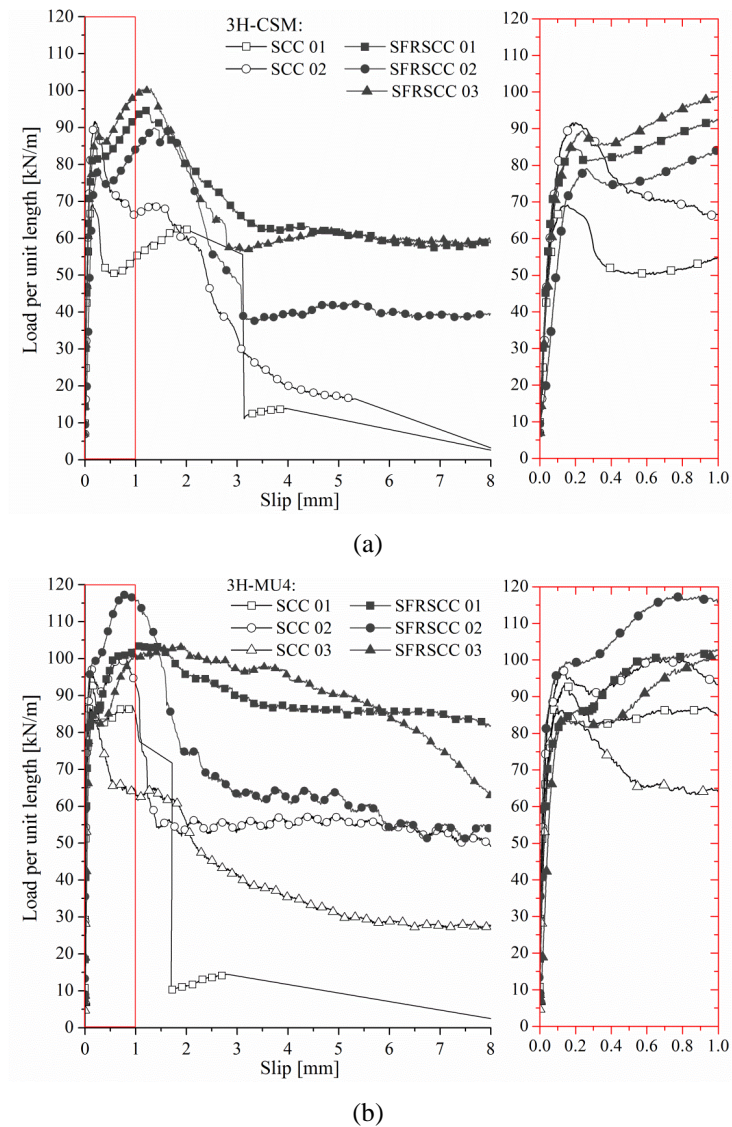
(a)

(b)

Figure 145: Influence of the concrete type on the pull-out load *versus* slip relationship: (a) 3H-CSM and (b) 3H-MU4.
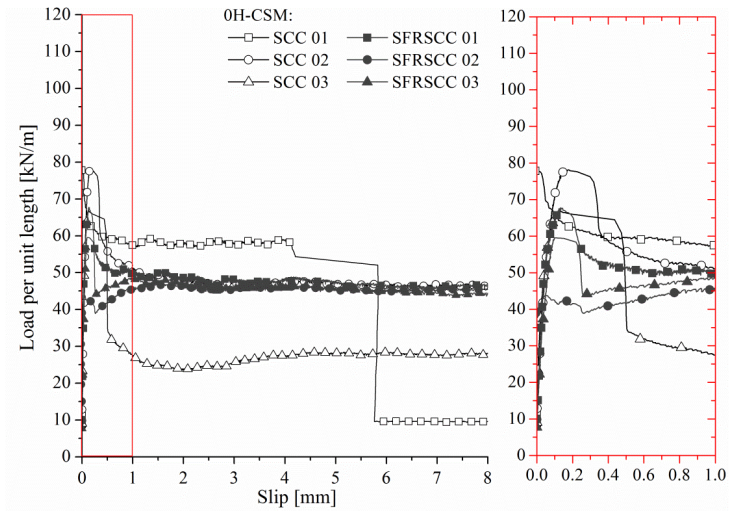
(c)
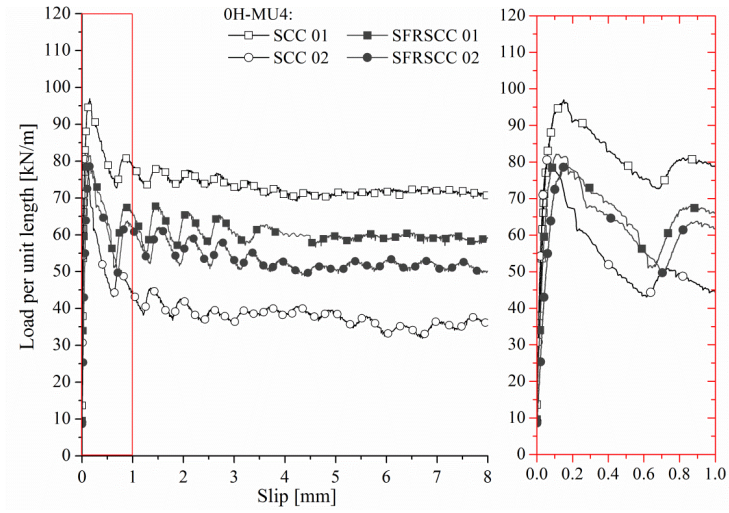
(d)

Figure 145: Influence of the concrete type on the pull-out load *versus* slip relationship: (c) 0H-CSM and (d) 0H-MU4.
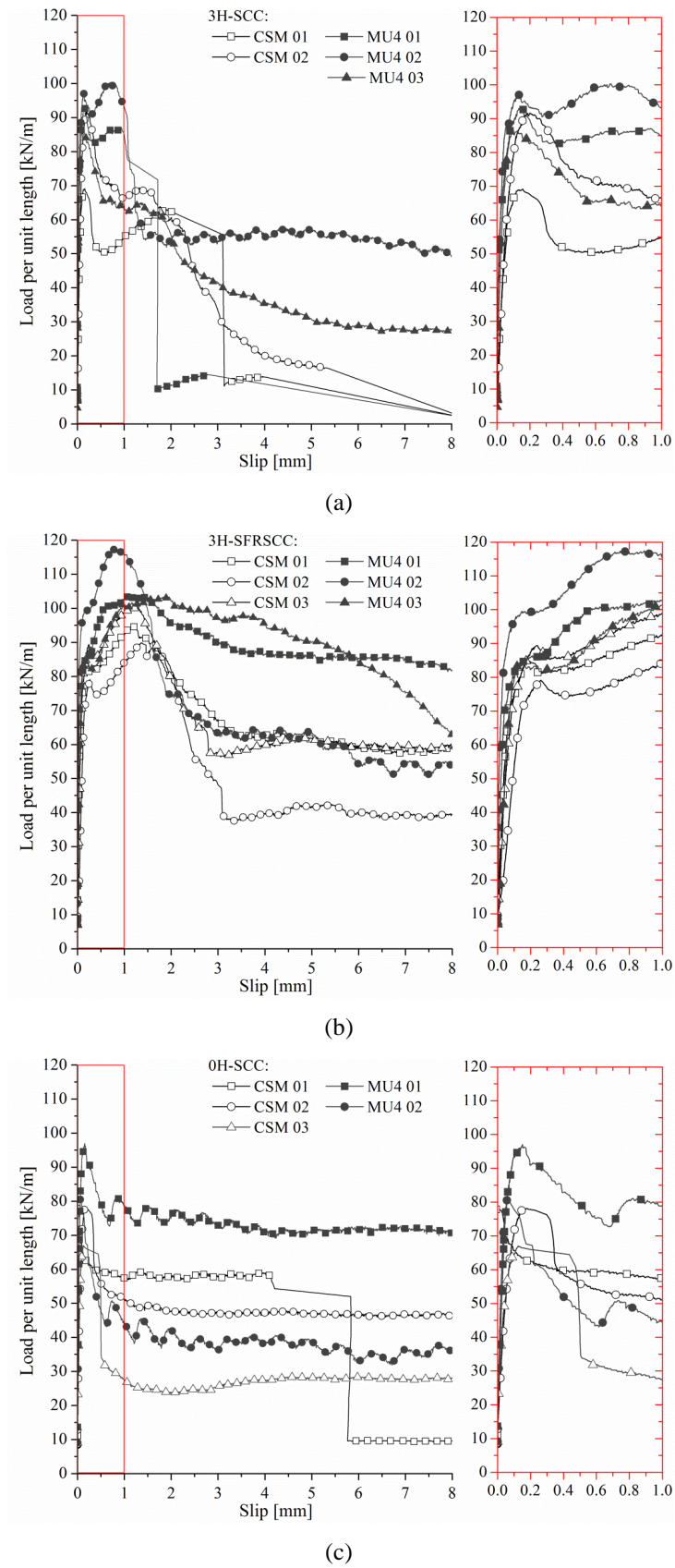
Figure 146: Influence of the GFRP laminate on the pull-out load *versus* slip relationship: (a) 3H-SCC; (b) 3H-SFRSCC and (c) 0H-SCC.

(d)
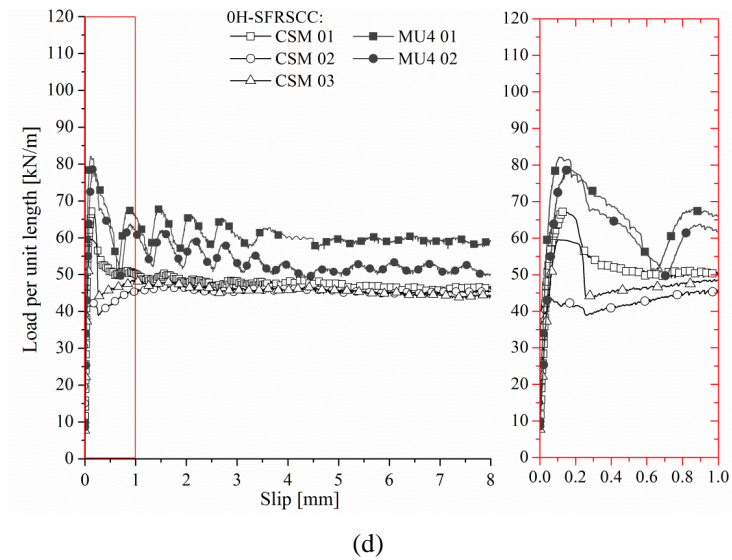
Figure 146: Influence of the GFRP laminate on the pull-out load *versus* slip relationship: (d) 0H-SFRSCC.
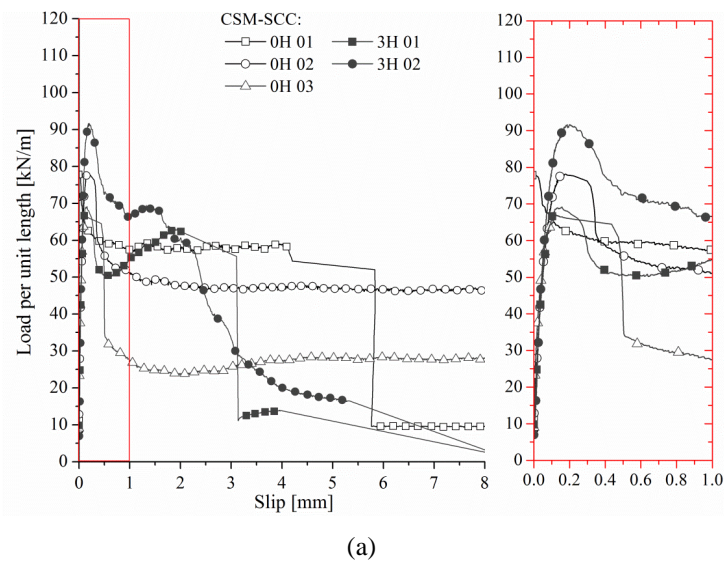
(a)

Figure 147: Influence of the number of holes in the connector on the pull-out load *versus* slip relationship: (a) CSM-SCC.
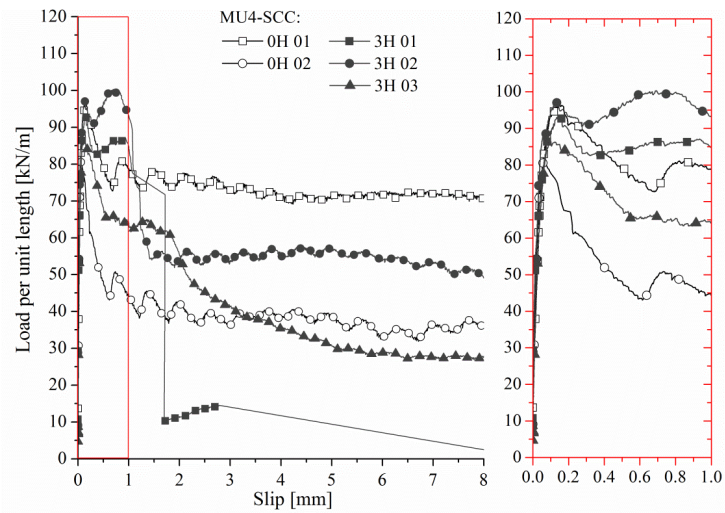
(b)
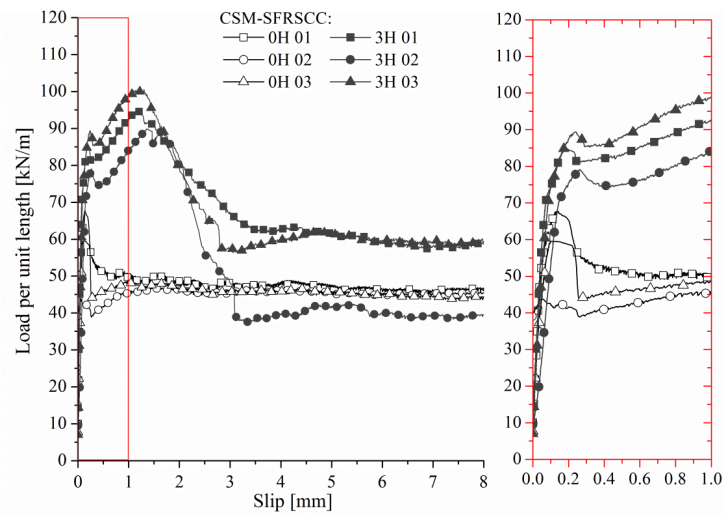
(c)
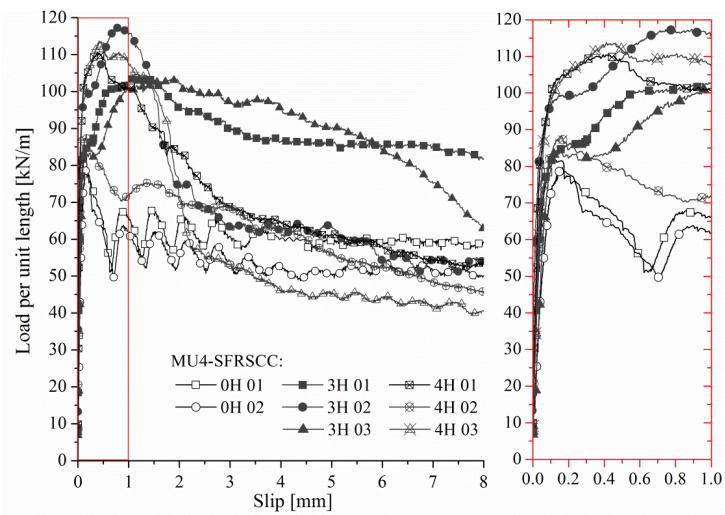
(d)

Figure 147: Influence of the number of holes in the connector on the pull-out load *versus* slip relationship: (b) CSM-SFRSCC; (c) MU4-SCC and (d) MU4-SFRSCC.

6.3   DISCUSSION

From the above mentioned figures it can be noted that the curves were all characterized by an initial stiff branch ($K_{tr.i}$ ranging from 78.8 to 193.3 kN/mm/m), up to the cracking load ($Q_{tr.cr}$) that ranged from 58.1 to 88.8 kN/m. The corresponding slip ($s_{tr.cr}$) varied from 0.05 to 0.18 mm. After this threshold, the response of the specimens significantly diverged from each other depending on the connection type (i.e., concrete type, GFRP type, and number of holes). In all the connection types, the dispersion of results becomes higher after concrete crack initiation.

For a better understanding of the effect of the studied variables on the pull-out load *versus* slip response, energy absorption indices were computed. Assuming a generic designation of η_j for this index, it was obtained through calculation of the area below the corresponding average load-slip curve up to the slip of reference *j*, given in millimetres. Three energy absorption indices were determined, η_1, η_2, and η_5, whose values are indicated in Table 34. Index η_1 was established considering that, in perforated specimens with SFRSCC, the maximum load capacity is attained for a slip value that is approximately equal to 1 mm. Index η_2, corresponds to post peak load levels that are always higher than 50% P_{max} measured in each test performed (with exception to specimen 3H-MU4-SCC 01) and index η_5, is calculated by computing a high slip deformation and is here used to assess the energy absorption of the connection.

From the results presented in Table 34 it can be also concluded that the ultimate loads ($Q_{tr.u}$) did not exhibit significant dispersion for the specimens of each group. The average and maximum values of the CoV obtained for the ultimate loads were, respectively, equal to 11% and 20%.

Table 34: Results of pull-out tests: energy absorption indices computed up to a slip equal to 1 mm (η_1), 2 mm (η_2) and 5 mm (η_5).

Connection	Energy absorption indices					
	η_1		η_2		η_5	
	Avg.	CoV	Avg.	CoV	Avg.	CoV
	[N·m/m]	[%]	[N·m/m]	[%]	[N·m/m]	[%]
3H-CSM-SCC	63.7	21	126.42	14	210.3	13
3H-CSM-SFRSCC	80.0	9	169.55	6	345.1	11
3H-MU4-SCC	82.8	14	142.78	8	240.8	36
3H-MU4-SFRSCC	94.9	11	194.83	4	445.2	9
0H-CSM-SCC	56.3	17	100.26	26	216.6	27
0H-CSM-SFRSCC	47.9	10	95.53	7	234.9	4
0H-MU4-SCC	67.4	28	126.11	34	293.5	39
0H-MU4-SFRSCC	63.9	5	123.39	5	294.2	8
4H-MU4-SFRSCC*	103.5	2.0	197.57	3.13	375.8	8.0

*- results of 4H-MU4-SFRSCC 02 were disregarded.

6.3.1 Effect of the steel fibre reinforcement of concrete

It was observed that the load-slip curves obtained from tests with 3H-SCC connections were affected by a significant level of variability, even for companion specimens. Conversely, specimens with 3H-SFRSCC exhibited a more regular behaviour.

From Figure 145 it can be noticed that the use of steel fibre reinforcement in the concrete only significantly affected the behaviour of the connections constituted by perforated plates (3H-CSM and 3H-MU4). In these cases, the use of SFRSCC has increased the load carrying capacity and, predominantly, the energy absorption capacity of the connections, demonstrated by the higher post-peak load capacity of these specimens when compared to those where SCC was used. The average maximum load carrying capacity of 3H-CSM and 3H-MU4 was 18% and 16% higher when using SFRSCC than SCC, respectively. The benefits of using SFRSCC instead SCC were even more notable when comparing the η_5 energy absorption index, since it was 64% and 84% higher for 3H-CSM and 3H-MU4, respectively.

The performance of the connections having steel fibre reinforcement for the concrete can also be examined by comparing the slip corresponding to the ultimate load ($s_{tr.u}$). Again, it was found that the use of SFRSCC led to an increase of $s_{tr.u}$ only in the case of specimens comprising perforated connectors. Tests 3H-CSM-SFRSCC and 3H-MU4-SFRSCC have

shown $s_{tr.u}$ about 3.0 and 5.6 times greater than the corresponding values computed for specimens 3H-CSM-SCC and 3H-MU4-SCC, respectively.

The key role played by the SFRSCC in the PERFOFRP is assured by the fibres that offer resistance to the crack propagation, resulting higher shear resistance of the SFRSCC dowels, not only by the direct contribution of the fibres, but also due to the higher aggregate interlock in consequence of the crack widening restriction. Consequently, when no concrete dowels exist (GFRP plates without holes), fibres do not assure any favourable contribution for the pull-out behaviour (see Figure 145). In general, all the connections comprising PERFOFRP plates presented a hardening stage after crack initiation. The abovementioned favourable effects of fibre reinforcement also justify the longer and stiffer hardening branch observed in the 3H-CSM-SFRSCC and 3H-MU4-SFRSCC specimens, when compared to the corresponding ones with SCC (see Figure 145). In the 3H-CSM-SFRSCC specimens, after crack initiation the load has increased up to the rupture of the GFRP connector. Conversely, in the 3H-MU4-SFRSCC specimens the concrete fracture capacity was exhausted prior to the bearing strength of the GFRP connector has been attained, leading to the formation of a concrete cone rupture.

In the connections comprising flat GFRP laminates without holes, the maximum load almost coincides with the crack formation in the concrete block, regardless the type of concrete adopted. Thus, since the concrete matrix of SFRSCC and SCC is almost equal, and considering that fibres do not affect the adhesion between the concrete and the GFRP laminate, no beneficial effects are expected from using fibres when the GFRP plates do not have holes.

6.3.2 Effect of the type of GFRP connector

The obtained results clearly show that when using PERFOFRP connectors, the larger is the load capacity of the GFRP laminate (MU4), the higher is the load carrying capacity and the more pronounced and stiffer is the hardening stage developed after crack initiation up to peak load (Figure 146(a) and Figure 146(b)). In fact, the average of peak load of 3H-MU4 was 15% higher than of the 3H-CSM.

In general, the connections with MU4 laminates presented a more ductile response, independently of the type of concrete, which can be justified by the nonlinear stress-strain response this GFRP develops (Figure 55(m)). The average values of η_1, η_2, and η_5 energy

absorption indices of 3H-MU4-SCC specimens were 30%, 13% and 15% larger than of the 3H-CSM-SCC specimens. Similar results were found for specimens produced with SFRSCC. However, particularly in these specimens, the greater increase on energy absorption capacity due to the use of 3H-MU4 connectors was noticed for higher slips. In these cases, η_1, η_2, and η_5 energy absorption indices increased 19%, 15% and 29% due to the adoption of MU4 laminates, respectively.

In the case of 0H tests, the maximum load of specimens comprising MU4-SCC and MU4-SFRSCC laminates were 19% and 39% greater than the average values obtained for the respective connections produced with CSM laminates. In fact, although both GFRP laminates were produced using the same resin type and manufacturing procedures, the GFRP laminates presented different superficial roughness induced by the use of different types of reinforcement (i.e., chopped strand mat for CSM laminate, and stitched roving fabric for MU4 laminate). This difference may have caused a higher friction strength for the MU4 laminate. Furthermore, in comparison to the 0H-CSM-SFRSCC, the 0H-MU4-SFRSCC connections also shown a slightly higher load level in the pseudo-yielding plateau observed after the concrete cracking.

6.3.3 Effect of the number of holes on the connector

It is possible to note in Table 33 that, in general, for a certain type of GFRP laminate and concrete, the holes in the connector led to an increase of the load capacity of the connection. Nonetheless, while this increase was statistically insignificant for the connections made with SCC (average increase of 8% and 5% for CSM-SCC and MU4-SCC, respectively), it became relevant for the connections produced with SFRSCC. For instance, the use of connectors with 3 holes led to a maximum load 64% and 34% higher than the one obtained in the connections 0H-CSM and 0H-MU4, respectively. Furthermore, the load capacity of connection 4H was, in average, 29% greater than the one of the connection 3H-SFRSCC. The influence of the holes in specimens made with SCC and SFRSCC is easily perceived in Figure 147, where the holes contributed for a substantial increase of maximum load and energy absorption, mainly when made with SFRSCC, due to the contribution of fibre reinforcement, as already reported. In fact, the average values measured for η_1, η_2, and η_5 energy absorption indices were 80.0 N·m/m, 169.5 N·m/m and 345.1 N·m/m for 3H-CSM specimens and 94.9 N·m/m,

194.8 N·m/m and 445.2 N·m/m for 3H-MU4 specimens. In average, these values were 47% to 78% higher than the values obtained in the tests performed with specimens comprising connectors without holes.

However, it is highlighted that even the GFRP connectors without holes presented a relatively high maximum load and post-peak resistance. The typical pull-out load *versus* slip response of the specimens 0H was characterized by maintaining a post-peak pseudo-yielding plateau at a relatively high load level up to a slip greater than 8 mm (exception is made for specimen 0H-CSM-SCC 01). For instance, at a slip of 8 mm the average load capacity of 0H-CSM-SFRSCC and 0H-MU4-SFRSCC connections was 45 kN/m and 55 kN/m, respectively. Thus, the experimental results proved that the friction plays an important role in the mechanical behaviour of the GFRP-concrete connections, which should not be disregarded for design purposes.

Finally, when the results presented in Figure 147(d) and Table 34 for 3H and 4H specimens are compared, it is noticed that when the number of holes per length of connector increased (i.e., spacing between holes was reduced), the response of the connection became slightly more ductile up to an approximate slip of 1.0 mm, but the response rapidly became more brittle for higher slips. In fact, 4H-MU4-SFRSCC showed an increase of 9.0% on the average value of η_1 energy absorption index, when compared to the value obtained for 3H-MU4-SFRSCC. Conversely, the average η_5 energy absorption index for 4H-MU4-SFRSCC was 16% lower than the respective value obtained for 3H-MU4-SFRSCC specimens. It is highlighted that the specimen 4H-MU4-SFRSCC 02 was not considered in this comparison since it exhibited a response significantly dissimilar from those of the same group of specimens (see Figure 147(d)).

6.4 ANALYTICAL MODEL FOR PREDICTING LOAD CAPACITY OF CONNECTIONS UNDER TRANSVERSAL LOADS

Based on the experimental evidence of the pull-out tests presented in the first part of this chapter and on the results from the bearing tests presented in section 4.5, an analytical model is proposed to predict the load carrying capacity of the developed PERFOFRP connectors when subjected to pull-out loads and embedded in plain or steel fibre reinforced concrete. The development of this analytical model was supported on a deeper interpretation of the

anchorage mechanics of the proposed connectors. For assessing the predictive performance of the model the pullout tests carried out with CSM and MU4 laminates were simulated.

As noticed in the performed experimental program on pull-out tests, one particularity of the connections consisting of PERFOFRP connectors and concrete is the fact that, when loaded transversally (under pull-out loads), the failure of the connection can be conditioned by the rupture of the connector itself. Thus, the formulation herein proposed to evaluate the load capacity of this type of connection needs to take into account both the possibility of rupture of GFRP connector and of concrete, as shown in Eq.(32).

$$Q_{tr.u}^{pr} = \min \begin{cases} Q_{tr.u.p}^{pr} \\ Q_{tr.u.c}^{pr} \end{cases} \tag{32}$$

where $Q_{tr.u.p}^{pr}$ is the predicted ultimate transversal load conditioned by the rupture of the GFRP connector, and $Q_{tr.u.c}^{pr}$ is the predicted ultimate transversal load conditioned by the rupture of concrete.

Based on the experimental observations of pull-out tests presented in sections 6.2 and 6.3, and on the experimental failure modes of the pin-bearing tests with the GFRPs, shown in section 4.5, the analytical framework was developed to predict the load capacity of PERFOFRP connections under transversal loads, $Q_{tr.u.p}^{pr}$. The framework considers the possibility of occurring the following four types of failure: net-tension ($Q_{tr.u.p.nt}^{pr}$), shear-out ($Q_{tr.u.p.so}^{pr}$), bearing ($Q_{tr.u.p.be}^{pr}$), or cleavage ($Q_{tr.u.p.cl}^{pr}$). In the proposed model, the load capacity of connection conditioned by the GFRP laminate is the minimum value among these values, as written in Eq. (33).

$$Q_{tr.u.p}^{pr} = \min \begin{cases} Q_{tr.u.p.nt}^{pr} \\ Q_{tr.u.p.so}^{pr} \\ Q_{tr.u.p.be}^{pr} \\ Q_{tr.u.p.cl}^{pr} \end{cases} \tag{33}$$

6.4.1 Net-tension failure

The maximum stress that can be introduced in net section ($\sigma_{nt.\max}$) is determined from Eq. (34), considering the following assumptions: the cumulative effect of multiple aligned holes is disregarded; Eq. (25) is used to obtain the stress introduced in net section between the holes; the strain/stress concentration observed in the pin bearing tests is taken into account (see Figure 97(a), Figure 98(a), Figure 99(a) and Figure 100(a)),

$$\sigma_{nt.\max} = K_I \cdot \frac{Q_{tr}}{(W - D_h) \cdot t_p}$$

(34)

where Q_{tr} is the applied load, W is the gross width of the laminate with one hole, D_h is the diameter of the hole, and t_p is the thickness of the laminate. K_I is the stress intensity factor under mode I fracture. K_I depends on the W/D_h ratio and of type of laminate (i.e., the stacking sequence and total content of fibres per direction) (Toubal *et al.*, 2005).

In the proposed model, it is considered that the failure mechanism in the connector takes place when $\sigma_{nt.\max}$ reaches the direct tensile strength of the composite in the load direction. Then, replacing $\sigma_{nt.\max}$ by the tensile strength of composite, $\sigma_{pt.u}$, and considering that the ultimate load of connector is related to the total number of holes, n_h, the load capacity of connector was predicted with the Eq. (35).

$$Q_{tr.u.p.nt}^{pr} = \frac{\sigma_{pt.u} (W - n_h \cdot D_h) t_p}{K_I}$$

(35)

K_I can be computed from Eq. (34) using the data obtained in bearing tests with LAT/CSM and LAT/MU4 specimens. In fact, in the bearing tests with single hole specimens consisting of CSM and MU4 laminates, a mix of bearing and net-tension failure was attained. (i.e., see results from Table 27 and failure modes of Figure 85). In the bearing tests with LAT specimens average failure loads equal to 9.74 kN and 26.93 kN were obtained for CSM and MU4 laminates, respectively. K_I equal to 2.33 and 1.23 were obtained replacing these values in Eq. (35), considering n_h equal to 1.0, W equal to the width of LAT specimens (75 mm),

and $\sigma_{pt.u}$ equal to the tensile strength of CSM and MU4 laminates in the load direction (252.54 MPa and 183.48 MPa, respectively). In the LAT specimens used for bearing tests the distance between the hole and the lateral edge of laminate was representative of a 3H connector. For the sake of simplicity and due the lack of data to estimate the effect of D_h/W ratio, K_I was considered constant independently of the distance between holes. This is a reasonable simplification, taking into account that the distance between holes is going to be always around the values representative for 3H and 4H connectors used in this research.

6.4.2 Shear-out:

The shear out stresses were computed considering Eq. (36). In this case, no stress concentration factors were considered because the shear strains along the lines that is supposed to obtain the maximum shear out stresses were almost uniform (see Figure 97, Figure 98, Figure 99 and Figure 100, (e) and (f)).

In the proposed model, it is considered that if the shear stress τ_{so} reaches the shear strength of composite, shear-out failure occurs. Thus, the ultimate load of connector conditioned by the shear-out failure can be obtained replacing the shear-out stress by the shear strength of laminate and taking into account the number of holes of connector, n_h (see Eq. (36)).

$$Q^{pr}_{tr.u.p.so} = 2 \cdot \tau_{xy.u} \cdot n_h \cdot e \cdot t_p \tag{36}$$

where $\tau_{xy.u}$ is the shear strength of the laminate corresponding to the direction where the $x-$axis of material is perpendicular to the fracture line (see Figure 79 (b)). This value was obtained only for the CSM laminate ($\tau_{xy.u} = 139.06\,MPa$), which is the reason for the absence of estimations for the load capacity of connectors with MU4 governed by the shear out failure of connectors in this work.

6.4.3 Bearing

As Eq. (27) indicates, the variation of compressive stress along the perimeter contact between the pin and the hole was disregarded in the proposed model, and the applied load was assumed acting uniformly on the perimeter of the bottom semi-circumference of the hole (see Figure 79 (c)). Thus, the ultimate load of connector governed by bearing was obtained

replacing the stress by the compressive strength of CSM and MU4 laminates. Taking into account that the load transferred for each hole is Q/n_h, where n_h is the number of holes of connector, the ultimate load governed by bearing is given by Eq. (37):

$$Q_{tr.u.p.be}^{pr} = \sigma_{pc.u} \cdot n_h \cdot D_h \cdot t_p \tag{37}$$

where $\sigma_{pc.u}$ is the compressive strength of the laminate corresponding to the load direction (0°/90°). The compressive strength of laminates used in this research work was not directly characterized. Nonetheless, in the bearing tests with LAT specimens the CSM and MU4 laminates presented a combined rupture mode, failing at similar load levels by net-tension and bearing failure. In this manner, the compressive strengths of CSM and MU4 laminates were estimated using Eq. (37) and the data obtained from bearing tests with CSM-LAT and MU4-LAT specimens for n_h equal to 1.0. Considering that the average load capacities of CSM-LAT and MU4-LAT specimens were equal to 9.74 kN and 26.93 kN (see Table 27), values equal to 162.33 MPa and 224.42 MPa were obtained for $\sigma_{pc.u}$ of CSM and MU4 laminates, respectively.

6.4.4 Cleavage

To estimate the maximum load that can be applied to the system prior the failure by cleavage, it was considered that the load applied to the connection (Q) is equally distributed among the holes (Q/n_h) and the load transferred to each hole is constant and uniformly distributed along the lower half of the hole (p_h), as shown in Figure 148. Thus, the distributed load in each hole (p_h) was obtained dividing the total load applied to the connector by the number of holes and by the arch length that is distributed, as given in Eq. (38).

$$p_h = \frac{2 \cdot Q}{n_h \cdot \pi \cdot D_h} \tag{38}$$

(a)

(b)
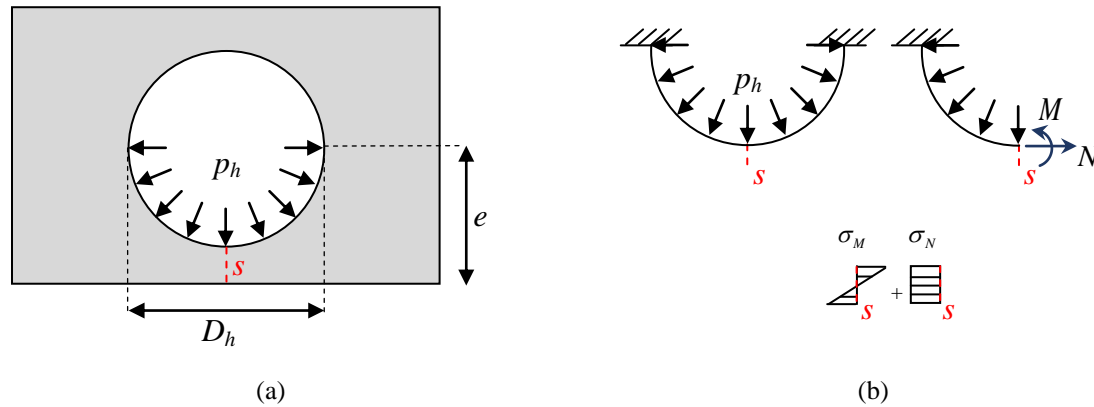
Figure 148: Model used to calculate the maximum axial stresses in the section *s*: (a) load uniformly distributed in the lower bound of the connector; (b) clamped arch used to compute the internal forces and axial stresses.

The internal forces and the engineering stresses along the *x*–direction in the section immediately below the hole (section *s* shown in Figure 148) were estimated by modelling the hole as a simply clamped arch with rectangular cross section of height equal to $(e - D_h/2)$ and thickness equal to t_p, as shown in Figure 148. In such a way, the maximum axial stresses in the crown of the clamped arch were computed using the formulae proposed by Dym and Williams (2011).

To take into account the uncertainties related to the problem (i.e., distribution of the load transferred from the concrete dowel to the connector, anisotropy of the MU4 laminate, among others), a correction factor ψ was introduced in the stress equation. The maximum normal tensile stress in the *x*–direction, developed in the section *s* was calculated by the Eq. (39).

$$\sigma_{x.\max} = \psi \cdot \frac{\pi^2 \cdot D_h^{\,2} \cdot p_h \cdot \left(30 \cdot t_p + \pi^2 \cdot D_h\right)}{2 \cdot t_p \cdot \left(e - \dfrac{D_h}{2}\right) \cdot \left(240 \cdot t_p^{\,2} + \pi^4 \cdot D_h^{\,2}\right)} \tag{39}$$

Replacing the equation Eq. (38) in Eq. (39), the maximum normal stress can be given by the Eq. (40):

$$\sigma_{x.\max} = \psi \cdot \frac{\pi \cdot D_h \cdot Q \cdot \left(30 \cdot t_p + \pi^2 \cdot D_h\right)}{n_h \cdot t_p \cdot \left(e - \dfrac{D_h}{2}\right) \cdot \left(240 \cdot t_p^2 + \pi^4 \cdot D_h^2\right)} \tag{40}$$

Considering that the rupture of the connection by cleavage happens when the ultimate tensile stress of the laminate in the x–direction, $\sigma_{pt.u}$, is attained in the section s, the load capacity of the connection governed by cleavage, $Q_{tr.u.p.cl}^{pr}$, can be predicted by the Eq. (41) isolating Q and replacing $\sigma_{x.\max}$ by $\sigma_{pt.u}$ in Eq. (40).

$$Q_{tr.u.p.cl}^{pr} = \frac{\sigma_{pt.u} \cdot n_h \cdot t_p \cdot \left(e - \dfrac{D_h}{2}\right) \cdot \left(240 \cdot t_p^2 + \pi^4 \cdot D_h^2\right)}{\psi \cdot \pi \cdot D_h \cdot \left(30 \cdot t_p + \pi^2 \cdot D_h\right)} \tag{41}$$

The values of the correction factor ψ can be determined applying the Eq. (41) to the pin-bearing tests that failed by cleavage, that is, tests with BEL specimens (see Table 27 and Figure 84). Using $n_h = 1$ and adopting for Q the ultimate load obtained in the bearing tests, ψ values equal to 1.534 and 0.991 were obtained for CSM and MU4 laminates, respectively.

As evidenced in the performed pull-out tests presented in the sections 6.2 and 6.3, when the rupture of concrete has governed the load capacity of connections, two main failure modes were evidenced: the concrete cone tensile fracture and the failure along the contact planes between the connector and concrete, i.e., a combination of failure of concrete dowels and by friction/adhesion. Thus, the predicted load capacity of connection governed by the rupture of concrete, $Q_{tr.u.c}^{pr}$, can be obtained as the minimum value between the predicted rupture load by concrete cone fracture, $Q_{tr.u.c.cf}^{pr}$, and by shear along the contact line between the connector and the concrete, $Q_{tr.u.c.df}^{pr}$, as given by Eq. (42).

$$Q_{tr.u.c}^{pr} = \min \begin{cases} Q_{tr.u.c.cf}^{pr} \\ Q_{tr.u.c.df}^{pr} \end{cases} \tag{42}$$

6.4.5   Concrete cone tensile fracture

Concrete cone failure was observed for the studied connections consisting of SCC and SFRSCC, as shown in the section 6.2.1. This failure mode, named after the roughly cone shape of the piece of concrete witch pulls out in this kind of failure, happens in the concrete block when principal tensile stresses transferred from the connector to the surrounding concrete reach its tensile strength and the concrete fractures along the surface that is the envelope of the compression isostatics. This is a failure mode commonly reported in pull-out tests with anchors, steel rebars and laminates embedded in concrete (Eligehausen and Balogh, 1995, Farrow *et al.*, 1996, Mansour Shirvani and Herman, 2004, Bianco *et al.*, 2009). Several equations have been already proposed to predict the concrete fracture capacity (Klingner and Mendonca, 1982, ACI Committee 349, 1985, Fuchs *et al.*, 1995, Farrow *et al.*, 1996, Eric J. Primavera and Edward, 1997). In general, predictions are made utilizing an idealized failure cone characterized by an effective height, h_e and considering a uniform tensile stress distribution in the concrete at failure (see Figure 149). In general, the existing equations compute the cone load capacity as the resultant of tensile stresses equal to concrete tensile strength, f_{ct}, directed parallel to the applied load and acting on the projected area of the failure cone, $A_{pr.0}$. Considering that the cone angle is θ (see Figure 149), the projected area can be estimated by $\frac{\pi}{2} \cdot \left(\frac{h_e}{\tan \theta} \right)^2$.

(a)   (b)
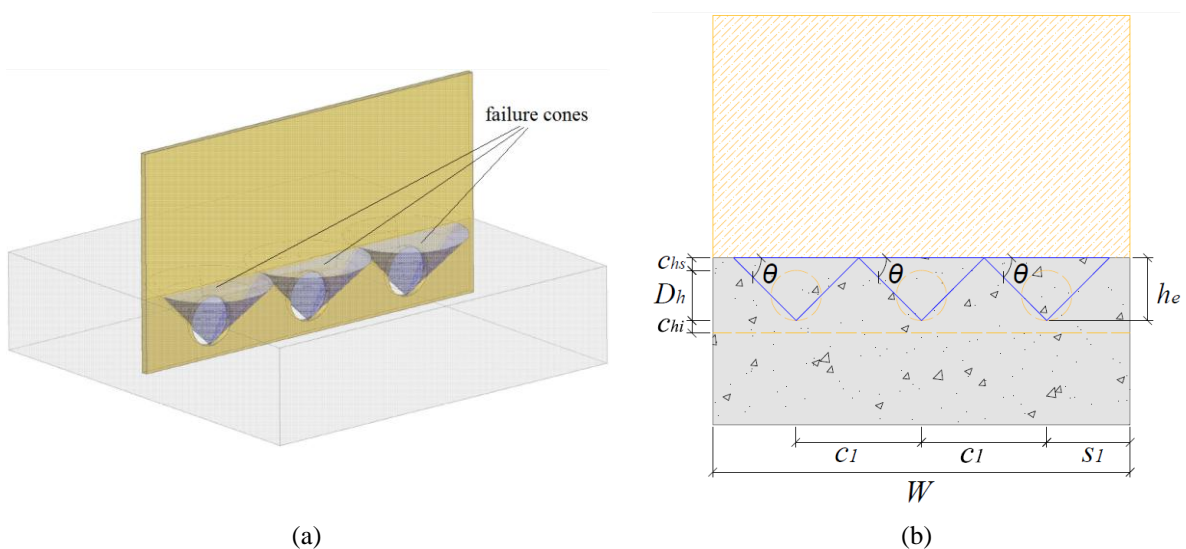
Figure 149: Schematic representation of concrete cone failure: (a) perspective; (b) cross-section.

Although primarily developed for headed anchors, the formulae proposed by ACI Committee 349 (ACI Committee 349, 1985) were adapted to estimate the load capacity of connections made with PERFOFRP connectors. As done by ACI Committee 349, a cone angle of 45° was considered. Based on the experimental observation, the apex of the cone failure was considered to be in the lower edge of the concrete dowels, aligned with the middle of hole and with the thickness of the connector, as shown in Figure 149. Thus, the load capacity of connector could be estimated by the Eq. (43).

$$Q^{pr}_{tr.u.cf} = f_{ct} \cdot A_{pr} \tag{43}$$

where f_{ct} is the tensile strength of concrete and A_{pr} is the sum of the projected area of individual cones in a surface normal to the load direction, minus the areas of overlap and areas cut off by intersecting edges (see Figure 150) (Barros *et al.*, 2009). The total projected area, $A_{pr.0}$, corresponding to all the cone failures, one for each of the n_h holes of connector, was computed from Eq. (44).

$$A_{pr.0} = n_h \cdot \frac{\pi}{2} \cdot \left(\frac{h_e}{\tan \theta} \right)^2 \tag{44}$$
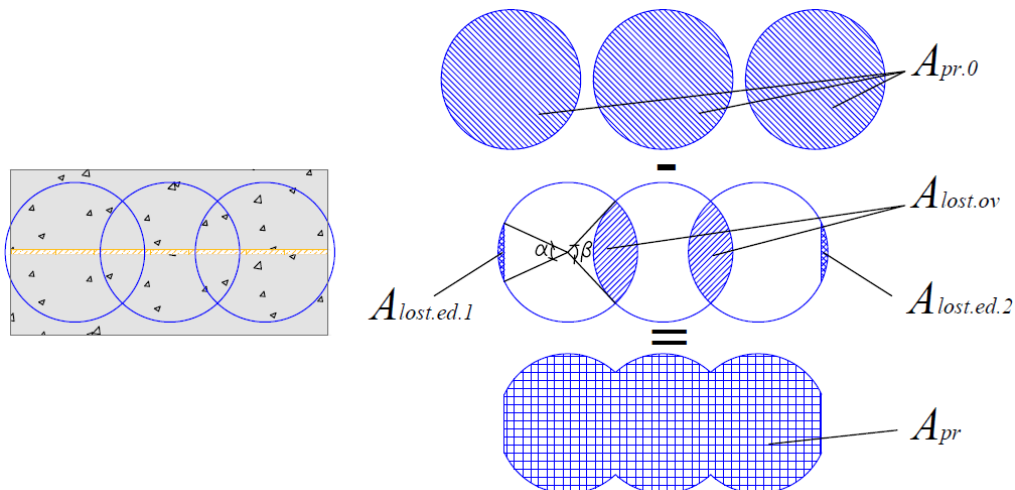
Figure 150: Determination of projected areas (plan view).

If the hole was located near a free edge, the projected area of the stress cone was reduced if the cone intersects the edge of the concrete (see Figure 150). The edge problem resulted if

$c_1/(h_e/\tan\theta) < 1$. The amount to be reduced can be found by calculating the areas lost due to the proximity of all the edges i, $A_{lost.ed.i}$, using the Eq. (45).

$$A_{lost.ed.i} = \pi \cdot \left(\frac{h_e}{\tan\theta} \right)^2 \cdot \frac{\beta}{360°} - c_1 \cdot \frac{h_e}{\tan\theta} \cdot \sin\left(\frac{\beta}{2} \right) \tag{45}$$

where β is the angle represented in Figure 150, given in degrees, and can be computed by Eq. (46).

$$\beta = \cos^{-1}\left[2 \cdot \left(c_1 \cdot \frac{\tan\theta}{h_e} \right)^2 - 1 \right] \tag{46}$$

The total projected area was also reduced in the presence of multiple closely spaced cones if their failure surfaces overlapped (Barros *et al.*, 2009). Considering an evenly distribution of holes spaced by s_1 (see Figure 149), the overlap problem resulted if $s_1/(2 \cdot h_e/\tan\theta) < 1$. Thus, the total overlapped area can be computed by Eq. (47).

$$A_{lost.ov} = (n_h - 1) \cdot \left(\frac{h_e}{\tan\theta} \right)^2 \cdot (\alpha - \sin\alpha) \tag{47}$$

where α was the angle represented in Figure 150, given in degrees, and was computed by Eq. (48).

$$\alpha = \cos^{-1}\left[2 \cdot \left(\frac{s_1}{\dfrac{2 \cdot h_e}{\tan\theta}} \right)^2 - 1 \right] \tag{48}$$

Finally, the net projected area was equal to the difference between the projected area corresponding to a hole, not limited by edge influences ($A_{pr,0}$), and the sum of the areas of segments formed by the n edges of the concrete acting as secant, as given by Eq. (49).

$$A_{pr} = A_{pr.0} - A_{lost.ov} - \sum_{i=1}^{n} A_{lost.ed.i} \tag{49}$$

The concrete average tensile strength, f_{ct}, was estimated from the compressive strength of SCC and SFRSCC by means of the formulae present in the *fib* Model Code 2010 (Fédération Internationale du Béton (fib), 2012), shown in Eq. (50), resulting in 4.41 MPa and 4.33 MPa for the SCC and SFRSCC, respectively. The contribution of steel fibres to the tensile strength of the SFRSCC was disregarded because the fibres volume fraction commonly used in steel fibre reinforced concretes are not sufficiently high to increases the the tensile strength of the cementitious composite (Bentur and Mindess, 2006a).

$$f_{ct} = \begin{cases} 0.3 \cdot f_{ck}^{2/3} & if \quad f_{ck} \leq 50 MPa \\ 2.12 \cdot \ln\left(1 + 0.1 \cdot \left(f_{ck} + 8 MPa\right)\right) & if \quad f_{ck} > 50 MPa \end{cases} \tag{50}$$

6.4.6 Shear along the contact line between the connector and the concrete (Shear in the Concrete Dowels plus Friction/Adhesion)

Two different mechanisms are associated to the failure by shear along the contact area of connector and concrete: shear in the concrete dowels and friction/adhesion between the concrete and the two connector's contact surfaces.

The shear along the concrete dowels can be computed considering the hypotheses of occurring a (1) single shear plane or (2) double shear planes. In the experimental study, after the pull-out tests it was evidenced that in some cases a slice of concrete remained in the hole of MU4 connectors, which corresponds to the case that double shear planes have occurred, due to the larger thickness of this type of laminate when compared to the CSM laminate.

The ultimate shear stress of concretes, v_c, were estimated using the empirical shear transfer model developed by Khanlou *et al.* (2013), presented in Eq. (51). This equation is based on regression analysis of data obtained from direct shear tests with hooked-end steel fibre reinforced concretes.

$$v_c = 0.75 \cdot \sqrt{f_{ck}} + 4 \cdot V_f^{0.9} \tag{51}$$

where v_c and f_{ck} are in MPa and V_f is the volume fraction of steel fibres, expressed as a percentage. Using $f_{cm} = 61.88\,\text{MPa}$ and $V_f = 0.774\%$ (i.e., 60kg/m^3), the ultimate shear stress of SFRSCC was estimated in 9.08 MPa. In the absence of fibres Eq. (51) reduces to

$v_c = 0.75 \cdot \sqrt{f_{ck}}$, which is the shear strength of plain concrete. This equation was used to compute the ultimate shear stress of SCC (found 5.9 MPa using $f_{cm} = 59.12\,\text{MPa}$).

The friction/adhesion contribution was estimated from the experimental data obtained in the pull-out tests for 0H specimens, where only the friction/adhesion is present. A uniform stress distribution was considered for the friction/adhesion stress, which is related to the GFRP and concrete types. The friction/adhesion strength then was computed dividing the peak load to the area of contact between the materials, considering the occurrence of double shear (the two faces of the connector in contact to the concrete). Thus, considering the average peak load obtained in the pull-out tests and the contact area, friction/adhesion strength, τ_{fr}, equal to 0.83 MPa, 0.65 MPa, 0.99 MPa and 0.90 MPa were obtained for connections: CSM-SCC, CSM-SFRSCC, M4-SCC and MU4-SFRSCC, respectively. Thus, the parcel of the load corresponding to the friction/adhesion is obtained multiplying τ_{fr} to the net contact area between the connector and the concrete. Differently from the equation of Sara and Bahram (2002), the second term of Eq. (52) considers the net contact area between the concrete and the connector.

Therefore, joining both effects, shear in the concrete dowels and friction/adhesion, the load capacity conditioned by this failure mode was estimated by Eq. (52), considering simple shear.

$$Q_{u.tr.c.df}^{pr} = \left[n_h \cdot \left(\frac{\pi \cdot D_h^2}{4} \right) \right] \cdot v_c + 2 \cdot \left[W \cdot (D_h + c_{hs} + c_{hi}) - n_h \cdot \left(\frac{\pi \cdot D_h^2}{4} \right) \right] \cdot \tau_{fr} \tag{52}$$

where $W \cdot (D_h + c_{hs} + c_{hi})$ is the gross area corresponding to the region of connector that is embedded in the concrete, as shown in Figure 149.

6.5 MODEL VALIDATION

The transversal load capacity of tested PERFOFRP connectors registered experimentally and predicted analytically are compared in Table 35 , an average error of 19.57% was obtained.

The proposed model was able to predict very well the failure modes observed in the different types of PERFOFRP connectors investigated. For instance, in the case of 3H-CSM-SCC and

3H-CSM-SFRSCC, a failure mode by cleavage of the CSM connector was predicted, which corresponds to what was experimentally observed. In average, the model underestimated the load capacity of 3H-CSM-SCC and 3H-CSM-SFRSCC connections on 1.05% and 16.36%, respectively.

In the case of connections consisted of MU4 PERFOFRP, the predicted load capacity of connections was always conditioned by the concrete fracture. For 3H-MU4-SCC, the predicted failure mode was due to shear along the contact plane between the connector and the concrete. In the other hand, for 3H-MU4-SFRSCC and 4H-MU4-SFRSCC a concrete cone failure was predicted. Nonetheless, attention should be paid to the fact that, for the MU4 PERFOFRP connectors, the values of $Q_{tr.u.cf}^{pr}$ and $Q_{tr.u.df}^{pr}$ were always quite similar. In fact, as reported in the section 6.2.1, it was experimentally observed that these connections presented both types of rupture.

Table 35: Comparison between experimental and analytically predicted pull-out resistance of connections.

Specimen	$Q_{tr.u}^{exp}$ [kN/m]	Conditioned by connector rupture					Conditioned by concrete failure			Predicted failure mode**	$Q_{tr.u}^{pr}$ [kN/m]	Error [%]
		$Q_{tr.u.p.nt}^{pr}$ [kN/m]	$Q_{tr.u.p.so}^{pr}$ [kN/m]	$Q_{tr.u.p.be}^{pr}$ [kN/m]	$Q_{tr.u.p.cl}^{pr}$ [kN/m]	$Q_{tr.u.p}^{pr}$ **[kN/m]**	$Q_{tr.u.c.cf}^{pr}$ [kN/m]	$Q_{tr.u.c.df}^{pr}$ [kN/m]	$Q_{tr.u.c}^{pr}$ **[kN/m]**			
3H-CSM-SCC 01	**69.1**	137.26	153.22	118.78	79.51	**79.51**	118.67	111.09	**111.09**	p.cl	**79.51**	15.1
3H-CSM-SCC 02	**91.6**	137.26	153.22	118.78	79.51	**79.51**	118.67	111.09	**111.09**	p.cl	**79.51**	-13.2
3H-CSM-SFRSCC 01	**94.8**	137.26	153.22	118.78	79.51	**79.51**	116.66	125.21	**116.66**	p.cl	**79.51**	-16.1
3H-CSM-SFRSCC 02	**89.9**	137.26	153.22	118.78	79.51	**79.51**	116.66	125.21	**116.66**	p.cl	**79.51**	-11.6
3H-CSM-SFRSCC 03	**100.5**	137.26	153.22	118.78	79.51	**79.51**	116.66	125.21	**116.66**	p.cl	**79.51**	-20.9
3H-MU4-SCC 01	**93.16**	379.50	*	328.41	158.05	**158.05**	129.65	122.65	**122.65**	c.df	**122.65**	31.7
3H-MU4-SCC 02	**100.3**	379.50	*	328.41	158.05	**158.05**	129.65	122.65	**122.65**	c.df	**122.65**	22.3
3H-MU4-SCC 03	**86.75**	379.50	*	328.41	158.05	**158.05**	129.65	122.65	**122.65**	c.df	**122.65**	41.4
3H-MU4-SFRSCC 01	**103.72**	379.50	*	328.41	158.05	**158.05**	127.45	143.65	**127.45**	c.cf	**127.45**	22.9
3H-MU4-SFRSCC 02	**117.48**	379.50	*	328.41	158.05	**158.05**	127.45	143.65	**127.45**	c.cf	**127.45**	8.5
3H-MU4-SFRSCC 03	**103.37**	379.50	*	328.41	158.05	**158.05**	127.45	143.65	**127.45**	c.cf	**127.45**	23.3
4H-MU4-SFRSCC 01	**110.45**	306.52	*	437.89	210.73	**210.73**	127.45	164.56	**127.45**	c.cf	**127.45**	15.4
4H-MU4-SFRSCC 03	**113.76**	306.52	*	437.89	210.73	**210.73**	127.45	164.56	**127.45**	c.cf	**127.45**	12.0

*- not enough data to predict the $\tau_{xy.u}$ of MU4 laminate.

**- p.cl: connector failure by cleavage; c.df: concrete failure by shear in the dowels plus friction/adhesion; c.cf: concrete cone failure.

6.6   FINAL REMARKS

In this chapter, a deeper investigation was conducted on the mechanical behaviour of connections between concrete and PERFOFRP connectors when subjected to transversal loads (pull-out tests). The experimental program consisted on 24 specimens made with two different GFRP laminates (CSM and MU4), two types of concrete (SCC and SFRSCC) and three different geometries for the connector (without holes, with 3 holes and with 4 holes). The main objective of this investigation was to obtain a better understanding of the proposed connections, evaluating the influence of the studied variables on the initial stiffness, load capacity and ductility of connections. Based on the observed experimental pull-out behaviour of connections, and on the results of the pin-bearing tests (section 4.5), a phenomenological model was proposed to predict the ultimate load capacity of the studied connections.

From the pull-out tests, the following conclusions can be drawn for connections made with materials and geometry similar to the used in this study:

- In general, connections made with CSM PERFOFRP connectors had the load carrying capacity limited by the rupture of the connector in the vicinity of the holes. The post testing inspection of the specimens pointed out that three typical failure lines appeared in the connectors that crossed the connector from the hole edge to the connector bottom edge: two inclined lines at about 45° and one 90° with the horizontal just below the holes. Nonetheless, one of specimens produced with SCC presented a distinct failure mode by shear in the planes of contact between the concrete and the connector (dowel effect + friction/adhesion), what can indicate that this failure mode happens for a load level not much different of the load that leads to the failure mode associated to the rupture of the connector itself.

- Premature ruptures of the concrete block were observed in specimens made with MU4 PERFOFRP connectors. In these specimens, the presence of two different failure patterns were observed: (1) rupture by shear along the interface surfaces between the connector and the concrete block, where prevails the combined effect of shear in the concrete dowels and in the net contact area by friction/adhesion; (2) concrete cone failure, with the formation of a cone type fracture surface with the apex located immediately below the holes and making and angle with the horizontal of approximately 47°.

- The load *versus* slip responses of all tested PERFOFRP–concrete connections were characterized by an initial stiff branch up to the cracking load. After this threshold, the response of the specimens significantly diverged from each other depending on the connection type.

- The use of steel fibre reinforcement in the concrete significantly affected the behaviour of connections that comprised PERFOFRP connectors, increasing the load carrying capacity and the energy absorption capacity of the connections. The load carrying capacity of 3H connections increased 17% in average. For the specimens with 0H, the use steel fibres did not significantly affect the friction/adhesion between the connector and the concrete, as expected.

- The connections with MU4 laminates presented a more ductile response, independently of the type of concrete.

- In average, the ultimate load capacities of connections made by SFRSCC and 3 holes increased 49% when compared with connections made with the same concrete and GFRP laminates without holes. Furthermore, the load capacity of connection with 4 holes was 29% greater than the one of the connection with 3 holes. Furthermore, when the number of holes per length of connector increased (i.e., spacing between holes was reduced), the response of the connection became slightly more ductile up to a slip approximately equal to 1.0 mm, but the response rapidly became more brittle for higher slips.

- When the results obtained in the pin-bearing tests (section 4.5) are taken into consideration it is possible to conclude that, for the geometries and materials used in this investigation, the load capacity of the connectors subjected to pull-out forces is limited by the distance between the hole and the bottom edge of specimen, independently of the composite used.

The proposed phenomenological model considered that the load capacity of the connection can be limited by all the possible failure modes that can occur in the connector itself and also by the different failure modes associated to the rupture of concrete. The validity of the proposed formulae was checked and its capability to predict accurately the failure modes observed in the pull-out experimental program was proved. When the predicted ultimate load capacities of connections were compared to the experimental results, an average error of 19.57% was obtained.

In further studies improvements should be implemented in the proposed model, namely in regard to considering the effect of the presence of multiple aligned holes in the connector or to explicit the effect of the properties of composites used in the connector. Also, the model shall be used to optimize the design of the connectors in terms of geometry and material properties in order to obtain a ductile failure mode at a certain required load level.

Chapter 7

PUSH-OUT TESTS

Along the building service life, the panels are subjected to lateral loads (e.g., wind and seismic loads) that introduce membrane and in-plane shear forces, as well as bending moments and out-of-plane shear forces. Depending on the level of in-plane shear stress transferred, the layers forming the sandwich panel can work as independent members (non-composite), partially-composite or in a full-composite manner. The transference of this stress component in a sandwich panel is schematically illustrated in Figure 1 (herein designated as longitudinal shear). In general, a full-composite action is desirable since it leads to lower stresses and smaller deflections, resulting a better structural performance and cost reductions.

The shear connectors are the elements responsible to transfer shear forces between outer layers. Their types and arrangement (i.e., number, spacing and distribution) must be designed for supporting the longitudinal shear stresses derived from the applied loadings. The design can also be performed to attain a particular level of composite action, for instance, in order to limit the stress level in the concrete layers.

Accordingly, the present chapter intends to analyze the behaviour of PERFOFRP connectors embedded into SFRSCC layers when subjected to longitudinal shear stresses. For this purposes push-out tests on PERFOFRP connectors were conducted by investigating the influence of the following variables: holes in the connector, type of GFRP, and the presence of concrete end-bearing in front of the rib connector. The experimental program was carefully planned in order to access the parcels of resisting mechanisms corresponding to the concrete

dowel action, frictional resistance and concrete end-bearing effect. In addition to the experimental work, an equation was proposed to predict the shear resistance of PERFOFRP when connected to SFRSCC layer.

7.1 ANALYTICAL MODELS TO PREDICT THE STRENGTH OF PERFOBOND CONNECTORS

In metallic Perfobond shear connectors, the load capacity results from the following mechanisms: 1) concrete end-bearing effect; 2) effect of transverse reinforcement (i.e., bars or fibres) in the rib holes, if present; 3) concrete dowel action; and 4) the tensile strength of the concrete layer along the Perfobond alignment (Oguejiofor and Hosain, 1994, Oguejiofor and Hosain, 1997, Verissimo, 2007, Vianna *et al.*, 2009, Ahn *et al.*, 2010). The three last effects are present when the connector is loaded in both the longitudinal and transversal directions, while the concrete end-bearing effect develops only when the connector works throughout the longitudinal direction, and when there is a concrete end-bearing zone (i.e., when discontinuous connectors are employed). In the specific case of SFRSCC the effect of transverse reinforcement can be replaced by the contribution of the steel fibres with a convenient adjustment.

In literature, there are some equations for predicting the shear resistance of Perfobond shear connectors longitudinally loaded. In this framework, Oguejiofor and Hosain (1997) proposed Eq. (53) to estimate the shear resistance of the connector, Q_{lo} [N], which was derived from regression analysis performed on the results obtained in experimental and numerical studies:

$$Q_{lo} = \beta_1 \cdot h \cdot t \cdot f_{ck} + \beta_2 \cdot A_{tr} \cdot f_y + \beta_3 \cdot n_h \cdot D_h^2 \cdot \sqrt{f_{ck}} + \beta_4 \cdot A_{cc} \cdot \sqrt{f_{ck}} \qquad (53)$$

The parcels of this equation simulate the contribution of the aforementioned four mechanisms, where h [mm] and t [mm] are the height and the thickness of connector, respectively, f_{ck} [MPa] is the concrete compressive strength, A_{tr} [mm^2] is the area of the transverse reinforcement, f_y [MPa] is the steel yielding strength, n_h [-] is the number of holes in the rib, D_h [mm] is the hole's diameter, A_{cc} [mm^2] is the shear area of concrete per connector and β_i are the coefficients obtained by regression analysis that best fitted the available experimental and numerical data. Ahn *et al.* (2010) have recently adopted a similar formulation, only differing on the values of β_i factors, since these were computed by considering the

experimental data obtained by these authors. The constants β_i obtained by Oguejiofor and Hosain (1997) and Ahn *et al.* (2010) are presented together in Table 36.

Eq. (53) does not consider the frictional resistance. To take into account the frictional resistance, Sara and Bahram (2002) proposed Eq. (54):

$$Q_{lo} = \alpha_1 \cdot b \cdot h_{ecs} \cdot \sqrt{f_{ck}} + \alpha_2 \cdot A_{tr} \cdot f_y + \alpha_3 \cdot n_h \cdot D_h{}^2 \cdot \sqrt{f_{ck}} + \alpha_4 \cdot b_f \cdot L_c \qquad (54)$$

where b_f [mm] is the width of the steel beam flange embedded into the concrete, and L_c [mm] is the contact length between the concrete layer and the steel beam flange. The same authors also proposed a slight modification on the term related to the end-bearing effect, first term of Eq. (54), that is now computed as function of the square root of the concrete strength and depends of b [mm] and h_{ecs} [mm], which are the thickness of the concrete layer and the distance between the end of the Perfobond rib and the end of the concrete layer, respectively. The parameters α_i included in Eq. (54), and listed in Table 36, were obtained from regression analysis by best fitting the experimental data performed by the authors.

Table 36: Parameters β_i and α_i of Eq. (53) and Eq. (54) (Oguejiofor and Hosain, 1997, Sara and Bahram, 2002, Ahn *et al.*, 2010).

Eq. (53)				
	Parameters:			
	β_1	β_2	β_3	β_4
Oguejiofor and Hosain (1997)	4.470	0.900	3.300	0.010
Ahn *et al.* (2010)	3.140	1.210	2.977	0.000
Q[N], h[mm], t[mm], f_c[MPa], A_{tr}[mm^2], f_y[MPa], n[-], D[mm], A_{cc}[mm^2].				

Eq. (54)				
	Parameters:			
	α_1	α_2	α_3	α_4
Sara and Bahram (2002)	0.747	0.900	1.304	0.413
Q[N], b[mm], h_{ecs}[mm], f_c[MPa], A_{tr}[mm^2], f_y[MPa], n[un.], D[mm], b_f[mm], L_c[mm].				

7.2   EXPERIMENTAL PROGRAM

Sixteen push-out tests were performed in the Laboratory of the Structural Division of the University of Minho. The tests aimed to provide information concerning the general behaviour and suitability for practical applications of PERFOFRP connectors, recently proposed for sandwich panels. In particular, the parameters studied were: the influence of holes in the GFRP, the type of the GFRP used in the connector, and the confinement provided by the presence of concrete in front of the rib connector. These parameters were selected due to their relevance for the performance of this type of connection. In fact, the presence of the holes contributes for the concrete dowel effect, the concrete in front of the connector for the end-bearing effect, and the properties of the GFRP for the tensile load level capable to be applied.

7.2.1   Push-out specimens and material properties

The specimens were produced in the Civitest company based on the standard push-out test recommended in EN 1994-1-1 (1994). The dimensions and arrangement of the push-out specimens were chosen in order to be representative of the connections in the sandwich panel previously proposed (see Chapter 5). The geometry of the specimens of different series was identical in order to distinguish the differences introduced by the aforementioned variables of the test program on the mechanical response of the connections. Each specimen consisted of two identical parts that were produced simultaneously and cast in the horizontal position, and later coupled (see Figure 151). Each part is composed of a SFRSCC layer (of the same thickness of the outer SFRSCC layers adopted in the sandwich panel) with an embedded PERFOFRP connector centered in its width. This procedure was adopted for simulating better the real manufacturing conditions of sandwich panels. The coupling was made with both halves in vertical position and two UPN 140 steel profiles, 350 mm long, each, positioned on the outside (see Figure 152). Twelve M8 bolts evenly spaced at 50 mm in the vertical direction were adopted to join the two halves of the GFRP connector. For this purpose 6 holes with approximately 9 mm diameter were drilled in each connector prior to joining. Another role of UPN 140 profiles was to transmit the load from the test machine to the GFRP connector. The bolts were firmly tightened in order the load be mainly transferred from the UPN 140 steel profiles to the GFRP connectors by shear friction between the profiles' webs and the GFRP laminate, thus avoiding local damage in the laminate that could be occurred by compressive stress concentration in the bolt/laminate contact. To increase the friction between

the UPN 140 and the GFRP, a rough surface finishing was done in the contact surfaces of both steel profiles. The UPN 140 profile was aligned with the GFRP connector at 50 mm above the top surface of the SFRSCC layers. This arrangement was adopted for an appropriate load application by the testing machine, and to guarantee a maximum SFRSCC/laminate slip of approximately 50 mm during this loading process. The layout of specimens used in the experimental program is represented in Figure 152. All the rib shear connectors used in this study consisted of a GFRP plate with the dimensions 125 mm $\times$ 350 mm, as represented in Figure 152(d). To evaluate the concrete dowel action, two different types of connectors were used: without holes (0H) and with holes (3H). In the case of PERFOFRP connectors (i.e., 3H), three uniformly spaced aligned holes of 30 mm diameter (D) were drilled, with a centre-to-centre distance between holes of 2.5D (75 mm). The spacing of the holes was based on the studies made by other researchers with Perfobond connectors (Oguejiofor and Hosain, 1994, Kim and Jeong, 2006), where a spacing between 2.0D and 2.5D is recommended for the attainment of the maximum shear resistance of the connection. The diameter of holes and hole spacing assumed in this study correspond to the same values adopted for the 3H specimens tested transversally in the Chapter 6. In order to keep the same configuration adopted in previous works, the nominal concrete cover thickness was kept equal to 15 mm. This cover thickness was guaranteed using plastic spacers, commonly employed for assuring aimed concrete cover thickness to steel rebars (see Figure 151(c)).
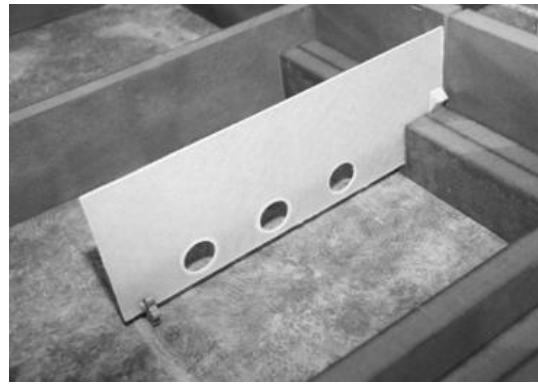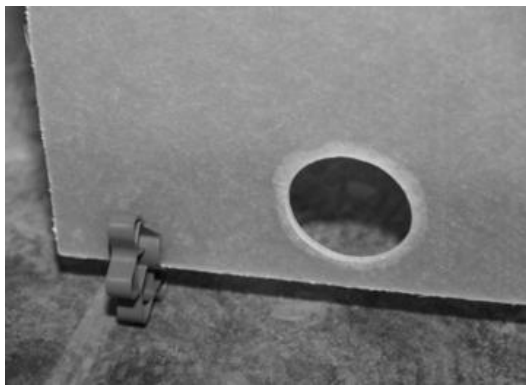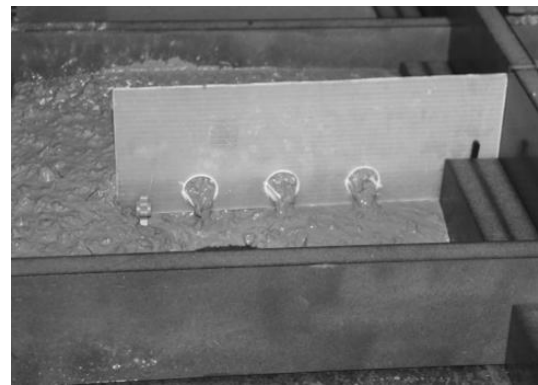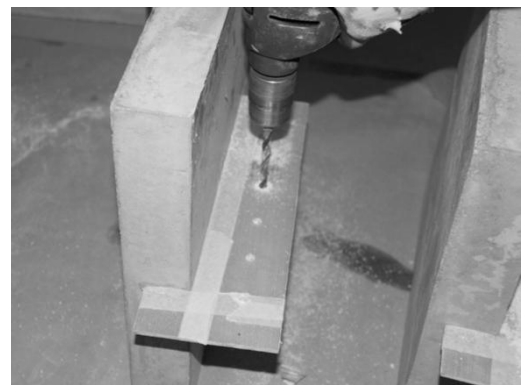
Figure 151: Fabrication of specimens used in push-out tests: (a) overall view; (b) connector ready for casting; (c) detail of plastic spacer; (d) casting one part of the specimen; (e) preparing each half part of specimens to be coupled; (f) detail of specimen ready to be tested.

The dimensions of SFRSCC layers used were 60 mm × 400 mm × 400 mm. The thickness of 60 mm was chosen based on the parametric studies presented in Chapter 5, where it was verified that it guarantees sufficient space for the anchoring of the PERFOFRP connector and assures the structural stability of the sandwich panels.

The other dimensions were defined considering the stress distribution in the concrete layers. It was important to guarantee that the failure modes associated with the GFRP connector could occurr without a premature concrete failure. Due to volume limitation of the mixer, the 16 specimens were produced in three different castings, using always the same concrete constituent materials, composition and manufacturing process.

To evaluate the end-bearing effect, specimens without concrete in front of the rib connector were fabricated. Hereinafter, these specimens will be labeled as WO, while the specimens that consider the end-bearing effect will be labeled as EB. The WO specimens were fabricated by sawing the concrete positioned in front of the connector, creating a groove with a thickness equal to 10 mm that extends from the connector end to the extremity of the layer. The geometry details of WO and EB specimens are given in Figure 152.

Push-out tests were performed with SFRSCC A from casting 4 (see Table 6). Two types of GFRP were used on the production of connections: CSM 1 and MU4 (see Table 19). Further details about the GFRPs can be seen in Chapter 4.
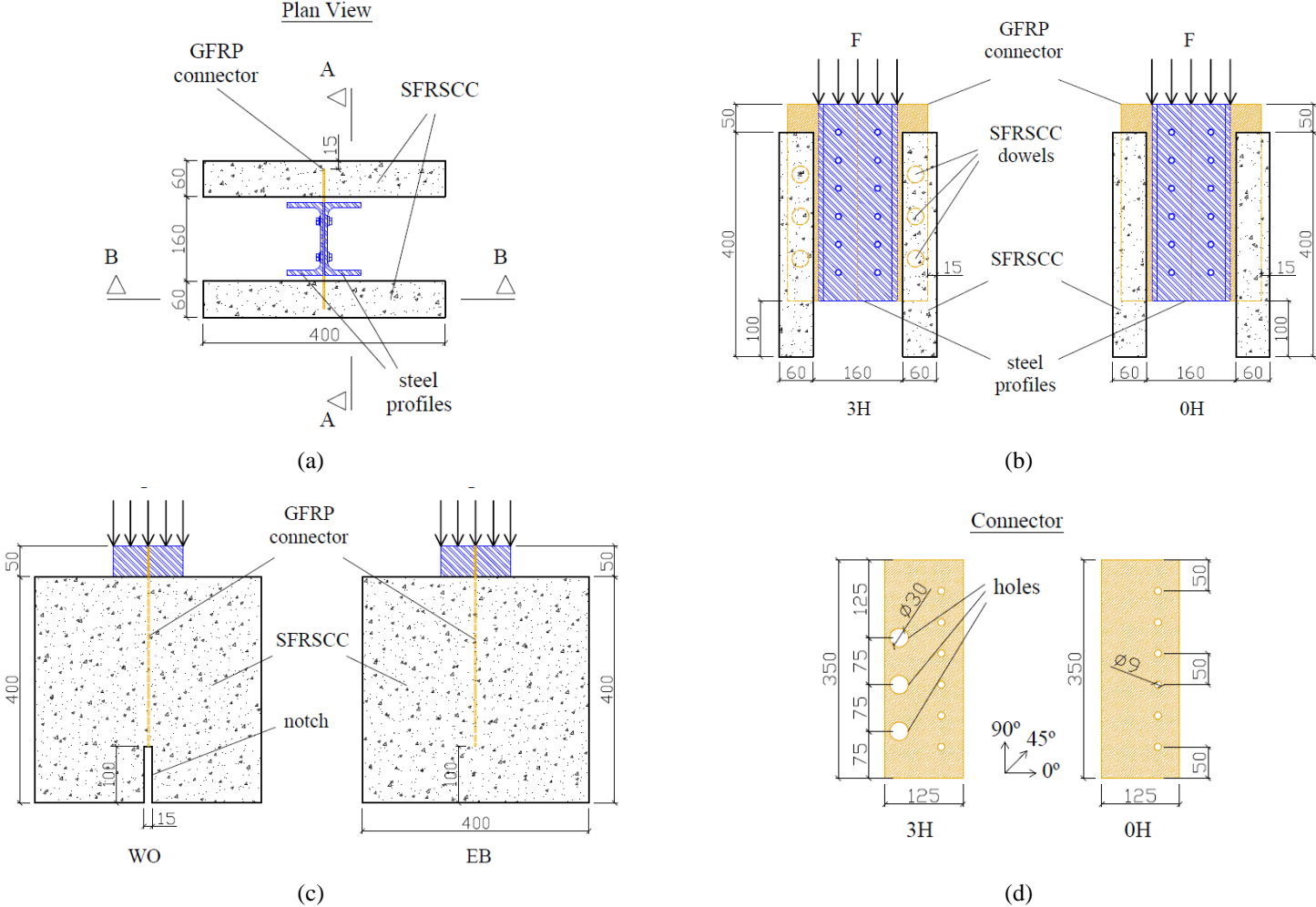
Figure 152: Layout of specimens used in push-out tests: (a) plan view; (b) section AA - 3H and 0H specimens; (c) section BB in WO and EB specimens; (d) lateral view of GFRP connectors used in 3H and 0H specimens (dimensions in millimeter).

Two identical specimens for each series were tested. The specimens were labeled in the format "XH-YYY-ZZ", where "X" refers to the number of holes in the connector (i.e., 0H or 3H), "YYY" indicates the type of GFRP laminate (i.e., CSM or MU4) and "ZZ" refers to the use, or not, of the end-bearing effect (i.e., WO or EB). The specimens making part of this experimental program are listed in Table 37.

Table 37: Push-out experimental program.

Number of holes in GFRP	Type of GFRP	End-bearing effect	Specimen	Number of specimens
0H	CSM	WO	0H-CSM-WO	2
0H	CSM	EB	0H-CSM-EB	2
0H	MU4	WO	0H-MU4-WO	2
0H	MU4	EB	0H-MU4-EB	2
3H	CSM	WO	3H-CSM-WO	2
3H	CSM	EB	3H-CSM-EB	2
3H	MU4	WO	3H-MU4-WO	2
3H	MU4	EB	3H-MU4-EB	2

7.2.2 Experimental procedure

The typical test setup is shown in Figure 153. Prior the load application, the concrete layers were braced laterally at their base using a frame that was firmly bolted. The bracing system was based on solutions adopted in previous works (Valente and Cruz, 2009, Ahn *et al.*, 2010) in order to prevent lateral movement, while permits free motion in the vertical direction. A steel plate was used in the top of the U steel profiles to ensure a uniform load application.
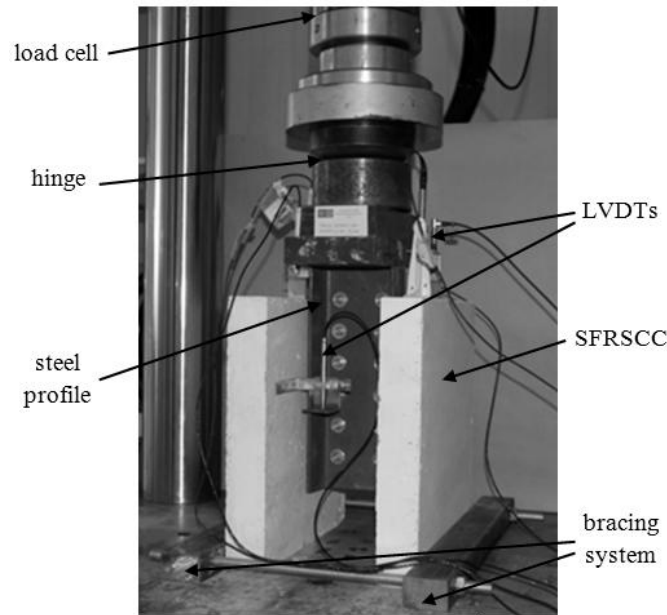
Figure 153: Push-out test setup.

The specimens were loaded in two stages, according to EN 1994-1-1 (1994). At the first stage, a cyclic sinusoidal loading of 10 cycles at a frequency of 0.01 Hz and amplitude of 5 kN was applied in the specimen. This cyclic loading stage intended to simulate the serviceability state of the actual structural element when inserted in a real building. In the second stage, a vertical monotonic compressive load was applied in displacement control with a rate of 0.10 mm/min. The load was applied to the specimens using a servo-controlled universal testing machine. A hinge was used between the piston of the machine's actuator and the specimen to accommodate any geometric irregularity.

7.2.3 Instrumentation

Figure 154 shows a schematic representation of the instrumentation layout adopted in push-out tests. Six Linear Variable Differential Transformers (LVDTs) were installed in the specimens to measure the slip between the GFRP connector and the SFRSCC layer. LVDTs A and B registered directly the relative displacement between the GFRP connector and the SFRSCC layer. These LVDTs were located on top of the specimen since this was the only accessible region of the connector, not covered by UPN 140 profiles. LVDTs E and F measured the relative displacement between UPN 140 profiles and the SFRSCC layers, in the mid height of the specimens. In order to obtain the slip between GFRP connector and the SFRSCC layer, the corresponding displacements between the GFRP connector and the UPN 140 profile, registered by LVDTs C and D, were subtracted from the data registered by

LVDTs E and F (it was assumed negligible the axial deformation of the UPN profiles, which is well acceptable). LVDTs A, C and E were related to the left SFRSCC layer, while the LVDTs B, D and F measured displacements related to the right SFRSCC layer. For instance, the slip corresponding to the left SFRSCC layer was obtained directly from the data registered by LVDT A (slip at loaded end) and subtracting from the difference between the measurements in the LVDT E and C (slip at mid height of the specimen). All the used LVDTs have a stroke range equal to ±10 mm.
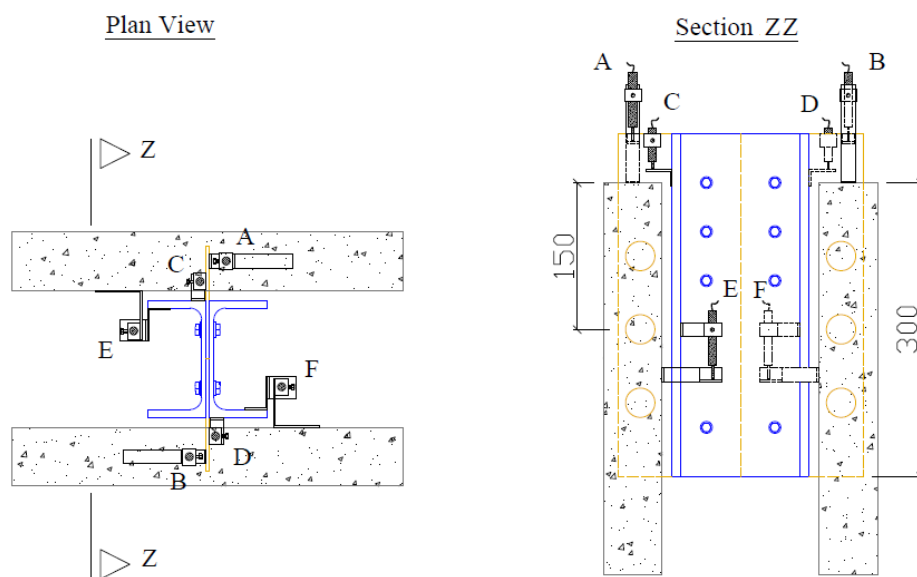
Figure 154: Schematic representation of instrumentation adopted in push-out tests (dimensions in millimeter).

All instruments were connected in a data acquisition system. The imposed displacement and the corresponding load were recorded as outputs of the testing machine. The later was registered by a 500 kN load cell arranged in parallel to the loading system. The acquisition system was set to continuously save the raw data to a file at 2 Hz. Load and displacements were continuously measured until the load value drops at least 20% of the maximum applied load in the post-peak stage.

7.3   EXPERIMENTAL RESULTS

7.3.1   Failure mechanisms

In general, the specimen's failure has initiated by the formation of longitudinal splitting crack in the SFRSCC layer, almost coinciding with the laminate plane, as shown schematically in

Figure 155. This vertical crack was first observed in the lower part of concrete layer, near the bottom extremity of the connector. Then, it moved towards the top part of the SFRSCC layer, by increasing its width with the applied load. In some specimens additional longitudinal cracks, parallel to the main crack, were also observed.

In the specimens comprising MU4 connectors with end-bearing effect (EB), other cracks were also observed in front of the rib connectors (Figure 155(b)). These cracks appeared in a later stage, both in the top and bottom zones of the layer, branching inclined from the inferior extremity of the connector towards the bottom surface of SFRSCC layer, and are associated to the concrete crushing (see Figure 155(b)). The crushing failure of SFRSCC layer was not observed in the CSM-EB connectors. In these specimens, the load capacity was limited by the rupture of the GFRP connectors. In the CSM-WO, only vertical cracks were observed in the SFRSCC layers.

(a)
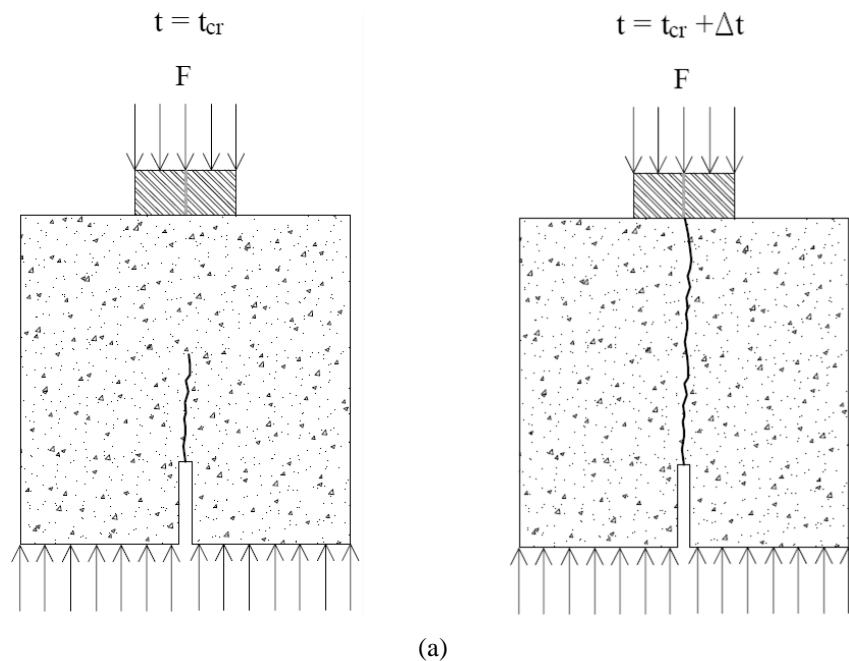
Figure 155: Typical evolution of cracking in the SFRSCC layers: (a) WO specimens

(b)
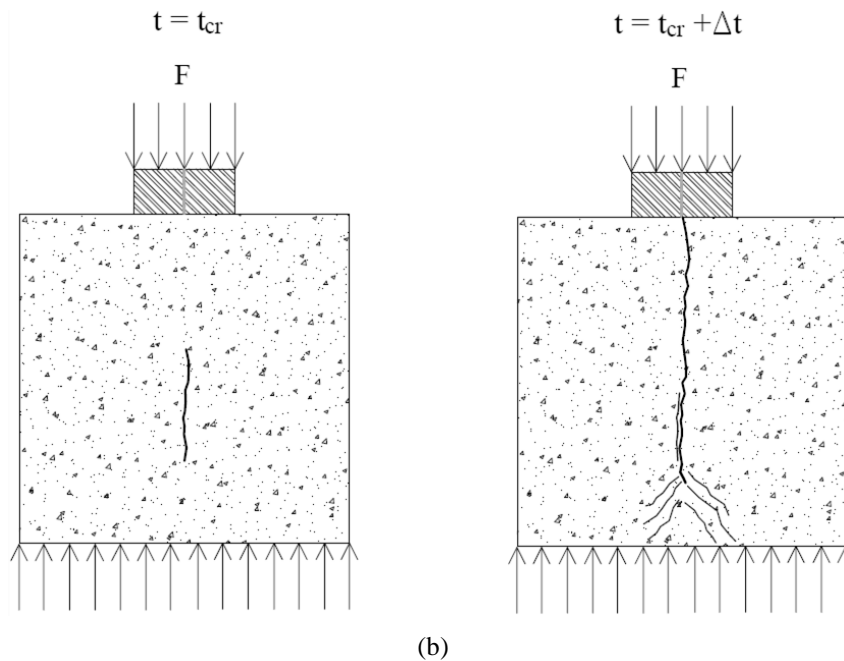
Figure 155: Typical evolution of cracking in the SFRSCC layers:(b) 3H EB specimens.

Figure 156 presents the typical final aspect of specimens' components after they have been tested and dismantled for the extraction of the GFRP connectors. Different failure mechanisms have occurred due to the presence, or not, of the concrete end-bearing effect, the existence, or not, of holes in the connector, and also the type of GFRP. Specimens comprising PERFOFRP connectors (3H) and without the end-bearing effect (Figure 9b, 9c) presented a failure mechanism associated to the shear failure of concrete dowels crossing the holes. In general, the PERFOFRP connectors were intact, independently of the type of GFRP used for the connector. Exception has occurred in the connectors of specimen 3H-CSM-WO 02, where a failure associated to the rupture of the connector between the holes was observed (see Figure 156(e)). In fact, in the tests with specimens WO, the displacement of the connector always made it appear in the notched section (see Figure 156(b)). Furthermore, some portion of SFRSCC generally remained in the holes at the end of tests with 3H-MU4-WO specimens. This SFRSCC was not crushed, which indicates that shear failure occurred in the concrete dowels.
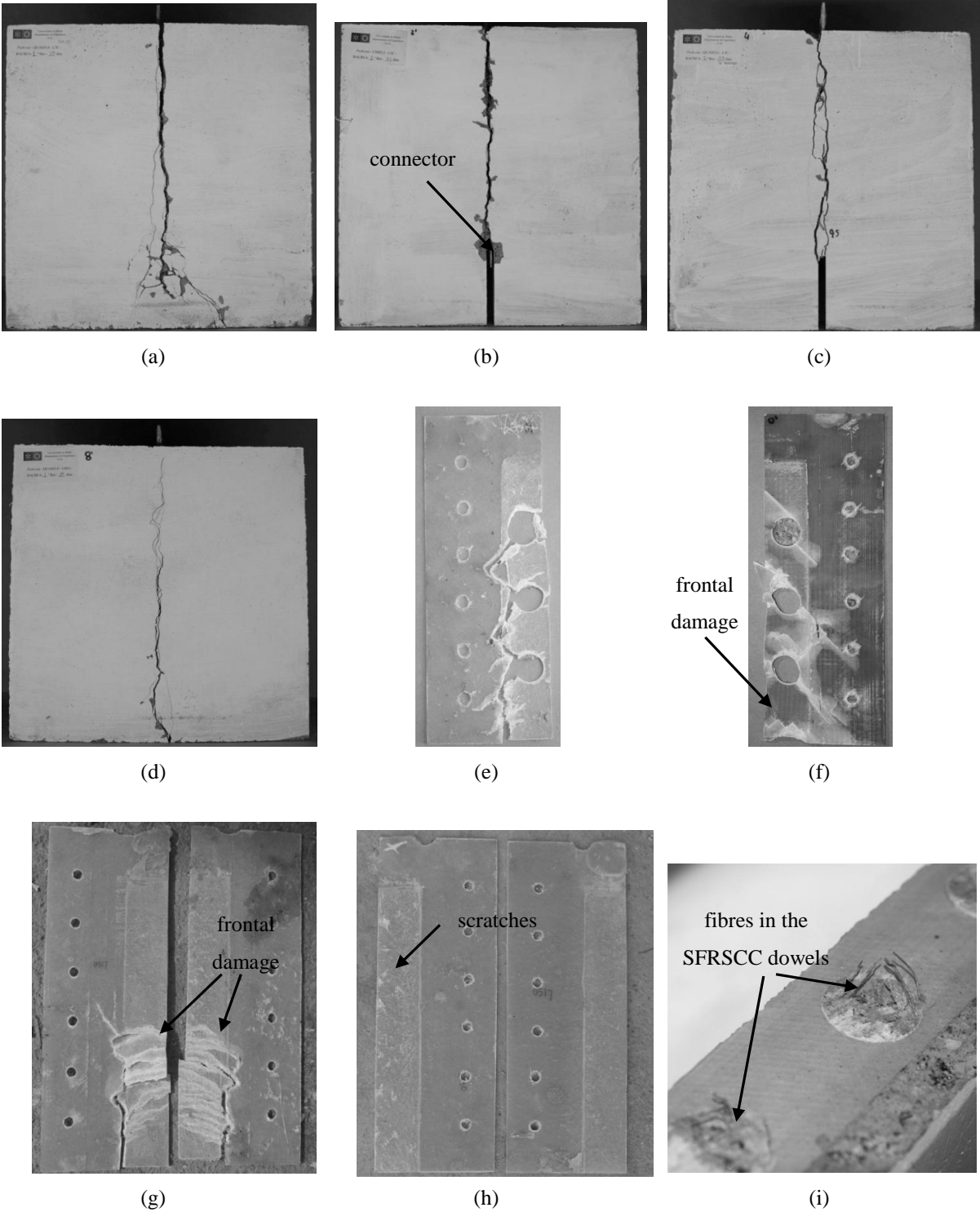
Figure 156: Final aspect of specimens after failure: (a) SFRSCC layer of 3H-MU4-EB; (b) SFRSCC layer of 3H-CSM-WO; (c) SFRSCC layer of 3H-MU4-WO; (d) SFRSCC layer of 0H-MU4-EB; (e) GFRP connector of 3H-CSM-WO; (f) GFRP connector of 3H-MU4-EB; (g) GFRP connector of 0H-CSM-EB; (h) GFRP connector of 0H-CSM-WO; (i) fibres in the SFRSCC dowels.

The GFRP connectors without holes and without concrete end-bearing effect (i.e., 0H-CSM-WO and 0H-MU4-WO) presented only superficial scratches (see Figure 156(h)). In the other hand, all the connectors with end-bearing effect (EB) presented some distortion in their lowest part, as shown in Figure 156(g). Similar failure mechanisms were observed in the specimens with connectors 3H-EB (see Figure 156(f)). However, in these specimens, the connectors also presented damage in the nearby of the holes (see Figure 156(f))., particularly in the case of 3H-CSM, where a shear rupture of GFRP has occurred. A main crack in the connector appeared aligned and in nearby of the interface between the SFRSCC layer and the UPN 140 steel profile. This crack run roughly along all the length of connector and led to a complete separation between the part of the connector embedded into the SFRSCC and the part attached to the steel profile (see Figure 156(e)).

Steel fibres were found in concrete dowels of all specimens comprising PERFOFRP connectors (see Figure 156(i)). The average and standard deviation associated with the number of steel fibres per hole/dowel were equal to 5.3 and 2.6, respectively.

7.3.2 Load-slip behaviour and load capacity

For some tests, it was observed that the top part of the GFRP connectors, where LVDTs A and B were positioned, presented some rotation. This rotation occurred in the plane of the connector towards the center of the specimen. It took place in the initial stage of test, probably due to the length of connector that was not embedded in the SFRSCC layer. This behaviour was more visible in tests with specimens comprising CSM connectors, probably due to their lower elastic modulus and thickness. The relative displacements between the GFRP connectors and the UPN 140 steel profiles were very small in all specimens. In fact, after the tests the connector surface in contact with the UPN 140 profiles shows no signal of scratching, indicating that no slippage occurred between both materials. Considering this, the measurements of LVDTs A and B were disregarded. Thus, the load *versus* slip response was established considering the average value computed from the subtraction between LVDT E and LVDT C and the subtraction between LVDT F and LVDT D.

Figure 157 displays the average load *versus* slip curves for each push-out specimen. These responses were determined averaging the two slip values corresponding to each load level. The load presented in the charts of Figure 157 corresponds to the load registered in the push-out tests divided by the number of similar loaded connectors in the specimen (i.e., two, for the tested specimens).

Until the load corresponding to the first crack has been reached the responses were very stiff . From this point on, the responses and the mechanisms that conditioned failure varied, depending on the type of connection tested. Nonetheless, in general, the decrease of load capacity was slow, and large slip values were measured, especially for EB specimens. In comparison to the response reported in the literature for Perfobond connectors (Valente and Cruz, 2009, Ahn *et al.*, 2010), in general, the connections consisting of PERFOFRP connectors presented a less ductile response.
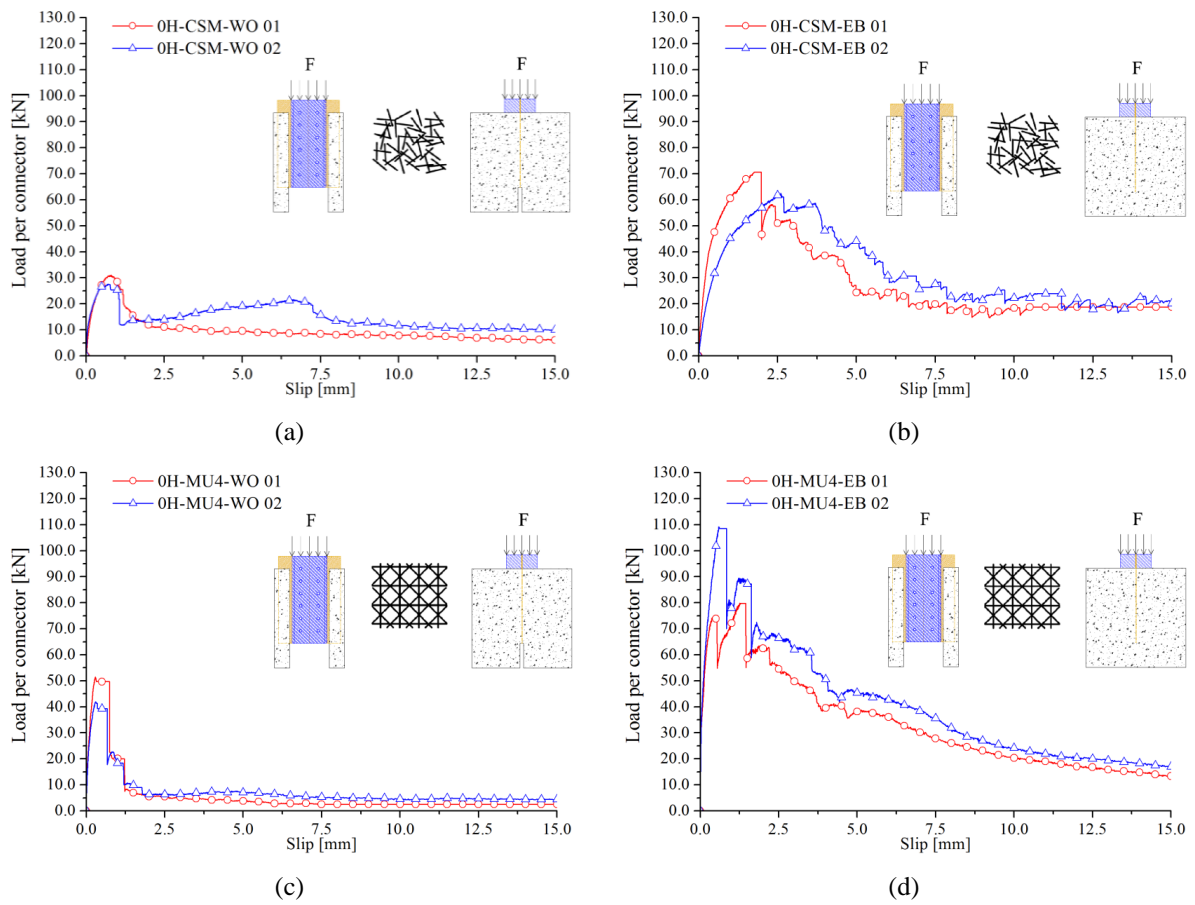
Figure 157: Load slip curves for: (a) 0H-CSM-WO; (b) 0H-CSM-EB; (c) 0H-MU4-WO; (d) 0H-MU4-EB.
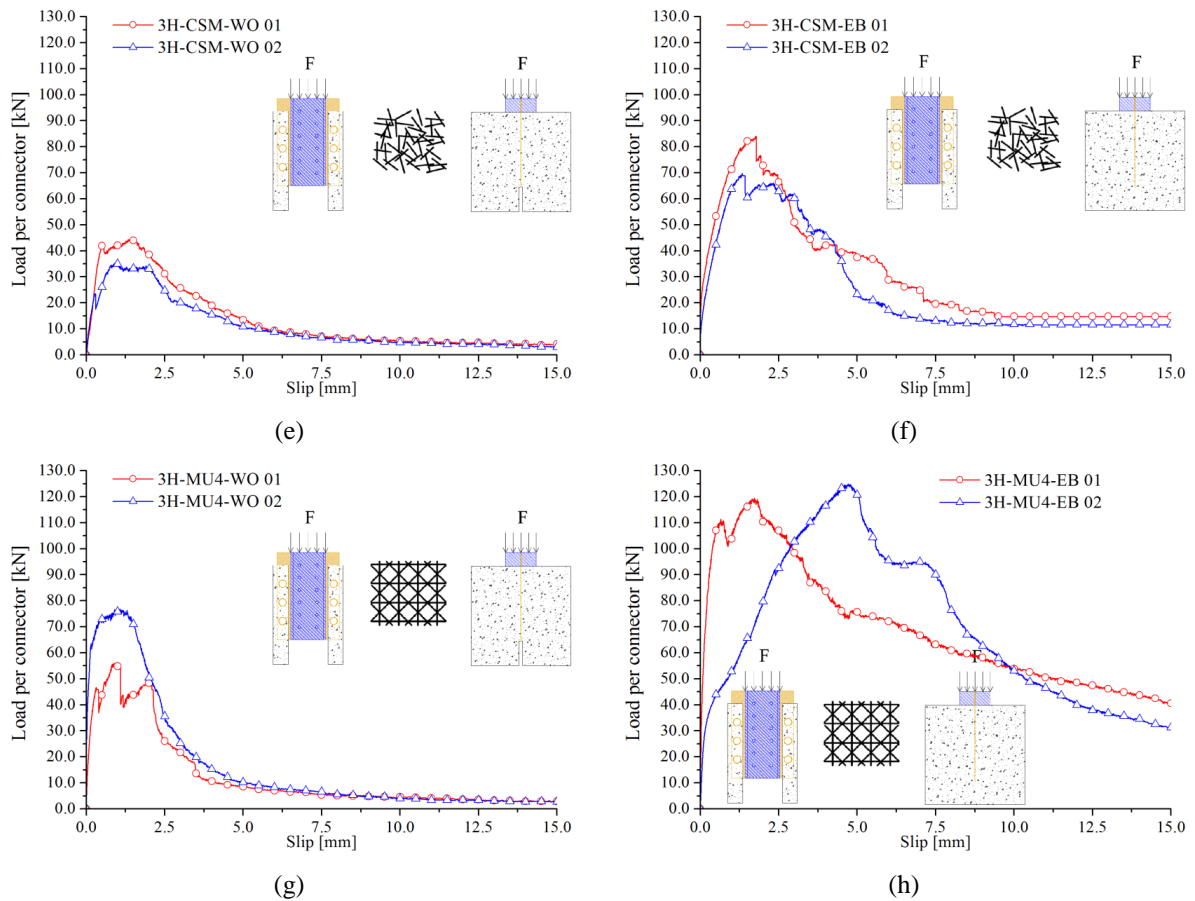
Figure 157: Load slip curves for: (e) 3H-CSM-WO; (f) 3H-CSM-EB; (g) 3H-MU4-WO and (h) 3H-MU4-EB.

Table 38 presents for each specimen: the load per connector corresponding to the peak ($Q_{lo.u}$), the corresponding slip ($s_{lo.u}$), the elastic slip corresponding to a load equal to $90\% \cdot Q_{lo.u}$ ($s_{el.90}$), the plastic slip for load $90\% \cdot Q_{lo.u}$ ($s_{pl.90}$) and the total slip for load $90\% \cdot Q_{lo.u.}$ ($s_{to.90}$). The aforementioned paramaters are explained in the following paragraphs. Furthermore, Table 38 shows the characteristic load capacity ($Q_{lo.k}$) and the characteristic slip ($s_{lo.k}$) for the group of identical specimens. $s_{lo.u}$, $s_{el.90}$, $s_{pl.90}$, and $s_{to.90}$ are ductility indicators established to evaluate the response of tested connections.

In comparison to the procedures indicated by EN 1994-1-1 (1994), the peculiarities of the analyses performed in this work were: 1) $Q_{lo.k}$ and $s_{lo.k}$ were obtained averaging the values computed for individual responses, while in EN 1994-1-1 (1994) the use of minimum values obtained for the group is recommended; 2) $s_{el.90}$, $s_{pl.90}$ and $s_{to.90}$ were obtained for a load corresponding to 90% of the maximum load registered for the test with the corresponding specimen, whilst the EN 1994-1-1 (1994) recommends to determine $s_{el.90}$, $s_{pl.90}$ and $s_{to.90}$ for a load equal to $Q_{lo.k}$ obtained for the group. These options were adopted due to the higher

variability on the obtained results when compared to the variability of the results registered in push-out tests with steel connectors.

Table 38: Experimental results corresponding to push-out tests.

Specimen Ref.	$Q_{lo.u}$			$s_{lo.u}$			$s_{el.90}$			$s_{pl.90}$			$s_{to.90}$			$Q_{lo.k}$	s_k
	Value	Avg	CoV	Value	Avg	CoV	Value	Avg	CoV	Value	Avg	CoV	Value	Avg	CoV		
	[kN]		[%]	[mm]		[%]	[mm]		[%]	[mm]		[%]	[mm]		[%]	[kN]	[mm]
0H-CSM-WO 01	31			0.8			0.52			0.5			1.02				
0H-CSM-WO 02	27.7	29.4	8	0.71	0.75	9	0.4	0.46	18	0.64	0.57	17	1.04	1.03	2	26.4	0.51
0H-CSM-EB 01	70.7			1.99			1.23			0.76			1.99				
0H-CSM-EB 02	62.5	66.6	9	2.61	2.3	19	1.89	1.56	30	1.9	1.33	60	3.78	2.88	44	59.9	1.19
0H-MU4-WO 01	51.5			0.29			0.22			0.53			0.75				
0H-MU4-WO 02	42	46.8	14	0.31	0.3	5	0.21	0.22	3	0.46	0.49	9	0.67	0.71	7	42.1	0.44
0H-MU4-EB 01	79.9			1.26			0.32			1.14			1.46				
0H-MU4-EB 02	109.3	94.6	22	0.59	0.92	52	0.46	0.39	25	0.38	0.76	70	0.84	1.15	38	85.1	0.68
3H-CSM-WO 01	44.8			1.41			0.46			1.4			1.86				
3H-CSM-WO 02	35.4	40.1	17	0.93	1.17	29	0.68	0.57	27	1.43	1.41	2	2.11	1.98	9	36.1	1.27
3H-CSM-EB 01	84.1			1.79			1.18			0.76			1.94				
3H-CSM-EB 02	69.7	76.9	13	1.34	1.56	20	0.96	1.07	15	0.47	0.62	33	1.43	1.68	21	69.2	0.55
3H-MU4-WO 01	56.1			0.88			0.71			0.39			1.1				
3H-MU4-WO 02	76.9	66.5	22	0.96	0.92	6	0.32	0.51	54	1.23	0.81	74	1.55	1.32	24	59.8	0.73
3H-MU4-EB 01	119.5			1.73			0.52			0.25			0.77				
3H-MU4-EB 02	124.9	122.2	3	4.71	3.22	66	3.69	2.1	107	1.46	0.86	100	5.15	2.96	105	110	0.77

A schematic representation of computing of $s_{lo.u}$, $s_{el.90}$, $s_{pl.90}$, and $s_{to.90}$ is presented in Figure 158. These properties were computed based on the procedures adopted by Valente and Cruz (2009) and on the recommendations of EN 1994-1-1 (1994). $Q_{lo.k}$ was considered 90% of average of the maximum loads obtained for a group of identical specimens:

$$Q_{lo.k} = 90\% \cdot \frac{\sum\limits_{i=1}^{n} Q_{lo.u.i}}{n} \tag{55}$$

where n is the number of identical specimens in each group.

The elastic slip value ($s_{el.90}$) corresponds to the slip value when $Q = 90\% \cdot Q_{lo.u}$ in the branch before the peak load (see Figure 158). From this point forward, all the slip was considered plastic. The plastic slip value ($s_{pl.90}$) was determined as the plastic displacement correspondent to $Q = 90\% \cdot Q_{lo.u}$. The total slip ($s_{to.90}$) is equal to the sum of $s_{el.90}$ and $s_{pl.90}$, corresponding to the total slip up to a load equal to $90\% \cdot Q_{lo.u,}$ attained in the pos-peak branch of the load-slip curve. The characteristic slip value ($s_{lo.k}$) was assumed as 90% of the average plastic slips for a group of identical specimens:

$$s_{lo.k} = 90\% \cdot \frac{\sum\limits_{i=1}^{n} s_{pl.90.i}}{n} \tag{56}$$

where n is the number of identical specimens of group.
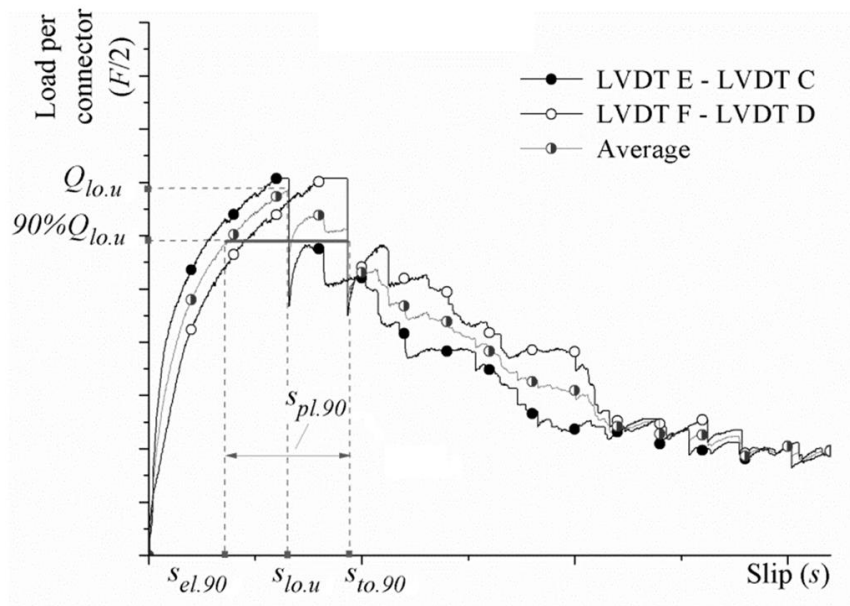
Figure 158: Schematic representation of computing representative loads and slips.

Box plots and scatter diagrams corresponding to the experimental data obtained are depicted in Figure 159, including the mean, median, 25 percentile, 75 percentile, minimum and maximum values obtained for each level of the studied variables. In this figure the experimental data and the normal distribution are illustrated by green triangles and red dashed lines, respectively.

The curves presented in Figure 159, in general, present a high variability associated with the results obtained within each group. Values of coefficient of variation of about 26%, 23% and 20% were obtained for $Q_{lo.u}$ related to the groups 3H-MU4-WO, 0H-MU4-EB and 3H-CSM-WO, respectively. Similar values of coefficient of variation, of around 24%, were registered by Naito *et al.* (2012) for push-out tests carried out with other types of GFRP connectors.
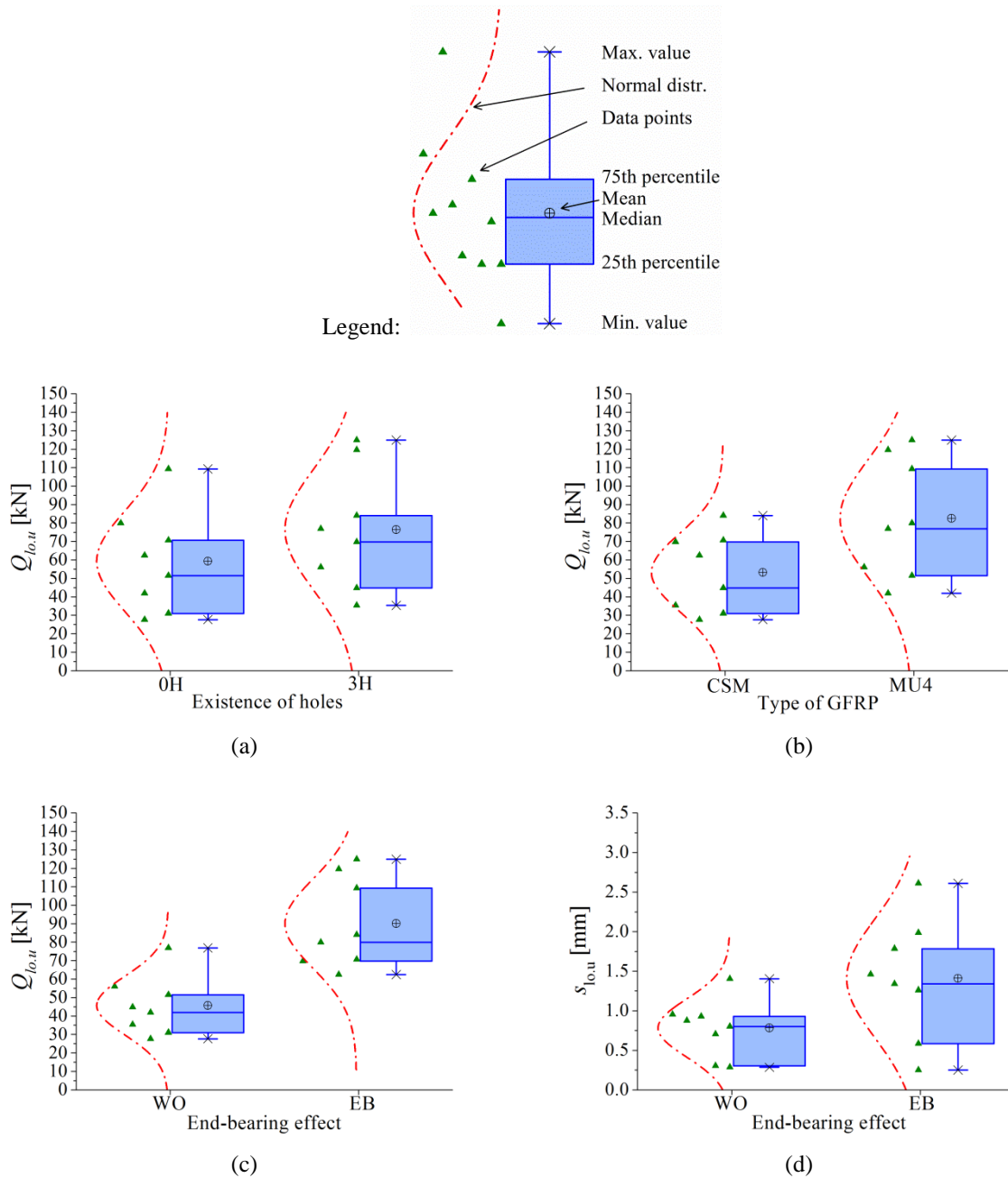
Figure 159: Box plots and scatter diagrams corresponding to the experimental data. (a) $Q_{lo.u}$ *versus* (non-)existence of holes; (b) $Q_{lo.u}$ *versus* type of GFRP; (c) $Q_{lo.u}$ *versus* (non-)presence of end-bearing effect and (c) $s_{lo.u}$ *versus* (non-)presence of end-bearing effect.

To obtain higher reliability in the interpretation of the experimental results, analysis of variance (ANOVA) and a multiple comparison method (Montgomery, 2009) were conducted with test results. The existence of holes, type of GFRP, and presence of concrete end-bearing were the considered factors. The analyses were developed to determine whether differences between fixed factors, two-way interactions and three-way interactions significantly affected $Q_{lo,u}$, $s_{lo,u}$ and $s_{pl,90}$. The interactions were studied to evaluate if the effect of one independent

variable (i.e., existence of holes, type of GFRP and end-bearing effect) depends on the level of the other independent variables. Due to the qualitative nature of the factors, dummy variables were employed, as follows: 1.0 for 0H, 2.0 for 3H; 1.0 for CSM, 2.0 for MU4 laminate and 1.0 for WO, 2.0 for EB. The Fisher´s least significant difference (LSD) method was adopted to compare all pairs of means and identify which means were different. Details about the statistical methods adopted can be found elsewhere (Montgomery, 2009). Table 39 summarizes the results of the statistical analyses. Two factor interactions of variables studied are given in Figure 160.
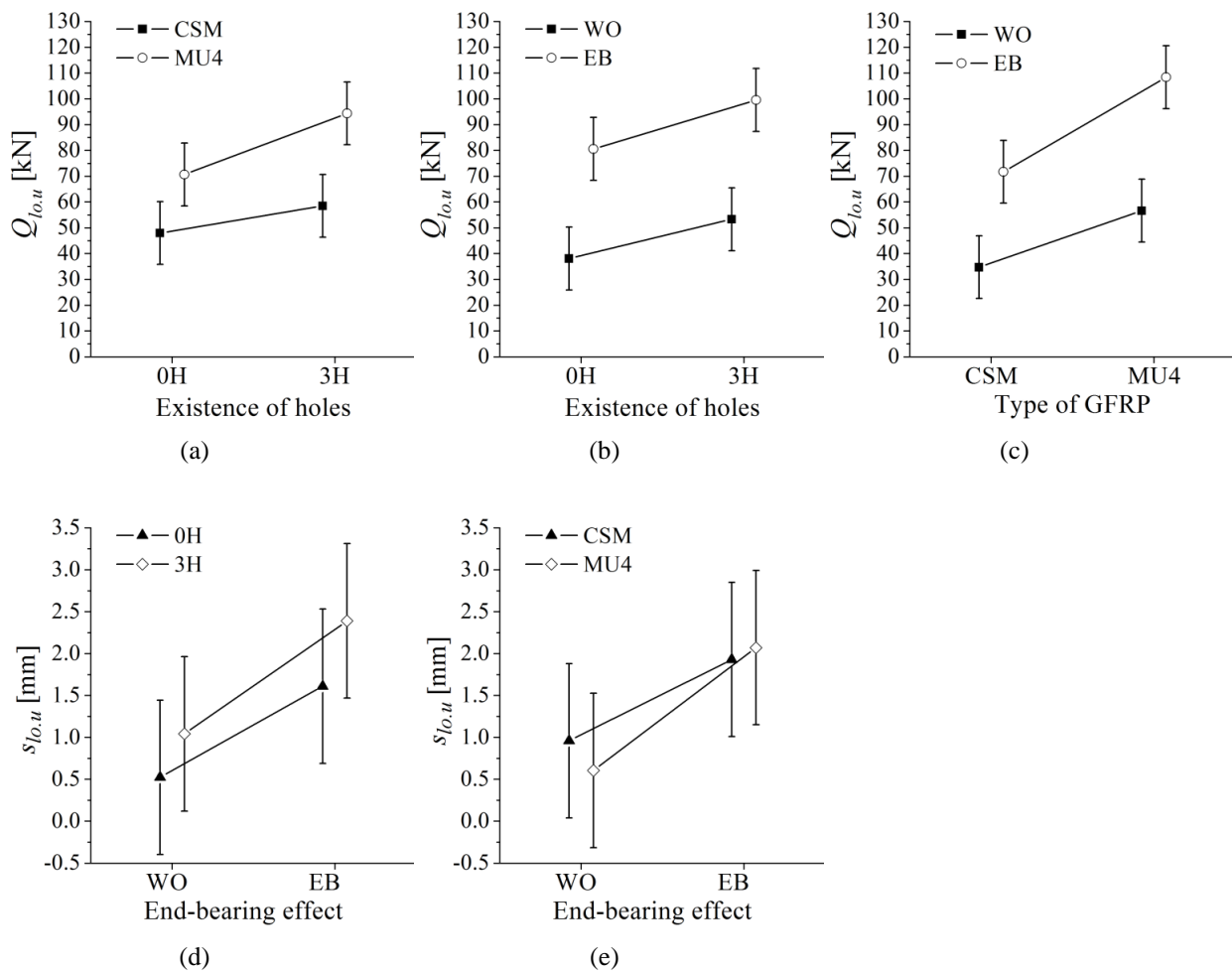
Figure 160: Two-factor interactions of variables studied: (a) existence of holes and type of GFRP on $Q_{lo.u}$; (b) existence of holes and presence of end-bearing effect on $Q_{lo.u}$; (c) type of GFRP and presence of end-bearing effect on $Q_{lo.u}$; (d) presence of end-bearing effect and existence of holes on $s_{lo.u}$ and (e) presence of end-bearing effect and type of GFRP on $s_{lo.u}$.

A factor was considered to have significant effect on the analyzed property if p-value was found to be less than 0.05 (95% confidence level). The F-ratio was obtained from Fisher´s

distribution table which depends on error degree of freedom (DF) and on the mean squares (MS). Table 39 shows that all the studied one-way factors significantly affected $Q_{lo,u}$. Furthermore, the F-ratios indicate that the concrete end-bearing was the studied variable with higher impact in the connections' load capacity ($Q_{lo,u}$). On the other hand, $s_{lo.u}$ was only influenced by the presence of end-bearing resistance. $Q_{lo,u}$, $s_{lo,u}$ and $s_{pl,90}$ were not significantly affected by neither two nor three-way evaluated interactions.

Table 39: ANOVA results for ultimate load ($Q_{lo,u}$) and slip corresponding to the ultimate load ($s_{lo.u}$).

Source	$Q_{lo,u}$				
	DF	MS	F-ratio	p-value	Significance
(A) Existence of holes	1	1171	10.47	0.012	yes
(B) Type of GFRP	1	3430	30.68	0.001	yes
(C) Presence of concrete end-bearing	1	7881	70.50	0.000	yes
(A)*(B)	1	173	1.55	0.248	no
(A)*(C)	1	14	0.13	0.732	no
(B)*(C)	1	217	1.95	0.201	no
(A)*(B)*(C)	1	18	0.16	0.702	no

Source	$s_{lo.u}$				
	DF	MS	F-ratio	p-value	Significance
(A) Existance of holes	1	1.684	2.64	0.143	no
(B) Type of GFRP	1	0.046	0.07	0.794	no
(C) Presence of concrete end-bearing	1	5.929	9.30	0.016	yes
(A)*(B)	1	2.616	4.11	0.077	no
(A)*(C)	1	0.069	0.11	0.751	no
(B)*(C)	1	0.245	0.39	0.552	no
(A)*(B)*(C)	1	1.995	3.13	0.115	no

7.4 DISCUSSION

In this section, only the factors found statistically significant in the ANOVA are commented. The discussions are made on basis of: the failure modes described in section 7.3.1; the data showed in Table 38 and Table 39 and the charts presented in Figure 157, Figure 159 and Figure 160.

7.4.1 Effect of existence of holes in the connector

Figure 159(a), Figure 160(a) and Figure 160(b) illustrate the effect of existence of holes in the load capacity of connection. The experimental results showed that, in average, the load capacity of 3H specimens was higher than the value obtained for 0H specimens. This effect was more relevant when connectors consisting of MU4 GFRP were used (see Figure 160(a)). In the case of connections consisting MU4 laminates, an average increase of 34% was obtained. On the other hand, the connections made with CSM laminate showed a smaller increase of load capacity due to the existence of holes, approximately equal to 22%. This difference is attributed to the fact that the load capacity of connections made with CSM laminates were limited by the premature rupture of connector. On average, $Q_{lo.u}$ increased 29% when 3H connectors were used rather than 0H connectors. This behaviour is attributed to the concrete dowels action in 3H specimens.

Additionally, the connectors presented an impressive high shear friction. In fact, the average load capacity of 0H-WO connections (without holes and neither end-bearing effect) represent 38% of the load capacity of the corresponding 3H-EB specimens. Thus, contrary to what is reported for the Perfobond connectors (Ahn *et al.*, 2010), in the case of PERFOFRP connectors, the parcel of load capacity transmitted across the connection by shear friction cannot be disregarded.

7.4.2 Effect of the type of GFRP of connector

The effect of the type of GFRP on the load capacity of connection is depicted in Figure 159(b), Figure 160(a) and Figure 160(c).

On average, an increase of 55% of the load capacity of connections was obtained for MU4 laminates, when compared with the values found for connections made of CSM laminates. The use of MU4 laminates in replacement of CSM laminates conducted to a gain in the load capacity of about 47% and 61% for 0H and 3H specimens, respectively.

7.4.3 Effect of presence of concrete end-bearing effect

Figure 159(c), Figure 160(b) and Figure 160(c) display the impact of concrete end-bearing effect on the load capacity of connections. The average $Q_{lo.u}$ obtained in specimens with concrete in front of rib connectors (EB) were 97% greater than the corresponding value obtained for notched specimens (WO). Furthermore, test results indicate that the presence of concrete end-bearing effect is the most relevant on the load capacity among the studied

variables (see the *F*-ratio column in Table 39). Nonetheless, the greatest increases due to the end-bearing effect were observed on the 0H and CSM specimens. The load capacities due to the end-bearing effect for these situations were, respectively, 112 and 107%.

Figure 160(d) and Figure 160(e) illustrate how the ductility of connection is affected by the end-bearing effect. In general, the $s_{lo.u}$ values of connections with concrete in front of GFRP rib connectors were 2.56 times higher than the corresponding values obtained for WO connections. Figure 160(d) indicates that the increase on the ductility due to the presence of concrete end-bearing was higher for MU4 specimens. However, end-bearing effect is equally important independently of the existence of holes in the connector.

7.5 ANALYTICAL MODEL FOR PREDICTING THE LOAD BEARING CAPACITY OF PERFOFRP CONNECTIONS UNDER LONGITUDINAL SHEAR

In this section an analytical model for predicting the ultimate load capacity of connectors under longitudinal shear is proposed, based on the experimental behaviour observed during the push-out tests and the obtained results.

One particularity of the mechanical behaviour of PERFOFRP connectors observed during the experimental program was the rupture of the connector itself. In all the connections where the end-bearing effect was present, the load capacity was conditioned by the failure of the connector itself. Therefore, the analytical model herein proposed is applied only to connections where the end-bearing effect is not present, i.e., to continuous connectors that are not confined in their extremities, as there isn't enough data available to validate the model with end-bearing effect.

Similarly to what was done in other works (Oguejiofor and Hosain, 1997, Sara and Bahram, 2002, Ahn *et al.*, 2010) for Perfobond connectors, this work considers that the ultimate load capacity of connection can be obtained as the sum of all the parcels related to the different mechanisms that contribute to the load carrying capacity of connection. In this work, it was possible to evaluate the contribution of the mechanisms associated with friction/adherence ($Q_{lo.fr}^{pr}$) and concrete dowel effect ($Q_{lo.do}^{pr}$), as given in Eq.(57).

$$Q_{lo.u}^{pr} = Q_{lo.fr}^{pr} + Q_{lo.do}^{pr} \tag{57}$$

Attention should be paid to the fact that in the tests with specimens without holes in the GFRP laminates and without end-bearing effect (specimens 0H-WO), the load carrying capacity was defined by the only mechanism present, which is friction/adhesion. Thus, the average peak load obtained from these tests was taken as the experimental value of ultimate load capacity that results from friction/adherence, $Q_{lo.u.fr}^{ex}$.

Considering a uniform distribution of shear stresses along the total contact area between the laminate and the SFRSCC, the friction strength associated to each type of laminate was estimated dividing the experimental value $Q_{lo.u.fr}^{ex}$, obtained in tests with each type of laminate (i.e., CSM and MU4), by the total contact area between both materials, considering the occurrence of double friction. Friction/adherence strength $\left(\tau_{fr} \right)$ equal to 1.05 MPa and 1.71 MPa was obtained for 0H-CSM and 0H-MU4 connections, respectively.

Once the friction/adherence strengths, τ_{fr}, associated to each type of laminate is known, and disregarding the contribution of the properties of SFRSCC for the friction/adherence, the parcel of the load capacity of a connection made with a PERFOFRP connector that is attributed to the friction/adherence mechanism can be predicted by Eq. (58),

$$Q_{lo.u.fr}^{pr} = \tau_{fr} \cdot A_{net} \tag{58}$$

where A_{net} is the net contact area between SFRSCC and PERFOFRP connector that can be expressed by Eq. (59).

$$A_{net} = b_{emb} \cdot L_{con} - \left(n_h \cdot \frac{\pi \cdot D_h^{\,2}}{4} \right) \tag{59}$$

In Eq. (59), b_{emb} is the embedded width of connector, L_{con} is the length of the PERFOFRP rib, n_h is the number of circular holes, and D_h is the diameter of holes. Specifically in the case of the PERFOFRP connectors studied in the experimental program, $b_{emb} = 45mm$, $L_{con} = 300mm$, $n_h = 3$ and $D_h = 30mm$ (see Figure 152).

The shear along the SFRSCC dowels was computed considering that single shear occurs in the dowels. The ultimate shear stress of SFRSCC, v_c, was estimated using the empirical shear transfer model developed by Khanlou *et al.* (2013), presented in Eq.(51).

Using f_{ck} = 66.1 MPa and V_f = 0.774 (i.e., considering the content of fibres equal to 60 kg/m^3 and the density of the steel equal to 7750 kg/m^3), the ultimate shear stress of SFRSCC, v_c, was estimated in 9.27 MPa.

Finally, the contribution to the load capacity of connection associated to the dowel effect was predicted by multiplying the cross-sectional area of all SFRSCC dowels by the direct shear strength of SFRSCC, as given in Eq.(60),

$$Q_{lo.u.do}^{pr} = \left(n_h \cdot \frac{\pi \cdot D_h^2}{4} \right) \cdot v_c \tag{60}$$

where n_h is the number of circular holes and D_h is the diameter of holes.

Table 40 shows the predicted results of $Q_{lo.u.fr}^{pr}$, $Q_{lo.u.do}^{pr}$, $Q_{lo.u}^{pr}$, and compares these values with the experimental ultimate loads of 3H-WO specimens. When the average ultimate load capacities of 3H-CSM-WO and 3H-MU4-WO are compared to the predicted values it was found that the values were overestimated and underestimated on 9% and 12%, respectively.

Table 40: Comparison between experimental and analytically predicted resistance of connections loaded longitudinally.

Specimen	$Q_{lo.u}^{exp}$ [kN]	$Q_{lo.u.fr}^{pr}$ Value	$Q_{lo.u.do}^{pr}$ Value	$Q_{lo.u}^{pr}$ Value	Error
3H-CSM-WO 01	44.80	23.90		43.56	9%
3H-CSM-WO 02	35.40		19.66		
3H-MU4-WO 01	56.10	38.92		58.58	-12%
3H-MU4-WO 02	76.90				

If the rupture of connections were conditioned by the concrete failure due to the end-bearing effect, the parcel corresponding to the end-bearing effect could be estimated considering the values of β_1 obtained by Oguejiofor and Hosain (1997) and Ahn *et al.* (2010) (shown in

Table 36), the geometric properties of specimens and the strength of concrete (i.e., $h = 60 - 15 = 45$ mm; $t_{CSM} = 2$ mm; $t_{MU4} = 4$ mm; $f_{ck} = 66.1$ MPa). Thus, the end-bearing contribution would be estimated on 27 kN and 19 kN for CSM laminates and 53 kN and 37 kN for MU4 laminates, respectively when the values of β_1 obtained by Oguejiofor and Hosain (1997) e Ahn *et al.* (2010) are adopted.

On the other hand, the contribution of the end-bearing effect in the tests with the PERFOFRP connectors can be evaluated subtracting the load capacities obtained in the tests with 3H-WO specimens from the values obtained in the tests with 3H-EB specimens. Therefore, the end-bearing contribution would be estimated on 37 kN and 56 kN for connections made with CSM and MU4 connectors, respectively. These values are quite similar to the values estimated by the use of equation proposed by Oguejiofor and Hosain (1997) for the case of Perfobond connectors (36% and 5% higher, respectively for CSM and MU4). This finding possibly indicates that the ultimate loads of connections made with PERFOFRP connectors were not too impaired by the damage of the connector in its frontal part.

7.6 FINAL REMARKS

In this study, push-out tests were conducted on connections comprising PERFOFRP connectors and self-compacting steel fibre reinforced concrete. The experimental program consisted on 16 specimens made with two different GFRP laminates (CSM and MU4). To evaluate the concrete dowel effect, tests were also conducted with PERFOFRP connectors with 3 evenly spaced holes and also with laminates without holes. Moreover, the end-bearing effect was isolated comparing the results of specimens with and without concrete in front of the PERFOFRP rib. Finally, an analytical formulae to predict the ultimate load capacity of connections consisted of unconfined connectors (i.e., without end-bearing effect) was proposed and its accuracy was evaluated. Based on the results of this investigation, the following conclusions may be drawn:

- differently to what happens with connections made with steel Perfobond connectors, it was observed that the failure in connections made with PERFOFRP connectors subjected to longitudinal shear has generally occurred due to the rupture of GFRP connector itself;

- contrary to what is reported for the Perfobond connectors, the PERFOFRP connectors presented an impressive high shear friction, corresponding to 38% of the load capacity of the 3H-EB specimens (with dowel effect and also end-bearing effect acting together). Thus, the parcel of load capacity transmitted across the connection by shear friction cannot be disregarded;

- the concrete dowels action significantly increased the load capacity of connections. On average, an increase of 29% was obtained for the load capacity of connections due to the existence of holes in the connectors. This effect was more relevant when MU4 connectors were used, because the load capacity of connections made with CSM laminates was limited by the premature rupture of the connector;

- when MU4 laminates were used rather than CSM laminates, the load capacity of connectors increased 55%, on average. The gain on load capacity due the use of MU4 laminates was more relevant for connectors with holes;

- among the studied variables, the concrete end-bearing effect showed to be the more relevant on the load capacity. On average, the specimens with concrete in front of rib connectors presented load capacity 97% greater than the corresponding value obtained for notched specimens;

- when compared to steel connectors, PERFOFRP connectors showed a smaller ductility, which seems to be justified by the premature failure of the GFRP plate. On average, the plastic slip for a load corresponding to 90% of the ultimate load ($s_{pl.90}$) was equal to 0.86 mm (standard deviation: 0.47 mm).

Chapter 8

FLEXURAL BEHAVIOUR

The shear behaviour of the PERFOFRP connectors used in the sandwich panels was already characterized by the pull-out and push-out tests previously presented in Chapter 6 and Chapter 7, respectively. However, in these tests the specimens are subjected essentially to shear forces, but in a real sandwich panel, due to bending loading configurations it is subjected, the PEFOFRP connectors are submitted to in plane shear and normal stress components.

It is well known that the connection between the concrete layers affects directly the degree of composite action of the sandwich panels and, consequently, their design (PCI, 2011). Depending on how the connection is materialized, the panel can behave, and should be designed, as having a non-, partial or full-composite behaviour. In general, the connections provide a partial-composite behaviour to the panels. The level of shear transfer between the concrete layers and, consequently, the degree of composite action of panel, greatly depends on the material and geometry of the connectors, but is also affected by the thermal insulating material used in its core (Choi *et al.*, 2015b). Tests results reported in different researches (Salmon and Einea, 1995, Benayoune *et al.*, 2008b) indicate that, despite their higher thermal efficiency, the panels including FRP connectors generally present smaller structural efficiency when compared with solutions having steel connectors and solid concrete zones. While the behaviour of non- and full- composite panels can be easily estimated since the degree of composite action can be established accurately, for panels working on a partially composite

mode the accurate evaluation of the specific composite action requires experimental research with these panels.

This chapter presents the results of an experimental work conducted with composite beam specimens and numerical studies that are part of a series of studies to determine the feasibility of using of the PERFOFRP shear connector in Steel Fibre Reinforced Self-Compacting Concrete (SFRSCC) structural sandwich wall panels.

The investigation presented in this chapter was executed to assess the performance of a PERFOFRP connector in loading conditions representative of the real application, as well as its effectiveness in transferring the stress components between the external SFRSCC layers. Specifically, the main objectives of the work presented in this chapter are:

- to explore the mechanical behaviour of the connections for SFRSCC sandwich panels made with PERFOFRP connectors when subjected to the combined effect of shear and flexural forces that are the mandatory load conditions in this structural element;
- to study the influence of the type of GFRP used in the connection on the ductility and strength capacity of the connections.

8.1   TEST PROGRAMME

Six composite small scale beam specimens were tested at Laboratory of the Structural Division of the University of Minho. The tests aimed to provide information concerning the general behaviour and suitability for practical applications of PERFOFRP connectors. In particular, the influence of type of GFRP used in the connector on the overall mechanical behaviour of the connection was investigated making use of composite beams subjected to a symmetrical two-point load. Details about the specimens, materials and experimental procedure are provided in the following sections.

8.1.1   Sandwich beam specimens

Each specimen consisted of a sandwich beam with length of 1245 mm, rectangular cross section with an overall thickness of 180 mm and width of 200 mm. Each specimen was composed of three layers with 60 mm thickness each, where the outer layers are made by SFRSCC, while the core layer is constituted by Expanded Polystyrene (EPS). The arrangement of the layers, their thickness and the materials were chosen to be representative

of the sandwich wall panels previously optimized through parametric studies with Finite Element analyses shown in Chapter 5. The SFRSCC layers were connected with a continuous PERFOFRP connector positioned in the middle of the beam's cross section along all its length, as shown in Figure 161.

The PERFOFRP connector used in this work was designed to have the same hole diameter and spacing used in the connectors previously tested under pull-out and push-out loads (Chapter 6 and Chapter 7). The diameter of holes (30 mm) and the SFRSCC cover thickness (15 mm) was determined for assuring the passage of the fresh SFRSCC through the holes and the gap between the connector and the formwork without the occurrence of segregation of aggregates and fibres. This thickness aims also to protect the GFRP connector, and avoid the formation of a line on the external surfaces of the panel coinciding with the location of the connector (due to the different physical properties of GFRP and SFRSCC), since the occurrence of these lines would have negative impact on the appearance of the panel. The diameter of the holes, as well as its cover thickness of 7.5 mm have also attended the stress concentration and failures modes observed in the pull-out and push-out tests (Chapter 6 and Chapter 7).

Front view:
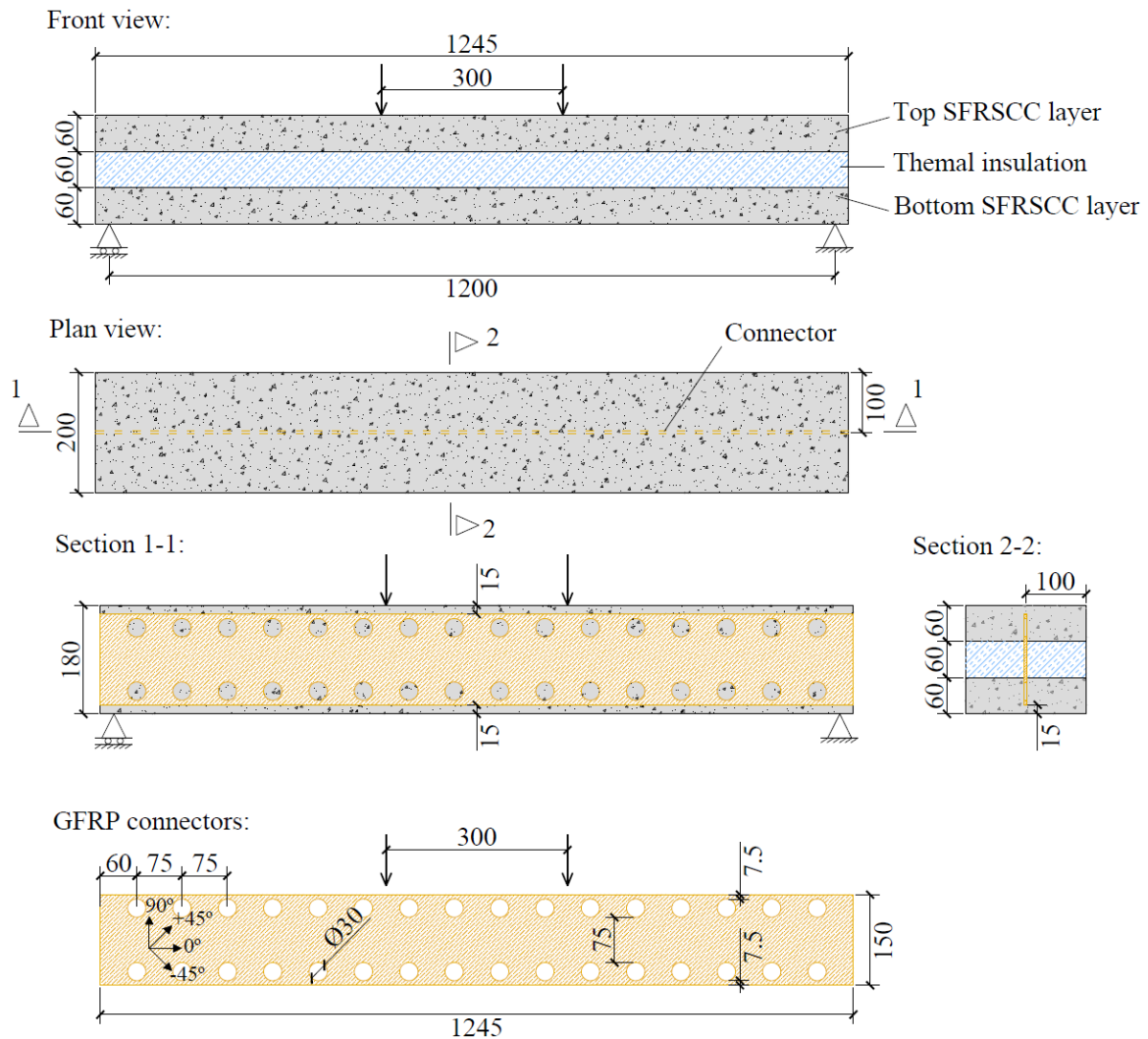
Figure 161: Geometry of test specimen (units in millimetres).

8.1.2   Material properties and preparation of specimens

The sandwich beam specimens were performed with SFRSCC B from casting 8 (see Table 6). Two types of GFRP were used on the production of connections: CSM 1 and MU4 (see Table 19). Further details about the GFRPs can be seen in Chapter 4. Three identical beams were cast for each type of GFRP used in the PERFOFRP connectors. The beams were cast in wood forms. Initially, the connector was positioned in the middle of each beam. The concrete cover was guaranteed by the use of plastic spacers commonly employed for steel reinforcement bars (see Figure 162). The bottom SFRSCC layer was poured up to the 60 mm level marked in the wood form. Two EPS blocks with the same length of the beam and 60 mm of thickness were positioned in each side of GFRP connector. The top SFRSCC layer was then poured. All the specimens were covered with plastic foil, and twenty four hours after the casting procedure

they were removed from mold to cure in air until testing. The tests were conducted when the specimens attained an age between 114 and 120 days.
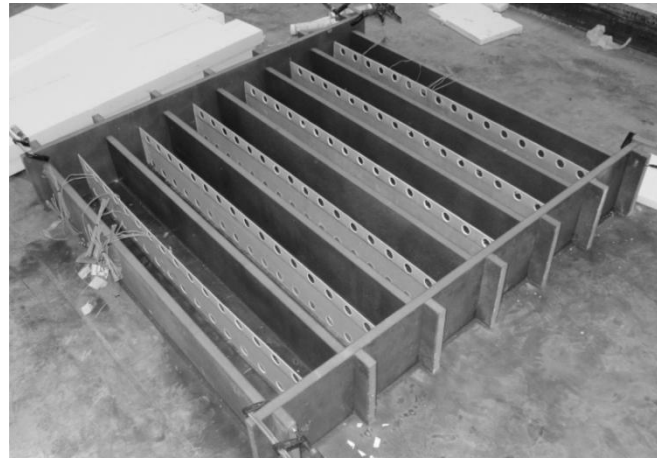
(a)
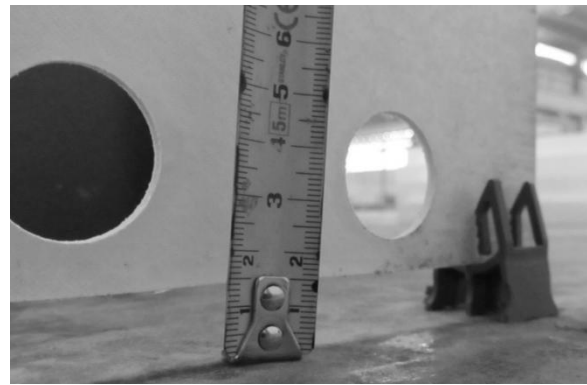
(b)

Figure 162: Preparation of test specimens: (a) formwork; (b) detail.

8.1.3   Test setup, instrumentation and test procedure

The beam specimens were tested under the four-point bending loading configuration represented in Figure 163. The load was applied by a 500 kN hydraulic jack via a load-spreader I-section steel beam and two halves of steel cylinders that were in contact to the top surface along all the width of the beam's cross section. The beams were simply-supported on steel rollers, with a span of 1200 mm. One of the supports had the rotation and sliding released in the direction parallel to the specimen's axis. All the specimens were tested with the beams positioned in the same direction that they were casted, that is, with their rough surface of the top SFRSCC layer upside.
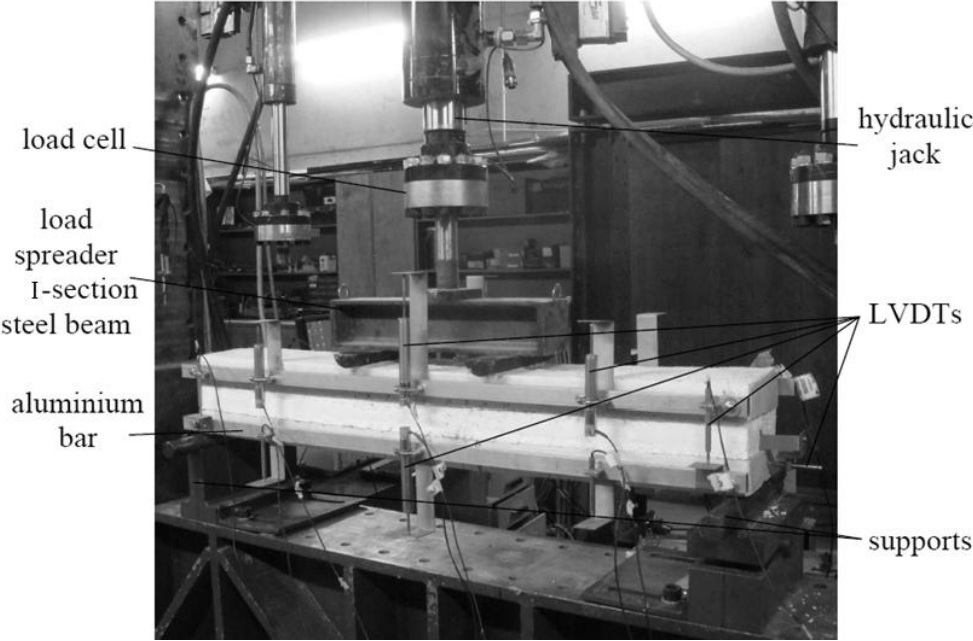
(a)
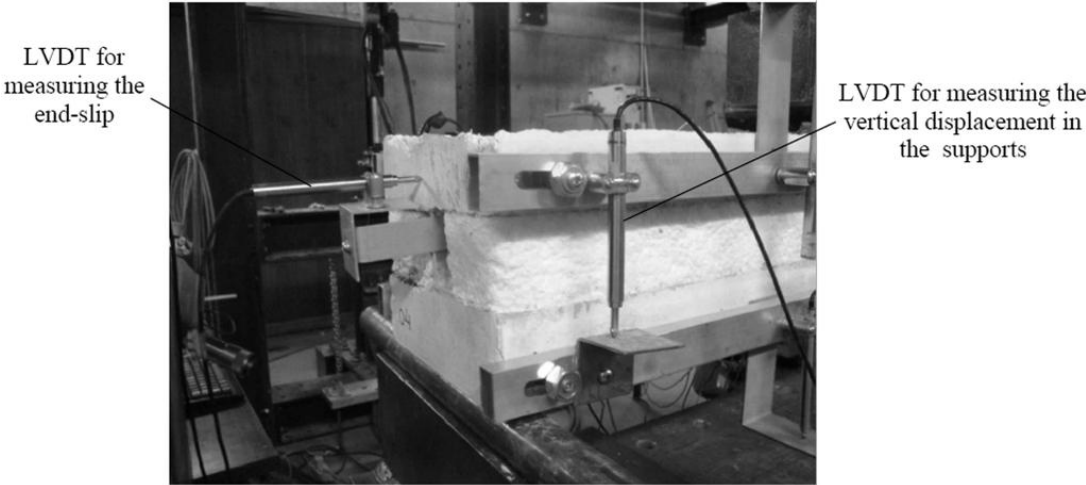
(b)

Figure 163: Four-point bending test setup: (a). overall view; (b) detail.

The load was registered by a 250 kN capacity load cell attached at the extremity of the hydraulic jack (see Figure 163(a)). The arrangement of LVDTs and strain gauges are shown in Figure 164. The following monitoring system was installed: (1) Ten LVDTs for measuring deflections along the beam's span (LVDTs C, G, L and O, with a stroke of ±50 mm) and at a distance of 225 mm from the supports (B, D, F, H, K and N, with stroke of ±25 mm). To evaluate possible misalignment of loading application, in the first and second specimens of each series, deflections were obtained in the front and rear sides of beams, as shown in Figure 164(a) and Figure 164(b). In the third specimen of each series, deflections were obtained only

in the rear side of beam. Deflections were obtained from measurements in the LVDTs fixed to an auxiliary steel bar in order do not include parasitic displacements in measurements (Japan Society of Civil Engineers, 1984). The measurements of deflections of top and bottom SFRSCC layers were made independently; (2) Eight bonded Electrical Strain Gauges (ESGs), with gauge length and resistance of 2 mm and 120 Ohm, respectively, were used to measure the strains in the PERFOFRP connectors of second specimen of each series (see s_1 to s_8 in Figure 164(c) and Figure 164(d)). Strains were obtained in the longitudinal direction at midspan (s_5 to s_8), loaded section (s_4) and at a distance equal to 225 mm from one of the supports (s_3). In this section, two other ESG were also positioned, at ±45° directions with the horizontal to measure the shear strains (s_1 and s_2); (3) Two LVDTs (stroke of ±10 mm) were used to measure the end slips (longitudinal direction) between the PERFOFRP and the SFRSCC layers (LVDTs I and P); (4) Four LVDTs (stroke of ±2.5 mm) were used to measure the relative displacement (i.e., transversal direction) between the top and bottom SFRSCC layers (LVDTs A, E, J and M).

A hundred unloading-reloading cycles between 0 to 14 kN were applied at the beginning of testing the third specimen of each series. During the load cycles, the test was load controlled at 1.02 kN/s, and afterwards the test was controlled by displacement rate, at 0.005 mm/s. The loading was conducted until the specimen's load carrying capacity drops at least 50% of its maximum capacity. All measurements made by the load cell, LVDTs and strain gauges were registered continuously along all the test at a rate of 2 Hz.

8.2 DISCUSSION OF TEST RESULTS

8.2.1 Experimental behaviour: failure modes, deflections and ultimate carrying capacities

The experimentally obtained cracking load, maximum applied load and maximum midspan deflection for each specimen are summarized in Table 41. The load-deflection curves are shown in Figure 165, where the contribution of the beam's self-weight and I-section spread load for the load and deflection is neglected due to its marginal influence of the global response of the beams.

Front view:

(a)

Rear view:

(b)

Strain gauges in connector:

(c)

(d)
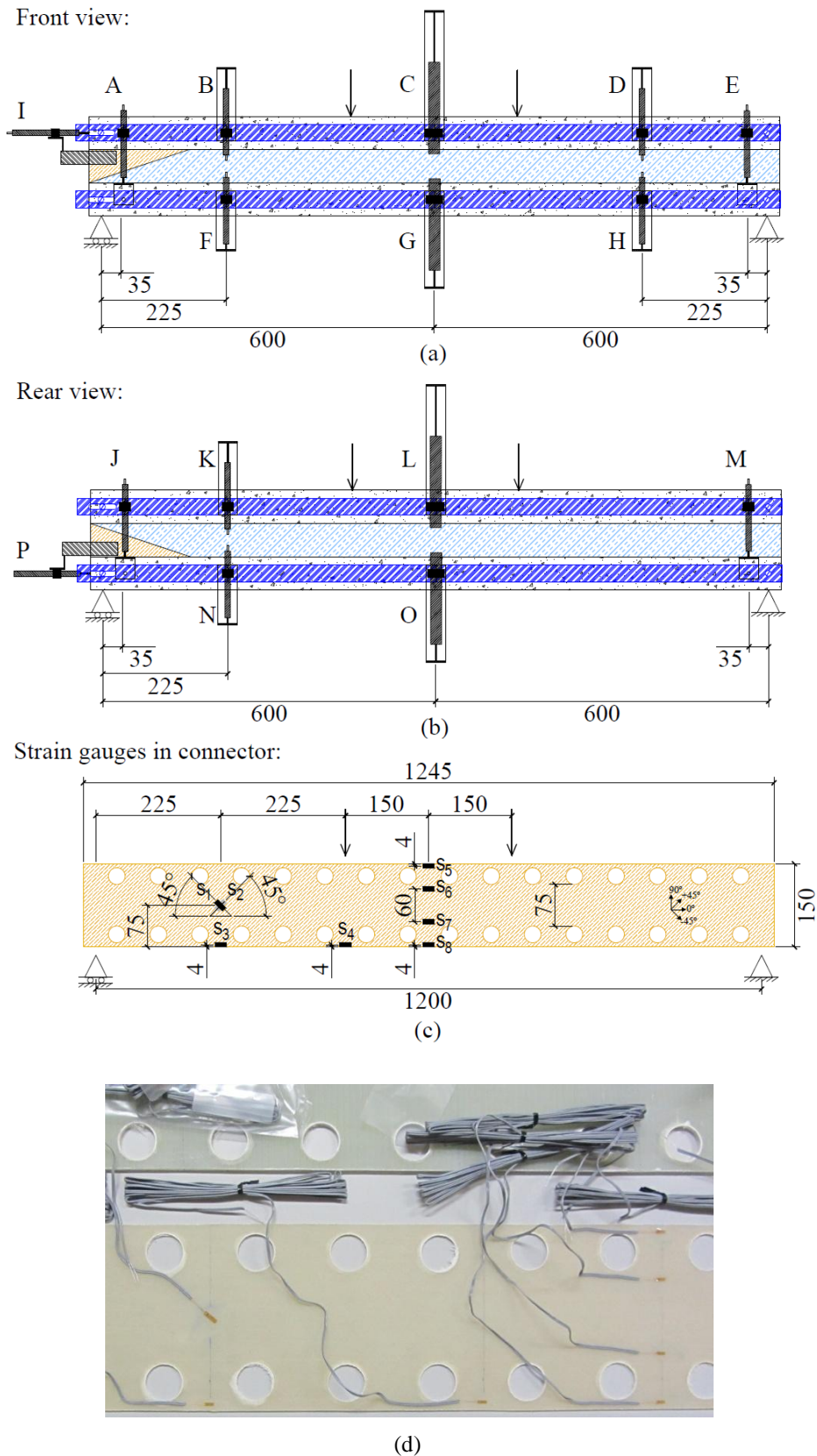
Figure 164: Instrumentation adopted in four-point bending tests (units in millimetres). LVDTs: (a) front view; (b) rear view. Strain gauges: (c) schematic representation; (d) overall view.

The deflections calculated for the upper concrete layer were obtained as the measured deflection diminished by the average vertical displacement recorded in the support ends (recorded in the LVDTs A, E, J and M).

Table 41: Cracking load, maximum applied load and midspan deflection corresponding to the maximum applied load for the tested beam specimens.

Specimen Ref.	Cracking load			Maximum applied			Midspan deflection		
	Value [kN]	Avg	CoV [%]	Value [kN]	Avg	CoV [%]	Value [mm]	Avg	CoV [%]
CSM 01	15.5			25.4			1.62		
CSM 02	14.3	14.7	5	28.3	26.1	7	1.77	1.6	12
CSM 03	14.2			24.7			1.40		
MU4 01	15.7			32.2			17.33		
MU4 01	15.6	15.6	1	27.9	29.6	8	17.01	16.2	11
MU4 03	15.5			28.8			14.11		

All the specimens of each group presented similar experimental responses. In general, the responses are characterized by an initial linear branch until the occurrence of the first crack, after which the initial stiffness of the specimen has decreased. Flexural cracks were first observed at the bottom and front sides of the bottom SFRSCC layer. The average cracking load was 14.7 kN (st. dev. equal to 0.74 kN) and 15.6 kN (st. dev. equal to 0.16 kN) for specimens made with CSM and MU4 laminates, respectively. These cracks progressed transversely across the underside of the bottom SFRSCC layer, and were located in the "pure" bending zone. Other hairline cracks occurred in the bottom SFRSCC layer within the flexure/shear spans.

At this stage, for CSM specimens, these cracks propagated progressively towards the top of the bottom SFRSCC of sandwich panel. Then, some hairline cracks also appeared in the bottom face of the top SFRSCC layer. The CSM specimens attained an average maximum load of 26.08 kN. For a deflection just after the one corresponding to the peak load a louder sound was heard, and the width of one of the cracks that appeared in the bottom SFRSCC layer started to increase, while the other cracks almost cease to propagate. Then, the load was decreasing pronouncedly with the increase of the deflection (structural softening).

For the MU4 specimens, after the cracks in the top SFRSCC layer have formed, a longitudinal crack appeared in the upper surface of the top SFRSCC layer, aligned with the PERFOFRP

connector. Subsequently, this longitudinal crack extended over the length of the beam, and the crack opening has increased (see the final aspect of this crack in the top view presented in Figure 168(b)). Thereafter, new cracks opened in the top SFRSCC layer, and similar to what occurred for the CSM specimen, a louder sound was heard, and one of the cracks of the bottom SFRSCC layer degenerated in a macro-crack. The main difference from the behaviour observed for the CSM specimens is that from this stage the load-deflection of MU4 specimens presented a deflection hardening stage, as can be observed in Figure 165.

A more intense cracking and wider cracks were also noticed for the specimens made with MU4 connector. The failure of these specimens occurred after a sequence of louder noises, typical of the failure of the GFRP laminates under direct tension. At this stage the load-carrying capacity of sandwich beam dropped suddenly.

(a)

(b)
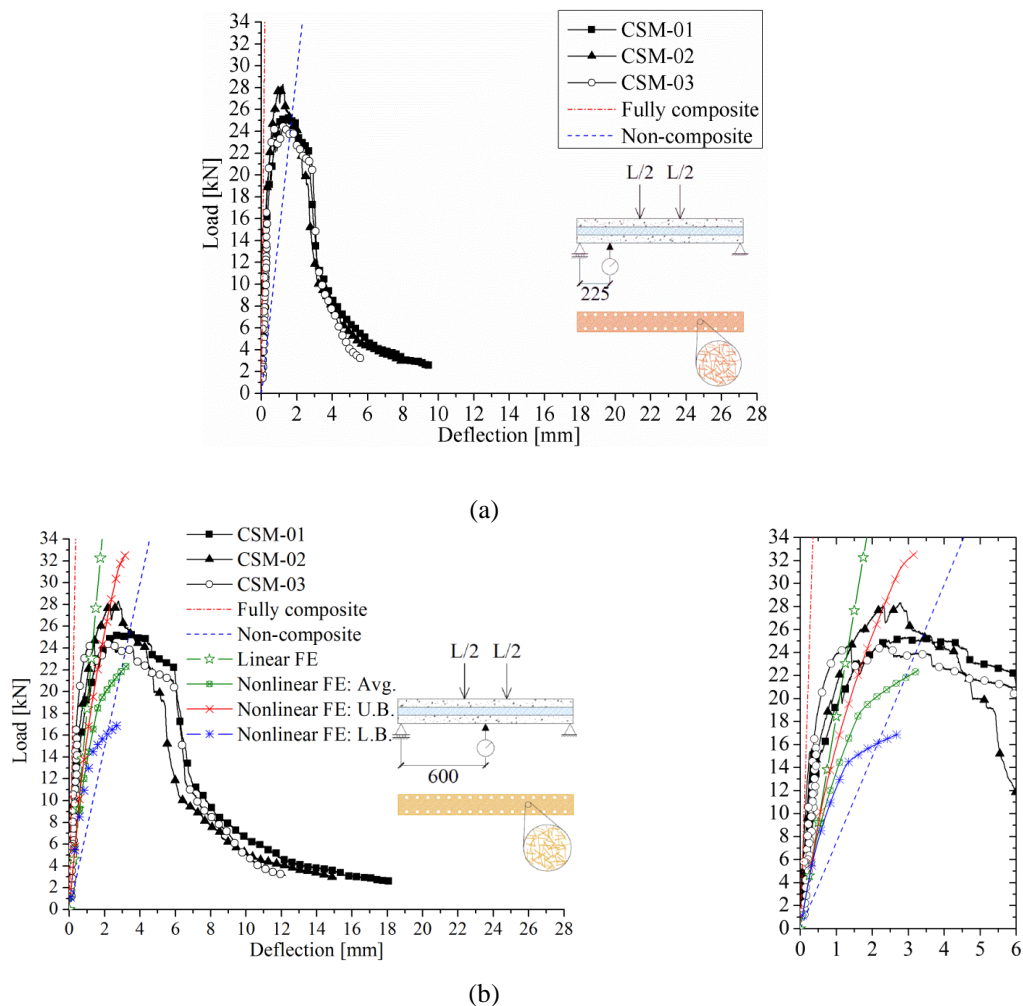
Figure 165: Average load-deflection curves. CSM specimens: (a) 225 mm far from the supports and (b) midspan; MU4 specimens.

(c)

(d)
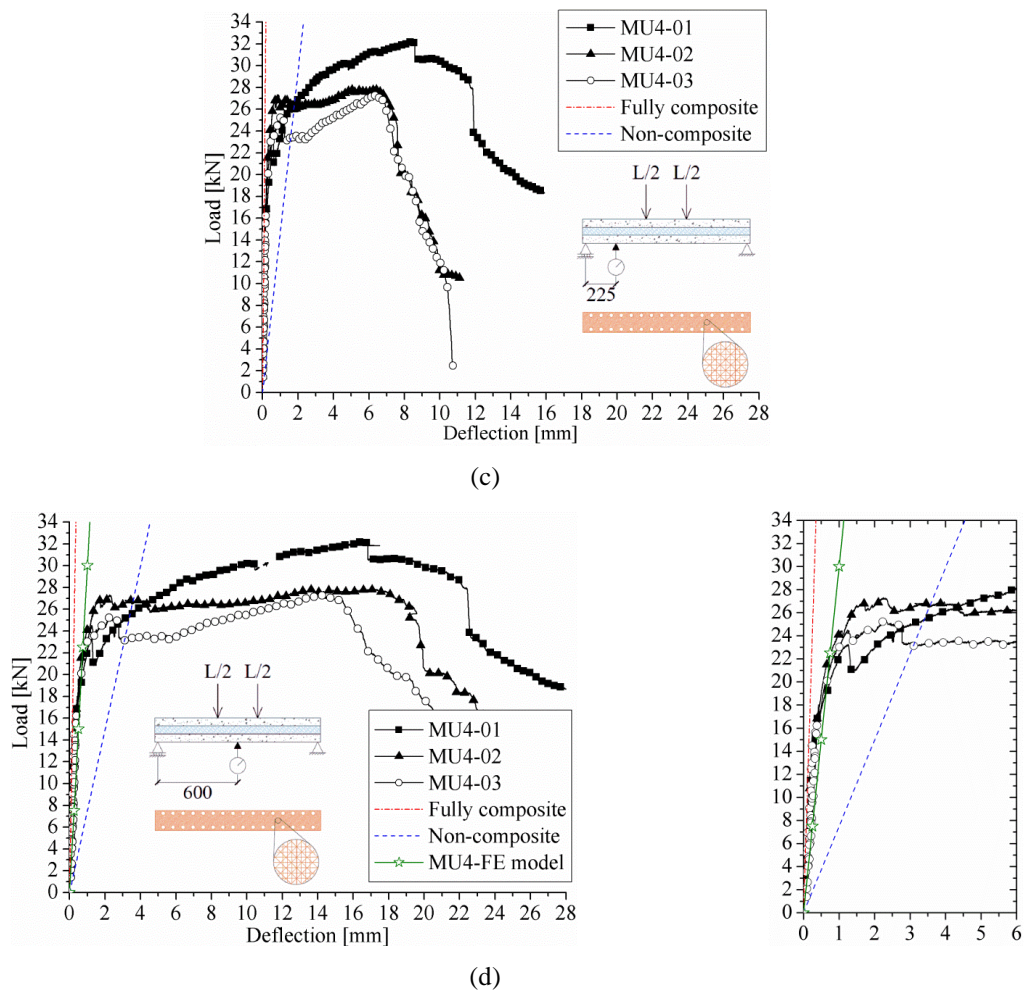
Figure 165: Average load-deflection curves. CSM specimens: (c) 225 mm far from the supports, (d) midspan.

From the load *versus* deflection curves shown in Figure 165 and Figure 166, it is possible to conclude that the connections between SFRSCC and CSM and MU4 connectors exhibited small stiffness degradation throughout the load cycles. A maximum residual deflection of 0.12 mm was registered after the 100 cycles in the sandwich beam fabricated with CSM connectors.

(a)   (b)
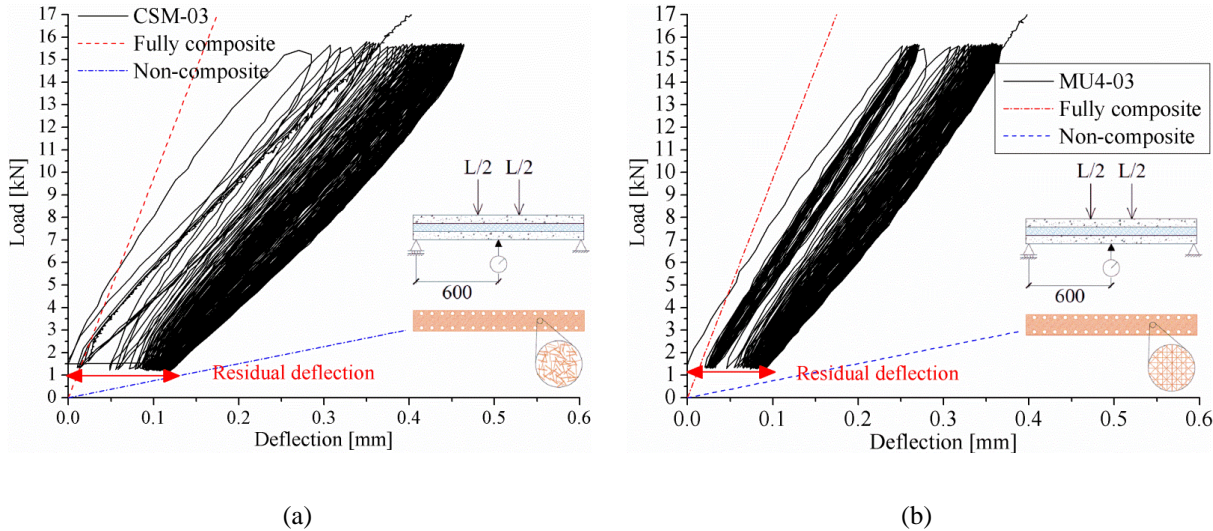
Figure 166: Load-deflection curves during the 100 loading-unloading cycles applied to the specimens: (a) CSM-03 and (b) MU4-03.

Representative evolution of cracking that occurred in the front side of beams during the tests is presented in Figure 167(a) and Figure 167(b) for specimens made with CSM (CSM 03) and MU4 (MU4 03) connectors, respectively.
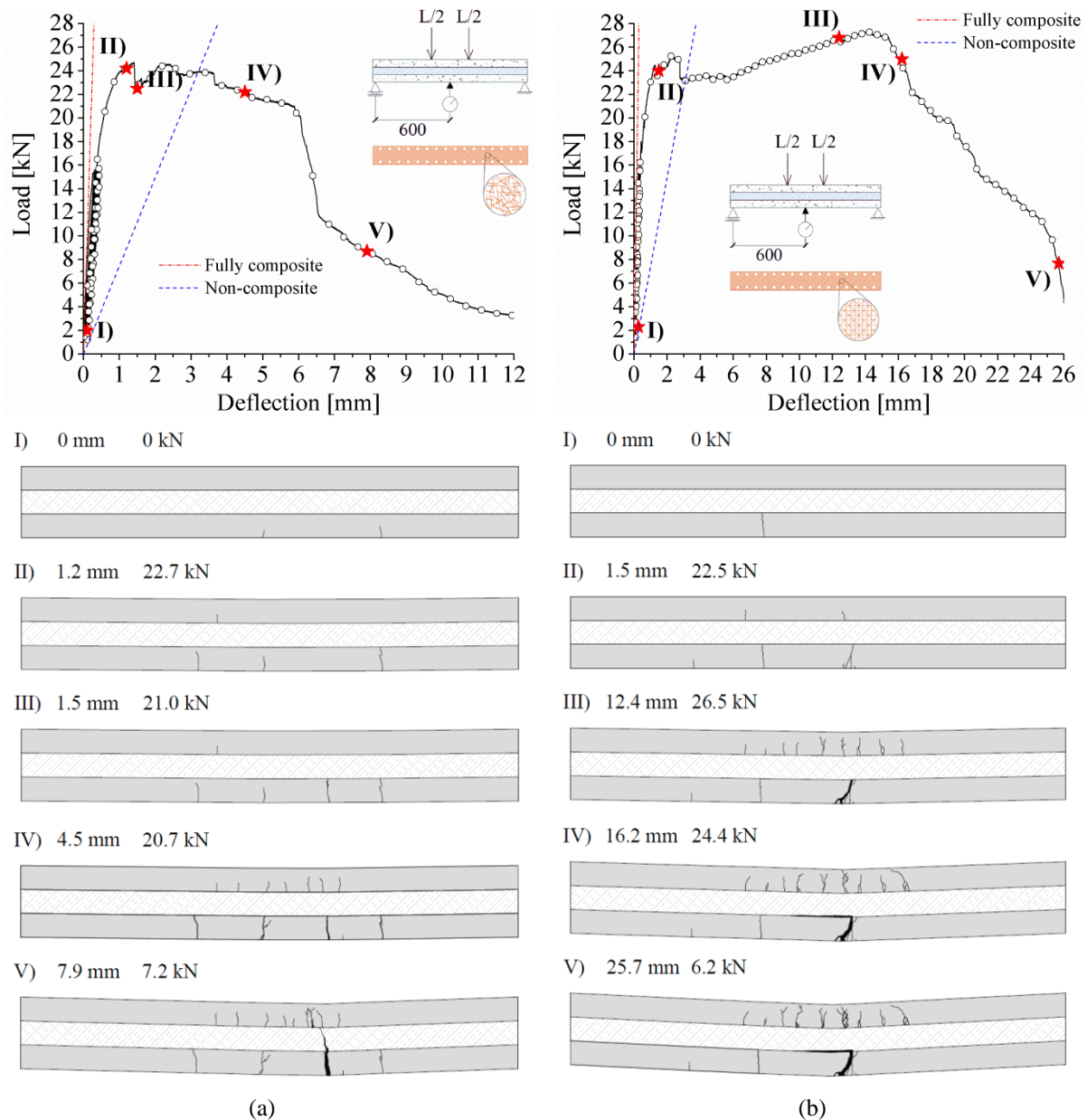
Figure 167: Crack pattern evolution for specimen: (a) CSM-03; (b) MU4-03.

After the tests, the specimens were disassembled in order to analyze the anchorage conditions of the connectors. The final aspect of some connectors are shown in Figure 168. After the observation of the final aspect of connectors, the failure of the sandwich beams was therefore attributed to the rupture of the GFRP connectors caused by the propagation of flexural cracks. Similarly to the behaviour of the composites under direct tensile tests (see section 4.3), the specimen made with CSM connectors presented a more brittle behaviour when compared to the behaviour of specimens with MU4 laminates. Moreover, the first sound heard during the tests was probably related to the failure of the laminates in the region right below the holes.

After this rupture the neutral axes of the beam's cross section in this region naturally was shifted upward. In the case of MU4 connectors, a new equilibrium was attained because the tensile strength of the laminate, together with the post-cracking residual strength of the SFRSCC, were able to carry the higher load transferred to the connector. Nonetheless, for the specimens made with CSM connectors, the smaller ductility of this type of connector (Figure 165) conducted to a more abrupt load decay of the beam just after damage initiation in the connector. Figure 168(e) and Figure 168(f) evidence that a "discrete crack" was formed in the CSM connector (localized failure), while a damage zone was developed in the MU4 connector (smeared damage).

(a)   (b)

(c)   (d)
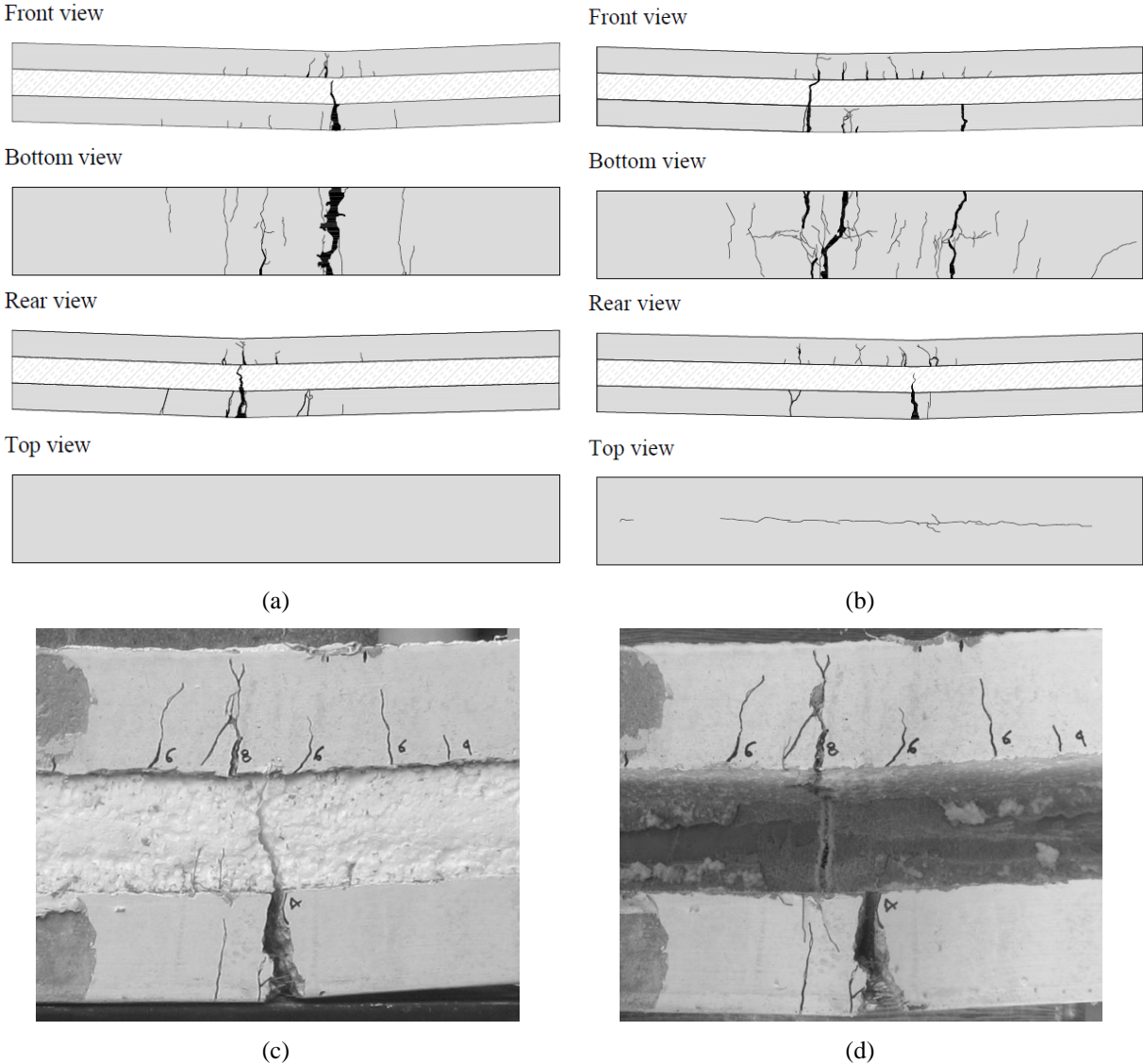
Figure 168: Final aspect of specimens after failure: (a) CSM-01; (b) MU4-02. Details: (c) CSM-01 and (d) CSM-01 after removal of EPS.

(e)   (f)
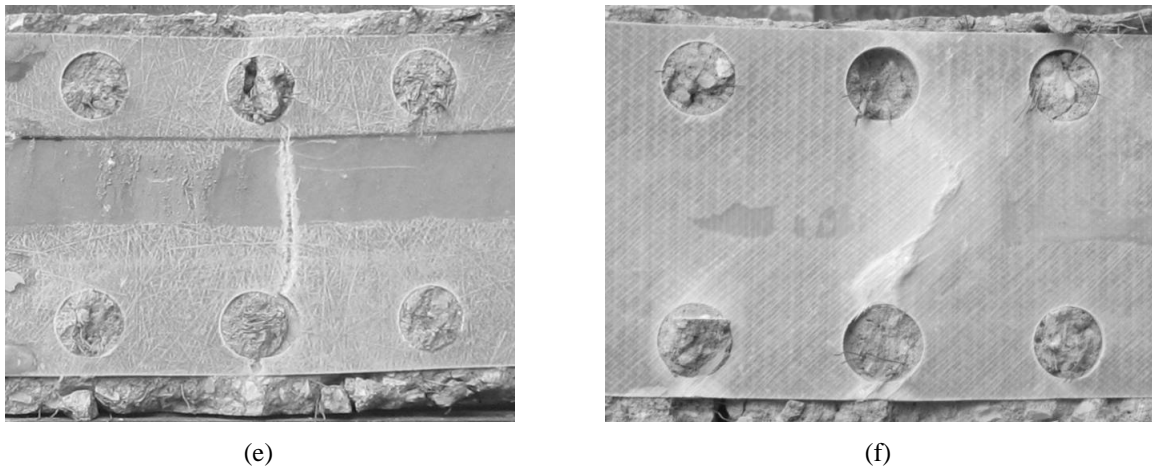
Figure 168: Final aspect of specimens after failure: (e) CSM-02; (f) MU4-01.

In general, the deflections obtained for the top and bottom layers of sandwich beams were similar. By comparing the deflections measured with the LVDTs installed in front and rear sides of the beams, and the deflections measured by the LVDTs positioned near the supports' cross section, it was possible to conclude that the specimens behaved symmetrically. From the measurements of vertical displacements recorded by the LVDTs positioned near the supports it was possible to conclude that no significant relative displacement between SFRSCC layers has occurred in the supports. Based on this observation, the deflections presented in this document are always average values obtained in the LVDTs positioned at the same distance from the mid-span. Figure 165 depicts the average of measured deflections at mid-span and at a distance equal to 225 mm from the supports for the different specimens. In general, the specimens made with the same type of connector behaved identically throughout the tests.

8.2.2   Normal strains in the connector

Representative strain profiles along the depth of the connector's cross section at the mid-section of the sandwich beams are shown in Figure 170(b), Figure 170(c), Figure 170 (e) and Figure 170(f). For the sake of conciseness the results of strain gauges s_3 and s_4 were omitted, since they were quite similar to the strain recorded in the strain gauge s_8.

For the CSM specimens it was evidenced that up to cracking load, the strain gauge s_8, located 4 mm from the bottom edge of the connector, registered only tensile strains. Nonetheless, the strain gauge s_7, located 45 mm from the bottom edge of the connector, registered only compressive strains. This suggests that the neutral axis of the composite beam is located in the bottom SFRSCC layer in the linear stage. However, attention should be paid that the strains

aforementioned were measured in the nearby of the holes. The existence of holes can lead to a specific strain distribution not being possible a simple interpretation of these results. The section corresponding to the numerical analysis will be also used to contribute for the analysis of the recorded strains.

After cracking, the response of strain gauges clearly deviated from the behaviour observed in the linear stage. While the loading was increased and, consequently, the cracks progressed to the top of the beam, the strain gauges positioned at 45 mm and 105 mm from the bottom edge of the connector have registered continuously increasing tensile strains, while the strains in strain gauge s_5 became even more compressed and s_8 more tensioned (see s_5 and s_8, presented in Figure 170(b), Figure 170 (c), Figure 170 (e) and Figure 170 (f)).
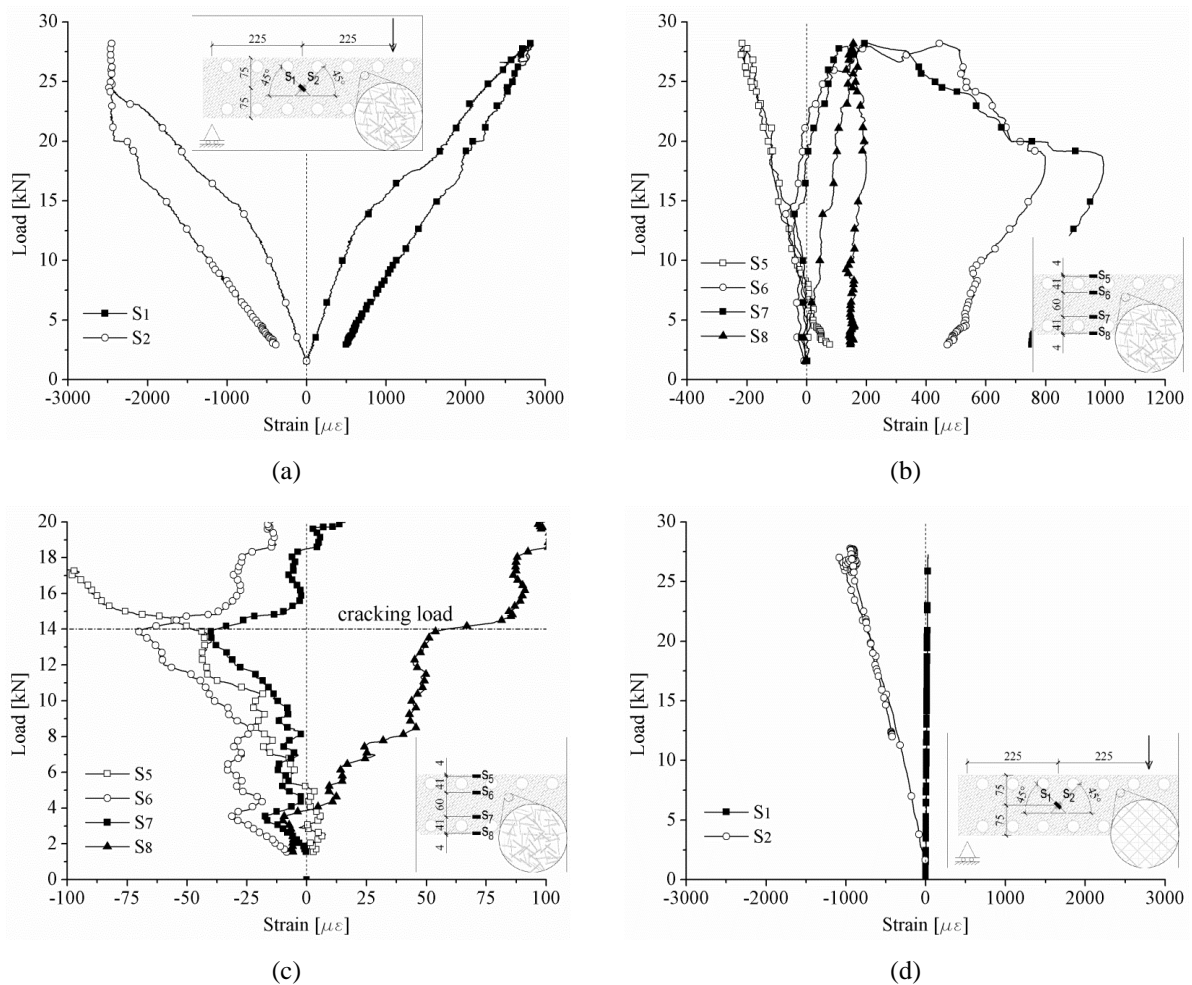
Figure 169: Force *versus* strain in the strain gauges (compression is negative): (a) s_1 and s_2 in CSM-02; (b) s_5 to s_8 in CSM-02; (c) s_5 to s_8 in CSM-02 (detail) and (d) s_1 and s_2 in MU4-02.

(e)   (f)
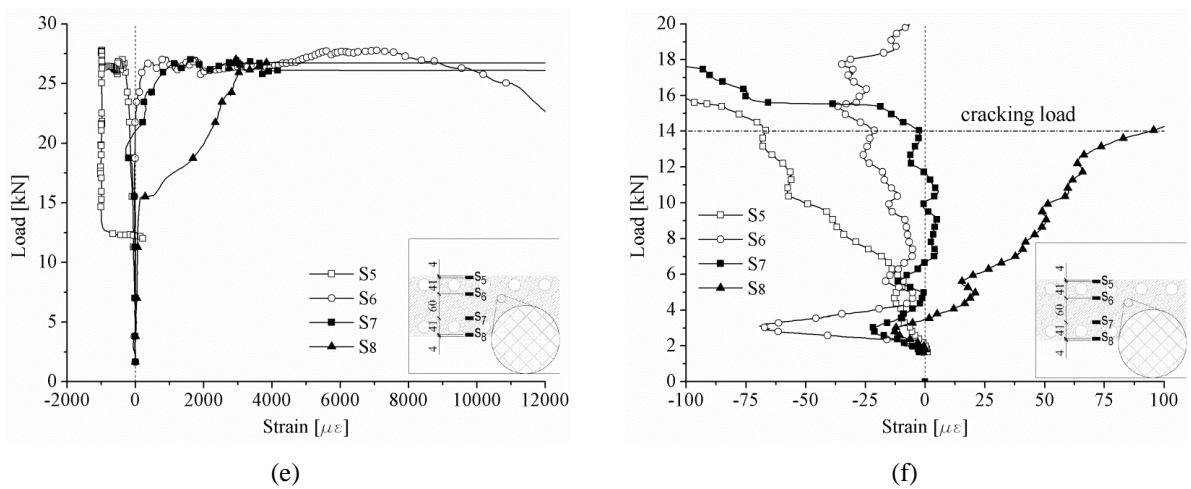
Figure 170: Force *versus* strain in the strain gauges (compression is negative): (e) s_5 to s_8 in MU4-02; (f) s_5 to s_8 in MU4-02 (detail).

Similar behaviour was observed in the test with MU4 02 specimen for the linear stage. The main difference is that the strain gauge s_7 registered values near zero.

Figure 171 shows the strain variation across the panel depth at the cracking load level.

(a)   (b)
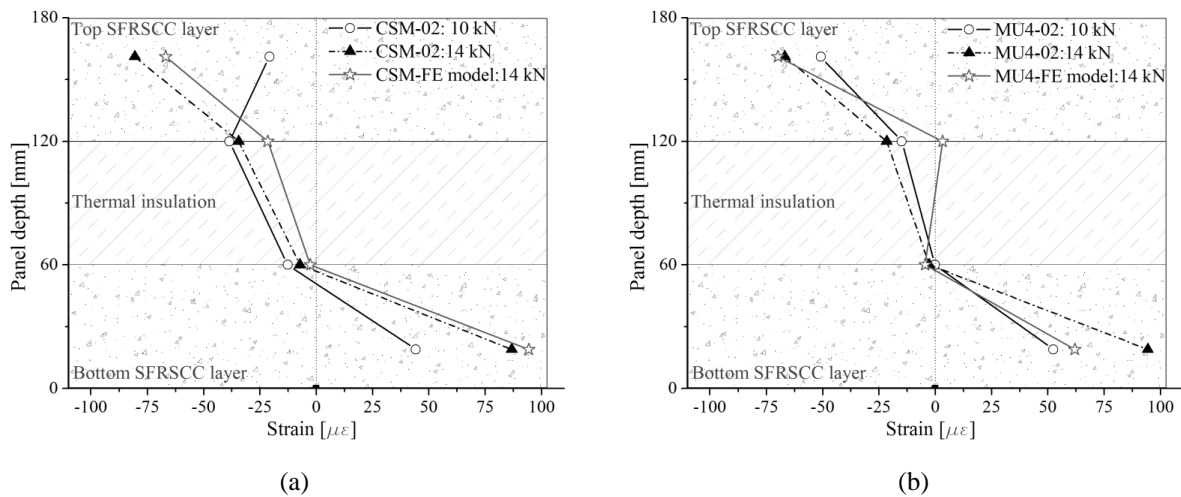
Figure 171: Strain variation across the panel depth for (compression is negative): (a) CSM-02 specimen; (b) MU4-02 specimen.

The strains registered in the post-cracking range is so dependent of the relative position of the strain gauges with respect to the cracks formed in the SFRSCC layers that a rational interpretation of the results is too difficult of assuring. Nonetheless, it is observed from Figure

170(b) and Figure 170(e) that the connectors were able to transfer forces from one SFRSCC layer to another efficiently up to failure, prolonging the composite behaviour of both layers.

8.2.3 Shear strains in the connector

From mechanics of materials, it is known that the difference in longitudinal strain registered by two arbitrarily oriented strain gauges in a uniform strain field is proportional to the shear strain along an axis bisecting the strain gauge axes and can be given by Eq. (61). Defining $0°$ axis as bisector of angle between gauge axes (see Figure 164), $\alpha = 45°$ as the angle between the strain gauges and the axis bisecting the strain gauge axes. Thus, the shear strain $\gamma_{0°90°}$ can be written as given be Eq. (61):

$$\gamma_{0°90°} = \frac{\varepsilon_{s1} - \varepsilon_{s2}}{\sin(2 \cdot \alpha)} = \frac{\varepsilon_{s1} - \varepsilon_{s2}}{\sin(2 \cdot 45°)} = \varepsilon_{s1} - \varepsilon_{s2} \tag{61}$$

where,

ε_{s1} is the strain registered by the strain gauge s_1.

ε_{s2} is the strain registered by the strain gauge s_2.

Therefore, considering that for the test configuration and for the arrangement of instrumentation shown in Figure 164, the normal strain registered by strain gauge s2 (ε_{s2}) is always negative (indicating compression). Thus, the shear strain $\gamma_{0°90°}$ can be calculated summing the absolute value of normal measurements registered with strain gauges mounted at +45° and −45° to the loading axis (s1 and s2, presented in Figure 170(a) and Figure 170(d)) at each data point. For the specimen MU4 02, the strain gauge s1 did not function, and the shear strain was taken equal twice the absolute value registered by the strain gauge s2.

In both specimens the shear strains presented a linear response with the load up to cracking. From this point on, the response presented a higher gradient of strains in consequence of the reduction of the stiffness due to cracking propagation, but the behaviour was kept almost linear up to the maximum load. By comparing the curves obtained for the specimen made with CSM and MU4 laminates, it can be observed that the maximum obtained shear strain was 5338 με and 2192 με, respectively. These values corresponds to 27.3% and 11.2% of the

ultimate shear strain of the CSM laminate. Although the MU4 laminate was not characterized under pure shear load conditions, it is expected that, due to its high content of fibres in ±45° directions, its ultimate shear strain is even higher than the value obtained for the CSM laminate.

8.2.4   Estimation of the degree of composite action attained with the connectors

The degree of compositeness of a sandwich panel is a quantitative concept for knowing how is the efficacy of both SFRSCC layers on acting together as a single unit to resist the applied loads. It also can be used to simplify the design of the panels, making possible to estimate the maximum deflections and stresses for a certain load level the panel is subjected. The degree of composite action of sandwich beams were evaluated considering the following two approaches: 1) the deflection obtained experimentally for the midspan section, similarly to what was done by Frankl *et al.* (2011); 2) the normal stress/strain distribution in the midspan section, as done by Benayoune *et al.* (2008b).

Differently from what is found in the literature (Benayoune *et al.*, 2008b, Frankl *et al.*, 2011), in this work a unified concept of degree of composite action was used. The idea is to compute the degree of composite level of beams as a function of the effective moment of inertia of these elements, independently on the parameter used (deflections or normal stresses/strains). This methodology differs from the adopted by Frankl *et al.* (2011), where the degree of compositeness of panels were computed making direct comparisons between the measured deflections with theoretical values. On the other hand, the degree of composite action proposed in this work is a percentage indicator of the two extreme situations in terms of moment of inertia of the beam considering the beam as a a noncomposite system and as fully composite system. This concept also differs from the degree of composite action calculated by Benayoune *et al.*(2008b) because in that work this concept represents the percentage of the theoretical moment of inertia of the panel acting in a fully composite way. Thus, the degree of composite action was computed using Eq. (62).

$$\varphi_i = \frac{I_{ef.i} - I_{nc}}{I_{fc} - I_{nc}} \tag{62}$$

where,

φ_i is the degree of composite action.

i is the load level that the degree of composite action is determined, given in kN.

I_{nc} is the theoretical moment of inertia assuming noncomposite behaviour.

I_{fc} is the theoretical moment of inertia assuming fully composite behaviour.

$I_{ef.i}$ is the effective moment of inertia (i.e., obtained from experimental data).

In this work the amount of composite action was determined only for a load equal to 14 kN, which corresponds to a load level immediately before the cracking load for all tested panels, based on the experimental observation.

The theoretical moments of inertia of sandwich beams were computed from Eqs. (63) and (64) for the noncomposite and fully composite cases, respectively:

$$I_{nc} = 2 \cdot \left(\frac{b \cdot h^3}{12} \right) \tag{63}$$

$$I_{fc} = 2 \cdot \left(\frac{b \cdot h^3}{12} + b \cdot h \cdot d^2 \right) \tag{64}$$

where b is the width of the sandwich beam's cross section (i.e., 200 mm for the sandwich beams tested in this work), h is the thickness of each SFRSCC layer (i.e., 60 mm for the sandwich beams tested in this work) and d is the distance from the centroid of a SFRSCC layer to the mid depth of the beam's cross section (i.e., 60 mm for the sandwich beams tested in this work). The values obtained for I_{nc} and I_{fc} are, respectively, 7.20×10^6 mm^4 and 9.36×10^7 mm^4. The values of I_{nc} and I_{fc} were obtained disregarding the contribution of the connector (GFRP) and of thermal insulation block (EPS). In fact, due to their very low elastic modulus, in comparison to the SFRSCC layers (and thickness in the case of GFRP plate), the moment of inertia of the homogenized composite system (i.e., considering the contribution of connector and thermal insulation to the moment of inertia), considering a fully composite behaviour and GFRP connectors made with CSM and MU4 laminate are, respectively, only 0.26% and 0.56% higher than the values obtained considering only the SFRSCC layers.

The effective moment of inertia obtained based on deflections corresponding to a load level equal to 14 kN $\left(I_{ef.14} \right)$ was calculated within the elastic range adopting the Euler-Bernoulli beam's equation and taking into account the deflections measured in the midspan of a beam and the support and loading conditions represented in Figure 161. Solving the Euler-Bernoulli beam's equation, the effective moments of inertia for the beam made with CSM and MU4 connectors were calculated with the average of the measured midspan deflections corresponding to the load level of 14 kN (i.e., average of deflections measured in front and rear sides of the beams, for the top and bottom SFRSCC layers, for the specimens 01 and 02). The values obtained for $I_{ef.14}$ were equal to $3.206 \times 10^7 \text{ mm}^4$ and $5.340 \times 10^7 \text{ mm}^4$ for the beam made with CSM and MU4, respectively. Thus, by applying Eq. (1) a degree of composite action of to 28.77% and 53.47%, was obtained for beam made with CSM and MU4 connectors respectively. If the methodology proposed for Frankl *et al.* (2011) was followed, the degree of composite action would be 84% for the beam made with CSM connector and 94% for the beam made with MU4 connector.

Figure 165 compares the experimentally obtained deflections with the theoretical deflections considering a non composite and fully composite behaviour of the beams. The results indicate that the deflections would be largely overestimated if a non-composite behaviour is considered for designing the panels.

8.3   PERFOFRP *VERSUS* SFRSCC SLIP

The end-slip values recorded by the LVDTs I and P indicated in Figure 164 were nearly zero until the end of the tests for all the specimens, having been 0.62 mm the maximum value. This value corresponds to the sum of the shear deformation and the slip between the PERFOFRP and the SFRSCC. The reduced end-slip observed in the tests reiterates the relatively high degree of composite behaviour of these panels.

8.3.1   Correlation between beam behaviour and push-out tests

From the experimental tests it can be stated that all tested sandwich beams have demonstrated adequate connection between the top and bottom SFRSCC layers, since no premature failures occurred, and the beams experienced relatively large deflections.

In the work presented in the Chapter 7, it was evaluated the direct shear capacity of connections made with the same CSM PERFOFRP connector consisted of 3 holes spaced

75 mm (center-to-center distance). In that study it was found that the shear strength of CSM PERFOFRP connectors embedded in SFRSCC A from casting 4 was equal to 174.22 kN/m (39.2 kN per 3×0.075 m of connection) and 341.78 kN/m (76.9 kN per 3×0.075 m of connection) for specimens without and with SFRSCC in front of connectors, respectively. Once it is not known what is the actual degree of confinement that the connectors are subjected in the sandwich beams, these values can be considered a lower and upper bound value of the shear strength of connections in the sandwich beams.

The failure by longitudinal shear of the connection would happen only if the longitudinal shear capacity of connection is surpassed by the value of the horizontal shear per unit length, also known as shear flow. In turn, the shear flow can be estimated by the following expression: $q_L = \dfrac{V \cdot Q}{I}$, where q_L is the shear flow, V is the vertical shear force, Q is the first moment with respect to the neutral axis of the portion of the cross section located either above or below the point at which q is being computed, herein taken as the area of the cross section of each SFRSCC layer, and I is the centroidal moment of inertia of the entire cross-sectional area. Thus, for the same load configuration and geometry of the beams, considering a linear elastic behaviour of materials and the effective moment of inertia determined by means of the registered deflections for the beams made with CSM connectors in the elastic range (i.e., $I_{ef.14}$ was equal to 3.206×10^7 mm^4), the shear flow corresponding to the highest cracking load and to the highest ultimate load registered in the test with the sandwich beams, i.e., 15.5 kN and 28.3 kN, respectively, would be 176.29 kN/m and 317.779 kN/m. These results indicate that, if there wasn't thermal insulation material contributing to resist the shear flow developed in the beam and if the shear strength obtained without end-bearing effect is representative of the shear strength of the connection in the beam, the failure by shear in the connection was near to occur even before the cracking of SFRSCC layers.

8.4 NUMERICAL STUDY

The main target of this numerical study is to contribute for a better understanding of the behaviour of the tested sandwich beams. More specifically, the interest of this investigation is to assess the stress distributions in the concrete layers and, mainly, in the PERFOFRP connectors during the loading process of the tested beams. In fact, investigations previously developed and described in Chapter 6 and Chapter 7, have shown that the ultimate shear

capacity of the sandwich panels can be conditioned by the rupture of the PERFOFRP connectors. However, since the anchorage parts of the connectors are embedded in the SFRSCC layers, the experimental evaluation of the strain field in these zones is quite difficult, and the failure mechanisms occurred cannot be followed.

General purpose software FEMIX, based on the Finite Element Method, was used for the analysis of a sandwich beam that reproduces the experimental test conditions. The SFRSCC layers and the thermal insulation were modelled by solid elements (20 nodes), while the connector was modelled by Reissner-Mindlin flat shell eight nodes finite elements. For both types of finite elements a Gauss-Legendre integration rule was adopted, with $2\times2\times2$ integration points (IP) for the solid elements, and 2×2 IP for the flat shell elements. The finite element mesh of the full beam is composed of 10032 elements and 43013 nodes. The dimensions attributed to the components forming the beams are equal to the ones of the representative tested beams. To obtain a more realistic stress/strain distribution in the GFRP, the holes were explicitly modelled, as shown in Figure 172. Perfect bond was considered between the PERFOFRP connector and the SFRSCC, since modeling the interface conditions between these two materials would require specific research in this topic, which is out-of-scope of the present work. A perfect bond was also assumed for the interface between EPS and SFRSCC/GFRP elements. An overall view of the mesh is illustrated in Figure 172.
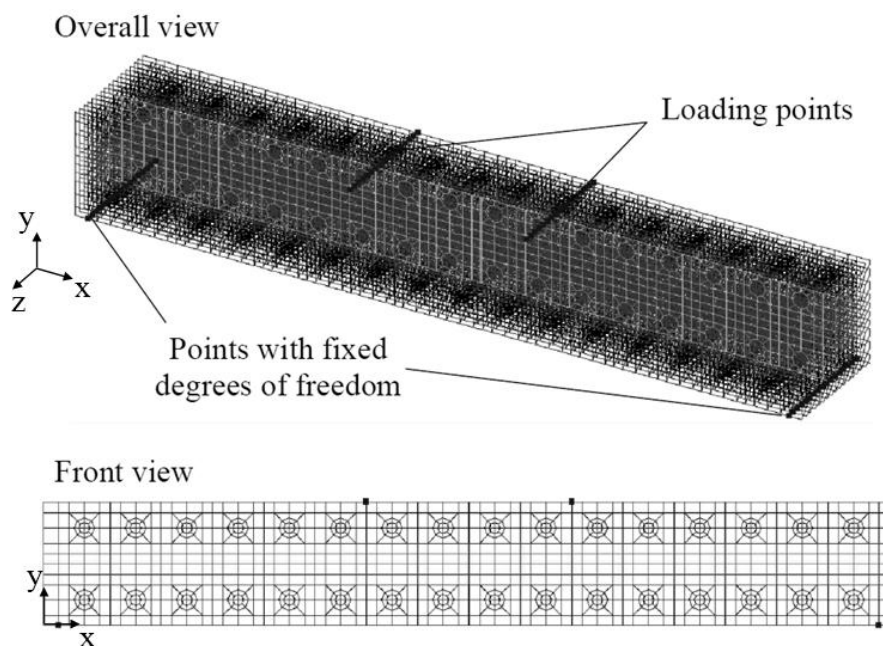
Figure 172: FE mesh adopted.

First, the SFRSCC, GFRP and EPS were simulated assuming a linear and isotropic behaviour, by considering the following values for the modulus of elasticity experimentally determined: 34.6 GPa (SFRSCC), 14.64 GPa (CSM), 16.70 GPa (MU4), and 7.5 MPa (EPS), this last one indicated by the supplier.

In a second stage, the beam was also modelled considering a multi-directional fixed smeared crack model for SFRSCC. In this model, the material was assumed as having a linear elastic behaviour under compression, since concrete crushing was not significant at failure of tested specimens. A quadrilinear stress–crack opening diagram was adopted to represent the post-cracking behaviour of the SFRSCC. The parameters used to represent the post-cracking behaviour of SFRSCC are schematically represented in Figure 37. Due to the uncertainties of the direction of fibres in the structural element, as discussed in the section 3.4, the sandwich beams were simulated considering the fracture parameters for the average, lower bound and upper bound behaviour of SFRSCC B obtained by inverse analysis of 3PBTs, as shown in Table 17.

The models considered the self-weight of the beam, assuming the specific weight of 25 kN/m^3, 18 kN/m^3 and 0.15 kN/m^3 for the SFRSCC, GFRP and EPS, respectively. The external vertical load was simulated by two line forces applied in the top surface of SFRSCC top layer, as schematically represented in Figure 172. The vertical displacement of the aligned nodes corresponding to the supports was restrained. For the nodes corresponding to one of the supports the horizontal displacement was also restrained.

8.4.1 Comparison between experimental and numerical responses

In Figure 165 the midspan deflections obtained experimentally are compared to the results obtained with the Finite Element simulations. The model was capable of fitting with reasonable accuracy the elastic stage of the tested beams, but a tendency for a softer prediction is visible, mainly in the beams with CSM connector. For this deviation can contribute uncertainties and inaccuracies inherent to the experimental behaviour (i.e., idealized boundary conditions, evolving of material properties, geometric inaccuracies, among others). In what concerns the nonlinear modelling, it is clear that a better fitting of the experimental response is attained when the upper-bound post-cracking behaviour is used to simulate the SFRSCC.

Figure 171 presents a comparison of the longitudinal strains in the GFRP connector at the midspan section of the beam, recorded experimentally and determined numerically (linear modelling). These strain values correspond to a load of 14 kN, when cracking is imminent in the bottom SFRSCC layer. The model predicted with sufficient accuracy the strain values registered experimentally in both types of connectors.

8.4.2   Stress pattern

Figure 173 to Figure 176 show the stress contour obtained with the numerical model for the SFRSCC layers and for the GFRP connector at a load level (14 kN) close to the cracking load.

As shown in Figure 173, tensile normal stress developed on bottom surfaces of both SFRSCC layers at the central region of beam. This behaviour was obtained for all models, independently of the properties attributed to the GFRP used in the connector. This response reiterates the fact that the connection does not provide a fully composite action to the beam. Maximum tensile stresses were installed in the beam with CSM laminate in the connector, indicating its relatively lower degree of composite action, due to the lower stiffness of this GFRP material.

A tensile strength equal to 3.9 MPa was estimated for the SFRSCC from its compressive strength through the equation proposed by the *fib* Model Code 2010 (*fib,* 2012a). Observing the stress levels attained in the SFRSCC layers (see Figure 173), the numerical simulations indicate that at a load level of 14 kN cracking would have already occurred in the bottom zones of both SFRSCC layers.

Tensile stresses developed in the SFRSCC layers along the width of the beam, attaining the maximum values in the nearby of the connector (see Figure 174). This stress concentration pattern is analogous to the longitudinal cracking observed in some beams during the tests (see Figure 168(b)).

In Figure 175 and Figure 176 are illustrated, respectively, the normal and shear stress contours in the CSM and MU4 laminate connectors, at a load level of 14 kN. At this load level, the maximum tensile stress developed in the connectors is less than 1.5% of the tensile strength of the corresponding laminate. For the same load level, the model estimates a maximum shear stress of about 13% of the shear strength of CSM laminate.
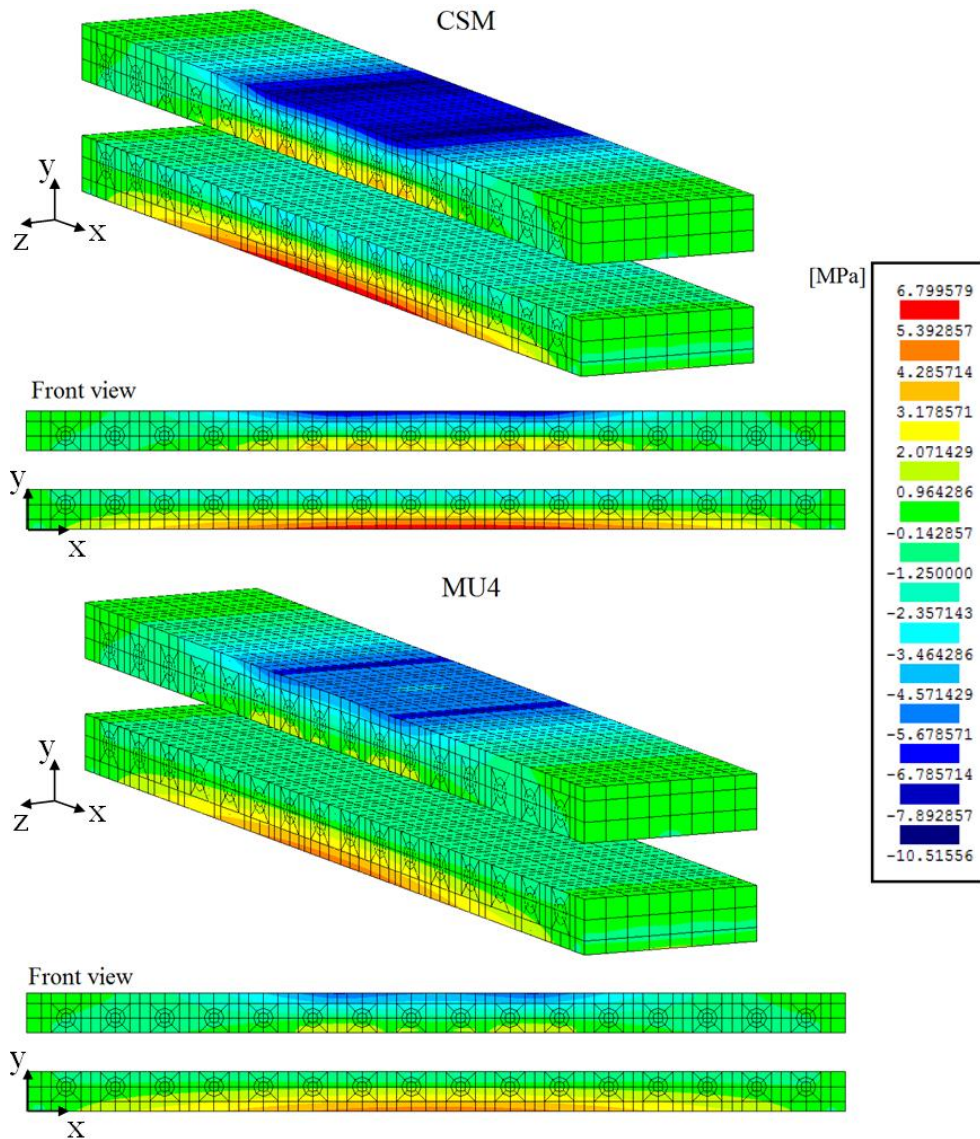
Figure 173: Normal stress σ_{xx} field in the SFRSCC layers corresponding to an applied load of14 kN (compression is negative).
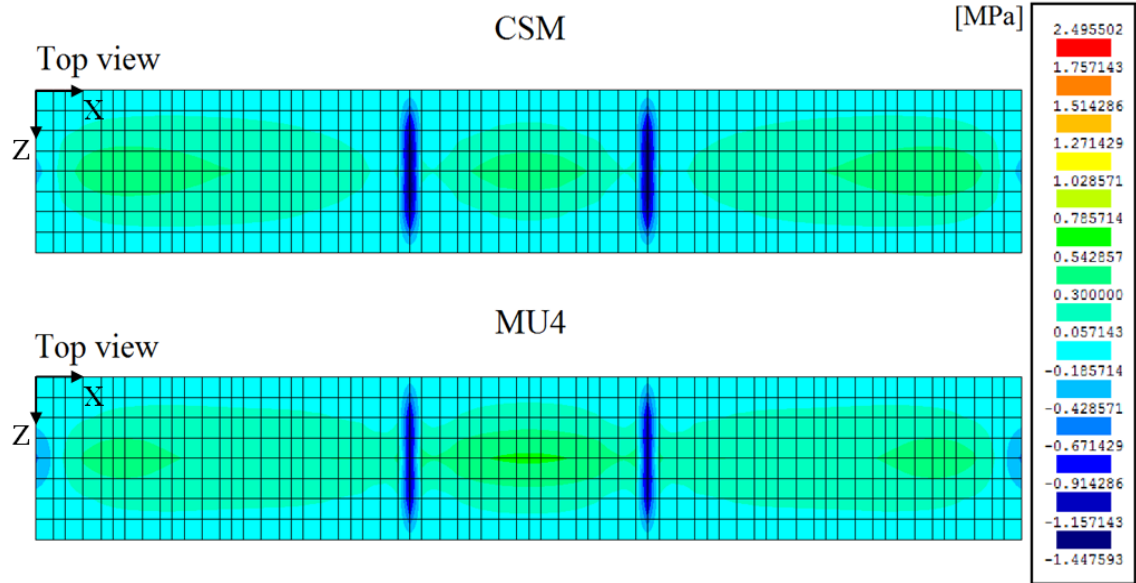
Figure 174: Normal stress σ_{zz} field in the SFRSCC layers corresponding to an applied load equal to14 kN (compression is negative).
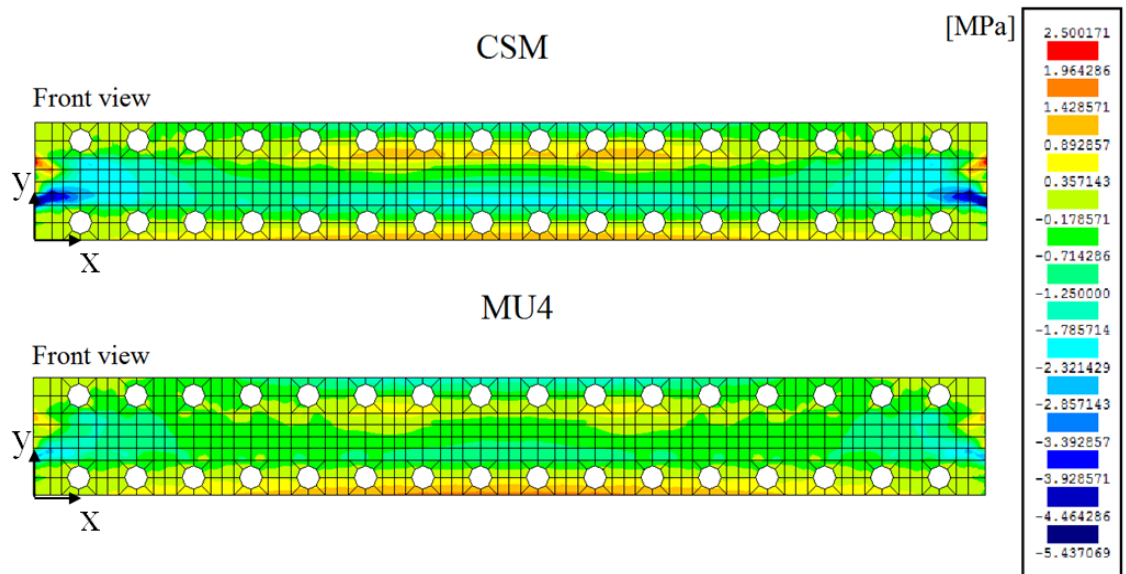
Figure 175: Normal stress σ_{xx} field in the GFRP connector corresponding to an applied load equal to14 kN (compression is negative).
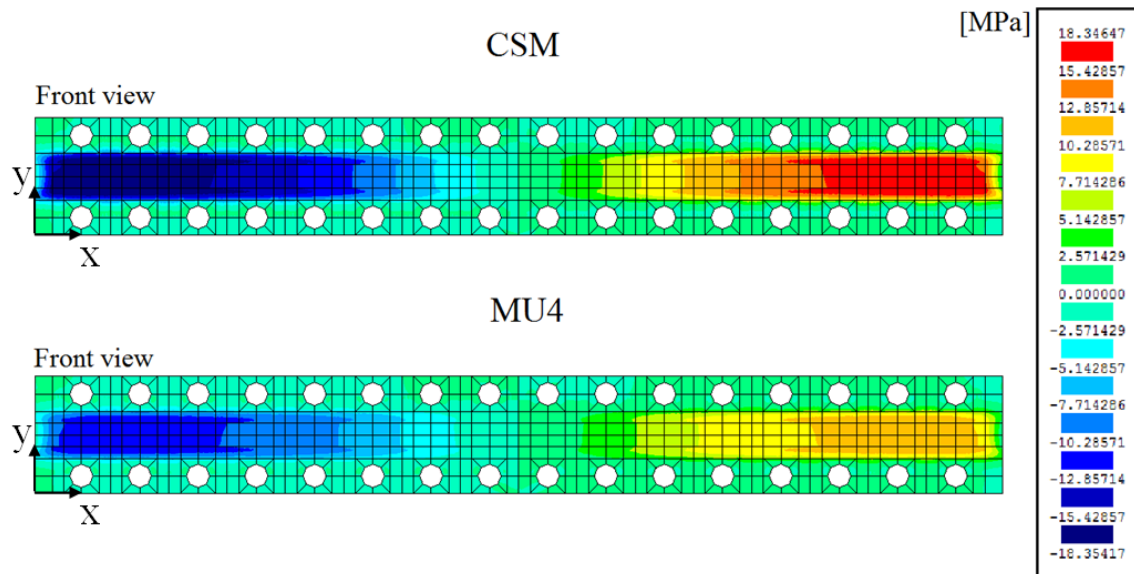
Figure 176: Shear stress γ_{xy} field in the GFRP connector corresponding to an applied load equal to14 kN.

8.5 FINAL REMARKS

This chapter performed an experimental and numerical investigation on the flexural behaviour of connections for sandwich panels containing PERFOFRP connectors and SFRSCC layers. Sandwich beams made with two different types of GFRP connectors (i.e., CSM and MU4) were tested under four-point bending, and the results were analyzed in terms of deflection, strain fields and failure mechanisms. For a better understanding of the flexural behaviour of connections, linear elastic and nonlinear material FE analyses were also performed. The model was validated with the experimental data and the stress fields were obtained. The main conclusions derived from the experimental and numerical investigations are the following ones:

- Independently on the type of laminate used in the connector, the ultimate failure mechanism of the connections under flexure is always associated to the flexural failure of the PERFOFRP connector after an extensive cracking in the SFRSCC layers.
- Although no significant increase on the cracking or ultimate load of the tested sandwich beams were obtained by replacing CSM connector by another stiffer connector, MU4, the failure mode obtained in the beams made with MU4 laminates was much more ductile.

- No significant slip was observed between the PERFOFRP connectors and the SFRSCC during the tests, at least in the parts where this slip was possible to be measured.

- A relatively low degree of composite action was achieved with both studied connections. The connections made with MU4 laminates presented a slightly high degree of composite action. When deflections were used, the connections made with CSM and MU4 laminates presented 28.77% and 43.47% of composite action, respectively.

- The general behaviour obtained with the FE model represented by load-deflection plots and strain variations in the midspan showed good agreement with the experimental data from sandwich beams tests.

- The stress contours obtained by the FE model of sandwich beams indicated that, for a load level corresponding to the imminence of SFRSCC bottom layer cracking, the maximum normal tensile stresses developed in the connectors were always less than 1.5% of the tensile strength of CSM or MU4 laminates. Furthermore, the maximum shear stresses attained in the laminates corresponded to only 13% of the shear strength of CSM laminate.

Chapter 9

IN-PLANE CYCLIC BEHAVIOUR

A main concern in the case of structural wall systems where the walls are used as the lateral force resisting system, similarly to the proposed in this thesis, is related to their capacity of bearing lateral loads (in-plane loads). It is highly desirable that they are designed to exhibit a ductile behaviour, which means demonstrating sufficient shear strength to favor a flexural yielding (Paulay *et al.*, 1982). In fact, design codes for seismic resistance of concrete buildings are more conservative for wall systems than for frame structures (CEN, 2005b). This is mainly attributed to the fact that the shear plays a superior role in seismic response of walls added to the smaller experimental-base knowledge on wall systems. An aggravating in the case of the proposed system is the fact that the panels are precast. The design of precast/prefabricated systems generally is even more conservative.

Since the 1950s, some research has been developed to access the behaviour of prestressed/reinforced concrete walls under monotonic or simulated earthquake loading (Barda *et al.*, 1977, Paulay *et al.*, 1982, Kypros and Amr, 1995, Hidalgo *et al.*, 2002, Cevdet K. Gulec and Bozidar, 2008, Kuang and Ho, 2008, Cevdet K. Gulec and Bozidar, 2009, Massone *et al.*, 2009). Nonetheless, few attention was given on the use of precast/prefabricated wall systems as primary lateral load resisting system for seismic regions (Crisafulli *et al.*, 2002, Holden *et al.*, 2003, Perez *et al.*, 2003, Todut *et al.*, 2014). The seismic performance of precast/prefabricated structural wall systems is not well understood because experimental research on walls is quite expensive and difficult of executing (Pavese

and Bournas, 2011). Moreover, most of these studies are focused on the behaviour of slender cantilever walls, giving relatively few attention for concrete walls with a height to length ratio of less than 2, hereinafter referred as squat walls.

Currently, there is still a lack of studies on the mechanical behaviour of structural concrete sandwich panels. The few works in this field are mainly dealing with the out-of-plane behaviour of panels (Bush and Wu, 1998, Pessiki and Mlynarczyk, 2003a, Benayoune *et al.*, 2008b, Frankl *et al.*, 2011). Only few and recent research works about their behaviour under seismic loads are available. The works developed by Pavese and Bournas (2011) and by Ricci *et al.* (2013) are dedicated to the assessment of the behaviour of single reinforced concrete cast-in-place squat sandwich panels under pseudo-static (cyclic) loadings. The behaviour of the complete structural system under earthquake (dynamic) loadings was investigated by Rezaifar *et al.* (2008) and Palermo *et al.* (2014). Nonetheless, the geometry, reinforcement of concrete layers, connections between concrete layers and constructive aspects of the sandwich panels tested in those researches are completely different from the solution proposed by Lameiras *et al.* (2013c, 2013b). The main differences that can be pointed out are the traditional materials (concrete reinforced with steel rebars and electro-welded meshes) and the cast-in-place technology for the sandwich panels, as well as steel connectors to link the external and internal RC concrete layers.

The investigation presented in this chapter was undertaken with the main aim of attaining a better insight of the in-plane cyclic behaviour of the sandwich panels comprising SFRSCC layers and PERFOFRP connectors. Experimental results of quasi-static in-plane cyclic tests performed on real scale sandwich panels were obtained, including failure modes, hysteresis diagram and shear behaviour. The option for the quasi-static in-plane cyclic tests relies on the available experimental facilities. Furthermore, stiffness degradation, ductility and energy dissipation capacity were also assessed from the experimental tests carried out.

9.1   TEST PROGRAMME

Real-scale tests with single walls were performed under combined in-plane loadings, which are: static horizontal cyclic loading and constant vertical loading (corresponding to the load transmitted by the upper stories for a low-rise residential building). In a simplified manner,

these tests on single walls can simulate the seismic action expected on the wall during an earthquake (Chopra, 1995).

The tests were performed with four prototypes, two of them without openings (NO) and the remaining two with a central opening (OP). These tests were carried out in the Laboratory of the Structural Division of the University of Minho.

9.1.1 Material properties

The materials used to build the prototypes were SFRSCC for the concrete layers, GFRP for the PERFOFRP connectors and Expanded Polystyrene (EPS) for the thermal insulation core. Different castings of SFRSCC B were used to produce the prototypes. In the prototypes NO02 and OP01, two castings were required for the bottom and top SFRSCC layers (see Table 42). In the Table 42 are presented the average values and CoV for the compressive strength and modulus of elasticity of used SFRSCC. Further data about the SFRSCC are given in Chapter 3.

Table 42: SFRSCC used in the production of the prototypes.

Panel / layer	SFRSCC B casting number	Compressive test			Modulus of elasticity test		
		Age [days]	N. of spec.	f_c [MPa] Avg. (CoV)	Age [days]	N. of spec.	E_c [Gpa] Avg. (CoV)
NO01/Both	10	94	4	45.60 (8.5%)	94	2	34.60 (3.5%)
NO02/Bottom	18	66	4	54.81 (2.7%)	66	2	35.97 (8.8%)
NO02/Top	19	66	4	64.83 (2.3%)	66	2	42.20 (2.6%)
OP01/Bottom	11	66	4	56.39 (3.4%)	66	2	35.06 (10.5%)
OP01/Top	12	66	3	61.23 (2.5%)	66	2	35.89 (16.1%)
OP02/All	13	67	4	61.94 (5.2%)	67	2	41.61 (6.0%)

Taking into account the performance and costs of the different GFRPs investigated in the experimental programs presented in Chapter 4, Chapter 6 and Chapter 7, and the required mechanical properties accessed in Chapter 5, the CSM GFRP was chosen to be used in the connectors of the present prototypes. Only the CSM 02 was used in the production of these connectors. Further information about the GFRP can be found in Chapter 4.

The EPS was used as the insulation material in the core, since it is economic and readily available. According to data supplied by the manufacturer, the expanded polystyrene adopted

in the middle layer has an apparent density equal to 15 kg/m^3, flexural strength equal to 100 kPa, obtained following the EN 12089 (CEN, 2013b), and develop compressive stresses at 2% and 10% strains, determined according to EN 826 (CEN, 2013a), equal to 15 kPa and 60 kPa, respectively.

9.1.2 Geometry and execution of prototypes

Figure 177 shows the dimensions and details of the prototypes used in the in-plane cyclic tests. All the prototypes have length (l_w) and height (h_w) equal to 2000 mm ($h_w / l_w = 1.0$). The thermal insulation material, the inner and the outer SFRSCC layers have thicknesses equal to 60 mm. The thickness of the inner SFRSCC layer was increased for 90 mm in a strip of 400 mm of height along the top boundary of panel. This solution reduces locally the thickness of thermal insulation what could jeopardize the thermal efficacy of sandwich panel, but it was the easier way to guarantee a suitable contact area to support the slabs in the modular construction developed in the scope of this research project. For the OP panels, a square opening with lengths equal to 900 mm × 900 mm was executed in its centre to simulate the effect of a window. For the sake of convenience, a solid SFRSCC zone with height equal to 150 mm was produced in their base, corresponding to the height of the panel that will be embedded in the foundation (see Figure 177). It is believed that the existence of this solid zone along the bottom edge of wall panel also helps to reproduce the effect of the cast-in-place foundation proposed for the modular construction system.
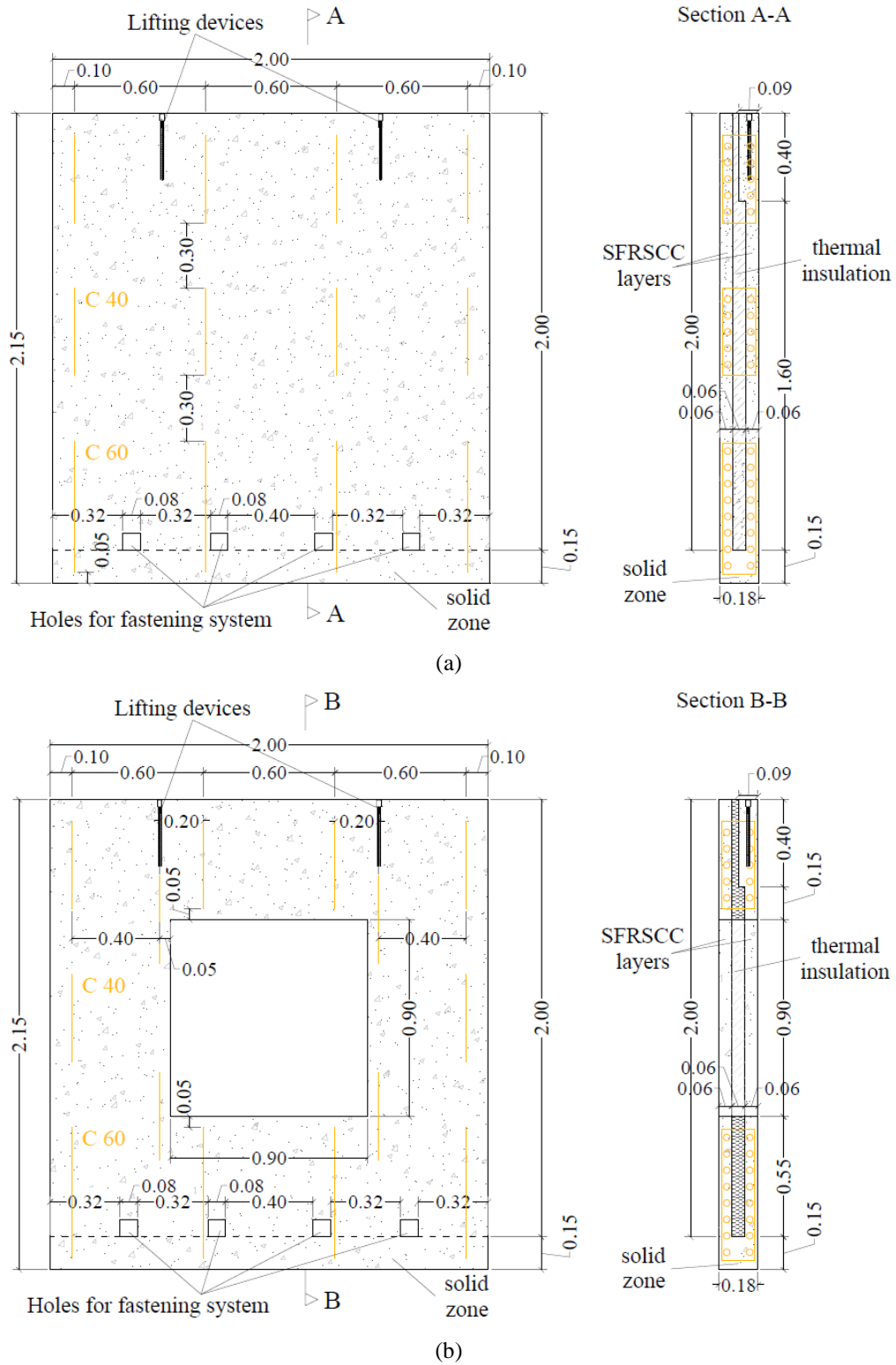
Figure 176: Details of the prototype (a) without opening and (b) with opening (dimensions in m).

(c)
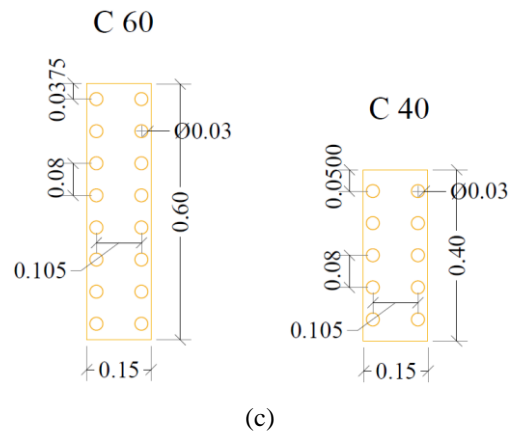
Figure 177: Details of the prototype: (c) connectors (dimensions in m).

Based on the numerical modelling of the sandwich panels under service conditions (see Chapter 5) and on the strength capacity of connections (see Chapter 6 and Chapter 7), it was decided to use discrete connectors (length equal to 400 mm) regularly distributed along the panel and arranged as shown in Figure 177(a) and Figure 177(b). These connectors are called C40 in Figure 177(c). All the connectors were positioned with their length parallel to the height of the prototypes. In the prototypes with opening, it was decided to use a connector in the proximity of each corner, as presented in Figure 177(b). Four connectors with length equal to 600 mm, hereinafter called C60, were positioned along the base of the prototype with 100 mm embedded in the SFRSCC solid zone (see Figure 177).

To enable the fastening system of the planed test setup, four square holes were produced immediately above the solid zone, through the all thickness of prototype (see Figure 177). The holes were produced using EPS prisms positioned appropriately during the casting of panels. Originally, also to enable the fastening of the wall to the reaction slab of the laboratory, the solid zone was planned and executed longer than the sandwich panel part (150 mm for each side), as shown in Figure 178. Nonetheless, the test setup was modified after some preliminary tests, and the regions of the solid zone longer than the wall panel were cut off using a diamond saw.

A wooden placeholder was used to materialize the window in the prototypes with openings, as shown in Figure 178(b). The thicker SFRSCC zone was materialized reducing the thickness of the thermal insulation to 30 mm in a strip of 400 mm of height along the top boundary of panel.

The execution of the prototypes followed the same sequence: (1) the thermal insulation plates (EPS) are previously cut in predefined dimensions according to the design of the prototype; (2) slots are opened in the EPS plates to allow the passage of the connectors; (3) The formwork is positioned in order to define the designed dimensions of the prototype; (4) EPS prisms for the fastening system are previously placed; (5) the first SFRSCC layer is poured; (6) the thermal insulation plates (EPS plates) and lifting inserts are placed; (7) the connectors are positioned prior the SFRSCC set time; (8) the second SFRSCC layer is poured and (9) after the initial curing (approximately 16h covered by a wet blanket), the prototype is removed from the mould and stocked, being cured under laboratory temperature and humidity conditions until the date of test. The employment of SFRSCC in replacement of the traditional reinforced concrete dismissed the execution of activities as cutting, bending, tying and placing of reinforcement as well as the vibration of the concrete of both layers.

(a)

(b)
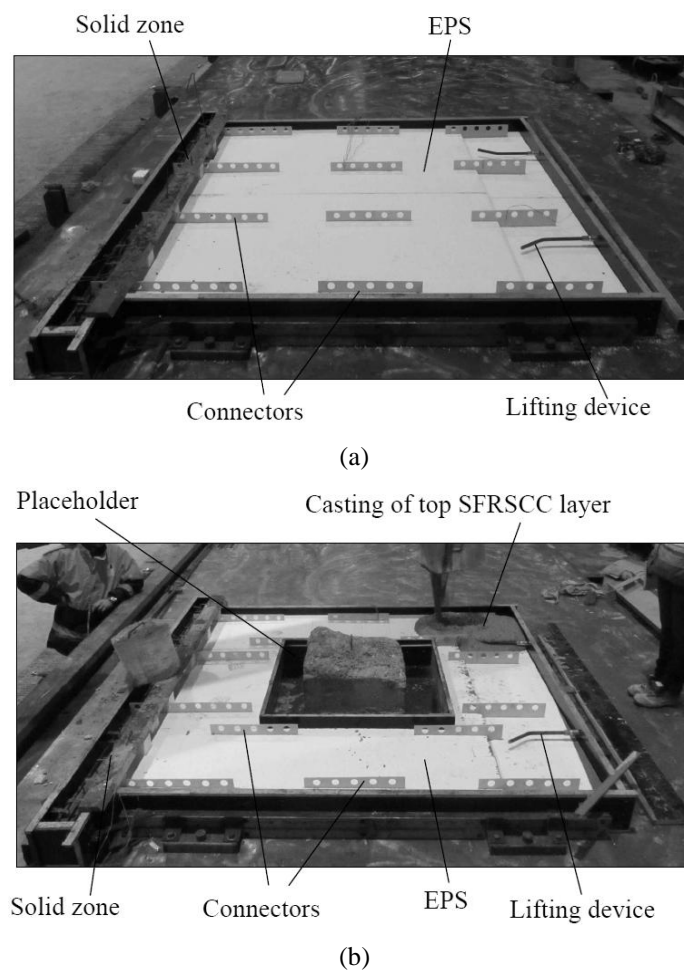
Figure 177: Manufacturing process of sandwich panels: (a) panels without opening and (b) panels with opening.

Spacers

(c)
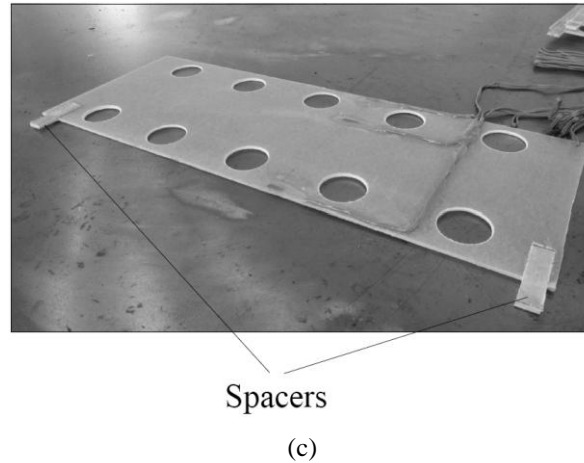
Figure 178: Manufacturing process of sandwich panels: (c) detail of connector with spacer.

All the prototypes were cast in the horizontal position, as shown in Figure 178. For the sake of simplicity on the manufacturing of sandwich panels, the connectors were positioned after the casting of the first SFRSCC layer. As noted in Chapter 5, this procedure reduces the probability of having fibres passing through the holes of the perforated GFRP connectors. Nonetheless, it disregards the use of temporary supports to keep the connectors positioned and held firmly while the first SFRSCC layer is poured. In the adopted procedure the connectors are positioned in slots previously made in the EPS plates (see Figure 178). In order to guarantee the specified SFRSCC cover (i.e., nominal distance between the GFRP connector and the mould equal to 15 mm), spacers made with the same GFRP used in the connectors were glued as shown in Figure 178(c).

9.1.3   Test setup, instrumentation and test procedure

Figure 179 illustrates the test setup used in the experimental program. It was conceived in order to apply almost constant in-plane vertical loads and cyclic lateral load in the prototypes. The prototypes were laterally loaded, reversed cyclic, displacement controlled, using a loading system consisting of an hydraulic servo-actuator acting in a rectangular loading area equal to 250 mm $\times$ 90 mm (height $\times$ width) with the gravity center passing 125 mm from the top surface of the prototype (see Figure 179). The actuator has a maximum capacity in terms of displacement and load equal to 100 mm and ± 250 kN, respectively. The loads and corresponding displacements are considered positive when the prototype is pushed. The actuator was connected to the reaction wall by means of a three-dimensional hinge and to the specimen by means of a two-dimensional hinge (see Figure 179). In order to impose the cyclic displacements to the prototype, the thicker part of the internal SFSCC layer was

confined by two steel plates connected through four sufficiently stiff steel threaded bars (nominal diameter: 40 mm).

The vertical load was applied by three hydraulic cylinders with automated pressure self-adjustment by means of a IPN 200 steel profile. Each hydraulic cylinder applied the load directly to the steel beam, acting against a T-shaped steel plate that is connected through four vertical steel threaded bars (nominal diameter: 17.5 mm) with hinges welded to the lower steel beam. This configuration allows the actuators to follow the horizontal movement of the prototype during the tests. For an adequate distribution of the vertical load, steel parts were welded to the top of the steel beam positioned in the top of the wall. The top surface of the wall that received the distributed load was leveled and regularized using high strength mortar. Finally, for a better distribution of load, one strip of a rigid rubber with 2 mm was positioned between the steel beam and the wall.

The prototype was connected to the bottom steel profile in 4 points in order to prevent the vertical movement of the solid SFRSCC zone (see Figure 179). For practical purposes, two different fastening systems were used to prevent the vertical displacements of specimens, as shown in Figure 179(c). Near the extremities of the wall panel were adopted a system where a high strength bolt was positioned in the solid SFRSCC zone. In the middle of panel were used steel bars with rectangular section passing throughout the holes produced during the casting of specimens (see Figure 179). Furthermore, the horizontal movement of the solid zone was restrained in the direction of the load confining it with two steel profiles, as shown in Figure 179. The out-of-plane displacements were prevented through means of punctual steel rollers distributed along the upper part of the specimen, on the both sides of the wall (see Figure 179(a)).
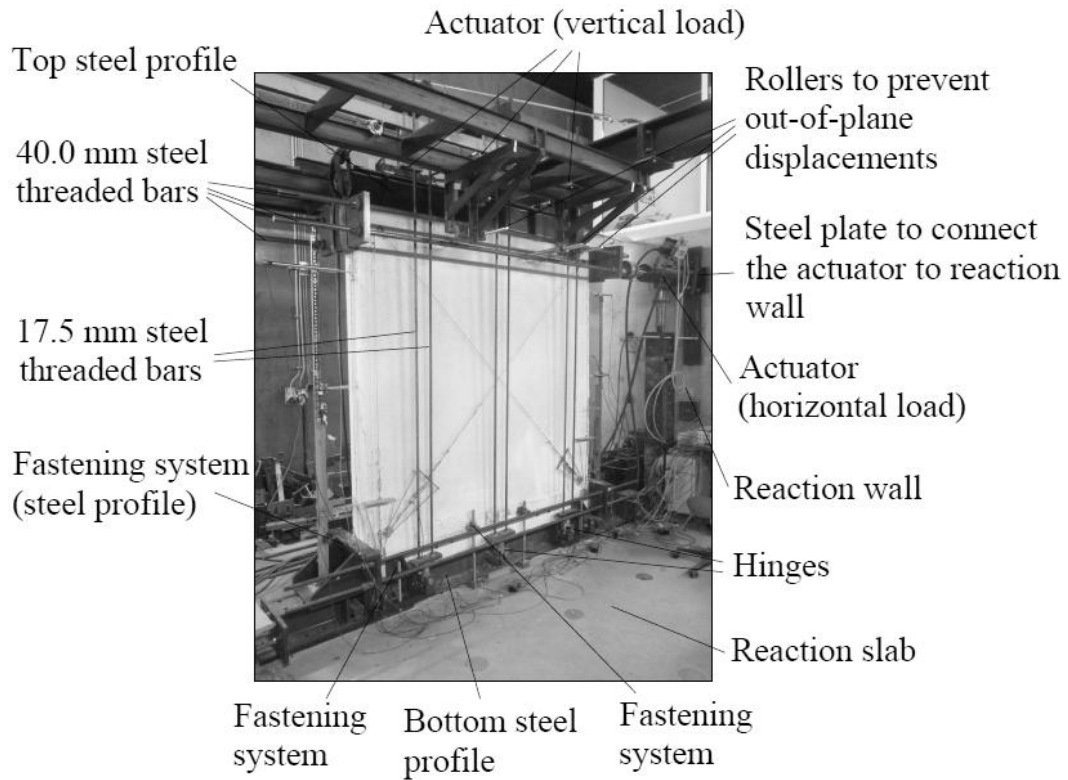
(a)
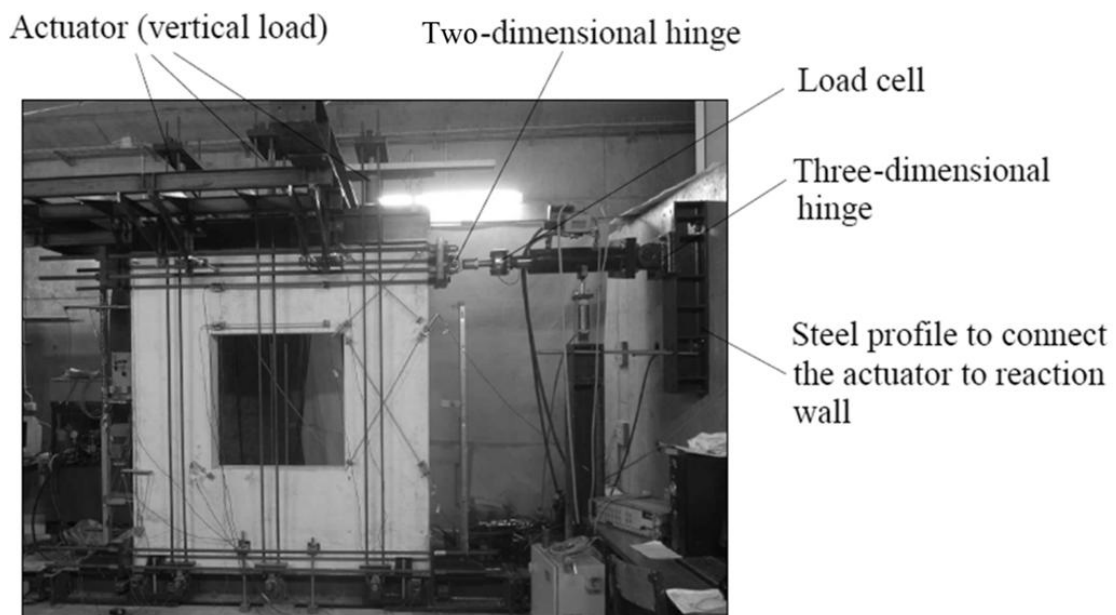
(b)

Figure 178: Experimental setup: (a) perspective of test setup adopted in NO 01 prototype; (b) lateral view of test setup adopted in NO 02, OP 01 and OP 02 prototypes (dimensions in m).

(c)
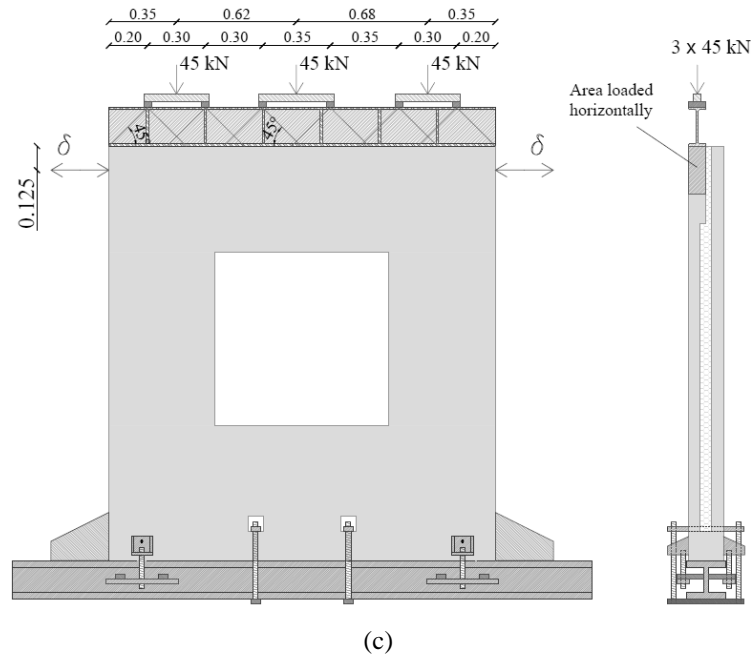
Figure 179: Experimental setup: (c) schematic representation of loading system (dimensions in m).

The displacements of specimens were measured using linear variable differential transformers (LVDT), as shown in Figure 180. Different instrumentation was used on the tests with NO and OP type walls. In general 16 LVDTs were used. In the specific tests of the prototypes without openings, 7 LVDTs were used to capture the horizontal displacement of these prototypes at different elevations (LVDTs 5 to 11, as presented in Figure 180). As shown in Figure 180, these horizontal displacements were registered in both SFRSCC layers, in order to capture any relative displacement that could occur due to the mode adopted to apply the load to the prototype. LVDT 16 was devoted to measure horizontal slip between the wall and the steel beam located in the base, LVDTs 13 to 15 were responsible for measuring vertical displacement at the bottom and top of wall (rocking displacement), LVDTs 1 and 2 were used to register the diagonal shear displacement, LVDTs 3 and 4 were adopted to register the vertical displacement and LVDT 12 was taken to evaluate any tendency for the separation of the SFRSCC layers in the middle height of the prototype. It is worth underlining that the horizontal displacements of the prototype were depurated from the horizontal rigid-body displacements of the solid SFRSCC zone, registered by LVDT 16.

Two different arrangements of LVDTs were used for the prototypes with openings. For both OP prototypes, their horizontal displacement type at different elevations were obtained with LVDTs 5 to 8, the horizontal slip between the prototype and the bottom steel beam were

measured by LVDT 16, and the rocking displacements by LVDTs 13 to 15. Moreover, the vertical displacement along the height of these prototypes was registered by one LVDT at the same position (LVDT 9 for OP 01 and LVDT 12 for OP 02). Nonetheless, while the LVDTs 1 to 5 were used in prototype OP 01 to measure the diagonal shear displacements (see Figure 180(b)), in prototype OP 02 the same LVDTs were used to register the crack opening displacements in the corners of the opening (see Figure 180(b)). Furthermore, the LVDTs 10 and 11 were used to measure the horizontal displacements in prototype OP 01, as shown in Figure 180(b). In prototype OP 02 the LVDTs 9, 10 and 11 were positioned in an attempt of registering the opening of horizontal cracks that had appeared in the first test with this type of prototype.

A constant vertical load of 45 kN (i.e., 22.5 kN/m) was applied to all the tested prototypes. The applied vertical load was calculated according to Eurocode 1 (CEN, 1991), considering a dead load of 4.3 kN/m^2, a live load of 2.0 kN/m^2 and assuming a slab of 10 m of span (the maximum value considered for the modular construction in the research project) of unidirectional behavior, simply supported on sandwich panels at its extremities. The partial safety coefficients were considered to be equal to 1.3 and 1.5 for dead and live loads, respectively. A total vertical load of 15 kN was applied by each of the three hydraulic cylinders for materializing the total load in the prototype. In the case of the horizontal load, the cyclic procedure adopted during the tests was based on ISO 21581 (ISO, 2010) and the procedures adopted by Poletti and Vasconcelos (2015). In summary, the lateral load procedure consisted of successive cycles progressively increasing in each direction of loading, according to predefined target drift ratios (i.e., cocient between the lateral displacement and the prototype's height). A total of nine target interstorey drifts were applied to investigate a wide range of phenomena from initial elastic phase up to the ultimate conditions, namely: 0.07%, 0.14%, 0.27%, 0.41%, 0.54%, 0.68%, 0.81%, 1.08% and 1.35%. In order to investigate the strength and stiffness degradation due to loading-unloading damage, the loading protocol consisted of three cycles at each level of displacement, as done by Poletti and Vasconcelos (2015), Pavese and Bournas (2011) and Ricci *et al.* (2013). Figure 181 shows the load history. The loading rate was of 0.3 mm/s, controlled by the LVDT positioned horizontally and aligned with the actuator (LVDT 6, shown in Figure 180).
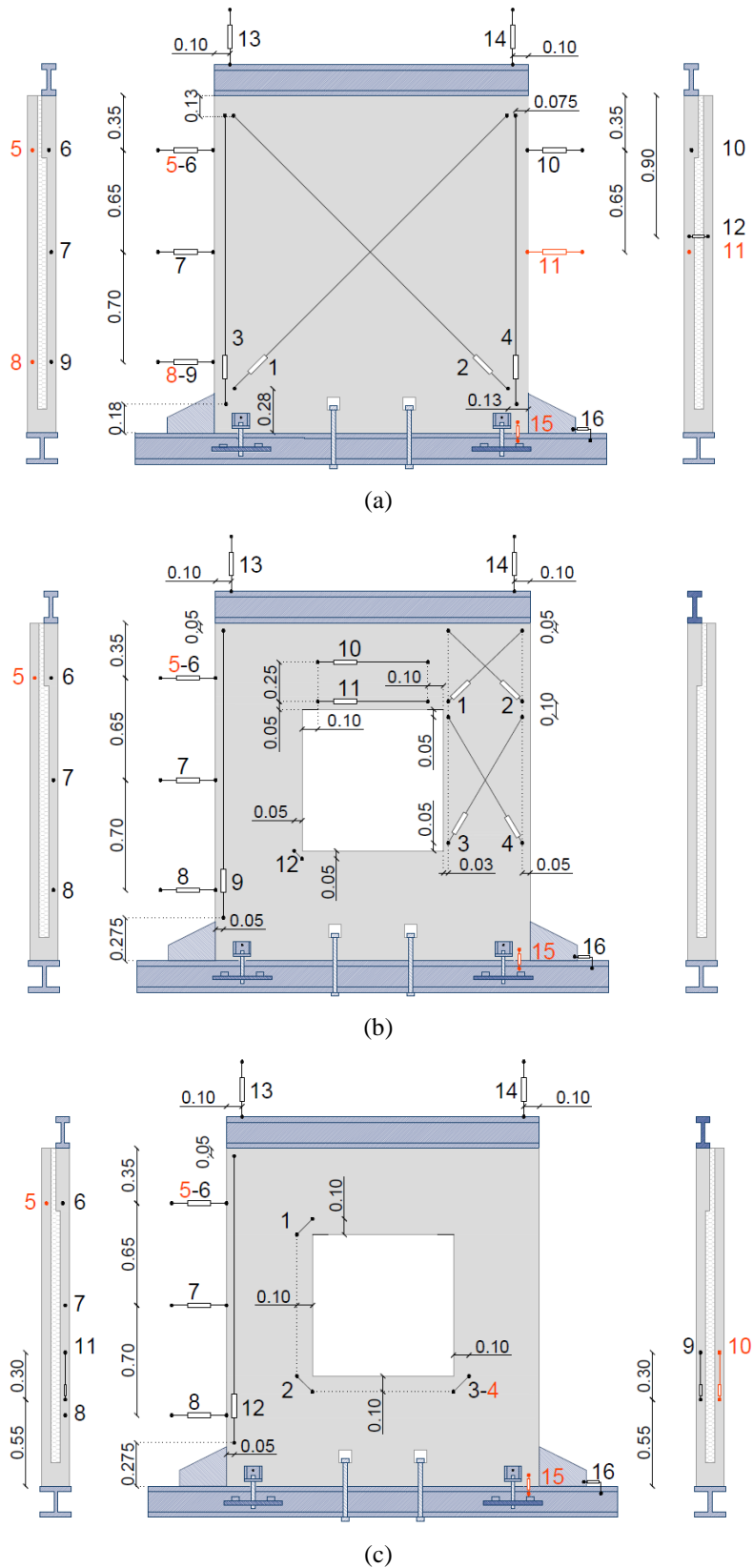
Figure 180: Schematic representation of instrumentation adopted: (a) prototypes without opening (NO 01 and NO 02); (b) prototypes with opening 01 (OP 01); (c) panel with opening 02 (OP 02) (dimensions in m).
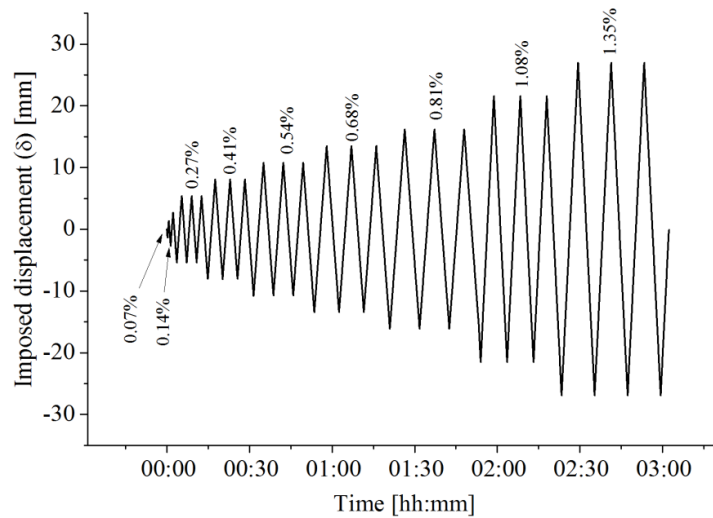
Figure 181: Test procedure used (pushing corresponds to a positive displacement).

9.2 EXPERIMENTAL RESULTS

9.2.1 Deformational features and typical damage patterns

Figure 182 and Figure 183 show the typical cracking patterns for each type of test performed. By observing the final aspect of the prototypes in Figure 182, no shear cracking pattern was detected in the prototypes without openings (type NO). In these prototypes, cracks are horizontal and concentrated at the transition between the solid zone and the sandwiched part (see Figure 182). These horizontal cracks started in the two corners, at drifts equal to 0.41%, and they are mainly caused by the applied flexural loading conditions. No additional cracks appeared during the test and the crack pattern alteration was resumed to the widening of the cracks in the base during the progress of test. The observed behaviour is strongly related to the specific constructive details at the part of the prototypes, where the abrupt transition from a solid zone to a sandwiched type section favour the localization and concentration of these type of cracks. Possibly, the use of conventional reinforcement in the lateral corners of the prototype could control the crack opening in these regions and take advantage of the higher shear strength of the wall panel, improving even more the lateral load capacity of the proposed panels. The main issues related to the use of conventional reinforcement along the base of panels are related to the decrease of the thermal efficacy of the sandwich panels and

also to the activities related to the preparation and installation of the steel bars (i.e., cutting, bending and positioning) that were avoided when using only fibre reinforced concrete. Alternatively, the connectors embedded in the solid zone (C60) could be done with higher content of fibres aligned in the prototype's height, increasing their load capacity along this direction and keeping this horizontal crack controlled, allowing to explore even more the shear capacity of sandwich walls. In fact, after the NO 02 prototype has been tested, it was dismantelled and it was verified that the C60 connectors located near the extremities of specimen were ruptured along the main crack that appeared in the SFRSCC layers (see Figure 184(a)).

Panel: NO 02 / Drift: 1.35% (front view)
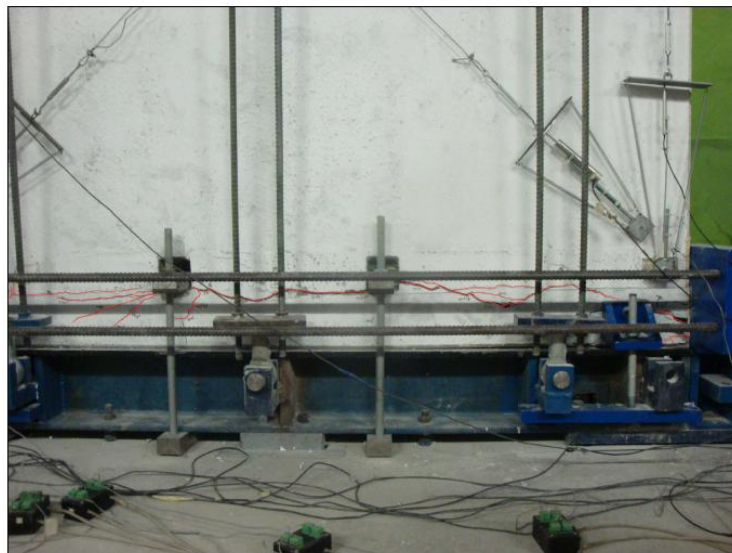
Figure 182: Typical cracking pattern of prototypes without opening (NO).

Figure 183 shows the typical evolving cracking pattern in the prototypes with openings, and the final aspect of these prototypes. In this case, due to the opening, the flexural cracks are less evident in respect to the prototypes without opening. As could be expected, inclined cracks concentrated around the opening have been formed. The first diagonal cracks appeared in the prototypes OP01 and OP02 for drifts equal to 0.54% and 0.41%, respectively (see Figure 183). Nonetheless, in the prototype OP01 the first crack appeared in the internal SFRSCC layer (i.e., with the thicker upper edge and that receives the vertical load) and the cracks that opening in the external layer were thinner than the cracks that formed in the internal layer until the end of test. In prototype OP02 the first crack appeared in the external layer and the cracking was more intense in this SFRSCC layer along the test.

Panel: OP 02 / Drift: 0.54% (front view)
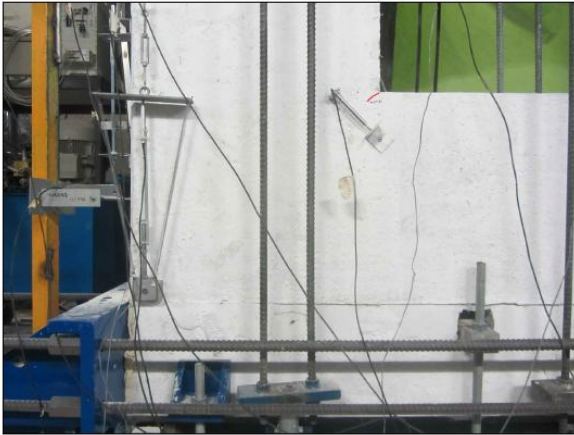
Panel: OP 02 / Drift: 0.68% (front view)
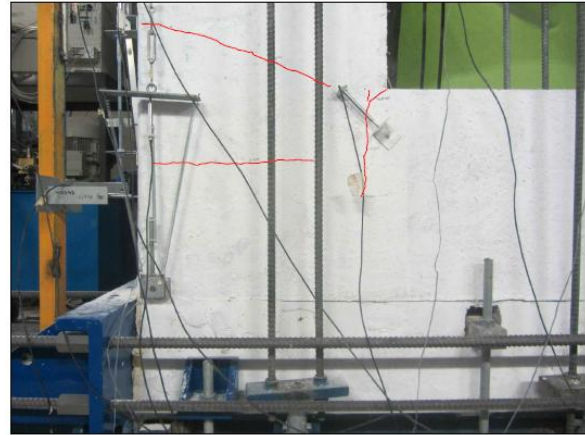
Panel: OP 02 / Drift: 0.81% (front view)
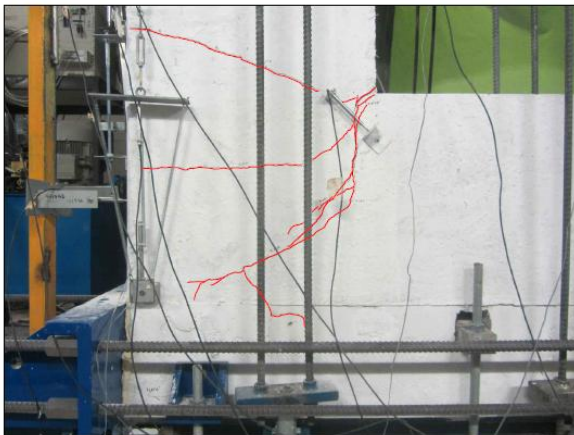
Panel: OP 02 / Final aspect (back view)

Figure 183: Typical cracking pattern of prototypes with opening (OP).

At 0.68% drift level, the diagonal cracks that appeared in the corners deviated towards the vertical direction in the nearby of GFRP connectors located in the proximity of corners of the central opening (see Figure 184). This observed behaviour indicates that the connector contributed to limit the widening of the cracks formed in these zones. At drifts equal to 0.81% and 0.68%, it was observed horizontal cracks rising from outer vertical edges of panels to the corners of openings of panels OP01 and OP02, respectively. These cracks appeared first in the lower corners and later in the upper corners of the prototypes. For both prototypes, at a drift equal 1.08%, the already opened cracks located above the opening became wider. At the same stage, sounds that seemed to be from the rupture of GFRP connectors were heard. After that, a clear rigid body movement of the prototype was observed until the end of tests.

The prototypes were dismantelled after have been tested in order to assess the final condition of GFRP connectors. It was observed that, in NO prototypes, the outmost C60 connectors (with 600 mm of length) were ruptured (see Figure 184(a)), while in all the other connectors there no apparent damage was detected. In the prototypes with openings, it was observed that the connectors C40 positioned in the nearby of opening corners, and the outmost C60 located in the beginning of horizontal cracking were ruptured (see Figure 184(b)). It was also observed that one of the outmost C60 connectors of prototype OP 01 was not ruptured, but the horizontal crack passed immediately above to the interruption of connector.

(a)

(b)
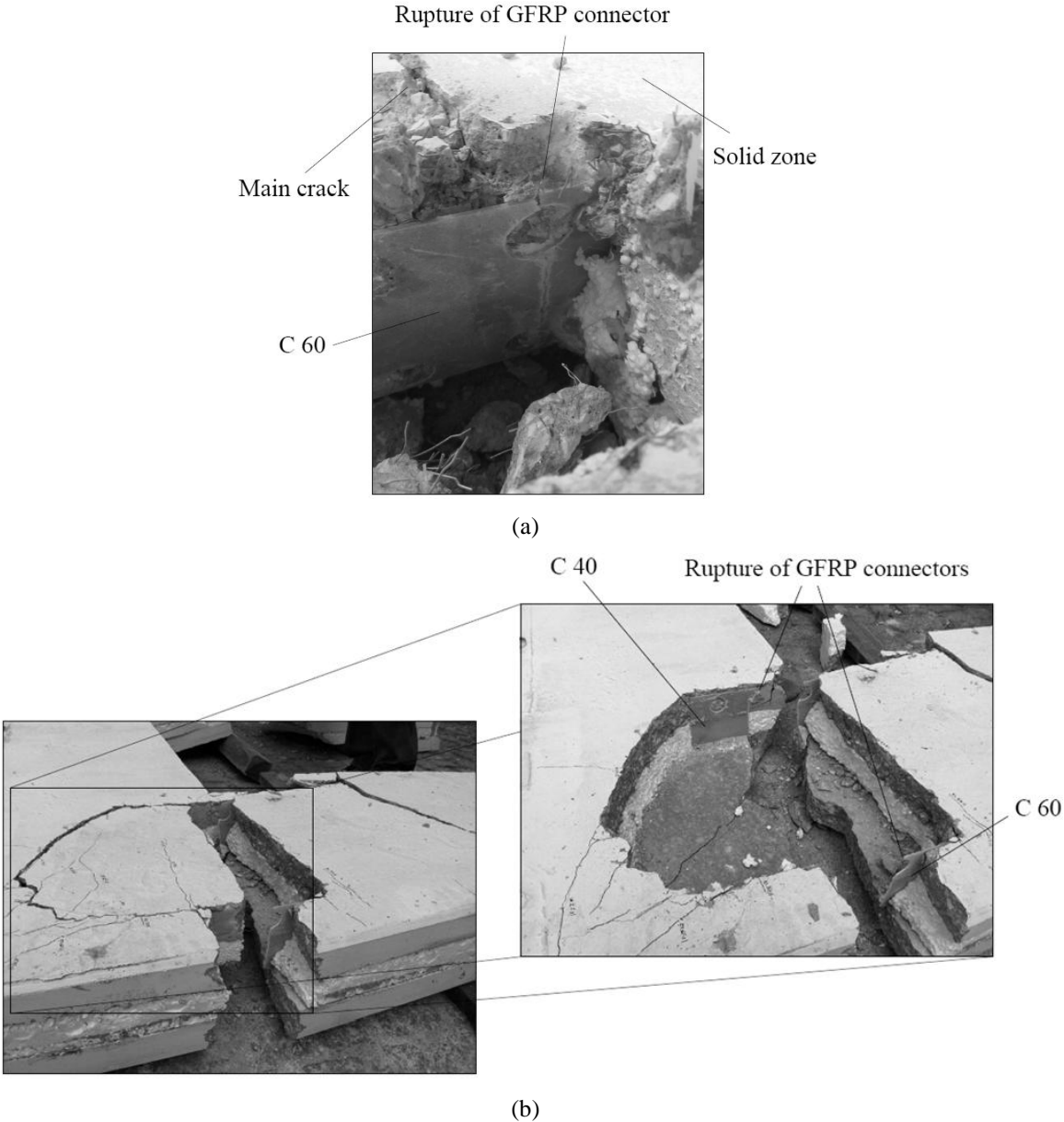
Figure 184: Damaged prototypes: (a) NO 02, (b) OP 02.

It is important to point out that no prototype have failed suddenly, presenting always a relatively gradual stiffness and strength degradation until the end of tests. Furthermore, all prototypes, with or without opening, displayed a moderate drift ratio at failure, of the order of 0.81-1.35%.

9.2.2 Typical hysteretic diagrams

The force-drift ratio hysteresis loops obtained in the tested prototypes are illustrated in Figure 185. The peak loads and corresponding drifts are summarized in Table 43, including: peak loads in two loading directions (pushing and pulling) and corresponding drift ratios.

From observation of Figure 185, it can be noted that all the tests presented some differences on their behaviour in positive and negative directions (pushing and pulling the prototype, respectively). Among different reasons that could be pointed out to the observed behaviour, the most acceptable are sliding of support. These differences are substantially higher in the test of NO 01 (the first one to be tested), due tothe use of a steel plate with relative low stiffness to connect the actuator to the reaction wall of laboratory (see Figure 179(a)). For the following tests this steel plate was replaced by an I-shaped steel profile, which has solved that issue (note the difference between the connection of actuator to the reaction wall, shown in Figure 179(a) and Figure 179(b)). Thus, the results of test NO 01 are always related only to the pushing cycles.
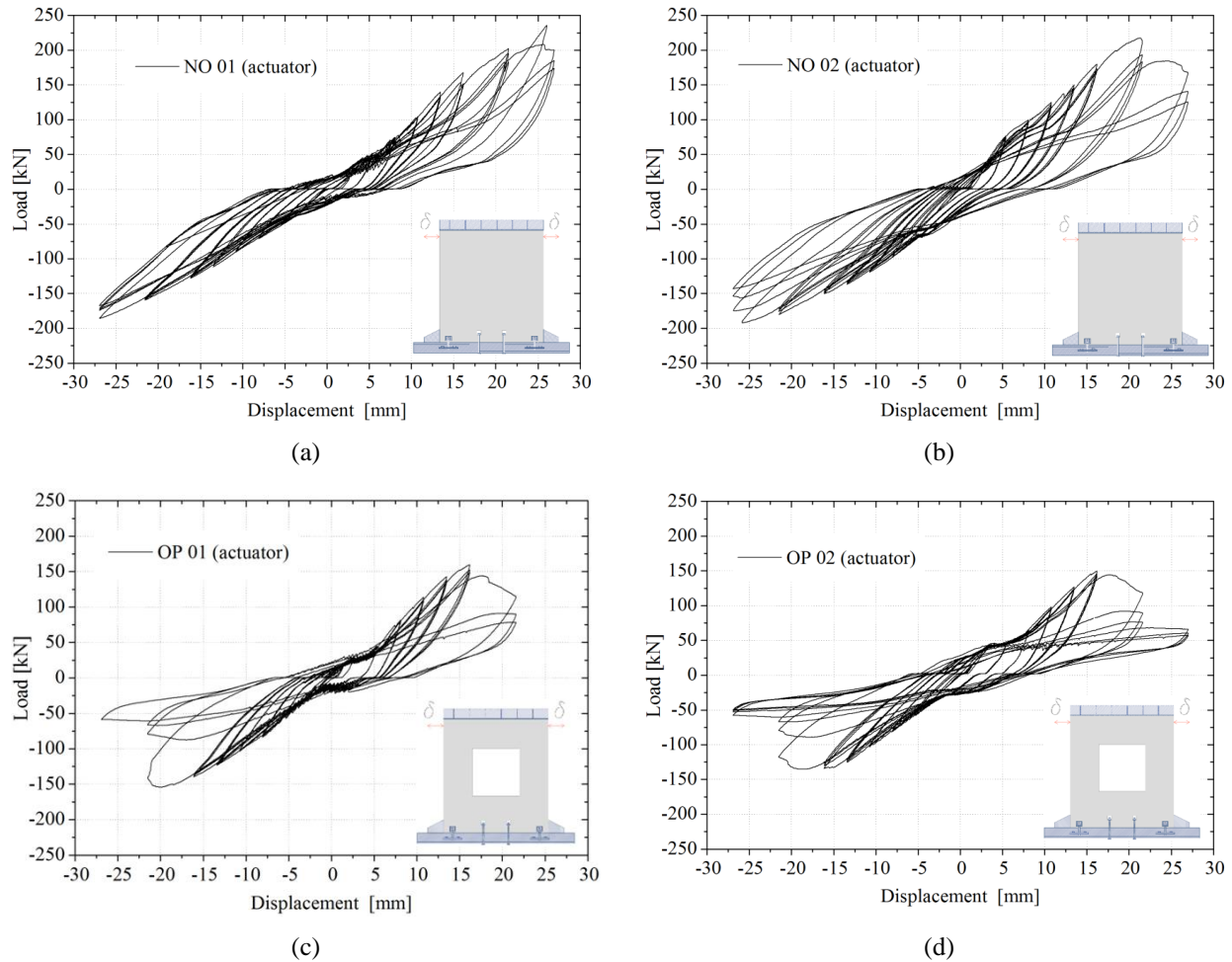
Figure 185: Hysteretic curves for: (a) NO 01; (b) NO 02; (c) OP 01; (d) OP 02.

Figure 185 shows that, for all specimens, up to a drift of 0.41% (corresponding displacement in the top of wall equal to 8.2mm), the curves exhibits low hysteresis, indicating no significant damage in the panels. Furthermore, up to this stage the loading and unloading stiffness remain quite similar. In general, the hysteretic loops become larger above a drift of 0.54%, indicating some damage increase in the prototypes. The hysteretic cycles become larger, and a cyclic strength degradation is observed above drift of 0.81%, for NO 01 prototype and above drift of 1.08% for the other tested panels. At his stage, the peak loads reached at the third pushing cycle corresponded to 89%, 85%, 54% and 53% of the load reached at the first cycle for NO 01, NO 02, OP 01 and OP 02, respectively. This indicates that the damage in SFRSCC was increased along the repeated cycles. Furthermore, this damage was higher for OP prototypes. Considering the first cycles and the pushing stages, the maximum loads were equal to 208.2, 217.2 kN and were reached at a drift of 1.35% and

1.08%, respectively for NO 01 and NO 02 prototypes, while they were reached 159.6 and 150.2 kN at 0.81% drift for OP 01 and OP 02 prototypes, respectively. The peak loads and corresponding drifts are presented in Table 43.

Table 43: Peak loads and drifts corresponding to the peak loads.

Spec. Ref.	Peak load [kN]						Drift corresponding to the peak load [%]					
	1st cycle		2nd cycle		3rd cycle		1st cycle		2nd cycle		3rd cycle	
	push	pull	push	pull	push	pull	push	pull	push	pull	push	pull
NO 01	208	-186	196	-174	184	-172	1.4	-1.4	1.1	-1.4	1.1	-1.4
NO 02	217	-192	194	-176	184	-172	1.1	-1.4	1.1	-1.1	1.1	-1.1
OP 01	160	-154	153	-137	149	-137	0.8	-1.1	0.8	-0.8	0.8	-0.8
OP 02	150	-135	146	-130	143	-127	0.8	-1.1	0.8	-0.8	0.8	-0.8

The presence of the opening in the prototypes reduced considerably the lateral resistance and stiffness when compared to those of prototypes without opening. The opening in the OP prototypes resulted in an average decrease in the strength equal to 27% in comparison with the NO prototypes (considering 1st cycles and pushing). Similarly, the stiffness of prototypes with opening was also affected, as can be noted observing the hysteretic loops in Figure 185.

The hysteretic curves obtained for the 4 tested prototypes are quite flat at the origin, which is justified by the fact that they experienced pinching in the cyclic response (see Figure 185), probably in consequence of slip between the specimen and the steel beam used as foundation and/or due to opening/closing of cracks.

The diagonal shear displacements were quite linear in the tests with prototypes without opening, as shown in Figure 186(a) for NO 02 prototype. This response reflects the fact that this prototype did not present any damage due to shear during the test. Moreover, averaging the values obtained for NO 01 and NO 02 specimens, it was noted that the maximum measured shear displacements in prototypes without opening represented only 1.0% of the corresponding lateral displacements imposed to the panels.

Figure 186(b) and Figure 187(a) show comparisons between the displacements read for both SFRSCC layers. From the observation of the hysteretic loops, it is noticed that the readings are quite similar, indicating that, although the load is imposed only to the internal SFRSCC layer (i.e., with the thicker SFRSCC in the upper border of the panel), both layers seem to work together, presenting very small relative lateral displacements.
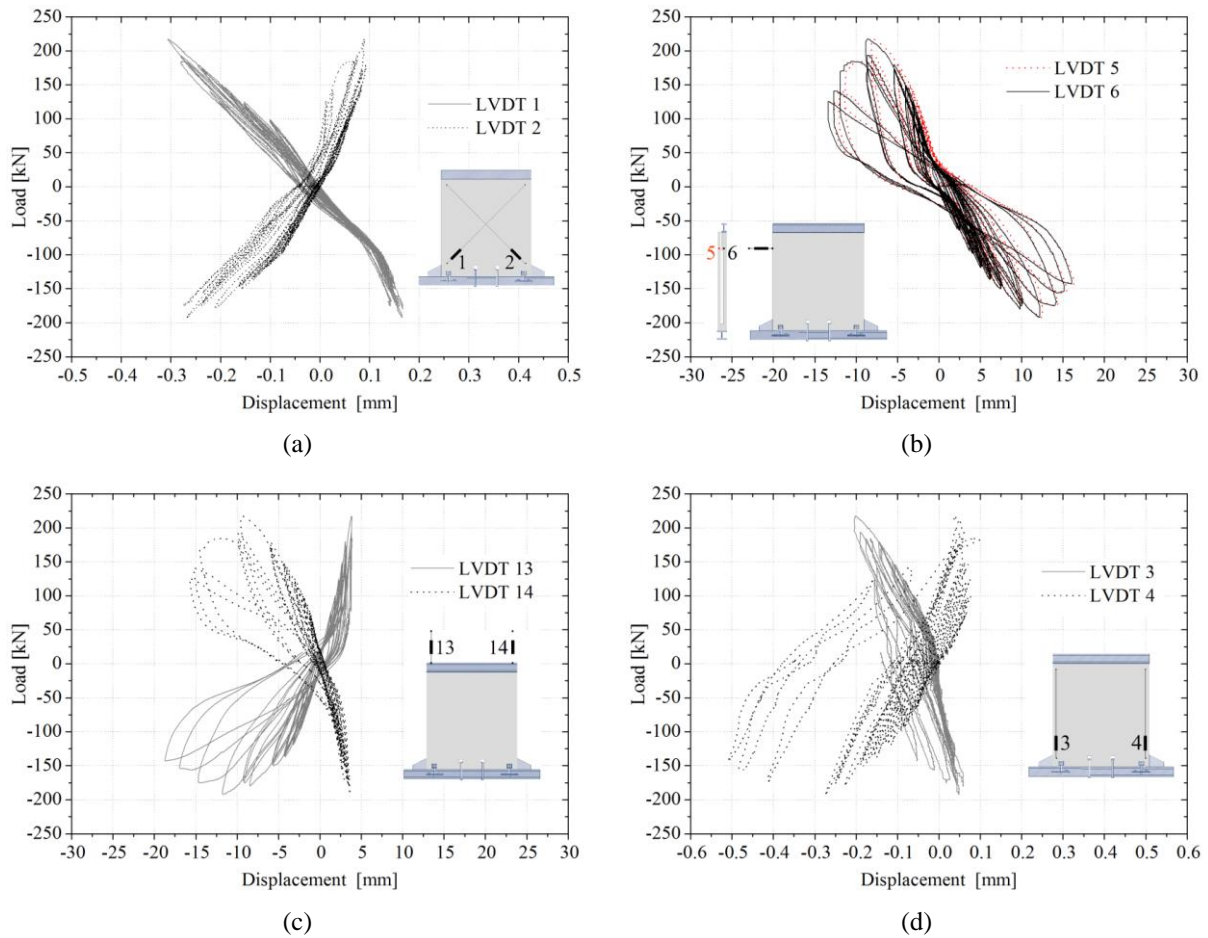
Figure 186: Force *versus* displacements for NO 02 prototype: (a) diagonal shear displacements; (b) lateral displacements in both SFRSCC layers; (c) rocking displacements; (c) vertical displacements.

From the analysis of Figure 186(c) and Figure 187(b), it is verified that the prototypes developed a rocking mechanism, with significant uplifting of the solid zone from the base beam. This rocking mechanism is more evident for tests with prototypes without opening. The upper steel beam of OP 02 prototype uplift as much as 7.5 mm (see Figure 187(b)), while this value reached 18 mm in the test with NO 02 prototype (see Figure 186(c)), pointing out the important rotation experienced by the tested prototypes.

(a)

(b)

(c)
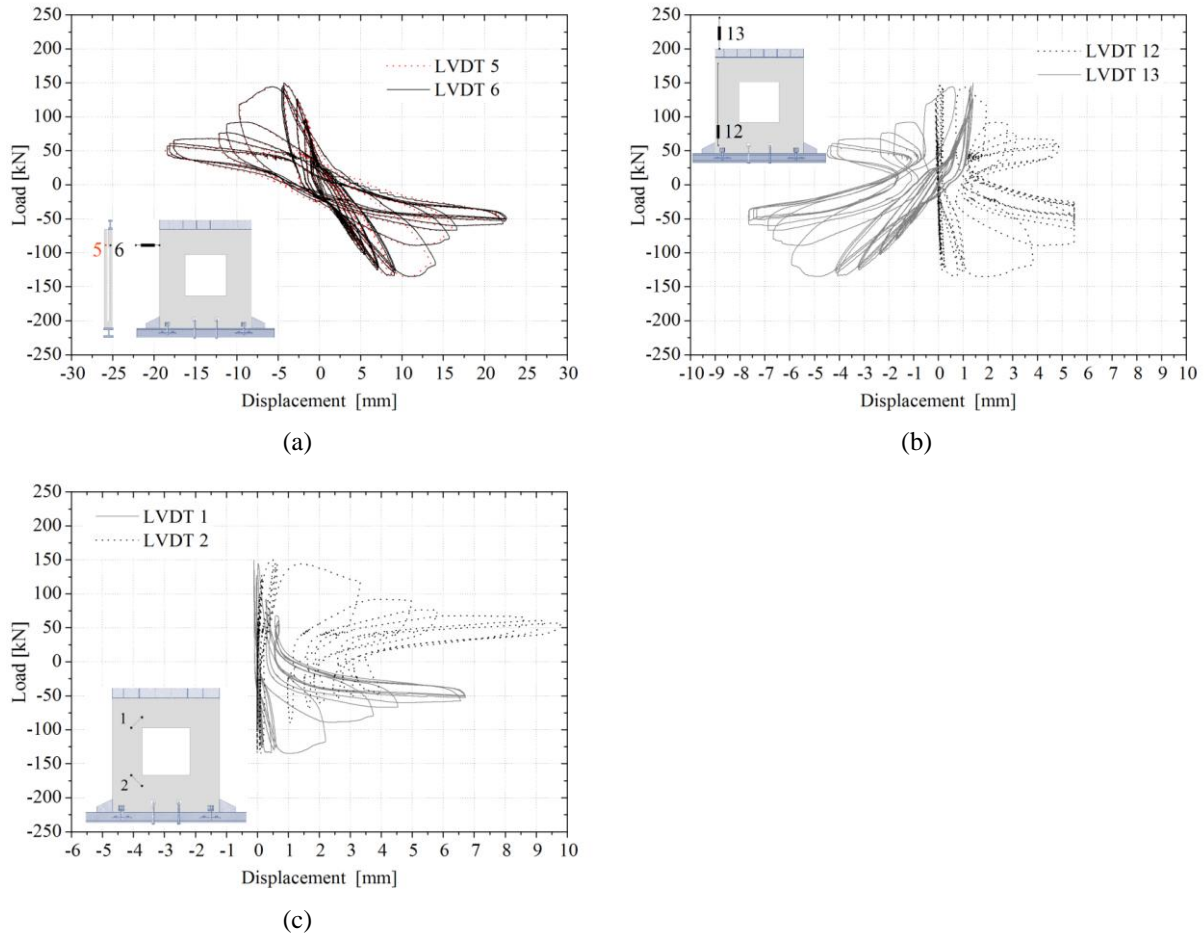
Figure 187: Force *versus* displacements for OP 02 prototype: (a) lateral displacements in both SFRSCC layers; (b) vertical and rocking displacements; (c) cracking opening width in the corners of opening.

9.3   SEISMIC PERFORMANCE

9.3.1   Monotonic envelope curves

The monotonic envelopes are curves obtained from the hysteresis loops connecting the points of maximum load in each drift level. Since the test protocol consisted on the application of three repetitions for each drift level (first cycle and two stabilization ones), three monotonic envelope curves were obtained: corresponding to the first cycle, second cycle and third cycle. Figure 188 shows the monotonic envelopes of the force-displacement curves as obtained for each of the three cycles corresponding to the same target drift level.
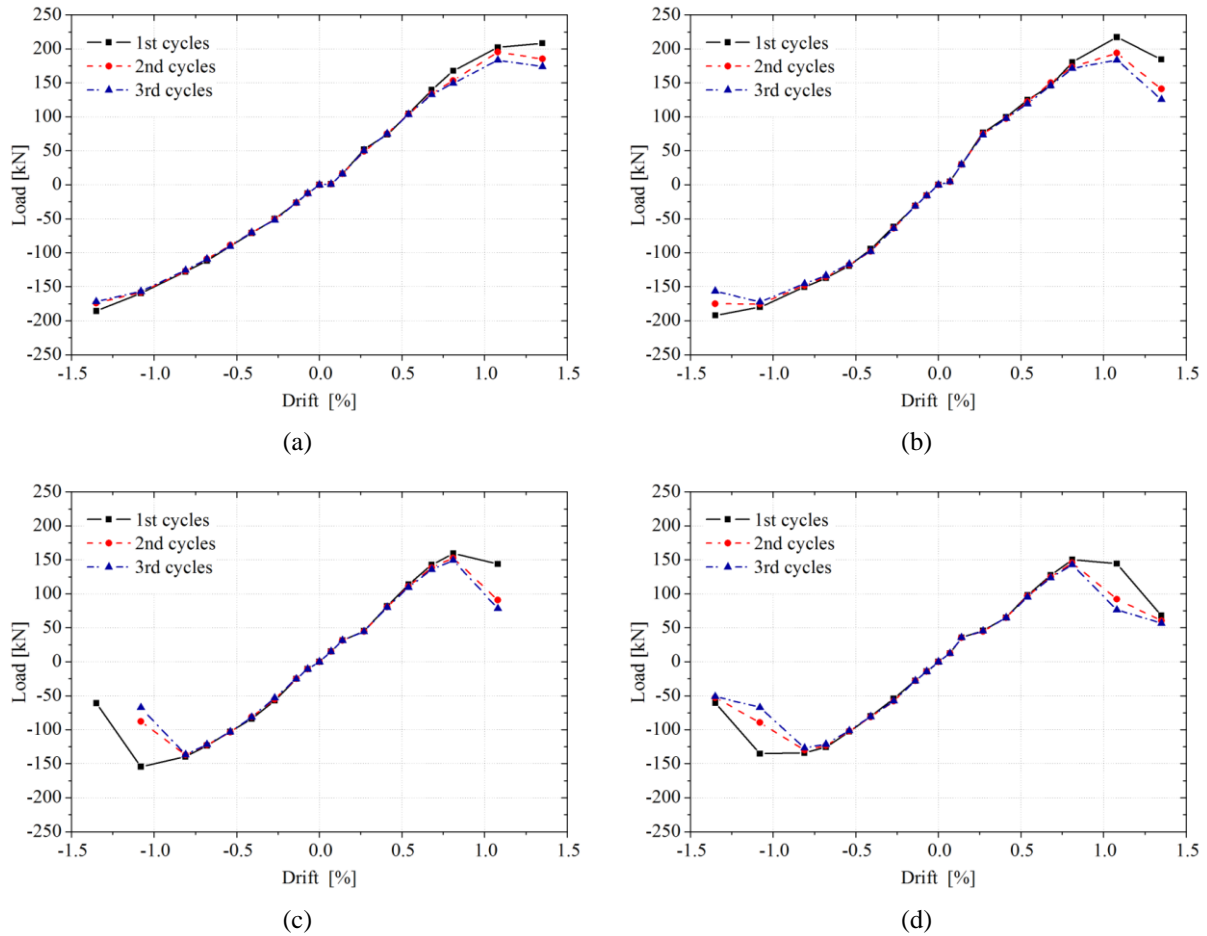
Figure 188: Envelopes of the force *versus* displacement responses: (a) NO 01; (b) NO 02; (c) OP 01; (d) OP 02.

9.3.2 Idealized bilinear behaviour

Figure 189 displays the equivalent bilinear force–displacement diagrams of tested prototypes. These diagrams assume a perfectly elasto–plastic behaviour for the prototypes, and were obtained from the monotonic envelopes. For the sake of conciseness, only the results during pushing stage of cycles (i.e., positive displacements) are presented. In order to take into account the cyclic degradation, bilinear curves corresponding to each of three different cycles were determined. The bilinearisation of the experimental curves was obtained based on the procedure adopted by Ricci *et al.* (2013). First, the initial stiffness, k_w, was set equal to the secant stiffness taking into account the origin and the load/displacement corresponding to the 0.27% drift. Thus, the pseudo yielding force, F_{wy}, was obtained through an energy criterion where the horizontal line segment of the idealized bilinear force-drift curve was located using an iterative graphic procedure that balanced the areas of the portions comprised between the real and the idealized curves above and below the horizontal line segment. The yielding

displacement, δ_{wy}, was defined as the intersection of the lateral load-displacement envelope curve and the initial slope, clearly given by F_{wy}/k_w (see Figure 190). Finally, the ultimate displacement, δ_{wu}, was set equal to the maximum imposed displacement (i.e., 21.6 mm for OP 01 prototype and 27.0 mm for all the other prototypes). Table 44 presents the main parameters that define the obtained bilinear curves the tested prototypes.
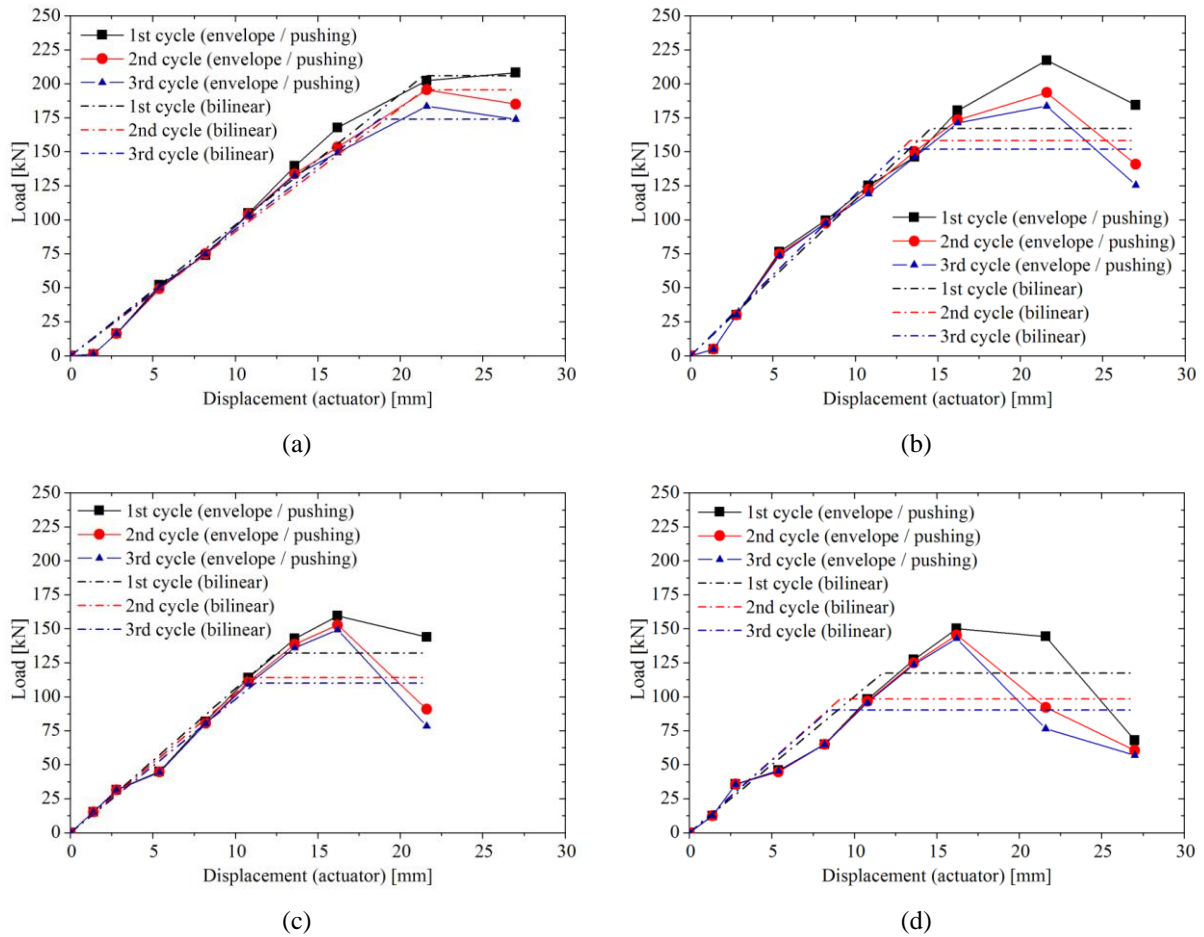
Figure 189: Equivalent bilinear curves: (a) NO 01; (b) NO 02; (c) OP 01; (d) OP 02.
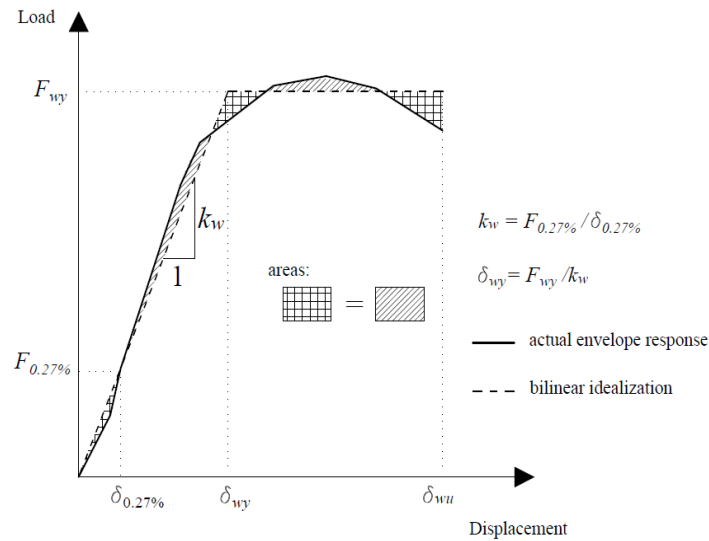
Figure 190: Schematic representation of equivalent energy method used to obtain the equivalent bilinear curve.

Table 44: Values of parameters that define the idealized bilinear behaviour for the tested walls.

Specimen	F_{wy} [kN]			δ_{wy} [mm]			δ_{wu} [mm]		
Ref.	1st	2nd	3rd	1st	2nd	3rd	1st	2nd	3rd
NO 01	206.0	195.5	174.0	21.4	21.4	18.7	27.0	27.0	27.0
NO 02	167.0	158.2	152.0	14.6	13.3	12.8	27.0	27.0	27.0
OP 01	132.2	114.1	110.2	12.5	11.1	11.2	27.0	27.0	27.0
OP 02	117.5	98.3	90.3	11.7	9.1	8.5	27.0	27.0	27.0

9.3.3 Initial stiffness and stiffness degradation

For comparison purposes, the initial stiffness of tested prototypes were calculated by two different methodologies. First, as made by Ricci *et al.* (2013), the initial stiffness was taken equal to the secant stiffness taking into account the origin and the load-displacement point corresponding to the 0.27% drift. In their work, Ricci *et al.* (2013) calculated the secant stiffness considering at a load-displacement point corresponding to 0.10% drift. Nonetheless, 0.27% drift was chosen for the present work in order to overcome some type of initial nonlinearity observed in the load *versus* displacement responses associated to initial adjustments of specimen at the beginning of tests. The second methodology chosen to calculate the initial stiffness is based on the ISO 21581 (2010), where the lateral stiffness of the walls are calculated according to Eq. (65).

$$k_{w2} = \frac{0.3F_{max}}{\delta_{40\%F\,max} - \delta_{10\%F\,max}} \tag{65}$$

where F_{max} is the maximum load attained in the test and $\delta_{40\%Fmax}$ and $\delta_{10\%Fmax}$ are, respectively, the displacement values obtained from the envelope curve corresponding to 40% and 10% of the maximum load. Table 45 summarizes the initial stiffness calculated by both methodologies.

The results shown in Table 45 indicate that the both adopted methodologies used to evaluate the initial stiffness lead to similar values. On average, the initial stiffness evaluated at 0.27% drift, considering the pushing branches, was equal to 10.54 and 11.38 kN/mm, respectively, for NO and OP prototypes. The respective values were equal to 10.35 and 10.81 kN/mm when the initial stiffness were computed by the Eq. (65).

Table 45: Values of initial stiffness calculated for the tested prototypes.

Specimen Ref.	Initial stiffness (k_w) [10^3 kN/mm]											
	$F_{0.27\%}$ / $\delta_{0.27\%}$						30% F_{max} / ($\delta_{40\%Fmax}$ - $\delta_{10\%Fmax}$)					
	1st cycle		2nd cycle		3rd cycle		1st cycle		2nd cycle		3rd cycle	
	push	pull	push	pull	push	pull	push	pull	push	pull	push	pull
NO 01	9.6	-	9.1	-	9.3	-	10.7	-	10.8	-	10.9	-
NO 02	11.5	14.2	11.9	13.9	11.9	13.7	11.6	15.1	12.2	16.6	12.1	17.1
OP 01	10.6	8.3	10.2	8.3	9.8	8.2	11.6	8.9	11.3	8.7	10.6	8.6
OP 02	10.0	8.5	10.8	8.3	10.7	8.4	9.9	7.6	10.8	7.6	10.7	7.7

When only the pushing branches are considered, the prototypes with opening exhibited initial stiffness slightly lower than the prototypes without opening. On average, the initial stiffness of prototypes with opening corresponded to 98% and 95% of the values obtained for the prototypes without opening, respectively when the initial stiffness is computed at 0.27% drift and when the methodology recommended by ISO 21581 is adopted.

The values of initial stiffness obtained by Ricci *et al.* (2013) for sandwich walls consisted on traditionally reinforced concrete layers (i.e., approximately equal to 35−40 kN/mm) were significantly higher than the values obtained in the current work. This difference can be attributed to the contribution of the following effects. Firstly, differently to what was done by Ricci *et al.* (2013), in the present work the load was applied in only one of the SFRSCC layers. Secondly, the foundation proposed by Ricci *et al.* (2013) for the walls consisted on a

stiff reinforced concrete slab, monolithically connected to the wall layers, resulting on a stiff connection. However, in the current work, due to the precast nature of the wall panels, the connection between the wall panel and the foundation is not as stiff as the connection adopted by Ricci *et al.* (2013).

To evaluate the degradation of stiffness experienced by the prototypes during the cyclic tests, the cyclic stiffness was computed for each drift ratio considering the average of the slopes of the line connecting the origin and the two points of loading corresponding to the maximum displacements (pushing and pulling). A schematic representation of the determination of cyclic stiffness is shown in Figure 191(a) (taking into account absolute values for loads and displacements). To compute the stiffness values of loads and displacements On the basis of the results presented in Figure 192, the stiffness of the prototypes without opening increased up to a drift ratio equal to 0.27% and decreased above this drift. In the case of the prototypes with opening, the overall stiffness starts to decrease from 0.14% drift. In general, the reduction in stiffness seems to be higher in prototypes with opening.

$$K = \frac{F_w^{+} + F_w^{-}}{\delta_w^{+} + \delta_w^{-}}$$

(a)

$$EVD_w = \frac{E_{dw}}{2\pi \cdot \left(E_{ew}^{+} + E_{ew}^{-}\right)}$$

(b)
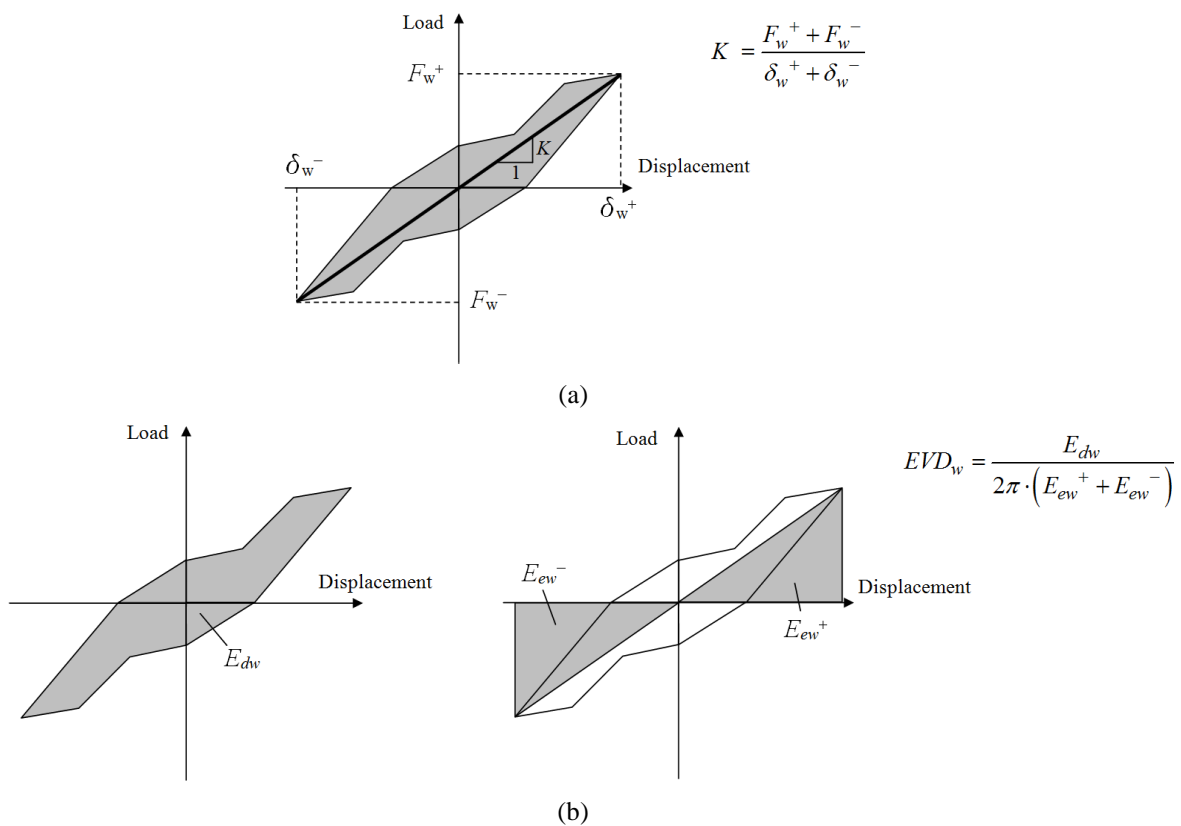
Figure 191: Evaluation of parameters: (a) overall stiffness (*K*); (b) Equivalent Viscous Damping (*EVD_w*).
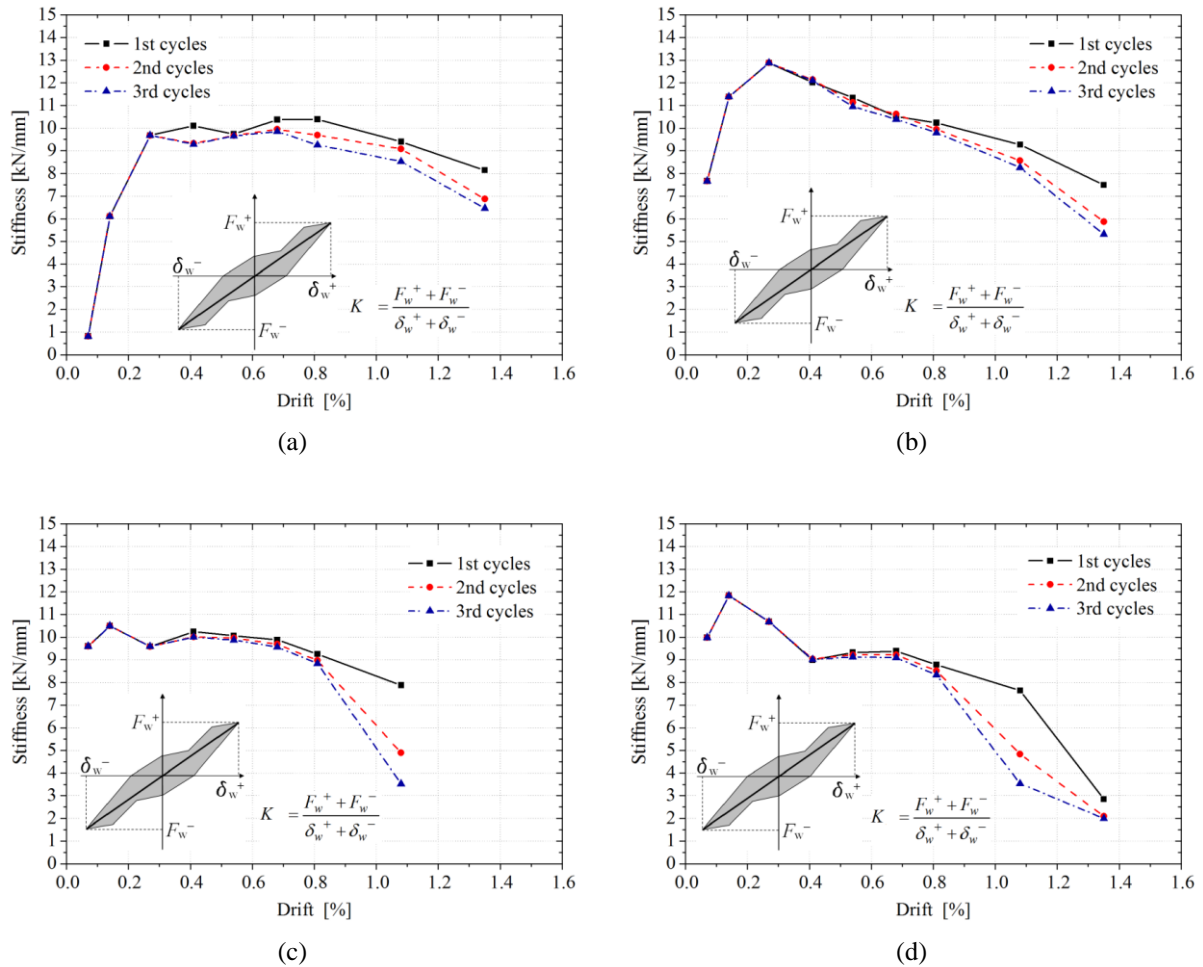
Figure 192: Overall stiffness degradation: (a) NO 01; (b) NO 02; (c) OP 01; (d) OP 02.

9.3.4 Ductility

The ductility of a wall subjected to in-plane loads can be defined as the capability of a structural system to undergo large amplitude of deformations without excessive strength deterioration. In other words, the ductility is the ability of the structural element to sustain several cycles of inelastic deformation without significant loss of strength. In earthquake-resistant design of structures, it is important to guarantee a ductile behaviour of the system and of the structural elements that are part of it.

In this work, the ductility is computed as the ratio between the ultimate displacement (δ_{wu}) and the pseudo-yield displacement (δ_{wy}) defined in the equivalent bilinear diagram. The ductility indexes, computed considering each of the three cycles, are presented in Table 46. It

is verified that the average values of ductility over cycles have ranged from 1.3 to 2.4, and that the displacement ductility was unaffected by the presence of opening in the wall.

Table 46: Values of ductility factor for the tested prototypes.

Specimen Ref.	Ductility factor = $\delta_{wu} / \delta_{wy}$ [ ]						
	1st cycle		2nd cycle		3rd cycle		Average over the
	push	pull	push	pull	push	pull	
NO 01	1.26	-	1.26	-	1.44	-	1.3
NO 02	1.85	2.17	2.03	2.35	2.11	2.42	2.2
OP 01	1.73	1.29	1.94	1.27	1.93	1.25	1.6
OP 02	2.30	1.72	2.95	2.05	3.19	2.26	2.4

In general, the ductility of the sandwich panels were quite low. For instance, Ricci *et al.* (2013) obtained ductility ratios ranging from 5.08 to 9.18 for cast-in-place sandwich panels consisting of 4 cm thick traditionally reinforced concrete layers and 10 cm thick layer of polystyrene foam.

9.3.5 Ability to dissipate energy

One major parameter usually adopted for the assessment of the seismic performance of walls is the ability of the structural element to dissipate energy during the cyclic test. According to FEMA-451 (FEMA, 2006), the more energy dissipated per cycle without excessive deterioration the better is the behaviour of the structure.

The dissipated energy by the walls per drift ratio, E_{dw}, was calculated using the area of the enclosed loop in the load−displacement curve (Figure 190b). Figure 193 reports the variation of the dissipated energy by the prototypes for each drift level.
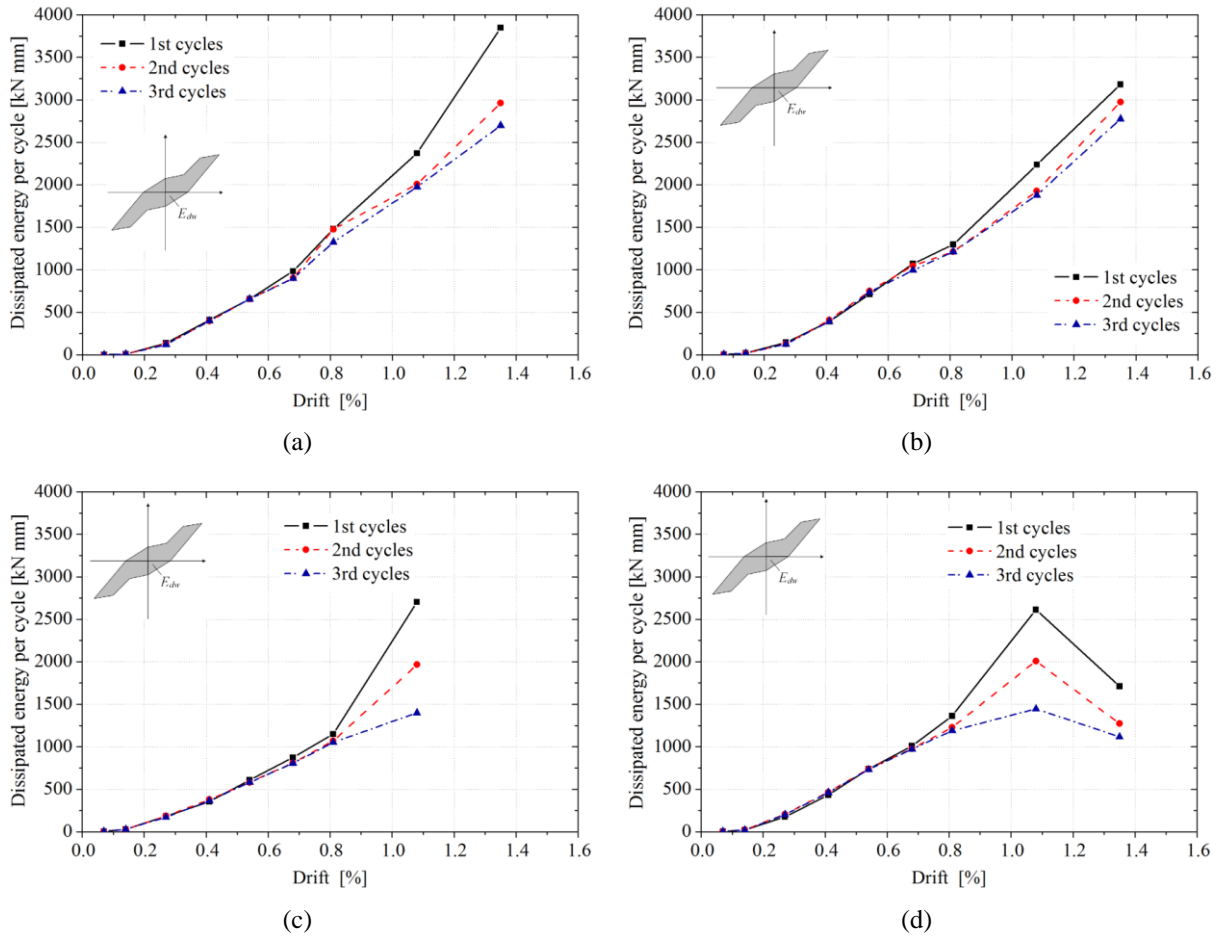
Figure 193: Dissipated energy per cycle: (a) NO 01; (b) NO 02; (c) OP 01; (d) OP 02.

As can be observed, the dissipation of energy found for both types of prototypes tends to increase with the lateral displacements.

From the observation of Figure 193, it can be noticed that the evolution of the dissipated energy is not directly proportional to the displacements, showing an exponential trend. This is possibly associated with the damage growth and with the consequent development of nonlinear displacements.

As shown in Figure 193, after a drift ratio equal to 1.08%, the dissipated energy per loop diminished for the test with prototype OP 02. This possibly happened due to the cracking of the panel prior to this drift.

In general, the results indicate that the energy dissipated by the proposed sandwich walls is rather low, when compared to the other structural walls.

9.3.6 Equivalent viscous damping

To evaluate further the effectiveness and seismic resistance of the sandwich walls, the Equivalent Viscous Damping (EVD_w) was also computed. It consists on a normalized energy dissipation capacity of panels that can be computed by Eq. (66), given by Chopra (1995).

$$EVD_w = \frac{E_{dw}}{2\pi \cdot \left(E_{ew}^{+} + E_{ew}^{-} \right)} \qquad (66)$$

where,

E_{dw} is the dissipated energy as discussed above and

E_{ew}^{+} and E_{ew}^{-} are the elastic energies of an equivalent viscous system calculated, respectively, at the maximum and minimum displacements reached in each loop (see Figure 191(b)).

Figure 194 illustrates how this property evolved with the increase of drift levels. Average values of the EVD_w at 0.41% drift equal to 9.50% and 10.54% were achieved for NO and OP panels, respectively.

As can be observed, the elastic viscous damping ratio found for all the prototypes without opening are almost constant between the 0.54% and 1.08% drift ratios, showing a trend to increase only between 0.14% and 0.41% drifts, and after 1.08% drift. In turn, the results for the prototypes with opening differed from the response of NO prototypes because their EVD_w decreased between 0.54% and 0.81% and presented a rapid increase between 0.81% and 1.08% drifts. After the 1.08% drift the prototype OP 02 presented a decrease of EVD_w when the second and third cycles are considered.
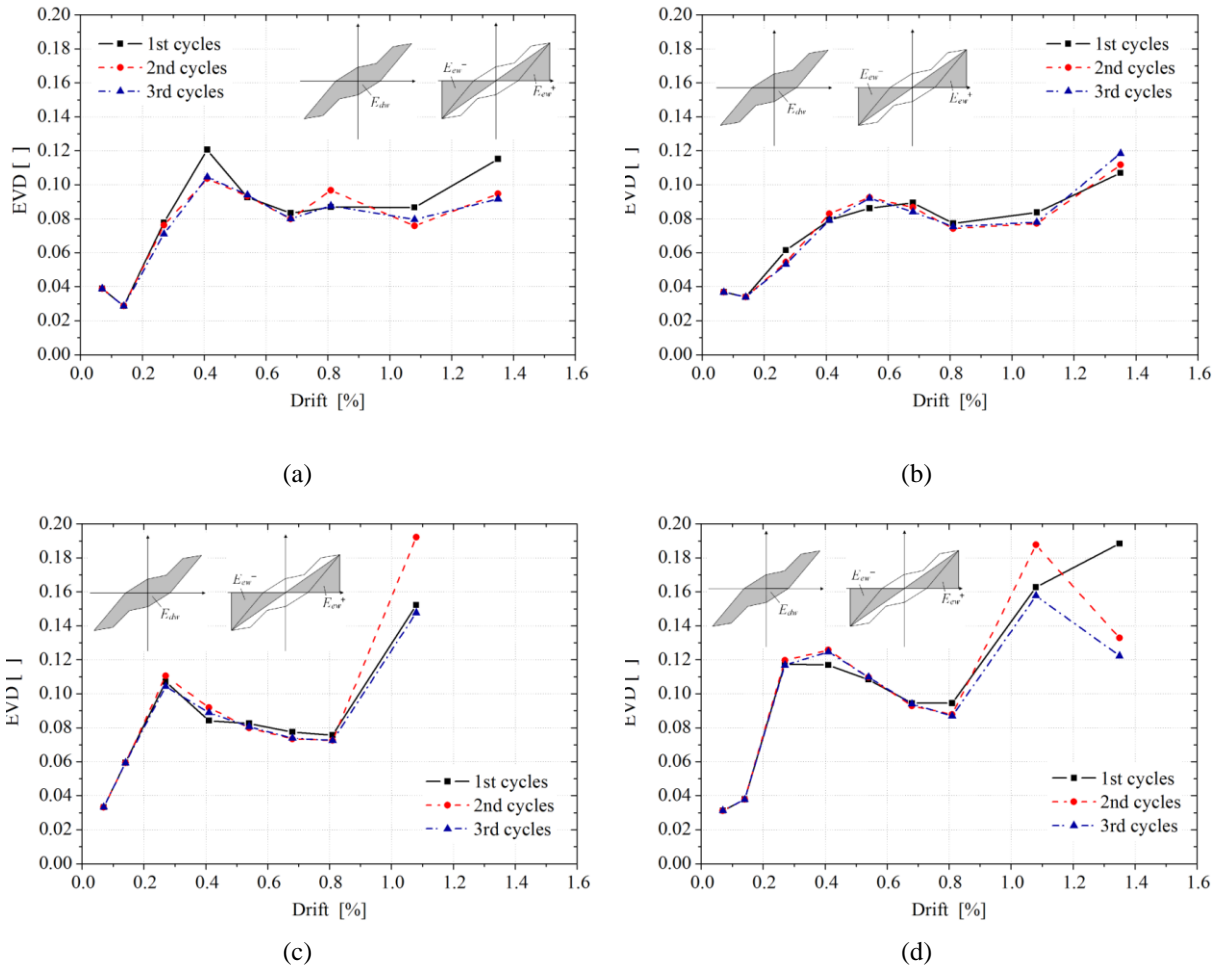
Figure 194: Equivalent viscous damping: (a) NO 01; (b) NO 02; (c) OP 01; (d) OP 02..

9.4 FINAL REMARKS

An experimental program was performed aiming at analysing the seismic behaviour of the developed precast sandwich wall consisted of two outer SFRSCC layers, GFRP connectors and EPS core. Its behaviour under in-plane lateral forces was assessed by pseudo-static cyclic tests performed on real scale panels, with and without opening. From the results presented in this chapter, the following conclusions can be drawn:

- when subjected to in-plane lateral loads, the sandwich panels present a flexure-dominant failure mode;

- the damage in panels without opening is concentrated in the toe regions of the wall. Possibly the failure mode of wall panels made with the real foundations could be different to what was obtained in this research. Further research is required to

investigate the failure mode of panels with the foundations chosen to be used in the building. The premature failure mode observed in the tests carried out could be avoided by using specific reinforcement to provide high strength and toughness in the critical regions. Nonetheless, the use of conventional reinforcement was avoided in the proposed system in order to keep the manufacturing of panels as simple and fast as possible. Independently of the foundation adopted in the field conditions, the results presented in this work can be considered a lower bound of the behaviour of the sandwich wall when subjected to lateral forces;

- the initial stiffness of sandwich walls is approximately equal to 10 kN/mm, apparently not being affected by the opening;

- the tested prototypes were able to withstand high values of lateral loads. Their lateral load capacity are approximately equal to 212 kN and 155 kN in the prototypes without and with opening, respectively;

- the minimum ductility registered in the prototypes has ranged from 1.3 to 2.4, apparently not being affected by the existence of opening in the prototype.

Chapter 10

CONCLUSIONS

10.1 MAIN CONCLUSIONS

Several structural concrete sandwich wall panels have been developed in the last years. Nonetheless, each of the available technologies has their limitations and still is necessary to seek for improvements in the current technology in order to achieve a more reasonable construction component. The main objective of this thesis was to propose a new structural wall panel and investigate its mechanical behaviour. The work consisted of experimental, numerical and analytical studies.

In the Chapter 3 was presented the results of experimental investigations focused on the determination of the mechanical behaviour of the SFRSCC and SCC used in the other experimental studies presented in the thesis. Special attention was given to the post-cracking tensile constitutive behaviour of SFRSCC (fracture mode I). A modified splitting test was proposed and making use of the developed test method, the influence of the flow driven orientation of fibres on the post-cracking behaviour of SFRSCC was assessed. Results from standard 3PBT method, proposed by RILEM TC 162-TDF for the characterization of regular FRC, were compared with the results obtained from specimens that are more representative of the actual structural element where the material is intended to be applied. Finally, the validity of *fib* MC 2010 approach for the constitutive modelling of SFRSCC applied to thin-section elements was questioned. From the research presented in this chapter it can be concluded that

the modified splitting test proposed in this work is a promising procedure to determine the values of the fracture parameters of SFRSCC to be adopted in the design of the thin-section structural elements. Also, the fibre orientation seems to be highly affected by the concrete flow. Specifically for the flow conditions used in this research, i.e., radial flow, the fibres tend to be oriented perpendicularly to the concrete flow. Furthermore, it was noticed that the *fib* MC 2010 approach for the constitutive modelling of fibre reinforced concrete seems to overestimate the energy absorption capacity even for the directions in which SFRSCC presents the uppermost energy absorption capacities (i.e., with the loading applied parallel to the concrete flow), due to the flow induced orientation of fibres.

In the Chapter 4, the manufacturing process used to produce different GFRP candidates to be used in the production of connectors was addressed. The main properties of interest of the GFRP candidates were evaluated. The characterization was limited to the determination of fibre content, direct tensile, shear and pin-bearing behaviour. The results of tests on different GFRP laminates allowed to conclude that a simple and low-cost GFRP such as the one made by chopped strand mat (CSM) can be used in the production of the connectors that are part of the sandwich panel. Furthermore, the characterization tests gave a better understanding of the overall behaviour of the connections and giving valuable information necessary to their correct design. From the shear tests,the measurements obtained by ESG demonstrated to be prone to inaccuracies for tests with laminates with high material anisotropy, due to the lack of uniformity of the shear strain in the gauge area. In the other hand, the Digital Image Correlation (DIC) demonstrated to be very useful because it allows measuring strains along a reduced area in the nearby of the notched section, not being necessary to use correction factors. The results of pin-bearing tests indicated that the load capacity of the connectors is limited by the distance between the hole and the bottom edge of specimen, independently of the composite used. Numerical modeling Finite Element Analysis (FEA) was used for modeling the pin-bearing tests, where it was found that it is possible to simulate the strain fields developed in the nearby of holes with acceptable accuracy.

In the Chapter 5 an innovative sandwich panel comprising SFRSCC layers and GFRP laminate connectors was proposed and its behaviour was investigated by numerical research. The geometry and arrangement of the panel components were optimized through a FE linear modelling. The structural behaviour of the sandwich panel was also assessed up to a relatively high damage level, by simulating the material nonlinear behaviour of SFRSCC layers due to crack initiation and propagation. The results of simulations allow to conlude that the

maximum tensile stress in the SFRSCC layers was significantly affected by the arrangement of the GFRP connectors. However, for a panel configuration comprising vertical GFRP connectors spaced 1 m from each other, the omission of the top horizontal connector did not imply relevant changes in the principal stresses in SFRSCC and GFRP. Furthermore, the obtained results have shown that it is possible to adopt an arrangement with only discrete vertical 0.40 m connectors, distanced vertically 0.60 m and horizontally 1.00 m from each other, keeping the ULS stress level in the SFRSCC layers and in the GFRP connectors comfortably under the corresponding strength of these materials. Furthermore, regardless of the arrangement and thickness of the SFRSCC layers, for serviceability limit state conditions, the maximum tensile stress in the GFRP connectors was always much lower than the tensile strength of the material, which leads to conclude that, disregarding local effects in the connections, the weakest components in the panel are the SFRSCC layers. However, even for the panels composed of SFRSCC layers of 35mm thickness, the maximum principal tensile stresses were lower than the characteristic tensile strength of SFRSCC. Nevertheless, as evidenced in the experimental program presented in the first part of this paper, using thicknesses of less than 60 mm for the SFRSCC may pose practical problems to the realization of the embedded connection to join the GFRP connector to the SFRSCC layers. The results obtained from the material nonlinear simulations of the sandwich panels have shown that the proposed configuration for the panel presents a ductile behaviour, even for wind load factor that is 23 times the load factor corresponding to the ULS. Ongoing experimental research with real scale prototypes is being carried out to appraise the relevant predictions provided by the FEM-based material nonlinear analysis carried out in this paper.

In the Chapter 6, a deeper investigation was conducted on the mechanical behaviour of connections between concrete and PERFOFRP connectors when subjected to transversal loads (pull-out tests). The experimental program consisted on 24 specimens made with two different GFRP laminates (CSM and MU4), two types of concrete (SCC and SFRSCC) and three different geometries for the connector (without holes, with 3 holes and with 4 holes). The main objective of this investigation was to obtain a better understanding of the proposed connections, evaluating the influence of the studied variables on the initial stiffness, load capacity and ductility of connections. Based on the observed experimental pull-out behaviour of connections, and on the results of the pin-bearing tests (section 4.5), a phenomenological model was proposed to predict the ultimate load capacity of the studied connections. From the pull-out tests, it was concluded that, in general, connections made with CSM PERFOFRP

connectors had the load carrying capacity limited by the rupture of the connector in the vicinity of the holes. The post testing inspection of the specimens pointed out that three typical failure lines appeared in the connectors that crossed the connector from the hole edge to the connector bottom edge: two inclined lines at about 45° and one 90° with the horizontal just below the holes. Nonetheless, one of specimens produced with SCC presented a distinct failure mode by shear in the planes of contact between the concrete and the connector (dowel effect + friction/adhesion), what can indicate that this failure mode happens for a load level not much different of the load that leads to the failure mode associated to the rupture of the connector itself. Premature ruptures of the concrete block were observed in specimens made with MU4 PERFOFRP connectors. In these specimens, the presence of two different failure patterns were observed: (1) rupture by shear along the interface surfaces between the connector and the concrete block, where prevails the combined effect of shear in the concrete dowels and in the net contact area by friction/adhesion; (2) concrete cone failure, with the formation of a cone type fracture surface with the apex located immediately below the holes and making and angle with the horizontal of approximately 47°. The use of steel fibre reinforcement in the concrete significantly affected the behaviour of connections that comprised PERFOFRP connectors, increasing the load carrying capacity and the energy absorption capacity of the connections. The load carrying capacity of 3H connections increased 17% in average. For the specimens with 0H, the use steel fibres did not significantly affect the friction/adhesion between the connector and the concrete, as expected. The connections with MU4 laminates presented a more ductile response, independently of the type of concrete. In average, the ultimate load capacities of connections made by SFRSCC and 3 holes increased 49% when compared with connections made with the same concrete and GFRP laminates without holes. Furthermore, the load capacity of connection with 4 holes was 29% greater than the one of the connection with 3 holes. Furthermore, when the number of holes per length of connector increased (i.e., spacing between holes was reduced), the response of the connection became slightly more ductile up to a slip approximately equal to 1.0 mm, but the response rapidly became more brittle for higher slips. When the results obtained in the pin-bearing tests are taken into consideration it is possible to conclude that, for the geometries and materials used in this investigation, the load capacity of the connectors subjected to pull-out forces is limited by the distance between the hole and the bottom edge of specimen, independently of the composite used. The proposed phenomenological model considered that the load capacity of the connection can be limited by all the possible failure modes that can occur in the connector itself and also by the different failure modes associated

to the rupture of concrete. The validity of the proposed formulae was checked and its capability to predict accurately the failure modes observed in the pull-out experimental program was proved. When the predicted ultimate load capacities of connections were compared to the experimental results, an average error of 19.57% was obtained.

In the Chapter 7, push-out tests were conducted on connections comprising PERFOFRP connectors and self-compacting steel fibre reinforced concrete. The experimental program consisted on 16 specimens made with two different GFRP laminates (CSM and MU4). To evaluate the concrete dowel effect, tests were also conducted with PERFOFRP connectors with 3 evenly spaced holes and also with laminates without holes. Moreover, the end-bearing effect was isolated comparing the results of specimens with and without concrete in front of the PERFOFRP rib. Finally, an analytical formulae to predict the ultimate load capacity of connections consisted of unconfined connectors (i.e., without end-bearing effect) was proposed and its accuracy was evaluated. Based on the results of this investigation, it is possible to conclude that, differently to what happens with connections made with steel Perfobond connectors, it was observed that the failure in connections made with PERFOFRP connectors subjected to longitudinal shear has generally occurred due to the rupture of GFRP connector itself. Also, contrary to what is reported for the Perfobond connectors, the PERFOFRP connectors presented an impressive high shear friction, corresponding to 38% of the load capacity of the 3H-EB specimens (with dowel effect and also end-bearing effect acting together). Thus, the parcel of load capacity transmitted across the connection by shear friction cannot be disregarded. The studies also evidenced that the concrete dowels action significantly increased the load capacity of connections. On average, an increase of 29% was obtained for the load capacity of connections due to the existence of holes in the connectors. This effect was more relevant when MU4 connectors were used, because the load capacity of connections made with CSM laminates was limited by the premature rupture of the connector. When MU4 laminates were used rather than CSM laminates, the load capacity of connectors increased 55%, on average. The gain on load capacity due the use of MU4 laminates was more relevant for connectors with holes. Among the studied variables, the concrete end-bearing effect showed to be the more relevant on the load capacity. On average, the specimens with concrete in front of rib connectors presented load capacity 97% greater than the corresponding value obtained for notched specimens;

In the Chapter 8 was presented an experimental and numerical investigation on the flexural behaviour of connections for sandwich panels containing PERFOFRP connectors and

SFRSCC layers. Sandwich beams made with two different types of GFRP connectors (i.e., CSM and MU4) were tested under four-point bending, and the results were analyzed in terms of deflection, strain fields and failure mechanisms. For a better understanding of the flexural behaviour of connections, linear elastic and nonlinear material FE analyses were also performed. The model was validated with the experimental data and the stress fields were obtained. From the observation of the experimental response of specimens, it can be concluded that, inpendently on the type of laminate used in the connector, the ultimate failure mechanism of the connections under flexure is always associated to the flexural failure of the PERFOFRP connector after an extensive cracking in the SFRSCC layers. Also, no significant increase on the cracking or ultimate load of the tested sandwich beams were obtained by replacing CSM connector by another stiffer connector, MU4, the failure mode obtained in the beams made with MU4 laminates was much more ductile. No significant slip was observed between the PERFOFRP connectors and the SFRSCC during the tests, at least in the parts where this slip was possible to be measured. Furthermore, a relatively low degree of composite action was achieved with both studied connections. The connections made with MU4 laminates presented a slightly high degree of composite action. When deflections were used, the connections made with CSM and MU4 laminates presented 28.77% and 43.47% of composite action, respectively. The general behaviour obtained with the FE model represented by load-deflection plots and strain variations in the midspan showed good agreement with the experimental data from sandwich beams tests. The stress contours obtained by the FE model of sandwich beams indicated that, for a load level corresponding to the imminence of SFRSCC bottom layer cracking, the maximum normal tensile stresses developed in the connectors were always less than 1.5% of the tensile strength of CSM or MU4 laminates. Furthermore, the maximum shear stresses attained in the laminates corresponded to only 13% of the shear strength of CSM laminate.

In the Chapter 9 an experimental program was presented aiming at analysing the seismic behaviour of the developed precast sandwich wall consisted of two outer SFRSCC layers, GFRP connectors and EPS core. Its behaviour under in-plane lateral forces was assessed by pseudo-static cyclic tests performed on real scale panels, with and without opening. From the results presented in this chapter, it can be drawn that when subjected to in-plane lateral loads, the sandwich panels present a flexure-dominant failure mode. Also, the damage in panels without opening is concentrated in the toe regions of the wall. Possibly the failure mode of wall panels made with the real foundations could be different to what was obtained in this

research. Further research is required to investigate the failure mode of panels with the foundations chosen to be used in the building. The premature failure mode observed in the tests carried out could be avoided by using specific reinforcement to provide high strength and toughness in the critical regions. Nonetheless, the use of conventional reinforcement was avoided in the proposed system in order to keep the manufacturing of panels as simple and fast as possible. Independently of the foundation adopted in the field conditions, the results presented in this work can be considered a lower bound of the behaviour of the sandwich wall when subjected to lateral forces. Furthermore, the initial stiffness of sandwich walls is approximately equal to 10 kN/mm, apparently not being affected by the opening. Moreover, the tested prototypes were able to withstand high values of lateral loads. Their lateral load capacity are approximately equal to 212 kN and 155 kN in the prototypes without and with opening, respectively. The minimum ductility registered in the prototypes has ranged from 1.3 to 2.4, apparently not being affected by the existence of opening in the prototype.

10.2 RECOMMENDATIONS FOR FUTURE RESEARCH

In the present work, a new structural sandwich panel was proposed and some preliminary studies were performed in the material, meso and full-scale in order to obtain a better understanding of the structural element proposed and to promote its utilization. Nonetheless, even though this thesis provides some answers regarding the properties of the constituent materials and regarding the structural behaviour of the proposed sandwich panel, several other questions have arisen during the development of this work. The following points are recommended for future research:

- Optimization of the geometry of modified splitting test specimen proposed for characterization of SFRSCC (i.e., diameter, dimensions of notches). This study should be done based on numerical studies in order to obtain an optimized geometry of specimen and notches.
- Development of inverse analysis of the modified splitting test should be performed in order to obtain the post-cracking parameters that characterize the SFRSCC. Genetic or evolutive algorithms should be checked.
- Optimization of the PERFORP connectors in terms of diameter of holes, distance between holes, distances between the holes and the edges, etc. This investigation could be done based on numerical studies.

- Assessment of the longitudinal shear behaviour of PERFOFRP $\times$ SFRSCC connections using specimens that includes the contribution of the insulating material, that is, more representative of the sandwich panels than the specimens used in the experimental program presented in this thesis.

- Further appraisal of the developed models for the pull-out and push-out performance of the PERFOFRP $\times$ SFRSCC connections.

- Establish axial-bending interaction curves for the proposed sandwich panels based on tests where the structural layer is axially loaded while the panel is loaded in flexure to failure.

- Development of an analytical model to predict the complete behaviouf of partially composite panels in flexure that takes into account the longitudial shear behaviour of the interfaces of SFRSCC layers and the insulation and connectors.

- Assessment of the thermal performance of the proposed sandwich panel and compare with similar sandwich panels made with commercially available technologies for the connectors.

- Assessment of the thermo-mechanical performance of the proposed sandwich panel and evaluate experimentally and numerically the cracking risks due to thermal gradients that the panels are subjected under service conditions.

- Evaluation of the performance of the proposed sandwich panels when subjected to fire loadings (push-out and flexural tests).

- Assessment of in-plane cyclic behaviour of the sandwich panels with different aspect ratios and with representative connections between wall $\times$ foundation.

- Assessment of seismic behaviour of the proposed building system by means of shaking table tests. The prototype may be as representative as possible of the real building, making use of the real connections expected to be employed between the wall $\times$ foundation, wall $\times$ wall and wall $\times$ slab.

- Development of comprehensive design rules for the building system that uses the proposed sandwich panels as main structural component.

REFERENCES

AASHTO 2011. *T 336 Standard Method of Test for Coefficient of Thermal Expansion of Hydraulic Cement Concrete*, American Association of State Highway and Transportation Officials, Washington D.C.

ABRISHAMBAF, A., BARROS, J. A. O. & CUNHA, V. M. C. F. 2013. Relation between fibre distribution and post-cracking behaviour in steel fibre reinforced self-compacting concrete panels. *Cement and Concrete Research,* 51**,** 57-66.

ACI COMMITEE 533 1993. ACI 533R-93: Guide for precast concrete wall panels.

ACI COMMITTE 544 1997. *Fiber reinforced concrete : ACI 544.1R-96,* Farmington Hills, Mich., American Concrete Institute.

ACI COMMITTEE 318 2005. Building Code Requirements for Structural Concrete (ACI 318-05) and Commentary (ACI 318R-05). Farmington Hills, MI: American Concrete Institute (ACI).

ACI COMMITTEE 349 1985. Code Requirements for Nuclear Safety Related Structures (ACI 349-85) (Revised 1990) (Reapproved 1997). *Technical Documents.* Farmington Hills, Mich.

ACI COMMITTEE 533 2012. *Guide for precast concrete wall panels (533R-11),* Farmington Hills, MI, American Concrete Institute (ACI).

ADAMS, D. F. & WALRATH, D. E. 1987. Further development of the Iosipescu shear test method. *Experimental Mechanics,* 27**,** 113-119.

AHN, J.-H., LEE, C.-G., WON, J.-H. & KIM, S.-H. 2010. Shear resistance of the perfobond-rib shear connector depending on concrete strength and rib arrangement. *Journal of Constructional Steel Research,* 66**,** 1295-1307.

References

AKCAY, B. & TASDEMIR, M. A. 2012. Mechanical behaviour and fibre dispersion of hybrid steel fibre reinforced self-compacting concrete. *Construction and Building Materials,* 28**,** 287-293.

ANDERSON, B. 2006. *Conventions for U-value calculations,* Garston, BRE Scotland.

ARCAN, M., HASHIN, Z. & VOLOSHIM, A. 1978. A method to produce uniform plane stress states with applications to fiber-reinforced materials. *Experimental Mechanics,* 18**,** 141-146.

ARRÊTÉ DU 24 MAI 2006 2006. Arrêté du 24 mai 2006 relatif aux caractéristiques thermiques des bâtiments nouveaux et des parties nouvelles de bâtiments

Présentation des textes réglementaires et de la méthode de calcul Th-CE. approuvée par l'Arrêté du 19 juillet 2006 (fascicule spécial n°2006-3 du BO en avril 2007).

ARRÊTÉ DU 26 OCTOBRE 2010 Arrêté du 26 octobre 2010 relatif aux caractéristiques thermiques et aux exigences de performance énergétique des bâtiments nouveaux et des parties nouvelles de bâtiments. JOURNAL OFFICIEL DE LA RÉPUBLIQUE FRANÇAISE.

ASHRAE 2009. *ASHRAE handbook. Fundamentals,* Atlanta (Ga.), American Society of Heating, Refrigerating and Air-Conditioning Engineers.

ASTE, N., ANGELOTTI, A. & BUZZETTI, M. 2009. The influence of the external walls thermal inertia on the energy performance of well insulated buildings. *Energy and Buildings,* 41**,** 1181-1187.

ASTM 2011. D2584 - 11: Standard Test Method for Ignition Loss of Cured Reinforced Resins. Philadelphia, PA: American Society for Testing and Materials (ASTM).

ASTM 2012a. D5379 - 12: Test method for shear properties of composite materials by the V-notched beam method. West Conshohocken, PA: American Society for Testing and Materials (ASTM).

ASTM 2012b. D7078 / D7078 M - 12: Standard Test Method for Shear Properties of Composite Materials by V-Notched Rail Shear Method. West Conshohocken, PA. USA.: American Society for Testing and Materials (ASTM).

ASTM 2013. D5961 / D5961M - 13: Standard Test Method for Bearing Response of Polymer Matrix Composite Laminates. Philadelphia, PA: American Society for Testing and Materials (ASTM).

ASTM C469 1994. Standard test method for static modulus of elasticity and poisson's ratio of concrete in compression. *Annual Book of ASTM Standards (04.02).* West Conshohocken, Pennsylvania: American Society of Testing Materials (ASTM).

ASTM STANDARD C1550 2010. Standard test method for flexural toughness of fiber reinforced concrete (using centrally loaded round panel). West Conshohocken, PA: ASTM International.

ASTM STANDARD D 3039/D 3039M 2008. Tensile Properties of Polymer Matrix Composite Materials. West Conshohocken, PA: ASTM International.

AZEVEDO, A. F. M., BARROS, J., SENA-CRUZ, J. M. & GOUVEIA, A. V. 2003a. Software in structural engineering education and design. *III Portuguese-Mozambican Conference of Engineering.*

AZEVEDO, A. F. M., BARROS, J. A. O., SENA-CRUZ, J. M. & GOUVEIA, A. V. 2003b. Software in structural engineering education and design. *III Portuguese-Mozambican Conference of Engineering.*

BAKIS, C. E., BANK, L. C., BROWN, V. L., COSENZA, E., DAVALOS, J. F., LESKO, J. J., MACHIDA, A., RIZKALLA, S. H. & TRIANTAFILLOU, T. C. 2002. Fiber-reinforced polymer composites for construction - State-of-the-art review. *Journal of Composites for Construction,* 6**,** 73-87.

BAMFORTH, P. B. 2007. *Early-age thermal crack control in concrete*, CIRIA.

BANK, L. 2013. Progressive Failure and Ductility of FRP Composites for Construction: Review. *Journal of Composites for Construction,* 17**,** 406-419.

BANK, L. C. & ARORA, D. 2007. Analysis of RC beams strengthened with mechanically fastened FRP (MF-FRP) strips. *Composite Structures,* 79**,** 180-191.

BARDA, F., HANSON, J. M. & CORLEY, W. G. 1977. Shear Strength of Low-Rise Walls with Boundary Elements. *Special Publication,* 53.

BARRAGÁN, B. E. 2002. *Failure and tougness of steel fiber reinforced concrete under tension and shear.* PhD Thesis, UPC.

BARROS, J. A. O. 1995. *Behaviour of fibre reinforced concrete, experimental analysis and numerical modelling.* PhD, University of Porto.

BARROS, J. A. O., BIANCO, V. & MONTI, G. 2009. NSM CFRP laminates for shear strengthening of RC beams: tests and mechanical model. *The Open Construction and Building Technology Journal,* 3**,** 12-32.

BARROS, J. A. O., CUNHA, V. M. C. F., RIBEIRO, A. F. & ANTUNES, J. A. B. 2005. Post-cracking behaviour of steel fibre reinforced concrete. *Materials and Structures,* 38**,** 47-56.

BARROS, J. A. O. & FIGUEIRAS, J. A. 2001. Model for the analysis of steel fibre reinforced concrete slabs on grade. *Computers & Structures,* 79**,** 97-106.

BARROS, J. A. O., PEREIRA, E. N. B. & SANTOS, S. 2007. Lightweight Panels of Steel Fiber-Reinforced Self-Compacting Concrete. *Journal of Materials in Civil Engineering,* 19**,** 295-304.

BAŽANT, P. Z. & PLANAS, J. 1998. *Fracture and size effect in concrete and other quasibrittle materials. New directions in Civil Engeneering,* Boca Raton (FL), CRC Press.

BAŽANT, Z. 1991. Why Continuum Damage is Nonlocal: Micromechanics Arguments. *Journal of Engineering Mechanics,* 117**,** 1070-1087.

BAŽANT, Z. 1994. Nonlocal Damage Theory Based on Micromechanics of Crack Interactions. *Journal of Engineering Mechanics,* 120**,** 593-617.

BAŽANT, Z. & OH, B. H. 1983. Crack band theory for fracture of concrete. *Matériaux et Construction,* 16**,** 155-177.

BAŽANT, Z. & PIJAUDIER-CABOT, G. 1989. Measurement of Characteristic Length of Nonlocal Continuum. *Journal of Engineering Mechanics,* 115**,** 755-767.

BENAYOUNE, A., ALI, A. A. A., SAMAD, A. A. A. & TRIKHA, D. N. 2007a. Response of Precast Reinforced Composite Sandwich Panels to Axial Loading. *Journal of Construction and Building Materials,* 21**,** 677-685.

BENAYOUNE, A., SAMAD, A. A. A., ABANG ALI, A. A. & TRIKHA, D. N. 2007b. Response of pre-cast reinforced composite sandwich panels to axial loading. *Construction and Building Materials,* 21**,** 677-685.

BENAYOUNE, A., SAMAD, A. A. A., TRIKHA, D. N., ABANG ALI, A. A. & ASHRABOV, A. A. 2006. Structural behaviour of eccentrically loaded precast sandwich panels. *Construction and Building Materials,* 20**,** 713-724.

BENAYOUNE, A., SAMAD, A. A. A., TRIKHA, D. N., ALI, A. A. A. & ELLINNA, S. H. M. 2008a. Flexural behaviour of pre-cast concrete sandwich composite panel – Experimental and theoretical investigations. *Journal of Construction and Building Materials,* 22**,** 580-592.

BENAYOUNE, A., SAMAD, A. A. A., TRIKHA, D. N., ALI, A. A. A. & ELLINNA, S. H. M. 2008b. Flexural behaviour of pre-cast concrete sandwich composite panel – Experimental and theoretical investigations. *Construction and Building Materials,* 22**,** 580-592.

BENTUR, A. & MINDESS, S. 2006a. *Fibre reinforced cementitious composites*, CRC Press.

BENTUR, A. & MINDESS, S. 2006b. *Fibre Reinforced Cementitious Composites, Second Edition*, Taylor & Francis.

BERNARD, E. S. 2004. Durability of Fibre-Reinforced Shotcrete. *Shotcrete: More Engineering Developments.* Queensland, Australia: Taylor and Francis.

BIANCO, V., BARROS, J. A. O. & MONTI, G. 2009. Three dimensional mechanical model for simulating the NSM FRP strips shear strength contribution to RC beams. *Engineering Structures,* 31**,** 815-826.

BIGAS, J. P. P., B.; DESCHRYVER, F.; MASSINARI, P.; PLIZZARI, G. 2007. Synthetic Macro-fibers Reinforced Self Compacting Concrete for Lightweight Precast Elements.

A Case Study. *5th International RILEM Symposium on Self-Compacting Concrete.* Ghent, Belgium.

BJØNTEGAARD, Ø. & SELLEVOLD, E. J. 2001. Interaction between thermal dilation and autogenous deformation in high performance concrete. *Materials and Structures/Materiaux et Constructions,* 34**,** 266-272.

BOLLER, K. H. 1969. A method to measure intralaminar shear properties of composite laminates. Dayton (OH): Air Force Materials Laboratory.

BOULEKBACHE, B., HAMRAT, M., CHEMROUK, M. & AMZIANE, S. 2010. Flowability of fibre-reinforced concrete and its effect on the mechanical properties of the material. *Construction and Building Materials,* 24**,** 1664-1671.

BROUGHTON, W. R., KUMOSA, M. & HULL, D. 1990. Analysis of the Iosipescu shear test as applied to unidirectional carbon-fibre reinforced composites. *Composites Science and Technology,* 38**,** 299-325.

BRÜHWILER, E. & WITTMANN, F. H. 1990. The wedge splitting test, a new method of performing stable fracture mechanics tests. *Engineering Fracture Mechanics,* 35**,** 117-125.

BS EN ISO 6946:1997 1997. Building components and building elements – Thermal resistance and thermal transmittance – Calculation method. London: British Standards Institution.

BUNN, W. G. 2011. *CFRP grid/rigid foam shear transfer mechanism for precast prestressed concrete sandwich wall panels.* M. Sc., North Carolina State University.

BUNSELL, A. R. & RENARD, J. 2005. *Fundamentals of fibre reinforced composite materials,* Bristol, UK, IOP Publishing.

BUSH, T. D. & STINE, G. L. 1994. Flexural Behaviour of Composite Precast Concrete Sandwich Panels With Continuous Truss Connectors. *Precast/Prestressed Concrete Institute Journal,* 39**,** 112-121.

BUSH, T. D. & WU, Z. 1998. Flexural Analysis of Prestressed Concrete Sandwich Panels with Truss Connectors. *Precast/Prestressed Concrete Institute Journal,* 43**,** 76-86.

CALLISTER, W. D. & RETHWISCH, D. G. 2009. *Materials science and engineering: an introduction*, John Wiley & Sons.

CAMPBELL, F. C. 2010. *Structural composite materials*, ASTM international.

CAPRINO, G., SQUILLACE, A., GIORLEO, G., NELE, L. & ROSSI, L. 2005. Pin and bolt bearing strength of fibreglass/aluminium laminates. *Composites Part A: Applied Science and Manufacturing,* 36**,** 1307-1315.

CARLSSON, L. A., ADAMS, D. F. & PIPES, R. B. 2014. *Experimental characterization of advanced composite materials,* Boca Raton, FL, USA, CRC Press.

CARMONA, S. & AGUADO, A. 2012. New model for the indirect determination of the tensile stress–strain curve of concrete by means of the Brazilian test. *Materials and Structures,* 45**,** 1473-1485.

CEN - EUROPEAN COMMITTEE FOR STANDARDISATION 1994. EUROCODE 4 EN 1994. Design of composite steel and concrete structures. Part 1.1 General rules and rules for buildings. Brussels.

CEN 1991. EN 1991: Eurocode 1 - Actions on structures. Brussels: European Committee for Standardization (CEN).

CEN 2004a. EN 1992-1 European Standard Eurocode 2: Design of concrete structures - Part 1: general rules and rules for buildings. Brussels.

CEN 2004b. EN 1994-1-1: Eurocode 4 - Design of composite steel and concrete structures. Part 1-1: General rules and rules for buildings. Brussels: European Committee for Standardization (CEN).

CEN 2005a. EN 14651:Test method for metallic fibered concrete - Measuring the flexural tensile strength (limit of proportionality (LOP), residual). Brussels: European Committee for Standardization.

CEN 2005b. European standard EN 1998-3: Eurocode 8: design of structures for earthquake resistance. Brussels: European Committee for Standardization.

CEN 2006a. EN 14488-3: Testing sprayed concrete. Flexural strengths (first peak, ultimate and residual) of fibre reinforced beam specimens. Brussels: European Committee for Standardization.

CEN 2006b. EN 14488-5: Testing sprayed concrete. Determination of energy absorption capacity of fibre reinforced slab specimens. Brussels: European Committee for Standardization.

CEN 2009. EN 12390-3. Testing hardened concrete – Part 3: compressive strength of specimens. Lisbon: European Committee for Standardization (CEN).

CEN 2013a. EN 826: Thermal insulating products for building applications: Determination of compression behaviour. European Committee for Standardization (CEN).

CEN 2013b. EN 12089: Thermal insulating products for building applications. Determination of bending behaviour. European Committee for Standardization (CEN).

CEVDET K. GULEC, A. S. W. & BOZIDAR, S. 2008. Shear Strength of Squat Rectangular Reinforced Concrete Walls. *Structural Journal,* 105.

CEVDET K. GULEC, A. S. W. & BOZIDAR, S. 2009. Peak Shear Strength of Squat Reinforced Concrete Walls with Boundary Barbells or Flanges. *Structural Journal,* 106.

CHAMIS, C. C. & SINCLAIR, J. H. 1977. 10º off-axis test for shear properties in fiber composites. *Experimental Mechanics,* 17**,** 399-346.

CHANG, F.-K., SCOTT, R. A. & SPRINGER, G. S. 1984. Failure of Composite Laminates Containing Pin Loaded Holes—Method of Solution. *Journal of Composite Materials,* 18**,** 255-278.

CHEN, A., NORRIS, T. G., HOPKINS, P. M. & YOSSEF, M. 2015. Experimental investigation and finite element analysis of flexural behavior of insulated concrete sandwich panels with FRP plate shear connectors. *Engineering Structures,* 98**,** 95-108.

CHO, J.-R., PARK, S. Y., CHO, K., KIM, S. T. & KIM, B.-S. 2012. Pull-out test and discrete spring model of fibre-reinforced polymer perfobond rib shear connector. *Canadian Journal of Civil Engineering,* 39**,** 1311-1320.

CHO, K., PARK, S., KIM, S., CHO, J.-R. & KIM, B.-S. 2010. Shear connection system and performance evaluation of FRP-concrete composite deck. *KSCE Journal of Civil Engineering,* 14**,** 855-865.

CHOI, I., KIM, J. & KIM, H.-R. 2015a. Composite Behavior of Insulated Concrete Sandwich Wall Panels Subjected to Wind Pressure and Suction. *Materials,* 8**,** 1264-1282.

CHOI, K.-B., CHOI, W.-C., FEO, L., JANG, S.-J. & YUN, H.-D. 2015b. In-plane shear behavior of insulated precast concrete sandwich panels reinforced with corrugated GFRP shear connectors. *Composites Part B: Engineering,* 79**,** 419-429.

CHOPRA, A. K. 1995. *Dynamics of structures: theory and applications to earthquake engineering,* Englewood Cliffs, New Jersey, Prentice-Hall.

COLLINGS, T. A. 1977. The strength of bolted joints in multi-directional CFRP laminates. *Composites,* 8**,** 43-55.

COLLINS, T. F. 1954. Precast Concrete Sandwich Panels for Tilt-Up Construction. *Journal of the American Concrete Institute,* 50**,** 149-164.

COMINOLI, L., FAILLA, C., MANZONI, M., PLIZZARI, G. A. & RIVA, P. Experimental study on SFRC precast panels. *In:* RILEM PRO 39, ed. Sixth RILEM symposium on fibre reinforced concrete (FRC) - BEFIB,, 2004 Varenna. RILEM, 1133-1142.

COMINOLI, L., MEDAL, A. & PLIZARRI, A. 2007. Fracture properties of high-strength hybrid fiber-reinforced concrete. *In:* GROSSE, C. U. & REINHARDT, S. H. W. (eds.) *Advances in Construction Materials.*

COOPER, C. & TURVEY, G. J. 1995. Effects of joint geometry and bolt torque on the structural performance of single bolt tension joints in pultruded GRP sheet material. *Composite Structures,* 32**,** 217-226.

CORNELISSEN, H. A. W., HORDIJK, D. A. & REINHARDT, H. W. 1986. Experimental determination of crack softening characteristic of normal weight and lightweight concrete. *Heron,* 31**,** 45-56.

CORREIA, J. R., FERREIRA, J. G. & BRANCO, F. A. 2006. A Rehabilitation Study of Sandwich GRC facade Panels. *Construction and Building Materials,* 20**,** 554-561.

CRISAFULLI, F. J., RESTREPO, J. I. & PARK, R. 2002. Seismic design of lightly reinforced precast rectangular wall panels. *PCI Journal,* 47**,** 104-121.

CUNHA, V. 2010a. *Steel Fibre Reinforced Self-Compacting Concrete (From Micro-Mechanics to Composite Behaviour).* University of Minho.

CUNHA, V. M. C. F. 2010b. *Steel fibre reinforced self-compacting concrete – from micromechanics to composite behaviour.* PhD thesis, University of Minho.

CUNHA, V. M. C. F., BARROS, J. A. O. & SENA-CRUZ, J. M. 2011. An integrated approach for modelling the tensile behaviour of steel fibre reinforced self-compacting concrete. *Cement and Concrete Research,* 41**,** 64-76.

CUSSON, D. & HOOGEVEEN, T. 2006. Measuring early-age coefficient of thermal expansion in high-performance concrete. *International RILEM Conference on Volume Changes in Hardening Concrete. Testing and Mitigation.* Technical University of Denmark, Lyngby, Denmark.

DAVIES, J. 2001. *Lightweight sandwich construction*, Wiley-Blackwell.

DAYTON SUPERIOR 2006. Insulated concrete panel tie – Precast edition. *P-24 Delta Tie.*

DECRETO-LEI 80/2006 2006. Regulamento das Características de Comportamento Térmico de Edifícios (RCCTE). *Decreto-Lei n.º 80/2006 de 4 de Abril.* Portugal.

DEPARTMENT OF THE ENVIRONMENT AND THE WELSH OFFICE 1991. The Building Regulations 1991: conservation of fuel and power. London.

DÉQUÉ, F., OLLIVIER, F. & ROUX, J. J. 2001. Effect of 2D modelling of thermal bridges on the energy performance of buildings: numerical application on the Matisse apartment. *Energy and Buildings,* 33**,** 583-587.

DESKOVIC, N., TRIANTAFILLOU, T. C. & MEIER, U. 1995. Innovative Design of FRP Combined with Concrete: Short-Term Behavior. *Journal of Structural Engineering,* 121**,** 1069-1078.

DI PERNA, C., STAZI, F., CASALENA, A. U. & D'ORAZIO, M. 2011. Influence of the internal inertia of the building envelope on summertime comfort in buildings with high internal heat loads. *Energy and Buildings,* 43**,** 200-206.

DI PRISCO, M., FERRARA, L. & LAMPERTI, M. L. 2013. Double edge wedge splitting (DEWS): an indirect tension test to identify post-cracking behaviour of fibre reinforced cementitious composites. *Materials and Structures,* 46**,** 1893-1918.

DI PRISCO, M., PLIZZARI, G. & VANDEWALLE, L. 2009. Fibre reinforced concrete: new design perspectives. *Materials and Structures,* 42**,** 1261-1281.

DIRECTIVE 2002/91/EEC 2003. Directive 2002/91/EC in press of the European Parliament and of the Council of 16 December 2002 on the energy performance of buildings. *In:* PARLIAMENT, E. (ed.). Official Journal of the European Communities.

DUPONT, D. & VANDEWALLE, L. 2005. Distribution of steel fibres in rectangular sections. *Cement and Concrete Composites,* 27**,** 391-398.

DYM, C. L. & WILLIAMS, H. E. 2011. Stress and Displacement Estimates for Arches. *Journal of Structural Engineering,* 137**,** 49-58.

EFNARC 2005. The European guidelines for self-compacting concrete.

EINEA, A. 1992. *Structural and thermal efficiency of precast concrete sandwich panel systems.* Ph.D, University of Nebraska.

EINEA, A., SALMON, D. C., FOGARASI, G. J., CULP, T. D. & TADROS, M. K. 1991. State-of-the-art of Precast Concrete Sandwich Panels. *Precast/Prestressed Concrete Institute Journal,* 36**,** 78-98.

EINEA, A., SALMON, D. C., TADROS, M. K. & CULP, T. D. 1994. A New Structurally and Thermally Efficient Precast Sandwich Panel System. *Precast/Prestressed Concrete Institute Journal,* 39**,** 90-101.

EKENEL, M. 2013. Testing and Acceptance Criteria for Fiber-Reinforced Composite Grid Connectors Used in Concrete Sandwich Panels. *Journal of Materials in Civil Engineering,* 26**,** 06014004.

ELIGEHAUSEN, R. & BALOGH, T. 1995. Behavior of fasteners loaded in tension in cracked reinforced concrete. *ACI Structural Journal,* 92**,** 365-379.

ELLIOTT, K. S. 2002. *Precast concrete structures,* Oxford, Butterworth-Heinemann.

EMANUEL, J. H. & HULSEY, J. L. 1977. Prediction of the thermal coefficient of expansion of concrete. *Journal of the American Concrete Institute,* 74**,** 149-155.

EN 1992-1-1 2004. Eurocode 2: Design of concrete structures. Part 1 - 1: General rules and rules for buildings. Brussels: European Committee for Standardization.

ENERGIEEINSPARVERORDNUNG FÜR GEBÄUDE 2007. Verordnung über energiesparenden Wärmeschutz und energiesparende. *Anlagentechnik bei Gebäuden vom 24, Juli 2007- seit dem 1. Oktober 2007 in Kraft.*

ENEV 2007 2007. Verordnung über energiesparenden Wärmeschutz und energiesparende Anlagentechnik bei Gebäuden (Energieeinsparverordnung – EnEV) vom 24.07.2007. Bundesgesetzblatt Jahrgang 2007, Teil I Nr. 34, ausgegeben zu Bonn am 26.07.2007.

ENEV 2009 2009. Verordnung über energiesparenden Wärmeschutz und energiesparende Anlagentechnik bei Gebäuden (Energieeinsparverordnung – EnEV) vom 29.04.2009, trat am 01.10.2009.

ENGSTRÖM, B., ALEXANDER, S., CHOLEWICKI, A., CHEFDEBIEN, A. D., BELLA, B. D., ELLIOTT, K. S., ORDOÑEZ, D. F., MENEGOTTO, M., NEWBY, M., RISE, G., ROMANES, H., SKJELLE, A., TSOUKANTAS, S., VAMBERSKY, N. J. A., ACKER, A. V. & VINJE, L. 2008. *fib* Bulletin 43: Structural connections for precast concrete buildings. Lausanne, Switzerland: *fib* - fédération internationale du béton.

ERIC J. PRIMAVERA, J.-P. P. & EDWARD, H. K. 1997. Tensile Behavior of Cast-in-Place and Undercut Anchors in High-Strength Concrete. *Structural Journal,* 94.

FARROW, C. B., FRIGUI, I. & KLINGNER, R. E. 1996. Tensile capacity design of single anchors in concrete: Evaluation of existing formulas on an LRFD basis. *ACI Structural Journal,* 93.

FÉDÉRATION INTERNATIONALE DU BÉTON (FIB) 2012. *fib* Model Code for Concrete Structures 2010 (MC2010). Lausanne, Switzerland: fédération internationale du béton.

FEMA 2006. FEMA-451: Recommended provisions: Design examples. Washington, USA: Federal Emergency Management Agency (FEMA).

FERRARA, L., BAMONTE, P., CAVERZAN, A., MUSA, A. & SANAL, I. 2012a. A comprehensive methodology to test the performance of Steel Fibre Reinforced Self-Compacting Concrete (SFR-SCC). *Construction and Building Materials,* 37**,** 406-424.

FERRARA, L., FAIFER, M., MUHAXHERI, M. & TOSCANI, S. 2012b. A magnetic method for non destructive monitoring of fiber dispersion and orientation in steel fiber reinforced cementitious composites. Part 2: Correlation to tensile fracture toughness. *Materials and Structures,* 45**,** 591-598.

FERRARA, L., FAIFER, M. & TOSCANI, S. 2012c. A magnetic method for non destructive monitoring of fiber dispersion and orientation in steel fiber reinforced cementitious composites—part 1: method calibration. *Materials and Structures,* 45**,** 575-589.

FERRARA, L., GRÜNEWALD, S. & DEHN, F. 2010. Design with Highly Flowable Fiber-Reinforced Concrete: Overview of the Activity of *fib* TG 8.8. *In:* RILEM (ed.) *Design, Production and Placement of Self-Consolidating Concrete - SCC2010.* Montreal, Canada: RILEM Bookseries 1,.

FERRARA, L. & MEDA, A. 2006. Relationships between fibre distribution, workability and the mechanical properties of SFRC applied to precast roof elements. *Materials and Structures,* 39**,** 411-420.

FERRARA, L., PARK, Y. & SHAH, S. 2008. Correlation among Fresh State Behavior, Fiber Dispersion, and Toughness Properties of SFRCs. *Journal of Materials in Civil Engineering,* 20**,** 493-501.

FIB 2012a. Model Code 2010 - Final draft, Volume 1. fédération internationale du béton/International Federation for Structural Concrete (fib).

FIB 2012b. Model Code 2010 - Final draft, Volume 2. fédération internationale du béton/International Federation for Structural Concrete (fib).

FIB T.G. 6.7 2011. Prefabrication for affordable housing. Lausanne, Switzerland: *fib* (fedération internationale du béton).

FRANKL, B. A. 2008. *Structural Behabior of Insulated Precast Prestressed Concrete Sandwich Panel Reinforced with CFRP Grid.* North Carolina State University.

FRANKL, B. A., LUCIER, G. W., HASSAN, T. K. & RIZKALLA, S. H. 2011. Behavior of precast, prestressed concrete sandwich wall panels reinforced with CFRP shear grid. *PCI journal,* 56**,** 42-54.

FUCHS, W., ELIGEHAUSEN, R. & BREEN, J. E. 1995. Concrete Capacity Design (CCD) Approach for Fastening to Concrete. *Structural Journal,* 92.

GALVIN, R. 2010. Thermal upgrades of existing homes in Germany: The building code, subsidies, and economic efficiency. *Energy and Buildings,* 42**,** 834-844.

GARA, F., RAGNI, L., ROIA, D. & DEZI, L. 2012. Experimental tests and numerical modelling of wall sandwich panels. *Engineering Structures,* 37**,** 193-204.

GAY, D., HOA, S. V. & TSAI, S. W. 2003. *Composite materials: design and applications*, CRC Press LLC.

GETTU, R., GARDNER, D. R., SALDÍVAR, H. & BARRAGÁN, B. E. 2005. Study of the distribution and orientation of fibers in SFRC specimens. *Materials and Structures,* 38**,** 31-37.

GLEICH, H. 2007. New carbon fiber reinforcement advances sandwich wall panels. *Structural Magazine***,** 61-63.

GODWIN, E. W. & MATTHEWS, F. L. 1980. A review of the strength of joints in fibre-reinforced plastics: Part 1. Mechanically fastened joints. *Composites,* 11**,** 155-160.

GOM 2009. ARAMIS, User Manual – Software – v6.0.2-6.

GRÉDIAC, M. 2004. The use of full-field measurement methods in composite material characterization: interest and limitations. *Composites Part A: Applied Science and Manufacturing,* 35**,** 751-761.

GROTH, P. 2000. *Fibre Reinforced Concrete - Fracture mechanics methods applied on self-compacting concrete and energetically modified binders.* Lulea University of Technology.

GRUNEWALD, S. 2004. *Performance-based Design of Self-compacting Fibre Reinforced Concrete.* Delft University of Technology.

GURTLER, H. 2004. *Composite Action of FRP Bridge Decks Adhesively bonded to Steel Main Girders.* Ecole Polytechnique Federale de Lausanne.

HALFEN-DEHA 2008. DEHA lifting anchor system: concrete.

HAMMER, T. & BJONTEGAARD, O. 2006. Testing of autogenous deformation (AD) and thermal dilation (TD) of early age mortar and concrete - Recommended test procedure. *International RILEM Conference on Volume Changes of Hardening Concrete: Testing and Mitigation.* Technical University of Denmark, Lyngby, Denmark.

HEGGER, J. & HORSTMANN, M. 2008. Light-weight TRC sandwich building envelopes. *Excellence in concrete construction through innovation: proceedings of the international conference on concrete construction.* Kingston University, London, UK: Taylor & Francis.

HIDALGO, P. A., LEDEZMA, C. A. & JORDAN, R. M. 2002. Seismic Behavior of Squat Reinforced Concrete Shear Walls. *Earthquake Spectra,* 18**,** 287-308.

HILLERBORG, A. 1980. Analysis of fracture by means of the fictitious crack model, particularly for fibre reinforced concrete. *International Journal Composites Cements,* 2**,** 177-184.

HILLERBORG, A. 1985. The theoretical basis of a method to determine the fracture energyG F of concrete. *Materials and Structures,* 18**,** 291-296.

HM GOVERNMENT 2010. The Building Regulations 2000: conervation of fuel and power. Coming into effect 1 October 2010. London.

HO, H., MORTON, J. & FARLEY, G. L. 1994. Non-linear numerical analysis of the iosipescu specimen for composite materials. *Composites Science and Technology,* 50**,** 355-365.

HODICKY, K., SOPAL, G., RIZKALLA, S., HULIN, T. & STANG, H. 2015. Experimental and Numerical Investigation of the FRP Shear Mechanism for Concrete Sandwich Panels. *Journal of Composites for Construction,* 19.

HOLDEN, T., RESTREPO, J. & MANDER, J. B. 2003. Seismic performance of precast reinforced and prestressed concrete walls. *Journal of Structural Engineering (ASCE),* 129**,** 286–296.

HORDIJK, D. 1991a. *Local approach to fatigue of concrete.* PhD thesis, Delft University of Technology.

HORDIJK, D. R. 1991b. *Local Approach to Fatigue of Concrete.* Delft University of Technology.

HUGHES BROTHERS 2008. Nu-Tie Sandwich Wall Connector. *Aslan 700.*

IMPRENSA NACIONAL CASA DA MOEDA - INCM 2006. Decreto-Lei n.º 80/2006 - Regulamento das Características de Comportamento Térmico de Edifícios (RCCTE). Lisbon, Portugal: Diário da República, I Série - A, n.º 67.

INCROPERA, F. P., DEWITT, D. P., L., B. T. & LAVINE, A. S. 2006. *Fundamentals of Heat and Mass Transfer*, Wiley.

INSEL, E., D., O. M., TANNER, J. E. & W., D. C. 2005. Carbon fiber connectors for concrete sandwich panels. *ACI Concrete International,* 28**,** 33-38.

IOSIPESCU, N. 1967. New accurate procedure for single shear testing of metals. *J. Mater.***,** 537-566.

ISO 2007. Thermal bridges in building construction - Linear thermal transmittance - Simplified methods and default values. Brussels: European committee for standardization (CEN) and International Organization for Standardization (ISO).

ISO 2010. ISO 21581: Timber structures – Static and cyclic lateral load test method for shear walls. Geneva, Switzerland: International Organization for Standardization (ISO).

ITALIAN DECREE 192/2005 2005. Attuazione della Direttiva 2002/91/CE relativa al rendimento energetico nell'edilizia. Italy.

JAPAN SOCIETY OF CIVIL ENGINEERS 1984. JSCE-SF4: Method of tests for flexural strength and flexural toughness of steel fiber reinforced concrete. Part III-2 Method of tests for steel fiber reinforced concrete. Concrete library of JSCE.

KADA, H., LACHEMI, M., PETROV, N., BONNEAU, O. & AÏTCIN, P. C. 2002. Determination of the coefficient of thermal expansion of high performance concrete from initial setting. *Materials and Structures/Materiaux et Constructions,* 34**,** 35-41.

KARAKUZU, R., ICTEN, B. M. M. & TEKINSEN, O. 2010. Failure behavior of composite laminates with multi-pin loaded holes. *Journal of Reinforced Plastics and Composites,* 29.

KARAKUZU, R., TAYLAK, N., İÇTEN, B. M. & AKTAŞ, M. 2008. Effects of geometric parameters on failure behavior in laminated composite plates with two parallel pin-loaded holes. *Composite Structures,* 85**,** 1-9.

KELLER, T., SCHAUMANN, E. & VALLÉE, T. 2007. Flexural behavior of a hybrid FRP and lightweight concrete sandwich bridge deck. *Composites Part A: Applied Science and Manufacturing,* 38**,** 879-889.

KHANLOU, A., MACRAE, G. A., SCOTT, A. N., HICKS, S. J. & CLIFTON, G. C. 2013. Shear performance of steel fibre-reinforced concrete. *Steel Innovations Conference 2013.* Christchurch, New Zeland.

KIM, H.-Y. & JEONG, Y.-J. 2006. Experimental investigation on behaviour of steel–concrete composite bridge decks with perfobond ribs. *Journal of Constructional Steel Research,* 62**,** 463-471.

KIM, J. & YOU, Y.-C. 2015. Composite behavior of a novel insulated concrete sandwich wall panel reinforced with GFRP shear grids: effects of insulation types. *Materials,* 8**,** 899-913.

KIM, Y. J. & ALLARD, A. 2014. Thermal response of precast concrete sandwich walls with various steel connectors for architectural buildings in cold regions. *Energy and Buildings,* 80**,** 137-148.

KIM, Y. J. & FAM, A. 2011. Numerical analysis of pultruded GFRP box girders supporting adhesively-bonded concrete deck in flexure. *Engineering Structures,* 33**,** 3527-3536.

KITSUTAKA, Y. 1997. Fracture Parameters by Polylinear Tension-Softening Analysis. *Journal of Engineering Mechanics,* 123**,** 444-450.

KLAPP, O. 2002. *Mechanisches Verhalten elastomerer Klebeverbindungen.* Universitat Kassel.

KLINGNER, R. E. & MENDONCA, J. A. 1982. Tensile Capacity of Short Anchor Bolts and Welded Studs: A Literature Review. *ACI JOURNAL,* 79**,** 270-279.

KOOIMAN, A. G. 2000. *Modelling steel fiber reinforced concrete for structural design.* PhD thesis, Delft University of Technology.

KOSSECKA, E. & KOSNY, J. 2002. Influence of insulation configuration on heating and cooling loads in a continuously used building. *Energy and Buildings,* 34**,** 321-331.

KRETSIS, G. & MATTHEWS, F. L. 1985. The strength of bolted joints in glass fibre/epoxy laminates. *Composites,* 16**,** 92-102.

KUANG, J. S. & HO, Y. B. 2008. Seismic Behavior and Ductility of Squat Reinforced Concrete Shear Walls with Nonseismic Detailing. *Structural Journal,* 105.

KUMOSA, M. & HULL, D. 1987. Mixed-mode fracture of composites using Iosipescu shear test. *International Journal of Fracture,* 35**,** 83-102.

KURIHARA, N., KUNIEDA, M., KAMADA, T., UCHIDA, Y. & ROKUGO, K. 2000. Tension softening diagrams and evaluation of properties of steel fiber reinforced concrete. *Engineering Fracture Mechanics,* 65**,** 235-245.

KYPROS, P. & AMR, E. 1995. Cyclic Behavior of RC Cantilever Walls, Part I: Experimental Results. *Structural Journal,* 92.

LAMEIRAS, R., BARROS, J., AZENHA, M. & VALENTE, I. B. 2013a. Development of sandwich panels combining fibre reinforced concrete layers and fibre reinforced polymer connectors. Part I: conception and pull-out tests. *Composite Structures,* 105**,** 446-459.

LAMEIRAS, R., BARROS, J., AZENHA, M. & VALENTE, I. B. 2013b. Development of sandwich panels combining fibre reinforced concrete layers and fibre reinforced polymer connectors. Part II: Evaluation of mechanical behaviour. *Composite Structures,* 105**,** 460-470.

LAMEIRAS, R., BARROS, J., VALENTE, I. B. & AZENHA, M. 2013c. Development of sandwich panels combining fibre reinforced concrete layers and fibre reinforced polymer connectors. Part I: Conception and pull-out tests. *Composite Structures,* 105**,** 446-459.

LAMEIRAS, R. M. 2007. *Contribuição ao Estudo das Propriedades Mecânicas dos Materiais Cimentícios Reforçados com Fibras de Vidro (Glass fibre reinforced cement – GRC).* Universidade Federal do Rio Grande do Sul – UFRGS.

LAMEIRAS, R. M., VALENTE, I. B., BARROS, J., AZENHA, M. & GONÇALVES, C. 2015. Pull-out behaviour of glass-fibre reinforced polymer perforated plate connectors embedded in concrete. Part I: Experimental program. *Composite Structures,* In this Volume.

LAPLANTE, P. & BOULAY, C. 1994. Evolution du coefficient de dilatation thermique du béton en fonction de sa maturité aux tout premiers âges. *Materials and Structures,* 27**,** 596-605.

LARANJEIRA, F. 2010a. *Design-oriented constitutive model for steel fiber reinforced concrete.* PhD Thesis, Universitat Politècnica de Catalunya.

LARANJEIRA, F. 2010b. *Design-Oriented Constitutive Model of Steel Fibre Reinforced Concrete.* Universitat Politècnica de Catalunya – UPC.

LARANJEIRA, F., AGUADO, A., MOLINS, C., GRÜNEWALD, S., WALRAVEN, J. & CAVALARO, S. 2012. Framework to predict the orientation of fibers in FRC: A novel philosophy. *Cement and Concrete Research,* 42**,** 752-768.

LEABU, B. V. F. 1965. Precast Concrete Wall Panels : Design Trends and Standards. *ACI Special Publication,* 11**,** 31-44.

LEE, B.-J. & PESSIKI, S. 2006. Thermal performance evaluation of precast concrete three-wythe sandwich wall panels. *Energy and Buildings,* 38**,** 1006-1014.

LEE, B.-J. & PESSIKI, S. 2008a. Experimental Evaluation of Precast, Prestressed Concrete, Three-Wythe Sandwich Wall Panels. *Precast/Prestressed Concrete Institute Journal,* 53**,** 95-115.

LEE, B.-J. & PESSIKI, S. 2008b. Revised zone method R-value calculation for precast concrete sandwich panels containing metal wythe connectors. *Precast/Prestressed Concrete Institute Journal,* 53**,** 86-100.

LEUNG, A. 1984. *Structural design and analysis of concrete sandwich panels and their practical application.* M. Eng, Memorial University of Newfoundland.

LEVITT, M. 1997. *Concrete materials: problems and solutions*, Taylor & Francis.

LINDBERG, R., BINAMU, A. & TEIKARI, M. 2004. Five-year data of measured weather, energy consumption, and time-dependent temperature variations within different exterior wall structures. *Energy and Buildings,* 36**,** 495-501.

LIU, D. & RAJU, B. B. 1999. Thickness effects on pinned joints for composites. *Journal of Composite Materials,* 33**,** 2-21.

LNEC E397 1993. Betões. Determinação do módulo de elasticidade em compressão (technical report). Lisbon: Laboratório Nacional de Engenharia Civil (LNEC).

LOSER, R., MÜNCH, B. & LURA, P. 2010. A volumetric technique for measuring the coefficient of thermal expansion of hardening cement paste and mortar. *Cement and Concrete Research,* 40**,** 1138-1147.

LOUKILI, A., CHOPIN, D., KHELIDJ, A. & LE TOUZO, J. Y. 2000. New approach to determine autogenous shrinkage of mortar at an early age considering temperature history. *Cement and Concrete Research,* 30**,** 915-922.

LOWE, R. & BELL, M. 1998. Towards sustainable housing: building regulations for the 21st century. Leeds: Leeds Metropolitan University.

LUCIER, G., RIZKALLA, S. H. & HASSAN, T. 2010. Thermally efficient precast concrete sandwich load bearing wall panels reinforced with CFRP. *3rd fib International Congress.* Washington D.C., USA.

LUO, Y., LI, A. & KANG, Z. 2012. Parametric study of bonded steel–concrete composite beams by using finite element analysis. *Engineering Structures,* 34**,** 40-51.

MANSOUR SHIRVANI, R. E. K. & HERMAN, L. G., III 2004. Breakout Capacity of Anchors in Concrete Part 1: Tension. *Structural Journal,* 101.

MARIKUNTE, S., ALDEA, C. & SHAH, S. P. 1997. Durability of Glass Fibre Reinforced Cement Composites: effect of silica fume and metakaolin. *Advanced Cement Based Materials,* 5**,** 100-108.

MARKOVIC, I. 2006. *High-performance hybrid-fibre concrete : development and utilisation.* PhD thesis, Delft University of Technology.

MARTINIE, L., ROSSI, P. & ROUSSEL, N. 2010. Rheology of fiber reinforced cementitious materials: classification and prediction. *Cement and Concrete Research,* 40**,** 226-234.

MARUYAMA, I. & TERAMOTO, A. 2011. Impact of time-dependant thermal expansion coefficient on the early-age volume changes in cement pastes. *Cement and Concrete Research,* 41**,** 380-391.

MASSONE, L., ORAKCAL, K. & WALLACE, J. 2009. Modelling of squat structural walls controlled by shear. *ACI Structural Journal,* 106**,** 646–655.

MAXIMOS, H. N., PONG, W. A. & TADROS, M. K. 2007. Behavior and design of composite precast/prestressed concrete sandwich panels with NU-Tie. *UNL Technical Report.* Lincoln: University of Nebraska.

MCCALL, W. C. 1985. Thermal Properties of Sandwich Panels. *Concrete International: Design and Construction,* 7**,** 34-41.

MCCARTHY, M. A. & MCCARTHY, C. T. 2003. Finite element analysis of the effects of clearance on single-shear, composite bolted joints. *Journal of Plastics, Rubber and Composites,* 32**,** 65-70.

MEDBERRY, S. B. & SHAHROOZ, B. M. 2002. Perfobond shear connector for composite construction. *Engineering Journal of American Institute of Steel Construction (AISC),* 39**,** 2-12.

MEHTA, P. K. & MONTEIRO, P. J. M. 2014. *Concrete: Microstructure, Properties, and Materials*, Mc-Graw Hill.

MICHELS, J., CHRISTEN, R. & WALDMANN, D. 2013. Experimental and numerical investigation on postcracking behavior of steel fiber reinforced concrete. *Engineering Fracture Mechanics,* 98**,** 326-349.

MONTAIGNAC, R., MASSICOTTE, B. & CHARRON, J.-P. 2012. Design of SFRC structural elements: flexural behaviour prediction. *Materials and Structures,* 45**,** 623-636.

MONTGOMERY, D. C. 2009. *Design and Analysis of Experiments,* New York, John Wiley & Sons.

MORCOUS, G., TADROS, M. K., LAFFERTY, M. & GREMEL, D. 2010. Optimized nu sandwich panel system for energy, composite action and production efficiency. *3rd fib Internation Congress.* Washington, DC, USA.

MORTON, J., HO, H., TSAI, M. Y. & FARLEY, G. L. 1992. An Evaluation of the Iosipescu Specimen for Composite Materials Shear Property Measurement. *Journal of Composite Materials,* 26**,** 708-750.

NAITO, C., HOEMANN, J., BEACRAFT, M. & BEWICK, B. 2012. Performance and Characterization of Shear Ties for Use in Insulated Precast Concrete Sandwich Wall Panels. *Journal of Structural Engineering,* 138**,** 52-61.

NAITO, C., HOEMANN, J., SHULL, J. S., SAUCIER, A., SALIM, H. A., BEWICK, B. T. & HAMMONS, M. I. 2011. Precast/prestressed concrete experiments performance on non-load bearing sandwich wall panels. Tyndall Air Force Base, FL: United States Air Force.

NEMEGEER, D., VANBRABANT, J. & STANG, H. 2003. Brite-Euram Program on Steel Fibre Concrete, Durability Corrosion Resistance of Cracked Fibre-Reinforced Concrete. *In:* SCHNÜTGEN, B. & VANDEWALLE, L. (eds.) *Test and Design Methods for Steel Fibre Reinforced Concrete-Background and Experiences. RILEM Technical Committee 162, TDF Workshop, Proceedings Pro 31.*

NEVILLE, A. M. 1996. *Properties of concrete. 4th Edition. 844pp.*, John Wiley & Sons.

ODEGARD, G. & KUMOSA, M. 2000. Determination of shear strength of unidirectional composite materials with the Iosipescu and 10° off-axis shear tests. *Composites Science and Technology,* 60**,** 2917-2943.

ODEGARD, K. S. M. K. G. 1999. Critical Examination of the Iosipescu Shear Test as Applied to 0degrees Unidirectional Composite Materials. *Mechanics of Composite Materials and Structures,* 6**,** 229-256.

OFFICE OF THE DEPUTY PRIME MINISTER 2006. The Building Regulations 2000: conservation of fuel and power. Coming into effect 6 April 2006. London.

OGOLI, D. M. 2003. Predicting indoor temperatures in closed buildings with high thermal mass. *Energy and Buildings,* 35**,** 851-862.

OGUEJIOFOR, E. C. & HOSAIN, M. U. 1994. A parametric study of perfobond rib shear connectors. *Canadian Journal of Civil Engineering,* 21**,** 614-625.

OGUEJIOFOR, E. C. & HOSAIN, M. U. 1997. Numerical analysis of push-out specimens with perfobond rib connectors. *Computers & Structures,* 62**,** 617-624.

OKUTAN, B. 2002. The effects of geometric parameters on the failure strength for pin-loaded multi-directional fiber-glass reinforced epoxy laminate. *Composites Part B: Engineering,* 33**,** 567-578.

OZAWA, M. & MORIMOTO, H. 2006. Estimation method for thermal expansion coefficient of concrete at early ages. *RILEM Int. Conf. Volume Changes of Hardening Concrete.* Lyngby, Denmark.

OZYURT, N., MASON, T. O. & SHAH, S. P. 2006. Non-destructive monitoring of fiber orientation using AC-IS: An industrial-scale application. *Cement and Concrete Research,* 36**,** 1653-1660.

OZYURT, N., MASON, T. O. & SHAH, S. P. 2007. Correlation of fiber dispersion, rheology and mechanical performance of FRCs. *Cement and Concrete Composites,* 29**,** 70-79.

PAHN, M. & HANZ, F. 2012. Influences of the production process on the load-deflection behaviour of three-layered sandwich panels with GFRP-connectors. *Architecture Civil Engineering Environment,* Vol. 5, no. 1**,** 37-46.

PALERMO, M., RICCI, I., SILVESTRI, S., GASPARINI, G., TROMBETTI, T., FOTI, D. & IVORRA, S. 2014. Preliminary interpretation of shaking-table response of a full-scale 3-storey building composed of thin reinforced concrete sandwich walls. *Engineering Structures,* 76**,** 75-89.

PANTELIDES, C. P., SURAPANENI, R. & REAVELEY, L. D. 2008. Structural Performance of Hybrid GFRP/Steel Concrete Sandwich Panels. *Journal of Composites for Construction,* 12**,** 570-576.

PAPADOPOULOS, A. M. 2005. State of the art in thermal insulation materials and aims for future developments. *Energy and Buildings,* 37**,** 77-86.

PAULAY, T., PRIESTLEY, M. J. N. & SYNGE, A. J. 1982. Ductility in earthquake resisting squat shearwalls. *ACI Journal,* 79**,** 257–269.

PAVESE, A. & BOURNAS, D. A. 2011. Experimental assessment of the seismic performance of a prefabricated concrete structural wall system. *Engineering Structures,* 33**,** 2049-2062.

PCI 2011. State-of-the-art of Precast/Prestressed Sandwich Wall Panels. *Precast/Prestressed Concrete Institute Journal,* 56**,** 131-175.

PCI COMMITTEE ON PRECAST SANDWICH WALL PANELS 1997. State-of-the-art of Precast/Prestressed Sandwich Wall Panels. *Precast/Prestressed Concrete Institute Journal,* 42**,** 1-61.

PCI INDUSTRY HANDBOOK COMMITTEE 2004. PCI Design Handbook: Precast and Prestressed Concrete - 6th ed. Chicago, IL: PCI.

PEREIRA, E. B., BARROS, J. A. O., RIBEIRO, A., CUNHA, V. M. C. F. & ANTUNES, J. A. B. 2004. Self-compacting steel fibre reinforced concrete for precasted sandwich panels - experimental and numerical research. *In:* DI PRISCO, M., FELICETTI, R. & PLIZZARI, G. A. (eds.) *6th International RILEM Symposium on Fibre-Reinforced Concretes (BEFIB 2004).* Ancona, Italy: RILEM.

PEREIRA, E. B., FISCHER, G. & BARROS, J. A. O. 2012. Direct assessment of tensile stress-crack opening behavior of Strain Hardening Cementitious Composites (SHCC). *Cement and Concrete Research,* 42**,** 834-846.

PEREIRA, E. N. B., BARROS, J. A. O. & CAMOES, A. 2008. Steel Fiber-Reinforced Self-Compacting Concrete: Experimental Research and Numerical Simulation. *Journal of Structural Engineering,* 134**,** 1310-1321.

PÉREZ-LOMBARD, L., ORTIZ, J., GONZÁLEZ, R. & MAESTRE, I. R. 2009. A review of benchmarking, rating and labelling concepts within the framework of building energy certification schemes. *Energy and Buildings,* 41**,** 272-278.

PEREZ, F. J., PESSIKI, S., SAUSE, R. & LU, L. W. 2003. Lateral Load Tests of Unbonded Post-Tensioned Precast Concrete Walls. *Special Publication,* 211.

PESSIKI, S. & MLYNARCZYK, A. 2003a. Experimental Evaluation of the Composite Behavior of Precast Concrete Sandwich Wall Panels. *Journal of Prescast/Prestressed Concrete Institute,* 48**,** 54-71.

PESSIKI, S. & MLYNARCZYK, A. 2003b. Experimental Evaluation of the Composite Behavior of Precast Concrete Sandwich Wall Panels. *PCI journal,* 48**,** 54-71.

PFEIFER, D. W. & HANSON, J. A. 1964. Precast Concrete Wall Panels: Flexural Stiffness of Sandwich Panels. *SP-11.* Farmington Hills: American Concrete Institute (ACI).

PIERRON, F. 1998. Saint-Venant Effects in the Iosipescu Specimen. *Journal of Composite Materials,* 32**,** 1986-2015.

PIERRON, F., CERISIER, F. & GREDIAC, M. 2000. A Numerical and Experimental Study of Woven Composite Pin-Joints. *Journal of Composite Materials,* 34**,** 1028-1054.

PIERRON, F. & VAUTRIN, A. 1998. Measurement of the in-plane shear strengths of unidirectional composites with the Iosipescu test. *Composites Science and Technology,* 57**,** 1653-1660.

POLETTI, E. & VASCONCELOS, G. 2015. Seismic behaviour of traditional timber frame walls: experimental results on unreinforced walls. *Bulletin of Earthquake Engineering,* 13**,** 885-916.

PRECAST/PRESTRESSED CONCRETE INSTITUTE – PCI 2001. *Recommended Practice for Glass Fibre Reinforced Concrete Panels,* Chicago, Precast/Prestressed Concrete Institute.

PRECAST/PRESTRESSED CONCRETE INSTITUTE – PCI 2006. Designer´s notebook: energy conservation.

PRISCO, M., PLIZZARI, G. & VANDEWALLE, L. 2009a. Fibre reinforced concrete: new design perspectives. *Materials and Structures,* 42**,** 1261-1281.

PRISCO, M. D. 2009. FRC: structural applications and standards. *Materials and Structures,* 42**,** 1169-1171.

PRISCO, M. D., PLIZZARI, G. & VANDERWALLE, L. 2009b. Fibre Reinforced Concrete: new design perspectives. *Materials and Structures,* 42**,** 1261-1281.

PURNELL, P. & BEDDOWS, J. 2005. Durability and Simulated Ageing of New Matrix Glass Fibre Reinforced Concrete. *Cement and Concrete Composites,* 27**,** 875-884.

PYNER, G. R. & MATTHEWS, F. L. 1979. Comparison of Single and Muilti-Hole Bolted Joints in Glass Fibre Reinforced Plastic. *Journal of Composite Materials,* 13**,** 232-239.

REAL DECRETO 314/2006 2006. Real Decreto 314/2006, de 17 de marzo, por el que se aprueba el Código Técnico de la Edificacíon. Spain: Boletín Oficial del Estado.

REZAIFAR, O., KABIR, M. Z., TARIBAKHSH, M. & TEHRANIAN, A. 2008. Dynamic behaviour of 3D-panel single-storey system using shaking table testing. *Engineering Structures,* 30**,** 318-337.

RICCI, I., PALERMO, M., GASPARINI, G., SILVESTRI, S. & TROMBETTI, T. 2013. Results of pseudo-static tests with cyclic horizontal load on cast in situ sandwich squat concrete walls. *Engineering Structures,* 54**,** 131-149.

RILEM TC 14-CPC 1975. Modulus of elasticity of concrete in compression (CPC8). *Materials and Structures,* 6**,** 25-27.

RILEM TC 162-TDF 2000a. Bending test. *Materials and Structures,* 33**,** 3-5.

RILEM TC 162-TDF 2000b. σ-ε-Design method. *Materials and Structures,* 33**,** 75-81.

RILEM TC 162-TDF 2001. Uni-axial tension test for steel fibre reinforced concrete. *Materials and Structures,* 34**,** 3-6.

RILEM TC 162-TDF 2002. Bending test. *Materials and Structures,* 35**,** 579-582.

RILEM TC 162-TDF 2003. σ-ε-Design Method. *Materials and Structures,* 36**,** 560-567.

RIZKALLA, S., HASSAN, T. & LUCIER, G. 2009a. FRP Shear Transfer Mechanism for Precast, Prestressed Concrete Sandwich Load-Bearing Panels.

RIZKALLA, S., HASSAN, T. & LUCIER, G. 2009b. FRP shear transfer mechanism for precast, prestressed concrete sandwich load-bearing panels. *Special Publ,* 265**,** 603-625.

RIZKALLA, S. H. & DAWOOD, M. 2009. Advances on the Use of FRP for the Precast Concrete Industry. *FRPRCS-9.* Sydney, Australia.

ROSEN, B. W. 1972. A simple procedure for experimental determination of the longitudinal shear modulus of unidirectional composites. *Composite Materials,* 6**,** 552-554.

ROSNER, C. N. & RIZKALLA, S. H. 1995. Bolted connections for fiber-reinforced composite material members: analytical model and design recommendations. *Journal of Materials in Civil Engineering,* 7**,** 232-238.

ROTS, J. G. & DE BORST, R. 1989. Analysis of concrete fracture in "direct" tension. *International Journal of Solids and Structures,* 25**,** 1381-1394.

SALEHIAN, H. & BARROS, J. A. O. 2014. Design and testing elevated steel fibre reinforced self-concrete slabs (accepted to be published). *Cement and Concrete Composites*.

SALMON, D. & EINEA, A. 1995. Partially Composite Sandwich Panel Deflections. *Journal of Structural Engineering,* 121**,** 778-783.

SALMON, D. C., EINEA, A., TADROS, M. K. & CULP, T. D. 1997. Full Scale Testing of Precast Concrete Sandwich Panels. *ACI Structural Journal,* 94**,** 354-362.

SARA, B. M. & BAHRAM, M. S. 2002. Perfobond shear connectors for composite construction. *Engineering Journal (AISC - American Institute of Steel Construction),* first quarter**,** 2-12.

SARKIS, M., GRANJU, J. L., ARNAUD, M. & ESCADEILLAS, G. 2002. Coefficient of thermal dilation of a fresh mortar. *Coefficient de dilatation thermique d'un mortier frais,* 35**,** 415-420.

SCHUMACHER, P. 2006. *Rotation Capacity of Self-Compacting Steel Fibre Reinforced Concrete.* Delft University of Technology.

SENA-CRUZ, J. M., BARROS, J. A. O., RIBEIRO, A. F., AZEVEDO, A. F. M. & CAMÕES, A. F. F. L. 2004. Stress-crack opening relationship of enhanced performance concrete. *9th Portuguese Conference on Fracture.* Setúbal, Portugal.

SHAH, S. P., SWARTZ, S. E. & OUYANG, C. 1995. *Fracture Mechanics of Concrete: Applications of Fracture Mechanics to Concrete, Rock and Other Quasi-Brittle Materials*, John Wiley & Sons, Inc.

SIMS, D. F. 1973. In-plane shear stress-strain response of unidirectional composite materials. *Composite Materials,* 7**,** 124-128.

SLAGTER, W. J. 1992. On the bearing strength of fibre metal laminates. *Journal of Composite Materials,* 26**,** 2542-2566.

SLOWIK, V., VILLMANN, B., BRETSCHNEIDER, N. & VILLMANN, T. 2006. Computational aspects of inverse analyses for determining softening curves of concrete. *Computer Methods in Applied Mechanics and Engineering,* 195**,** 7223-7236.

SMITH, P. A. & PASCOE, K. J. 1986. The effect of stacking sequence on the bearing strengths of quasi-isotropic composite laminates. *Composite Structures,* 6**,** 1-20.

SORIANO, J. & RIZKALLA, S. 2013. Use of FRP grid for the composite action of concrete sandwich panels. *In:* BARROS, J. (ed.) *FRPRCS11 – 11th International Symposium on Fiber Reinforced Polymer for Reinforced Concrete Structures.* Guimarães, Portugal.

SOUSA, A. M. R., XAVIER, J., MORAIS, J. J. L., FILIPE, V. M. J. & VAZ, M. 2011a. Processing discontinuous displacement fields by a spatio-temporal derivative technique. *Optics and Lasers in Engineering,* 49**,** 1402-1412.

SOUSA, A. M. R., XAVIER, J., VAZ, M., MORAIS, J. J. L. & FILIPE, V. M. J. 2011b. Cross-correlation and differential technique combination to determine displacement fields. *Strain,* 47**,** 87-98.

SOUSA, A. M. R., XAVIER, J., VAZ, M., MORAIS, J. J. L. & FILIPE, V. M. J. 2011c. Cross-Correlation and Differential Technique Combination to Determine Displacement Fields. *Strain,* 47**,** 87-98.

STÄHLI, P., CUSTER, R. & MIER, J. M. 2008. On flow properties, fibre distribution, fibre orientation and flexural behaviour of FRC. *Materials and Structures,* 41**,** 189-196.

STÄHLI, P. & VAN MIER, J. G. M. 2007. Manufacturing, fibre anisotropy and fracture of hybrid fibre concrete. *Engineering Fracture Mechanics,* 74**,** 223-242.

ŠVEC, O., ŽIRGULIS, G., BOLANDER, J. E. & STANG, H. 2014. Influence of formwork surface on the orientation of steel fibres within self-compacting concrete and on the mechanical properties of cast structural elements. *Cement and Concrete Composites*.

TARNOPOL'SKII, Y. M., KULAKOV, V. L. & ARANAUTOV, A. K. 2000. Measurements of shear characteristics of textile composites. *Computers & Structures,* 76**,** 115-123.

TEIXEIRA, N. 2015. *Connections and fatigue behaviour of precast concrete insulated sandwich panels.* M. Sc., Queen's University.

TODUT, C., DAN, D. & STOIAN, V. 2014. Theoretical and experimental study on precast reinforced concrete wall panels subjected to shear force. *Engineering Structures,* 80**,** 323-338.

TOMLINSON, D. G. 2015. *Behaviour of partially composite precast concrete sandwich panels under flexural and axial loads.* PhD, Queen´s University.

TORRENTS, J., BLANCO, A., PUJADAS, P., AGUADO, A., JUAN-GARCÍA, P. & SÁNCHEZ-MORAGUES, M. 2012. Inductive method for assessing the amount and orientation of steel fibers in concrete. *Materials and Structures,* 45**,** 1577-1592.

TORRIJOS, M. C., BARRAGÁN, B. E. & ZERBINO, R. L. 2010. Placing conditions, mesostructural characteristics and post-cracking response of fibre reinforced self-compacting concretes. *Construction and Building Materials,* 24**,** 1078-1085.

TOUBAL, L., KARAMA, M. & LORRAIN, B. 2005. Stress concentration in a circular hole in composite plate. *Composite Structures,* 68**,** 31-36.

TURCRY, P., LOUKILI, A., BARCELO, L. & CASABONNE, J. M. 2002. Can the maturity concept be used to separate the autogenous shrinkage and thermal deformation of a cement paste at early age? *Cement and Concrete Research,* 32**,** 1443-1450.

UNFCCC 2015. Adoption of the Paris Agreement. *Paris Climate Change Conference - November 2015, COP 21.* Geneva (Switzerland): United Nations Office at Geneva.

UNITED NATIONS ENVIRONMENT PROGRAMME 2007. Buildings and Climate Change: Status, Challenges and Opportunities. *UNEP Publications.*

VALENTE, I. & CRUZ, P. J. S. 2004. Experimental analysis of Perfobond shear connection between steel and lightweight concrete. *Journal of Constructional Steel Research,* 60**,** 465-479.

VALENTE, I. B. & CRUZ, P. J. S. 2009. Experimental analysis of shear connection between steel and lightweight concrete. *Journal of Constructional Steel Research,* 65**,** 1954-1963.

VALENZA, A., FIORE, V., CALABRESE, L. & DI BELLA, G. 2007. Failure map of composite laminate mechanical joint. *Journal of Composite Materials,* 41.

VAN MIER, J. G. M. 1997. *Fracture processes of concrete: assessment of material parameters for fracture models,* Boca Raton (FL), CRC Press.

VAN TITTELBOOM, K., GRUYAERT, E., DE BACKER, P., MOERMAN, W. & DE BELIE, N. 2015. Self-repair of thermal cracks in concrete sandwich panels. *Structural Concrete,* 16**,** 273-288.

VANDEWALLE, L., HEIRMAN, G. & VAN RICKSTAL, F. 2008. Fibre orientation in self-compacting fibre reinforced concrete. *7th RILEM International Symposium on Fibre Reinforced Concrete 2008 (BEFIB 2008).* Chennai: Curran Associates, Inc.

VERISSIMO, G. S. 2007. *Development of a shear connector plate gear for composite structures of steel and concrete and study their behavior.* Ph.D. thesis, Universidade Federal de Minas Gerais.

VIANNA, J. D. C., COSTA-NEVES, L. F., DA S. VELLASCO, P. C. G. & DE ANDRADE, S. A. L. 2009. Experimental assessment of Perfobond and T-Perfobond shear connectors' structural response. *Journal of Constructional Steel Research,* 65**,** 408-421.

VIVIANI, M., GLISIC, B. & SMITH, I. F. C. 2007. Separation of thermal and autogenous deformation at varying temperatures using optical fiber sensors. *Cement and Concrete Composites,* 29**,** 435-447.

WALRATH, D. E. & ADAMS, D. F. 1983. The Iosipescu shear test as applied to composite materials. *Experimental Mechanics,* 23**,** 105-110.

WALRAVEN, J. C. 2009. High Performance Fiber Reinforced Concrete: Progress in Knowledge and Design Codes. *Materials and Structures,* 42**,** 1247-1260.

WHITNEY, J. M. & HALPIN, J. C. 1968. Analysis of laminated anisotropic tubes under combined loading. *Composite Materials,* 2**,** 360-367.

WIGHT, J. K. & MACGREGOR, J. G. 2012. *Reinforced concrete: mechanics and design,* Upper Saddle River, Prentice Hall.

WOLTMAN, G. D. 2014. *Structural and steady-state thermal experimental investigations of an insulated sandwich panel.* M. Sc., Queen's University.

WOLTMAN, G. D., TOMLINSON, D. G. & FAM, A. 2010. A comparative study of various FRP shear connectors for sandwich concrete walls. *CICE 2010 - The 5th International Conference on FRP Composites in Civil Engineering.* Beijing, China.

WOLTMAN, G. D., TOMLINSON, D. G. & FAM, A. 2013. Investigation of various GFRP shear connectors for insulated precast concrete sandwich wall panels. *Journal of Composites for Construction,* 17**,** 711-721.

WU, T. J. & HAHN, H. T. 1998. The bearing strength of e-glass/vynil-ester composites fabricated by vartm. *Composite Science and Technology,* 5**,** 1519-1529.

XAVIER, J., DE JESUS, A. M. P., MORAIS, J. J. L. & PINTO, J. M. T. 2012. Stereovision measurements on evaluating the modulus of elasticity of wood by compression tests parallel to the grain. *Construction and Building Materials,* 26**,** 207-215.

XAVIER, J., OLIVEIRA, M., MONTEIRO, P., MORAIS, J. J. L. & MOURA, M. F. S. F. 2014. Direct Evaluation of Cohesive Law in Mode I of Pinus pinaster by Digital Image Correlation. *Experimental Mechanics*, 1-12.

YUN, H. D., JANG, S. J. & YOU, Y. C. 2012. Direct shear responses of insulated concrete sandwich panels with GFRP shear connectors. *Applied Mechanics and Materials,* 204-208, 803-806.

YÝLMAZ, T. & SÝNMAZÇELIK, T. 2007. Investigation of load bearing performances of pin connected carbon/polyphenylene sulphide composites under static loading conditions. *Materials & Design,* 28, 520-527.

ZERBINO, R., TOBES, J. M., BOSSIO, M. E. & GIACCIO, G. 2012. On the orientation of fibres in structural members fabricated with self compacting fibre reinforced concrete. *Cement and Concrete Composites,* 34, 191-200.